The Structure and Eruptive History of Rotorua Caldera, Taupo Volcanic Zone, New Zealand.

A thesis
submitted in fulfilment
of the requirements for the degree
of
Doctor of Philosophy in Geological Sciences
at the
University of Canterbury
by

David M. Milner

University of Canterbury
2001

Lake Rotorua from Mt Ngongotaha. In the upper left a scarp marks the northern boundary of Rotorua Caldera. The southeastern caldera margin is defined by topography to the right. In the middle background are Tikitere Graben and Lake Rotoiti, and Mokoia Island is to the right of centre.

Abstract

Mamaku Ignimbrite erupted 220-230 ka, is a voluminous deposit that is exposed over c. 3100 km^2 predominantly NNE, NW, and SW of Rotorua Caldera, and has a maximum measured outflow thickness of 145 m. Rotorua Caldera is a 21×22 km complex collapse structure in southwest Bay of Plenty, Taupo Volcanic Zone, New Zealand.

The Mamaku Ignimbrite sequence can be divided into basal tephra and main ignimbrite sequences. The basal tephra sequence comprises pyroclastic fall and density current deposits and records progression of the eruption from wet to dry. The main ignimbrite sequence has been separated into lower, middle and upper parts based on crystal content, welding, and extent of vapour phase alteration and devitrification. Boundaries between lower, middle, and upper ignimbrite are always gradational, and lithic and pumice content and size also vary stratigraphically throughout the deposit.

Lateral variations in upper Mamaku Ignimbrite include areas of high lithic concentration, and lithic lag breccias, at and within the Rotorua Caldera margin with size and concentration of lithic fragments decreasing away from the caldera. At medial distances the ignimbrite is internally massive with occasional zones of pumice clast concentration, and varying lithic content. Boundaries of these lithic and pumice concentration zones are gradational and no sharp flow unit boundaries exist. At distal localities a crystal-rich band is present at the base of the ignimbrite and crystal-rich lenses are present at higher levels. These crystal-rich lenses suggest that distally the pyroclastic flow was moving in a dominantly non-particulate manner.

XRF analysis has revealed three silicic pumice types in Mamaku Ignimbrite that range from dacite to high silica rhyolite (66-76 wt% SiO_2). No large compositional gaps exist between the pumice types and they provide evidence for the evacuation of a gradationally zoned magma chamber. The more silicic pumice compositions were probably derived by 20 % crystal fractionation of the dacitic magma. Andesitic blebs in upper Mamaku Ignimbrite are a fourth juvenile component which had a different petrogenesis to the silicic pumice types. The andesitic magma probably resided as a sill towards the base of the dacitic magma.

Maximum lithic size variation shows Rotorua Caldera to be the source of upper Mamaku Ignimbrite. Gradational contacts between lower, middle, and upper ignimbrite suggest that the ignimbrite was deposited during a single eruptive event from one source. Coexistence of the three pumice types at all stratigraphic levels is further evidence for a single eruptive source. Variations in lithic content, and coexistence of different pumice types through the ignimbrite stratigraphy, indicate that caldera collapse occurred throughout the eruption, but particularly during the eruption of middle Mamaku Ignimbrite and in later stages of the eruption of upper Mamaku Ignimbrite.

Rhyolite domes of Rotorua Caldera can be separated into seven groups, two of which are related to adjacent volcanic centres. Fragments of rhyolite lava are also a major component of lithic lag breccias at caldera margin sites. The domes that are related to Rotorua record the eruption of five different rhyolitic magma bodies. The largest rhyolite dome complexes are located around the area of deepest caldera subsidence. These domes have similar phenocryst assemblages and phenocryst chemistries to silicic Mamaku Ignimbrite pumice clasts suggesting that they are from the same magma. Rhyolite lava fragments in the lag breccias also have similar phenocryst assemblages

and phenocryst chemistry to Mamaku pumice clasts and may represent initial extrusions from the Mamaku magma chamber. All other rhyolite lavas in Rotorua Caldera have different phenocryst assemblages to Mamaku Ignimbrite pumice clasts and are probably not consanguineous with them.

Mokai Ignimbrite outcrops in an 8 km wide (east to west) band between lakes Taupo and Whakamaru. It has the same unusual paleomagnetic direction as Mamaku Ignimbrite, is the same age, and has similar pumice chemistry. Upper Mokai Ignimbrite is vapour phase altered and has a similar appearance to upper Mamaku Ignimbrite. Three distinct units define Mokai Ignimbrite's stratigraphy, each separated by ash deposits. Internal variations suggest that Mokai Ignimbrite formed a compound cooling unit. The three flow unit compound cooling unit stratigraphy, phenocryst assemblage of juvenile mafic fragments, presence of mafic blebs at all stratigraphic levels, and thickness of Mokai Ignimbrite suggest that it is distinct from Mamaku Ignimbrite.

Rotorua Caldera is described as a rhyolitic, single event, asymmetric, multiple block, single locus caldera on the basis of published geophysical data, caldera geomorphology and geology, location and thickness of Mamaku Ignimbrite and the nature of intra-caldera rhyolite domes. The timing of collapse is deduced, from Mamaku Ignimbrite stratigraphy, to have started at least by the time that middle Mamaku Ignimbrite erupted, but probably occurred throughout the eruption of the main ignimbrite sequence. The caldera formed during a single eruption, but cannot be well described by current caldera classifications, as it has characteristics that can be attributed to trapdoor, downsag, piecemeal and piston processes of collapse. Taupo Volcanic Zone is dominated by NE-SW striking faults with more widely spaced NW-SE striking structures. This fault pattern inhibits the formation of simple caldera structures. The regional fault pattern is interpreted to have cut the Rotorua Caldera floor into a number of blocks that subsided to varying depths towards a single collapse locus.

Table of Contents

CHAPTER 1
Introduction

1.1 Introduction

Mamaku Ignimbrite was erupted from Rotorua Caldera approximately 225 ka (Shane et al., 1994; Houghton et al., 1995; Black et al., 1996). It is one of the most widespread ignimbrites of Taupo Volcanic Zone (TVZ), is one of the youngest welded ignimbrites of TVZ (Murphy and Seward, 1981) and until this thesis was one of the least studied. This thesis presents field and laboratory data obtained for the ignimbrite which has been used to constrain the ignimbrite's source and to interpret possible methods for its emplacement, magma chamber configuration and magma withdrawal dynamics. Structure and evolution of Rotorua Caldera are also described, with collapse inferred, from stratigraphic variation in Mamaku Ignimbrite pumice chemistry and lithic content, to have begun early in the eruption of Mamaku Ignimbrite, continuing until the eruption ceased.

Mamaku Ignimbrite was named by Martin (1961) probably after the Mamaku Plateau which it caps. The name **Mamaku** means *black tree fern* or *edible tree fern*. The plateau most likely takes its name from the tree fern that is prolific in the native forest that much of it is covered by.

Rotorua Caldera is a 21×22 km depression that contains Lake Rotorua. It is a single event caldera formed during the eruption of Mamaku Ignimbrite. It is now an area of major tourism and is steeped in Maori legend. Rotorua takes its name from Lake Rotorua which was named by Ihenga of the Te Arawa tribe who discovered Rotoiti while on a hunting trip from Maketu (Stafford, 1999). He later returned with his family to claim the area for Te Arawa and discovered Lake Rotorua (although it is written that another tribe already lived in the area (Reed, 1958)). The name Rotorua was given to the lake and is thought to have been derived by one of two ways. **Roto**- means *lake* referring to the body of water. **Rua** has multiple meanings two of which are *pit* or *depression*, and *two* or *second*. Rotorua means either *lake in a pit* referring to the caldera in which the lake lies or *second lake* referring to the chronology of its discovery, since Ihenga had discovered Lake Rotoiti first (Stafford, 1999).

Other legends of Rotorua include the origins of the geothermal areas, for which Rotorua is famous, and of the tors that are prominent on the proximal to medial surface of Mamaku Ignimbrite on the Mamaku-Kaimai plateau. Fire demons from Hawaiki are said to have created the hot springs by coming to the surface while searching for Ngatoro-i-rangi (an explorer) who lay freezing on Mt Ngauruhoe (Reed, 1958). The tors are said to be a party of warriors intent on attack that was turned to stone by a fair-skinned people (Patupaiarehe) who, legend has it, lived on Mt Ngongotaha prior to the Maori arrival (Stafford, 1999).

1.2 Taupo Volcanic Zone

The Taupo Volcanic Zone (TVZ) is the result of the oblique subduction of the Pacific Plate beneath the Indo-Australian Plate that begins at the Hikurangi margin off the east coast of New Zealand (Figs 1.1 and 1.2; Cole, 1990; Wilson et al., 1995). TVZ is a NE-SW oriented zone of volcanic activity that extends from Ruapehu in the south to beyond White Island in the north and has maximum dimensions 300 km long × 60 km wide as defined by active volcanic centres (Fig. 1.3; Wilson et al., 1995). It can be split into three parts: A southern andesite-dominated section, a central rhyolite-dominated section, and a northern andesite-dominated section (Fig. 1.3 inset; Wilson et al., 1984; some rhyolite eruptives have also been reported in submarine TVZ, Bay of Plenty by Gamble et al. (1993)).

The spatial relations of volcanism in TVZ are still debated. Ballance (1976), Cole and Lewis (1981), and Cole (1990) view TVZ as a volcanic arc and backarc basin. The arc comprises dominantly andesitic cones (subordinately dacite and basaltic andesite; Cole et al., 1995). Volcanism in the backarc area (of Cole, 1990) is bimodal, dominantly rhyolitic, with minor basaltic activity (Cole et al., 1995). The existence of an arc-backarc is controversial. Wilson et al. (1995) show that volcanism of all compositions overlap in time and space and consider TVZ an arc disrupted by rifting. Also rhyolitic volcanism is restricted to a central portion of TVZ (Fig. 1.3 inset) and not present along the whole length of the zone as in classic backarc situations. A suggestion for the restricted locality of the rhyolitic volcanism is the Coromandel arc extending beneath the central portion of TVZ with rhyolite being sourced by melting of these older igneous rocks (Cole, 1990).

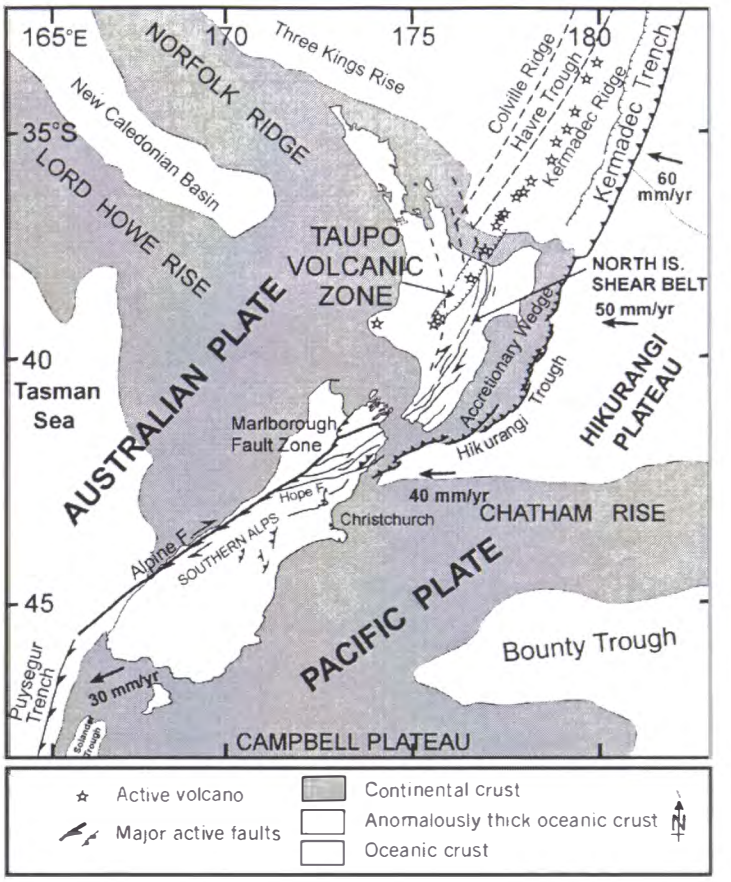

Figure 1.1. New Zealand's geological setting. TVZ is situated in the North Island and occurs in response to subduction of the pacific plate beneath the Indo-Australian Plate along the Hikurangi Margin. Arrows represent motion of the Pacific Plate relative to the Indo-Australian Plate. Rates are from Walcott (1987). F= Fault. After Cole (1990) and Pettinga (1998).

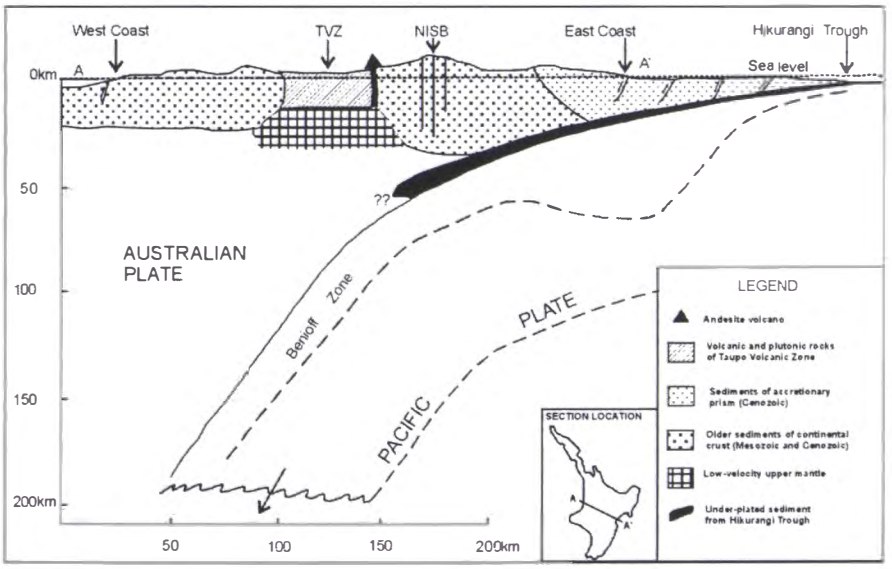

Figure 1.2. Cross-section through the Pacific/Indo-Australian subduction system through the central North Island. TVZ comprises thin continental crust due to extension (after Walcott, 1987; Smith et al., 1989; in Cole, 1990). NISB= North Island Shear Belt.

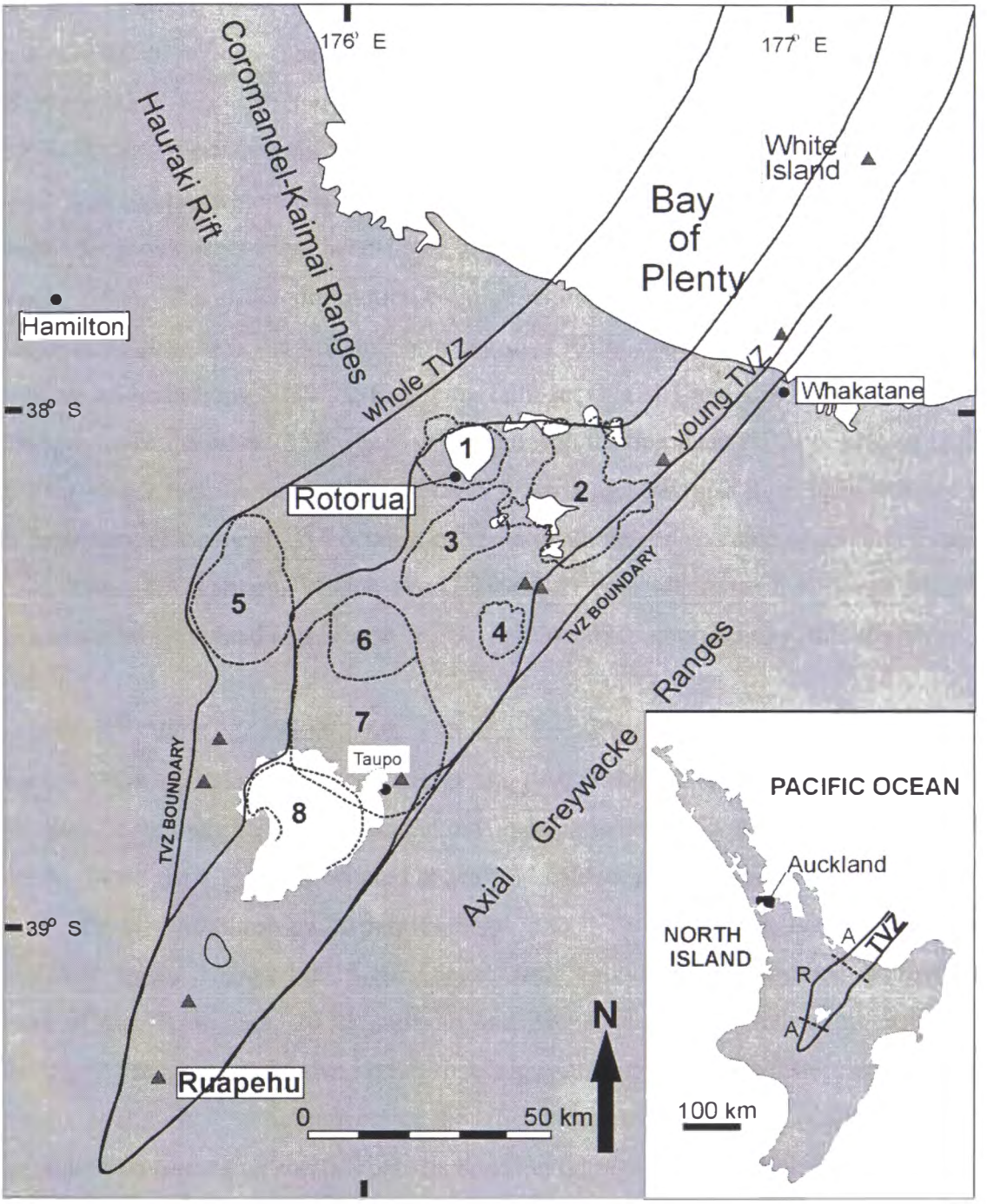

Figure 1.3. TVZ is located in central North Island and contains eight identified calderas or caldera complexes: 1) Rotorua, 2) Okataina, 3) Kapenga, 4) Reporoa, 5) Mangakino, 6) Maroa, 7) Whakamaru, 8) Taupo. The whole TVZ boundary encompasses all centres active since 2 Ma. Young TVZ includes only those centres active in the last 0.34 Ma (Onshore after Wilson et al., 1995; offshore after Wright, 1990, Gamble et al., 1993, and Davey et al., 1995). The inset shows the segregation of compositionally dominated segments within TVZ with northern and southern andesite/dacite dominated parts (A) and a central rhyolite dominated segment (R) (after Houghton et al., 1995)

TVZ is a zone of active rifting within continental crust and is extending at ~7-12 mm/year (Sissons, 1979; Walcott, 1987; Crook and Hannah, 1988; Darby et al., 2000) in a NW-SE direction. The extension has lead to thin continental crust beneath TVZ 15-17km thick (Fig. 1.2; Stern, 1987; NB new data may increase this by up to 10 km, C.J.N. Wilson, pers. comm. to G. Leonard, 2001). East of TVZ is the North Island Shear Belt (NISB) which is a zone of dextral strike-slip movement (Cole, 1990). Large strike-slip movements have been noted from first motion studies in TVZ (Smith and Webb, 1986). The strike-slip motion coupled with dip-slip movement creates a zone of transtension in which the volcanic activity of TVZ is taking place and is thought to generate an underlying NNW-SSE striking fault set (Fig. 1.1 and 1.3; Cole, 1990). The relationship of the NNW-SSE trending structures to the dominant NE-SW striking faults of TVZ is not well known but the NNW-SSE striking structures have been inferred to be important in terms of: 1) Location of some of the larger volcanic vents (e.g. Taupo, Cole, 1990; Whakamaru, Wilson et al., 1995), 2) coincidence with zones of magma accumulation (Rowland and Sibson, 1999), and 3) caldera morphology (this study).

Activity of TVZ commenced 2 Ma with eruption of the andesites of the Hauhangaroa Ranges (west of Lake Taupo; Wilson et al., 1995). Rhyolitic activity began with the eruption of ignimbrites from Mangakino approximately 1.68 Ma (Houghton et al., 1995). Since then TVZ has erupted at least 34 caldera-forming ignimbrites (Houghton et al., 1995) over three main periods (Fig. 1.4). Throughout its activity TVZ has produced up to 10,000 km^3 DRE (dense rock equivalent) of dominantly rhyolitic material (80 % rhyolite, 20 % andesite and dacite, and <1 % high alumina basalt), making it the most productive active rhyolitic centre on earth (Hochstein et al., 1993; Wilson et al., 1995). The thinness of the crust and rapid extension may allow the swift accumulation of magma and promote its eruption (Houghton et al., 1995).

Eight calderas or caldera complexes have been identified in TVZ (Fig. 1.3) and other possible caldera structures are also noted (Wilson et al., 1995). Caldera-forming rhyolitic activity in TVZ has occurred during three main periods I, II, and III (Figs 1.4 and 1.5; Houghton et al., 1995). Period I occurred between 1.68-1.53 Ma and involved eruption of ignimbrites from Mangakino volcanic centre. Period II can be split into two parts A, and B. Period IIA spanned 1.21-0.89 Ma and involved eruptions from Mangakino volcanic centre. Activity during period IIB was intense and involved eruption of the voluminous Unit E and Rocky Hill ignimbrites from Mangakino. Period

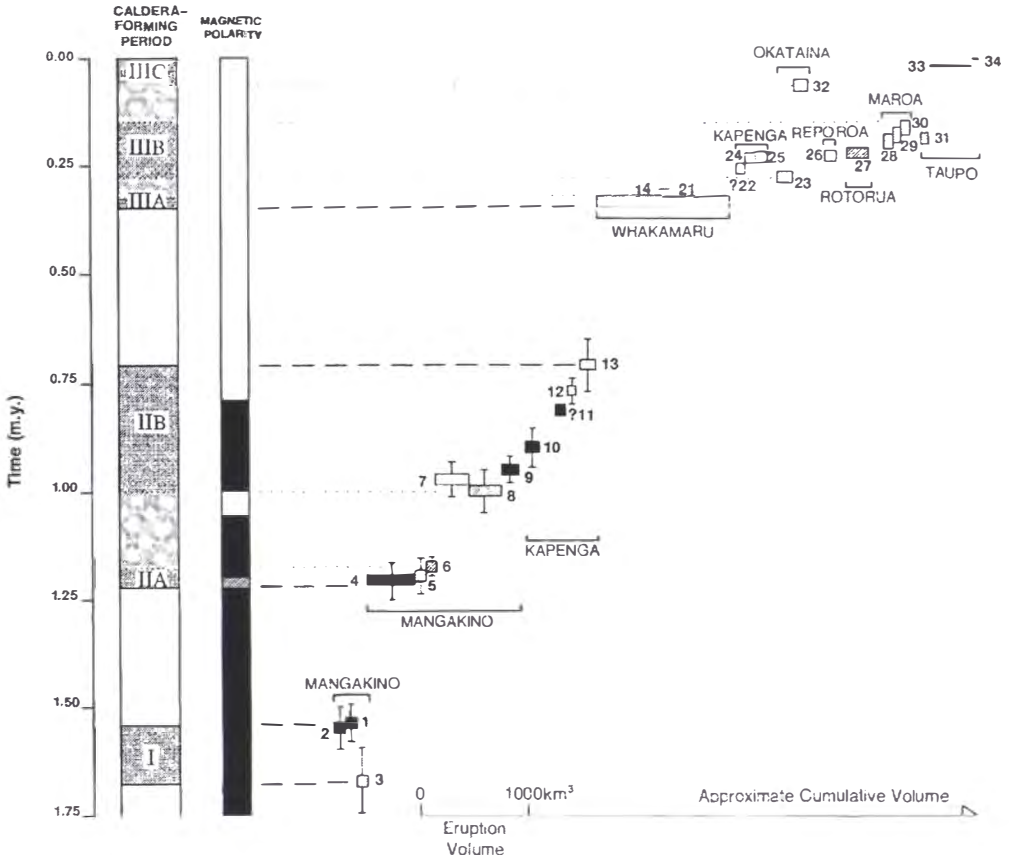

Figure 1.4. Caldera forming rhyolitic activity of TVZ can be split into three main periods based on ages of exposed deposits. The three main periods can be further subdivided into lesser interval groupings. Mamaku Ignimbrite was erupted during period IIIB. From Houghton et al. (1995).

IIB lasted from 0.77-0.68 Ma and also involved eruptions from Kapenga volcanic centre including the andesitic Tikorangi (Hildyard et al., 1999) and widespread high grade Waiotapu ignimbrites (Ritchie, 1996). Period three stretches from 0.34 Ma-present and may be divided into IIIA, IIIB, and IIIC each spanning 0.34-0.32 Ma, 0.28-0.15 Ma, and 0.065 Ma-present respectively. Period IIIA erupted the voluminous Whakamaru Group ignimbrites. Mamaku Ignimbrite was erupted during period IIIB, a period when 5 caldera's were active. The youngest ignimbrites (IIIC) of TVZ have been erupted from Taupo and Okataina Volcanic Centres and include the Oruanui and Taupo ignimbrites and the Rotoiti Breccia.

1.3 Mamaku Ignimbrite

The Mamaku Ignimbrite caps the Mamaku Plateau north, northwest and west of Rotorua, as a broadly domed fan (Briggs et al., 1996) that covers an area of 3200 km^2

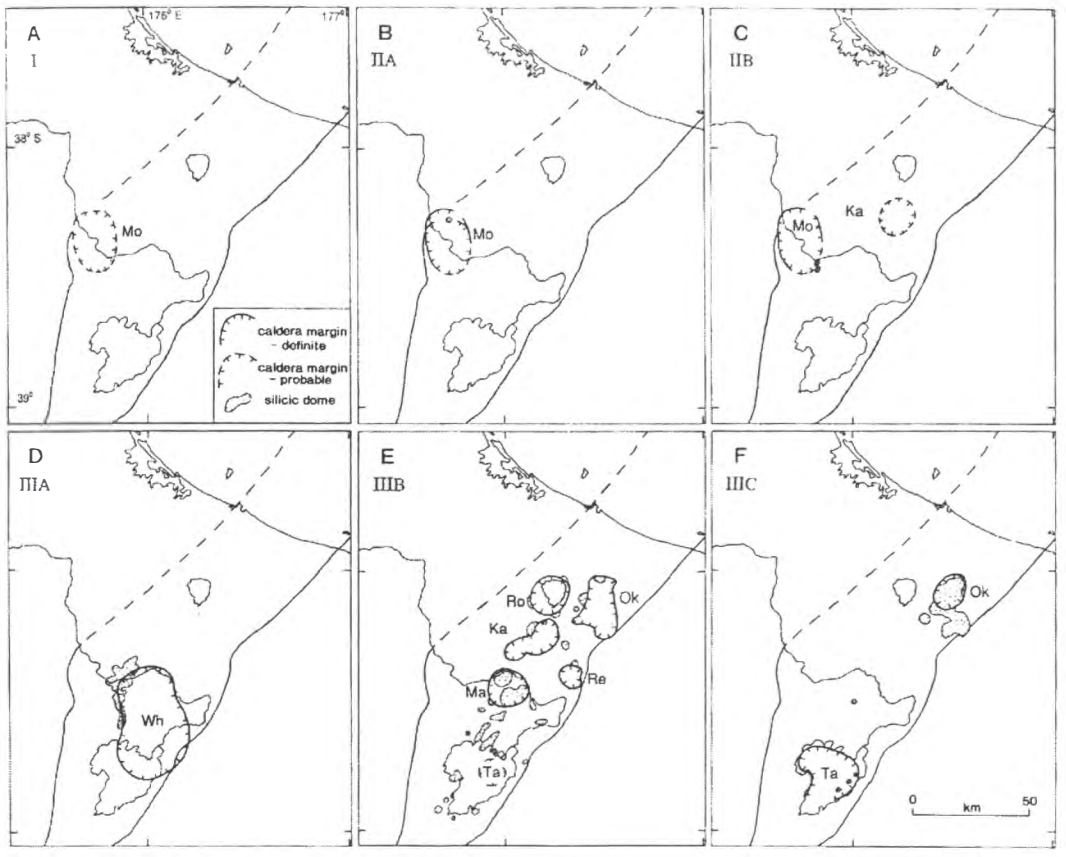

Figure 1.5. Caldera structures active during periods I-III. Five caldera structures were active during the period in which Rotorua Caldera formed. From Houghton et al. (1995).

(see chapter 2). The Taupo Fault Belt in the south, Hauraki Rift in the northwest, and the Kaimai Range and Tauranga Basin in the north bound the Mamaku Plateau. Mamaku Ignimbrite is also exposed east and south of Rotorua Caldera with limited outcrops in Okataina Volcanic Centre (OVC) and in the Taupo Fault Belt (Fig. 1.1). In upper parts it is characterised by extensive vapour phase alteration (VPA) that may have discouraged in-depth study.

This thesis is the first major study undertaken on Mamaku Ignimbrite defining its internal stratigraphy, geochemistry, source, and relationship to rhyolite domes of Rotorua Caldera.

1.3.1 Exposure

Mamaku Ignimbrite is exposed primarily in road cuts (state highways and forest roads), deeply incised streams and valleys, and in tors that rise from the Mamaku Plateau

Figure 1.6. Exposure of Mamaku Ignimbrite on farmland. The bluffs at lower left are Pokai Ignimbrite. Above this is the eroded lower part of Mamaku Ignimbrite forming a shallow slope with no outcrop. Exposed at the top are middle to upper parts of Mamaku Ignimbrite. Upper Mamaku Ignimbrite is also easily eroded and often does not outcrop in natural settings.

surface at proximal to medial distances from Rotorua Caldera. Exposure is mainly restricted to upper vapour phase altered levels of Mamaku Ignimbrite. Levels below this chiefly outcrop in streams or valleys and road cuts (where roads follow these valleys) towards the limit of the ignimbrite's extent. Much of the area underlain by Mamaku Ignimbrite is utilised for forestry, or is covered by native forest, diminishing exposure. Only welded levels of the ignimbrite are commonly exposed in areas of forest cover or farmland due to the ease of erosion of softer upper and lower parts (Fig. 1.6). Exposure southwest of Rotorua is limited to Mamaku Plateau. Southeast of Rotorua Caldera extension and downfaulting in Taupo Fault Belt along with sedimentation and further volcanic activity has caused the burial of most of the Mamaku Ignimbrite. North and east of Rotorua, Mamaku Ignimbrite outcrop is limited due to activity of OVC (see chapter 2).

1.4 Mokai Ignimbrite

Mokai Ignimbrite is exposed southwest of the southernmost outcrops of Mamaku Ignimbrite. It is a small isolated ignimbrite that is exposed in an 8 km wide zone, between lakes Whakamaru and Taupo, mainly near its margins where it has been eroded by rivers and streams. Mokai and Mamaku ignimbrites are the same age and have been suggested as correlatives (Black, 1995; Tanaka et al., 1996).

1.5 Rotorua Caldera

Rotorua Caldera is a well defined (largely in-filled) 22×21 km depression that is located in the northeastern part of TVZ (Fig. 1.3). It is adjacent to Okataina and Kapenga volcanic centres and is one of two single event calderas of TVZ (the other being Reporoa Caldera (Beresford and Cole, 2000)). Its single event history and its reasonably well-preserved surface morphology make it one of the best places to study the dynamics of caldera collapse at a young volcanic centre.

1.6 Aims

Prior to this work Mamaku Ignimbrite has not been studied in detail. Formation of calderas in TVZ has also not been investigated in depth. The primary aims of this thesis are to:

1) Define the internal stratigraphy (lithologically and geochemically) of Mamaku Ignimbrite to infer its mode of emplacement, source magma chamber characteristics, and to constrain its source.
2) Determine the relationship between Mamaku and Mokai ignimbrites.
3) Determine the relationship between Mamaku Ignimbrite and rhyolite domes of Rotorua Volcanic Centre (RVC), to ascertain whether a single magma body was involved or whether multiple chambers have been active during the evolution of RVC.
4) Study the morphology of Rotorua Caldera, assessing the role of NE-SW striking faults and NNW-SSE striking faults in controlling caldera structure, and, using Mamaku Ignimbrite stratigraphy, determine the timing and evolution of caldera collapse.

5) Deduce the eruptive history of Rotorua Caldera.

Unless otherwise stated, all grid references in this thesis refer to New Zealand Map Series 260, 1:50,000.

CHAPTER 2
Mamaku Ignimbrite

2.1 Previous Work

Grange (1937) grouped Mamaku Ignimbrite in Patetere Ignimbrite, a term that included most of the ignimbrites from north of Rotorua to Taupo. Healy (1957) called the unit "Omanawa Ignimbrite" in an area close to the Kaimai Range. Martin (1961) named Mamaku Ignimbrite in a general TVZ ignimbrite overview. He designated the type locality at the Tauranga Direct Road bridge over Mangorewa River at U15/886551 (Fig. 2.1). Other studies incorporating Mamaku Ignimbrite have involved mapping of parts of Mamaku Plateau (Fransen, 1982; Morgan, 1986; Hughes, 1993; Whitbread-Edwards, 1994; Lynch-Blosse, 1998) and economic mineral reconnaissance surveys also of the Mamaku Plateau.

Thompson (1958), Nathan, (1975), Fransen (1982), and Morgan (1986) looked at Mamaku Ignimbrite stratigraphy. The findings of these authors are discussed in section 2.5.2.

2.2 Distribution

Outcrop of Mamaku Ignimbrite outflow covers c. 3100 km^2 and is exposed radially around Rotorua Caldera (Fig. 2.1). The area of Mamaku Ignimbrite was estimated using a method outlined by Streck and Grunder (1995) using insitu outcrop and topography for probable and possible original extents (Fig. 2.2). The original total area covered by the ignimbrite was likely at least 3200 km^2, and may have been up to 3900 km^2 immediately post-emplacement. The main exposure forms a fan extending between Te Puke in the north and Atiamuri in the southwest, capping the Mamaku-Kaimai Plateau (Fig. 2.1). The surface of the Mamaku-Kaimai Plateau dips gently northwards at c. 2° (Briggs et al., 1996) and c. 3° to the northwest and west. Between Mamaku township and Hamurana, the ignimbrite surface dips back towards Lake Rotorua due to downsagging during caldera formation (see chapter 6). In the northeast the Mamaku Ignimbrite rides up onto the Papamoa Ranges and to the north it wraps around the southern extension of the Kaimai Ranges. It extends to the southern edge of the

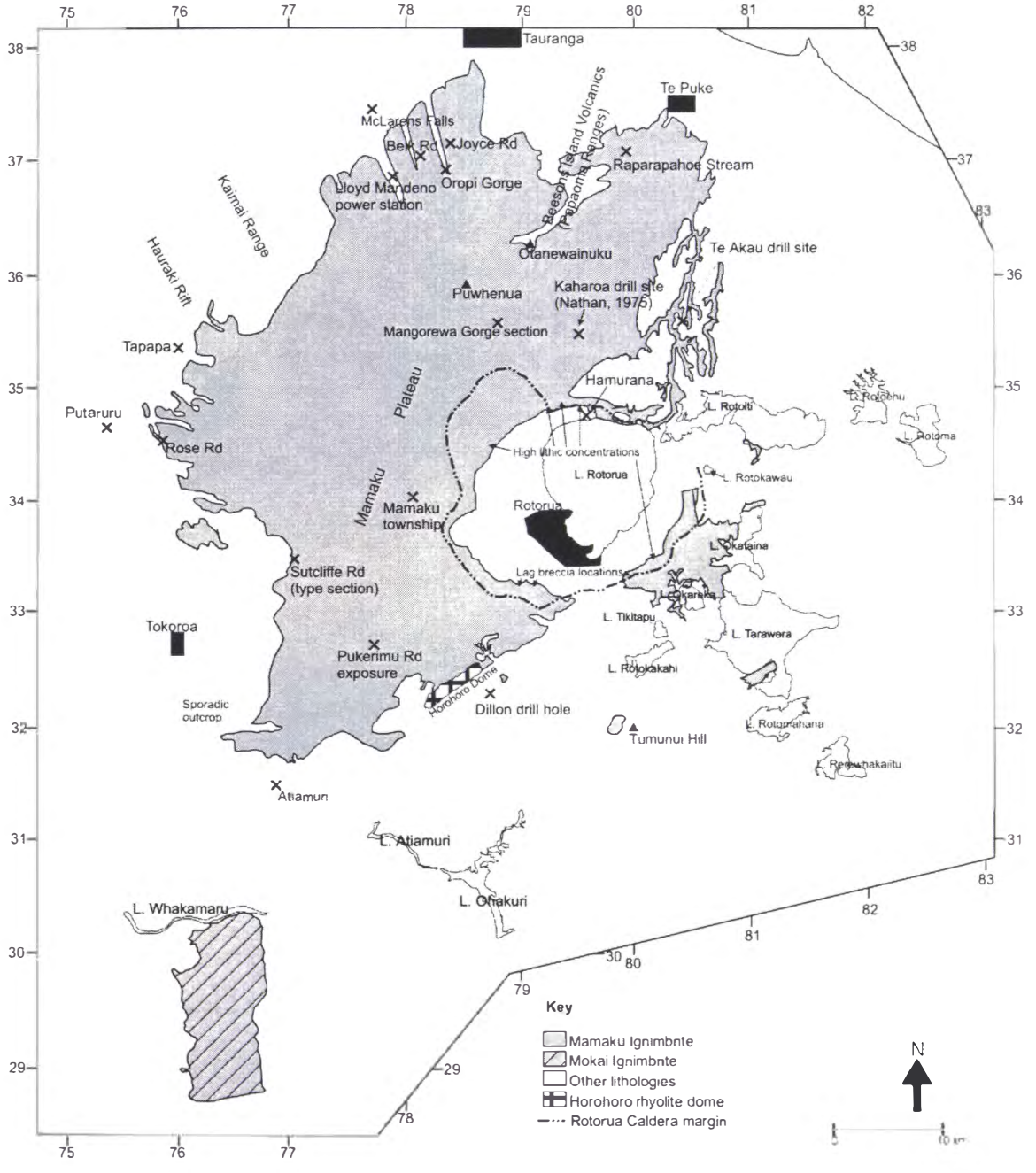

Figure 2.1. Current outcrop distribution of Mamaku Ignimbrite and locations mentioned in the text. See back pocket for second copy. Grid from NZMS 262, 1:250,000.

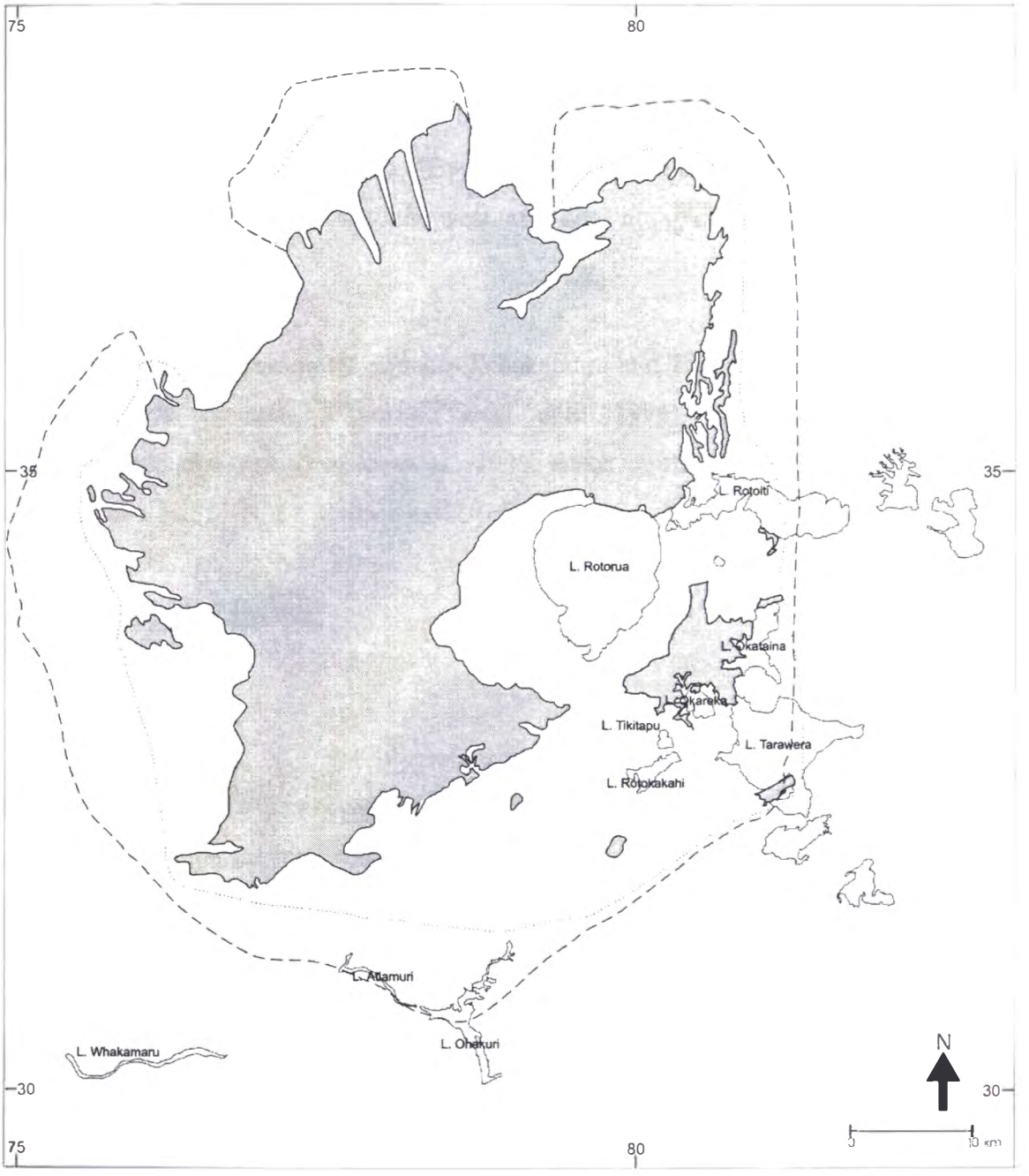

Figure 2.2. Current (shaded), probable (dotted), and possible (dashed) distributions of Mamaku Ignimbrite based on methods used by Streck and Grunder (1995). Grid taken from NZMS 262, 1:250,000.

Tauranga Basin where it overlies the Waimakariri Ignimbrite of Briggs et al. (1996). Mamaku Ignimbrite is not present west of Tokoroa or Putaruru and thins towards the Hauraki rift, with no exposure beyond Tapapa. In the southwest the Mamaku Ignimbrite pyroclastic density current moved around the Horohoro rhyolite dome without over-topping it. East of the Horohoro dome Mamaku Ignimbrite is present in the Dillon drill core near Guthrie (Fig. 2.1) and as an outlier on the northwestern side of Tumunui Hill. East of Rotorua it occurs adjacent to Lake Tarawera and between lakes Rotorua, Okataina, and Okareka, but its outcrop has been disrupted by activity of the Okataina Volcanic Centre (OVC). The ignimbrite could not have been as widespread east of Rotorua Caldera as it is to the west, as it does not overlie older ignimbrites north or east of OVC.

Mokai Ignimbrite occurs between lakes Whakamaru and Taupo (Fig. 2.1) and has been associated with Mamaku Ignimbrite (Tanaka et al., 1996). It has an identical unusual paleomagnetic direction (Tanaka et al., 1996; Black et al., 1996) and is the same age (Houghton et al., 1995). It is discussed in chapter 7.

2.3 Thickness and Volume

2.3.1 Outflow

Mamaku Ignimbrite thickness varies greatly, and is chiefly dependent on the underlying topography. Adjacent to the southern rim of Rotorua Caldera, Mamaku Ignimbrite is 30-40 m thick. At Raparapahoe Stream close to Te Puke, 21 km from source, an 80 m section is exposed (the base does not outcrop). 145 m of Mamaku Ignimbrite occurs in a drill hole near Kaharoa (U15/948542; Nathan, 1975) and is the greatest thickness of outflow measured. Drill core at Te Akau (Fig. 2.1) penetrates 123 m (U15/047549; Fransen, 1982; this study), and beneath Mamaku Township 58 m has been drilled (Wood, 1985). At its distal localities Mamaku Ignimbrite thins and is 2-5 m thick on Rose Rd (T15/586428), and in drill holes near Te Puke it is 2 m thick (U14/033702). At the northern margin the ignimbrite terminates in either a 20 m high scarp or gradually pinches out.

Ignimbrites that are not entirely welded have original thicknesses and distributions reduced by erosion and total thickness and distribution estimates based on current

outcrop are minima. An average thickness of 72.5 m was used for volume calculations, which gives volumes of 225 km^3, 232 km^3, and 283 km^3 for current outcrop, probable, and possible extents respectively. Dense Rock Equivalent (DRE) was calculated by determining the density of Mamaku Ignimbrite at various levels (and finding the average based on volume of each level), finding the ratio between those and the density of non-vesicular rhyolite lava (assumed as primary magmatic density) and dividing calculated and estimated volumes by this ratio (see Appendix 6). Taking maximum density of rhyolite lava leads to outflow DRE between 96-121 km^3.

2.3.2 Intracaldera ignimbrite

Thickness of intracaldera ignimbrite has been estimated at ≥ 1000 m beneath Rotorua City and Mt Ngongotaha by Rogan (1982, based on gravity and magnetic surveys; Fig. 2.3) and 279 m near the caldera rim northeast of Whakarewarewa by Lamarche (1992, seismic reflection surveys). A volume estimate for intra-caldera Mamaku Ignimbrite based on caldera volume and depth to the ignimbrite's upper surface in drill core yields 114 km^3 or 48.7 km^3 DRE (see Appendix 7).

Rogan (1982) found a disparity of depth to basement calculations of 1 km between gravity and magnetic data (magnetism estimates were 1 km shallower than gravity). She suggested the presence of at least a kilometre of non- or reversely magnetised material caused the disparity (Fig. 2.3). Although that actual make up of the caldera fill will not be proven unless a deep hole is drilled, Mamaku Ignimbrite had since been shown to have an intermediate paleomagnetic direction (Black et al, 1995; Tanaka et al., 1996) backing up Rogan's postulate.

Lamarche's (1992) seismic reflection estimate is based on two seismic lines run perpendicular to each other, close to Whakarewarewa thermal reserve. His estimate is equivocal. There is a seismic reflector where he interprets the base of the ignimbrite (Fig. 2.4). There are other reflectors that have not been interpreted however and there is no borehole data to confirm reflector characteristics.

Drill core has confirmed at least 120 m of altered Mamaku Ignimbrite east of the racecourse in Rotorua, but the base has not been reached (Wood, 1992). It is white and extensively altered due to geothermal activity (C.P. Wood, pers comm., 1999).

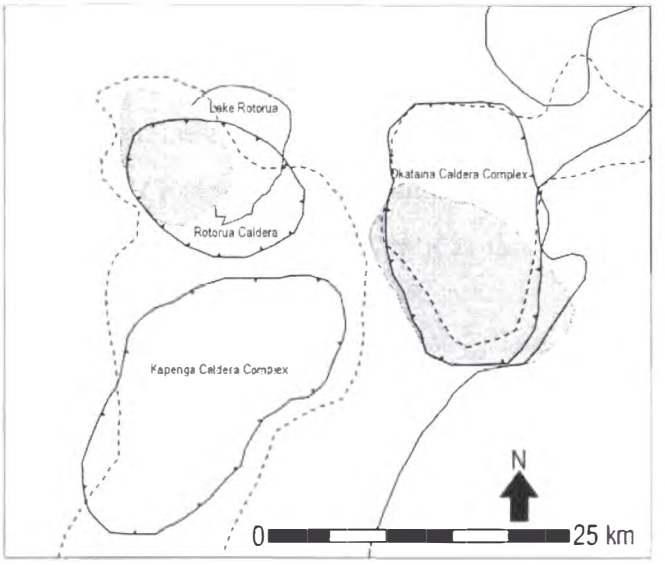

Figure 2.3. Rogan's (1982) interpretation of caldera boundaries and location of non- or reversely magnetised material giving rise to the disparity between gravity and magnetic basement depth calculations. Grey shaded areas were interpreted as underlain by at least 1 km of non- or reversely magnetised material. Toothed lines represent collapse structures. Dashed and solid lines represent 500 m contours (depth below mean sea level) of magnetic and gravity data respectively.

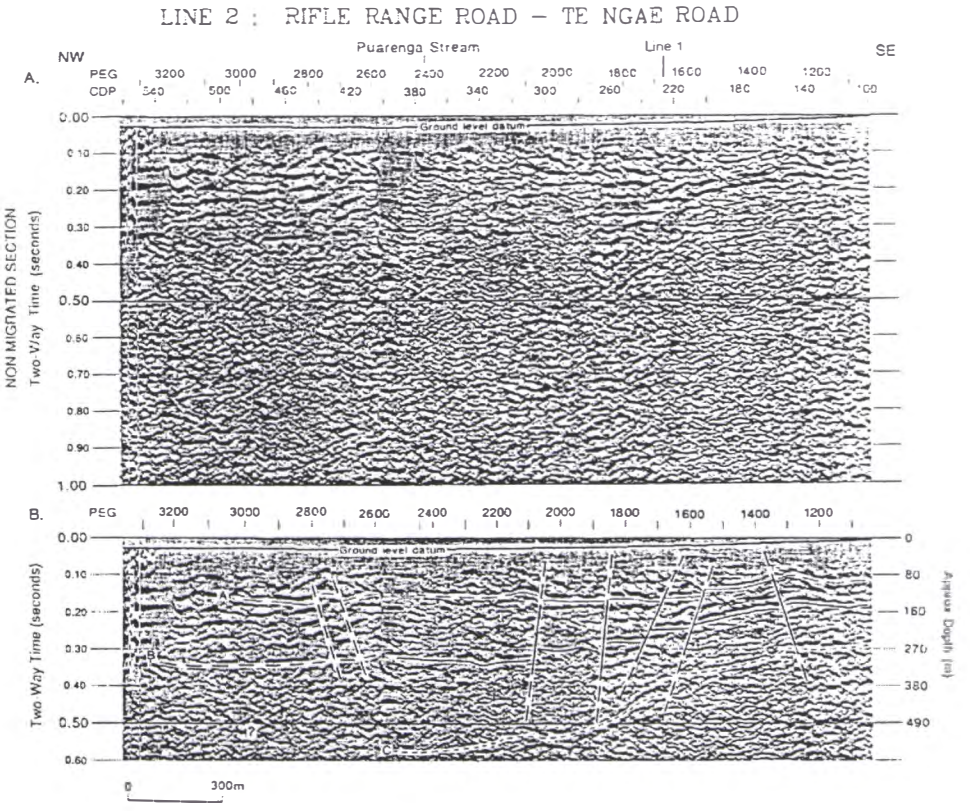

Figure 2.4. One of Lamarche's (1992) seismic lines and his interpretation. Horizon A is the top of lacustrine sediments, horizon B the top of Mamaku Ignimbrite, and horizon C the ignimbrites suggested base. Other reflectors exist that could also be interpreted as the lower Mamaku contact. Drill core is required to confirm or deny Lamarche's interpretation.

Hunt (1992) based on gravity data suggested that the caldera is filled to a depth >1 km with sediment (a similar thickness to Rogan's (1982) estimate of non- or reversely magnetised material), and that Rotorua is not a caldera. Evidence presented throughout this thesis suggests otherwise, and because of this it is thought that the majority of the caldera is filled with Mamaku Ignimbrite.

2.4 Age and stratigraphic relations

Murphy and Seward (1981) dated Mamaku Ignimbrite at 140 ± 80 ka (fission track estimate). Dates calculated since 1994 suggest an older age: Shane et al. (1994) obtained an isothermal plateau fission track (ITPFT) age of 230 ± 12 ka, Houghton et al. (1995) an age of 220 ± 10 ka from $^{40}Ar/^{39}Ar$, and Black et al. (1996) 230 ± 10 ka also from ITPFT. Mamaku Ignimbrite was erupted during a geomagnetic incursion which has been correlated with the Pringle Falls event (Black et al., 1996; Tanaka et al., 1996) which occurred 218 ± 10 ka (Herrero-Bervera et al., 1994). The 220-230 ka age is accepted here because of the agreement of dates calculated since 1994. 220 ka is within error of Murphy and Seward's (1981) age.

Mamaku Ignimbrite is exposed predominantly northwest of the TVZ margin. It immediately overlies Pokai Ignimbrite in Kinleith Forest, and in the Matahana Basin area it overlies Whakamaru Ignimbrite (320 ± 20 ka, Houghton et al., 1995) and densely welded Waiotapu Ignimbrite (580 ± 50 a, Houghton et al., 1995). At Sutcliffe Rd a tephra and aeolian sequence at least 2 m thick (overgrown) separates the Pokai and Mamaku ignimbrites. At distal localities north and northnortheast of Rotorua the Waiteariki and Waimakariri ignimbrites, Beeson's Island Volcanics and Minden Rhyolite (Otanewainuku, Puwhenua and Mt Misery) all underlie Mamaku Ignimbrite.

2.5 Internal stratigraphy

Mamaku Ignimbrite can be separated into a basal tephra sequence, and a main ignimbrite sequence. The main ignimbrite sequence can be further split into lower, middle and upper ignimbrite based on crystal content, welding and vapour phase alteration intensity (Fig. 2.5). Boundaries between lower, middle and upper ignimbrite

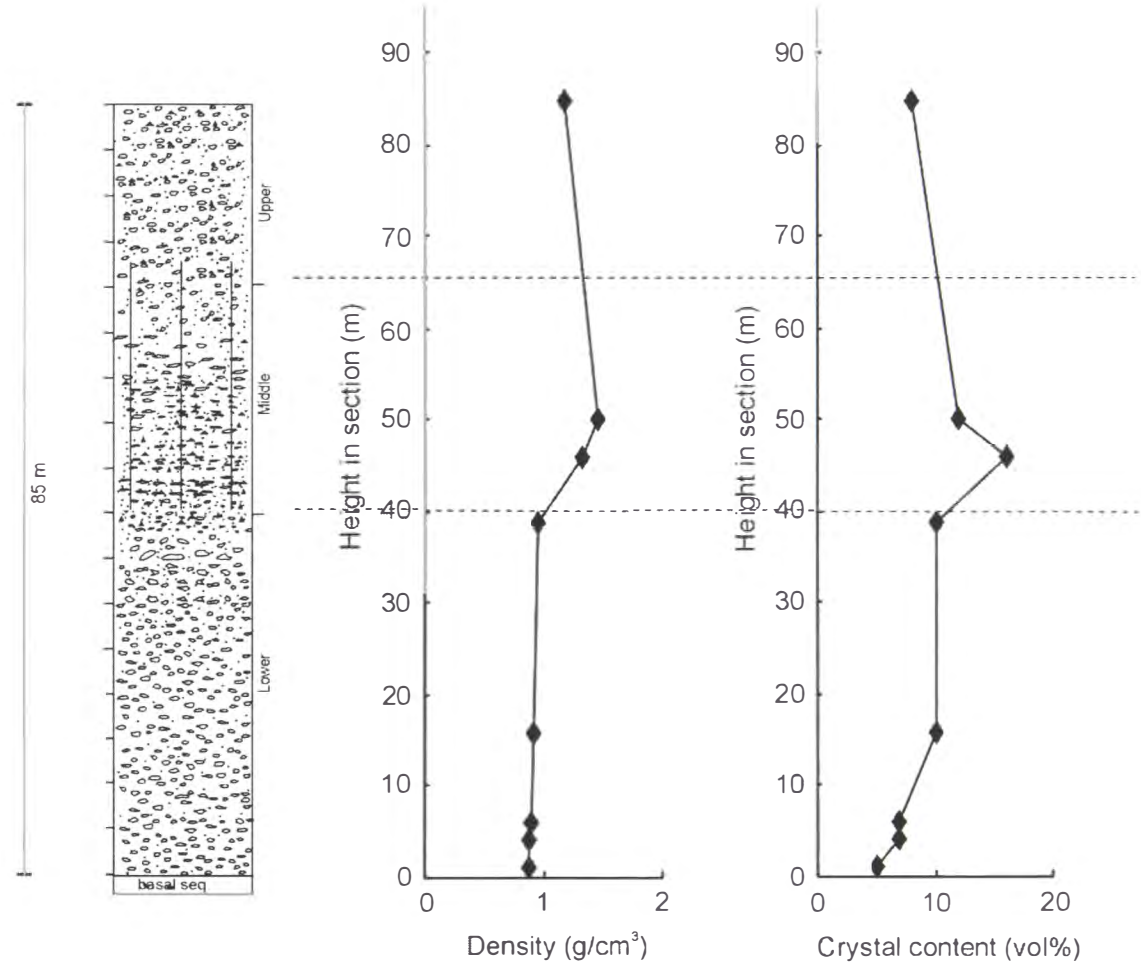

Figure 2.5. Sutcliffe Rd section (Mamaku Ignimbrite type section from U16/733344). Density and crystal contents increase markedly in middle ignimbrite. Jointing starts in middle ignimbrite and gradually stops in upper ignimbrite. Pumice clasts compact forming fiamme in middle ignimbrite. Open shapes are pumice clasts, black triangles are lithic fragments, and black spots are crystals.

are gradational. The type section of Mamaku Ignimbrite is here designated as Sutcliffe Rd in Kinleith Forest (between U16/733344 and U16/742338). At this locality all levels of the ignimbrite are exposed including some of the underlying tephras.

2.5.1 Basal tephra sequence

The base of Mamaku Ignimbrite is exposed at six localities. The basal tephra sequence comprises pyroclastic fall and density current beds and is best exposed at Pukerimu Rd (U16/777177, Fig. 2.1). At this locality the pyroclastic fall and density current beds total 2.3-2.4 m thickness and comprise 14 easily identifiable units (Fig. 2.6). Of these

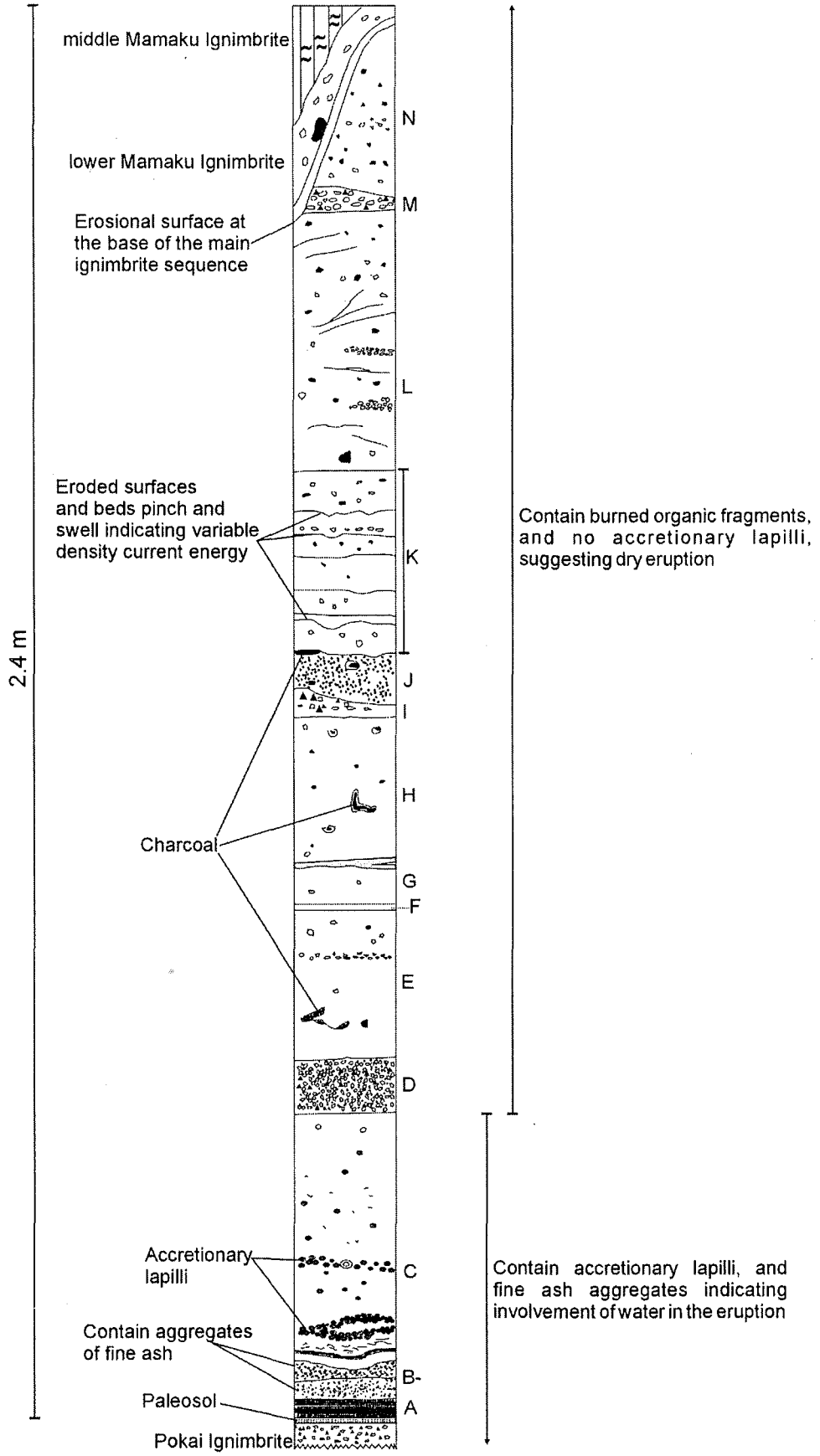

Figure 2.6. Graphic log of the basal sequence at Pukerimu Rd, labelled units are discussed in the text.

14 units only 5 are exposed elsewhere. Beneath the basal sequence at Pukerimu Rd is either 1 m of brown, fine tuff the surface of which is a hard iron stained band or the eroded surface of Pokai Ignimbrite on which a well developed paleosol is present.

The lowest unit exposed (unit A) is 30 mm thick, green-grey to pale yellow, fine to coarse ash that mantles the underlying topography with no thickness variation. The ash layer is predominantly small (up to 6 mm diameter) rounded to subangular aggregates of fine ash and contains 15 vol% rhyolite (including obsidian) rock fragments up to 6 mm diameter, and 10 vol% crystals. Fine ash aggregate size increases away from the band's centre imparting a doubly graded appearance. The colour variation is probably due to post-deposition water movement. Granulometric analysis (after Walker, 1983; Fig. 2.7) suggests a fall origin for this unit, as does its lack of thickness variation and it perhaps represents a vent clearing blast. The fine ash aggregates are similar to those described by Smith (1998) and suggest this phase of the eruption was phreatomagmatic.

Above unit A, unit B is 50 mm thick and comprises pale brown-grey, bedded, poorly sorted, coarse grained, crystal-rich ash with rare pumice clasts up to 10 mm across. The surface of this ash was eroded during the emplacement of unit C, which is also found at Pine and Sutcliffe roads (Fig 2.1). It is 50-450 mm thick, grey-white, very fine grained ash with numerous accretionary lapilli (up to 10 mm diameter) and ~2 vol% pumice clasts (up to 15 mm across). Small, sub mm size, angular obsidian fragments occur towards its base. Accretionary lapilli (broken and whole) are visible throughout this unit, and are concentrated in places to form discrete lenses. Accretionary lapilli are slightly compacted and elongate with long axes sub horizontal.

Its thickness varies irregularly, usually thickest in paleotopographic depressions, but in some places thickening upslope. 100m from the type section laminae of lighter grey material are sub-parallel to the unit margins. These laminae are interpreted as products of shear down slope under weight of unit C immediately after deposition, and/or during emplacement of the main Mamaku Ignimbrite sequence. Pieces of units A and C are incorporated into Mamaku Ignimbrite (Fig. 2.8) that can sometimes be traced to their points of origin. The increased thickness of unit C in depressions is thought to be dominantly primary (accretionary lapilli are not broken as would be expected if the thickness difference was due to a large amount of post-depositional movement) but may have been accentuated by downslope creep under its own weight, or by deposition of

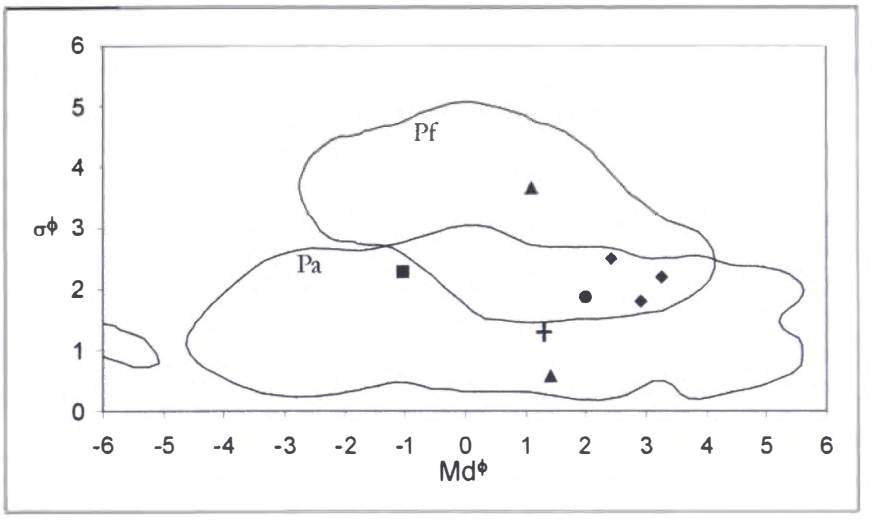

Figure 2.7. Granulometry of lower Mamaku Ignimbrite (lMI) and basal layers. Following Walker (1971). += basal tephra sequence unit A (Pukerimu Rd), •= basal tephra sequence unit M (Pukerimu Rd), ■= bottom layer at Oropi Gorge, ▲= Oropi Gorge lMI, ♦= Sutcliffe Rd lMI.

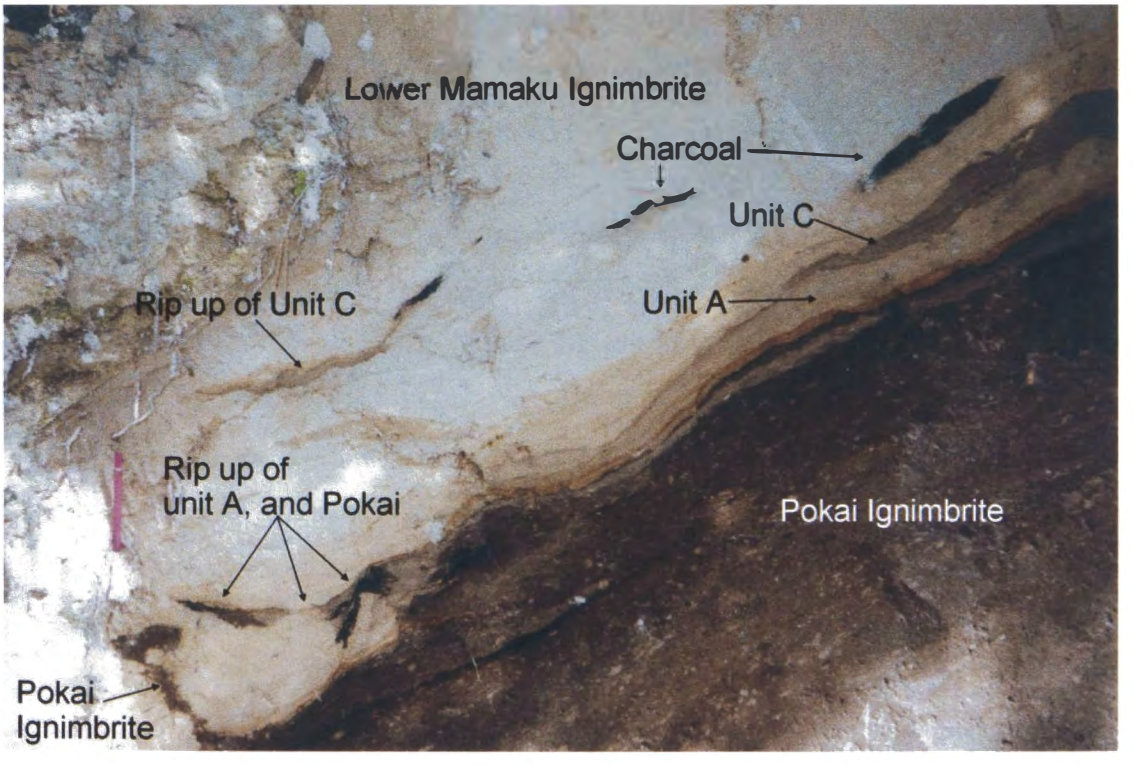

Figure 2.8. Photograph of lMI and part of the basal tephra sequence. lMI has ripped up and sheared out unit C, eroded unit A and ripped up Pokai Ignimbrite.

the main ignimbrite sequence or during passage of the pyroclastic density current adding an overlying load or causing deformation by shear causing the wet band to move into lower paleotopographic areas. The thickness differences, presence of accretionary lapilli and local scouring of underlying material suggest unit C is the deposit of a wet, turbulent pyroclastic current.

Above unit C is a bedded pyroclastic density current sequence. Charcoal is present in nearly all the layers precluding involvement of water during the eruption. The organic fragments are twigs and sticks rather than leaves indicating that the host material is a density current deposit rather than air fall. Deposition from a pyroclastic density current is also suggested by irregular basal contacts (eroded during passage of the succeeding current), internal thickness variation of each bed, and presence in some units of lithic and pumice concentration lenses.

Immediately on top of the phreatomagmatic band (C) is 100 mm of poorly sorted fine to coarse ash (unit D) containing pumice lapilli (5 vol%, up to 21 mm), small lithic lapilli (5 vol%, up to 5 mm) and 20 vol% coarse ash sized crystals. This band interfingers with the unit below. The interfingering relationship is post-depositional caused by loading and/or shearing within the phreatomagmatic band after unit D deposition (possibly due to weight of Mamaku Ignimbrite main sequence).

Unit E is much finer grained than the unit it overlies. It is fine, grey ash containing very occasional accretionary lapilli (<1 vol%), 1-2 vol% rounded pumice lapilli up to 4 mm width, and 2-3 vol% charcoal. Pumice lapilli are present throughout the band and are concentrated in two areas; in a pumice lens where pumice content reaches approximately 10 vol%, and around charcoal fragments. Vaporisation of volatiles within the organic matter elutriated fine material leaving coarse pods, which are oriented sub-parallel to the organic fragment they surround, not vertically as is usual in pyroclastic deposits. Presence of charcoal indicates this unit was drier than unit C. The presence of accretionary lapilli points to moisture involvement, but their paucity and lack of other moisture indicators suggests its influence was small (from a small amount of magma-water contact or external influences such as rain or steam evaporate from overridden material) rather than an integral part of the eruption (as it was with unit C).

Unit F is a 10 mm thick pumice-rich (10-20 vol%, up to 4 mm across), lithic-bearing (1-2 vol%, sub millimetre size), fine to very fine ash.

Unit G is fine to coarse ash grading to very fine ash at its top. Pumice clasts are up to 11 mm diameter, and <1 vol%, no lithic fragments were identified in the band and crystals are too small to be seen in hand specimen.

Unit H is 600 mm thick, grey, poorly sorted, very fine to coarse ash containing pumice lapilli (1 vol%, 12 mm maximum width), small lithic lapilli (<<1 vol%), and organic fragments (2-3 vol%). Crystal fragments dominate the matrix. Larger organic clasts are surrounded by black-yellow alteration halos. As with unit G the matrix in this unit fines and becomes darker grey towards its upper surface.

Unit I is a lens of poorly sorted coarse grey ash with 5-10 vol% small pumice lapilli and 1 vol% organic fragments. Coarse ash-size lithic fragments, crystals and shards comprise the matrix.

Light grey fine to coarse ash with 3 vol% crystals and occasional lithic lapilli with shards dominating the matrix comprise unit J.

Unit K is a sequence of alternating coarse and very fine to fine ash bands containing varying pumice (<1-3 vol%), lithic (0-1 vol%), and charcoal (1-2 vol%) contents. The units pinch and swell, and irregular boundaries indicate erosion of previous deposits by succeeding phases of the pyroclastic current.

The 450 mm thick unit L is poorly sorted fine to coarse ash, with 5 vol% pumice lapilli (present throughout the unit and concentrated in lenses, 22 mm maximum diameter), <1 vol% lithic lapilli (lithic fragments comprise ~3 vol% matrix), and 5 vol% charcoal. Short discontinuous iron stained bands are locally present. Pumice lenses are also local, flat-lying and do not occur behind topographic obstacles. They represent isolated periods where density current conditions allowed their deposition.

Unit M is poorly sorted white-pale grey fine to coarse ash. Pumice clasts are up to 10 mm across, fibrous and comprises 40 vol% of the unit. Rhyolitic lithic fragments (up to 10 mm across) make up 10 vol% of the unit, crystals 40 vol%, and fine ash 10 vol%.

Thickness varies between 20 and 50 mm and the unit plots in the pyroclastic flow field of the Walker's (1983) fall/flow diagram (Fig. 2.7).

Unit N is pale grey-light brown, up to 250 mm thick, poorly sorted, fine to coarse ash with small pumice lapilli (up to 12 mm in length), and coarse ash-sized lithic fragments (2 vol%). Pumice content is up to 5 vol% for the whole unit but in lenses is concentrated to 7-8 vol%.

There appear to be no extensive time breaks between the units of the basal sequence, some beds pinch and swell, often truncate or have eroded previously deposited beds (Fig. 2.6) suggesting variations in density current energy. They are interpreted as deposited from a continuous eruption and illustrate variations in eruptive style and energy.

The main sequence of Mamaku Ignimbrite at this site truncates both units M and N. One hundred metres to the south, only units A and C are present and 100 m further south units A, C, and N can be seen with disrupted relations. The base of the main body of Mamaku Ignimbrite is marked at Pukerimu Rd by a pale orange band the colour of which is probably due to post-depositional processes such as water movement.

2.5.2 Main ignimbrite sequence

The main Mamaku Ignimbrite sequence is predominantly massive, and mineralogically monotonous. Here distinctions are made between upper, middle, and lower Mamaku Ignimbrite based on welding, crystal content, and changes in vapour phase alteration. No single flow units have been identified. Correlation of internal stratigraphy delineated in previous studies with that described here is made in Figure 2.9.

Thompson (1958) logged 130 m Mamaku Ignimbrite in the Te Akau 5 (Fig. 2.9) drill core as part of a potential dam site investigation, and recognised soft pink ignimbrite at the top, hard off white-grey lenticulite at mid-low levels, and a white sandy base.

Nathan (1975) recorded 145 m of Mamaku Ignimbrite from a drill hole near Kaharoa (U15/948542; Fig. 2.9) and found approximately 85 m of upper porous ignimbrite, a 45

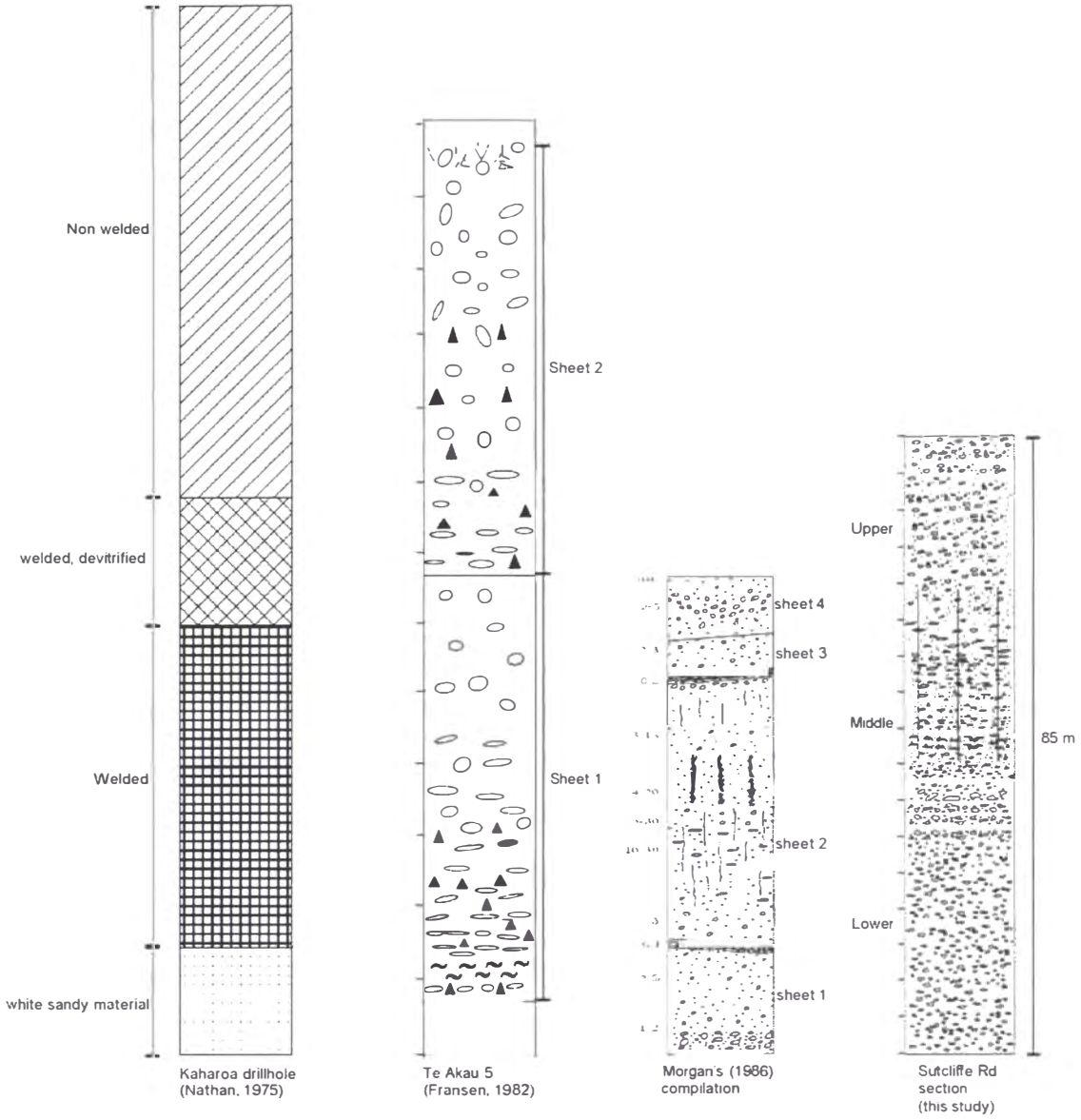

Figure 2.9. Comparison of Mamaku Ignimbrite stratigraphy used in this study with that of other workers. Open shapes are pumice clasts, small black shapes are crystals, black triangles are lithic clasts, and black wavy lines are fiamme.

m yellowish-brown welded facies, and lower unit comprising soft ash or pumice sand (although there were no core samples of this unit) approximately 15 m thick.

Fransen (1982) relogged the Te Akau 5 core originally logged by Thompson (1958) and defined two flow units based on pumice compaction and lithic content (Fig. 2.9). The change in pumice flattening used as evidence for the second flow unit is questionable however as pumice clasts are absent in the upper part of the lower sheet where he has inferred them to be open. Fransen's increase in lithic content is consistent with sections logged during this study, but a change in lithic content may also mean a change in lithic

supply or pyroclastic current energy/steadiness rather than a second flow unit (Branney and Kokelaar, 1992). This core was again logged during this study but some of the core has been lost and a full reinterpretation could not be made.

Morgan (1986) identified 4 flow units in distal Mamaku Ignimbrite, based on a compilation of graphic logs (Fig. 2.9). Bedded surge deposits separate sheets 1, 2 and 3 and sheet 4 separated from sheet 3 by a manganese band. Presence of the bedded deposits was confirmed during this study and they are discussed in section 2.5.3. The manganese band is here interpreted as precipitated from groundwater, and not a flow unit boundary.

Lower Mamaku Ignimbrite (lMI)

Lower Mamaku Ignimbrite is best exposed at Sutcliffe Rd in Kinleith Forest (Fig. 2.1) (U16/735344). Here it is 40-45 m thick and comprises pale brown to creamy white to grey, non-welded, non-jointed, mostly massive, poorly sorted, pumice containing (7-10 vol%), lithic-poor (<1 vol%), crystal-bearing (7-10 vol%) ignimbrite with fine to coarse ash matrix. Granulometric analysis after Walker (1983) indicates lMI was deposited from a pyroclastic density current (Fig. 2.7). Density varies between 0.79 g/cm^3 and 0.95 g/cm^3.

Maximum pumice clast diameter is 230 mm. Pumice concentrations define crude layers at some levels. At Sutcliffe Road concentrated bands of large pumice clasts are present with gradational upper and lower contacts. Thin pumice "trains", in which the concentration of pumice clasts reaches 15-20 vol%, can be traced for the extent of some outcrops towards the base of lMI (up to 5-7 m) without thinning and without any defined upper or lower contacts.

Where found lithic fragments are almost all rhyolite lava with rare accidental ignimbrite fragments (dominantly Pokai Ignimbrite).

Towards its base lMI contains rip up clasts of Pokai Ignimbrite, charcoal and parts of the basal sequence (Fig. 2.10). At Pukerimu Road trees and shrubs were uprooted pulling Pokai Ignimbrite and unit A of the basal sequence with them, and small scale

Figure 2.10. Rip up clast of Pokai Ignimbrite partially encasing organic material in lMI at Pukerimu Rd. The organic matter was probably part of the root system of a tree. Arrival of Mamaku Ignimbrite uprooted the tree which pulled Pokai with it. Also at this locality a small paleotopographic irregularity was flattened overturning part of the basal tephra sequence.

topographic irregularities were destroyed or overturned (Fig. 2.10) indicating high pyroclastic density current energy. At Pine Rd (U16/761192) crystal content increases (reaching 50 vol%) in a 5 mm band at the base of lMI imparting a layer 2a-like (of Sparks et al., 1973; section 2.7) appearance. Such a crystal-rich band is not seen at any other basal lMI outcrop.

Thickness of lower Mamaku Ignimbrite varies between 1 m and 45 m (1 m is seen at Pukerimu Rd (U16/777177). The Te Akau core 18 (U15/046527; Thompson, 1963) log has up to 4 m lower Mamaku, Nathan (1975) found up to 15 m, Te Akau 5 core possibly 3 m (Thompson, 1958; Fransen, 1983; this study), 5 m at Oropi Gorge (U15/876686), and 1.5 m at Lake Rotokawau (U15/065418). Diatoms were found in a sample from below 3 m depth in this layer in Te Akau 5 casting doubts about its origin(Thompson, 1958). The full thickness of the sandy material in Te Akau core 5 is 10 m (Thompson, 1958; Fransen, 1983); the lower 7 m has not been included as Mamaku Ignimbrite here. "Sandy white" material beneath welded Mamaku Ignimbrite

in core described by Nathan (1975) and Thompson (1958) is consistent with lMI seen in the outcrop.

Middle Mamaku Ignimbrite (mMI)

A sudden increase in welding, crystal content and jointing is indicative of middle Mamaku Ignimbrite. mMI is light-brown to dark-grey, jointed (spacing 0.5-4 m); moderately to very strongly welded (non-rheomorphic) ash with a dense vitrophyre in places near its base. Crystal content is 17-26 vol%, pumice clasts up to 20 vol%, and lithic fragments 0-4 vol%. In thin section the matrix is brown and dominated by clear, cuspate shards that impart a vitroclastic texture (Fig. 2.11). Density is up to 2.2 g/cm^3.

Pumice clasts are flattened and lenticular (fiamme) with flattening ratios (long axis/short axis) of 6-13 decreasing to 3-4 near the top. Lithic fragments are again almost entirely rhyolite lava and are sporadic throughout the section.

The increased hardness causes this unit to form bluffs that are prominent in the Kinleith Forest landscape. Above and below mMI ease of erosion causes surface slopes to have gentle gradients with relatively poor exposure.

The greatest thickness of exposed middle ignimbrite is at the type section of Mamaku Ignimbrite designated by Martin (1961), U15/886551 (Mangorewa Gorge; Fig. 2.1). Here approximately 50 m of middle ignimbrite is exposed but the lower contact cannot be seen. Near Kaharoa ~45 m of middle Mamaku ignimbrite was drilled (Nathan, 1975), ~70 m in Te Akau core 5 (Thompson, 1958; Fransen, 1983), and 40 m outcrops in Waiteti Stream (U15/875435, base not exposed). Approximately 25 m and 40 m are present at Sutcliffe Road and Raparapahoe Stream respectively. It thins northwards and is 5-7m thick at Oropi Gorge and Lloyd Mandeno power station (U15/786684). Mamaku Ignimbrite is not present 500 m west of the Lloyd Mandeno power station exposure (U15/781684).

mMI contains no rheomorphic structures that would indicate agglutination and secondary flow and fiamme long axes are predominantly horizontal suggesting an origin predominantly by compaction. But presence of mMI lithic fragments in upper Mamaku Ignimbrite suggests that, at least close to source, some agglutination occurred during, or

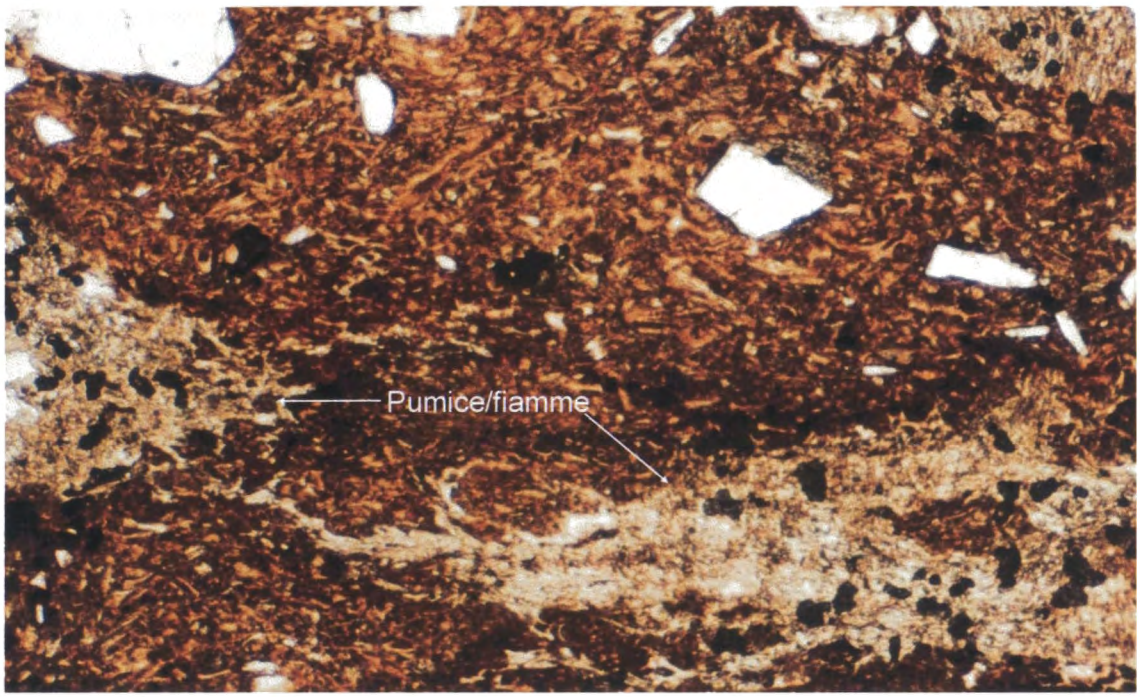

Figure 2.11. Photomicrograph of mMI showing vitroclastic and eutaxitic textures. Cuspate glass shards are still clearly visible in the matrix. Pumice clasts are compacted but still have fibrous structure. Picture is 4 mm left to right.

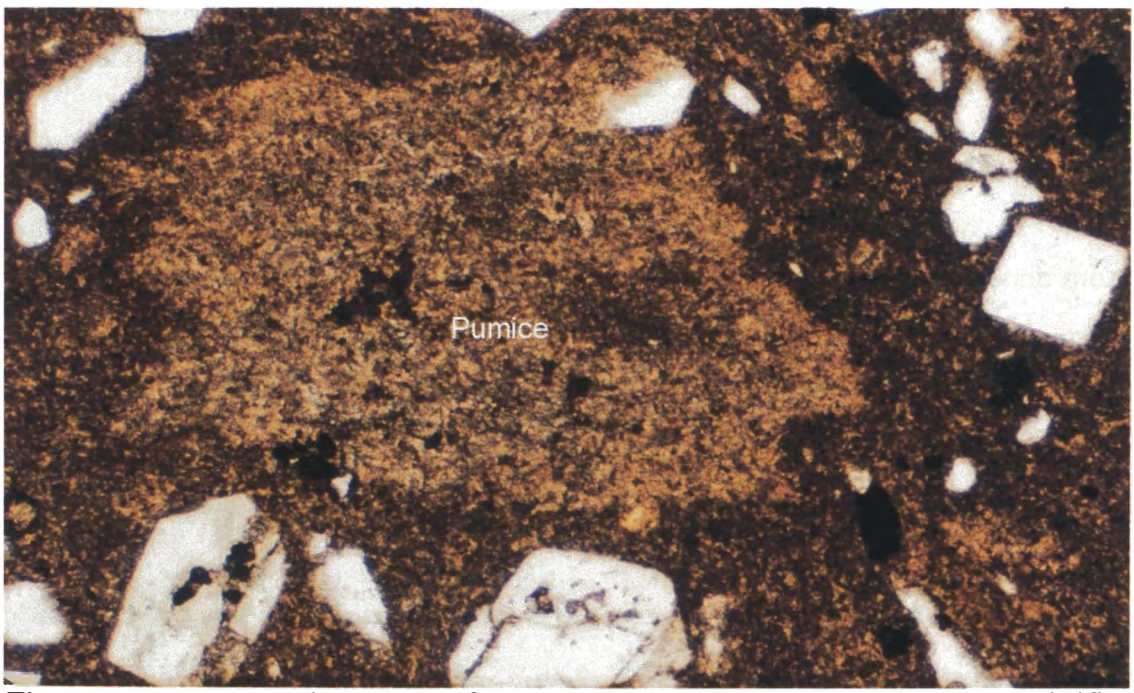

Figure 2.12. Photomicrograph of uMI. Pumice clasts are completely devitrified. Small radiating crystal can just be made out in the pumice clasts. Relict glass shards can be seen but the matrix is mostly structureless. Micrograph measures 4 mm left to right.

welding occurred immediately after mMI deposition. This would give it the competence required for eruption and transport for deposition in uMI. The welding of mMI may have also been influenced by an increase mass eruption rate (MER). An increase in MER would lead to a higher particle concentration pyroclastic density current, and a higher aggradation rate, thereby promoting heat retention and welding. An increase in MER would also account for the slight increase in the concentration of lithic fragments in mMI. mMI-lMI and mMI-uMI boundaries are gradational. lMI grades into mMI over 1-2 m, but the boundary between mMI and uMI is much more difficult to determine. Welding decreases and devitrification increases with height above the base of mMI; at both Sutcliffe Road and Oropi Gorge exposures mMI grades into uMI over about 10 m.

Upper Mamaku Ignimbrite (uMI)

Upper Mamaku Ignimbrite is grey-pink-red, non- to moderately welded, non-jointed to jointed, friable, fine to coarse ash. Density varies between 0.84 and 1.1 g/cm^3. Crystal content varies between 10-15 vol%, lithic content 0-2 vol% and pumice clasts 10-20 vol%. It is characterised upwards from mMI where pumice clasts become totally devitrified (Fig. 2.12) and is also typified by the presence of irregularly shaped andesitic blebs (Fig. 2.13) and influx of lithic fragments of mMI. uMI is exposed over much of the Mamaku Plateau, predominantly in road cuts.

Lithic fragments in uMI are mostly pieces of mMI, with rhyolite lava fragments, muddy argillic clumps and rare plutonic fragments. mMI fragments are angular to rounded, pink, welded, crystal-rich (up to 25 vol%) fiamme-bearing fine ash. They occur mostly towards the top of the ignimbrite away from the mMI-uMI boundary and are thought to be vent derived. Rare segregation pipes in exposures at Rotorua Caldera rim indicate high fluidisation of the parent pyroclastic density current (Wilson, 1986). They are 300-500 mm high, and contain lithic fragments (mainly mMI) up to 50 mm diameter.

uMI has been extensively affected by vapour phase alteration (VPA) post deposition causing colour changes within it. Pumice clasts have devitrified and characteristic fibrous textures have been replaced by microspherulites (<<1 mm) of feldspar and silica (Fig. 2.12). Microspherulites also occur at the margins of some primary crystals. The matrix often comprises small needle-like crystals and contains aggregates of platy

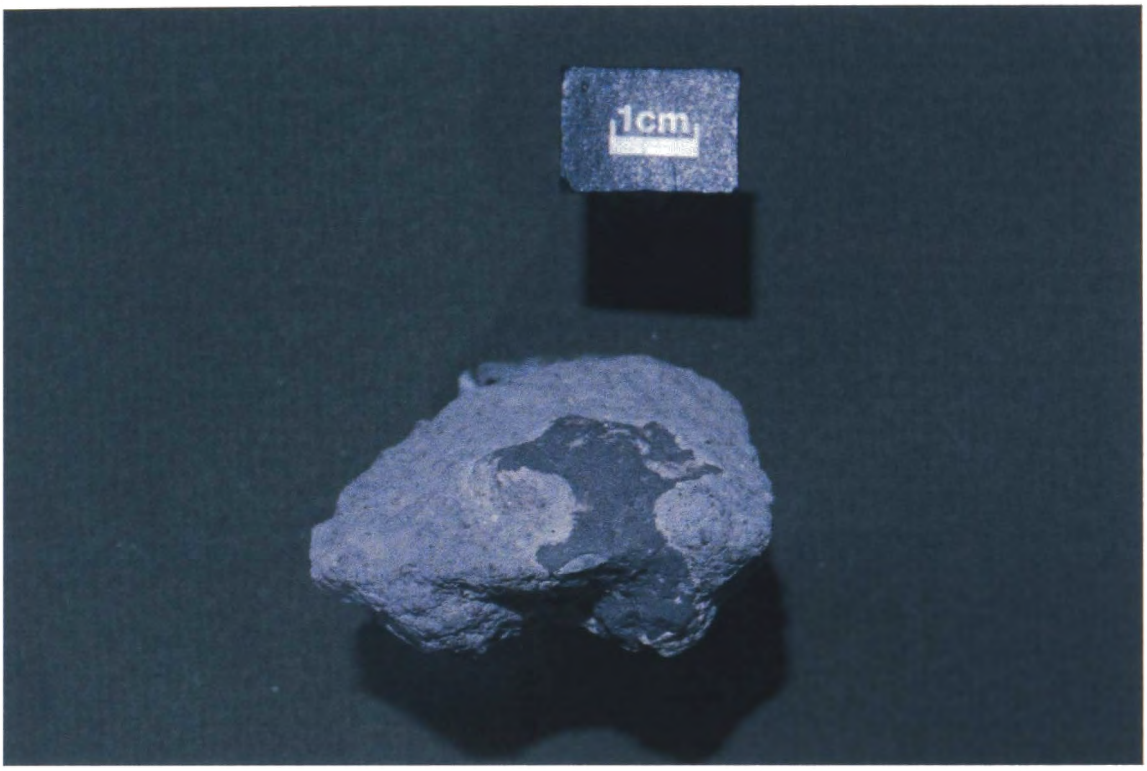

Figure 2.13. Hand specimen of an andesitic bleb in uMI. Note the morphology of the bleb that suggests it was liquid on eruption.

Andesitic blebs are up to 70 mm long, dark-grey to black, massive, and irregular shaped with 4.5 vol% phenocrysts in a very fine-grained holocrystalline groundmass (see next chapter, section 3.3). They are found exclusively in uMI. Their presence is important in deciphering magma chamber configuration and eruption dynamics. Mafic injection has been invoked as a trigger of other rhyolitic ignimbrite eruptions in TVZ (Tikorangi (Hildyard, 1996; Hildyard and Cole, 2000), Oruanui (Sutton, 1995), Whakamaru (Brown et al., 1998)). The same is interpreted for the Mamaku Ignimbrite eruption. The chemistry of the andesitic blebs and an eruption model are discussed in chapters 3 and 8 respectively.

Crystal and lithic content

Crystal content varies between 7-26 vol% depending on stratigraphic position (disregarding the small crystal-rich band in lMI at Pine Rd) and comprises plagioclase + quartz + clinopyroxene + iron/titanium oxides ± alkali feldspar ± orthopyroxene with trace amounts of hornblende and biotite. Crystal content is greatest (17-26 vol%) in the welded mMI (probably due to pore space decrease, and density increase) and lowest (7-10 vol%) in its non-welded lower part. Mamaku Ignimbrite is generally lithic-poor (<1

quartz + clinopyroxene + iron/titanium oxides ± alkali feldspar ± orthopyroxene with trace amounts of hornblende and biotite. Crystal content is greatest (17-26 vol%) in the welded mMI (probably due to pore space decrease, and density increase) and lowest (7-10 vol%) in its non-welded lower part. Mamaku Ignimbrite is generally lithic-poor (<1 vol%) with abundance of lithic fragments increasing in welded middle ignimbrite (up to 4 vol%) and near the top of uMI (up to 2 vol% in medial exposure).

2.5.3 Lateral variations

Layer 1-like lenses

At the base of lMI and within distal mMI at Oropi Gorge (U15/876686) coarse crystal-rich (50-60 vol%) layers are present. The layer beneath lMI is coarse to fine with pumice lapilli, but is not an equivalent to unit A of Pukerimu Rd as it is coarser grained (M_d= -1.05 ϕ at Oropi Gorge vs 1.3 ϕ for unit A) and less sorted. Within mMI at Oropi Gorge a crystal-rich lens with a maximum height of 120 mm extends for c. 15 m along the outcrop (Fig. 2.14) similar to those noted elsewhere in uMI by Morgan (1986). mMI beyond the lens does not contain a flow unit boundary. Crystal-rich lenses are not seen in mMI at Sutcliffe Rd. The lens in mMI and the layer beneath lMI may be layer 1-type deposits from a fully deflated pyroclastic density current, as described by Druitt (1998); the lens in mMI is possibly due to temporary migration of the pyroclastic density current direction. Sutcliffe Rd is a medial exposure where the pyroclastic density current probably had not fully deflated. Deposition of Mamaku Ignimbrite is discussed later in this chapter (section 2.7) and further in chapter 8.

Lithic lag breccias

Size and concentration of lithic fragments in uMI increase towards Rotorua with lithic concentration zones and lag breccias present around the caldera rim.

Lithic lag breccias occur at three caldera margin localities on top of uMI, while lithic concentration zones (up to 20 vol% lithic clasts) have been found at a number of caldera margin sites (Fig. 2.1). The type exposure of a Mamaku Ignimbrite lithic lag breccia is in a gully on Wharenui Farm past the end of Basley Rd (U16/996342) where a 1 m thick band is exposed in the side of a bulldozed track for ~10 m (dipping gently towards the

Figure 2.14. A crystal rich lens in mMI exposed at Oropi Gorge. The lens reaches a maximum thickness of 150 mm (A) before pinching out (B). Beyond the lens there is no flow unit boundary in mMI. The crystal-rich lens is traceable for 15 m across the outcrop before exposure is terminated by landslip debris. It possibly represents a temporary migration of the pyroclastic density current direction.

caldera) and contains 80-90 vol% lithic fragments. Lithic fragments comprise 46 vol% mMI, 48.5 vol% rhyolite lava, 3.8 vol% other ignimbrites (Waiotapu, Pokai, and Whakamaru mainly), and 1.7 vol% plutonic clasts (comprising clasts of microgranite, granite, microdiorite, diorite and very rare gabbro). uMI grades quickly (over c. 100 mm) into the breccia; lithic fragments are set in the same pink, fine to coarse matrix of uMI, and devitrified pumice clasts of uMI type are present. The top of uMI is generally forested and hence has little outcrop. It is likely that lithic lag breccias are present at other localities particularly along the southwest and west caldera margin but as a result of forest cover none were found during the study. Lag breccias may be present in proximal mMI but also are not exposed.

Beresford (1997) interpreted lag breccias in Kaingaroa Ignimbrite as signifying a change in eruption dynamics (vent widening, vent multiplicity and onset of caldera collapse). Those of Mamaku Ignimbrite are interpreted the same way. Increase in lithic content is sharp, and there is a change in composition of lithic fragments (from dominantly rhyolite to dominantly mMI), as there is in Kaingaroa Ignimbrite. Lithic lag breccias in uMI are not extensive laterally or vertically and beyond the caldera margin breccias are not seen. At medial to distal localities lithic content increases towards the top of uMI (at the same stratigraphic level as the lag breccias). The stratigraphic position of the lag breccias points to an episode of caldera collapse at the end of the Mamaku Ignimbrite eruption. Lithic content also increases in lower mMI (Fransen, 1982; this study) and may signify an earlier caldera collapse event, but lack of mMI exposure prohibits confirmation of possible lag breccias. The collapse history and evolution of Rotorua Caldera structure is discussed in chapter 8.

2.6 Source of Mamaku Ignimbrite

Anisotropic magnetic susceptibility (AMS, Rochette et al., 1992), clast imbrication, ignimbrite thickness, maximum lithic size (M_L), and location of lithic lag breccias are all useful techniques for determining ignimbrite source direction (Wright and Walker, 1977; Walker, 1985).

2.6.1 Maximum lithic data

To determine Mamaku Ignimbrite source, measurements were made of the long axes of the 5 largest lithic fragments seen at 110 uMI sites. The 5 values were averaged and an isopleth map constructed (Fig. 2.15a). Maximum lithic data (M_L) from mMI and lMI are of limited use because of lack of exposure close to source. M_L of uMI decreases from 192 mm at the northern margin of Rotorua Caldera to 11-15 mm at Oropi Gorge. North of Oropi Gorge lithic fragments are rare and were not measured. West and southwest M_L diminishes from 100-1000 mm near the caldera rim to between 4–15 mm at its western margin near Tokoroa and Atiamuri (Fig. 2.15a). Isopleths (Fig. 2.15a) centre on the area southwest of Lake Rotorua, with size decreasing away from Rotorua Caldera (Fig. 2.15b).

Lithic lag breccias, considered proximal deposits (Wright and Walker, 1977; Bacon, 1983; Walker, 1985; Branney and Kokelaar, 1997; Nairn et al, 1993; Beresford and Cole, 2000; Brown, 1994), are present at three localities on the western rim. Lithic concentration zones are located at various sites around the rim. They are likely present but are not exposed at other sites around the caldera rim.

2.6.2 Anisotropic magnetic susceptibility (AMS)

Magnetic fabrics form by the alignment of magnetic grains that may result from flow during emplacement of an ignimbrite and impart anisotropic magnetic susceptibility (Ellwood, 1982; Cagnoli and Tarling, 1997). The magnetic susceptibility of an ignimbrite is often anisotropic and greatest parallel to the pyroclastic density current flow direction (e.g. Knight et al. (1986), Macdonald and Palmer, (1990), and Ort et al. (1999)). Ideally maps of magnetic susceptibility measurements will exhibit a radial pattern about the source vent. AMS studies were carried out on a number of TVZ ignimbrites by Black (1995). In general her results show a radial AMS pattern for Mamaku Ignimbrite about a source in the western part of Rotorua Caldera (Fig. 2.16). Places where the magnetic susceptibility does not align with a Rotorua source is likely due to local changes in pyroclastic density current direction. An area northwest of Rotorua yielded inconclusive AMS long axes. This area is interpreted to have sagged during caldera collapse (see chapter 6) and the AMS directions may represent a small amount of secondary flow back into the caldera in response to collapse or a change in

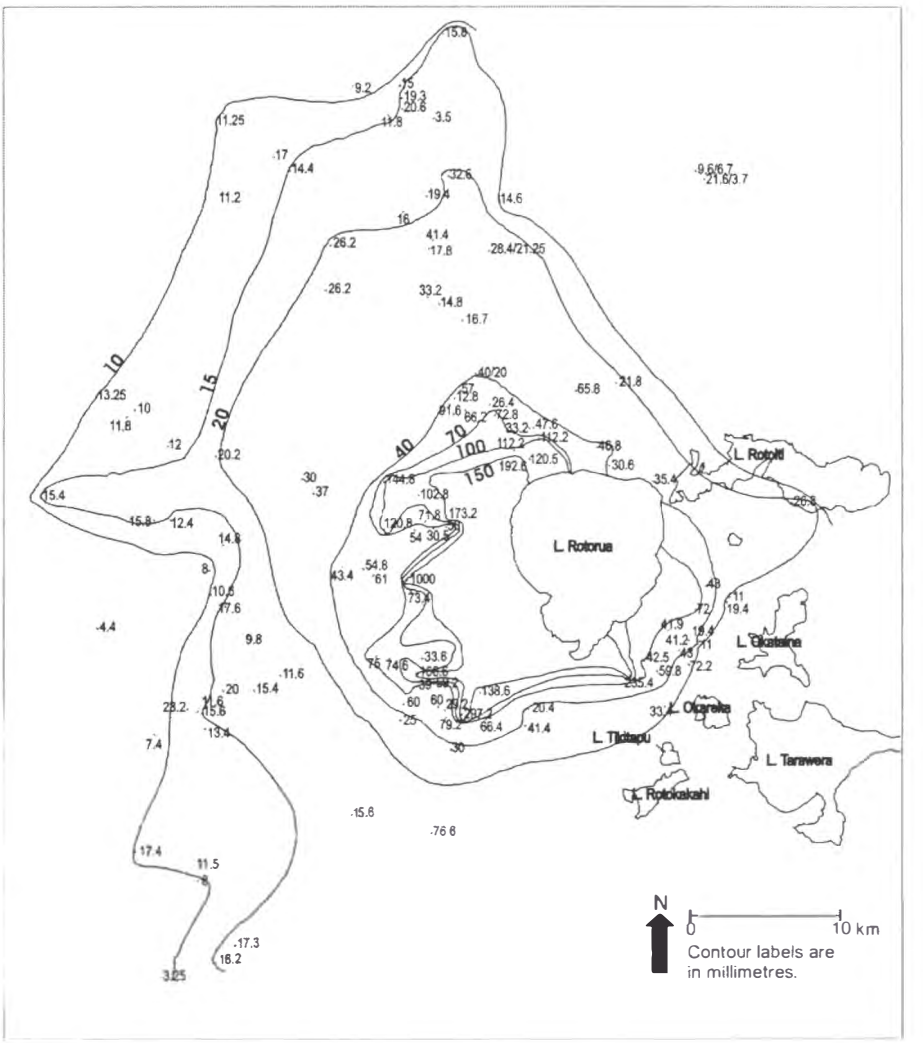

Figure 2.15a. Maximum lithic (M_L) isopleth map for uMI. Isopleths centre on the area southwest of Lake Rotorua, the inferred main source area of the ignimbrite. Isopleths labels are in millimetres.

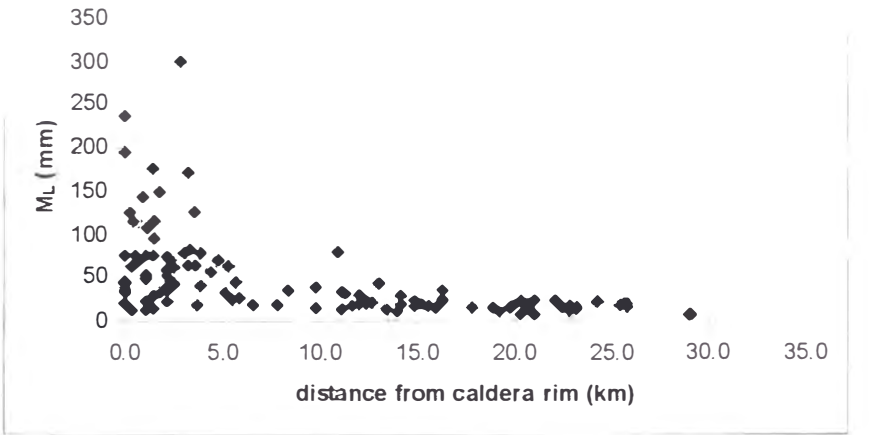

Figure 2.15b. Maximum lithic size vs distance from Rotorua Caldera rim. Lithic size clearly decreases away from the rim of Rotorua Caldera.

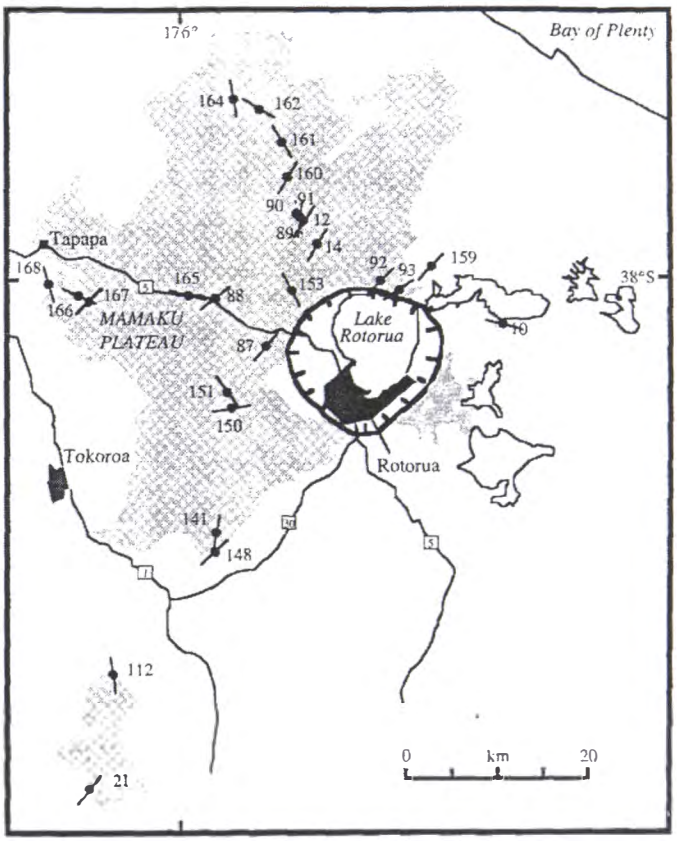

Figure 2.16. Black's (1995) interpretation of Mamaku Ignimbrite's magnetic susceptibility. Long axes of the magnetic susceptibility ellipsoids generally radiate out from Rotorua Caldera suggesting this as its source. Note that AMS measurement 87 is parallel to the caldera margin and probably represents secondary flow or change in density current direction due to caldera collapse. Analyses 21 and 112 are in Mokai Ignimbrite.

flow direction in response to the topographic barrier the forming caldera probably created.

2.6.3 Thickness

Thickness of total Mamaku Ignimbrite outflow varies irregularly according to paleotopography, but generally thickness increases towards Rotorua Caldera (Fig. 2.17).

2.6.4 Kapenga Caldera as a possible source

Rotorua Caldera has been the assumed source of Mamaku Ignimbrite (Healy, 1963; Wilson et al., 1984; Wood, 1992). More recently I.A. Nairn and C.P. Wood (pers. comm., 1999) have suggested that Kapenga and Rotorua calderas were concurrently active with eruption of Mamaku Ignimbrite either directly from the Kapenga area or

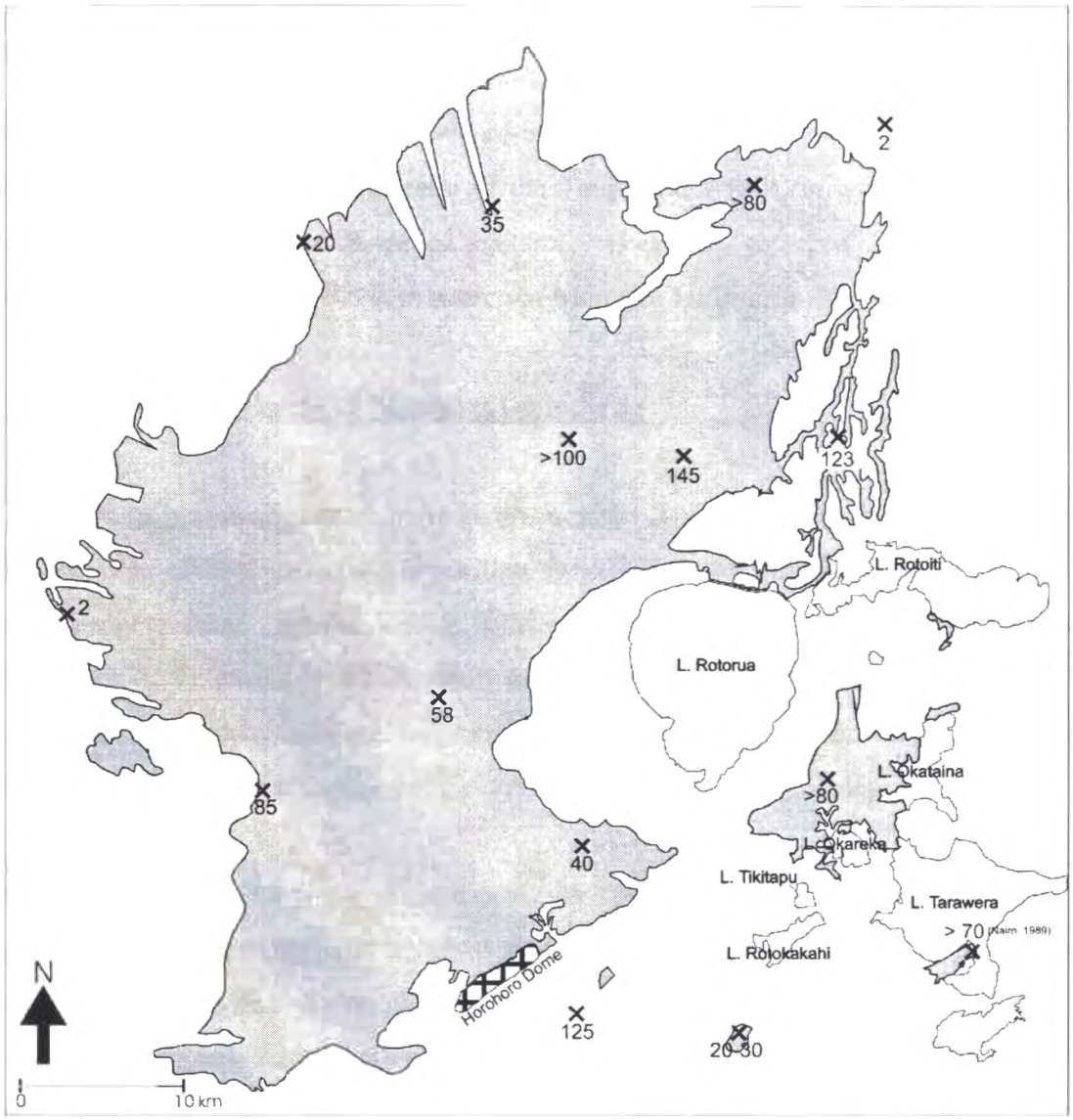

Figure 2.17. Maximum thickness (in metres) of complete sections of Mamaku Ignimbrite. Paleotopography causes anomalies but there is a general increase towards Rotorua.

migration of magma from Kapenga to Rotorua allowing collapse of Kapenga Caldera without eruption from it (see Fig. 1.3 for location). Similar events of magma migration with accompanying caldera collapse have occurred elsewhere e.g. Katmai, Alaska (Hildreth, 1991) and Vulsini, Italy (R.A.F. Cas, pers comm., 1999). Lack of Mamaku Ignimbrite outcrop in the Kapenga area was sited as evidence for its concurrent collapse (I.A. Nairn pers. comm., 1999). Mamaku Ignimbrite outcrops on Apirana Rd (U16/874245), west of Tumunui Hill (U16/971182) and ~125 m thickness is present in a geothermal exploratory drill hole at U16/876230. The Apirana Rd and Guthrie localities are approximately 250 m lower than outcrop on Mamaku Plateau. The

Horohoro Fault that defines the northwest margin of the Taupo Fault Belt lies between Mamaku Plateau and Kapenga. The TVZ is actively extending at 7-12 mm/yr (Cole et al., 1995, and references therein). This rate allows 1600-2800 m of extension since eruption of Mamaku Ignimbrite. Lack of outcrop in Kapenga is more likely due to this extension and subsequent subsidence of the Taupo Fault Belt (in which Kapenga lies) than volcanic collapse of Kapenga caldera. Evidence gathered during this study indicates that Rotorua was the sole source of Mamaku Ignimbrite.

2.7 Mode of emplacement of Mamaku Ignimbrite

Deposition of ignimbrites from pyroclastic density currents remains controversial. Two main schools of thought exist, deposition from pyroclastic density current by: 1) *en masse* emplacement (Sparks, 1976; Walker, 1983), or 2) progressive aggradation (Fisher, 1966; Valentine, 1987; Branney and Kokelaar, 1992). Progressive aggradation and *en masse* emplacement are end member methods of deposition. It is likely that a spectrum of depositional regimes exists giving rise to the variety of deposits observed.

En masse advocates view pyroclastic rocks as deposited from either airfall, surges or flows. *En masse* emplacement involves almost instantaneous "freezing" of a flow over its entire thickness and extent. For *en masse* deposition to occur the pyroclastic flow must be moving in a dominantly laminar or plug-like fashion and have a yield strength. Once the shear stress falls below that required to overcome yield strength the pyroclastic flow stops in a fashion akin to a mud flow or debris flow. Ignimbrites that were deposited *en masse* are compacted analogues of the pyroclastic flow with internal variations reflecting flow processes (Wilson, 1993). Because the pyroclastic flow moves in a laminar fashion any vertical variation in the ignimbrite must have been present prior to deposition (e.g. Palladino and Valentine, 1996). The height of topography traversed by a pyroclastic flow that deposited *en masse* is deemed to reflect its momentum (Sparks, 1976; Sheridan, 1979; e.g. Taupo Wilson 1985; 1997). The pyroclastic flow is regarded as having a head, body and tail (Fig. 2.18a, Wilson and Walker, 1982; Wilson, 1986) creating an ignimbrite with ordered facies variations (layers 1, 2, and 3, Fig 2.18b, Sparks et al., 1973).

Layer 1 or the ground layer is enriched in the dense components of the pyroclastic flow (crystals and/or lithic fragments). It may comprise three units deposited from: 1) A

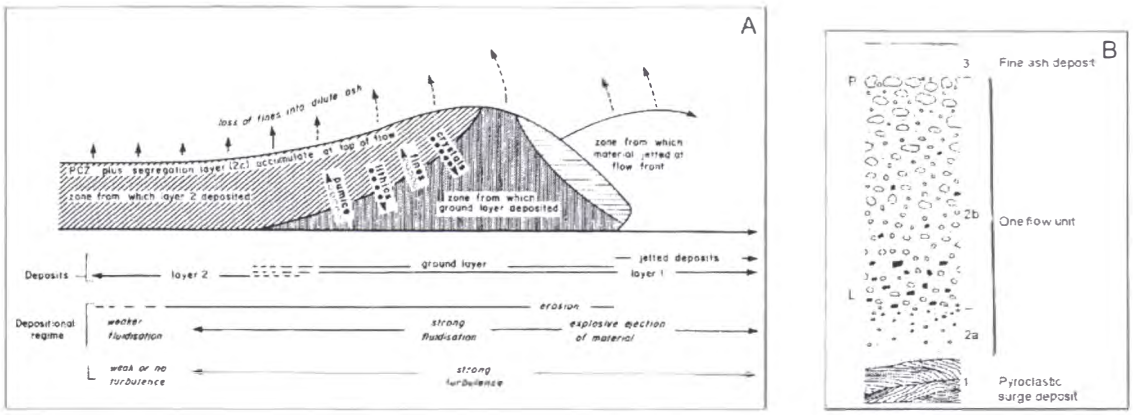

Figure 2.18. A) Morphology of a pyroclastic flow that deposits en masse showing the expanded head from which the ground layer is deposited and body from which layers 2a and b are deposited. The ground layer is also deposited from material jetted from the flow head. Overriding the pyroclastic flow is an ash cloud (from Wilson, 1985). B) The ideal flow unit stratigraphy (P= maximum concentration of pumice clasts, L= maximum concentration of lithic clasts; from Sparks et al., 1973).

ground surge that advances immediately in front of the pyroclastic flow (Sparks et al., 1973), 2) produced in the turbulent, expanded head of the pyroclastic flow (ground layer, Fig. 2.18), 3) material jetted (jetted deposits) through the front of the pyroclastic flow by rapidly expanding air ingested at the flow front (Wilson, 1993). Turbulence and expansion are caused by ingestion of air at the flow head. Turbulence carries the lighter components (pumice clasts and ash) up either into the body of the flow or the overriding ash-cloud surge (Fig. 2.18, Wilson, 1985). Loss of fines and expansion of the flow head results in diminished buoyancy of the dense components (crystals and lithic fragments) causing their deposition.

Layer 2 is deposited from the body of a pyroclastic flow and forms the main bulk of an ignimbrite (Wilson, 1986, 1993). Layer 2 is of two parts: 2a (basal layer) and 2b. The basal layer is finer grained than layer 2b (Sparks, 1976) and has reversely graded lithic and pumice clasts (indicating shear during emplacement; Wilson, 1986). The contact between layer 2a and 2b may be sharp or gradational depending on shear-strain rate gradient (Wilson, 1993). Layer 2b is the main mass of layer 2. Coarse fragments in layer 2b may be graded or ungraded induced by gravity/buoyancy, or shear within the flow (Sparks, 1976). Grading of pumice clasts may be opposite to that of lithic fragments illustrating the particulate concentration or fluidisation of the parent pyroclastic flow (Sparks, 1976). Interaction with the substrate may impart a shear gradient to the pyroclastic flow that decreases away from the pyroclastic flow-substrate

interface. In high concentration, low fluidisation flows grading may be absent (high particle concentration impedes vertical clast movement) or both lithic fragments and pumice clasts may be reversely graded as larger clasts migrate away from the zone of maximum shear (Cas and Wright, 1987). Normal grading of both pumice clasts and lithic fragments occur in expanded flows due to settling of the heavier, coarser clasts under gravity (Cas and Wright, 1987). Reverse grading of pumice clasts and normal grading of lithic fragments will occur in intermediate concentration pyroclastic flows, with lithic fragments settling under gravity and larger pumice clasts rising due to their greater buoyancy (Cas and Wright, 1987). In the case of highly fluidised pyroclastic flows, sharply bounded lithic and pumice concentration zones occur at the bottom and top of the ignimbrite respectively (Wilson, 1980). In some ignimbrites deposited from highly fluidised pyroclastic flows there is a fine grained layer 2c, representing fines elutriated from the flow that have rafted along the flow surface (Wilson, 1993).

Layer 3 is deposited by surge or fall from the cloud that overrides the pyroclastic flow (Sparks et al., 1973). The cloud overriding is composed of fines elutriated from the flow (Wilson, 1993). Layer 3 deposited when all movement of the flow ceases, is rich in fines, is commonly bedded and may have pinch and swell structures (Sparks et al., 1973; Cas and Wright, 1987).

Of these 3 layers only layer 2 need be present; layer 3 is easily eroded, and layer 1 may not be deposited depending the density of the pyroclastic flow (Wilson, 1993).

In progressive aggradation a pyroclastic density current is regarded as a sustained current rather than a discrete body or plug and covers the range between surges and flows (Branney and Kokelaar, 1995). A pyroclastic current is separated into: 1) particulate and 2) non-particulate components and is sustained (Branney and Kokelaar, 1995). The two layers are separated by the depositional boundary layer (DBL; Fig. 2.19, Branney and Kokelaar, 1992). The depositional boundary layer moves progressively upwards at a rate dependent on the stability of the pyroclastic current. Above the DBL the particulate component is an expanded, turbulent gas-solid dispersion. Particles above the DBL travel by saltation, kept aloft by interparticle collision and interparticle gases. Beneath the DBL grains are in constant contact with each other (non-particulate) and the density current moves by traction under the influence of gravity. The particulate and non-particulate components move

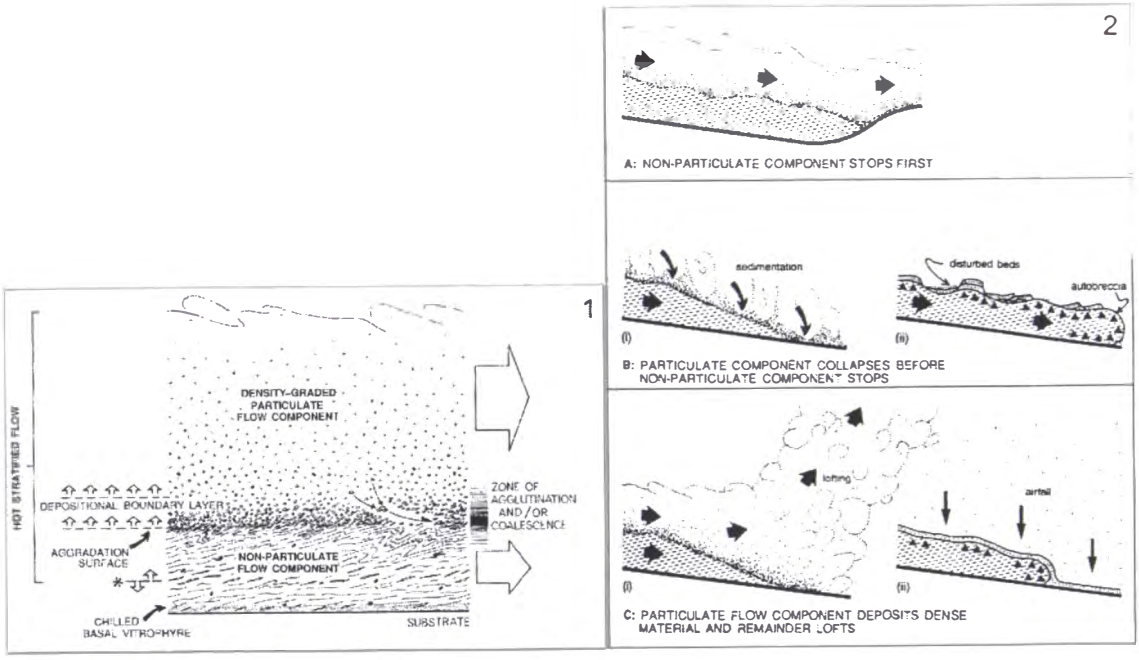

Figure 2.19. Emplacement of an ignimbrite by progressive aggradation, as envisaged by Branney and Kokelaar (1992). 1) a schematic cross-section through a pyroclastic flow. Material of the particulate flow component is entrained into the non-particulate flow component through the depositional boundary layer (DBL). The DBL migrates up through the current at a rate dependent on the current's steadiness. The particulate and non-particulate parts of the current act independently and may move in different directions. 2) Either may stop first leading to characteristic deposit features.

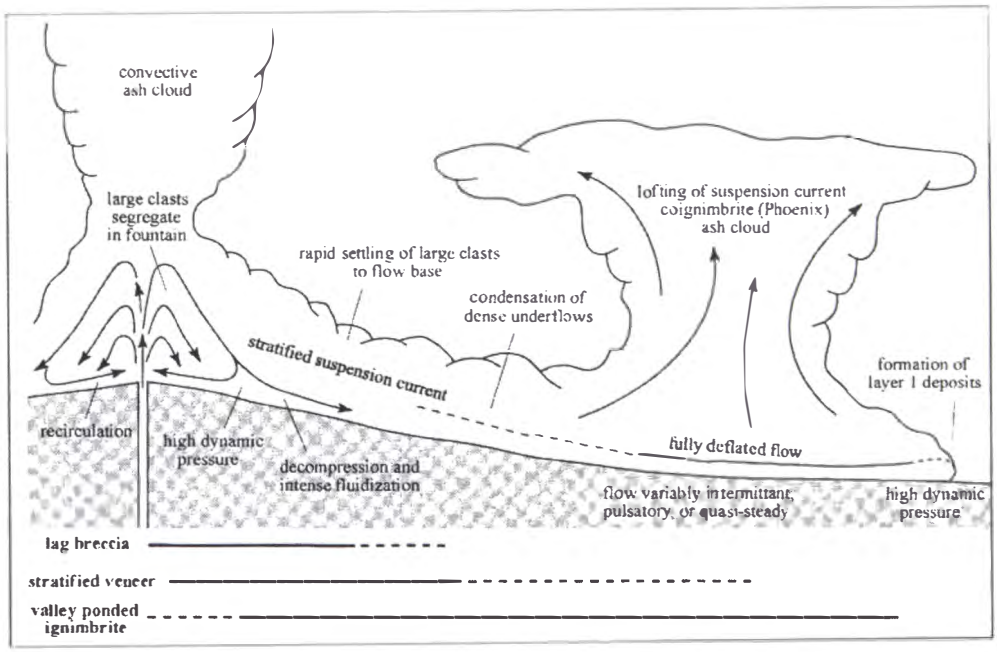

Figure 2.20. Druitt's (1998) high aspect ratio ignimbrite forming pyroclastic density current morphology. Close to source particles travel in suspension, and larger heavier clasts are deposited. Further away the flow deflates and has a head, body and tail morphology. Very fine and light material rises creating a co-ignimbrite ash cloud.

independently of one another and may move in different directions. Stratigraphic variation in concentration of components depends on their rate of supply to the particulate component at the source and their rate of entrainment into the DBL (which is governed by the energy of the current; Branney and Kokelaar, 1992; Kokelaar, 1993). As a density current becomes more distal it may become fully deflated and a dense undercurrent may form (Fig. 2.20; Sparks, 1976; Druitt, 1998). When fully deflated the pyroclastic current may move in a laminar fashion and create a deposit with layer 1, 2 and 3 morphology (Druitt, 1998).

Vertical variation in an ignimbrite deposited by progressive aggradation reflects steadiness of the pyroclastic density current (Branney and Kokelaar, 1992; Kokelaar, 1993). If the pyroclastic density current energy at a given point remains constant through time it is said to be steady. If the energy changes the current is deemed to be unsteady (Kokelaar, 1993). Massive deposits result from steady currents (e.g. Branney and Kokelaar, 1997). Any vertical variability reflects changing current conditions or unsteadiness. Increases in energy may result in stripping of material deposited earlier by the same pyroclastic density current or deposition of coarser and/or denser material (Kokelaar, 1993), while decreases in energy lead to normally graded deposits (Branney and Kokelaar, 1992). If a pyroclastic current is turbulent and thick enough it will move over the topography. Anything higher than the current is left untouched.

Ignimbrites are often classified by aspect ratio. The aspect ratio (AR) is determined by dividing an ignimbrite's average thickness by the diameter of a circle with the same area as the ignimbrite (Walker, 1983). High aspect ratio ignimbrites (HARIs) are thick compared to their extent (e.g. Valley of Ten Thousand Smokes, AR=1:135; Wilson, 1986). Conversely low aspect ratio ignimbrites (LARIs) are thin in comparison to their extent (e.g. Taupo Ignimbrite, AR= 1:107,000; Wilson, 1986). LARIs are thought to be emplaced by highly energetic pyroclastic density currents produced from eruptions with high magma discharge rates and HARIs from low eruption rates and lower energy pyroclastic density currents (Wilson, 1993). For the HARI/LARI classification scheme to be applicable the ignimbrite needs to have discrete flow units that deposited more or less *en masse*. HARI/LARI classification of ignimbrites that have been deposited by a mechanism closer to the progressive aggradation end of the pyroclastic density current depositional spectrum is more difficult. Mamaku Ignimbrite shows evidence of having

been progressively aggraded (see chapter 8) and no discrete flow units can be identified within it. An aspect ratio value for the Mamaku Ignimbrite is therefore inappropriate.

Two notable features of Mamaku Ignimbrite are: 1) a number of rhyolite domes rise above its surface (Puwhenua and Otanewainuku north of Rotorua, Horohoro dome to the southwest, and Endean dome on the western rim of the caldera; Fig. 2.1); and 2) Local thickness variations are rapid and of high magnitude. The ignimbrite onlaps both the southern extension of the Kaimai Ranges and Beesons Island Volcanics (Papamoa Ranges; Fig. 2.1). Its surface is 120 m lower than the top of Horohoro dome on the north side of the dome and has been downfaulted to the south in the Guthrie Graben. Mamaku Ignimbrite is not apparent on top of rhyolite domes or ranges mentioned. The thickness is variable laterally as it is in excess of 80 m thick at Raparapahoe stream, yet at U14/033702 (8 km from Raparapahoe stream and only 5 km further from source from source) the thickness is only 2 m. Also the ignimbrite is in excess of 100 m thick at Mangapapa River, whereas at Mamaku Township (approximately half the distance from the Rotorua Caldera rim) it is 58 m thick (Fig. 2.1 and 2.17). These features indicate that Mamaku Ignimbrite was deposited from a pyroclastic density current that was controlled by topography even at medial localities. Deposition was either from a dense flow, or an expanded cloud that was lower than the domes or deposited a thin layer on them that has since been eroded.

Mamaku Ignimbrite is interpreted as deposited by a mechanism closer to the progressive aggradation end of the spectrum although it exhibits some features that are more characteristic of *en masse* emplacement (layer 1- and 2a-like layers at distal localities). The vertical variations are too complex to be deposited from a pyroclastic density current that stopped entirely *en masse* and moved in a laminar fashion. Vertical variations in pumice clast and lithic content and size, and erosion of earlier deposited beds are consistent with deposition from a pyroclastic density current of variable energy. Features close to source illustrate high current energy, and stratigraphic variation further from source indicates increased deflation of the pyroclastic current. Mamaku Ignimbrite is thus interpreted as deposited progressively from an unsteady pyroclastic current in which density increased with distance from source. Its mode of deposition is discussed further in chapter 8.

2.8 Post-emplacement alteration

Mamaku Ignimbrite has been altered post-emplacement in three ways: 1) welding in mMI, 2) devitrification and 3) alteration by vapour phase activity.

Welding resulted dominantly from compaction (although some agglutination must have occurred) of hot ignimbrite immediately post emplacement, and is at a maximum towards the base of mMI.

Devitrification is the crystallisation of glass into its constituents (usually alkali-feldspar or albite, and silica polymorphs, Smith, 1960a) and is illustrated in Mamaku Ignimbrite by the break down of pumice clasts and glass shards. Towards the zone of maximum welding in mMI the fibrous texture of pumice remains intact (in thinsection) and the ignimbrite matrix has a vitroclastic texture (Fig. 2.11). Upward from the zone of maximum welding, pumice and vitroclastic textures gradually break down, pumice clasts become collections of microspherulites, and the matrix becomes massive and structureless with occasional lenses of needle-like crystals and patches with relict shard textures (Fig. 2.12). In uMI pumice clasts have been completely devitrified, are soft, and very friable (powdery). Frequently pumice clasts have been eroded completely from an outcrop and only holes remain.

Vapour phase alteration (VPA) is the dissolution or precipitation of minerals by gases moving through an ignimbrite (Smith, 1960b). The sources of gases involved in VPA include:

1) Volatiles involved in the eruption itself (including gases released during explosive expansion of pumice, Smith, 1960b).
2) Volatiles released during devitrification (e.g. Papike, 1992).
3) Ingested air (Smith, 1960).
4) Water from streams or ponds (Keith, 1984).
5) Volatiles released from organic matter (Carr, 1984; Keith, 1984).
6) Meteoric water. Depending on their thicknesses ignimbrites can take tens to hundreds of years to cool. Meteoric water may be responsible for VPA long after ignimbrite deposition.

Microscopic crystals of tridymite, cristobalite, alkali feldspar and albite (EDAX identifications and XRD; Appendix 4; Fig. 2.21) are located in pore spaces of uMI (including pumice vesicles). Tridymite crystals are platy and form crystal aggregates while albite and alkali feldspar crystals radiate from various nucleation points. The effect of deposition of tridymite and feldspar crystals in pumice clasts of uMI is discussed in chapter 3. In thin section magnetite is also identified, concentrated in samples taken from joint margins and fossil fumarole conduits. Hematite (XRD analysis) is present in the same areas. Clay minerals such as halloysite have been identified (XRD analysis, this study) at the margins of fumarolic structures and pyroxene crystals are usually broken down leaving iron stained spots (Fransen, 1982; this study).

In outcrop colour changes along joints and around fossil fumarole pipes are the most vivid illustration of vapour phase activity. Fossil fumarole pipes are classified into the following:

1) Bleached conduits. Leaching of minerals by passage of fumarolic gases along fractures or up open pipes bleaches the rock. Such structures have been noted in other ignimbrites by Wilson (1986).
2) Vertical to near vertical fractures or fracture zones either empty or filled with amorphous material. Gas escapes along the fractures breaking the ignimbrite down. Clay (halloysite 10Å) is often present in the altered material, and the fractures are usually surrounded by colour variations.
3) Open and/or infilled with exotic material. Fumarolic conduit material is sometimes completely eroded and replaced by slope wash. In some places the fumarolic conduits have undergone more than one phase of opening for example On Tauranga Direct Rd (U15/901528) a fumarolic pipe exhibits evidence of vertical gas discharge at its margins (clast long axes oriented vertically) inside which are subhorizontal bands with meniscus morphologies more consistent with settling of material downwards (Fig. 2.22). The meniscus structures indicate a second phase of opening of this pipe.
4) Colour changes from grey or pink most commonly to red, purple and yellow and sometimes black. These colour changes are due to the deposition of magnetite and hematite (colours probably reflect the oxidation state of iron and concentration of magnetite and hematite). Red and purple colour bands often

occur outside central bleached zones suggesting conditions changed away from the main zone of gas movement. Carr (1984) and Stimac et al. (1996) identified magnetite as the main iron vapour phase mineral in the Matahina Ignimbrite and Bandelier Tuff respectively. Both Carr (1984) and Stimac et al. (1996) found that K-feldspar, tridymite, cristobalite and magnetite were the dominant minerals deposited from the vapour phase. The same minerals occur in Mamaku Ignimbrite with inclusion of hematite.

Deposition of vapour phase minerals can cement the rock increasing its induration (Wilson, 1986). Mounds and ridges are prominent in the landscape northwest and west of Lake Rotorua (Fig. 2.23). These mounds usually contain one or more fumarolic conduits (Fig. 2.24). The ignimbrite in these mounds is more indurated than in surrounding areas and subsequent erosion has left them as tors. Similar structures have been documented in the Bishop Tuff (Sheridan, 1970).

In an effort to prove the origin of the mounds and ridges, pipes and fissures were counted at a number of sites within mounds and also in ignimbrite with no mounds along a section of Galaxy Rd in Kinleith Forest, and the induration noted. Mounds have an average of 1 pipe or altered fissure every 3-4 m and are well indurated. Exposure in areas without mounds have 1 pipe or fissure every 7 m and is moderately to poorly indurated. Fumarolic mounds are 25-60 m diameter and rise 5-15 m above the surrounding landscape. Depth of their conduits cannot be ascertained and lack of deep ignimbrite exposure means control of their location is not determinable. Fumarolic ridges are up to 1 km long, 20-60 m wide and up to 20 m higher than the surrounding landscape. They are aligned sub-parallel to the northwestern caldera margin. Their origin is equivocal but it is postulated that fumarolic activity concentrated along zones of extension created during caldera formation. Extension created lines of weakness along which gases preferentially migrated cementing sub-parallel zones rather than points as seen west of here outside the caldera rim (see chapter 6). Ridges in the Bishop Tuff are attributed to ascent of vapour along joints (Sheridan, 1970).

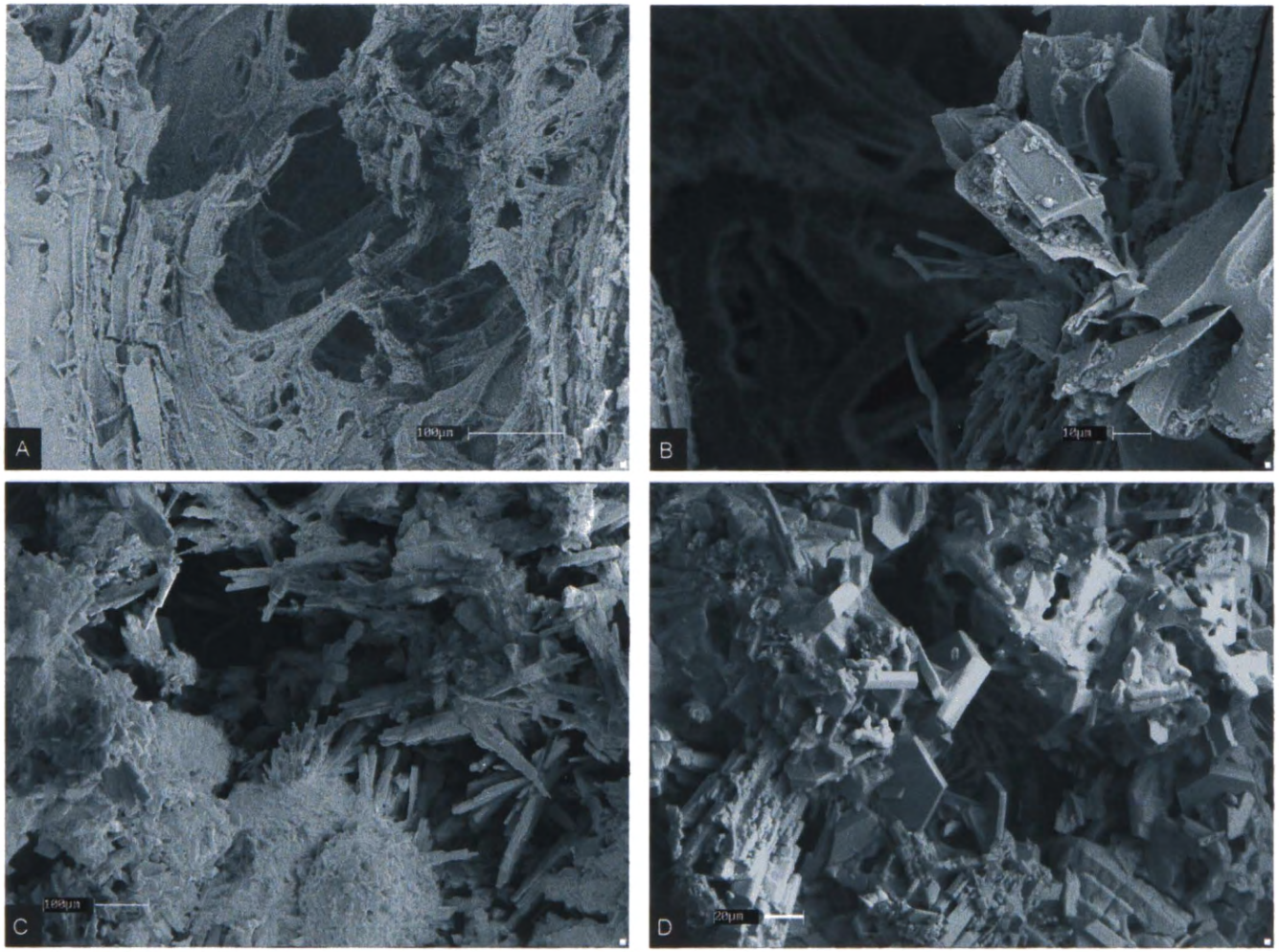

Figure 2.21. Effects of vapour phase alteration (VPA) and devitrification on Mamaku Ignimbrite pumice. A and B are from lMI and virtually unaffected by VPA. Note the fibrous texture of A and the smooth surfaces and broken fibres of B. C and D are pumice from uMI. Radiating crystals in C are albite growing into a vesicle. Platy crystals in D are silica polymorphs (probably tridymite). The original pumice texture in C and D has been completely destroyed by devitrification and VPA.

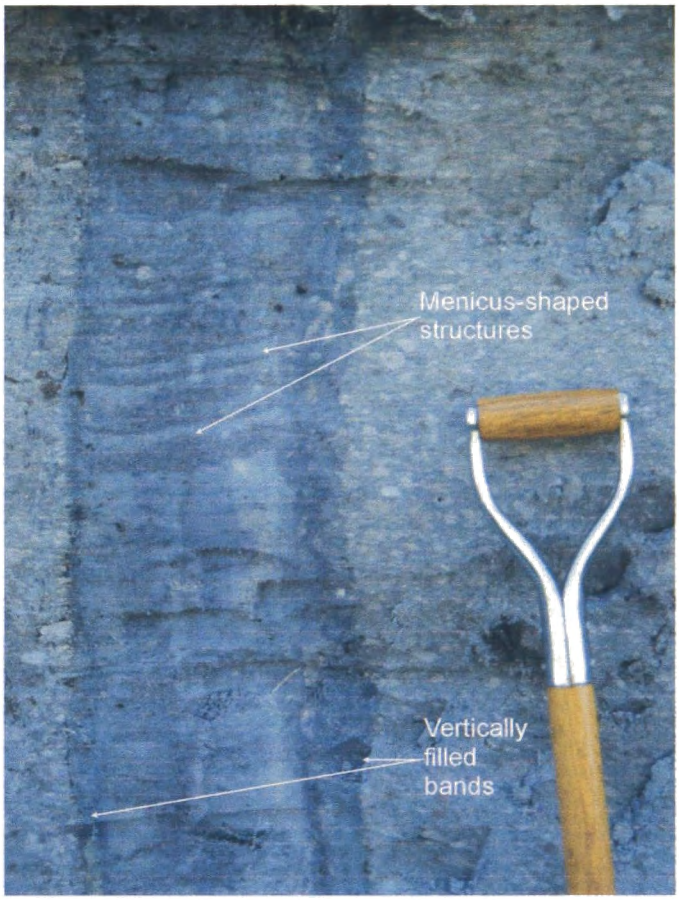

Figure 2.12. A fumarolic pipe that has been filled in two stages. Outer bands are interpreted to have been created during the ascent of fumarolic gas. Meniscus shaped structures are thought to have formed during the settling of material from above upon further opening of the pipe.

Figure 2.23. Fumarolic mounds in uMI northwest of Rotorua Caldera. Deposition of tridymite, cristobalite, albite, magnetite and hematite has cemented the uMI surrounding the fossil fumarole conduits. Subsequent erosion causes their prominence in the landscape.

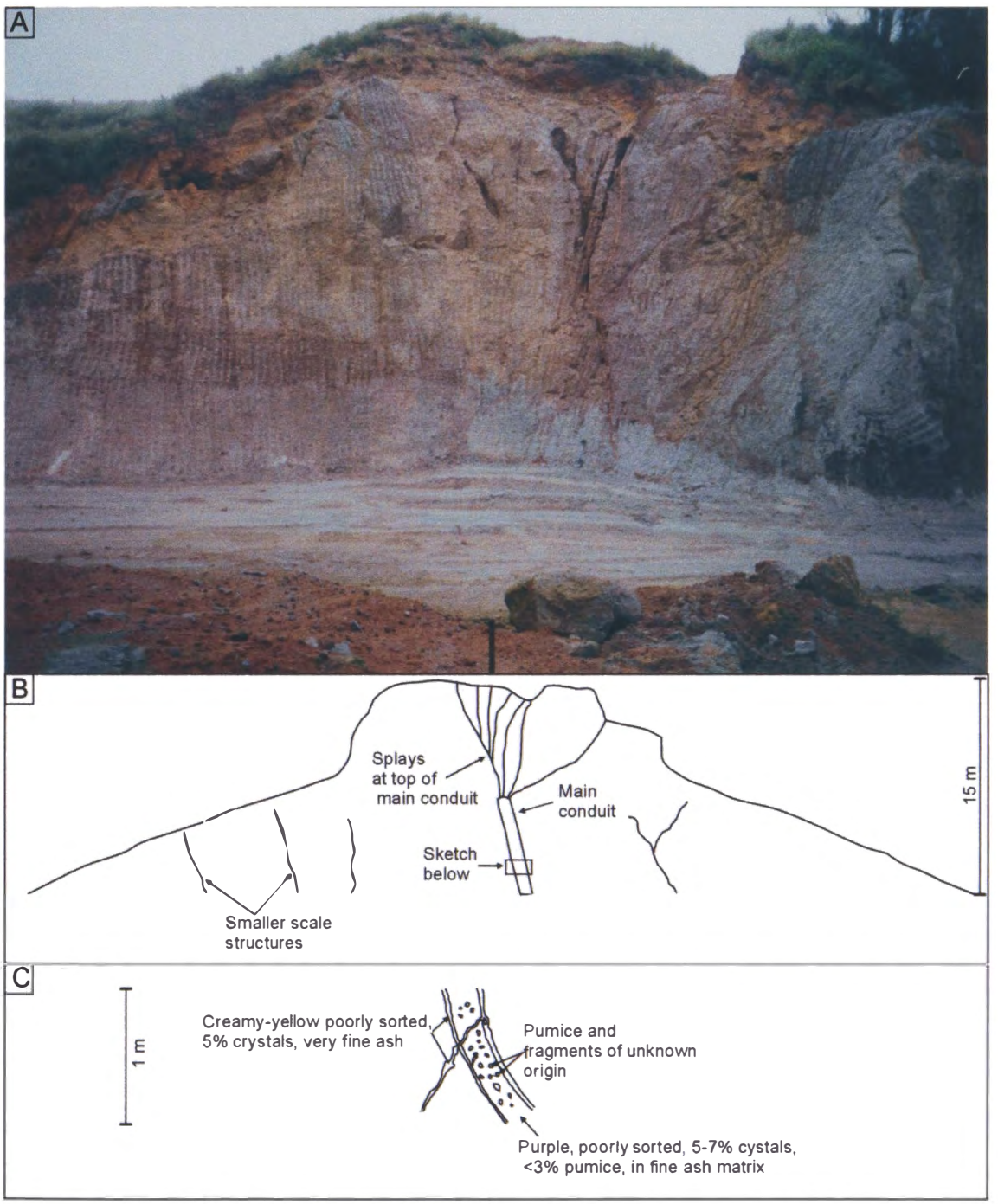

Figure 2.24. A quarried fumarolic structure reveals an internal conduit that splays at the top. Gases escaping up the conduit would have deposited minerals thereby cementing the ignimbrite and making it harder than in the surrounds. Material in the conduits is often eroded leaving a cavity, that may or may not be filled with eroded material. A) Photograph of the central portion of the fumarolic structure. B) Sketch of A). C) Close up sketch of the fumarole conduit. The material inside the conduit is probably derived from the surrounding ignimbrite.

CHAPTER 3
Geochemistry and Petrography

3.1 Introduction

Zonation of large volume rhyolitic magma chambers has been well studied since Smith (1979) suggested that all caldera-forming ignimbrites (ash-flow sheets) should show some chemical or thermal zonation. Hildreth (1981) went further saying that every large volume non-basaltic eruption taps a magma reservoir that is thermally and compositionally zoned. Later work (e.g. de Silva, 1991) suggested that zoning is mainly isolated to small volume cylindrical magma chambers (<100 km^3) that allow efficient convective fractionation, and that large volume chambers are more slab-like making efficient convection difficult and creating homogeneous magmas. To analyse the possibility of zoning in the Mamaku Ignimbrite magma chamber, pumice samples were taken from lower and upper ignimbrite levels (fiamme from mMI were unable to be extracted in quantities needed for analysis). Pumice clasts are pieces of the erupting magma quenched upon fragmentation and their analysis provides direct evidence of magma chamber configuration and eruption progression. Pumice clasts in many ignimbrites may be grouped according to chemical, petrographic, and/or thermal composition (Smith, 1979; Hildreth, 1981). The different pumice types may be separated stratigraphically indicating increasing depth of magma chamber evacuation, or mixed together indicating chaotic eruption of a zoned magma chamber, or coincident or sequential eruption of two or more adjacent chambers.

TVZ ignimbrites show a variety of styles of zonation. Beresford, (1997) delineated vertical isotopic variation in Kaingaroa Ignimbrite. Ignimbrites from Mangakino Volcanic Centre show vertical changes in pumice types (Briggs et al., 1993) as does Pokai Ignimbrite (Karhunen, 1993). Dunbar et al. (1989) illustrated existence of weakly zoned and long-lived homogeneous magma chambers beneath Okataina and Taupo volcanic centres respectively. Brown et al. (1998) found well developed zoning of pumice chemistry, temperature and phenocryst populations in Whakamaru Group ignimbrites and concluded that magma erupted from two or three chambers (three consanguineous magma types).

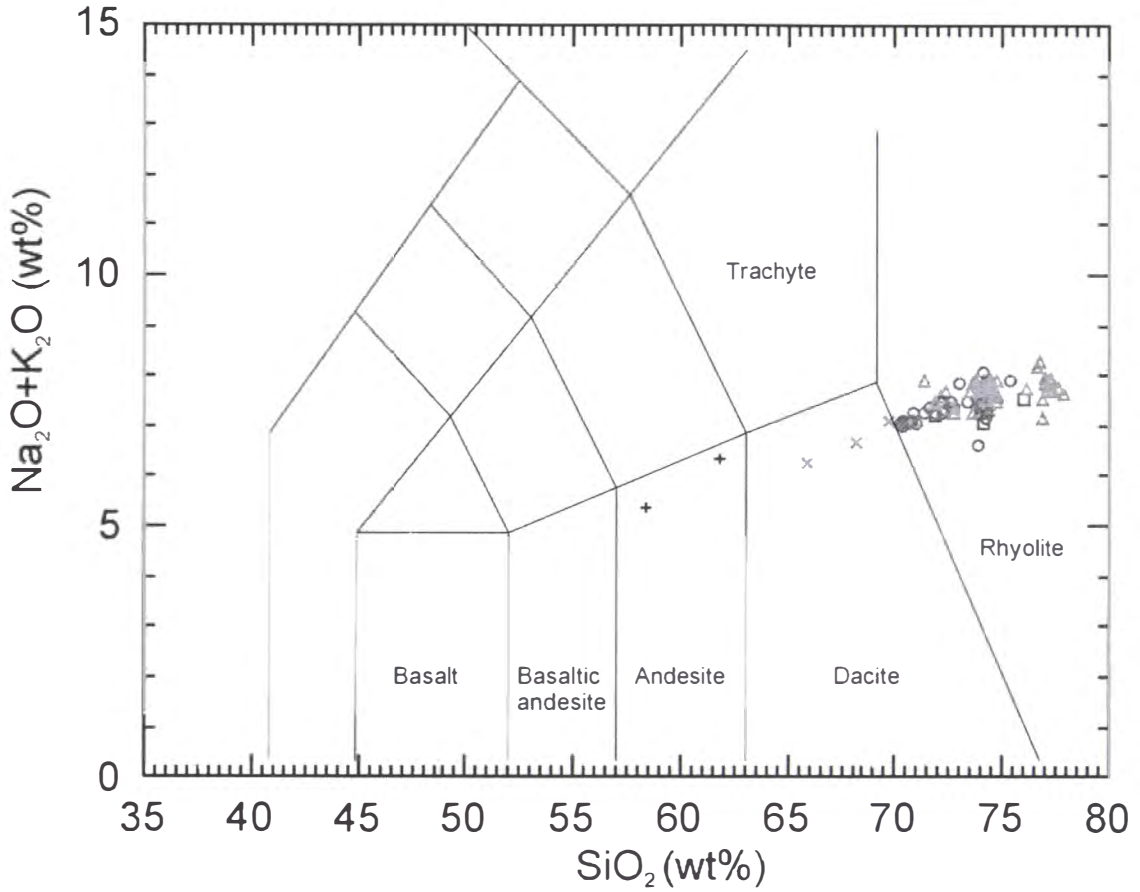

Figure 3.1. All samples analysed by XRF from Mamaku Ignimbrite. Juvenile components vary between andesite and high silica rhyolite. After Le Maitre (1989).

Previous geochemical work on Mamaku Ignimbrite includes pumice chemistry by S.D. Weaver and B.F. Houghton (unpublished data), glass analyses by Black et al. (1996), and whole rock chemistry by Fransen (1982). Whole rock geochemistry and petrology of Fransen (1982) shows slight decreases in plagioclase, silica, CaO, Na_2O, K_2O contents and a slight increase in Al_2O_3 content upwards through the ignimbrite.

Geochemical analysis was carried out on 143 juvenile clasts that range from andesite to high silica rhyolite (Fig. 3.1). Fifty six of these samples had Loss on Ignition >3% and were not included in interpretation. Fifty four pumice clasts were from upper Mamaku Ignimbrite (uMI) and extensively affected by vapour phase alteration (VPA; see chapter 2) and devitrification, so have been left out of the geochemical discussion. They have been included in a discussion about the effects of VPA on pumice chemistry. Two andesitic blebs from uMI have also been analysed and have been included in the ignimbrite chemistry discussion. Pumice clasts from sites in lMI were analysed by X-ray fluorescence (XRF) and 4 of these were further investigated using the electron probe microanalyser (EPMA) facility at Victoria University of Wellington. At Sutcliffe Rd

(Fig. 1.1) an attempt was made to sample pumice clasts from regular vertical intervals through lMI. lMI forms 40-45 m of an 85 m section exposed here. Sampling was only successful at medial to distal localities due to the lack of lMI exposure close to source. In addition EPMA analysis was also carried out on a collection of small pumice clasts from unit M of the basal sequence at Pukerimu Rd and an andesitic bleb of uMI.

Petrographic analysis was carried out on ignimbrite and pumice samples to determine characteristics and variations between pumice types and in ignimbrite stratigraphy.

3.2 Ignimbrite petrography

Mamaku Ignimbrite varies vertically from light grey, non-welded, unconsolidated, pumiceous and sandy, through dark grey, welded and lenticular, to pink-purple, devitrified and vapour phase altered. The progressions from non-welded to welded to devitrified and vapour phase altered are all gradational. The most obvious petrographic differences are in the textures of pumice clasts and glass shards, and in crystal concentration. All crystals are euhedral to subhedral or broken, and often contain cracks probably caused by stresses imparted during eruption, transport and deposition.

lMI is sandy and unconsolidated, poorly indurated with occasional thin pumice clast beds. It contains up to 10 vol% crystals, 10 vol% pumice clasts and, <1 vol% lithic fragments. Crystals, glass shards and ash form the matrix. Glass shards are cuspate to elongate and undeformed. Crystals comprise plagioclase + quartz + pyroxene + Fe/Ti oxides. Pumice clasts are open and vesicular, show no signs of compaction, and have not devitrified.

mMI is moderately to very strongly welded (not rheomorphic) and contains up to 26 vol% crystals, up to 4 vol% lithic fragments and 20 vol% pumice clasts and glass shards in the matrix. Crystals comprise plagioclase + quartz + clinopyroxene + orthopyroxene + Fe/Ti oxides ± hornblende (trace amounts). Pumice clasts are broken and flattened, becoming glassy with very low vesicularity towards the area of maximum welding. Glass shards are mostly cuspate, but have deformed around crystals. The glass shards and flattened pumice clasts impart eutaxitic texture.

Pumice structure and glass shards in uMI have all but been destroyed due to devitrification. The ignimbrite is pink-purple, poorly indurated, contains 7-15 vol%

crystals, up to 20 vol% pumice clasts and up to 2 vol% lithic fragments (although lithic content varies with proximity to source). The crystal assemblage is plagioclase + quartz + clinopyroxene + orthopyroxene + Fe/Ti oxides ± hornblende (trace amounts). Fransen (1982) noted that pyroxenes and Fe/Ti oxides were often broken down or destroyed leaving only brown spots. This study concurs. The mafic components in uMI are usually surrounded by a spherical alteration halo, and they are thought to have broken down in response to vapour phase activity while the ignimbrite was cooling.

3.3 Pumice clast petrography

Juvenile components in Mamaku Ignimbrite include silicic pumice clasts and andesitic blebs. Mamaku Ignimbrite pumice clasts cannot be distinguished in hand specimen but in thin section there are subtle differences from which three pumice types can be established.

Type 1 pumice clasts comprise 6-7 vol% phenocrysts, and up to 60 vol% vesicles. The phenocryst assemblage is plagioclase + quartz + orthopyroxene + Fe/Ti oxides ± augite (trace) ± hornblende (trace). In one type 1 pumice sample a number of phenocrysts of quartz-feldspar graphic intergrowths were found, mostly surrounding plagioclase phenocrysts. These are thought to be glomerocrysts stripped from the magma chamber wall during its evacuation.

Type 2 are made up of 5-7 vol% phenocrysts and 30-60 vol% vesicles. Phenocrysts comprise plagioclase + quartz + orthopyroxene + Fe/Ti oxides ± augite (trace).

Type 3 pumice clasts contain 4-5 vol% crystals and are up to 60 vol% vesicles. The crystal assemblage is plagioclase + orthopyroxene + Fe/Ti oxides ± quartz ± augite (trace) ± hornblende (trace).

In all pumice samples plagioclase and pyroxene often occur together in crystal aggregates that are likely to be glomerocrysts stripped from the magma chamber walls.

Andesitic blebs are dark grey-black, and irregular shaped with up to 10 vol% phenocrysts in a very fine-grained holocrystalline matrix. Pyroxene is the dominant phenocryst mineral with plagioclase + amphibole + biotite ± olivine (trace).

Groundmass microphenocrysts comprise amphibole (~35 vol%) and plagioclase (~45 vol%), and 10 vol% Fe/Ti oxides. The appearance of the andesitic material in uMI has important implications for the magma chamber configuration and eruption dynamics of Mamaku Ignimbrite.

Crystallisation of the andesitic blebs occurred in two stages. The first is indicated by growth of the pyroxene and plagioclase, and biotite phenocrysts up to 1.5 mm long, the second by crystallisation of the hydrous groundmass. Microphenocrysts making up the groundmass are long and thin (amphiboles are up to 0.3 mm long by 0.02mm wide). Groundmass amphibole crystals often splay at the ends forming fan or bowtie textures and, in extreme cases, star-shaped clusters (Fig. 3.2a). Plagioclase microphenocrysts are commonly skeletal and many have swallowtail terminations (Fig. 3.2b). The morphologies of groundmass amphibole and plagioclase indicate chilling of the andesitic magma.

The margins of some andesitic blebs are cracked consistent with quenching upon entry into a cooler medium. The margin of one andesitic bleb has a rhyolitic coating that is discordant with the matrix. This coating is probably a sample of the original magma involved in the Mamaku Ignimbrite eruption.

While the morphology of groundmass microphenocrysts and fracturing of the margins of the andesitic bleb indicate rapid cooling, the larger phenocrysts of pyroxene, plagioclase and biotite indicate an earlier, drier, phase of crystallisation. The sudden transition between the two crystallisation phases suggests intrusion of the andesitic magma into the silicic chamber. The temperature difference between rhyolitic and mafic magmas would probably have been sufficient to cause the rapid cooling apparent in the andesitic blebs of uMI and the transfer of heat from mafic magma may have caused vesiculation of the rhyolitic melt possibly leading to eruption initiation.

3.4 Major and trace elements

Pumice clasts and andesitic blebs were extracted and analysed by XRF at the University of Canterbury following the method outlined in Appendix 2.

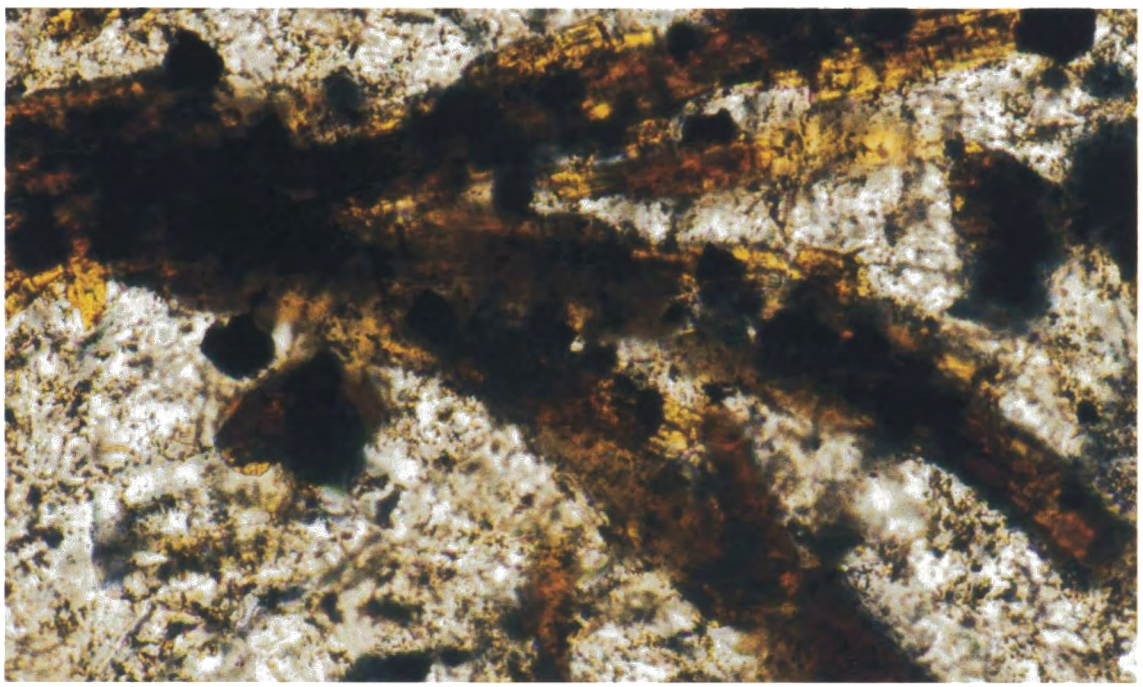

Figure 3.1a. The splayed terminus of a hornblende microphenocryst in the groundmass of an andesitic bleb. These hornblende crystals are long and thin often with splayed ends indicating undercooling of the magma. View is 1 mm left to right.

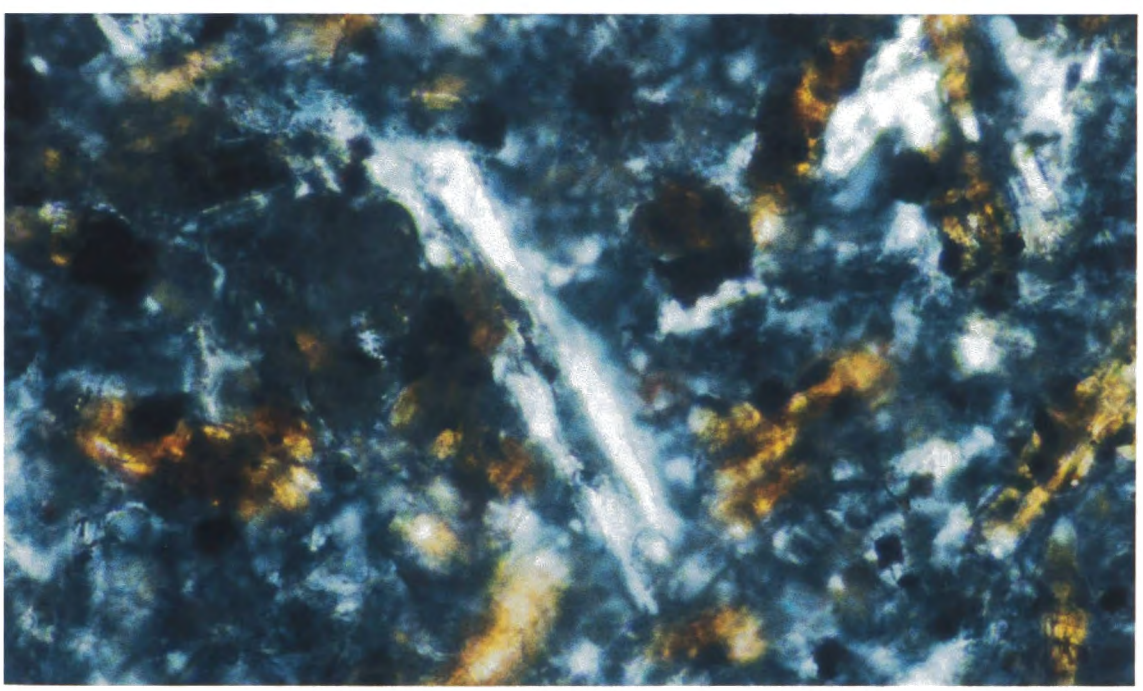

Figure 3.2b. A skeletal plagioclase crystal from the groundmass of an andesitic bleb also indicative of undercooling. View is 1 mm left to right.

3.4.1 Whole pumice chemistry from lower Mamaku Ignimbrite

Pumice clasts from the lower ignimbrite range from dacitic (66.0-69.7 wt% SiO_2; type 3 pumice) to rhyolitic (70.2-76.0 wt% SiO_2; pumice types 1and 2; Fig 3.3). All lMI pumice clasts are metaluminous to peraluminous and have possibly been affected by secondary leaching of alkalis (Fig. 3.4). There is a slight increase in K_2O content with increasing SiO_2 with one high-K pumice clast (Fig. 3.5). The rhyolitic pumice types 1 and 2 can be clearly separated based on Rb/Sr ratios (Fig. 3.6).

Type 1 pumice clasts vary between 71.9-76.0 wt% SiO_2. Type 1 is low in Al_2O_3, Fe_2O_3, TiO_2, CaO and Na_2O, and high in K_2O when graphed against SiO_2 (Fig. 3.7) and high in Ba, and low in Sr, Zr and Zn against Rb (Fig. 3.8) compared with types 2 and 3.

Type 2 pumice clasts range between 70.2-74.1 wt% SiO_2 and has chemistry intermediate between pumice types 1 and 3. Zn, Zr and Sr concentrations all decrease with increasing Rb. Ba exhibits no distinct pattern having a wide range of values over a small variation in Rb abundance. Al_2O_3, Fe_2O_3, TiO_2 and CaO all decrease whereas K_2O increases in concentration with increasing SiO_2. Na_2O abundance in type 2 pumice clasts shows no clear relationship with increasing SiO_2. A trend line through the chemistry of type 2 pumice would connect types 1 and 3 on most chemical plots.

Only three dacitic type 3 pumice samples have been analysed. K_2O concentration is low whereas Al_2O_3, Fe_2O_3, TiO_2, CaO and Na_2O are all high compared with types 1 and 2. Zn, Zr and Sr are of relatively high abundance in type 3 pumice clasts.

The enrichment in K_2O and depletion of other majors with increasing silica content is consistent with fractionation of mafic minerals from the magma and crystallisation of plagioclase feldspar. Rb concentration increases gently with increasing SiO_2 whereas Sr content decreases sharply. Enrichment of Rb and depletion of Sr with increasing SiO_2 from type 3 → 1 is also consistent with crystallisation of plagioclase feldspar. Decreasing CaO, and Na_2O is also consistent with removal of plagioclase from the system. Pumice types 1, 2, and 3 lie on the same major and trace element trends suggesting all 3 types are petrogenetically related. No major compositional gaps exist between the three pumice types suggesting they evolved in a gradationally zoned magma chamber. The decrease in TiO_2, Fe_2O_3 (type 3 → type 1) is thought to represent crystallisation of mafic phases such as magnetite and pyroxene.

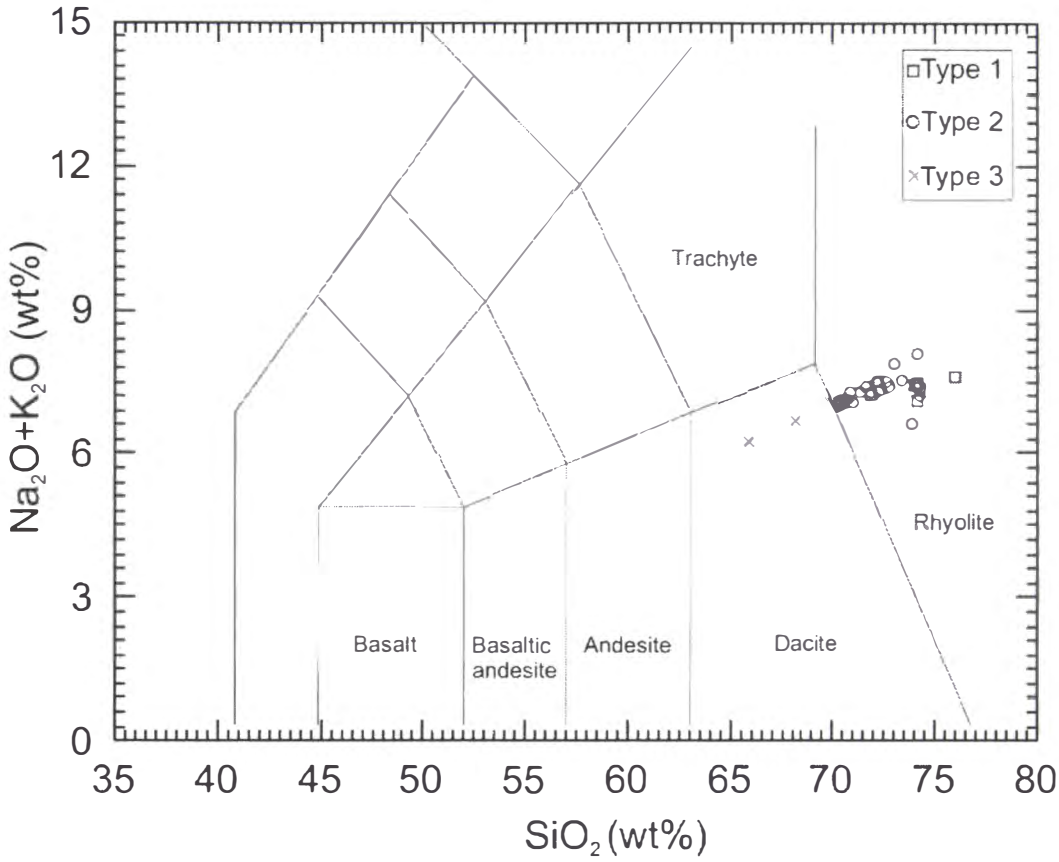

Figure 3.3. Total alkalis-silica diagram of pumice clasts from lMI (after Le Maitre, 1989). Pumice clasts range from dacite to high silica rhyolite.

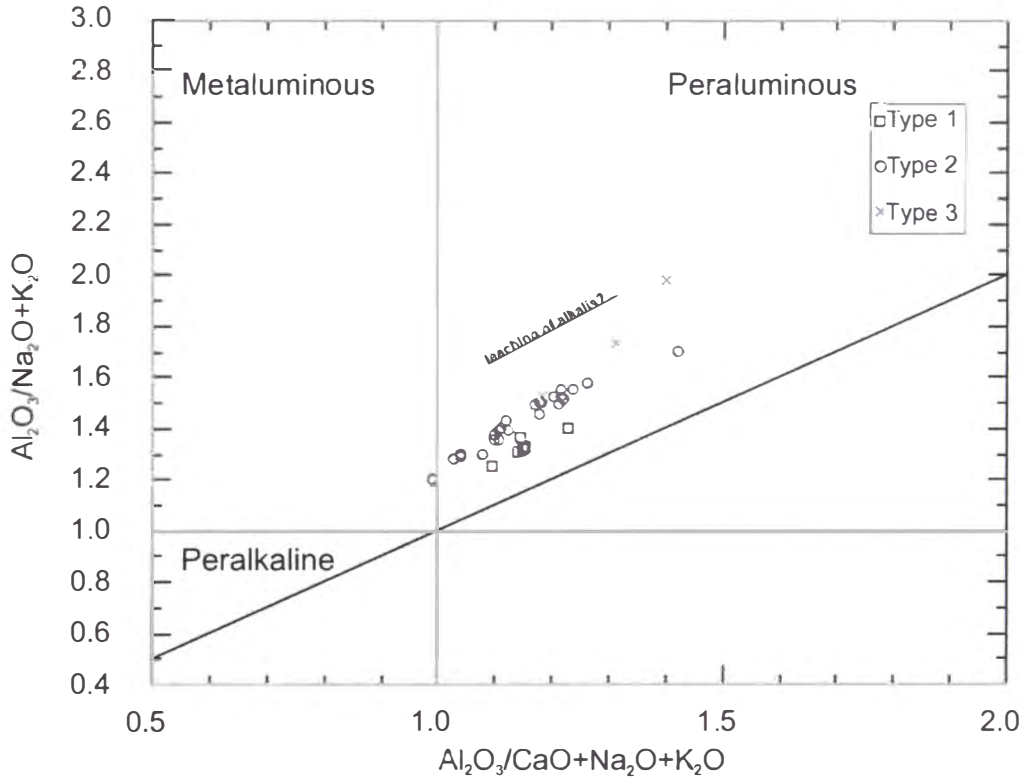

Figure 3.4. Alumina saturation index plot of Mamaku Ignimbrite pumice chemistry. The range may be due to some secondary leaching of alkalis from the pumice clasts. After Maniar and Piccoli (1989).

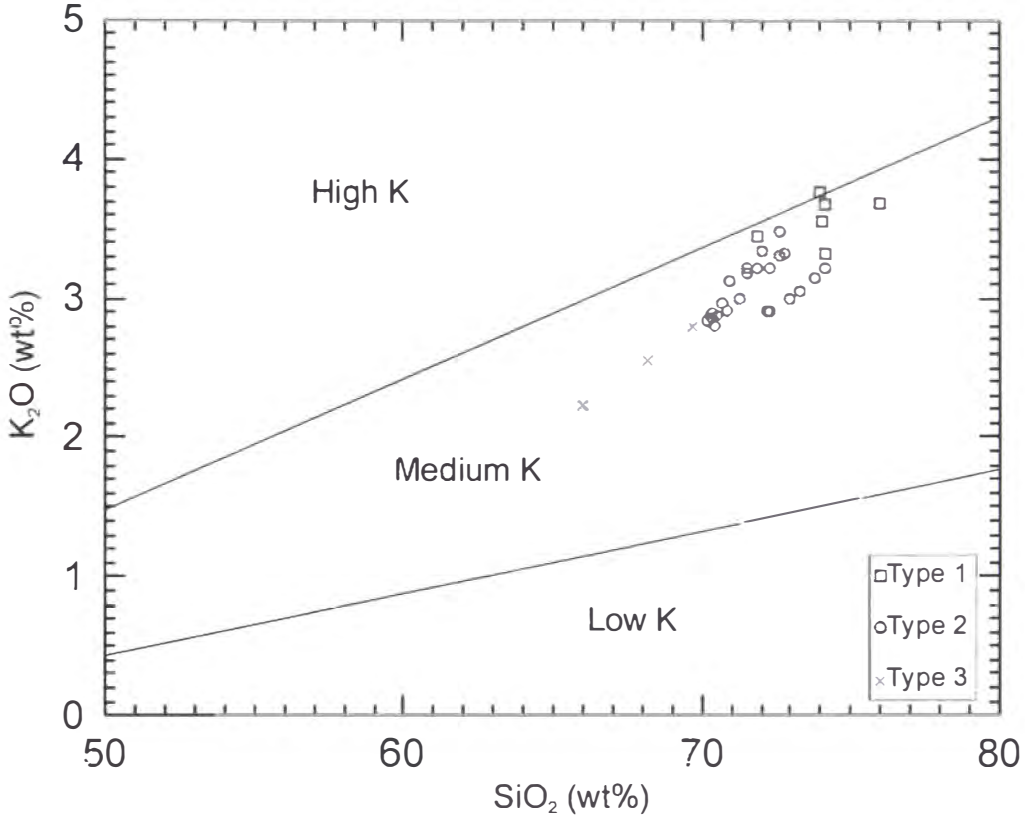

Figure 3.5. K_2O versus SiO_2 plot showing the increase of both components from less to more evolved pumice types.

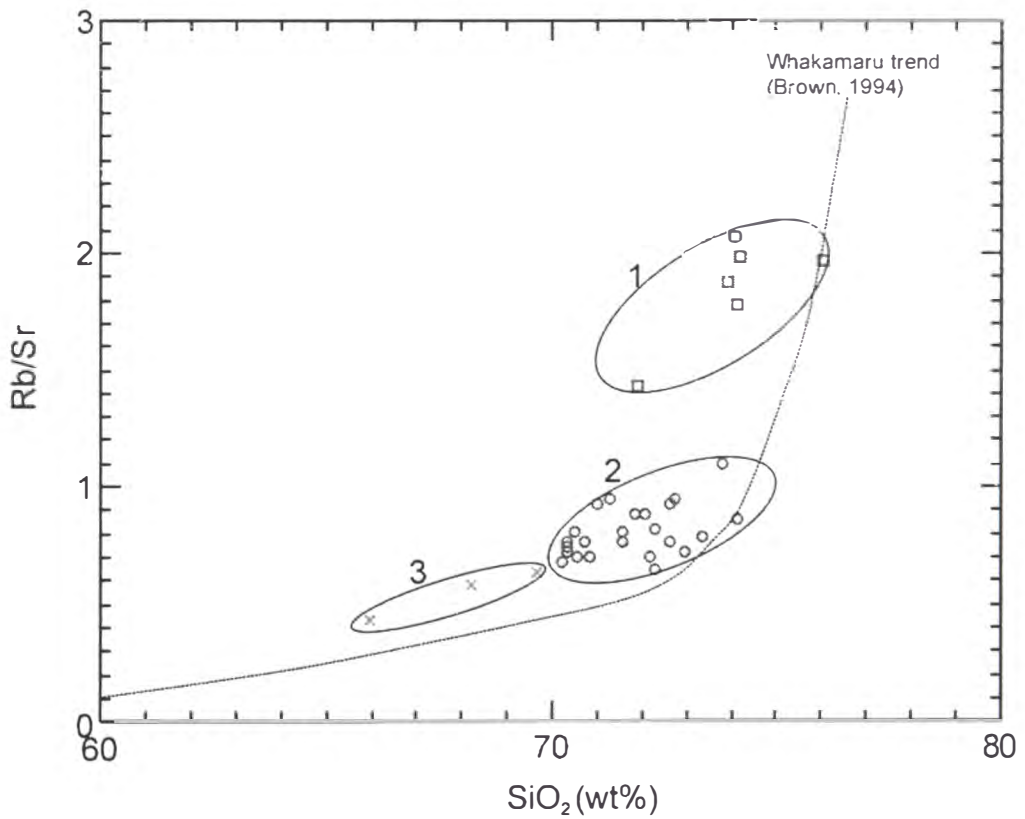

Figure 3.6. The three pumice types can be separated according to their Rb/Sr ratios. Types 1 and 2 are clearly distinguishable from each other.

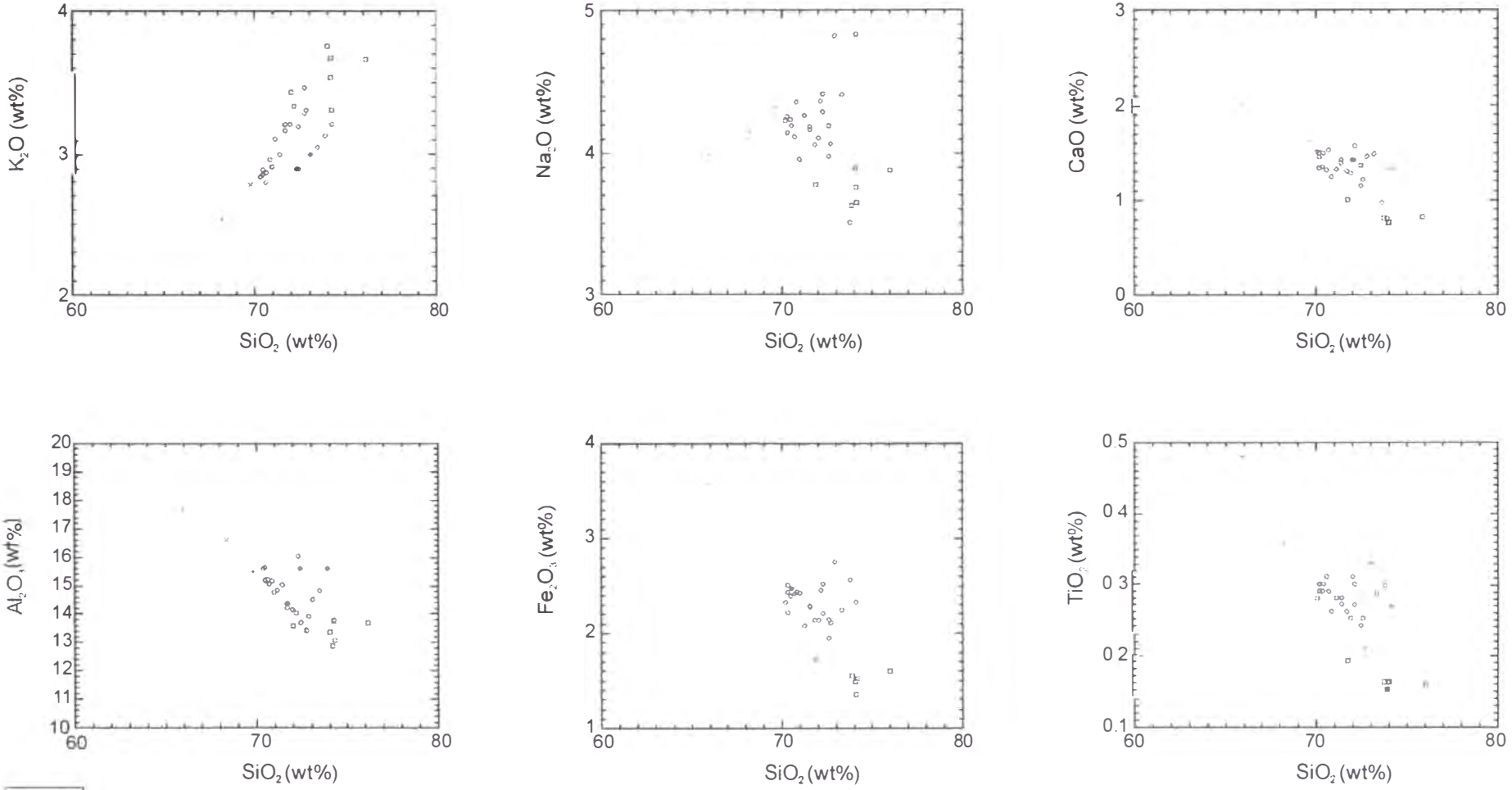

Figure 3.7. Major element variation versus silica content. The increase in K_2O and decrease in Na_2O and CaO is consistent with the removal of plagioclase from the melt. Decreases in TiO_2 and Fe_2O_3 are likely caused by crystallisation of pyroxene and magnetite.

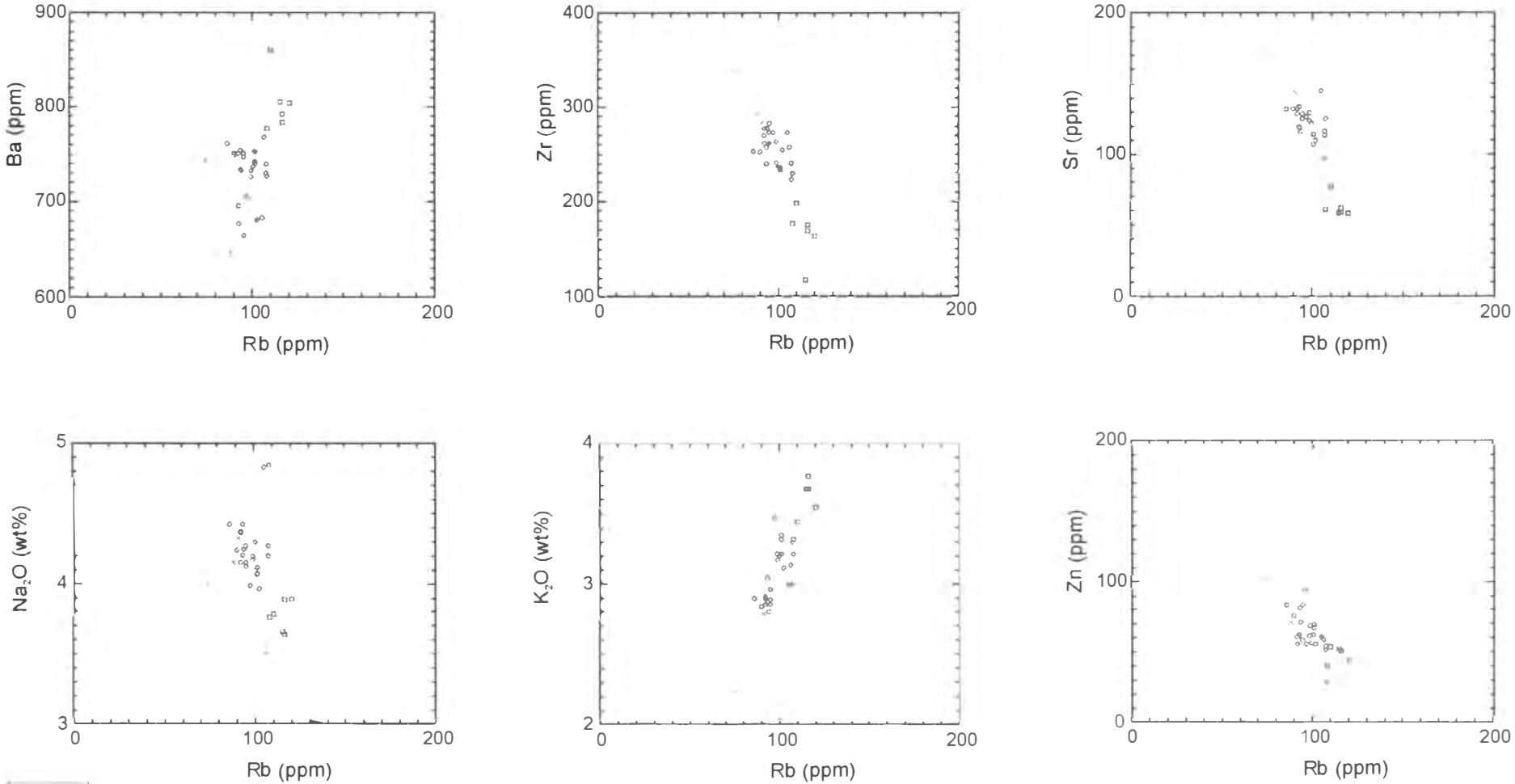

Figure 3.8. Major and trace element data plotted against Rb. Sr and Na both decrease with increasing Rb, while K_2O and Ba increase consistent with plagioclase dominated fractionation. The increase in Ba is inconsistent with plagioclase fractionation and is probably due to fractionation of pyroxene and quartz.

The different pumice types are not separated stratigraphically in Mamaku Ignimbrite. This indicates contemporaneous eruption of all pumice types. Type 2 pumice is by far the most common type suggesting it dominated the pre-eruptive magma chamber. All pumice types (1, 2, and 3) lie on the same major and trace (standard and normalised) element trends (Figs 3.7, 3.8, and 3.9) further suggesting a petrogenetic relationship between all the corresponding magma types (normalised trace element trends are typical of TVZ rhyolite).

Raleigh fractionation vector modelling using the dominant phenocrysts of the various pumice types demonstrates that type 1 pumice compositions can be formed from a type 3 magma parent (Fig. 3.10, table 3.1); 20% crystal fractionation of type 3 magma will generate a daughter of type 1 with type 2 magma composition intermediate stage.

Trace element plots show enrichment of large ion lithophiles elements (LILE) relative to high field strength elements (HFSE). Sr is strongly depleted from type 3 → type 1 indicating fractionation of plagioclase. Sr is most strongly depleted in type 1 pumice clasts consistent with lower CaO and Na_2O contents of this pumice type.

Mineralogy of the different pumice types is consistent with whole pumice chemical trends. Quartz content increases from type 3 → 1 consistent with the increase in SiO_2 content on chemical plots (see section 3.4). The decrease in abundance of plagioclase, pyroxene, and Fe/Ti oxides is consistent with concentration decreases in FeO, Al_2O_3, Na_2O, CaO, and TiO_2 type 3→ type1.

3.4.2 Pumice chemistry from upper Mamaku Ignimbrite

Pumice clasts from uMI have been extensively affected by VPA. VPA is most noticeable in the distribution of the major elements. Two groups of pumice can be distinguished in accepted uMI analyses. The two groups correspond to pumice types 1 and 2 of lMI. uMI pumice chemistry is separated from that of lMI pumice by an approximately 2-3 wt% increase in SiO_2 (Fig. 3.11). There is also a slight increase in K_2O (Fig. 3.11). The increase in SiO_2 and K_2O in turn reduces all other major element percentages. VPA is characterised in Mamaku Ignimbrite by the deposition of tridymite, cristobalite, alkali feldspar, and albite. Minerals deposited from the vapour phase fill pore spaces in the rock including pumice vesicles. Tridymite crystals are commonly seen as hexagonal plates under SEM (see Fig. 2.21). Albite, alkali feldspar

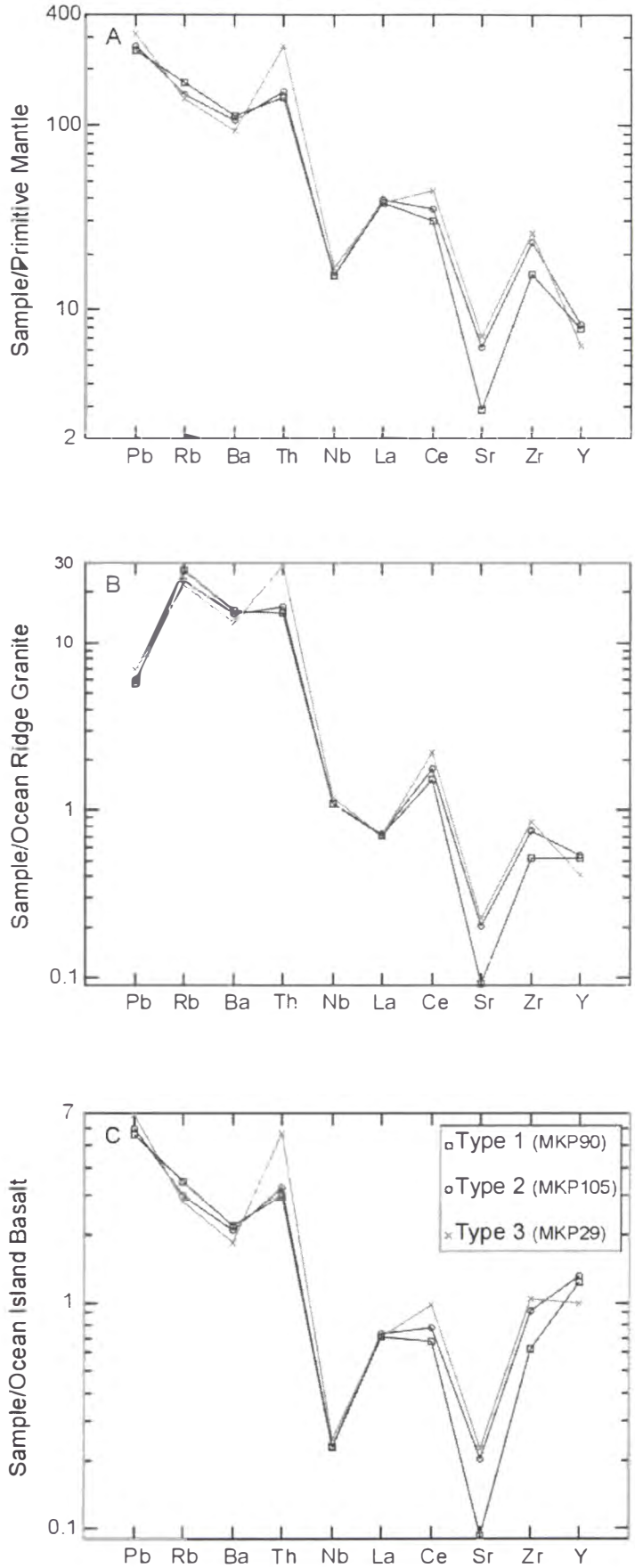

Figure 3.9. Trace element geochemistry normalised against: A) Primitive mantle (from Sun and McDonough, 1989), B) Ocean Ridge Granite (from Pearce et al., 1984), and C) Ocean Island Basalt (from Sun and McDonough, 1989). Normalised trends are typical of TVZ trends.

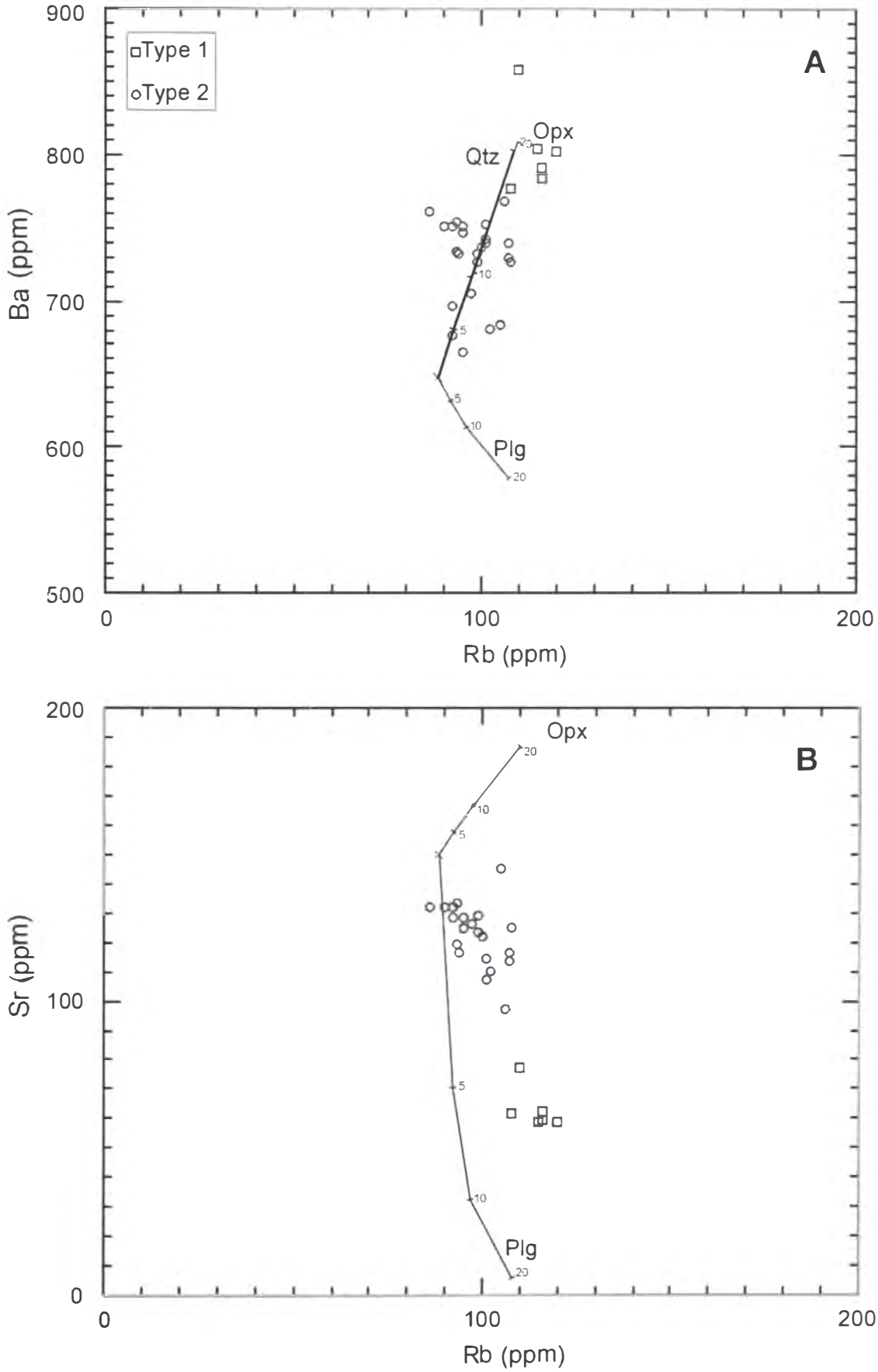

Figure 3.10. Vector modelling of magma evolution by Raleigh fractionation of a type 3 parent magma (MKP29). The trace element distribution of type 1 and 2 pumice clasts can be achieved by 20% fractionation of a type 3 parent. Distribution coefficients are from Arth (1976) and Nash and Crecraft (1985), as quoted by Rollinson (1993).

Calculation of Raleigh fractionation vector paths

Partition coefficients for rhyolitic liquids

	Plagioclase	Orthopyroxene	Quartz
Rb	0.105	0.003	0.041
Sr	15.633	0.009	N/A
Ba	1.515	0.003	0.022

Initial composition: Rb 88 ppm; Sr 150 ppm; Ba 648 ppm type 3 pumice (MKP29)

Using Raleigh fractionation equation:

$C_L/C_O = F^{(D-1)}$

C_L = wt concentration of trace element
C_O = wt concentration of trace element in parent liquid
F = Fraction of melt remaining
D = Distribution coefficient

	Plagioclase	Orthopyroxene	Quartz
5%			
Rb	92.1	92.4	92.4
Sr	70.8	157.8	-
Ba	631.1	682.0	681.3
10%			
Rb	96.7	97.7	97.4
Sr	32.1	166.5	-
Ba	613.8	719.8	718.3
20%			
Rb	107.5	109.9	109.0
Sr	5.7	187.1	-
Ba	577.7	809.5	806.0

Table 3.1. Method of calculation of Raleigh fractionation vector paths shown in Fig. 3.10. Partition coefficients from Arth (1976) and Nash and Crecraft (1985). Raleigh fractionation equation taken from Rollinson (1993).

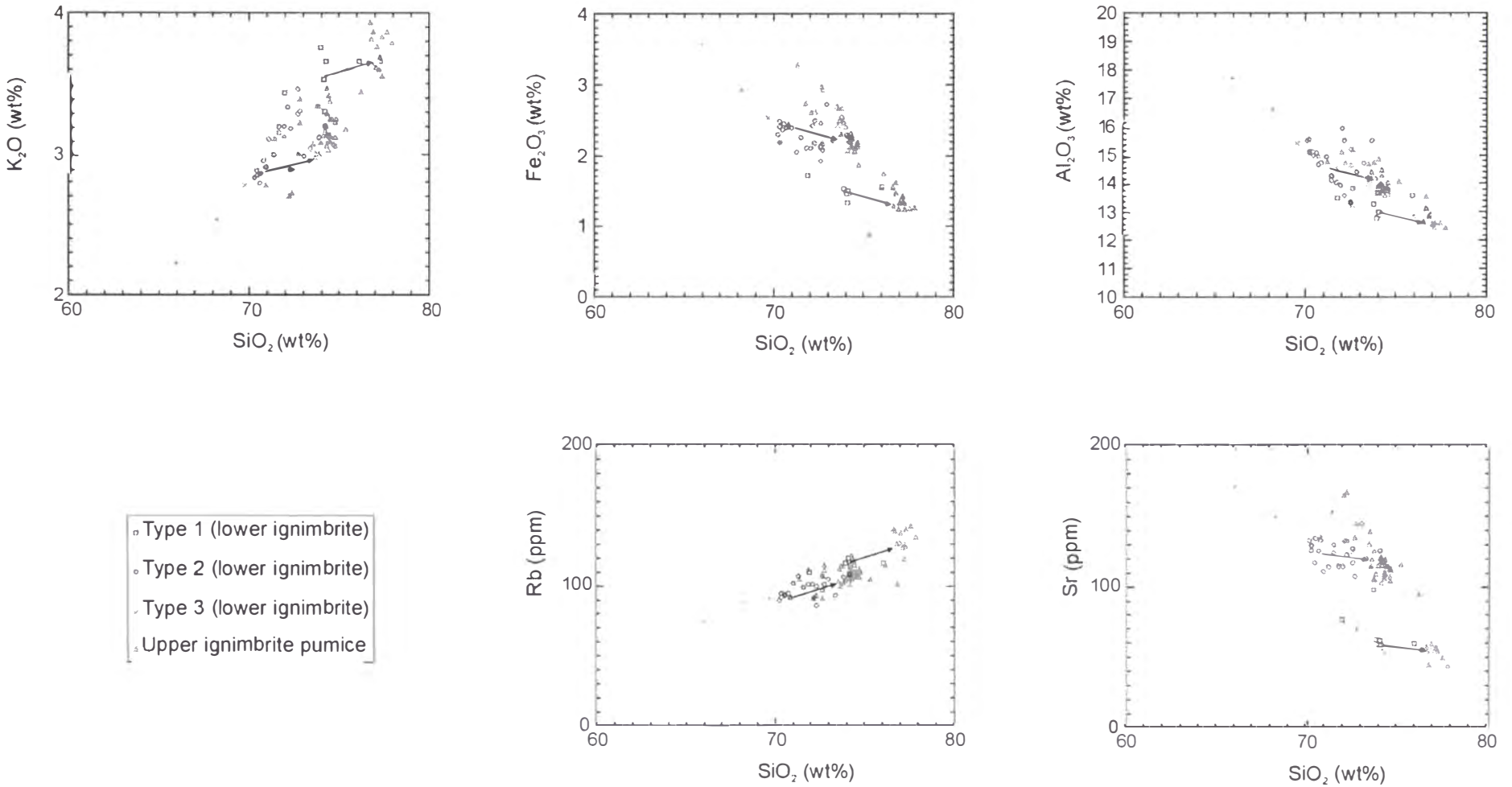

Figure 3.11. Trace and major element abundances of lMI and uMI pumice. Note the higher K_2O and Rb abundances in uMI pumice. This is probably due to the deposition of alkali feldspar from the vapour phase. Decreases in the concentrations of Al_2O_3 and Fe_2O_3 are probably due to increases in SiO_2 and K_2O.

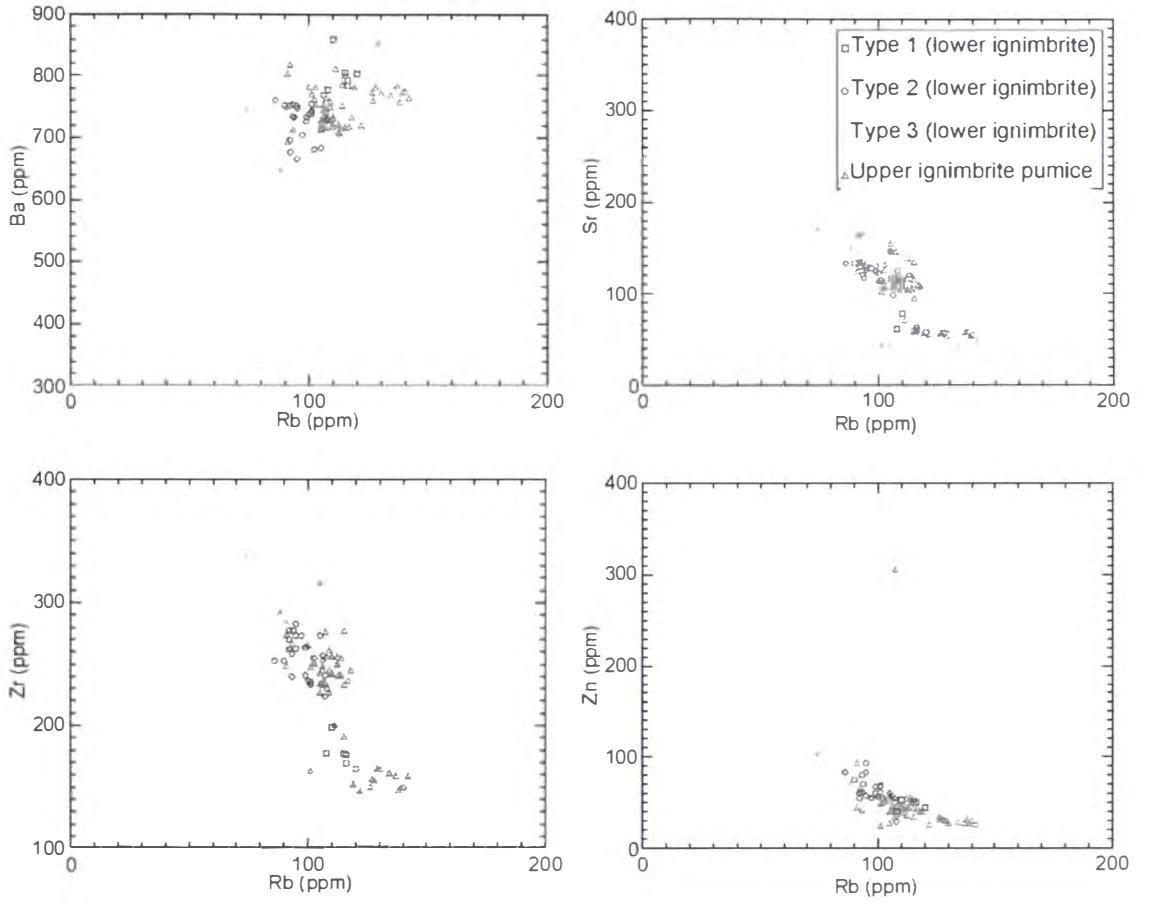

Figure 3.12. Selected trace element plots for lMI and uMI pumice clasts. VPA has had little effect on trace element abundance with only small variations in Ba, Sr, Zr, and Zn.

and cristobalite are seen as radiating crystal aggregates (similar to spherulitic growths; see Fig. 2.21). It is the deposition of these minerals that cause the SiO_2 and K_2O enrichment. Interestingly Loss on Ignition values are less in pumice clasts altered by vapours than pumice clasts that appear unaffected. This is most likely due to the loss of water contained in glass during the devitrification of uMI pumice clasts.

VPA seems to have had little affect on pumice trace element composition with only slight variations (Figs 3.12). Rb has increased slightly whereas other trace elements are little affected. The increase in Rb concentration can be accounted for by the deposition of alkali feldspar during vapour phase alteration and devitrification.

Normalised trace element plots show that uMI pumice clasts have the same variations as those from lMI (Fig. 3.13).

3.4.3 Andesitic blebs of upper Mamaku Ignimbrite

Andesitic blebs are located entirely within uMI, and because of this have all been affected by VPA. Although pumice clasts from uMI were omitted from geochemical interpretation the presence of the andesitic blebs is important to the interpretation of the magma chamber dynamics and have been included. The blebs range between 58.4-61.8 wt% SiO_2. SiO_2 content will have been raised slightly due to the effects of VPA, although these effects will be less than has occurred in silicic pumice clasts as the andesite blebs are of much lower vesicularity (<1 vol%). Normalised trace element plots do not follow the same path as pumice types 1, 2, and 3 (Fig. 3.14), suggesting that the andesitic magma had a different petrogenesis. Morphology of the andesite blebs suggests they were liquid on eruption (see Fig. 2.13). No mixed or mingled andesite-rhyolite pumices has been found in Mamaku Ignimbrite.

3.5 Mineral chemistry

Mineral chemistry was analysed using the JEOL Superprobe 733 at the Analytical Facility of Victoria University of Wellington. Methods of analysis are outlined in Appendix 3.

3.5.1 Plagioclase

Plagioclase is the dominant phenocryst in all Mamaku Ignimbrite pumice clasts. Crystals are up to 2 mm long, euhedral to subhedral or broken. Plagioclase in plagioclase-pyroxene aggregates are thought to represent fragments of the magma chamber wall and not representative of magmatic conditions. Crystals in such aggregates were avoided during EPMA analysis.

Plagioclase is normally zoned in all pumice types varying between An_{31-17}, An_{47-15}, and An_{43-20}, all andesine-oligoclase, for pumice types 1, 2 and 3 respectively. Composition of plagioclase varies between An_{46-25} in andesitic blebs and An_{33-17} in pumice clasts from the basal sequence. The generally less calcic plagioclase of pumice types 1 and 2 compared with plagioclase of type 3 pumice is consistent with magma evolution from type 3→ type 1 (and associated increase in SiO_2 content).

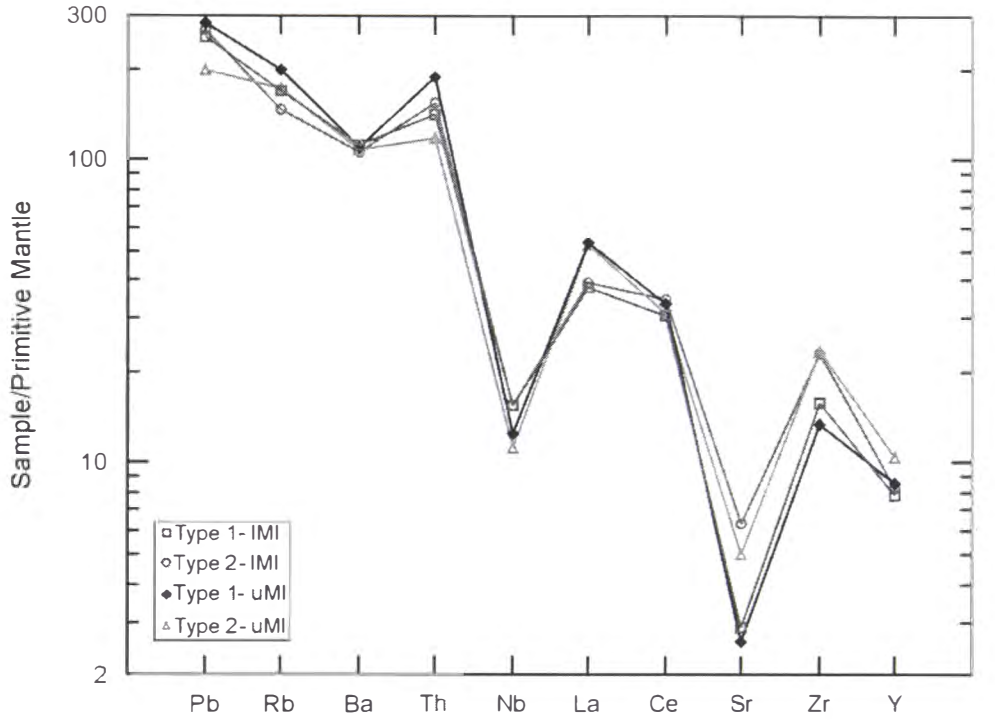

Figure 3.13. Spider diagram of uMI and lMI pumice trace and rare earth element chemistry normalised by primitive mantle chemistry (from Sun and McDonough, 1989). uMI pumice trace element chemistry is similar to that from lMI and variations typical of TVZ rhyolite.

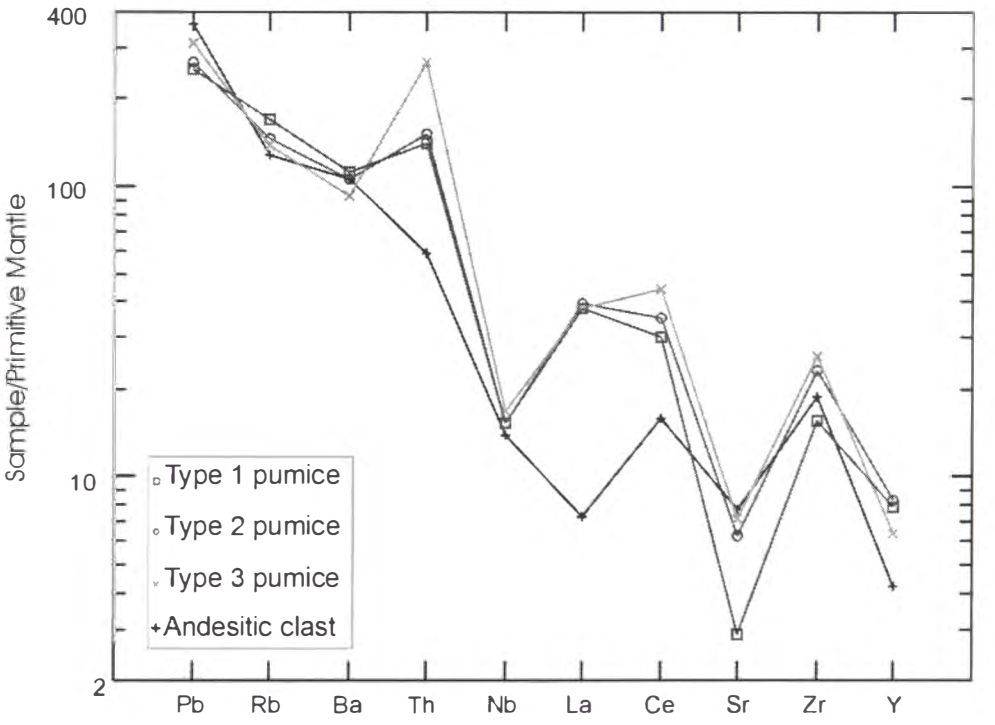

Figure 3.14. Spider trace element plot for lMI pumice and andesitic blebs normalised against primitive mantle (from Sun and McDonough, 1989). The andesitic bleb is notably depleted in Th, La and Ce compared with lMI pumice clasts and has a discordant normalised pattern suggesting that the andesitic and silicic magmas were not petrogenetically related.

3.5.2 Pyroxene

Orthopyroxene is the dominant mafic phenocryst typically comprising 0.5-1% (by volume) of pumice clasts. Augite is also present but in much lesser quantities (<<1 vol%). Pyroxene crystals are up to 2 mm long and 0.25-0.5 mm in cross section (perpendicular to their c-axes). Pyroxenes were analysed from mineral separates and polished thin sections. As with plagioclase, pyroxene crystals in glomerocrysts were avoided during analysis.

Pyroxene crystals in Mamaku Ignimbrite pumice clasts are often zoned, becoming more Fe-rich towards their margins. They vary between $En_{56-34}Wo_{3-2}Fs_{63-43}$, $En_{59-40}Wo_{3-2}Fs_{57-38}$, and $En_{48-41}Wo_{3-2}Fs_{56-50}$ in pumice types 1, 2, and 3 respectively, and $En_{43-39}Wo_{2}Fs_{59-55}$ in pumice clasts from the basal tephra sequence (Fig. 3.15). Two populations of pyroxene exist in the andesitic blebs, high and low Ca (orthopyroxene and augite respectively; Fig. 3.16). Orthopyroxene in andesitic blebs vary between $En_{74-50}Wo_{3-2}Fs_{47-23}$, whereas augite varies between $En_{45-44}Wo_{42-37}Fs_{19-13}$.

3.5.3 Glass

Mamaku Ignimbrite pumice glass is all high silica rhyolite varying between 75-79 wt% SiO_2 (75-79 wt%, 70-76 wt%, and 75-77 wt% for types 1, 2, and 3 respectively).

Pumice clasts of the basal sequence vary between 72 and 75 wt% SiO_2. The groundmass of the andesitic blebs is microcrystalline and analysis by EPMA is not feasible.

3.5.4 Accessory minerals

Hornblende is present in trace amounts in pumice types 1 and 3 and identified by EPMA as calcic hornblende (edenite). In andesitic blebs rare olivine phenocrysts were seen and are Fo_{85}.

3.6 Water content

Water content estimates are based on experiments carried out by Naney (1983). Naney used set compositions and applied varying temperatures and pressures to determine the stability fields of ferromagnesian minerals in silicate melts. The mineral assemblage

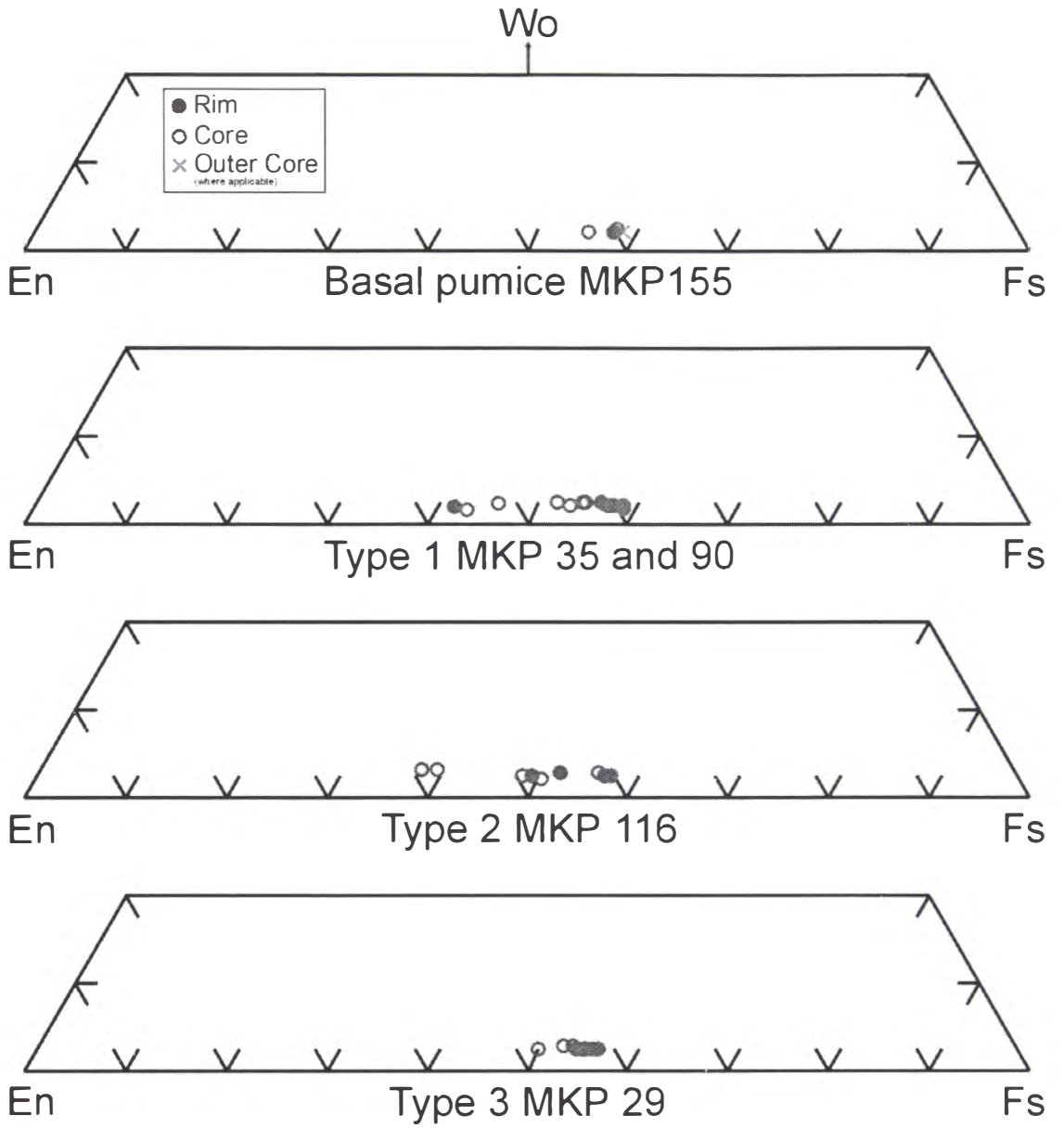

Figure 3.15. Composition of orthopyroxene from pumice clasts of lMI and the basal sequence. Orthopyroxene are dominantly ferrosilite becoming more Mg enriched towards their rims.

seen in all Mamaku Ignimbrite pumice types suggests the magma contained between 2.5 and 5 wt% water immediately prior to eruption (N.B. This is a 'best fit' situation, as not all the minerals present in Naney's descriptions occur in Mamaku pumice clasts).

3.7 Geothermometry

Analysis of Fe/Ti oxide pairs is one of the most common and reliable methods of estimating the temperature of an eruption. The method was pioneered by Buddington and Lindsley (1964) and further developed by Andersen and Lindsley (1988). More

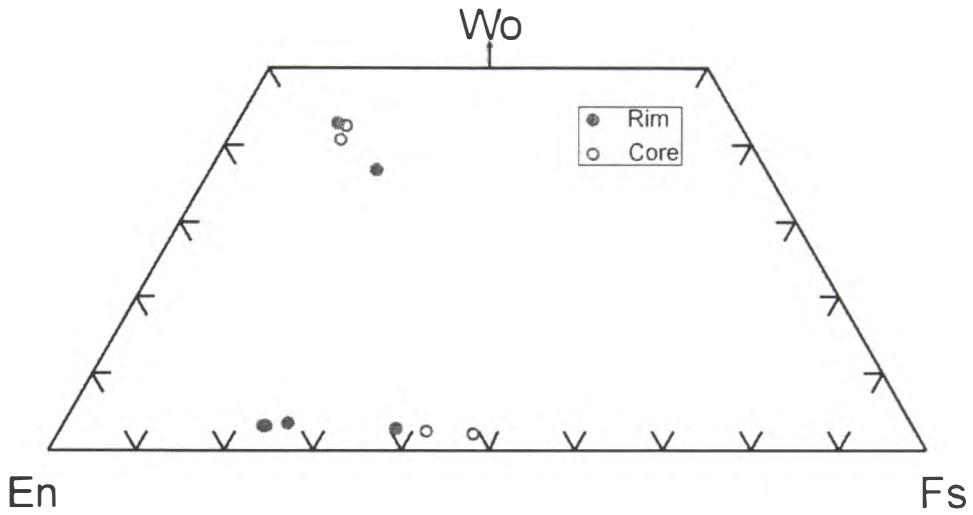

Figure 3.16. Compositions of pyroxene in MKP120 (andesitic bleb). Andesitic blebs contain both orthopyroxene and augite. This again suggests that they had a different petrogenesis to the silicic pumice types. Orthopyroxene becomes more En-rich towards rims.

recently Sack and Ghiorso (1991) have refined the Fe/Ti oxide geothermometer to give more accurate temperature estimates and their method is used here. Analysis of obviously exsolved magnetite was avoided. Magnetite and ilmenite analysed were predominantly inclusions in pyroxene crystals. Crystals in contact with pumice glass or at the margins of pyroxene phenocrysts were favoured during analysis as these were assumed to be in contact with the melt immediately prior to eruption.

Temperatures calculated from Mamaku Ignimbrite pumice clasts are anomalously low. Temperature estimates for a type 1 pumice clast range between 630-664 °C (with the exception of one calculation of 780 °C), a type 2 pumice clast vary between 718 and 740 °C, and a type 3 pumice clast vary between 665-724 °C. Pumice clasts from the basal sequence were erupted at approximately 750 °C. Oxygen fugacity varies between log fO_2 -18.58 to -21.98 for type 1, -16.07 to -16.59 for type 2, and -16.96 to -18.81 for type 3 pumice clasts.

Magnetite and ilmenite from andesitic blebs were all extensively resorbed, considered not in equilibrium, and therefore not analysed.

The temperatures calculated here are low compared with other TVZ ignimbrites (cf. 802-820 °C for Kaingaroa (Beresford, 1997), and 730-820 °C for Whakamaru (Brown,

1993) ignimbrites (Whakamaru dominantly ranged between 795-821 °C, with only one pumice type ranging between 730-750 °C)). Only one temperature calculated from the type 1 pumice clast, the three from type 2, and the estimate from the pumice clasts of the basal sequence are comparable. Low magma temperatures are usually accompanied by a high phenocryst content (indicated by phenocryst abundance histograms of Ewart (1967)). Mamaku Ignimbrite pumice clasts are of low phenocryst contents (4-7 vol%; cf. 10-40 vol% of Whakamaru Ignimbrite pumice clasts, Brown (1994)). Low temperature estimates of some rhyolite lava analyses noted by P. Shane (pers. comm., 2000) are often due to disequilibrium of Fe/Ti oxide phases. These two lines of evidence suggest that although magnetite and ilmenite pairs were sought that should have been in equilibrium (avoiding magnetite with lines of exsolution, probing grains that would have been in contact with the magma) they were not, and that the temperatures calculated here should be treated with caution.

3.8 Comparison with other TVZ rhyolites

Mamaku Ignimbrite pumice chemistry has been compared with the TVZ pumice data of B.F. Houghton and S. D. Weaver (unpublished data), Briggs et al. (1993), and Sutton et al. (1995) as outlined in Brown (1994; Fig. 3.17). Mamaku Ignimbrite pumice clasts lie wholly within the Zn-Zr range of other TVZ rhyolites. The Zr variation of Mamaku Ignimbrite pumice clasts of 221 ppm is large. Only Ohakuri pumice samples have a larger range, and in Ohakuri this may be attributable to more than one magma chamber (M. Nakagawa, pers. comm., 1997). Similar to the Zn-Zr plot, the Rb-Sr variation is large relative to other TVZ ignimbrites. The Sr range is comparable only with the Whakamaru group pumice types and Zn-Zr range is broad compared with all other TVZ ignimbrites. Both plots illustrate fractionation trends of the Mamaku magma system similar to Whakamaru (Rb-Sr, and Zn-Zr), and Marshall (Zn-Zr) ignimbrites. The wide range of compositional values outlined in Fig. 3.17 (A and B), along with their linear fractionation trend indicate strong zonation of whole pumice chemistry compared with other TVZ ignimbrites (with the exception of Whakamaru Ignimbrite).

Briggs et al. (1993) observed two styles of zoning in Mangakino ignimbrites: 1) Ignimbrites with continuous compositional variations in major and trace element chemistries, and similar isotopic compositions (due to fractional crystallisation of a single magma body), and 2) those with major and trace element and isotopic compositions resulting due to pre- and syn-eruptive mixing i.e. eruption of multiple

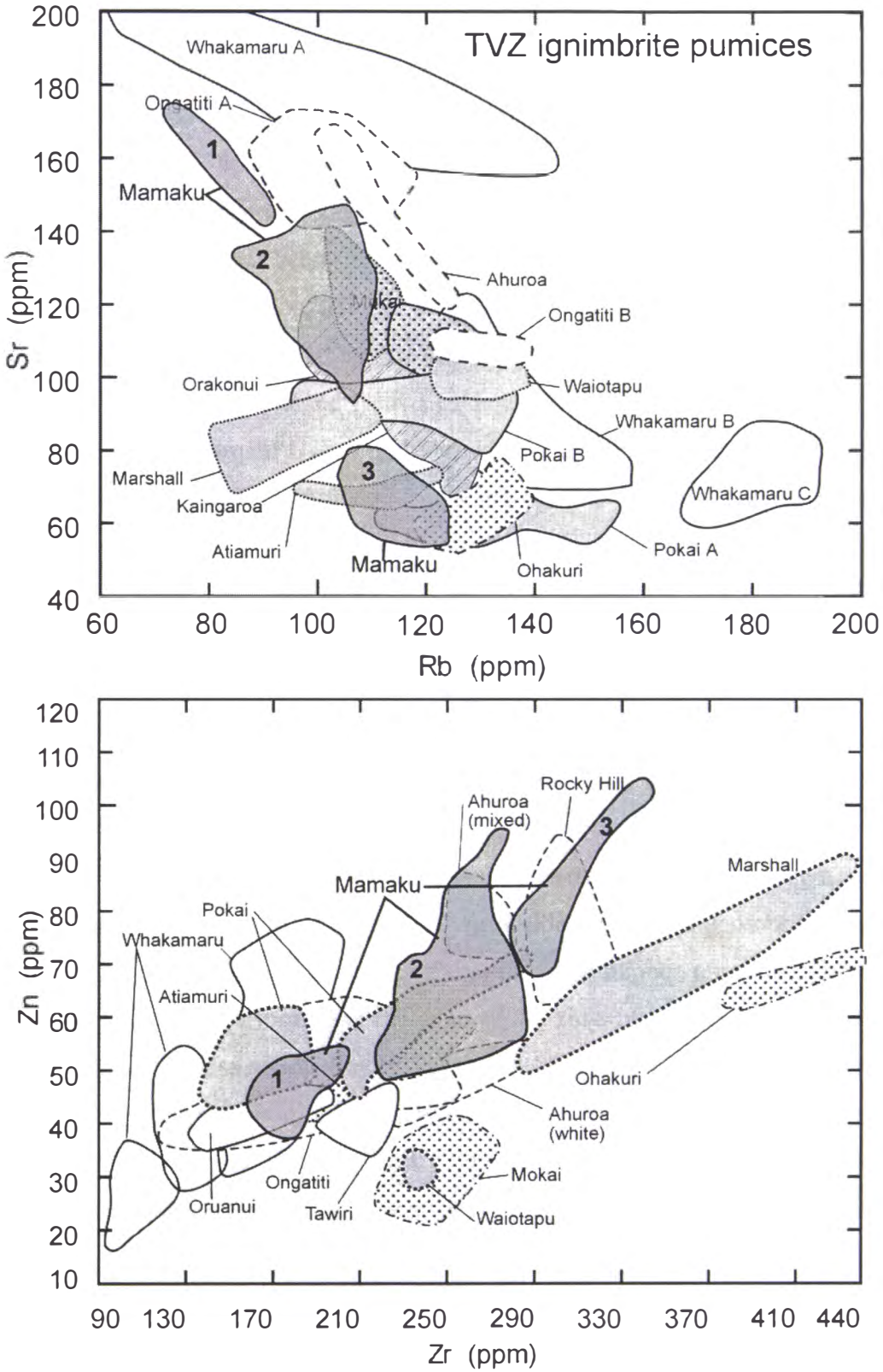

Figure 3.17. Comparison of Mamaku Ignimbrite pumice chemistry with other ignimbrites of TVZ. TVZ ignimbrite data taken from B.F. Houghton and S.D. Weaver (unpublished data), Briggs et al. (1993), Brown (1994), and Sutton et al., (1995) as outlined in Brown (1994), and Beresford (1997). Mamaku Ignimbrite pumice clasts have wide Sr, Zr, and Zn ranges compared with most other TVZ ignimbrites. Fields 1, 2 and 3 correspond to pumice types 1, 2, and 3 respectively.

magma bodies. Briggs et al. (1993) interpreted type 1 zonation is a function of residence time in the magma chamber. Mangakino is the oldest known rhyolitic centre of TVZ active perhaps before inauguration of rifting and crustal thinning, which would have allowed magma to accumulate and fractionate without much tectonic disturbance (Briggs et al., 1993). Most other authors have noted homogeneous or weakly zoned deposits sourced from central TVZ (e.g. Dunbar et al. (1989), Sutton et al. (1995), and Beresford (1997)) and it has been suggested that the high rate of extension and high heat flow inhibits magma zonation (Briggs et al., 1993; Beresford, 1997). Whakamaru Ignimbrite pumice clasts, studied by Brown et al. (1998), are strongly chemically and thermally zoned and were sourced from a caldera that straddles the present day Taupo Fault Belt. The Whakamaru Group ignimbrites have a combined volume of 1000km^3, the most voluminous single eruptive sequence known in TVZ and were erupted following a quiescent period in TVZ activity (Houghton et al., 1995). Beresford (1997) suggested that it was this period of tectonic and volcanic stability that allowed the large volume of magma to accumulate and fractionate to the extent it did. This may be so, but the same argument does not hold for Mamaku Ignimbrite.

Mamaku Ignimbrite is the youngest welded ignimbrite of TVZ (Murphy and Seward, 1981). It was emplaced following an energetic phase of TVZ activity during which eruption of Matahina, Pokai and Kaingaroa ignimbrites also occurred (Houghton et al., 1995). The combined volume of intra- and extra-caldera Mamaku Ignimbrite was up to 397 km^3 (170 km^3 DRE) making it one of the most voluminous eruptions recorded in TVZ. Rotorua Caldera is located at the edge of the zone of active extension and as a result may have been less affected by rifting than other volcanic centres. The dominant fault trend changes in the vicinity of Rotorua Caldera from NE-SW strike to the south to ENE-WSW strike toward the northeast. Its location therefore may have allowed accumulation and fractionation, in a similar way to the type 1 zoning described by Briggs et al. (1993) at Mangakino Volcanic Centre, by being tectonically less active compared with the rest of TVZ.

3.9 Discussion

A variety of zonation styles (homogeneous to strongly zoned) have been deduced for TVZ ignimbrites and attributed to vigorous magma chamber convection (Blake et al., 1992) strong zonation in the magma chamber (Brown et al., 1998), rhyolite-rhyolite mixing (Carr, 1984), and evacuation of numerous magma chambers (Briggs et al.,

1993). If erupted from multiple magma chambers or from a mixed rhyolite-rhyolite magma chamber the various pumice types in the resultant deposit should lie on discordant major and trace element trends (Briggs et al., 1993; Brown, 1993; Cambray, 1995). Such discordant trends are not seen in Mamaku Ignimbrite pumice chemistry and pumice types 1-3 interpreted to represent a single magma body

Pumice types 1, 2, and 3 are consanguineous based on geochemical trends and fractionation modelling with pumice types 1 and 2 forming in response to plagioclase dominated fractionation from dacitic type 3 magma. This would create a zoned magma chamber, and the similar phenocryst assemblages and lack of large compositional gaps in pumice chemistry suggests that the zonation was gradational.

Andesitic blebs of uMI have distinctly different major and trace element trends, and show evidence of chilling. Because of this the andesitic blebs are thought to represent a discrete magma, unrelated to the dacitic and rhyolitic pumice types, which injected into the magma chamber where it accumulated beneath type 3 magma.

A model of the proposed magma chamber immediately prior to eruption of Mamaku Ignimbrite is shown schematically in Figure 3.18. Only erupted magma has been included in the diagram and layering in the chamber is based on their probable densities. The andesitic magma is only found towards the top of the ignimbrite and it is proposed that it formed a sill-like body immediately beneath type 3 magma.

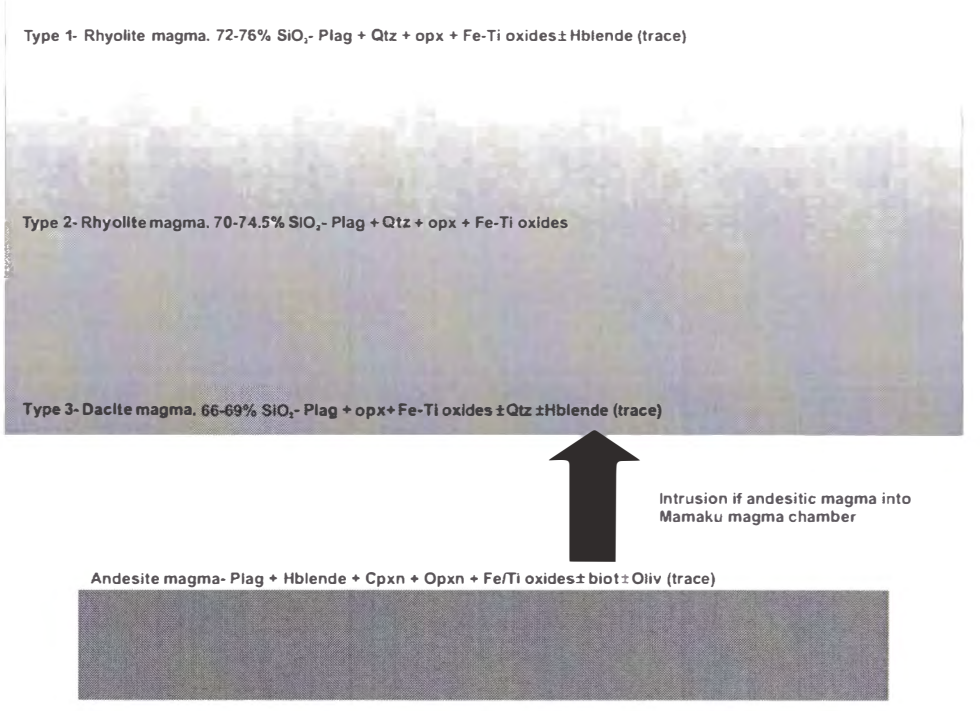

Figure 3.18. Schematic model of the Mamaku magma system. Zonation of the silicic chamber is thought to have been gradational and the andesitic magma to have accumulated as a sill within, or at the base of the type 3 magma.

CHAPTER 4

Rhyolite Domes of Rotorua Caldera

4.1 Introduction

Extrusive rhyolite lavas may both precede and postdate caldera forming activity (Smith and Bailey, 1968), and rhyolite lavas of Rotorua Caldera may equally be split into pre- and post-caldera ages (Fig. 4.1). No dates have yet been published concerning the ages of the lava domes, but relative ages can be determined from relationships with Rotorua Caldera, dome morphology, and cover. Pre-caldera rhyolite domes are present at or just outside the caldera margin, while post-caldera rhyolite lava is present as domes or dome complexes within the caldera.

In this chapter all rhyolite domes associated with Rotorua Caldera have been re-examined geochemically and petrographically in an effort to determine their characteristics, inter-relationships, and their affiliation to Mamaku Ignimbrite pumice types.

4.2 Previous work

Previous work on the Rotorua rhyolite lavas has involved mainly geochemical and petrographic analysis concentrating dominantly on the lavas of Mt Ngongotaha.

Grange (1937) classified all TVZ rhyolite lavas as Haparangi rhyolite. Later Healy et al. (1964) segregated the Haparangi rhyolites into ha_1 and ha_2 based on their relation to various caldera structures. Rhyolite domes surrounding Maroa, and Okataina volcanic centres and Rotorua Caldera termed ha_1 were deemed older than their respective structures, and described as spherulitic and lithic (devitrified). Inside these structures the younger glassy lavas associated with post-caldera dome building were termed ha_2. In recent work Nairn (in prep) has further subdivided the young rhyolite domes based on their ages relative to the Rotoiti Tephra. Those that postdate the tephra are collectively termed ha_3. Nairn (in prep.) further reassigned the rhyolites in order to associate them with specific volcanic centres or calderas, rhyolite lavas of Rotorua termed hr ($hr_{1,2,\text{ and }3}$ referring to pre- and post caldera formation and post Rotoiti Tephra respectively).

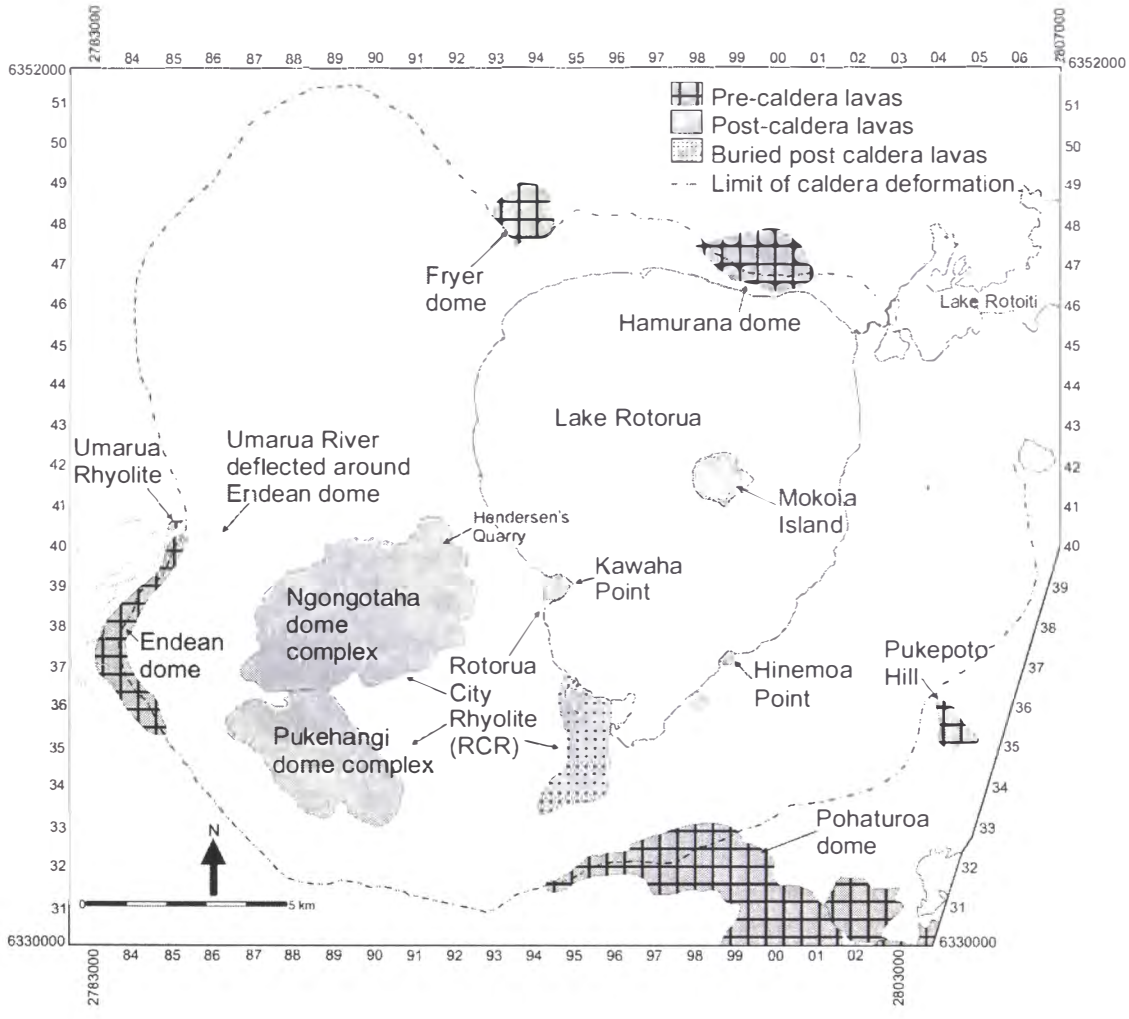

Figure 4.1. Map showing locations of pre- and post-caldera rhyolite domes in and around Rotorua Caldera. Also note Umarua River that diverts around Endean dome before entering Rotorua Caldera.

Ewart (1967 and 1968) analysed the rhyolite domes of Rotorua as part of a general petrographic and geochemical study of TVZ rhyolite lavas. Ewart (1968) grouped the rhyolite lavas of Rotorua according to their crystal contents (modal %) and ferromagnesian assemblages (Fig. 4.2). Crystal content was observed to be between 0 and 30% and ferromagnesian assemblages comprised combinations of hypersthene, hornblende and biotite. He also suggested that all the rhyolite lavas of Rotorua erupted from a single, high level, magma chamber that was recharged with fresh pulses of magma (accounting for domes at various stages/assemblages of crystallisation), but pointed out that Pohaturoa dome has a similar phenocryst assemblage to rhyolite lavas further south.

Shepherd (1991) worked specifically on the post-caldera rhyolites of Rotorua Caldera. He concentrated on Mt Ngongotaha concurring with Ewart's (1968) findings about all

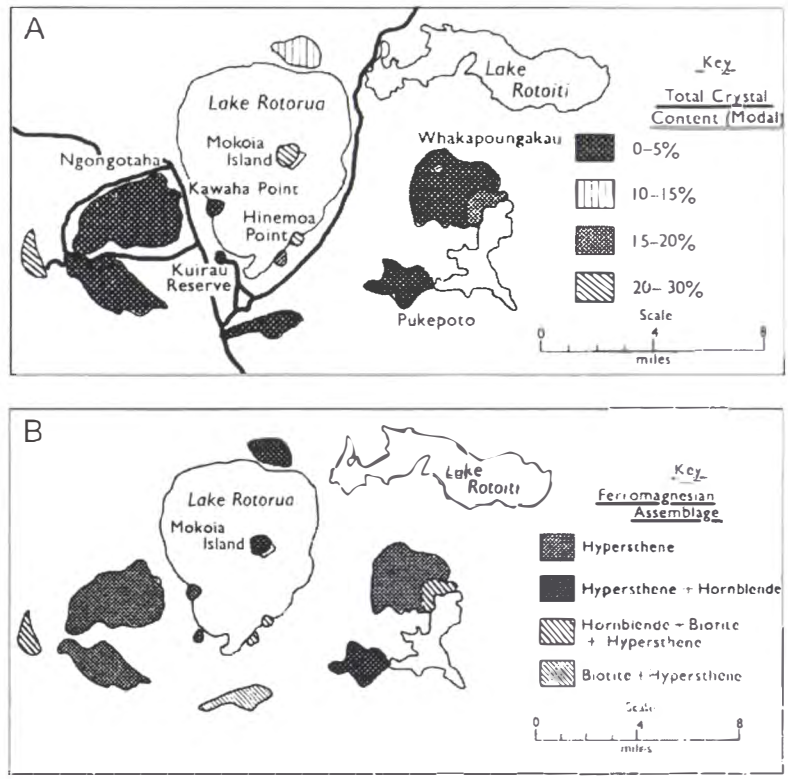

Figure 4.2. Ewart's (1968) classification of Rhyolite domes of Rotorua Caldera. A) According to modal crystal content, and B) according to ferromagnesian assemblages.

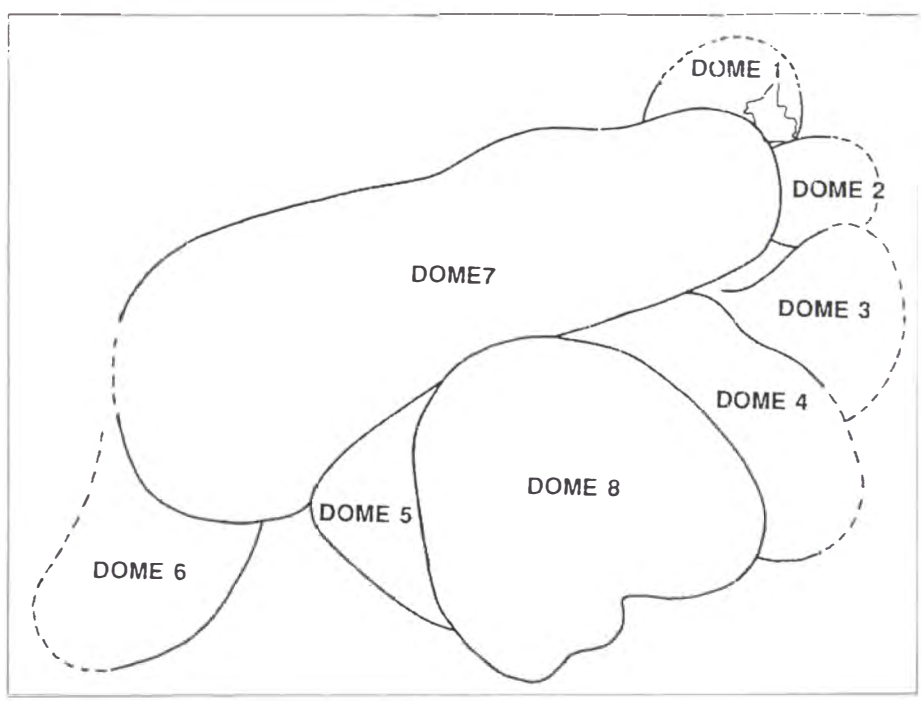

Figure 4.3. Shepherd's (1991) view of Mt Ngongotaha dome complex comprising eight domes. The jagged shape in dome one is Henderson's quarry.

the other rhyolite domes associated with Rotorua. He gathered information on dome morphology, geochemistry and determined a chronology of the Mt Ngongotaha dome complex. He interpreted the surface morphology of the complex to comprise eight separate domes (Fig. 4.3). He also noted vapour phase olivine deposited in lithophysae of Mt Ngongotaha lava and concluded that all the post-caldera rhyolite domes were sourced from a single magma chamber.

Dravitzki (1999) looked at Mt Ngongotaha, Pukehangi and Endean domes, and found the Umarua rhyolite (Fig. 4.4). He grouped Pukehangi dome complex and Mt Ngongotaha as a single complex based on geochemical grounds and proximity, and interpreted Mt Ngongotaha as comprising eight domes and the Pukehangi complex as comprising five. Small pyroclastic deposits were described and assigned to Ngongotaha and Pukehangi domes according to geochemistry. Although geochemically analysed, Endean dome and Umarua rhyolite were not discussed.

Richnow (1999) studied only rhyolite exposed in Henderson's Quarry in the northeastern most dome of the Mt Ngongotaha dome complex determining the history of dome growth, cooling, and alteration. Eruption mode was interpreted to have been dominantly exogenous and fissure fed.

4.3 Pre-caldera Rhyolite domes

Pre-caldera rhyolite domes surround Rotorua Caldera (Fig. 4.1). Of these Pukepoto Hill has been associated with activity of Okataina Volcanic Centre (Nairn, in prep), and Pohaturoa has been associated with Kapenga and Rotorua (Ewart, 1968). Hamurana dome is located at the eastern end of a fault scarp that controls the northern margin of Rotorua Caldera and Endean dome occurs at the caldera's western rim. A mostly buried, previously undocumented rhyolite dome outcrops at the western end of the fault scarp north of Lake Rotorua and is here termed Fryer dome. Rhyolite lava fragments (expanded and unexpanded types) form a large proportion of lithic lag breccias of upper Mamaku Ignimbrite indicating that other rhyolite domes were present in the Rotorua area but were destroyed or buried during caldera formation.

4.3.1 Petrography

Petrography of the pre-caldera rhyolite domes is variable.

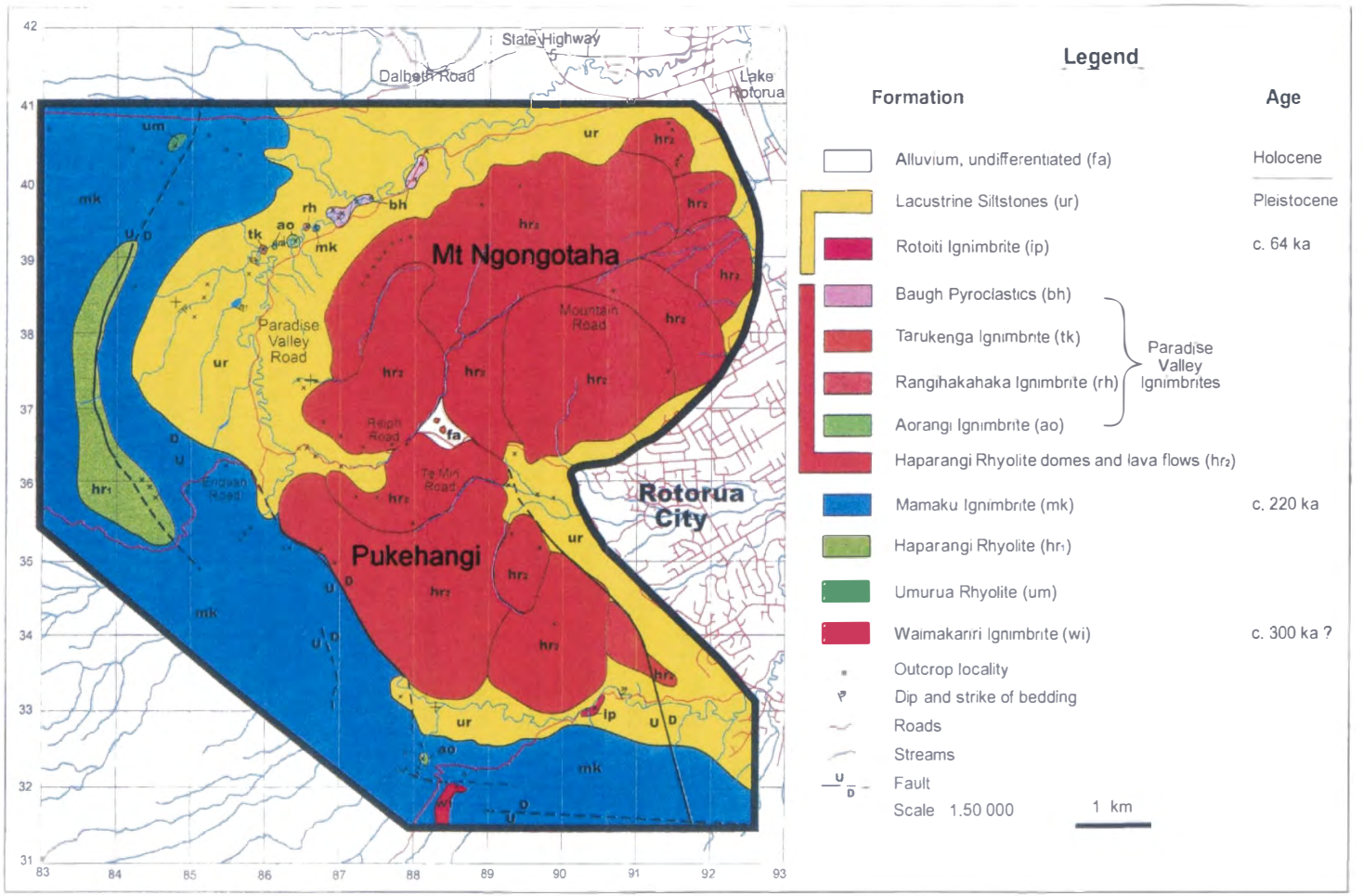

Figure 4.1. Dravitski's (1999) map of Paradise Valley, Utuhina Stream area. Note the positions of Endean dome, and Umarua rhyolite. Also note the make-up of the Ngongotaha-Pukehangi dome complex and the numerous outcrops of pyroclastic deposits in Paradise Valley that have been attributed to the dome complex.

Hamurana dome is flow banded and contains 15 vol% phenocrysts which comprise plagioclase + orthopyroxene + clinopyroxene + Fe/Ti oxides. The groundmass, although containing obvious flow bands, is totally devitrified and felsitic.

Fryer dome is exposed in a small outcrop of altered pink-grey flow banded rhyolite. The dome is buried underneath Mamaku Ignimbrite at the eastern end of the scarp that marks part of Rotorua Caldera's northern margin. Fryer dome contains 20 vol% phenocrysts that comprise plagioclase + orthopyroxene + Fe/Ti oxides. As with Hamurana dome, flow banding is still obvious but the groundmass has devitrified. Spherulites have developed and the felsitic textures predominate.

Endean dome is light grey and contains between 20-30 vol% crystals. The groundmass is entirely spherulitic due to devitrification and the phenocryst assemblage comprises plagioclase + quartz + biotite + hornblende + orthopyroxene + Fe/Ti oxides. Plagioclase, at 15-25 vol%, dominates the crystal assemblage. Umarua rhyolite, named by Dravitzki (1999), also comprises plagioclase + hornblende + biotite. An Umurua rhyolite sample was examined during this study and quartz, orthopyroxene and Fe/Ti oxides were also identified within it. The groundmass is totally spherulitic. Dravitzki interpreted it as a very local rhyolitic extrusive north of Endean dome (Fig. 4.1). In this study the Endean dome has been extended north, based on aerial photography, to the point where Umurua River enters Rotorua Caldera. Umurua rhyolite is on the opposite side of Umurua River at this point. Umarua rhyolite has a similar phenocryst assemblage to Endean dome and the newly interpreted extent of the latter suggests that the two are closely related, if not the same.

Pohaturoa dome outcrops in Hemo Gorge at the caldera's southern margin. It is grey, has an entirely spherulitic groundmass and is crystal-poor (~1 vol% phenocrysts). The phenocryst assemblage is almost entirely plagioclase with trace amounts of Fe/Ti oxides. Ewart (1968) also noted biotite and hypersthene in these lavas.

Pukepoto Hill is located at the eastern margin of the caldera (Fig. 4.1) and is thought to be associated with Okataina Volcanic Centre (Nairn, in prep). It is grey-brown, spherulitic with remnant flow bands and crystal-poor, containing 5 vol% phenocrysts. Plagioclase + orthopyroxene + hornblende + Fe/Ti oxides make up the phenocryst assemblage.

Expanded rhyolite lithic fragments of uMI lithic lag breccias comprise up to 60 vol% vesicles and 20 vol% phenocrysts. Plagioclase dominates the phenocryst assemblage (18 vol%) with subordinate quartz and orthopyroxene (1 vol% each). Plagioclase is up to 1 mm length, pyroxene <0.3 mm and quartz resorbed and <0.5 mm. Most crystals are broken which is probably due to secondary expansion during reheating of the clasts during the Mamaku Ignimbrite eruption.

4.3.2 Geochemistry

Only three pre-caldera rhyolite domes analysed by XRF during the course of this study: Endean, and Hamurana domes, and Umarua rhyolite (identified by Dravitzki (1999)). All are rhyolitic, and weakly peraluminous (probably due to slight alteration and devitrification since eruption; Fig. 4.5). All are high in CaO, Al_2O_3, and Fe_2O_3, and low in Na_2O when plotted against SiO_2 (Fig. 4.6). K_2O content is comparable to that of post-caldera domes that surround the gravity low (see below; Fig. 4.6). They contain high amounts of Sr and low amounts of other trace elements relative to post-caldera rhyolite lavas when plotted against Rb (Fig. 4.7).

The pre-caldera rhyolite domes analysed plot over a wide range when compared with the post-caldera rhyolite groups (Fig. 4.6 and 4.7). Umarua Rhyolite plots away from the other Endean dome analyses in trace element graphs (Fig. 4.7). Hamurana dome has variable chemistry compared with Endean dome suggesting they had independent petrogenetic histories.

4.4 Post-caldera rhyolite domes

Most of the post-caldera rhyolite domes are located close to Rotorua City surrounding a basement depression determined using geophysics (Rogan, 1982; Hunt, 1992) that is associated with caldera collapse (see chapter 6). In total 7 post-caldera domes or dome complexes are exposed. The morphology of the largest of these, Mt Ngongotaha, is controlled by at least eight domes or dome lobes (Shepherd, 1991; Dravitzki, 1999; Fig. 4.4). The rhyolite domes that surround the low gravity anomaly (including Mt Ngongotaha, Pukehangi, Kawaha Point and buried rhyolite domes beneath Rotorua City) are herein termed Rotorua City rhyolite (RCR). Mokoia Island and Hinemoa Point are the only two areas that rhyolite lavas occur away from the basement depression. An age of less than 50,000 yrs has been ascribed to both Mokoia Island and

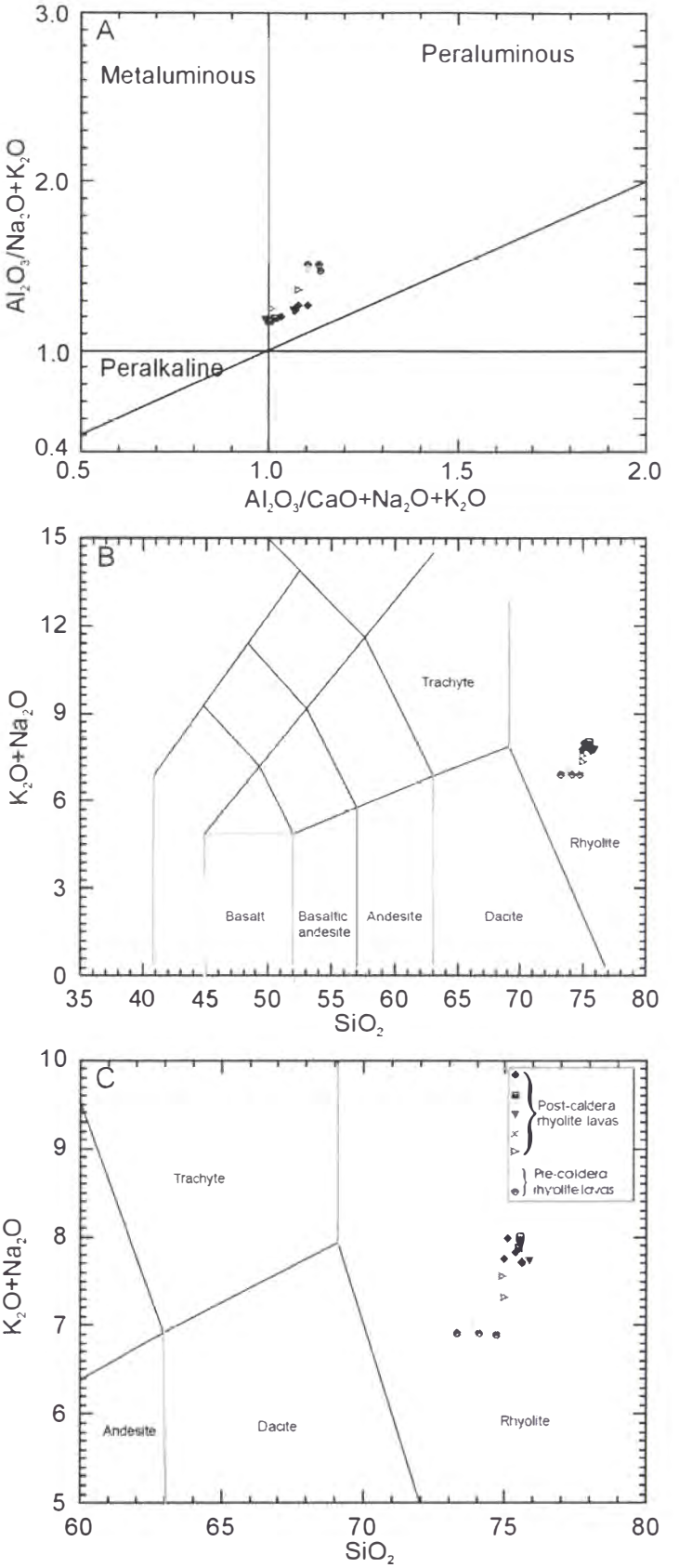

Figure 4.5. ASI (A) (after Maniar and Piccoli, 1989) and TAS (B and C) (after Le Maitre, 1989) diagrams for rhyolite lavas present in Rotorua Caldera. Pre-caldera domes are rhyolitic, and are weakly peraluminous. Post-caldera lavas are all also entirely rhyolitic, and are metaluminous-weakly peraluminous.

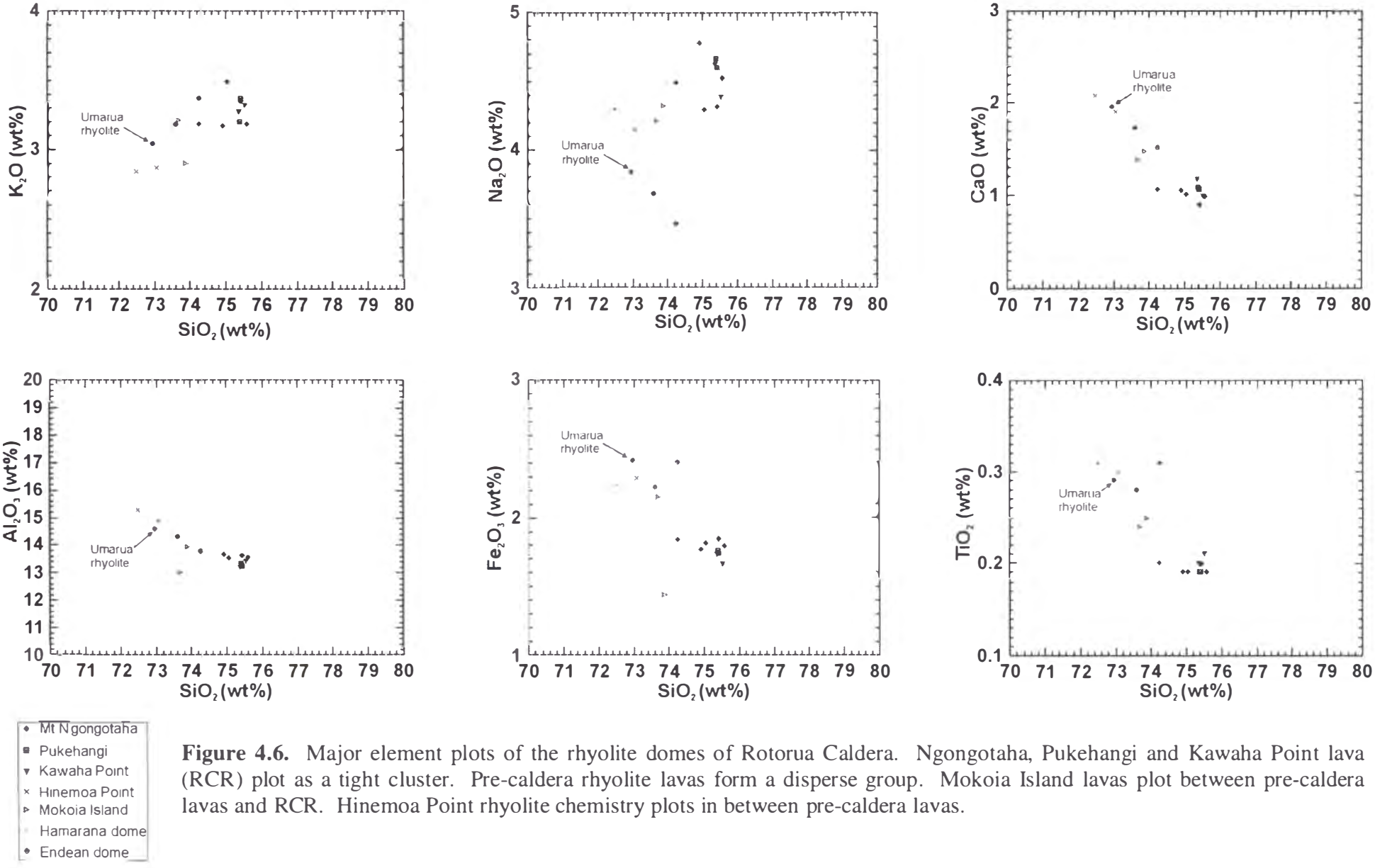

Figure 4.6. Major element plots of the rhyolite domes of Rotorua Caldera. Ngongotaha, Pukehangi and Kawaha Point lava (RCR) plot as a tight cluster. Pre-caldera rhyolite lavas form a disperse group. Mokoia Island lavas plot between pre-caldera lavas and RCR. Hinemoa Point rhyolite chemistry plots in between pre-caldera lavas.

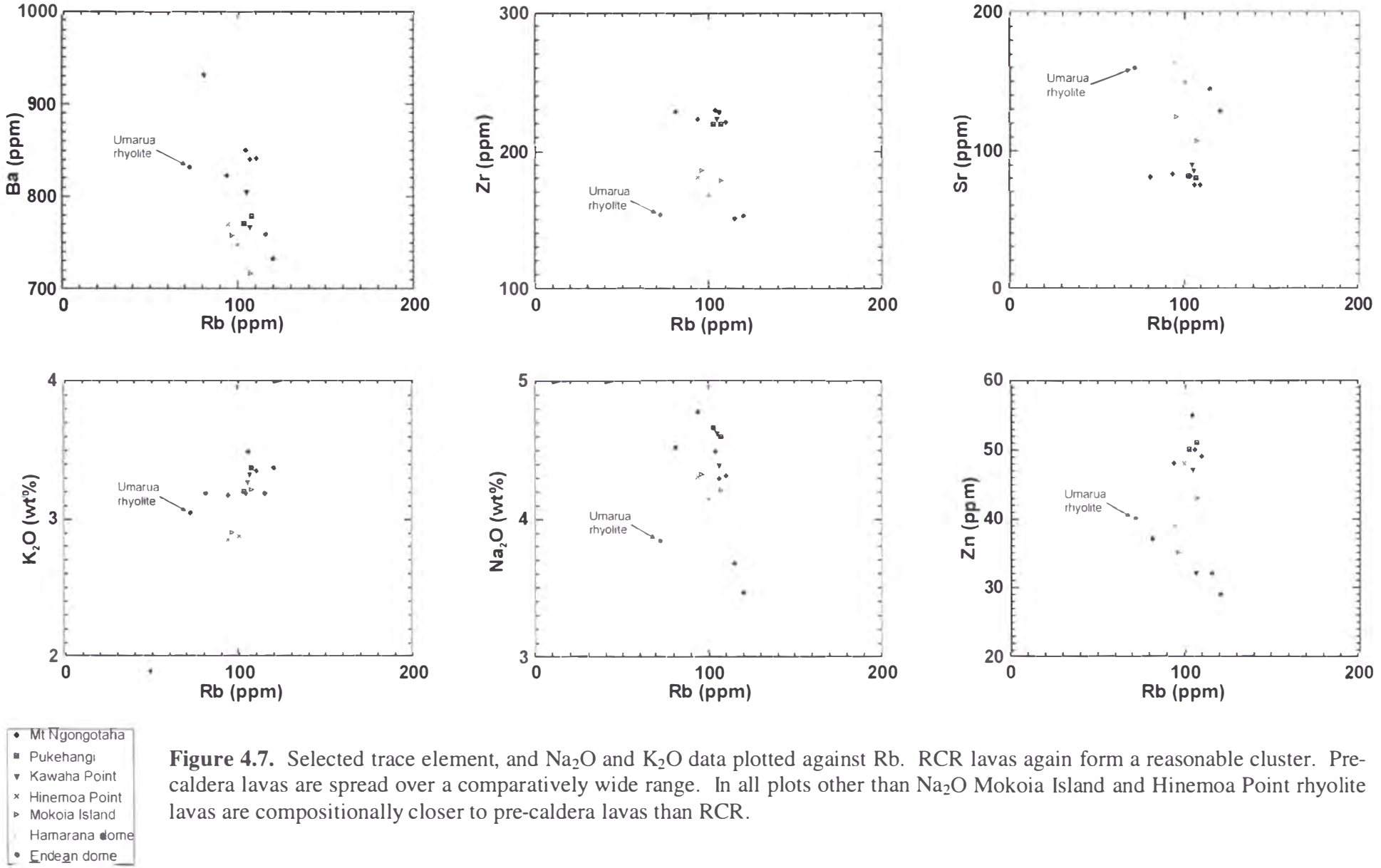

Figure 4.7. Selected trace element, and Na_2O and K_2O data plotted against Rb. RCR lavas again form a reasonable cluster. Pre-caldera lavas are spread over a comparatively wide range. In all plots other than Na_2O Mokoia Island and Hinemoa Point rhyolite lavas are compositionally closer to pre-caldera lavas than RCR.

Hinemoa domes (Nairn and Wood, 1987), but remains to be confirmed.

4.4.1 Petrography

Domes of the Mt Ngongotaha complex contain bands of spherulitic (in places the groundmass is entirely spherulitic) and glassy material. Lava of this complex is crystal-poor, containing only 3-5 vol% phenocrysts that comprise plagioclase + orthopyroxene + Fe/Ti oxides ± quartz (trace).

Pukehangi dome complex comprises up to 5 domes (Dravitzki, 1999; this study) and has very similar mineralogy to Mt Ngongotaha. Phenocrysts comprise only 2-3 vol% and again comprise plagioclase + orthopyroxene + Fe/Ti oxides with rare quartz. The groundmass alternates glassy to spherulitic.

At Kawaha Point glassy to devitrified rhyolite is exposed. It is 3-4 vol% phenocrysts comprising mainly plagioclase + Fe/Ti oxides ± orthopyroxene with rare quartz. Some plagioclase has been resorbed. In places the groundmass is entirely spherulitic and felsitic while in others it is still vitric and glassy.

Southsoutheast of Kawaha Point a rise in the ground surface indicates the presence of buried rhyolite lava. The extent of the lava has been inferred by Wood (1992) and is shown in Fig. 4.1. This lava is flow banded (red/pink to grey to white bands) and contains 3-4 vol% phenocrysts consisting of plagioclase + orthopyroxene + Fe/Ti oxides.

Mokoia Island rhyolite contains 20-25 vol% phenocrysts that are made up of euhedral-subhedral plagioclase + quartz + orthopyroxene + hornblende + Fe/Ti oxides. The matrix is mainly glass with occasional spherulites and 1-2 mm long lithophysae.

At Hinemoa Point, lava of Hinemoa dome is crystal-rich containing 20-25 vol% phenocrysts of plagioclase + quartz + biotite + Fe/Ti oxides. The groundmass is glassy, flow banded, and contains a small number of vesicles. Plagioclase phenocrysts are often embayed. Close by, to the southwest, another outcrop of rhyolite occurs which has a similar mineralogy to Hinemoa Point. The two are inferred to be the same.

4.4.2 Geochemistry

Post-caldera rhyolite lavas can clearly be split into three groups based on geochemistry (Fig. 4.6 and 4.7). The domes of RCR form one group whereas Mokoia Island and rhyolite outcropping at Hinemoa Point both have distinctive geochemistries. All are rhyolitic, and are metaluminous to weakly peraluminous (Fig. 4.5).

The domes of RCR are the most silica rich and form a reasonably tight cluster when all major element concentrations are plotted against SiO_2. They are all high in Na_2O and K_2O, and low in CaO relative to all other Rotorua rhyolite lavas and low in Fe_2O_3 and Al_2O_3. They also form tight clusters when Sr and Zr concentrations are plotted against Rb. These domes are not so tightly grouped when other trace elements are plotted against Rb. A reasonably tight grouping is also seen on the Zn vs Rb plot (Fig. 4.7) with 2 samples (one from Kawaha point and one from Mt Ngongotaha) plotting outside the main field. Ba content of these rhyolite domes ranges over 200 ppm.

Hinemoa Point dome chemistry has more in common with pre-caldera rhyolite lavas than with either Mokoia Island lava or with RCR domes. It is lowest of all domes in SiO_2 and K_2O and highest in CaO (Fig. 4.6). Hinemoa Point dome Na_2O concentrations are intermediate between pre- and other post-caldera domes. Rb versus Sr and Zr abundances plot among pre-caldera dome compositions (Fig. 4.7).

Mokoia Island chemistry is intermediate between that of Hinemoa Point and RCR (Figs 4.6 and 4.7).

The geochemistry of the three groups of post-caldera rhyolite domes is consistent with the mineral assemblages with both Mokoia Island and Hinemoa domes comparatively rich in mafic crystals (leading to high Ca, Fe and Ti contents) with the only exception being one Mokoia Island sample that has a low iron content (Fig. 4.6).

4.5 Mineral chemistry

EPMA was carried out on Hamurana, Kawaha Point domes, and an expanded rhyolite fragment from a lithic lag breccia to assess the chemistry of orthopyroxene, plagioclase,

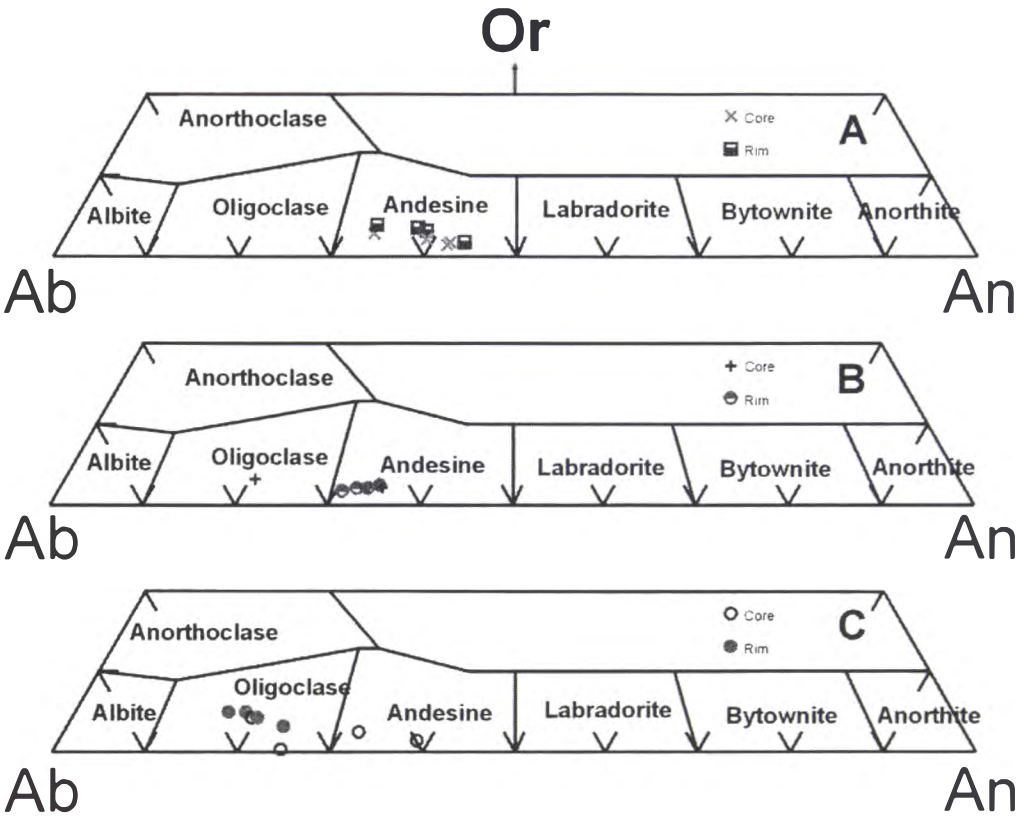

Figure 4.8. Plagioclase chemistry for rhyolite lavas of Rotorua Caldera. A) Hamurana dome. B) Kawaha Point dome (RCR). C) An expanded rhyolite lithic fragment from a lithic lag breccia. Plagioclase of Kawaha Point and the expanded rhyolite lithic fragment are normally zoned. Plagioclase crystals of Hamurana dome are both normally and reversely domed

and glass. Where possible cores and rims of minerals were analysed to investigate zoning characteristics.

4.5.1 Hamurana dome

Plagioclase phenocrysts constitute 13 vol% of Hamurana dome. Plagioclase crystals are up to 1 mm long, and mostly normally zoned, varying between An_{42}-An_{33} with only one reversely zoned crystal varying An_{42}-An_{44} identified (Fig 4.8).

Pyroxene comprises 1 vol% of Hamurana dome and is often present as euhedral, zoned crystals up to 0.2 mm length. Composition varies between $En_{63}Wo_{1.5}Fs_{35.5}$ to $En_{54}Wo_2Fs_{44}$ from the core to the rim (Fig. 4.9).

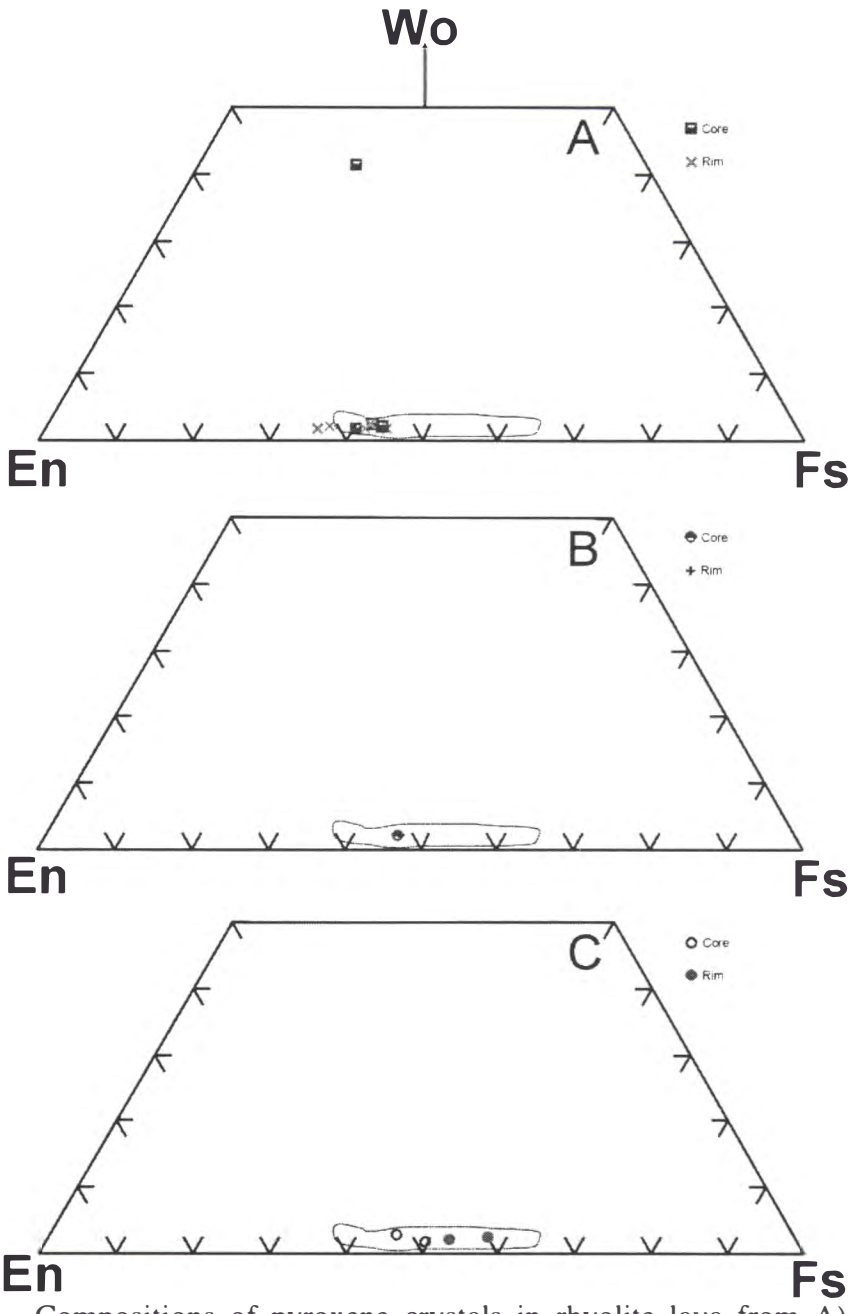

Figure 4.9. Compositions of pyroxene crystals in rhyolite lava from A) Hamurana dome, B) Kawaha Point, and C) a lithic lag breccia. Rings represent total fields for pyroxene from Mamaku Ignimbrite pumice clasts.

4.5.2 Expanded rhyolite lava fragment

One rhyolite lava fragment from a lithic lag breccia was analysed by EPMA. Plagioclase is broken, up to 1.5 mm long, and normally zoned An_{39}-An_{17} (Fig. 4.8).

Pyroxene crystals are zoned varying from $En_{52}Fs_{45}Wo_3$ to $En_{40}Fs_{57}Wo_3$ (core to rim) and are up to 0.5 mm in length (Fig. 4.9).

4.5.3 Kawaha Point dome

Kawaha Point (RCR) dome is crystal-poor. Plagioclase constitutes only 3 vol%. Four plagioclase crystals were analysed, two of which were normally zoned An_{35}-An_{30} and two reversely zoned varying between An_{33}-An_{34} and An_{20}-An_{33} (Fig. 4.8).

Orthopyroxene makes up much less than 1 vol% of Kawaha Point rhyolite. Only 1 pyroxene was analysed and yielded $En_{52}Fs_{46}Wo_2$ composition for both the core and rim (Fig. 4.9).

Glass varies between 63 and 77 wt% SiO_2 although the majority vary between 76-77 wt%.

4.6 Discussion

4.6.1 Rhyolite dome inter-relations

Ewart (1968) considered that all the rhyolite lava domes of Rotorua Caldera were erupted from a single magma chamber. Evidence found during this study suggests that the lavas can be split into a number of distinct groups.

The similarity of the RCR domes suggests that they are related, and may have erupted from the same magmatic source. All are crystal-poor, glassy to devitrified, and contain dominantly plagioclase and orthopyroxene with rare quartz. These lavas were also grouped based on phenocryst content and phenocryst composition by Ewart (1968). The mineralogy and chemistry of the RCR is distinct from those that occur away from the gravity low suggesting that they were sourced from different chambers.

Mokoia Island and Hinemoa Point rhyolite domes have distinctly different chemical compositions and phenocryst assemblages, suggesting that they were erupted from separate, small rhyolitic magma chambers.

Endean, Umarua and Hamurana rhyolite domes are chemically different to all post-caldera domes except for Hinemoa dome (Hinemoa dome can be separated from the pre-caldera domes based on Na_2O content; Fig. 4.6). Umarua rhyolite is separated from

Endean dome in geochemical plots (Fig. 4.6 and 4.7), but the two have been grouped together due to their geographic proximity and similar phenocryst assemblages. The phenocryst assemblage of Fryer dome is similar to that of Hamurana dome suggesting that the two are related. The formation of Rotorua Caldera between the extrusions of Hinemoa dome and the pre-caldera domes suggests that these domes were not sourced from the same magma chamber. The phenocryst assemblage of Hamurana and Fryer domes is different from that of Endean and Umarua rhyolites suggesting a different petrogenetic path.

Both the rhyolite lavas of Pukepoto Hill and Pohaturoa dome are crystal poor (up to 5 vol%). They have both been related to other volcanic centres (Nairn, 1989; Ewart, 1968). Pukepoto Hill has similar mineralogy to the post-caldera domes of RCR, but contains hornblende, similar to rhyolite of the Okataina Volcanic Centre. It is thought to be unrelated, other than spatially, to Rotorua Volcanic Centre. Pohaturoa dome is petrographically dissimilar to other RVC rhyolite domes and is suggested to be unrelated (Ewart (1968) indicated that Pohaturoa Dome was similar to rhyolite lavas further south).

The rhyolite lava fragments (expanded and non-vesicular) in the lag breccias illustrate the existence of rhyolite domes prior to the caldera's development that were completely destroyed or buried during the climactic eruption and no longer exposed. The phenocryst assemblage is similar to that of RCR and pumice clasts of the Mamaku Ignimbrite and they may be related (see section 4.6.2). Further geochemical work needs to be carried out, but the rhyolite lava fragments in the lag breccias may represent the first extrusions from the Mamaku Ignimbrite magma chamber.

The pre-caldera rhyolite domes have been suggested to be extruded remnants of the Waimakariri Ignimbrite magma chamber (Lynch-Blosse, 1998). This was suggested when Lynch-Blosse (1998) postulated Rotorua Caldera as the source of Waimakariri Ignimbrite. The volume of Rotorua Caldera is insufficient to accommodate Waimakariri Ignimbrite (see chapter 6). While this does not preclude the suggestion that the domes are related to Waimakariri Ignimbrite, the characteristics of the pre-caldera domes suggest they are probably not related to one another, and the other postulated source at the southern end of the Kaimai Range (Lynch-Blosse, 1998) shows petrogenetic relationships between the domes and Waimakariri Ignimbrite to be unlikely.

4.6.2 Relationship between Mamaku Ignimbrite and Rotorua rhyolite lavas

Suggestions about the relationships of the various exposed lavas to Mamaku Ignimbrite are based on major and trace element geochemistry and phenocryst assemblages. Isotope work and/or rare earth element analysis of both the rhyolite lavas and Mamaku Ignimbrite pumice clasts need to be carried out before these suggestions can be confirmed.

Magma is often extruded preceding and following the climactic eruption of a caldera creating dome complexes especially in the vicinity of faults and fractures involved in the caldera's formation (e.g. Smith and Bailey, 1968; Self et al.,1986).

When whole rock chemistry of all the rhyolite lavas is compared with that of juvenile pumice clasts of Mamaku Ignimbrite a close association is seen (Fig. 4.10 and 4.11). All rhyolite lava groups overlap with the pumice compositions in major and trace element plots. The overlaps are, however, inconsistent and a particular dome or a particular group of rhyolite lavas does not always overlap with the same pumice group leading to difficulty in association.

The post-caldera rhyolite lavas of RCR have a similar phenocryst concentration and assemblage to the juvenile pumice types found in Mamaku Ignimbrite and when modelled according to Raleigh fractionation these rhyolite lavas plot close to, or between, type 1 and 2 pumice clasts indicating the possibility of their formation from the Mamaku magma chamber (Fig. 4.12). RCR lavas plot closest to type 1 pumice compositions on most major element plots (exception being SiO_2 vs Na_2O and K_2O) but have trace element chemistry that is variable compared with Mamaku Ignimbrite pumice clasts. Mineral chemistry of Kawaha Point rhyolite is also very similar to that of Mamaku Ignimbrite pumice with the chemistry of plagioclase phenocrysts and the pyroxene crystal analysed plotting within the Mamaku Ignimbrite pumice ranges. The domes of RCR are thought to be the final extrusions from the Mamaku magma chamber.

Endean dome has a different phenocryst assemblage from juvenile Mamaku Ignimbrite pumice clasts, is comparatively crystal-rich, and thought to be unrelated petrogenetically to Mamaku Ignimbrite. Hamurana dome is also comparatively crystal

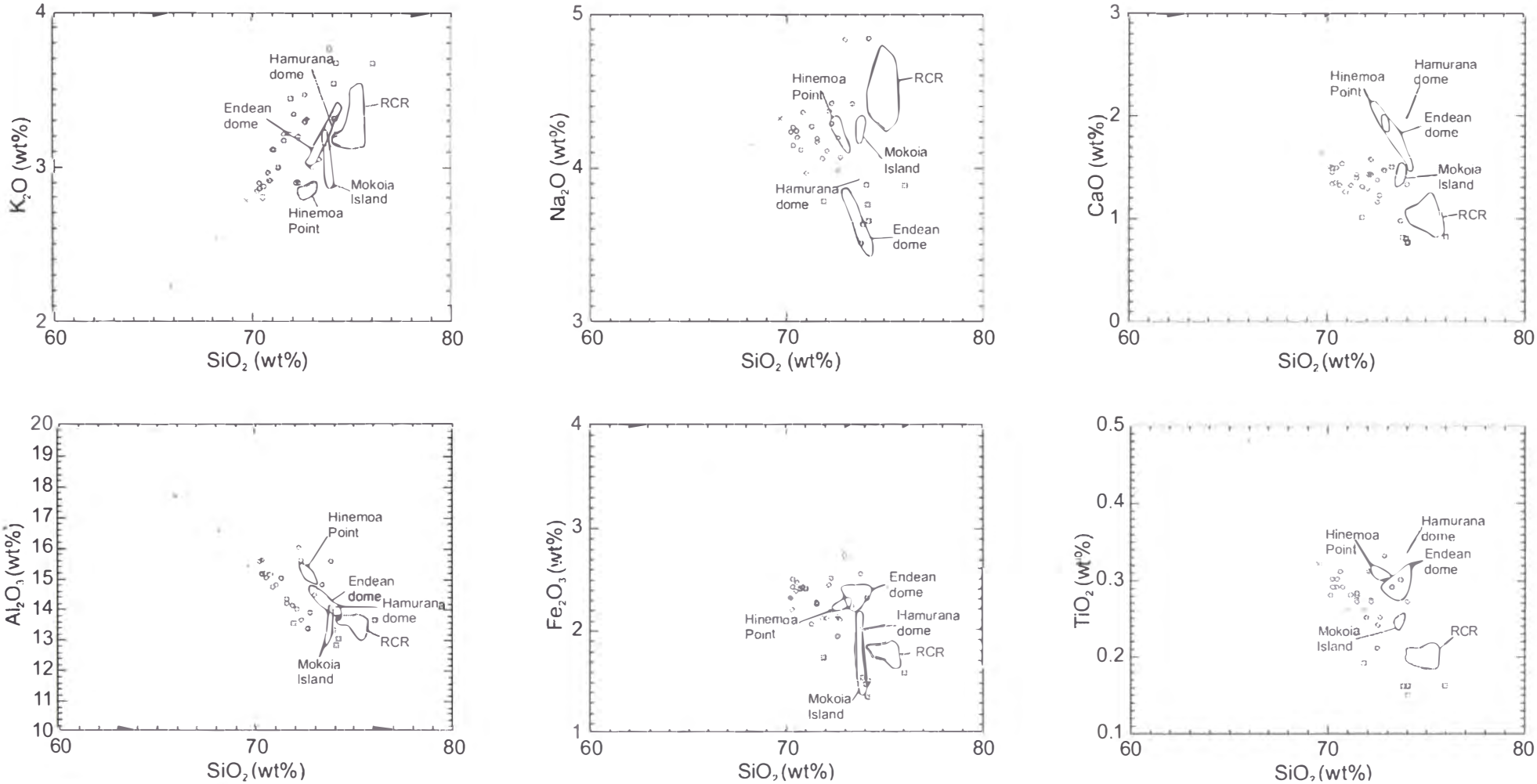

Figure 4.10. Comparison of juvenile Mamaku pumice and Rotorua Caldera rhyolite lava major chemistry. Chemistry of the lavas often overlaps with that of Mamaku Ignimbrite pumice, but the same group does not often overlap consistently with the same pumice group. RCR rhyolite composition is close to type 1 pumice on all plots except Na_2O

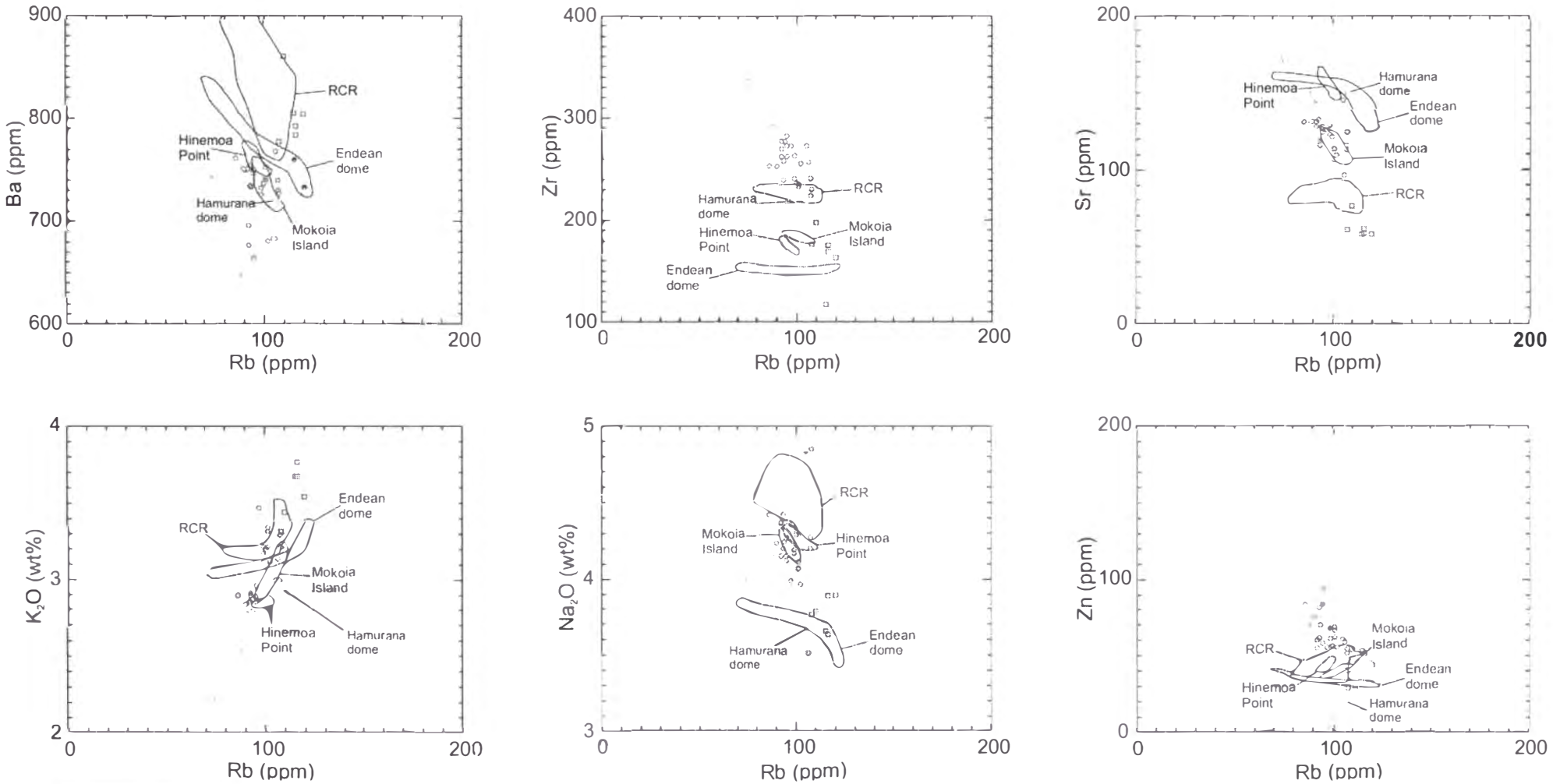

Figure 4.11. Comparison of juvenile Mamaku and rhyolite lava of Rotorua Caldera trace and major element chemistry. Again no rhyolite group overlaps consistently with the same pumice type.

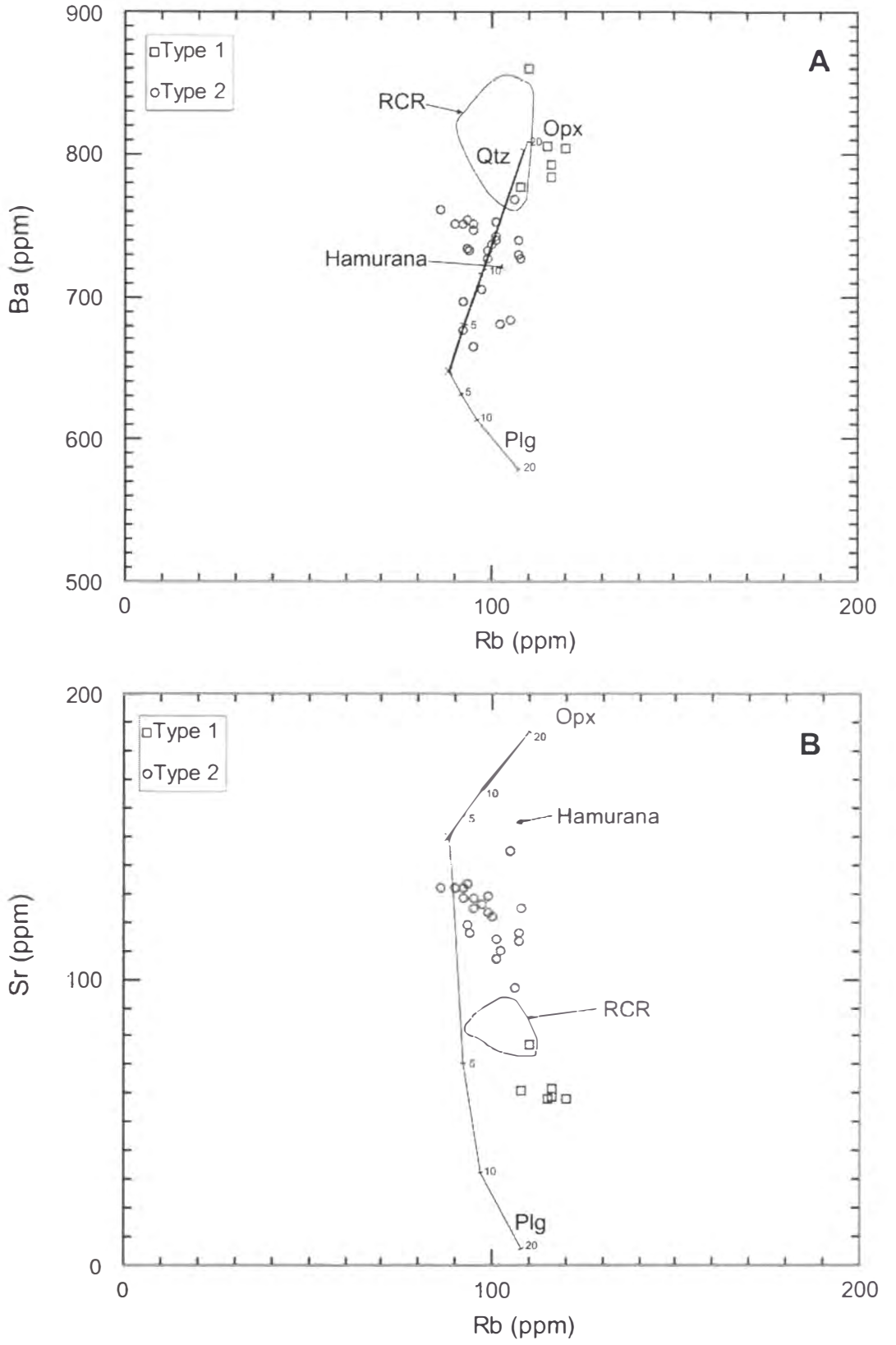

Figure 4.12. Vector modelling by Raleigh fractionation of a Mamaku Ignimbrite type 3 parent magma (MKP29) and comparison with RCR and Hamurana dome lavas. The RCR field plots between pumice types 1 and 2 but closer to type 1. Hamurana dome plots among Mamaku Ignimbrite pumice chemistry on only the Rb vs Ba plot. No other rhyolite lavas have been shown, as their phenocrysts assemblages require other Raleigh fractionation vectors that would not be consistent with Mamaku Ignimbrite pumice data. Trace element distribution coefficients are from Arth (1976) and Nash and Crecraft (1985), as quoted by Rollinson (1993).

rich. The compositions of Hamurana dome plagioclase plot within the range of plagioclase from Mamaku pumice clasts, but pyroxene is up to 2% more En-rich than corresponding Mamaku pumice phenocrysts, and vector modelling (Fig. 4.12) suggests that Hamurana dome lava is not consanguineous with Mamaku Ignimbrite pumice types.

An expanded rhyolite lava fragment from a lithic lag breccia has a similar phenocryst assemblage to Mamaku Ignimbrite pumice clasts. Plagioclase and pyroxene phenocryst compositions of the expanded rhyolite lava fragment plot wholly within those of Mamaku Ignimbrite pumice clasts. The presence of such fragments in the lag breccias proves the previous existence of rhyolite domes in the area now occupied by Rotorua Caldera and the similarity of the phenocryst content and phenocryst chemistry (Fig. 4.9) hint at a petrogenetic relationship between the lavas and Mamaku Ignimbrite pumice clasts. It is likely that these fragments represent the first extrusions from the Mamaku magma chamber.

Rhyolite of Mokoia Island and Hinemoa domes have distinctive phenocryst assemblages and are also crystal-rich compared with Mamaku Ignimbrite pumice clasts. Both domes are suggested to be younger than 50,000 yrs BP (Nairn and Wood, 1987; Kennedy et al., 1978; Healy, 1963). Chemistry of Hinemoa dome is similar to that of Endean and Hamurana domes and this, along with its phenocryst assemblage, suggests it is unrelated to Mamaku Ignimbrite. Mokoia Island is also thought to be unrelated to Mamaku Ignimbrite due to its dissimilar phenocryst assemblage and chemistry.

CHAPTER 5
Calderas and Caldera Structure

5.1 Introduction

Calderas and caldera complexes have been recognised in nearly all volcanic environments on earth and in the solar system. The largest caldera known is that of Olympus Mons on Mars, which measures 80×65 km and is a nested structure containing 6 collapse centres (Mouginis-Mark and Robinson, 1992). On earth caldera complexes range in size from <1 km diameter up to 35×100 km (La Garita Caldera; Lipman, 2000). Historic eruptions associated with caldera collapse have lead to huge fatalities in Indonesia (Krakatau; van Bemmelen, 1932), and are considered to have caused the destruction of the Minoan civilisation at Santorini (Druitt et al., 1999). Calderas are also often the sites of vigorous geothermal activity making them potential sites for electricity generation.

The last 20 years has seen significant advancement in the understanding of caldera structures and caldera forming processes with a number of classification schemes developed. Lipman et al. (1984) indicated the importance of finding eroded calderas where remnants of pyroclastic material and source magma chambers are exposed. In this situation crustal structures involved in caldera formation can be directly analysed and interpreted. Also of importance are young calderas with well preserved surface morphologies. Comparisons between old deeply eroded and young well preserved structures should lead to a much better understanding of caldera forming processes.

There are a number of classification methods using composition, collapse process, and type example as main criteria. All calderas can be described according to composition and collapse process and most calderas can be likened to type examples, or they may define a new type themselves.

The earliest reference to collapse at a volcano was by Pegues (1842) who thought Santorini formed by volcanic collapse of a previously larger island. Fouque (1879) also studied Santorini and was the first to come up with the idea of collapse as a result of eruption (Druitt et al., 1999). He described the steep slopes of the escarpment that form

the inner (discontinuous) crater wall, and petrography of the latest deposit, noting the lack of clasts corresponding to the old structure. Fouque deduced that rather than explosive destruction of a previous structure, "concomitant subsidence" best explained these features. Verbeek (1885, translation in Simkin and Fiske, 1983) described the structures at Krakatau in the year after its 1883 eruption. Sonar was used to map the sea floor, geologic descriptions were made of 1883 pyroclastic deposits and surveys of the devastated region carried out. He considered that the part of Krakatau that was missing after the eruption was either blown into the air or collapsed. Like Fouque, he considered the lack of clasts of the previous structure in the erupted deposits as evidence against explosive destruction of the previous cone preferring a collapse explanation for its disappearance. Verbeek also noted a very deep sea floor between the islands and a change in sea floor depth outside the previous volcanic structure, which was also better explained by collapse. Clough et al. (1909), after mapping in Scotland, interpreted Glencoe as a collapsed cauldron with a distinct ring fault. It became the type example of a caldera that had collapsed along a ring fault despite geologic descriptions that indicated more than one period of collapse occurred there.

Many classification schemes for calderas exist in the literature. Williams (1941) summarises early classification schemes as follows:

Daly's (1914) classification:

Calderas- Produced by explosion. May be simple or nested.

Sinks- Formed by collapse. Also may be simple or nested.

Sunken calderas- Resulting from subsidence after explosion.

Volcanic rents- Due principally to horizontal tearing apart of cones.

Walker's (1928) classification:

Explosion related calderas- Volcanic depressions more than a mile across.

Subsidence calderas-

i) Kilauea type- Formed by engulfment following a recession of lava in a conduit as a result of outpourings at lower levels.

ii) Katmai type- Formed by explosion of viscous, siliceous magmas and subsequent collapse of the crater walls.

Tanakadate's (1930) classification:

Crater type- A circular or oval caldera at the summit of a volcanic cone, for example Aso and Hakone, Japan.

Depression type- Basins without distinct rims that are deeply sunk in mountain regions or a plateaux of volcanic origin. Many are irregularly outlined and heavily modified by erosion.

Conca type- Shallow depressions with gently sloping walls. For example Bolsena Caldera.

Central calderas- resulting from collapse around a summit vent.

Lateral calderas- Resulting from eruption at a vent adjacent to the collapse site.

Van Bemmelen's (1932) classification:

Central type- Formed at the summit of cones.

Depression type- Of eccentric and irregular plan.

Conca type- Shallow basins with gently sloping sides.

Reck's (1936) classification:

Type I- Calderas associated with endogenous forces.

i) Explosion calderas- such as Krakatau, and Santorini.

ii) Ruckflussencaldren- resulting from withdrawal of magma.

iii) Intrusion calderas- including depressions produced by cryptovolcanic activity.

iv) Collapse calderas- such as Kilauea, and Askja.

Type II- Calderas formed by exogenous forces, i.e., modified forms.

i) Erosion calderas.

ii) Deflation calderas.

Williams (1941) himself classified calderas as 6 types that could be further subdivided based on collapse morphology:

Explosion calderas- Rare and relatively small calderas, such as Tarawera.

Collapse calderas- Result from withdrawal of magmatic support at depth, and occasionally from internal solution of volcanic cones. May be split into:

i) Krakatau type- Engulfment follows repeated and usually short-lived explosions of pumice and juvenile ash. Examples include Crater Lake, Aso, and Santorini.

ii) Kilauea type- Rapid effusion of lava from fissures on the flanks of a cone or intrusion of magma as dikes or sills drains the central conduit and causes foundering of the central vent.

iii) Katmai type- Produced by a combination of internal solution, pumice explosion and avalanching of the crater walls.

iv) Cryptovolcanic type- Formed by subsidence following subterranean explosions when little or no magma escapes at the surface.

v) Glencoe type- Cauldron subsidences resulting from the collapse of the roof of a magma chamber along ring fractures, that is, stoping of cylindrical blocks of the crust.

vi) Miscellaneous calderas- Produced by changes in shape and/or volume of magma bodies at depth (including lateral spreading of magma).

Erosion calderas- May result from any of the preceding types from enlargement of the crater to form gigantic amphitheatres, e.g. Banks Peninsula.

Volcanic graben- More or less straight walled depressions formed by collapse.

i) Summit graben.

ii) Sector graben- On the flanks of a cone, e.g. Stromboli.

Volcanic rents or fissure troughs- Caused by tearing apart of volcanic cones by movements that are mainly horizontal. Injection of dike swarms or overloading of cones on a weak substratum may induce this sliding.

Major-volcano-tectonic depressions- Subsidences related to areal eruptions, generally from fissures rather than from central vents. e.g. TVZ.

Since this seminal work of Williams (1941), many of the calderas on which he based his caldera classification scheme have been reinterpreted as involving structures that are often more complex than their surface morphology indicates. For example the caldera at Katmai is thought to have formed mainly due to magma migration to Novarupta (Williams and McBirney, 1979; Hildreth, 1991) and Glencoe has been interpreted as piecemeal, forming by volcano-tectonic subsidence (Moore and Kokelaar, 1997; 1998). Erosion calderas are not primary forms and although still described (e.g. Karatson et al., 1999) the term is not widely used.

Williams and McBirney (1979) built on Williams (1941), modifying and adding caldera types:

Krakatoan type- formed by the foundering of the tops of large composite volcanoes following explosive eruptions from one or more vents or arcuate fissures on the flanks. Volume is usually much less than 100 km^3.

Katmai type- Collapse due to drainage of a central magma chamber to feed eruptions at other volcanoes or fissures beyond the base of the cone.

Valles type- Foundering occurs along arcuate fractures independent of pre-existing volcanoes as a consequence of, and simultaneously with, a discharge of huge volumes of siliceous pumice. Usually >100 km^3.

Hawaiian type- Collapse of the top of shield volcanoes during late stages of growth. Prior tumescence is followed by subterranean drainage of basic magma from beneath the summit region into rift zones and, in many cases, by flank eruption of lava.

Galapagos type- Collapse during late stages of growth of basaltic shields. Unlike Hawaiian type, collapse occurs in response to injection of magma and eruptions of lava from circumferential fissures near the summit and less frequently from radial fissures on the flanks.

Masaya type- Piecemeal subsidence of a shallow broad depression in the central portion of a shield. Nearly all lavas are contained within the boundary scarps.

Atitlan type- cauldron subsidence unrelated to an earlier cone, but associated with eruptions from volcanoes near the rim or nearby fissures.

All of these types are based on type examples. Other calderas may have similarities but usually have structures and morphologies divergent from type examples. Also, many of the caldera types outlined have overlapping eruptive and collapse styles. Atitlan type is classed only on non-association with pre-existing extrusions. Valles-type calderas also need not be associated with a pre-existing cone. Masaya has since been reinterpreted, and Galapagos and Hawaiian collapse types are very similar.

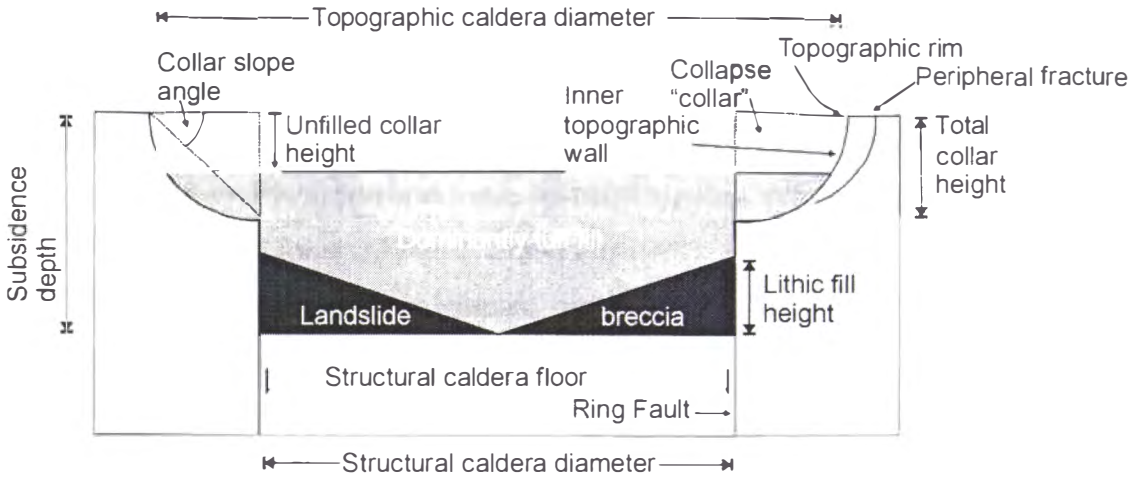

Figure 5.1. Lipman's (1997) model of a caldera's components and structure.

The definitions used in this thesis are taken from Cole et al. (1996) and Cole, et al. (in prep) that read:

Caldera- A volcanic depression, generally large, which is principally the result of collapse into the top of a magma reservoir during or immediately following eruptive activity.

Caldera complex- Spatially and structurally associated nested calderas. As structures are generally poorly or incompletely preserved ignimbrites should be assigned only on the basis of volcanological criteria.

Cauldron- An eroded caldera in which features immediately below the floor of the caldera are exposed, but no surface expression of the caldera remains.

Ring structure- Plutonic equivalent of a caldera where deep erosion (generally >1 km) has exposed the magma chamber or chambers.

Crater- A volcanic depression at the top of a volcano that is the result of explosion.

Calderas may be considered in terms of topographic and structural elements (Fig. 5.1). Lipman (1984; 1997; 2000) identifies calderas as bounded by structural and topographic boundaries (Fig. 5.1) within which are the collapse collar, inner topographic wall,

caldera floor and caldera fill (Fig. 5.1). The structural boundary comprises that part of the caldera that has collapsed due to movement along faults. The topographic boundary joins the high points that surround the caldera. The topographic boundary is normally wider than the structural rim and forms by mass wasting, erosion and "scalloping" after caldera formation (Lipman, 1984; Nairn et al., 1994). Collapse of a caldera often leads to deformation outside the topographic rim (B.P. Kokelaar, pers. comm., 1999) and post-caldera erosion can make defining a topographic rim difficult or of little use in defining the extent of a caldera. In this thesis a *limit of deformation* associated with caldera collapse is also used in observation of Rotorua Caldera. The *limit of deformation* encompasses all structures associated with a particular caldera's formation.

Calderas may also be described according to their processes of collapse, composition of volcanic eruptives, and tectonic setting.

5.2 Calderas of differing composition

Calderas may vary slightly with composition and may be subdivided into peralkaline, basaltic, andesitic-dacitic and rhyolitic.

5.2.1 Peralkaline calderas

Peralkaline calderas are typically associated with zones of rifting, unrelated to a subduction system; e.g. Pantelleria, Sicily associated with a submerged continental rift (Mahood, 1983; Mahood, 1984; Mahood and Hildreth, 1986; Orsi et al., 1991), Mayor Island, New Zealand, associated with NNE striking Ngatoro Basin and normal faults of the Mayor Island fault belt (Cole, 1990; Houghton et al., 1992), and calderas of the K'one (Gariboldi) volcanic complex, Ethiopia, associated with the Main Ethiopian Rift (Cole, 1969).

Calderas tend to be of small volume and the volcanoes tend to be shield-like. Collapse heights are usually <300 m and they form in response to small volume pyroclastic eruptions e.g. Mayor Island, caldera wall height ~350 m, with pyroclastic units of one collapse episode 1-10 km^3 (Houghton et al., 1992), Pantelleria, wall height ~90m (youngest episode, Hildreth and Mahood, 1986), estimated eruption volume 7 km^3 (Green Tuff, Wolff and Wright, 1981). Notable exceptions exist e.g. Gran Canaria has

a caldera wall up to 1 km high, and has erupted pyroclastic material in the order of 100 km^3 (Schmincke, 1967) although numerous collapse events have probably occurred here (as have occurred at Las Canadas close by (Marti et al., 2000)).

Formation is usually in response to explosive eruption of tuffaceous material (e.g. Schminke, 1967; Mahood and Hildreth, 1983; Houghton et al., 1992; Marti et al., 2000), and is often succeeded by extrusion of lavas from a central vent, which may eventually fill the caldera (Mahood, 1984). Also at some peralkaline calderas post-caldera lava extrusion is associated with magma intrusion into the root zone of the caldera that leads to uplift (resurgence) of the central portion of the caldera floor (e.g. Pantelleria; Johnson, 1969; Mahood and Hildreth, 1983; Mahood, 1984; Orsi et al., 1991). Peralkaline volcanic edifices are usually shield-like (Mahood, 1984; Houghton, et al., 1992) and go through stages of caldera collapse and caldera filling (similar to explosive basaltic calderas, see section 5.2.2).

5.2.2 Basaltic calderas

Basaltic calderas can be considered as either dominantly explosive or dominantly effusive.

Dominantly effusive calderas are associated with shield volcanoes at hotspots such as Hawaii and the Galapagos Islands and calderas created by tumescence and magma drawdown, sometimes with associated explosive eruptions (Simkin and Howard, 1970; Decker, 1987; Walker, 1988). Tumescence is related to intrusion of sills, which expand and inflate the top of the shield. This inflation leads to expansion at the surface creating normal faults. At Hawaii the caldera often contains a lava lake, and the volcano goes through caldera collapse and caldera filling cycles. The caldera eventually fills with successive layers of lava and may over flow. Caldera collapse is associated with lateral magma migration from the chamber often accompanied with eruption elsewhere, often through fissures in the shield flanks (Simkin and Howard, 1970; Munro and Rowland, 1996). As magma migrates the lava lake drains and support is removed from the magma chamber roof leading to caldera formation (Decker, 1987). Calderas form in a similar way at Galapagos, the only difference being the absence of linear rift zones at the surface as seen in Hawaiian examples (Walker, 1988; Munro and Rowland, 1996). The 1968 collapse event in Fernandina (Galapagos) created a caldera with a volume that

was 10 times greater than the erupted products (Simkin and Howard, 1970). This is possibly because faults created by expansion/tumescence are already unstable and collapse is triggered by a small amount of magma withdrawal thereby creating a comparatively large volume caldera (Simkin and Howard, 1970; Munro and Rowland, 1996).

Hawaiian calderas are up to 5×3.1 km diameter with caldera walls up to 140 m high (Walker, 1988). Calderas of the Galapagos are up to 9.3×7.4 km diameter, and 1100 m deep (Munro and Rowland, 1996). The difference in size between Hawaiian and Galapagosian calderas has been suggested as due to storage of magma dominantly beneath the central portion of Galapagos shields whereas at Hawaiian volcanoes magma may be present beneath rift zones that extend well beyond their summit regions (Munro and Rowland, 1996). This would focus the area affected by magma drawdown at Galapagos volcanoes to the area of the caldera causing greater displacement.

Magma rise injects sills in to the country rock (Walker, 1988). Magma accumulation in these sills causes doming of the surface and may lead to opening of radial or concentric fractures at the ground surface (Fig. 5.2; Walker, 1988) and may lead to formation of a lava lake (Decker, 1987). Subsequent magma drawdown leads to failure of the overlying rock and formation of the caldera (Decker, 1987; Munro and Rowland, 1996). Further rise of magma can gradually fill the caldera and may eventually overflow, before the next collapse phase (Decker, 1987; Walker, 1988).

The type example of explosive basaltic calderas is Masaya Volcano in Nicaragua. Masaya is a nested structure that was also thought to have formed dominantly by magma drawdown and collapse into the magma chamber (Walker and McBirney, 1979). More recent work shows this not to be the case and that collapse was concurrent with explosive eruptions that produced basaltic ignimbrites and widespread basaltic plinian fall deposits up to 8.9 km^3 and 12 km^3 respectively (Williams and Stoiber, 1983). Masaya Caldera measures 11.5×6 km and has scalloped margins due to the influence of regional structures (Williams and Stoiber, 1983; Walker et al., 1993). It has formed within a low basaltic shield (Rymer et al., 1998) in an andesite dominated volcanic arc (Walker et al., 1993). It contains a shallow (maybe 500 m depth), low volume (>10 km^3) magma chamber and both its composition and form set it apart from the surrounding volcanics (Walker et al., 1993).

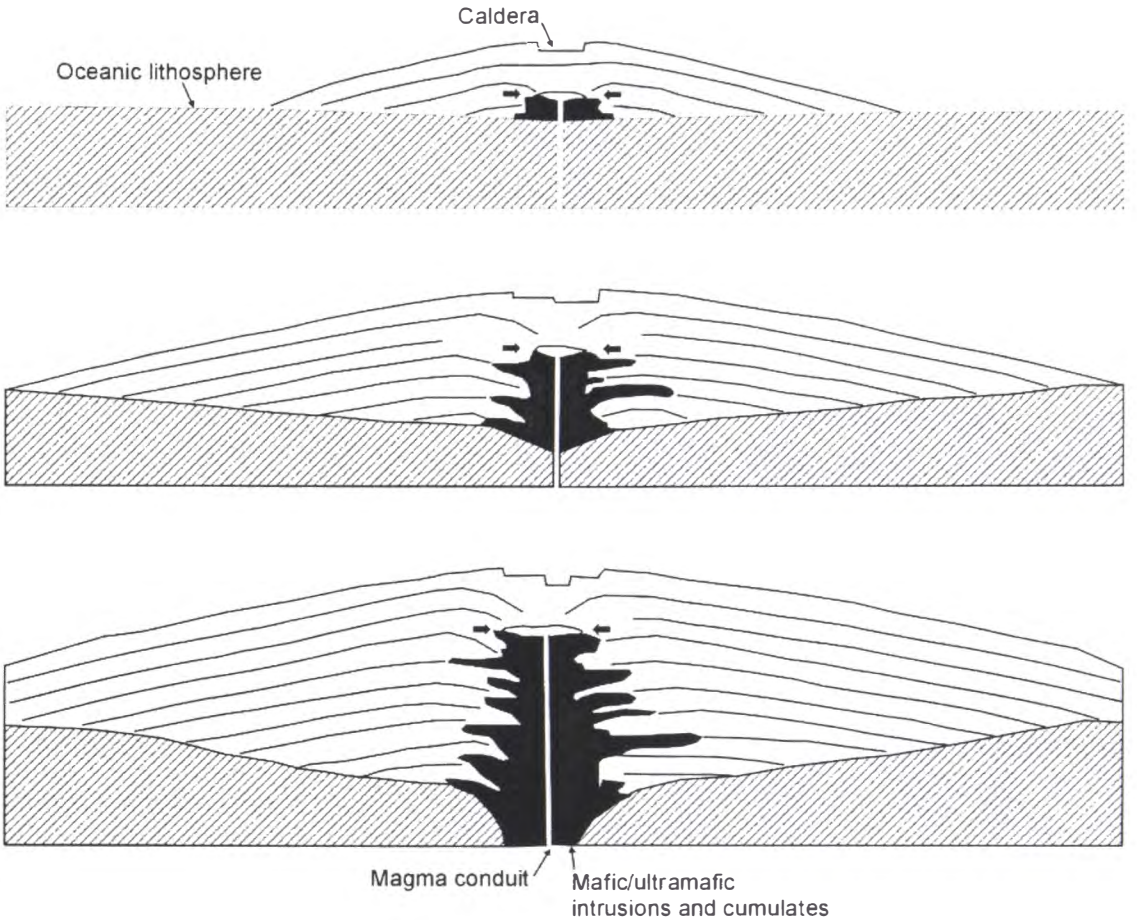

Figure 5.2. Walker's (1988) suggested mechanism for the formation of calderas and shield evolution at Hawaiian volcanoes. The intruding magma and sills can expand the shield thereby causing extension and collapse at the surface. These models assume the magma chamber (between the arrows) remains at a constant depth beneath the edifice. Caldera formation may also be caused by magma withdrawal. Extension due to magma intrusion may lead to an unstable situation which along with magma withdrawal leads to caldera formation.

Masaya Caldera now contains lava flows and cinder cones (Williams, 1983) which may represent a phase of shield building. The structure is nested with numerous pits (Rymer et al., 1998) and it is unclear how many eruptions were involved in the caldera's formation. Masaya Caldera goes through periods of intense degassing (Walker et al., 1993) and eruption of the lava flows is likely from a degassed magma produced during these phases. Periods where the magma is not allowed to degas may cause the magma to become supersaturated with volatiles leading to explosive eruptions and caldera collapse (Williams and Stoiber, 1983; Walker et al., 1993) and it is likely that Masaya goes through periods of shield building and caldera collapse. Collapse is interpreted (based on gravity data and small observed pit crater collapses) to have occurred on faults that dip outwards (Rymer et al., 1998).

5.2.3 Andesite-dacite calderas

Calderas associated with andesitic-dacitic volcanism usually involve the destruction of stratocones. The collapse of Mt Mazama to form Crater Lake, USA (studied by Bacon, 1983), Krakatau, Indonesia (Self and Rampino, 1981), and Santorini, Greece (Druitt et al., 1999) are the best studied examples of this caldera type.

Crater Lake Caldera formed ~6800 yr BP with the eruption of the spectacularly compositionally zoned Mazama Ash (51-59 km^3) and was described by Bacon (1983). During the eruption 40-52 km^3 of the stratocone Mt Mazama collapsed into the caldera. The eruption cycle began with the extrusion of dacite domes on the flanks of Mt Mazama. The climactic eruption started with eruption of the Wineglass Welded Tuff (~4-12 km^3) that was followed by a ring vent phase (ejection of Mazama Ash) during caldera collapse (Fig. 5.3).

The eruptions of Krakatau, Mt Mazama, Batur, and Santorini volcanoes all resulted in the collapse of a caldera and destruction of well formed volcanic cones of basalt to basaltic andesite to andesite composition (Self and Rampino, 1981; Bacon, 1983; Wheller and Varne, 1986; Druitt et al., 1999). The material erupted in the climactic phases was either totally dacitic or was from a zoned magma chamber in which there was a significant amount of dacitic material. The dacitic material is usually consanguineous with andesitic or basaltic material erupted during the same eruption or during later phases and often the dacitic magma is formed by fractionation from the co-eruptive mafic magma (e.g. Self and Rampino, 1981; Bacon, 1983; Wheller and Varne, 1986). This fractionation requires a reasonable residence period in the magma chamber (e.g. 15,000-40,000 yrs suggested for Mazama Ash fractionation (Bacon, 1983)). So the presence of dacite in the eruptive sequence implies formation of a magma chamber during a period of repose that allowed crystal fractionation and probably time for accumulation of a moderate volume of magma. In the above examples caldera collapse follows a period of cone building in which lava and small volume pyroclastic units are erupted. It may be the presence of a large stratocone that inhibits eruption thereby causing the accumulation and fractionation of a moderate volume of magma.

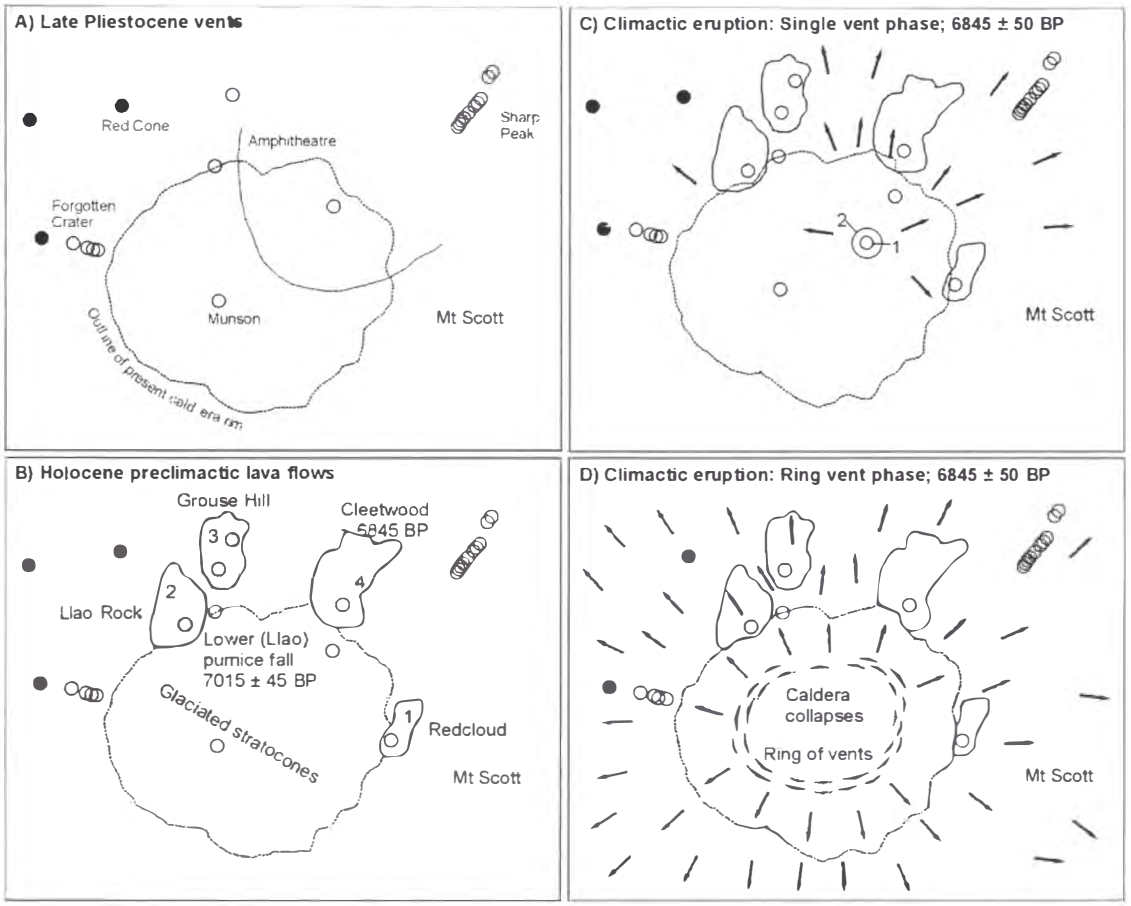

Figure 5.3. The 6845 BP eruption of Mt Mazama and formation of Crater Lake. Eruption began with the extrusion of lava flows and domes (1-4) on the flanks of the cone (B). The climactic phase started with eruption of pyroclastic material (Wineglass Tuff) from a central vent (C). Caldera collapse occurred coherently in a piston-like manner, and eruption took place from a ring of vents at the margins of the collapsing block (D). From Bacon (1983).

5.2.4 Rhyolitic calderas

Formation of rhyolitic calderas has produced the largest volume pyroclastic deposits recorded and created huge collapse depressions. The calderas that form are often >10 km diameter and subsidence of the caldera floor is regularly over 1 km. The largest recorded is La Garita Caldera in the San Juan Mountains, USA that measures 100×35 km and formed on eruption of the >5000 km^3 Fish Canyon Tuff (Lipman et al., 1997).

The classic resurgent rhyolitic caldera cycle envisaged by Smith and Bailey (1968) consisted of seven stages based on Valles Caldera, USA (stages 1-6 are shown in Fig. 5.4):

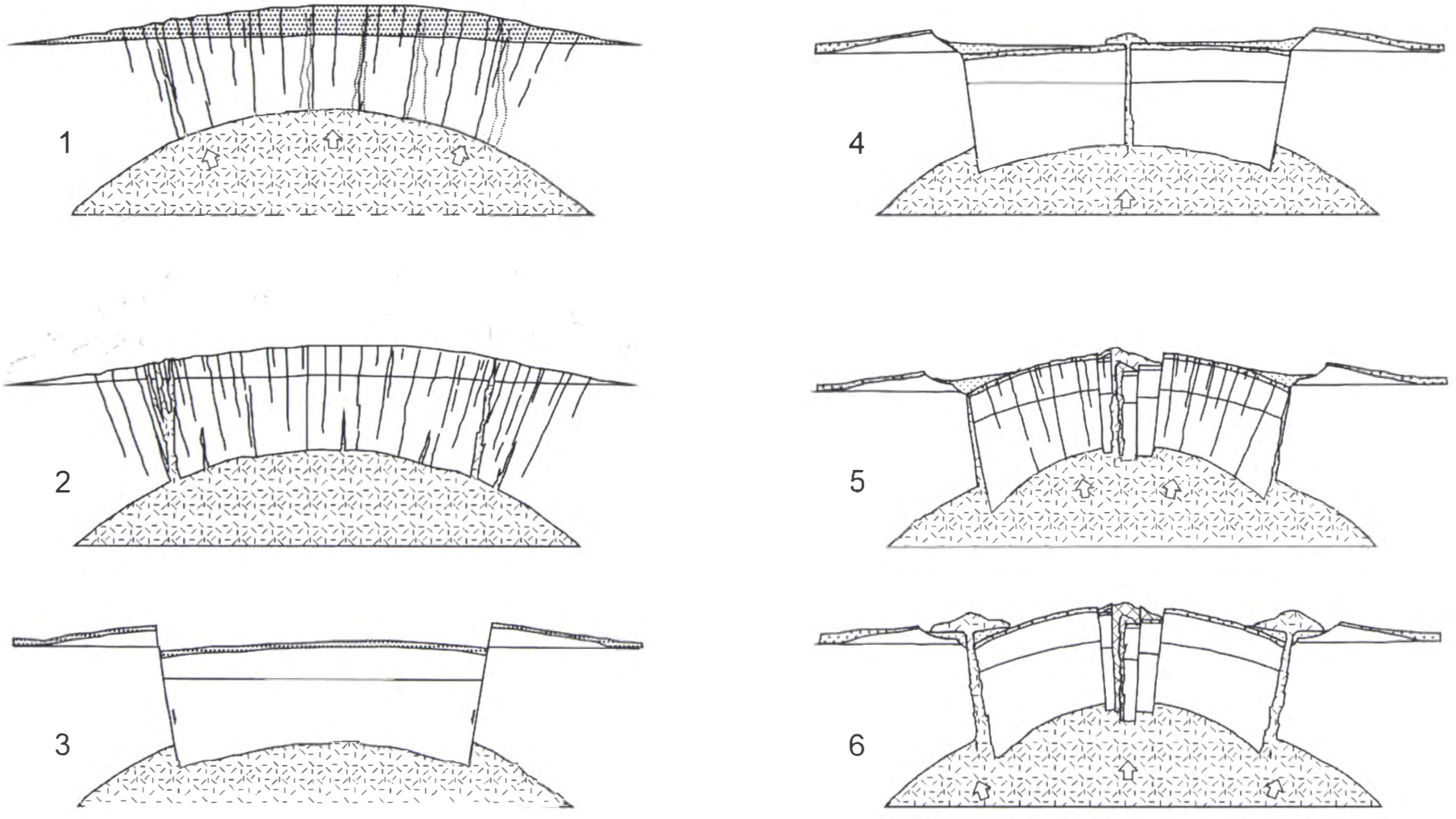

Figure 5.4. Six of the seven stages of a rhyolitic caldera's evolution as envisaged by Smith and Bailey (1968). 1) Magma emplacement and tumescence, 2) large volume pyroclastic eruptions which cause 3) caldera collapse, 4) pre-resurgent, post-collapse volcanism and sedimentation, 5) resurgent doming and 6) major ring fracture volcanism. The seventh stage involves hydrothermal and solfataric activity that proceeds until the magma chamber completely cools.

1) Tumescence and generation of ring fractures- Formation of the magma chamber and magma accumulation causes doming of an area larger than that of the magma chamber. Ring fractures form accommodating ground expansion in response to doming.

2) Caldera-forming eruptions- Regional tumescence is ended by eruption of large volume ignimbrites. Pressure of the rising/accumulating magma becomes greater than lithostatic pressure imparted by the rocks above and eruption the climactic eruption is initiated.

3) Caldera collapse- Caldera collapse usually occurs concurrently with eruption of an ignimbrite. As support is removed from beneath the overlying rocks, collapse is initiated along ring fractures. Ring dikes may be injected during this stage. The caldera usually collapses along vertical or steeply inclined ring fractures.

4) Pre-resurgence volcanism and sedimentation- The caldera is unstable immediately after its formation and the caldera walls undergo caving, gravity sliding, and avalanching. Magma pressure may be partially restored and caldera wall modification may be accompanied by explosive or extrusive eruptions.

5) Resurgent doming- Renewed magma pressure and perhaps isostatic rebound cause the centre of the caldera to dome. Formation of longitudinal, or radial or apical grabens accompanies the ground distension associated with this doming. Volcanism often occurs at the sites of ring fracture and dome complexes may form. The distinction between domes of lava and domes of resurgent origin can be made by observing of sediment deformation. Resurgence causes uplift and deformation of the whole sediment pile. Lavas will be extruded on top of sediments with little disturbance caused.

6) Major ring-fracture volcanism- This is the period of greatest post-collapse surface volcanism. Eruptions occur from the moat or from ring fractures. Volcanics produced during this stage overlie, or are interbedded with, lake sediments and post-resurgence caldera fill. Pyroclastic eruptions and dome

collapse may add to the caldera fill. Distribution of domes may illustrate the presence of a ring fault as at Valles (Fig. 5.5).

7) Terminal solfataric and hot spring activity- Hot springs and solfataras are active throughout the caldera cycle. At all volcanoes this represents the last stage of volcanic activity after all eruptions have ceased. This is an important time for deposition of ore deposits and probably relates to the crystallisation of the pluton involved in caldera activity. The length of stage 7 probably relates to the size of the underlying pluton and, indirectly, to the size of the ignimbrite erupted.

The whole cycle is envisaged to take a million years to complete, but depends on the size of the underlying pluton.

Lipman (1984; 2000) breaks the caldera cycle down into 4 stages:

1) Pre-collapse volcanism- Tumescence is thought to involve surface volcanism. Tumescence is not easily preserved and formation of pre-caldera lava domes and small explosive eruptions are usually the only record of magma accumulation and migration to shallow crustal levels.
2) Caldera subsidence.
3) Post-collapse magmatism and resurgence- Volcanism after caldera formation can be randomly scattered within the caldera or localised along regional structural trends. Renewed rise of magma may uplift the central portion of the caldera either by doming or block uplift. This uplift may also be caused by intrusion of sill complexes.
4) Hydrothermal activity and mineralisation- This may occur throughout the life of the caldera, and may or may not lead to ore deposition.

Both the Smith and Bailey (1968) and Lipman (1984; 2000) models are general caldera cycles and may not continue to completion. Lipman's (1984; 2000) caldera cycle seems based largely on that of Smith and Bailey (1968), varied according to recent research, and grouping Smith and Bailey's original stages 2+3, and 4+5+6 into his stages 2 and 3 respectively. Lipman says that this kind of caldera cycle is dominantly seen where there is thick continental crust, although it was first associated with Toba in Sumatra (a volcano-tectonic depression (Williams, 1941)). The Lipman (1984; 2000) and Smith

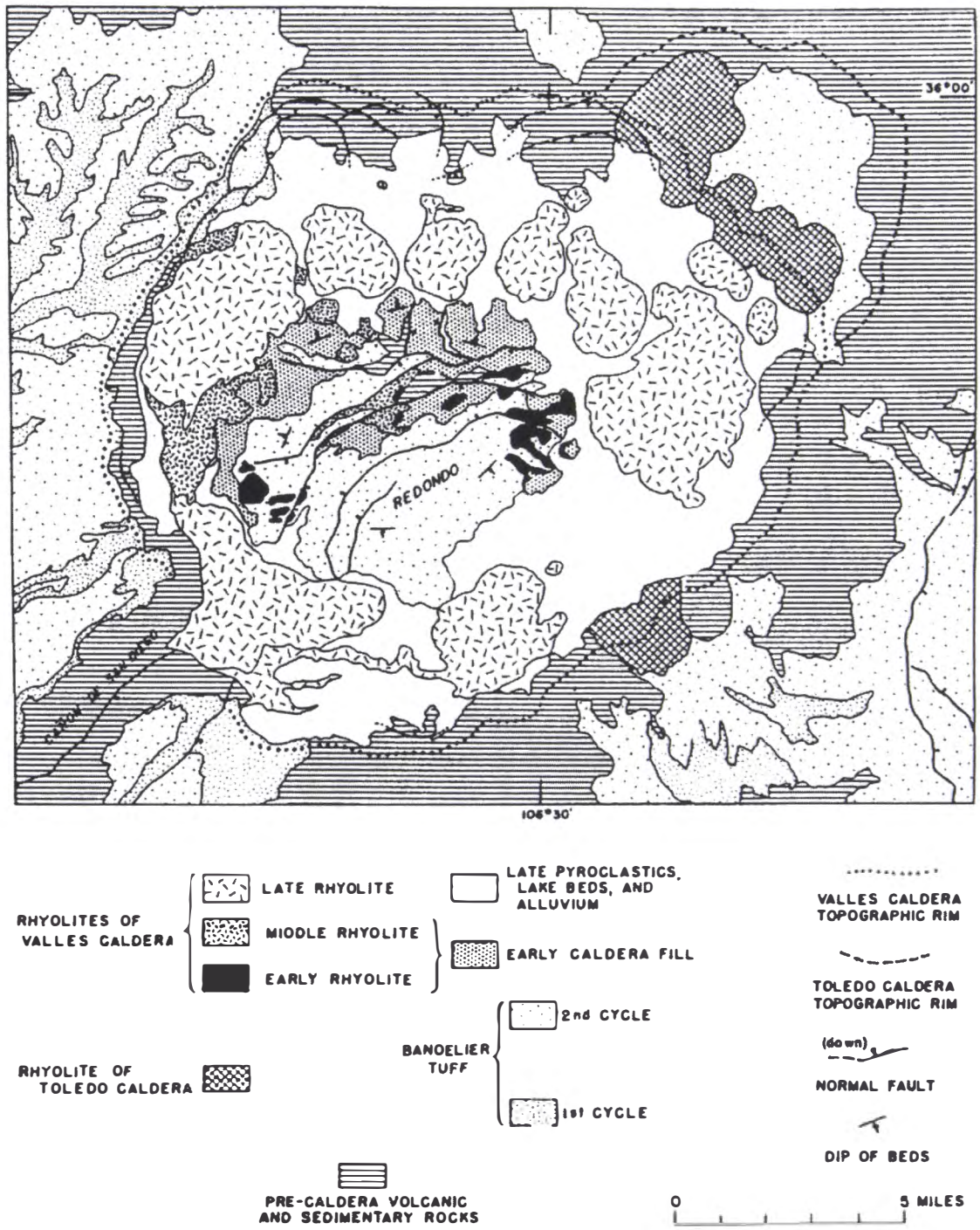

Figure 5.5. Geological map of Valles Caldera on which the 7 stage caldera cycle is based (from Smith and Bailey, 1968). Redondo dome is the resurgent peak on which early caldera fill and Bandelier Tuff are exposed (eruption of the Bandelier Tuff over two episodes caused formation of the caldera). Later rhyolite extruded along a ring fracture, and fractures cross-cutting the dome formed in response to resurgence. The embayment in the northeast is the Toledo embayment and represents pre-Bandelier caldera formation (Self et al., 1986).

and Bailey (1968) models are also associated with relatively stable crust which, when thick and continental, allows accumulation of huge volumes of magma (Wilson et al., 1984; Houghton et al., 1995). Stages may overlap or be by-passed depending on the properties of the magma system, and regional tectonics.

5.3 Processes of caldera collapse

Numerous models for the process of caldera collapse exist in the literature. Five end member collapse processes are: Plate or piston, piecemeal, trapdoor, downsag, and funnel collapse (Fig 5.6).

5.3.1 Plate/piston collapse

Plate/piston collapse involves the subsidence of a coherent block of rock into an evacuating chamber down a ring fault (Fig. 5.6). The caldera floor may be variably faulted but the displacement along intra-caldera floor faults is at least an order of magnitude less than that of the ring fault (Lipman, 2000). Syn-collapse intra-caldera eruptive units should be planar within the caldera without significant thickness variation anywhere across the caldera floor. Numerous North American calderas are interpreted as of this type, e.g. Creede (Steven and Lipman, 1976), Crater Lake (Bacon, 1983; Williams, 1941), and Valles (Self et al., 1984). The dip of the ring fault may be steeply inward, outward, or vertical and may vary with depth and/or proximity to the magma chamber (e.g. Lipman, 1997; Roche et al., 2000). Inward dipping ring faults create a space problem in areas of stable crust requiring either extension, or substantial excavation of the margins of the caldera floor block or surrounding country rock for collapse to proceed.

5.3.2 Piecemeal

Piecemeal refers to a caldera with numerous floor blocks and/or multiple collapse centres (Lipman, 1997; 2000; Fig. 5.6). Branney and Kokelaar (1994) defined piecemeal calderas as ranging from those with highly block faulted floors to those that lack coherent caldera floors because the entire collapsing block has been reduced to a mega-breccia (they provide Aira Caldera, Japan as an example where this has occurred). Collapse may be due to multiple magma chambers with overlapping eruption times

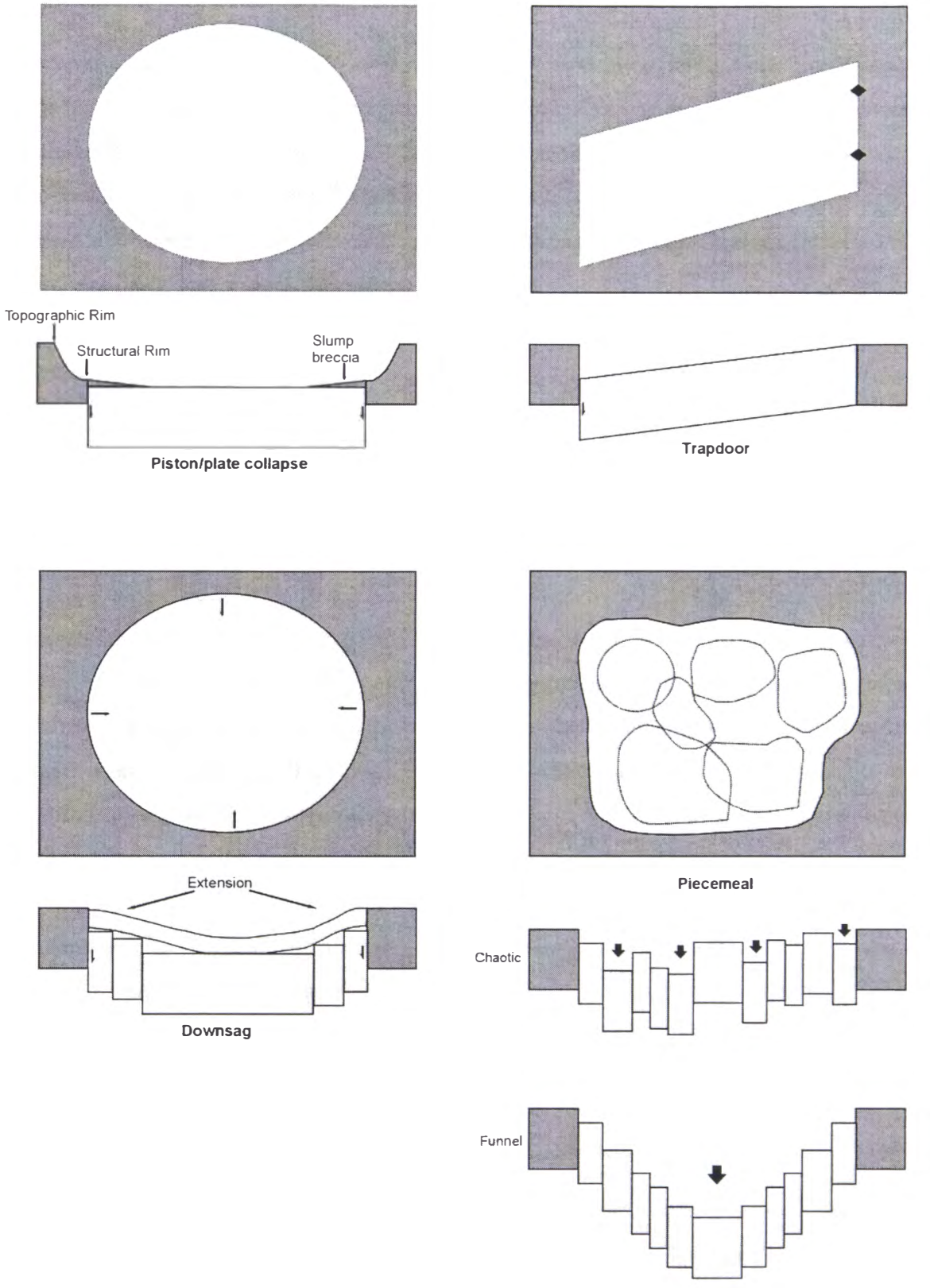

Figure 5.6. Four end members of caldera collapse. Funnel collapse is classed here as a type of piecemeal collapse and is expanded on in Figure 5.8.

(eruption of one may trigger eruption of the other (e.g. Scafell Caldera, England; Kokelaar and Branney, 1994; 1999), or where caldera collapse which is spatially overlapping thereby creating a caldera complex (e.g. Haroharo Caldera, Okataina Volcanic Centre; Nairn, 1989), where tectonically controlled faults break the caldera floor into numerous blocks prior to eruption and control collapse location (e.g. Glencoe Caldera; Moore and Kokelaar, 1997; 1998), or where the entire caldera floor has been rendered a megabreccia (Branney and Kokelaar, 1994). Syn-eruptive caldera fill shows marked and rapid thickness increase in the corresponding collapse centre (Moore and Kokelaar, 1998; Kokelaar and Branney, 1999).

5.3.3 Downsag

This type of collapse occurs where ring faults do not form. Instead the rocks overlying the magma chamber deform by bending without fracture (Walker, 1984). No distinct caldera walls form and the ground surface dips gently towards the caldera collapse centre (Walker, 1984). It is also observed at mine sites where the overburden relaxes in response to removal of subterranean material (Scandone, 1990). Downsag without fracturing creates a space problem and usually requires either extension at the surface, removal of a large amount of subsurface material in the collapsing block, block rotation or bed over bed sliding (Fig. 5.7; Branney an Kokelaar, 1994). Components of downsag often occur in association with other collapse processes including mild flexuring and fracturing immediately prior to formation of a well defined faulted caldera boundary, processes that accompany inception of faulting in brittle upper crustal rocks, incomplete ring fault subsidence, (e.g. hinge of trapdoor collapse), and late inward dipping tilting and fracturing of the topographic wall after collapse (Branney, 1995; Lipman, 2000). Bolsena Caldera, Italy and Taupo and Rotorua calderas, New Zealand have been used as examples of downsag collapse (Walker, 1984).

5.3.4 Trapdoor

Trapdoor collapse is envisaged to occur where formation of a ring fault is incomplete. Collapse is hinged on one side and is deepest towards the other side (Fig. 5.6). The hinged side has to deform in a downsag manner (Lipman, 2000). It is also conceivable that a complete ring fault forms and the encompassed block subsides asymmetrically leading to a trapdoor-like structure.

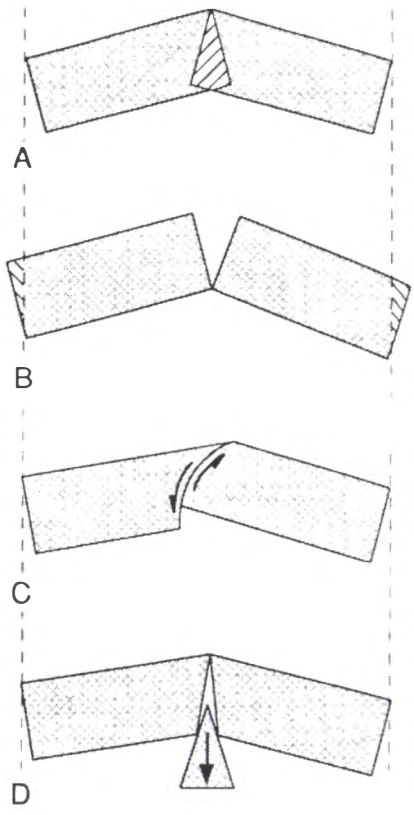

Figure 5.7. Space problems created by warping of a lithologic block. Either destruction of the rock (A), extension at the surface (B), block rotation (C), detachment of a lower block (D), or bed over bed sliding (not shown) are required to allow bending of a crustal block. During downsag it is supposed that the crustal block warps into the space created upon eruption of a large amount of magma. These diagrams show that it is difficult to deform a rock by downsag alone. From Branney and Kokelaar (1994).

5.3.5 Funnel

Funnel calderas may be formed by a number of methods including chaotic collapse where the entire caldera floor is broken up and consists of numerous blocks (megabreccia) that can subside and rotate independently, non-chaotically where coherent blocks are displaced by sequentially greater amounts towards the collapse centre with or without ring faults (Scandone, 1990; Halinan, 1993), collapse into a small or deep magma chamber, (either a tilted block (Roche et al., 2000; see section 5.4) or the collapse collar (Lipman, 1997) dominates the caldera fill), or explosive coring of the conduit (Aramaki, 1984). Funnel calderas have been inferred mainly from the geophysical response of some volcanic depressions but have also been interpreted from drill hole evidence. Geophysical responses often show a flared or broadly V-shaped structure (Aramaki, 1984; Halinan, 1993) (Fig. 5.8). Many Japanese calderas are

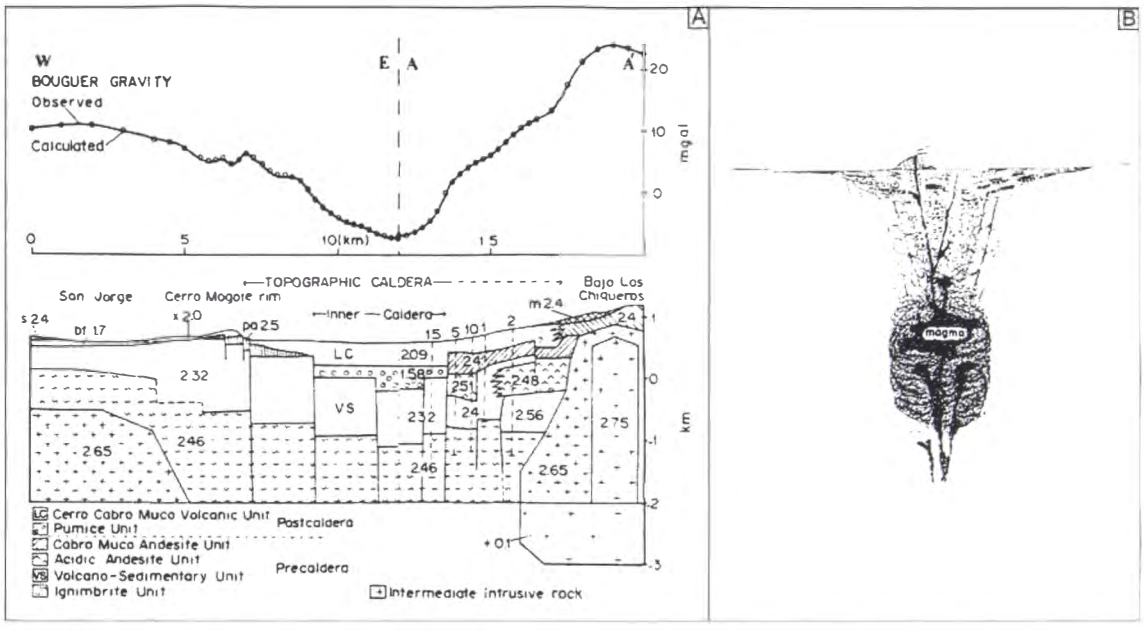

Figure 5.8. Two of three ways in which a funnel-shaped caldera may form (the third is outlined in section 5.4). A) Guayabo Caldera in Costa Rica comprises multiple blocks that have been displaced by increasing amounts towards its centre giving rise to a funnel shaped geophysical response (from Halinan, 1993). B) The model of Aira Caldera formation of Aramaki (1984). The entire central part of the caldera floor has been rendered megabreccia down to the magma chamber, with outer stepped faults. This would also give a funnel-shaped geophysical response. Scandone (1990) shows that creating a caldera by the method shown in B), while possible, is unlikely as it would require a huge amount of energy.

interpreted to have a funnel shaped geometry e.g. Hakone (Kuno et al., 1970), and Aira, and Aso calderas (Aramaki, 1984). Halinan (1993) interprets Guayabo Caldera, Costa Rica to have formed by collapse along concentric ring faults ("telescoping" towards the area of deepest collapse) that gives rise to a similar geophysical response (Fig. 5.8A). Japanese calderas with funnel-shaped geophysical responses are interpreted to have formed by explosive coring of the volcanic vents where the calderas, down to their magma chambers, are filled by material that was explosively ejected and fell back from the eruption column (Fig. 5.8B; Aramaki, 1984). Scandone (1990) says that such explosive coring is unlikely due to the extremely high amount of energy it would require.

5.3.6 Combinations and irregularities

Nearly all calderas are piecemeal by Branney and Kokelaar's (1994) definition. Their piecemeal description includes the funnel calderas of Aramaki (1984) and Halinan (1993) and, in its strictest sense would include Crater Lake caldera as described by

Williams (1941), which is one of the type examples of piston collapse. Lipman (1997) noted that most piston-like caldera floors contain faults that break them up; he suggests that where displacement down the bounding (ring) fault is greater than the subsidence down faults within the subsiding block by at least an order of magnitude it should be termed a piston or plate caldera.

Ring faults associated with piston collapse can be inward dipping to outward dipping or vertical. Inward dipping ring faults, inferred to exist by Smith and Bailey (1968) and Lipman (1984), require an extensional environment otherwise a space problem exists that prohibits collapse. In many eroded calderas the ring faults described are very steeply inward dipping or vertical (e.g. Grizzly Peak; Fridrich et al., 1991). Outward dipping faults are now thought to be more common (Branney, 1995; Roche et al., 2000; see caldera analogues section 5.4), have been observed at eroded calderas (e.g. Yoshida, 1984; John, 1995), and interpreted from geophysical analysis (Mori and McKee, 1987; Rymer et al., 1998).

Many structural characteristics may be attributed to the same caldera collapse process. Numerous collapse processes may occur at the same caldera and surficial features that appear generated by one collapse process may be controlled, at depth, by blocks subsiding by a different process (see section 6.3).

5.4 Caldera Analogues

Caldera collapse has been compared to craters produced by subsurface nuclear explosions (Scandone, 1990), mining subsidence and ice melt pits (Branney, 1995), and laboratory models (Komuro et al., 1984; Komuro, 1987; Marti et al., 1994; Roche et al., 2000). Collapse structures associated with withdrawal of oil from a reservoir are also analogous to caldera collapse (Odonne et al., 1999). Experimental analogues have enhanced understanding of how calderas collapse, but the resulting models lack realism because they have been carried out under static conditions. External forces that modify stress regimes around a magma chamber, and cause disruption to overlying strata, are missing in analogue models and substances used for analogue crust commonly have uniform properties throughout their thickness, a condition not often found in nature.

5.4.1 Tumescence

Tumescence is the doming of overlying strata as a magma chamber intrudes and accumulates within the crust. This accumulation causes semi-spherical uplift of the surface and the resultant extension causes formation of faults approximately radial to, and/or concentric with the apex of the dome (Komuro et al., 1984; 1987; Marti et al., 1994; Roman-Berdiel et al., 1995). Radial and ring dikes may be intruded along the fractures in response to magmatic pressure (Lipman, 2000). Doming of the surface also leads to tension in the crust above the chamber and requires formation of an apical graben (Fig. 5.9), the shape of which is governed by the shape of the magma reservoir (Komuro et al., 1984; Marti et al., 1994).

5.4.2 Caldera collapse

Marti et al. (1994), Branney (1995), Odonne et al. (1999), Roche et al. (2000), and Acocella et al. (2000), all show that the faults that bound the caldera floor are outward dipping reverse faults at the surface that steepen with depth, becoming vertical or steeply inward dipping (Fig. 5.10 and 5.11). Outward dipping faults have also been shown at Rabaul and Masaya calderas (Mori and McKee, 1987; Rymer et al., 1998). The caldera floor block may also break up into a series of conical blocks depending in the depth and size of the magma chamber (Fig. 5.11; Marti et al., 1994; Roche et al., 2000). Usually bounding these conical blocks is a near vertical ring fault that extends upwards from the magma chamber becoming reverse at the surface (Fig. 5.11). Radial and concentric faults formed during tumescence may be reactivated during magma withdrawal (Fig. 5.9). Normal fault movement may dominate during the early stages of caldera formation but as collapse proceeds fault movements are dominantly along the ring fault and reverse faults that break up the caldera floor (Fig. 5.9; Komuro et al., 1984; Marti et al., 1994). The surface expression of the ring fault in analogue models is seen to propagate parallel to the caldera margins away from a single point, "unzipping" in a fashion that has been inferred from stratigraphic variations in ignimbrites (e.g. Valles Caldera, Self et al. (1986) Long Valley Caldera, Hildreth and Mahood, (1986), and Wilson and Hildreth (1997) in Roche et al. (2000), and Reporoa Caldera, Beresford and Cole (2000)).

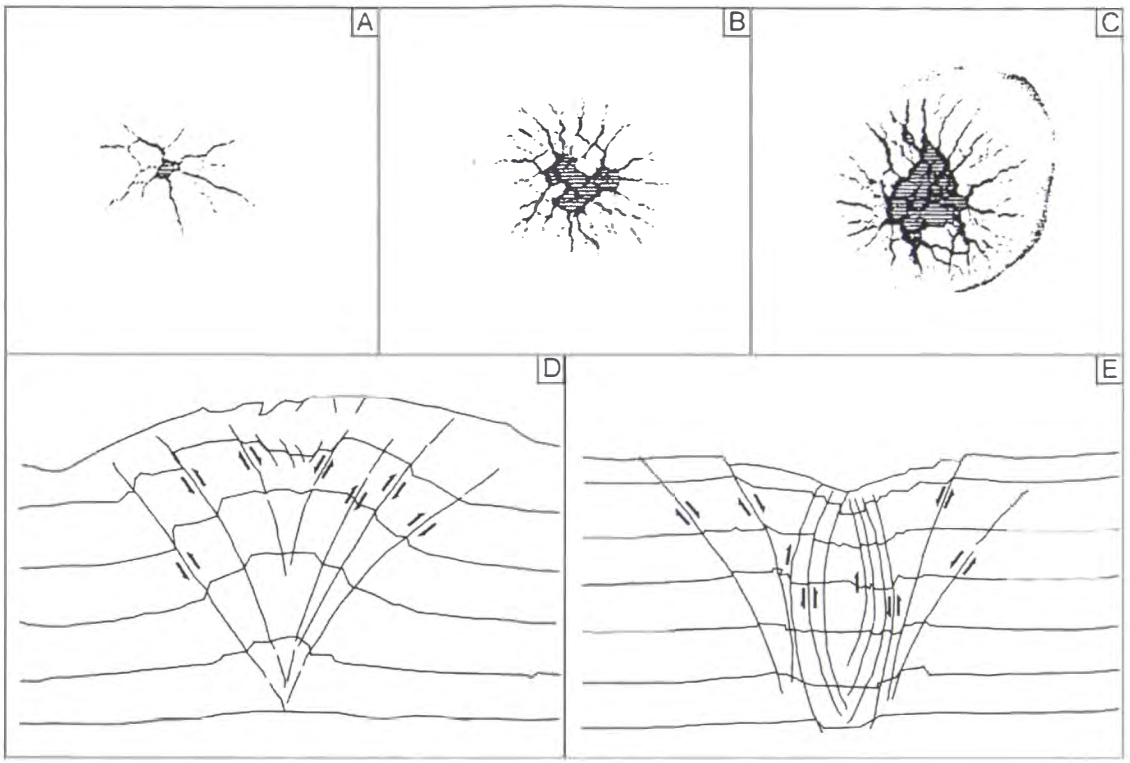

Figure 5.9. A, B, and C are plan views of the area deformed during a tumescence experiment. The ground domes and extends, and eventually the apex subsides. D shows a cross section through an experimental tumescent dome showing reverse faults accommodating the uplift and the start of apical collapse. E illustrates that faults active during tumescence can reverse their sense of movement during caldera collapse. A, B, and C from Komuro (1987). D and E from Marti et al. (1994).

Roche et al. (2000) showed in their experiments that the morphology of the collapse structure depends on the depth, size, and shape of the magma chamber. Shallow magma chambers with large diameters lead to downsag or piston collapse calderas, whereas deep chambers, with small diameters lead to funnel shaped structures. Of great importance in Roche et al.'s (2000) models was the formation of an extensional tilted block beyond the margin of the subsiding caldera floor (Fig. 5.12). Odonne et al. (1999) and Branney (1995) also identified the presence of a tilted block and marginal extension. The percentage of the surface of the caldera that the tilted block makes up is directly proportional to the aspect ratio of the caldera floor (thickness/diameter) that is governed by the depth and size of the magma chamber. With small deep magma chambers the aspect ratio of the caldera roof is high and the tilted block may make up to 80% of the calderas surface morphology and imparts a funnel-shaped geometry. The tilted block is also a potential explanation for downsag towards the margins of calderas where shallow sloping ground surfaces are often observed (e.g. Walker, 1984).

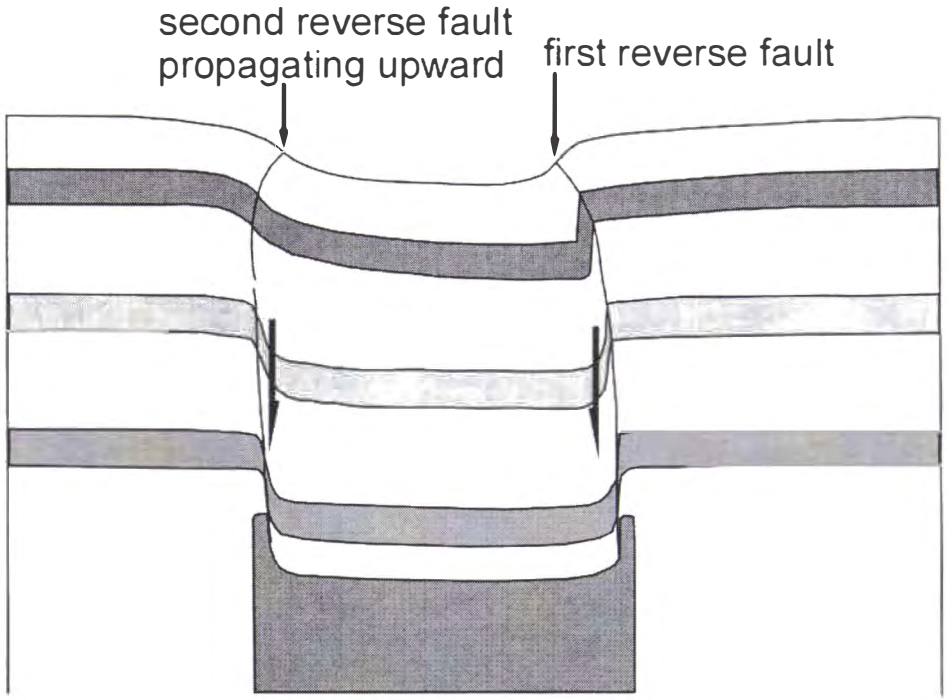

Figure 5.10. The result of one of Roche et al.'s (2000) laboratory experiments. Note the caldera block bounding fault is outward dipping and reverse at the surface, steepening to vertical at depth.

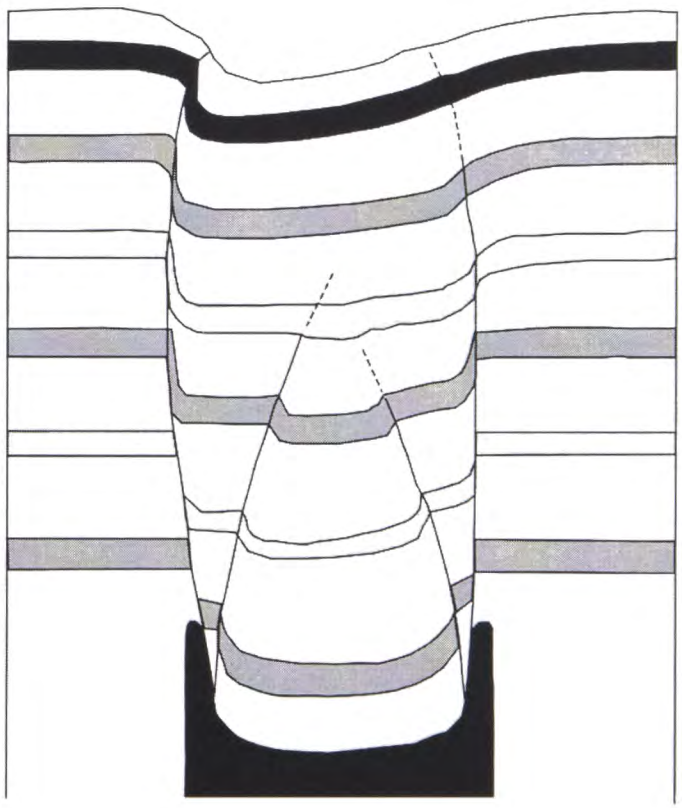

Figure 5.11. Sketch showing a conical mass forming in the subsiding caldera floor block. With increasing depth to the magma chamber more conical blocks are created during caldera formation. Note also that the ring fault dips outwards at shallow depths. From Roche et al. (2000).

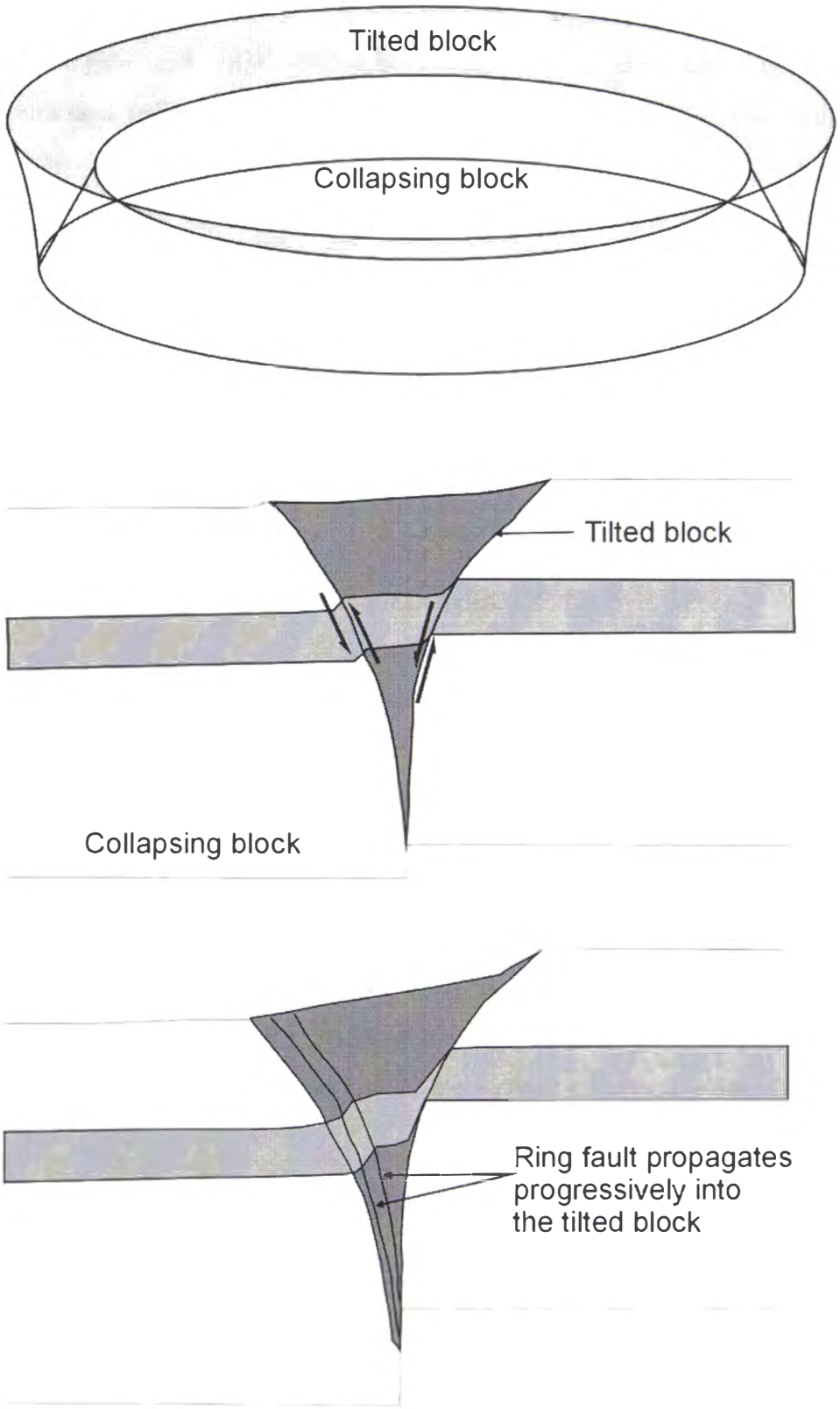

Figure 5.12. Sketches and location of the tilted and collapsing blocks (A and B) seen in Roche et al.'s (2000) experiments. The "ring fault" propagates progressively into the tilted block as subsidence proceeds (C). The tilted block may account for downsag structures seen towards the margins of caldera collapse. Funnel shaped calderas result with small or deep magma chambers as the tilted block takes up a greater proportion of the surface.

Roche et al. (2000) also found that magma chamber shape has a substantial influence on the stress regime around the chamber and on the initiation and shape of collapse. Square, rectangular and elliptical chambers with flat roofs were modelled along with half spheres and half cylinders. For square and rectangular chambers, initiation of collapse was observed to begin from the middle of one side (above the chamber), with the fault propagating away from this point until it reached the corner that inhibited further growth. Collapse proceeded in a trapdoor manner before a fault was initiated on the opposite side (from its middle) which, in turn, was followed by fault formation on the other two sides in the same way. For rectangular, elliptical and half cylinders, faults propagated from the middle of one of the longest sides first, followed by the opposite side for rectangles and ellipses. For half cylinders the collapse was strongly asymmetric parallel to the cylinder long axis with subsidence very much deeper at the side where the first faults initiated than the side opposite. In the tilted block grabens began to form in the case of half cylinders, squares and rectangles.

Scandone (1990) drew comparisons between caldera collapse, mining subsidence, and surface craters formed by subsurface nuclear explosions. He viewed caldera formation to occur in the same way mining subsidence and nuclear explosion collapse pits proceeded; by chaotic collapse of successively higher blocks of rock beneath a zone of relaxation into the magma chamber (Fig. 5.13). The "peeling" of successively higher blocks continues until a stable shape is reached. If a stable shape cannot be reached before the collapse reaches the surface, or if the zone of relaxation penetrates the surface, a depression results (Fig. 5.13). If the ratio between the width of the cavity to its depth is large, shear cracks can rise to the surface causing a piston-like collapse (Wisser, 1927, in Scandone, 1990; Fig. 5.13A). If the magma chamber is wide enough, and ring fractures do not form, sagging can occur at the surface above the area of detaching subsurface blocks (Fig. 5.13C). Scandone notes that the surface depression formed in such a way will always be of less volume than the volume of the initial cavity beneath, due to the chaotic or broken nature of the collapsing block.

Analogue models and comparisons with other collapse structures have significantly advanced the understanding of processes by which caldera formation proceeds. All of the models to date, however, have been carried out under static conditions. Roche et al. (2000) acknowledge that their models do not take in to account the effect of pre-existing structures such as faults associated with both regional tectonics and earlier formed

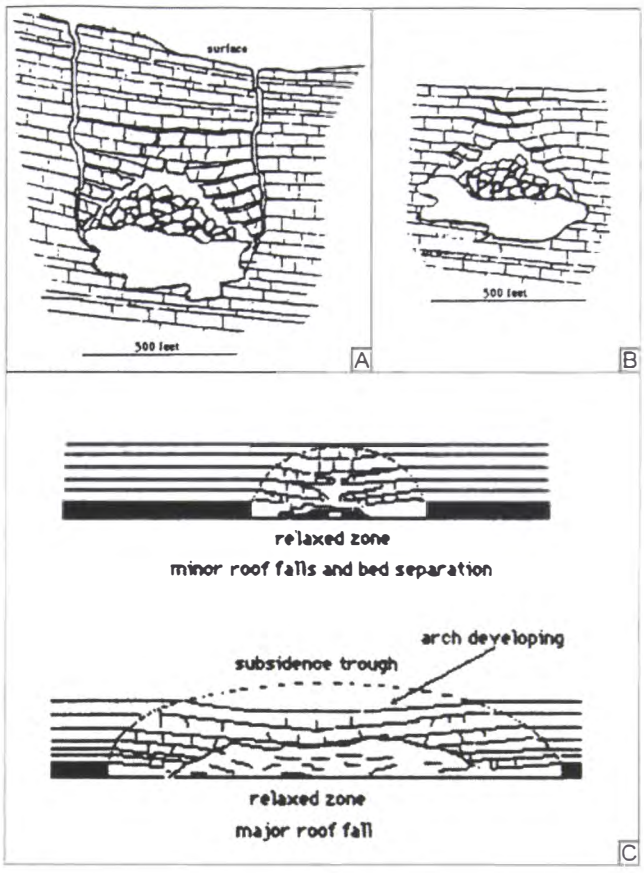

Figure 5.13. Scandone (1990) drew comparisons between mining (A and B) and nuclear blast collapse pits, and calderas. He views such depressions as forming as successively higher layers peel off in a zone of relaxation (C) and sink into the cavity until a stable shape is reached. If the relaxation zone reaches the surface a depression will form akin to a downsag caldera. If the relaxation zone doesn't reach the surface the ground surface remains unchanged unless the cavity is large enough and deep enough in which case a central fault-bounded block forms and can collapse like a piston (A). A) and B) are from Wisser (1927) and C) from Thomas (1973) in Scandone (1990).

caldera structures. Other problems with analogue models are the mediums in which the collapse is studied. Usually the models use sand or sometimes flour. Neither have significant cohesion and the properties of the collapsing block are uniform from the top to the base of the experimental pile. Caldera floor rocks may contain much heterogeneity and are often lithified complicating both the formation and propagation of structures involved in caldera formation. The structures formed during analogue models thus far are ideal structures and further experimentation is required to resolve the types of structure that form when external forces are applied to non-uniform strata with pre-existing defects during caldera collapse.

5.5 Stress regimes associated with caldera formation and initiation of collapse

Gudmundsson (1988; 1998) and Gudmundsson et al. (1997) have modelled the stress trajectories around a magma chamber and the formation of ring faults mathematically. Models were calculated based on spherical and sill-like magma reservoirs that were subjected to varying external stress regimes. They found that ring fault formation is unlikely when a magma chamber is subject only to internal magmatic overpressure. Spherical over or under-pressured chambers, and sill-like chambers under tensile stress, were also not likely to initiate rings faults. Only when the magma chamber has a sill-like geometry, is over-pressured, and has excess vertical pressure applied to its base causing doming of overlying rocks is ring fault formation probable. The stress field that surrounds a magma chamber is a function of forces acting on (e.g. regional tectonics), and within, that magma chamber. For a ring fault to form the area of maximum stress needs to be at a point or points above the magma chamber radially away from its centre (Fig. 5.14). If the maximum stress is located at the magma chamber margin then faults initiate there leading to ring dikes or cone sheet emplacement that would inhibit further fault propagation (Fig. 5.14). With all spherical chambers, and in sill-like chambers where the only forces acting were external, the area of maximum stress was located at the magma chamber margins or above the centre of the chamber which is not favourable for ring fault formation. Only where a sill-like chamber existed that had caused doming in the ground surface did this area of maximum stress occur away from the chamber margin allowing a ring fault to form. The conclusion reached by Gudmundsson (1988; 1998) and Gudmundsson et al. (1997) was that the collapse occurs in response to doming of the overlying crust, this collapse opens conduits for the magma and that the collapse drives the eruption rather than vice versa.

The collapse in response to doming is verified by laboratory models (Komuro et al., 1984; Komuro, 1987; Marti et al., 1994), but this collapse may block conduits rather than open them (Legros et al., 2000) and withdrawal of magma from the magma chamber is seen to reactivate these faults (Marti et al., 1994). Also, in laboratory models the withdrawal of magma leads to initiation of ring faults at the magma chamber margin that migrate towards the surface (Roche et al., 2000). Gudmundsson (1988; 1998) and Gudmundsson et al. (1997) do not take into account the possibility of withdrawal of magma causing collapse in their calculations, and the only scenario really provided for is that of magma accumulation and associated tumescence that does lead to

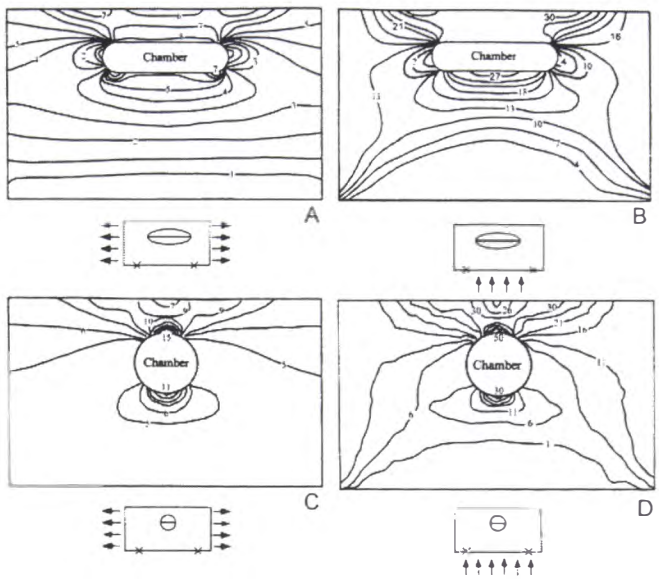

Figure 5.14. Gudmundsson's (1998) computer generated models of stress fields around magma chambers. For a ring fault to form Gudmundsson considers that it must initiate somewhere above the magma chamber and propagate downwards. If it initiated at the magma chamber, dike intrusion would occur stabilising the crust and inhibiting further fault growth. In A) extension is applied to a magma chamber, stress reaches a maximum at the magma chamber margin and faults would initiate here. In B) upward force is applied to the chamber simulating magma accumulation and doming at the surface, maximum stress occurs at the surface creating favourable conditions for ring fault formation. In both circumstances with a spherical chamber (C and D) maximum stress occurred at the chamber margin. Gudmundsson's models do not use removal of magmatic support as a cause of caldera collapse.

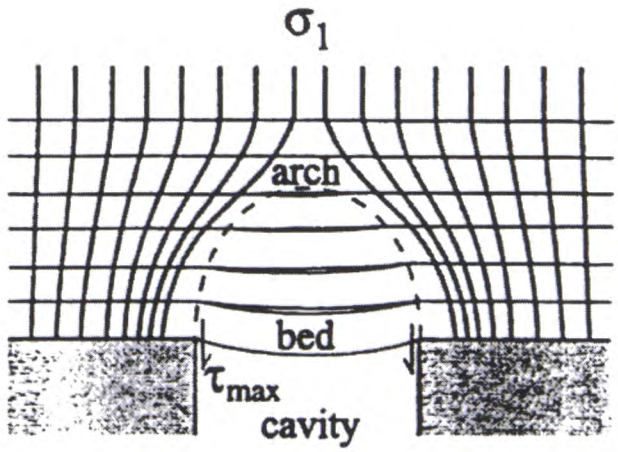

Figure 5.15. How the principal stress is affected by the presence of an underlying cavity. Lines of principal stress σ_1 curve above the cavity and converge towards its margin. This creates an arch beneath which pressure is less than lithostatic and collapse occurs. Outside the arch a limit of influence (not shown) bounds an area of rock in which principal stress lines are deflected and σ_1 is greater lithostatic. The limit of influence marks the area in which the principal stress lines are affected by magma withdrawal. Maximum shear stress (τ_{max}) is vertical near the cavity margin leading to vertical normal faults. Away from the cavity the τ_{max} dips outwards leading to reverse faults. Modified from Vidal (1961) and Given (1973) in Roche et al. (2000).

an apical depression but this is succeeded in importance as a caldera morphology control by removal of support of the caldera floor through magma withdrawal (Marti et al., 1994).

Deposits have been described that show that many caldera forming eruptions begin with a central vent phase before moving to a ring vent and collapse phase (e.g. Crater Lake (Bacon, 1983), and Reporoa Caldera (Beresford and Cole, 2000)) suggesting that the eruption of magma controls collapse and not vice versa. Gudmundsson (1988; 1998) says that his calculations conform well to observed structures at Icelandic Calderas. Many authors have suggested calderas in Iceland originate by lateral magma movement (e.g. Sigurdsson and Sparks, 1978) and Gudmundsson (1987) concurs, contradicting his inference of caldera collapse causing eruption.

Roche et al. (2000) predicted the angle of faults that would form in their models based on the stress fields that should surround a magma chamber and the internal angle of friction. They drew a parallel between the stress field surrounding a mining cavity and that surrounding a magma chamber. The maximum principle stress axis is vertical at the edge of the chamber, but curves towards a central point when above the chamber (Fig. 5.15). This suggests that the first faults to form are reverse that dip outward at the surface and increase dip with depth. This occurred in their models.

5.6 Caldera Size

Spera and Crisp (1981) studied the horizontal caldera surface area and magma chamber zonation. They compiled a list of studied calderas and compared their areas with the volume of erupted material. Plotting the log of the erupted volume vs the log of caldera area they found an approximately 1:1 relationship although there is a large amount of scatter (the ratio of magma volume: caldera area may be up to 100:1 km). They also say that a caldera associated with a cylindrical magma chamber is approximately 3 times greater in area than for a conical chamber that erupts the same volume of magma.

Caldera horizontal surface area is highly variable depending on the amount of magma erupted. Similar volumes of erupted material can lead to very different caldera areas and volume, for example Krakatau, Indonesia and Pinatubo, Philippines erupted between 1 and 10 km^3 and resulted in well formed calderas while Quizapo, Chile and

Santa Maria, Guatemala erupted 4 km^3 and 8.5 km^3 respectively and did not result in any collapse at all (Gardner and Tait, 2000 and references therein). Generally the greater the amount of material ejected the greater the horizontal caldera surface area will be, but it will also depend on the magma chamber geometry and depth below the surface. The area of collapse is chiefly dependent on the surface area and shape of the magma chamber roof, and the depth and amount of material extracted (Roche et al., 2000).

5.7 Discussion: Factors affecting caldera morphology and collapse processes

The caldera types and processes described above represent ideal structures or end members that are rare in nature. There are variations to each type structure and many factors contribute to final caldera morphology and mode of collapse. Numerous examples exist that cannot be attributed to any one particular type.

The main factors likely to exist that affect caldera collapse and morphology are defects in the country rock. Any faults that are present will provide lines of weakness along which caldera collapse should preferentially occur and they can break up the caldera floor into numerous blocks. Depending on the dip of pre-existing faults, caldera floor blocks can be created that have roughly uniform cross sectional area from the ground surface to the magma chamber (vertical block bounding faults, Fig. 5.16A, e.g. Moore and Kokelaar, 1997; 1998) or can be irregularly shaped prisms with limited vertical and horizontal extents (Fig. 5.16B). When caldera collapse proceeds these blocks will probably move and/or rotate with a dependency on adjacent blocks that is governed by their size, their proximity to the main locus of collapse, and the amount of subsidence. The ultimate situation of this crustal break-up is the sandy material used as crust in laboratory experiments where each grain acts as a block of limited 3-dimensional proportions that can move and rotate as adjacent grains do the same.

At Ischia pre-existing structures have a great effect on the shape of the resurgent block. Uplifted sections are bounded by regional tectonic structures (Fig. 5.17; Orsi et al., 1991; Acocella and Finiciello, 1999). Pre-existing structures have also been shown to affect the morphology of resurgence at Pantelleria (Fig. 5.17; Orsi et al., 1991; Tibaldi and Vezzoli, 2000), Campi Flegrei, and Rabaul (De Natale et al., 1997). In the same

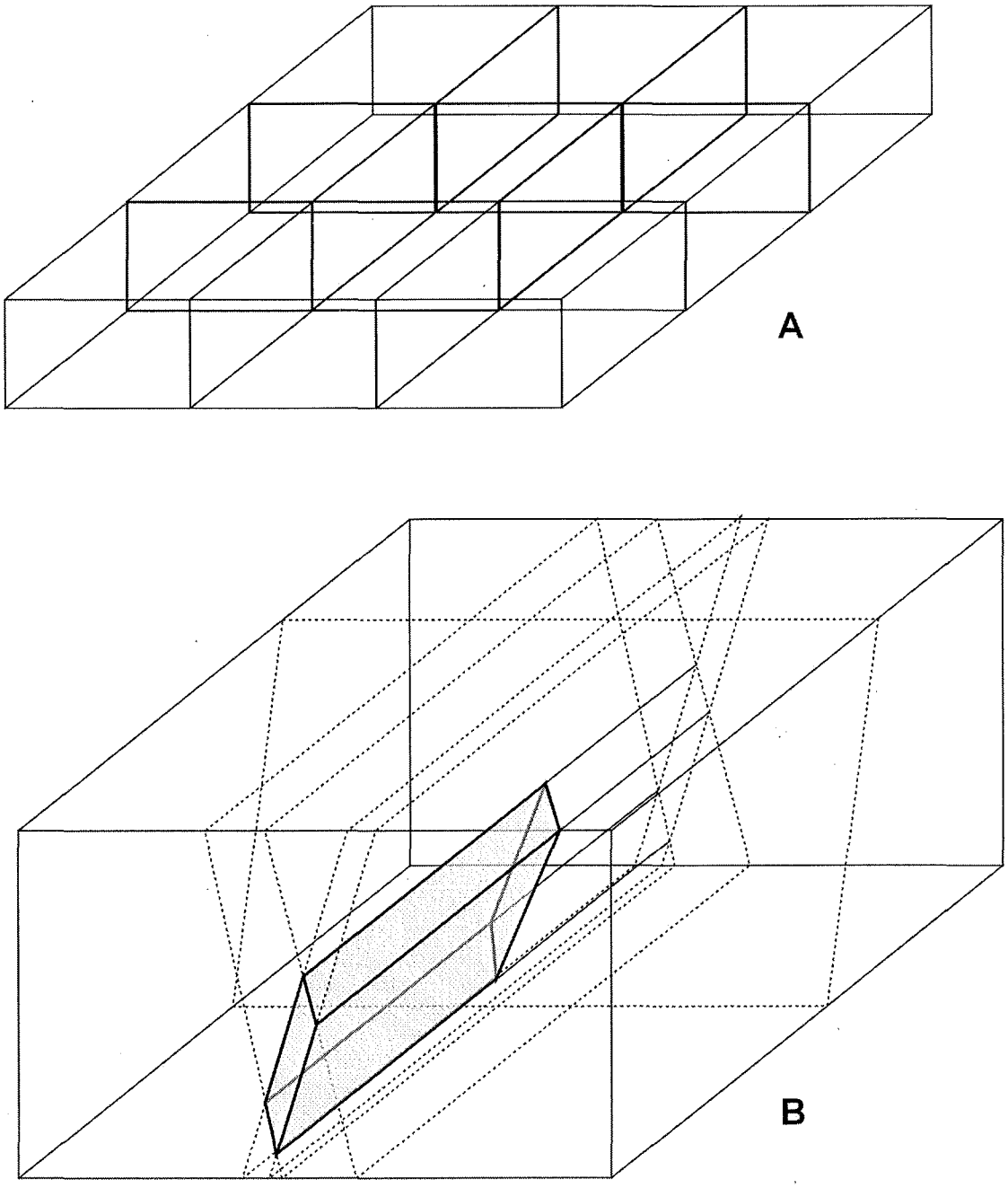

Figure 5.16. Simple block diagram showing how crustal blocks can be created by intersecting fault planes (bounding the blocks in A, and bounded by dashed lines in B). In A all fault planes are vertical leading to blocks with uniform cross-sectional area (horizontally and vertically). In B, dipping faults intersect with sub-parallel or orthogonal fault traces. For simplicity no movement has occurred on any of the faults. In nature this would displace older intersected faults. The block created would rotate and move as those around it do creating a complex 3-dimensional collapse situation.

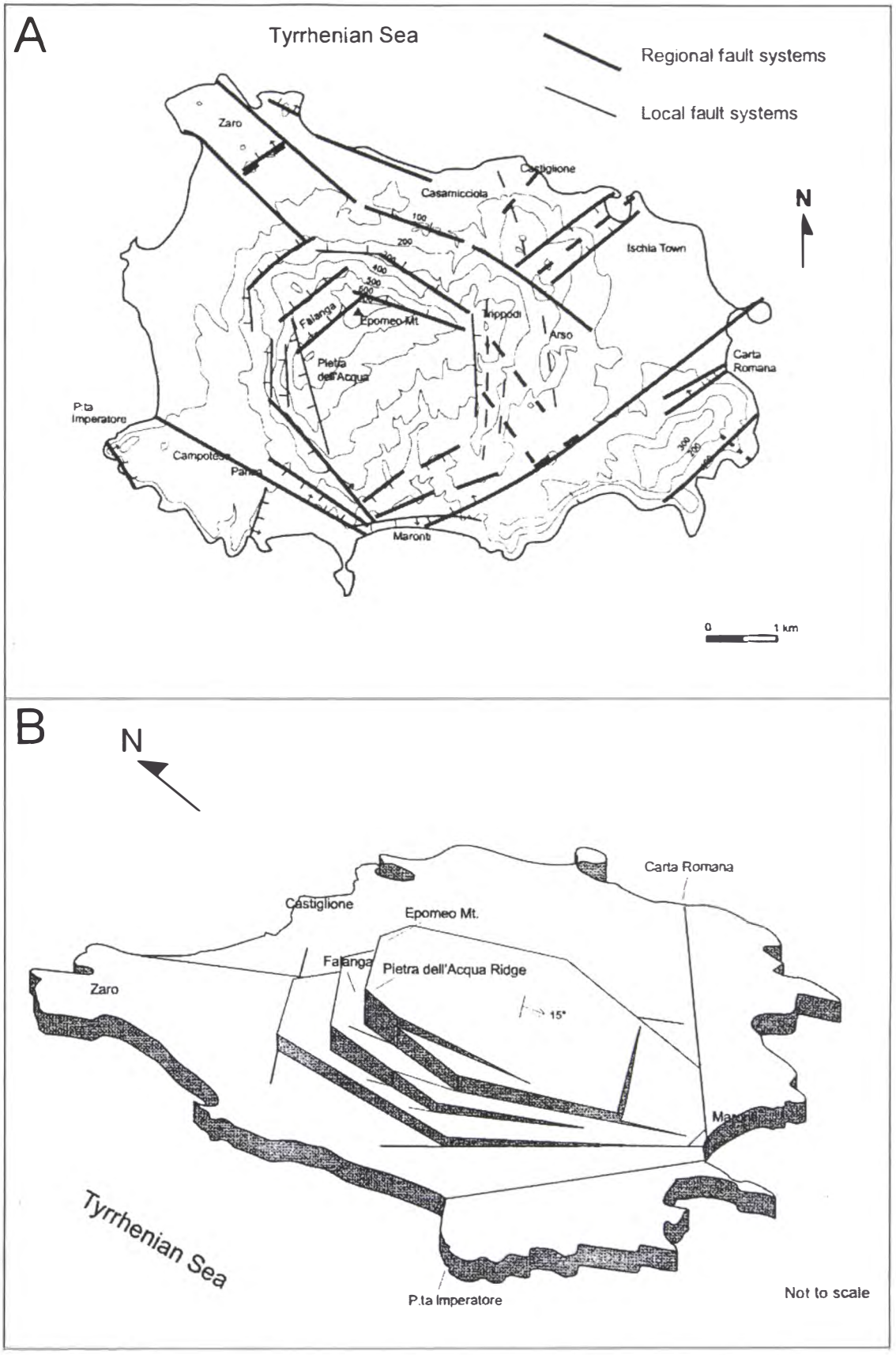

Figure 5.17. The island of Ischia, an example of the affects of pre-existing structures on resurgence. Regional and local fault patterns are shown in A. B is a block diagram (not to scale) of the shallowest part of the resurgent block. The affect of pre-existing structures on the morphology of the resurgent block is obvious. From Acocella and Funiciello (1999).

way, pre-existing structures are likely to affect caldera collapse and morphology of the collapsing block.

Faults also provide potential paths for ascending magma, can control the location of erupting vents (Druitt and Sparks, 1984; e.g. Nappi et al. (1991), and Smith and Houghton (1995)), and may play a role in magma chamber formation (e.g. Nappi et al., 1991). The maximum depth and area of caldera collapse will always depend on the dimensions and depth of the magma chamber and the volume of material that erupts from it, but faults in the caldera floor will control the way it breaks up and, to a certain extent, the way it subsides.

Caldera floor heterogeneities are also likely to affect the mode by which collapse takes place. The ease at which the different lithologies can dislocate from one another and their ability to bend can generate surface morphology that suggests formation by a different process than has occurred at depth (e.g. downsag and/or deformation of flat lying strata above an area of brittle basement collapse as at Scafell Caldera, Branney and Kokelaar, 1994; Kokelaar and Branney, 1999).

Any topography that exists is likely to affect the way stress concentrates above the magma chamber also affecting the way in which the caldera subsides.

5.8 Case studies

The five calderas discussed below are good examples of the role of tectonics in caldera collapse and eruption location.

5.8.1 Snowdon Caldera, Wales

Snowdon Caldera was active during the Ordivician and formed during the eruption of the Lower Rhyolitic Tuff Formation (Kokelaar, 1988; Branney and Kokelaar, 1999). It formed in a transtensional environment that was compositionally bimodal (rhyolite and basalt). The volcanism occurred in response to subduction, probably in the present day northwest, during the closure of the Iapetus Ocean (Kokelaar, 1988). Structures that were associated with transtension in the area of volcanism dominantly strike northwest-southeast (Howells et al., 1987; Kokelaar, 1988; Kokelaar and Branney, 1999; Fig.

5.18). Volcanism was controlled by these fractures with vent sites at various localities along them (Howells et al., 1987). This fault pattern broke the area up into a series of blocks that would have affected caldera formation (in a similar way to TVZ; see section 5.9). Kokelaar and Branney (1999) suggest that volcanic activity in North Wales during the Ordovician was similar to central TVZ in terms of production and that the rate of extension was probably also comparable, the main difference being that North Wales during the Ordovician was submarine.

The Snowdon Volcanic Group comprises, in order of decreasing age, the Lower Rhyolitic Tuff Formation (LRTF), Bedded Pyroclastic Formation (BPF), and Upper Rhyolitic Tuff Formation (URTF), which are rhyolitic, basic and rhyolitic respectively (Fig. 5.19; Campbell et al., 1987; Kokelaar, 1988). The control of structures relating to both caldera collapse and regional tectonics on volcanism is evident with post-caldera vent locations aligned along regional structures and along local faults caused by caldera subsidence and observation of LRTF thickness increasing into both the caldera and tectonically controlled depressions (Fig. 5.19; Campbell et al., 1987; Kokelaar, 1988; Kokelaar and Branney, 1999). Snowdon Caldera itself (Fig. 5.19) formed by eruption of the LRTF and was also the site of later activity that formed the BPF and URTF (Howells et al., 1987; Kokelaar, 1988; Kokelaar, and Branney, 1999). Collapse of the caldera occurred in a trapdoor-like fashion with sides controlled by the regional tectonic grain (Campbell et al., 1987; Kokelaar and Branney, 1999; Fig. 5.19). The caldera floor was broken up into a number of blocks, with long axes parallel to the tectonic grain, that subsided together but to different depths (B.P. Kokelaar, pers. comm., 1999). This disparity of subsidence depths has imparted a piano key-like morphology to the caldera floor (Dr B.P. Kokelaar pers. comm., 1999; Fig. 5.20), a divergence from the classical trapdoor structure of Lipman (1997; 2000). Snowdon caldera also underwent resurgence during its evolution, that was affected by extension, between the eruptions of the LRTF and URTF (during eruption of BPF; Kokelaar, 1992), but uplift due to resurgence totalled >340 m while subsidence due to rifting was >500 m leading to a net subsidence (Kokelaar and Branney, 1999).

5.8.2 Glencoe Caldera, Scotland

Glencoe Caldera has been referred to in the past as the type example of collapse along a

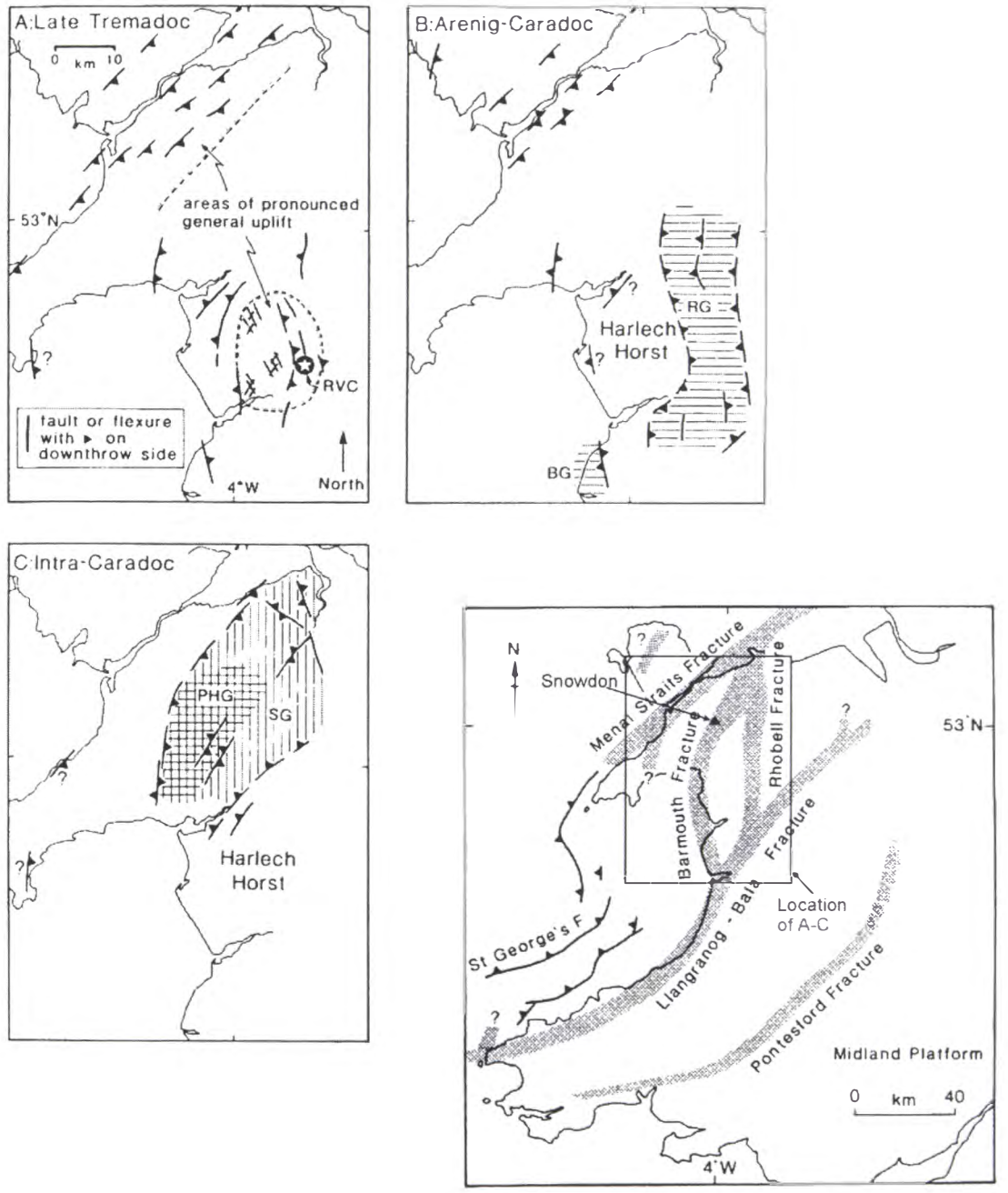

Figure 5.18. Tectonic developments in Wales during the Ordovician in response to subduction of the Iapetus Ocean in the northwest. A-C show active structures at various stages of the Ordovician. The area was structurally complex complicating formation of an "ideal" caldera. Snowdon is located in the proximity of the Barmouth fracture. RVC= Rhobell Volcanic Complex, RG= Rhobell Graben, PHG= Pitts Head Graben, SG= Snowdon Graben. From Kokelaar (1988).

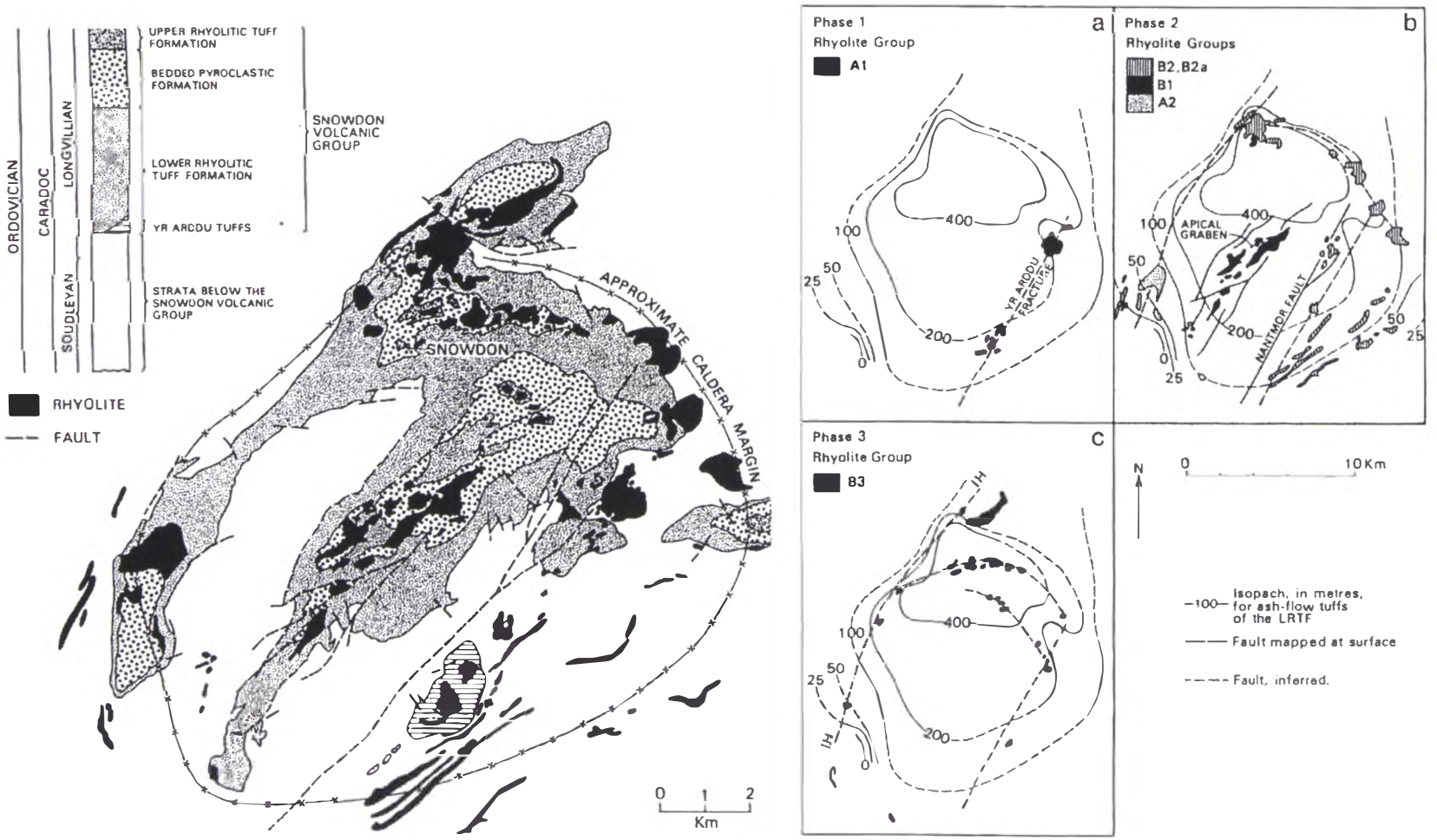

Figure 5.19. The geology of Snowdon Caldera (left). The caldera formed during the eruption of the LRTF. The thickness variation of LRTF (a-c) in Snowdon Caldera shows that the caldera is asymmetric and trapdoor-like. Collapse is suggested to have occurred in a "piano-key"-like fashion. Rhyolite lava has subsequently extruded along tectonic faults and faults created during caldera collapse (prior to caldera formation (a), and after caldera formation (b and c)). From Campbell et al (1987).

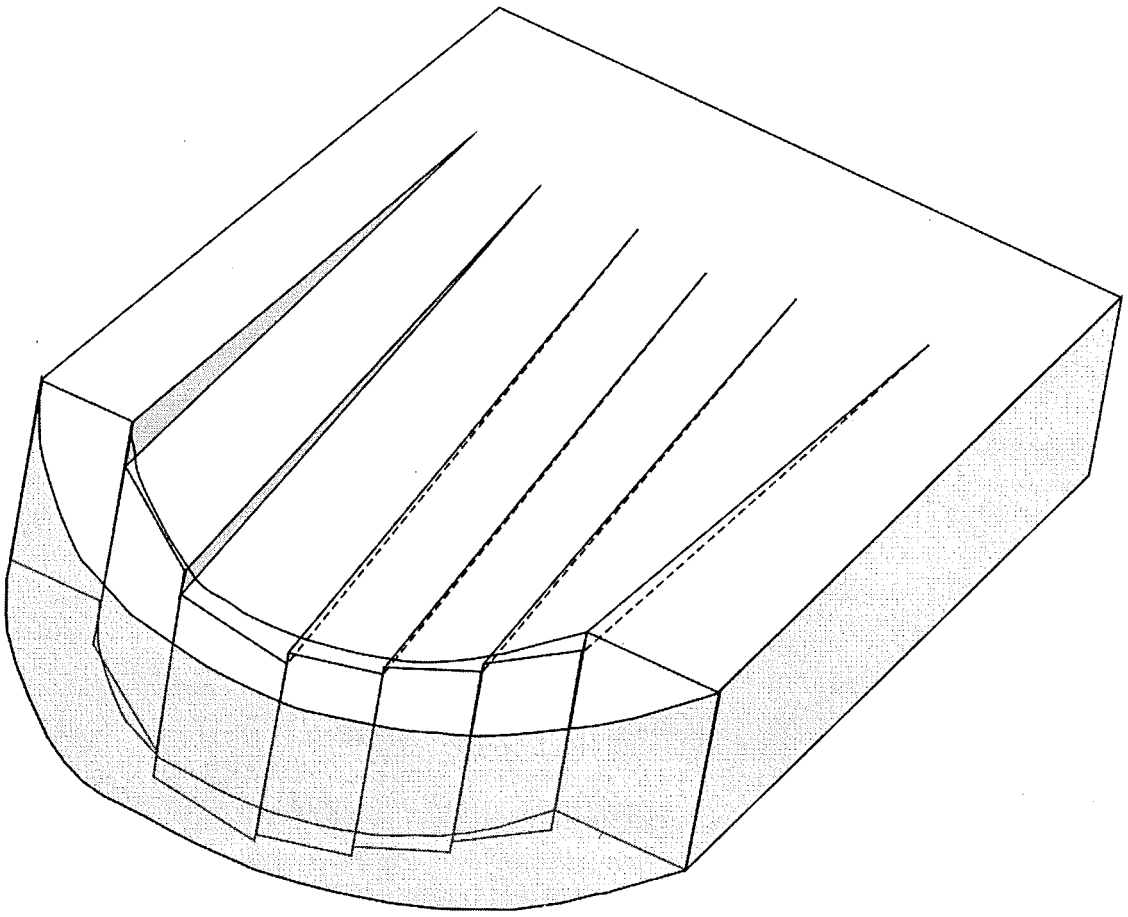

Figure 5.20. "Piano key"-like trapdoor collapse. If pre-existing structures exist and asymmetric subsidence takes place along adjacent caldera floor blocks, a "piano key" morphology can be imparted. Such collapse is interpreted to have occurred at Snowdon Caldera (Kokelaar and Branney, 1999).

ring fault (Clough et al., 1909; Williams, 1941). Glencoe Caldera was active 421 Ma after formation of the Caledonide Orogen (Moore and Kokelaar, 1998). At the time the tectonics of the area were dominated by major sinistral movements along the Great Glen and Highland Boundary faults, two major terrane bounding structures (Fig. 5.21; Moore and Kokelaar, 1998). Displacement along these structures lead to complex fault block rotations, dextral movements, and transtension in the terrane between them (Jacques and Reavy (1994), in Moore and Kokelaar, 1998). The structure of Glencoe caldera has been described by Taubeneck (1967) and more recently by Moore and Kokelaar (1997; 1998). Taubeneck (1967) found that a number of ignimbrites occur in the area, confirming repeated eruptions, and identified an inner ring fault that dipped outwards. He suggested that caldera collapse occurred mainly on the outer steeply dipping ring fault.

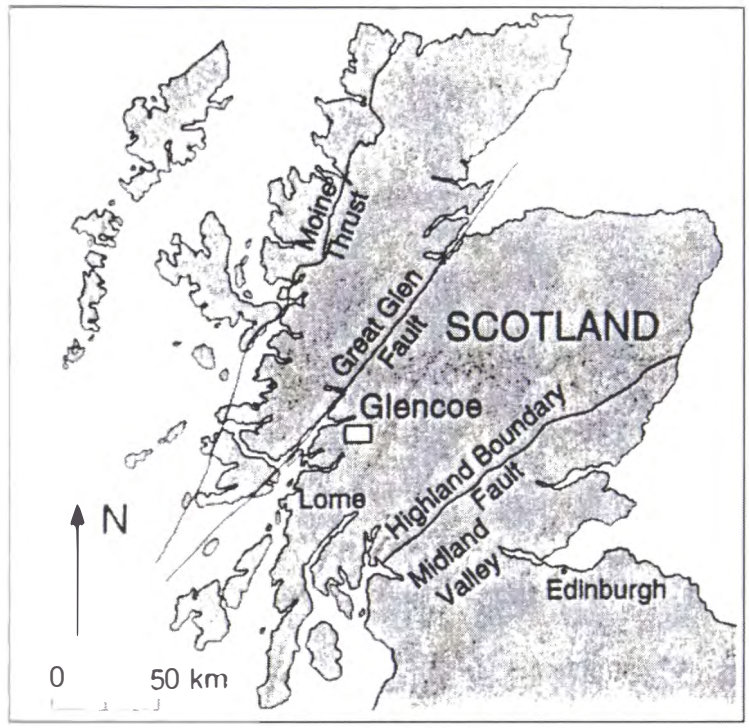

Figure 5.21. Glencoe Caldera is situated between the Highland Boundary Fault and the Great Glen Fault. The two were concurrently active major sinistral strike slip faults and are terrane boundaries. The terrane between them was subject to a complex tectonic situation with orthogonal fault patterns and complex block rotations. Volcanism at Glencoe took place while the terrane bounding faults were active. After Clough et al. (1909) in Moore and Kokelaar (1998).

Moore and Kokelaar (1997; 1998) offer an alternative explanation for the formation of Glencoe Caldera. They show that the area is cut by a number of orthogonal graben structures that formed in response to the regional tectonic environment (Fig. 5.22). Sites of volcanism and collapse were controlled by the bounding faults of these grabens and collapse was achieved both by withdrawal of magmatic support, and by tectonic movements. The bounding "ring fault" has up to 1 km of displacement. Displacement varies around the ring fault, may not have been temporally coincident at different points around it, and may be related to processes other than volcanic eruption. Activity began with intrusion of an andesitic sill complex followed by tectonic faulting and formation of alluvial fans. Eruptive activity commenced with the formation of a tuff cone, which was followed by 5 caldera forming eruptions that caused collapse at different areas of the final structure and the caldera is concluded by Moore and Kokelaar (1997; 1998) to be piecemeal rather piston-type.

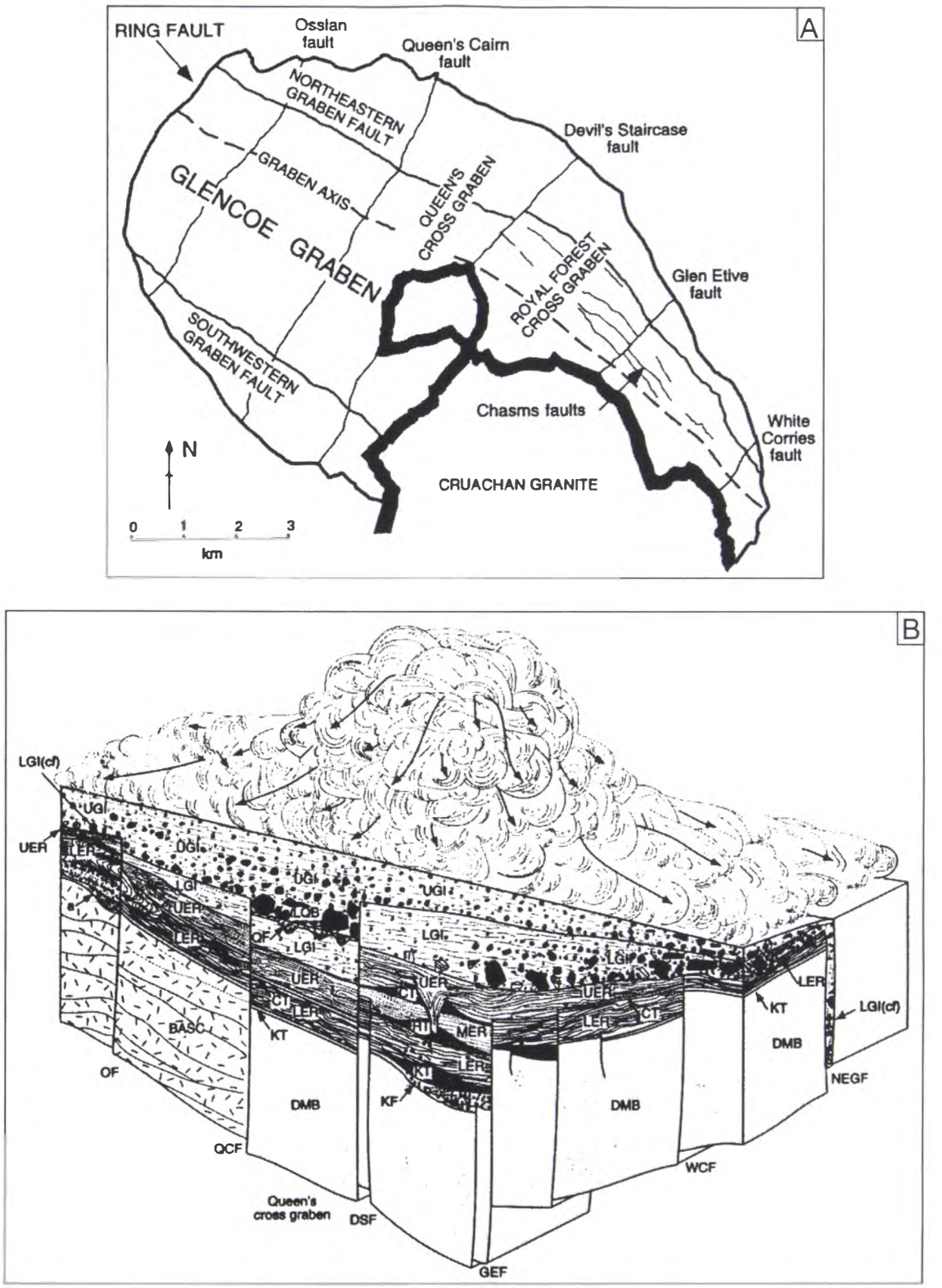

Figure 5.22. The fault pattern and structure of Glencoe Caldera. A) A plan view showing the orthogonal fault pattern mapped at Glencoe. The faults are cross-cutting grabens that were ultimately effected by major strike slip movements on terrane bounding faults. Glencoe Caldera formed during the eruption of at least the 5 exposed pyroclastic units. B) The orthogonal structures broke the proto-caldera up into a number of blocks and controlled the location of vents (and likely magma chamber occurrence) causing piecemeal collapse. From Moore and Kokelaar (1998).

Lipman (2000) still believes Glencoe is a piston type collapse structure saying movement of faults inside the main ring fault is less by an order of magnitude than along the ring fault itself. Evidence put forward by Moore and Kokelaar (1997; 1998) and Kokelaar and Branney (1999), however, clearly refutes this assertion and Glencoe is a classic case where regional tectonics greatly affect the morphology and collapse dynamics of a caldera and, along with numerous caldera forming eruptions, created a complex collapse structure.

5.8.3 Scafell Caldera, England

Scafell Caldera of the English Lake District is a piecemeal caldera that formed in response to eruption of the Ordovician Borrowdale Volcanic Group (Branney and Kokelaar, 1994). It also occurred in response to subduction of the Iapetus Ocean beneath the continental crust of Britain (Branney and Soper, 1988). It is described by Branney (1988), Branney and Kokelaar (1994) and Kokelaar and Branney (1999). Volcanism here ranged in composition including rhyolitic through basaltic material.

Like Glencoe, collapse at Scafell occurred in a piecemeal fashion and was controlled by tectonic faulting and voluminous volcanism involving a number of magma chambers. Eruption of material occurred at various sites controlled by pre-existing faults. Eruption of one magma chamber caused sufficient instability to trigger eruption of another and is evidenced by the interfingering of tuffs of different composition. The piecemeal nature of Scafell is characterised by the dramatic thickening of ignimbrites at various stratigraphic levels into geographically separate depressions. Each of these depressions signifies a caldera collapse centre that may or may not overlap with an adjacent one. Previously formed faults have also, in places, reversed throw in subsequent volcano-tectonic collapse events. While collapse occurred in different areas in response to eruption of separate magma chambers, Scafell Caldera is thought to have formed during a single event, and while eruption and collapse in one area waned, it began in another, finally resulting in a nested collapse structure or piecemeal caldera (Fig. 5.23 and Fig. 5.24).

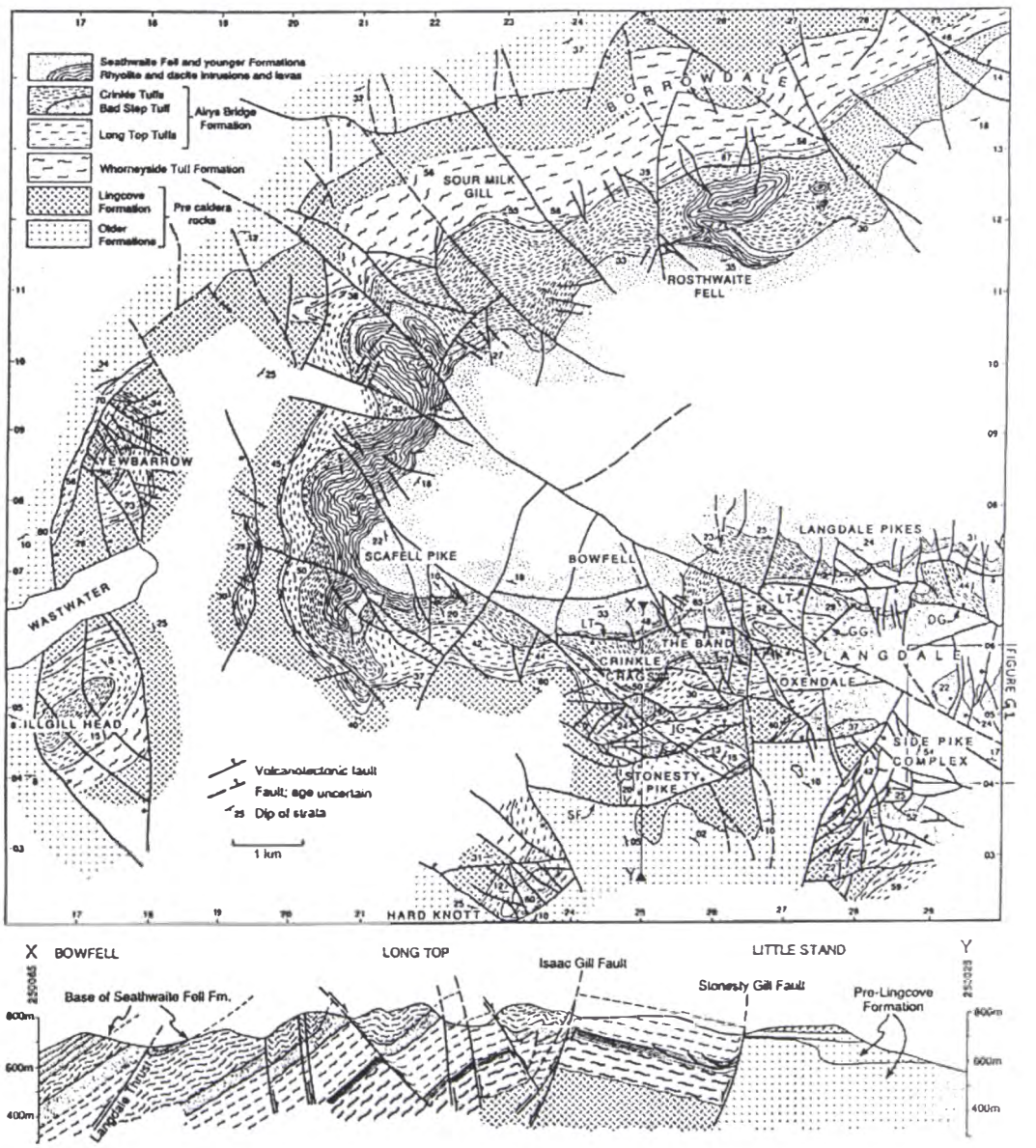

Figure 5.23. Geological map of part of Scafell Caldera. Note the large number of crosscutting volcanotectonic faults. In the cross-section notice the thickening and thinning of some strata on opposite sides of these faults that indicates caldera collapse prior to or during their deposition. From Branney and Kokelaar (1994).

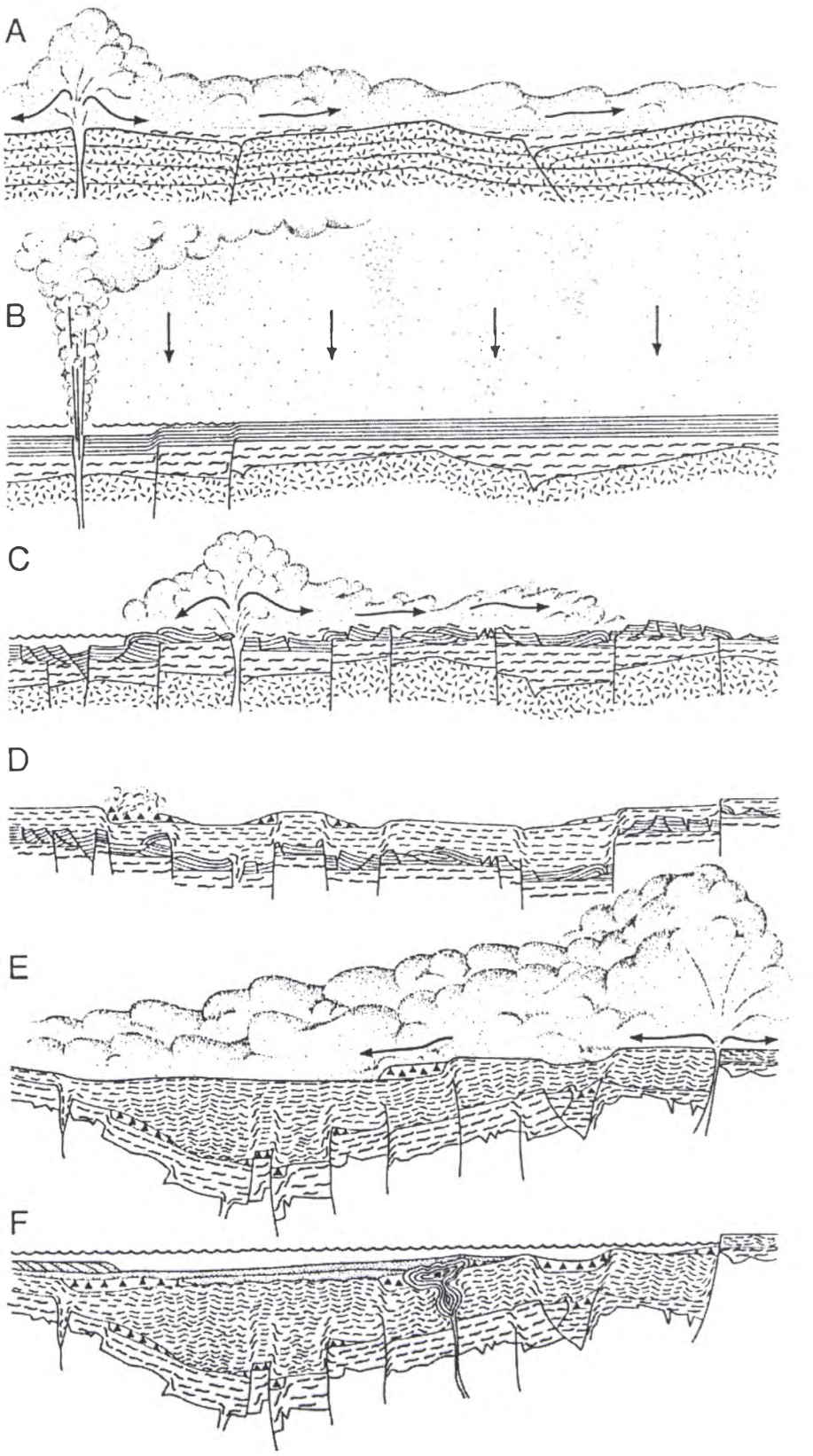

Figure 5.24. Schematic diagram showing the piecemeal development of Scafell Caldera. A) Eruption of Whorneyside ignimbrite, and B) Whorneyside phreatomagmatic tuff. C) Onset of piecemeal collapse with eruption of Long Top Tuffs from new vents. D) Continued subsidence. E) Eruption of Crinkle Crag Tuffs causes further caldera collapse and reactivation of some faults with a reversed sense of motion. F) Caldera occupied by lake with associated sedimentation. From Branney and Kokelaar (1994).

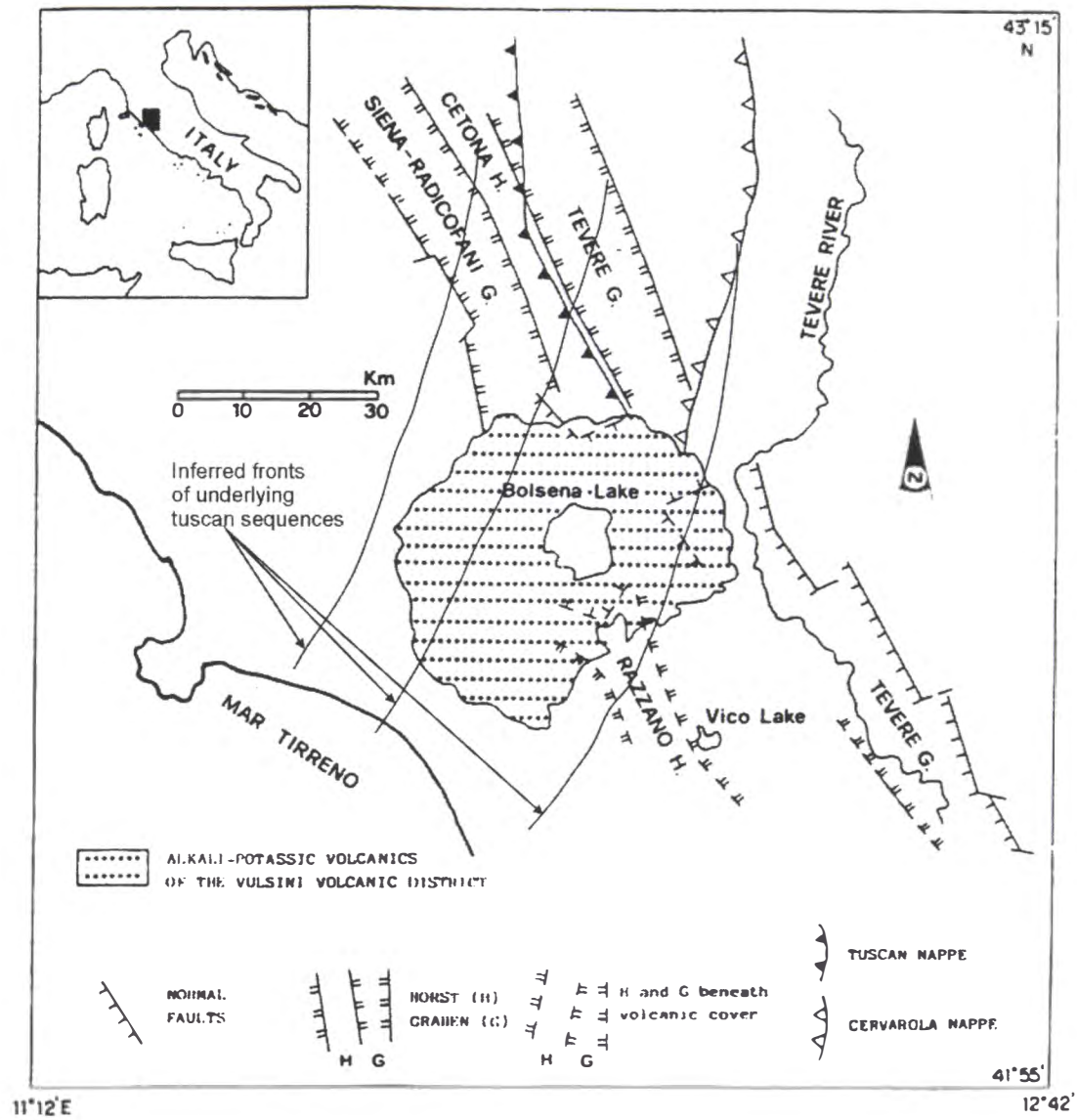

Figure 5.25. Tectonic structures cutting Bolsena Caldera. After Nappi et al. (1991), and Nappi et al. (1998).

5.8.4 Bolsena Caldera, Italy

Bolsena Caldera is located in the currently active Vulsini volcanic district in Italy. Bolsena Caldera has been compared with Rotorua and classified as a downsag structure by Walker (1984) based on the dip of the intra-caldera ground surface (between 5 and 15°). Walker's (1984) classification of downsag structures at Taupo, Rotorua and Bolsena took account only of the surface rocks where downsag looks obvious. However, ignimbrites that have erupted from Bolsena Caldera are insufficient to account for its volume, and its development much more complex with tectonic activity thought to have accounted for at least as much (if not more) subsidence as magma chamber evacuation (Nappi et al., 1991). The tectonic regime of the Vulsini district is

complex and contains orthogonal fault sets under WNW-ESE extension. The dominant fault set strikes NNW-SSE, whereas an underlying fault set strikes NE-SW and relates to the fronts of Tuscan sequences that underlie the Vulsini district (Nappi et al., 1991; Nappi et al., 1998; Fig. 5.25). Overprinted on these are "fundamental tectonic lines of weakness" that strike N-S and WNW-ESE (Nappi et al., 1998). The intersection of these fault sets is thought to have allowed the shallow intrusion of magma (Nappi et al., 1998). Explosive deposits from the caldera are numerous, small to moderate volume and have lead to incremental caldera development (Nappi et al., 1991; Nappi et al, 1998). Again, caldera morphology diverges from a simple structure and is something more complex. Close by, Latera caldera has formed entirely by subsidence associated with volcanic eruptions (incrementally) with magma accumulation and vent location associated with the regional tectonic regime (Nappi et al., 1991).

5.8.5 Newberry Caldera, USA

Newberry Caldera is situated at the top of a broad currently active shield just north of the Basin and Range province, behind the Cascade Range in Oregon, USA. The shield measures 63×45 km and has at least 200 basaltic cinder cones on its flanks (G. Goles pers. comm., 1999). The caldera is at the apex of the shield and has formed in response to the eruption of many pyroclastic units (Fig. 5.26; Macleod and Sherrod, 1988).

Three fault zones meet at Newberry Volcano (Fig. 5.26; Fitterman, 1988; G. Goles, pers. comm., 1999) which is the likely reason for its presence. Magma probably uses this intersection (being a point of weakness) intermittently as a path of ascent.

Newberry is a piecemeal caldera. Collapse is thought to occur on many "ring faults", starting from about 2 km outside the caldera wall, with displacement increasing progressively on adjacent faults towards the current centre (G. Goles pers. comm., 1999). The caldera floor is broken up into many blocks by the intersecting fault zones but the numerous phases of collapse that have occurred there are more likely controlled by the continual ascent and eruption of varying volumes of magma from a single magma chamber (G. Goles, pers. comm., 1999). There appear to have been no phases of resurgence at Newberry (G. Goles, pers. comm., 1999), which may also be due to its tectonic situation.

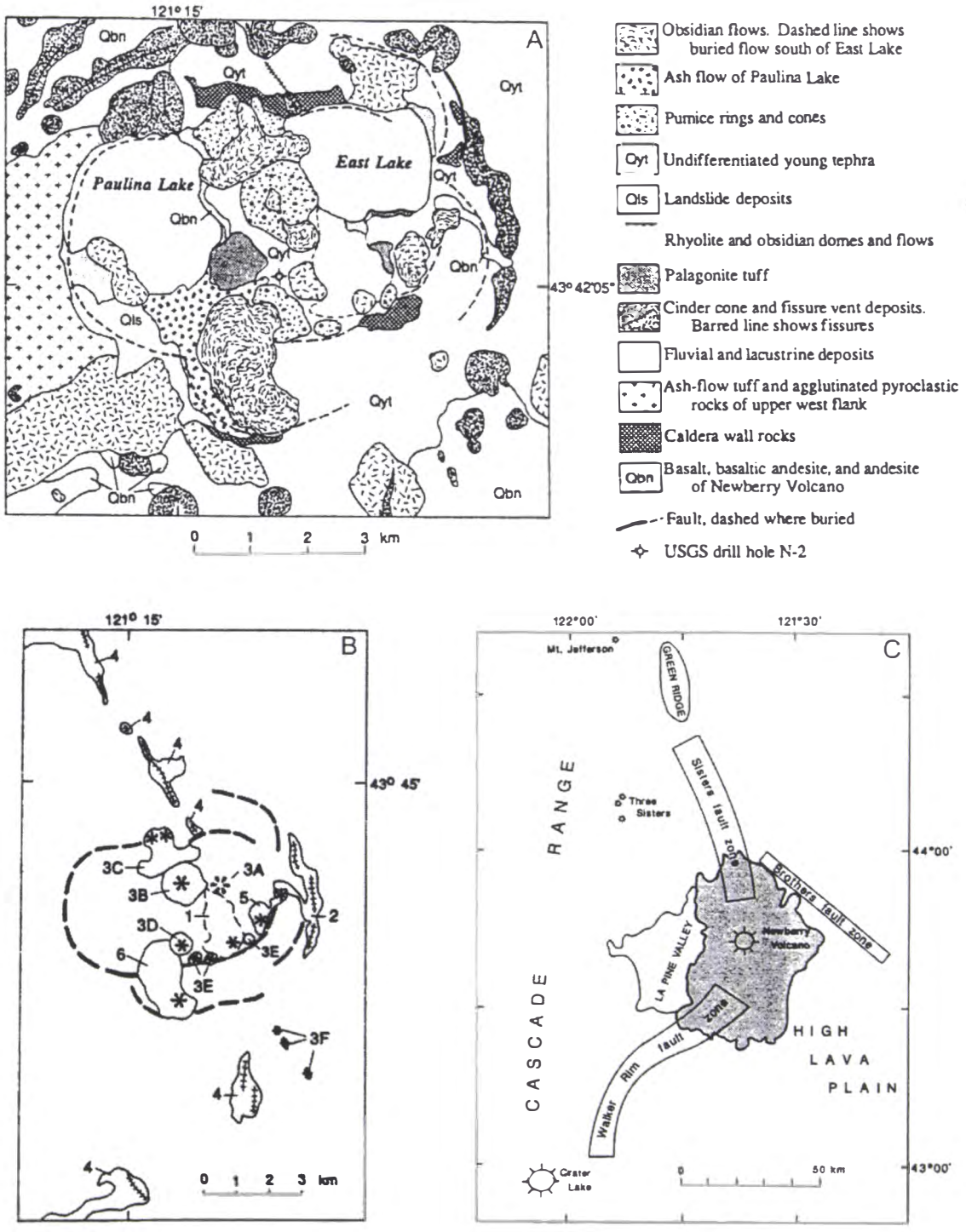

Figure 5.26. A) Geological Map of Newberry Caldera (from Macleod et al., 1982). B) Holocene eruptive episodes, and clearly shows the caldera faults (from Macleod et al., 1982). Inner and outer collapse structures in A and B show that the caldera formed during more than one episode with younger faults truncating older ones. C) The tectonic environment of Newberry illustrating the intersection of three major fault systems (from Fitterman, 1988).

5.8.6 Discussion

All of the above calderas, with the exception of Snowdon, have formed in response to evacuation of multiple magma chambers. All the calderas emphasise the importance of regional tectonics on their morphology and location of eruption. Tectonic processes are also controls of magma chamber location and accumulation (as at Newberry, and Bolsena), and likely control chamber shape, which in turn affects caldera morphology (Roche et al., 2000).

The calderas show the varying styles of piecemeal caldera collapse (as defined by Branney and Kokelaar, 1994). Glencoe, Scafell, and Bolsena exhibit piecemeal form due to eruption from multiple magma chambers through a caldera floor already broken up by intersecting faults. Magma withdrawal and pre-existing structures in the caldera floor probably contributed equally to overall caldera shape. Snowdon Caldera formed dominantly during a single event, the piecemeal nature being due to the pre-existing structural grain. The Newberry Caldera floor is undoubtedly broken up into numerous parts, but collapse dominantly occurs towards one centre, with the piecemeal nature caused by repeated replenishment and evacuation of magma from a one or more centrally located magma reservoirs.

5.9 Calderas of TVZ

Eight calderas have been identified in TVZ and are as follows: Rotorua, Haroharo (in Okataina Volcanic Centre), Kapenga, Reporoa, Mangakino, Maroa, Whakamaru, and Taupo (Fig. 5.27; Wilson et al., 1984; Nairn et al., 1994; Wilson, et al., 1995). Various other depressions have been suggested as possible calderas. Caldera forming activity in TVZ began with initiation of activity at Mangakino volcano 1.6 Ma (Briggs et al., 1993; Houghton et al., 1995) and, as mentioned in chapter one, occurred over three main periods.

TVZ is actively extending at between ~7 and 12 mm/yr (Sissons, 1979; Walcott, 1987; Crook and Hannah, 1988; Darby et al., 2000) in a NW-SE direction along a zone striking approximately NE-SW. The extension imparts a distinct structural grain to TVZ that is evidenced by the numerous fault scarps in the region (Fig. 5.28). A second,

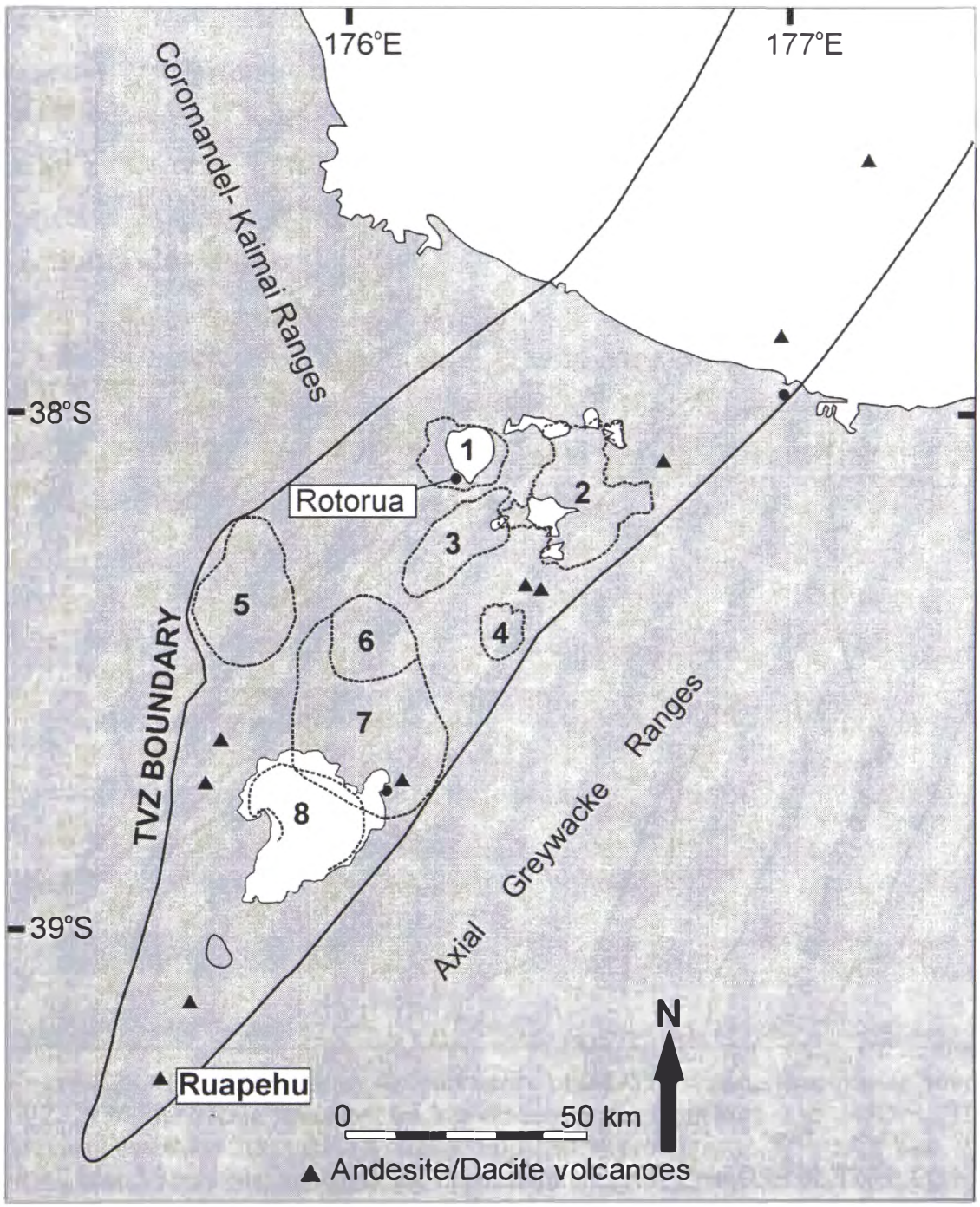

Figure 5.27. TVZ calderas. 1) Rotorua, 2) Haroharo, 3) Kapenga, 4) Reporoa, 5) Mangakino, 6) Maroa, 7) Whakamaru, 8) Taupo. Only Rotorua and Reporoa calderas formed during single eruptions. After Houghton et al. (1995).

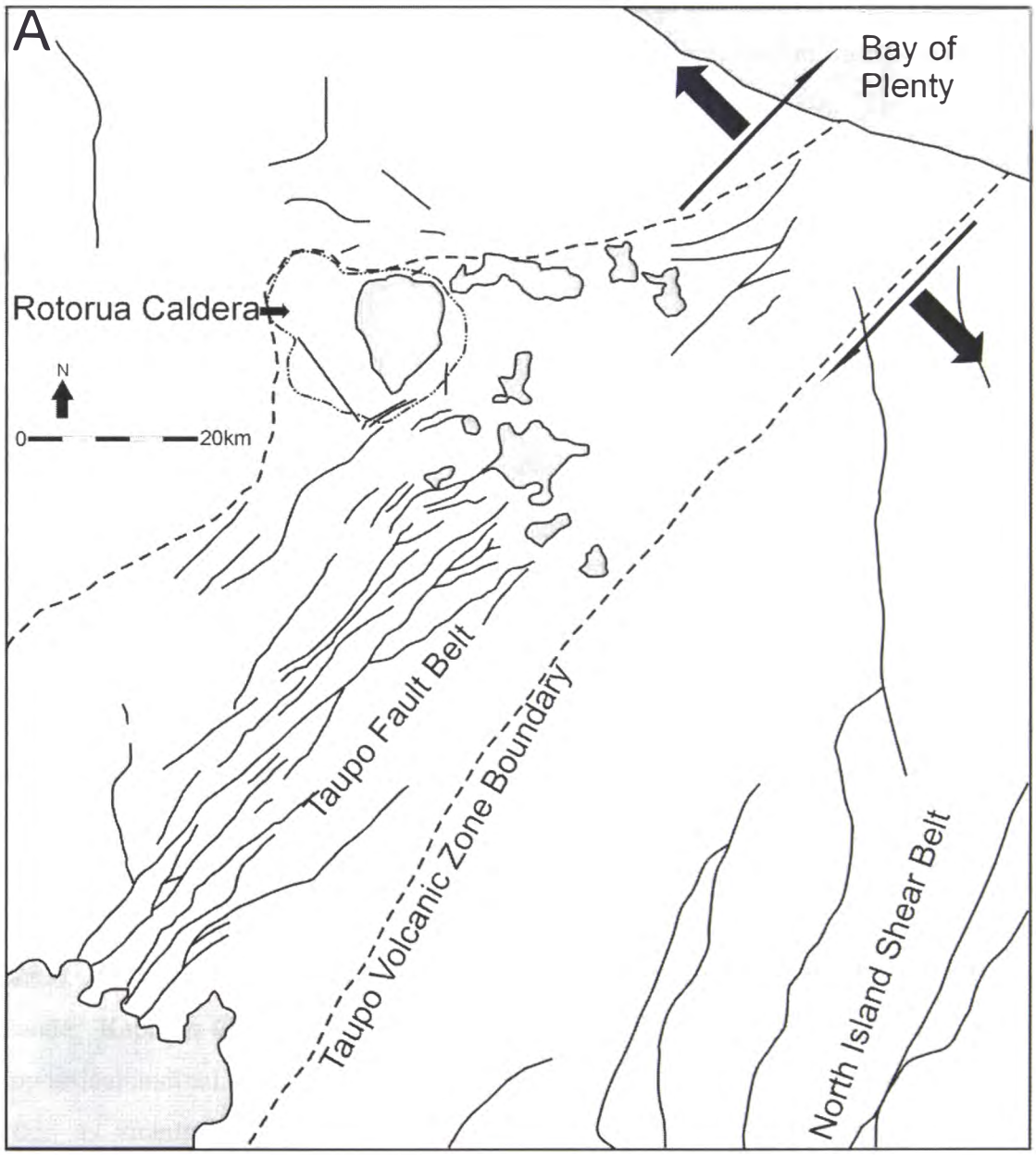

Figure 5.28. Diagram showing the prevalence of NE-SW striking structures in young TVZ. NW-SE striking structures are less obvious and seldom seen at the surface. The dominant extension direction and rotation imparted by proximity to, or overlap with, the North Island Shear Belt shown in the upper right are from Cole (1990). The influence of the shear belt may cause transtension in TVZ resulting in en echelon pull aparts (as seen with the Tarawera vent sites; Cole, 1990). Rotorua Caldera is located towards the edge of the main axis of rifting in TVZ perhaps allowing NW-SE striking structures to exert greater influence on its morphology. Solid lines are faults. Map taken from Berryman et al. (1998).

less dominant, set of faults strikes NW-SE (Wan and Hedenquist, 1981; Cole, 1990). These two sets of faults have probably been created under a transtensional regime in response to oblique subduction at the Hikurangi margin and proximity to the North Island Shear Belt (Fig. 5.28 and 5.29; Cole, 1990). Alternatively, Rowland and Sibson (1999) regard the NW-SE cross cutting features as "accommodation" zones (also areas of magma accumulation) between offset spreading centres (Fig. 5.30). The interaction of both fault sets likely provides paths of preferred magma ascent and breaks the crust up into blocks that will preferentially subside in the event of caldera collapse, thereby inhibiting formation of simple calderas.

The cycle of caldera formation in TVZ is not typical of cycles outlined by Smith and Bailey (1968) or Lipman (1984). Ring fractures associated with tumescence and resurgence have not been identified at TVZ calderas, (although evidence for tumescence is often not seen at calderas). Existing crustal defects may reduce the likelihood of radial and conical fracture formation masking tumescence and resurgence. It may be that resurgence is prohibited by extension in TVZ or that it occurs by a similar process to that described at Snowdon Caldera (in Kokelaar, 1992). Smith and Bailey's (1968) stages 2-4 and 7 obviously happen in TVZ, as shown by numerous ignimbrites, calderas, lakes and geothermal areas, but resurgence has not been observed.

Reporoa (Beresford and Cole, 2000) and Rotorua calderas are the only two known to have formed during a single eruptive event in TVZ (resulting in the Kaingaroa and Mamaku ignimbrites respectively). The rest have formed by more than one collapse episode. Kapenga Caldera has no topographic expression and is defined on the basis of geophysical anomalies (Rogan, 1982). Up to seven ignimbrites have been sourced from within its vicinity (Houghton et al., 1995) and Kapenga Caldera is thought to be a buried collapse structure. Haroharo is a nested collapse structure and has formed in response to eruption of at least 3 ignimbrites (Nairn, 1989; Bailey and Carr, 1994; Beresford, 1997). Since 26.5 Ka Taupo Caldera has undergone at least 3 periods of collapse (Sutton et al., 1995; Wilson et al., 1995) and may have erupted as many as 4 major ignimbrites (Cole et al., 1998). Maroa is considered a composite complex (Wilson et al., 1995), and Whakamaru erupted 4 ignimbrites termed the Whakamaru Group (Brown, 1994). At least 9 caldera forming ignimbrites have been erupted from the Mangakino centre (Houghton et al., 1995). Other calderas may exist in TVZ but

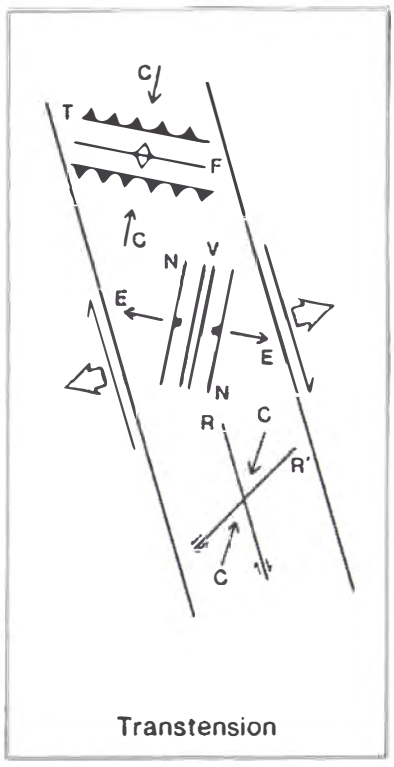

Figure 5.29. When extensional and strike slip regimes interact a transtensional environment may result causing formation of orthogonal fault sets and en echelon basins and folds. In TVZ en echelon volcanic vents are often seen (e.g. the Tarawera vent alignment; Cole, 1990). C- compression axis, E- extension axis, N- normal faults, T- thrust faults, R- reidal shears or strike slip faults, V- veins, dikes or extension features, and F- fold axes. After Sanderson and Machini (1984) in Cole (1990).

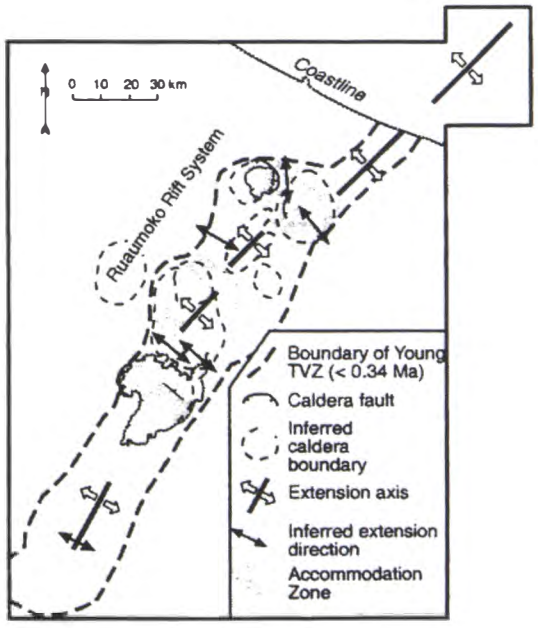

Figure 5.30. Rowland and Sibson's (1999) view of structural controls in TVZ. NW-SE extension occurs along axes sub-parallel to the TVZ axis. NW-SE trending accommodation zones are interpreted as zones of magma accumulation and offset adjacent axes of extension.

have either been buried by younger pyroclastics and/or totally disrupted due to extension.

Wilson et al. (1995) view two possible end member models for central TVZ: 1) that all of central TVZ represents a giant composite caldera volcano, and 2) that caldera collapse is confined to the areas identified as caldera volcanoes and little silicic volcanism occurs elsewhere. The second end member requires the rest of central TVZ to be subsiding solely in response to extension. Wilson et al. (1995) also indicate that lithic-rich deposits at various locations in TVZ indicate that further caldera structures are yet to be identified, suggesting Broadlands and a location in the southern Kaimai Range (both now buried) as two possible caldera locations. A depression near Atiamuri is also a suspected caldera; J.W. Cole pers. comm., 1997; D. Gravley, work in progress). As Wilson et al. (1995) admit it is impossible to say which if either of the two possible TVZ end member models is correct, but it is the author's view that the first suggestion provides a better explanation.

CHAPTER 6
Rotorua Caldera

6.1 Terminology

The following section describes aspects of Rotorua Caldera's structural evolution. Classification of calderas as either simple piston, trapdoor, piecemeal or downsag is viewed here as too restrictive, and while giving general overviews of structural styles, they give no indication of the caldera's overall geometry or evolution. A caldera should be described in terms of magma composition, caldera floor collapse symmetry (symmetric or asymmetric instead of piston or trapdoor), caldera floor coherency (single block or multiple block rather than piston and piecemeal), number of collapse loci (chaotic or non-chaotic), and number of events (single or multiple, referring to the number of pyroclastic deposits erupted during its formation). Inclusion of all these terms in a caldera's description provides a much better understanding of its structure and formation history.

6.2 Rotorua Caldera

Rotorua Caldera is located towards the northern part of the rhyolite-dominated central portion of TVZ at its western margin (Fig. 6.1) and is an irregularly shaped depression with maximum dimensions of 21×22 km (Fig. 6.2). Rotorua Caldera's geometry can be defined by two ellipses that create a structural boundary of 21×20 km. One ellipse has a long axis oriented NE-SW and the other a long axis oriented NW-SE running through the embayment in the caldera's northwest margin (Fig. 6.2). The two overlap towards the southwest of the caldera around Rotorua City.

The caldera was formed during a single event, the eruption of Mamaku Ignimbrite. Its location towards the edge of the TVZ is away from the main axis of extension and it may be less affected by tectonic faulting than many other TVZ eruptive centres. Rotorua is a young TVZ caldera (Houghton et al., 1995), was created by one of the most voluminous eruptions known from TVZ, and has been modified only slightly by other volcanism since its collapse. These factors make it one of the best preserved and most

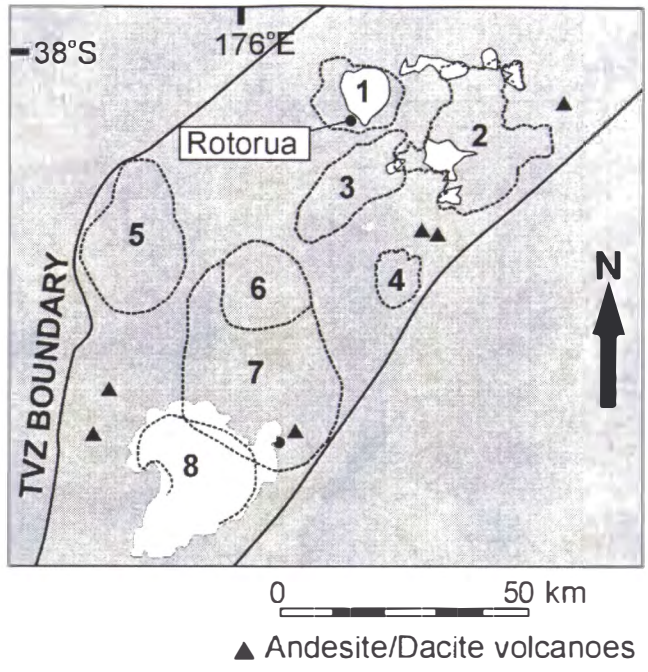

Figure 6.1. Map of central TVZ showing recognised caldera structures. Rotorua Caldera is located in the northern part of central TVZ. Only Rotorua and Reporoa (1 and 4 respectively) calderas formed during single events and are best suited for structural study based on geomorphology. After Houghton et al. (1995).

obvious calderas of TVZ, comparable only with Reporoa Caldera (Beresford, 1997; Beresford and Cole, 2000) further south.

6.2.1 Previous work

Most previous work on Rotorua Caldera has concentrated on aspects of its geothermal field including heat flow and water properties.

Geology

Hochstetter (1864) in his landmark description of the geology of New Zealand described the hot springs of Rotorua. He suggested that rather than the area being a volcanic crater, the depression originated through collapse of the ground in the volcanic plateau, perhaps following volcanic activity. Park (1910), Marshall (1905; 1912), and Cotton (1922) also discussed the formational processes of the Rotorua depression.

Marshall (1905) and Park (1910) favoured the formation of Rotorua through volcanic explosion, whereas Marshall (1912) and Cotton (1922) both suggested its formation by

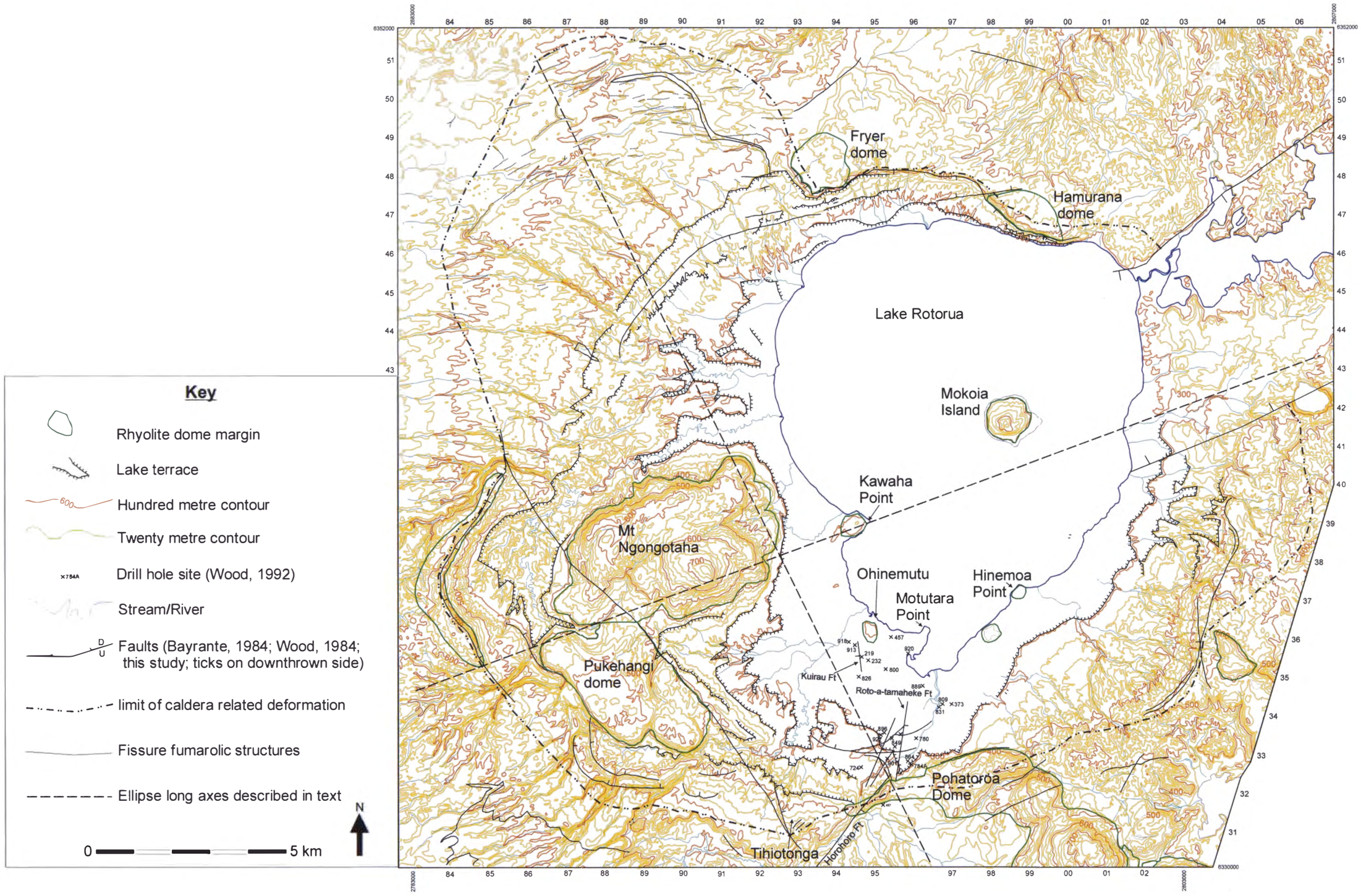

Figure 6.2. Topographic map showing geomorphic aspects of Rotorua Caldera and location of Wood's (1992) logged drill holes. Note that drainage north of the scarp at the head of the embayment is away from the caldera. Inside the embayment drainage is towards the lake and, where present, controlled by fumarolic ridges. Lake terraces reflect lake levels since 42,000 yr BP (Kennedy et al., 1978).

subsidence. Grange (1937) wrote generally about the geology surrounding and between Rotorua and Taupo, agreeing with Hochstetter's interpretation that the depression formed by structural collapse, probably after volcanic activity.

Healy (1964) and Thompson (1964) referred to the depression surrounding Lake Rotorua as a caldera. Ewart and Healy (1965) looked at both Rotorua Caldera and Okataina Volcanic Centre mainly describing rhyolitic eruptive deposits. They regarded the Rotorua depression as being of caldera origin. Healy et al. (1974) mapped the Rotorua depression as part of a regional geological map. Thompson (1974) produced the first detailed geological map of the Rotorua district, noting the distribution of major pyroclastic and sedimentary lithologies and suggesting a caldera margin (Fig. 6.3). His map became the basis from which many workers have studied the geology of Rotorua. He viewed the caldera as enclosed by a single fault that marked the caldera margin with a second fault inside this only on the caldera's eastern edge. Thompson (1974) also suggested that inside the ring fault the caldera was step-faulted towards its centre (Fig. 6.4).

Crafar (1974a) and Nairn (1974) noted the locations of existing drill holes and made recommendations for the sites of new drill holes respectively. Crafar (1974b) also looked at the geology of the Rotorua City geothermal area based on drill hole information, interpreting the step-faulting of Mamaku Ignimbrite as down from Tihiotonga towards Kawaha Point (locations on Fig. 6.2). Nathan (1976) wrote about the geology of the Rotorua district as part of a conference field guide, pointing out fault scarps and suggesting downwarping of the ground surface in the caldera's northwest.

Wood (1985b; 1992) described the subsurface geology and hydrology of the geothermal field (from drill core) demonstrating that the Mamaku Ignimbrite surface has been progressively downfaulted northwards from outcrop at the southern caldera rim (concurring with Crafar's (1974) suspicion). Wood (1992) noted buried post-caldera rhyolite domes beneath Rotorua City and the presence of buried, massive slumped blocks of pre-caldera rhyolite immediately within the southeast caldera margin, beneath lake sediments, that he interpreted formed by collapse of the caldera wall. Nairn and Wood (1988) gave a brief description of the geology and geologic history of Rotorua Caldera including its formation due to the eruption of Mamaku Ignimbrite, extrusion of post-caldera rhyolite domes and aspects of Rotorua geothermal field.

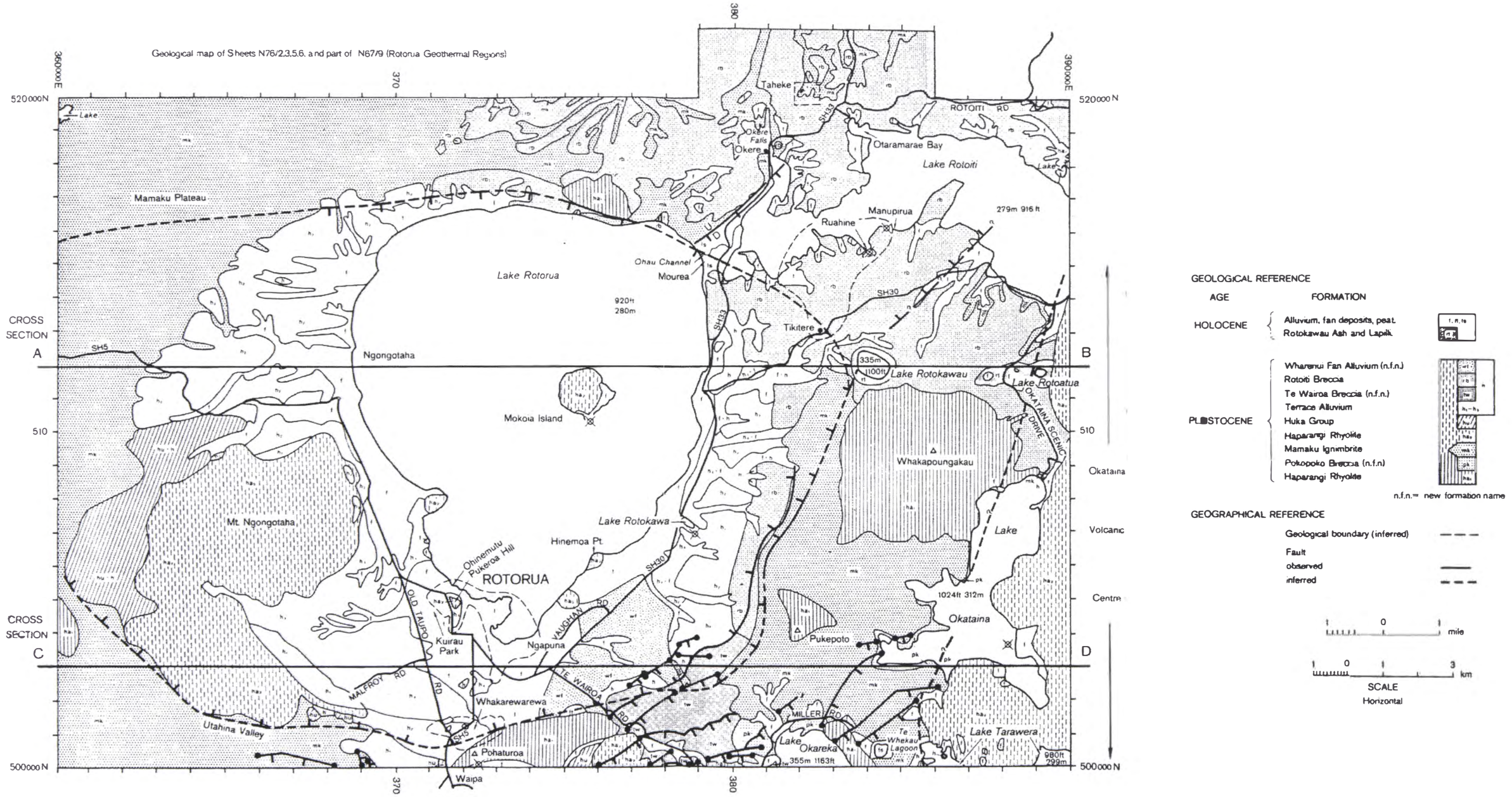

Fig. 6.3. Thompson's (1974) map of the geology of the Rotorua District. Note the single fault marking the caldera margin and a second fault in the south-southeast. Cross sections are shown in Figure 6.4.

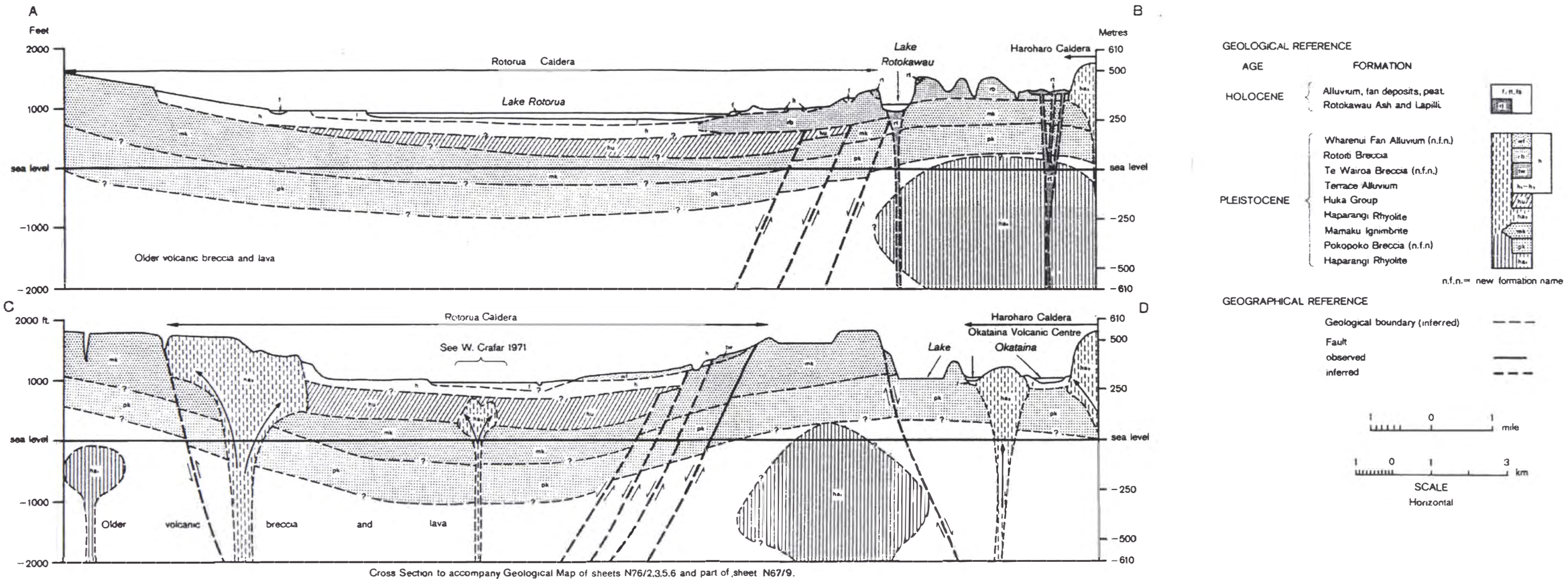

Cross Section to accompany Geological Map of sheets N76/2,3,5,6 and part of sheet N67/9.

Fig. 6.4. Cross sections of Thompson (1974). Thompson viewed the caldera as step-faulted in the east. This is concurred with in this study, although it is now thought that the structure is more complex than that shown here. Vertical exaggerration approximately 4 times.

Dravitzki (1999) described the geologic and mechanical properties of lake sediments and local pyroclastic flow deposits in Paradise Valley in the southwest part of the caldera. He produced a detailed map of the Paradise and Utuhina valleys including maps of the lavas that comprise the Pukehangi and Ngongotaha rhyolite dome complexes. Dravitzki (1999) also noted a number of small pyroclastic deposits that he inferred to be sourced from the dome complexes based on geochemical grounds (see Fig. 4.4).

Ewart (1967; 1968), and Shepherd (1991) have carried out studies on the rhyolite lavas of Rotorua Caldera. These were discussed in chapter 4.

Late Quaternary land surfaces and geomorphology of Rotorua Caldera have been studied by Kennedy et al. (1978). They documented lake level changes, fan building episodes, primary tephra sequences, and aeolian deposits. They then interpreted the geomorphic development of the area since the lake drained from its maximum level at c.42 ka based on ^{14}C ages of tephra marker beds.

Nairn (1989) and Bellamy (1991) studied volcanology and deposits of the Okataina Volcanic Centre with limited overlap into the eastern part of Rotorua Caldera. Bellamy (1991) mapped the Te Wairoa breccia's extent into Rotorua Caldera from its Okataina Volcanic Centre source.

It has been suggested that two other ignimbrites erupted from Rotorua Caldera. These are the Pokai (Wood, 1992), and Waimakariri (Lynch-Blosse, 1998) ignimbrites. Karhunen (1993) suggested that Pokai Ignimbrite was sourced from Kapenga Caldera based on sparse lithic data, ignimbrite flow direction indicators, and thickness determinations. Karhunen noted a lithic lag breccia in Pokai Ignimbrite just 1.2 km southwest of Rotorua City, but re-examination suggests it is not a lithic lag deposit, but rather lithic-rich (7-10 vol%) ignimbrite. At a site marginal to both Rotorua and Kapenga structures (U16/929307) is a lag deposit that is of part of Pokai Ignimbrite (50-60 vol% lithic clasts). The location of the lag deposit between Rotorua and Kapenga structures makes it speculative to assign either as its source, but Karhunen's data suggests that Kapenga is more likely. Lynch-Blosse's (1998) suggestion of Rotorua as a source for Waimakariri Ignimbrite is based on thickness variation and distribution (Waimakariri Ignimbrite distribution is similar to Mamaku Ignimbrite). Lynch-Blosse

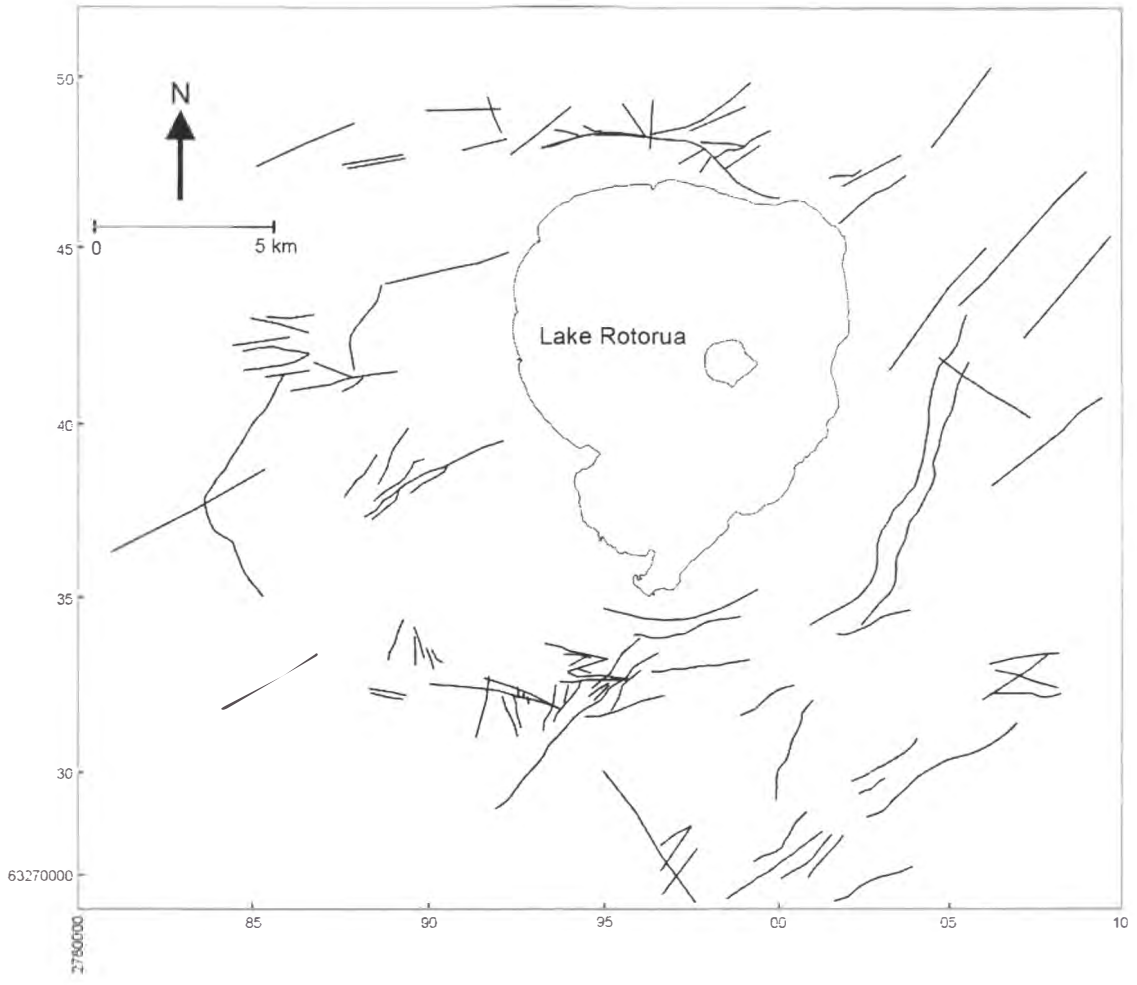

Figure 6.5. Bayrante's (1984) map of lineaments in the Rotorua District. Many are not related to the formation of Rotorua Caldera.

also suggests an alternative source may be buried beneath Mamaku Ignimbrite in the Mamaku Plateau. Volume calculations in chapter 8 indicate that Rotorua Caldera is an unlikely source for any ignimbrites other than Mamaku Ignimbrite.

Lloyd (1975) was the first to look at Rotorua structurally, identifying faults subparallel to the caldera margin in the south of the caldera. Bayrante (1984) documented many lineaments and faults in and around Rotorua Caldera, but mainly in its southern part (mainly associated with the geothermal field, Fig. 6.5). In a brief overview Bayrante noted that structural elements of Rotorua Caldera were dominated by three patterns: NE-SW and NW-SE lineaments and arcuate or concentric patterns (Fig. 6.5). Arcuate and concentric patterns run sub-parallel to the caldera margins. Reanalysis during this study suggests that, while present, many of Bayrante's lineaments are not of tectonic or

volcanic origin. Alternative explanations for some of these lineaments include fluvial and fumarolic activity.

Geophysics

Watson-Munro (1938), Jones (1940), Modriniak (1949), Woodward and Ferry (1973), Macdonald (1974), Rogan (1982), Bibby et al., (1992), and Hunt (1992) have all investigated the geophysical response of the Rotorua area. Watson-Munro (1938), Jones (1940), and Modriniak (1949) all investigated the magnetic properties of the area around Rotorua City. Their data have been incorporated into most later magnetic surveys as their surveys were made when Rotorua City was much smaller and the magnetic response was less affected by artificial structures.

Modriniak (1949) supported the idea that formation of the Rotorua depression occurred by collapse. Woodward and Ferry (1973) and Rogan (1982) looked at Rotorua as part of regional gravity and magnetic surveys and identified a geophysical depression. Macdonald (1974) used resistivity, gravity, heat flow and magnetic techniques to assess three geothermal fields, including that of Rotorua. He suggested that Rotorua Caldera was not a true caldera due to the lack of a circular gravity anomaly that paralleled the caldera margin, proposing instead that Rotorua Caldera was a "down-warped block structure". Hunt (1992) investigating the caldera structure around Rotorua City agreed with Macdonald's finding that geophysical evidence did not support the caldera hypothesis in the sense of a caldera being a roughly circular region of subsidence.

Bibby et al. (1992) published results of an aerial magnetic survey, and measured resistivity around the Rotorua District. Their magnetic data were added to Macdonald's (1974) map, as access to take measurements within Rotorua City was not granted. Bibby et al., (1992) suggested that geothermal areas at Ohinemutu (on the lake shore, Fig. 6.2) and Rotorua City relate to deep plumes of heated water rising up possible faults.

Both Davy (1992) and Lamarche (1992) used seismic equipment to investigate the subsurface structure of Rotorua and found it difficult to get a deep response. Lamarche estimated Mamaku Ignimbrite thickness near the southeastern caldera margin to be 279 m. Lamarche's lower Mamaku Ignimbrite boundary (see Fig. 2.4) is equivocal, but the

top agrees with drill hole information (C.P. Wood, pers. comm., 2000), and he interprets Mamaku Ignimbrite as thickening towards the northwest, away from the southeast caldera margin. Davy studied the shallow structure of the floor of Lake Rotorua inferring dipping gas charged sedimentary strata.

6.2.2 Methods of study

Interpretation of Rotorua Caldera has involved:

- Assessment and reinterpretation of published geophysical data.
- Geomorphic interpretation
  -Analysis of aerial photography and satellite imagery.
  -Ground based confirmation of structures identified in aerial photographs
- Geological examination
  -Relationship of Mamaku Ignimbrite stratigraphy and thickness variation to caldera collapse.
  -Study of pre- and post-caldera rhyolite domes.

All available geology is compiled into a new map presented in Figure 6.6. It will be referred to throughout the rest of this chapter and provides the basis for discussion.

6.2.3 Geophysical response

The most useful geophysical techniques for studying caldera structure are magnetism and gravity (e.g. Pakiser, 1961; Kane et al., 1976). Gravity is affected by the depths of different density rocks, and in the case of a caldera collapse structure the dense basement rocks will be deeper and buried by a greater thickness of lower density pyroclastic material inside its margins than outside, leading to a low anomaly (Kane et al., 1976). Therefore a caldera structure has a low gravity signature that is sometimes circular and parallel to the caldera margins (Macdonald, 1974; Hunt, 1992, and references therein). Magnetism is also susceptible to the depth of lithologies. Deeper magnetic rocks will give a weaker response than those at shallow levels (e.g. Kane et al., 1976; Rogan, 1982). Macdonald (1974), Woodward and Ferry (1973), Rogan (1982), and Hunt (1992) have all undertaken magnetic and/or gravimetric surveys of Rotorua Caldera.

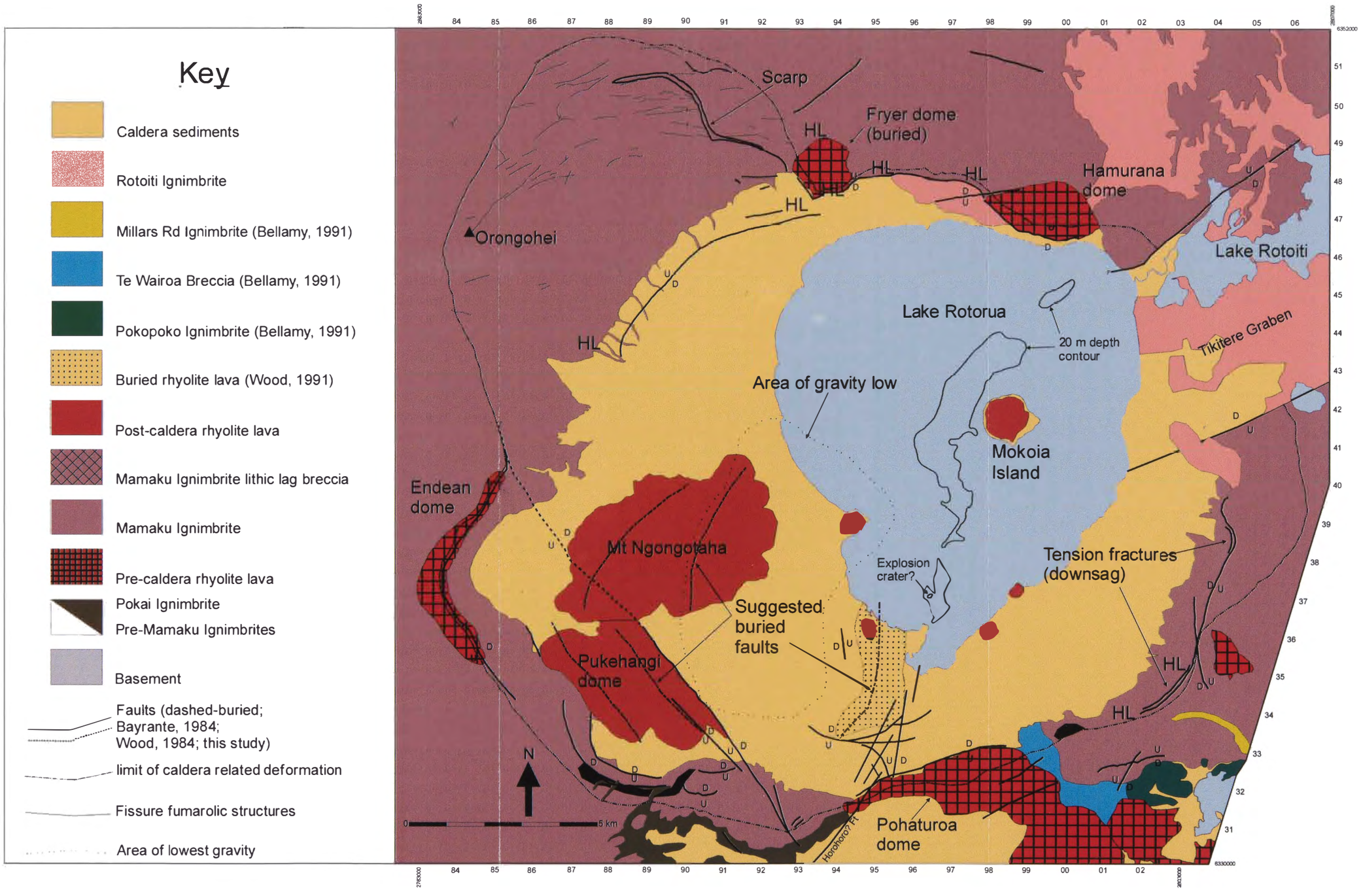

Figure 6.6. Geology of Rotorua. Post-caldera rhyolite domes surround the area of lowest gravity. Pre-caldera rhyolite domes have been cut by caldera forming faults. Numerous lineaments are present in the southern part of the caldera. Faults mark the emergence of Mamaku Ignimbrite from beneath lake sediments towards the southwestern and western caldera margins, and at the opening of the embayment in the northwest. Tikitere Graben and activity of Okataina Volcanic Centre have destroyed surficial Rotorua Caldera structures in the northeast. HL denotes areas of high lithic concentration (other than lithic lag breccias).

Woodward and Ferry (1973) showed a gravity trough extending NNW-SSE through Rotorua (Fig. 6.7). It branches off a deeper gravity trough that runs NE-SW through Taupo, Kapenga and Okataina volcanic centres following the main axis of extension. There is a deviation in the contour pattern across Rotorua City that probably represents an area of collapsed basement.

Rogan (1982) was the first to look at all TVZ volcanic centres using geophysics. Using gravity and magnetism she calculated the depth to basement using assumptions of the basement properties. Interpreting gravity, she found the deepest basement (lowest gravity anomaly) beneath Rotorua City, and low gravity readings extended NW-SE (Fig. 6.8). Maximum depth to basement was calculated at 2500 m below sea level, 1500 m lower than the surrounding basement. Depth calculations using magnetic data suggested a depth to basement of ~1000 m below sea level. To account for the disparity Rogan suggested the presence of non-magnetic, or reversely magnetised rock at least 1 km thick southwest of the centre of the caldera (Fig. 6.9). There is no way of telling exactly what rocks are present in the area of Rogan's anomaly without deep drilling, but it has been shown that Mamaku Ignimbrite was erupted during a polar excursion when the North Pole was located in the equatorial Atlantic (Shane et al., 1994; Tanaka et al., 1996). This could mask the magnetic response (D.C. Nobes, pers. comm., 2000), and ponding of Mamaku Ignimbrite in the caldera may have lead to the depth disparity.

More recently Hunt (1992) measured gravity around Rotorua City with much closer station spacings than in previous studies. He correlated his data with previous studies outside the city, and found three gravity low anomalies (Fig. 6.10) in the area of deepest basement determined by Rogan (1982). Two of these are situated beneath Rotorua City and the other beneath Mt Ngongotaha. Hunt added to Macdonald's (1974) list of calderas that have circular/subcircular geophysical anomalies and concluded that while present the low gravity anomalies of Rotorua were not subcircular or parallel to the caldera margin confirming Macdonald's conclusion that Rotorua is not of caldera origin. He goes further saying that the gravity low lies at the northeastern end of a low gravity trough that extends from Oturoa in the northeast for 35 km southwest and may extend 70 km further to the southern end of Lake Taupo. He says that the western side of Rotorua Caldera is associated with the gravity low but that the eastern side is associated with gravity highs and that there is no clear spatial relationship between Rotorua Caldera and the gravity low. The gravity low beneath Rotorua City (labelled L

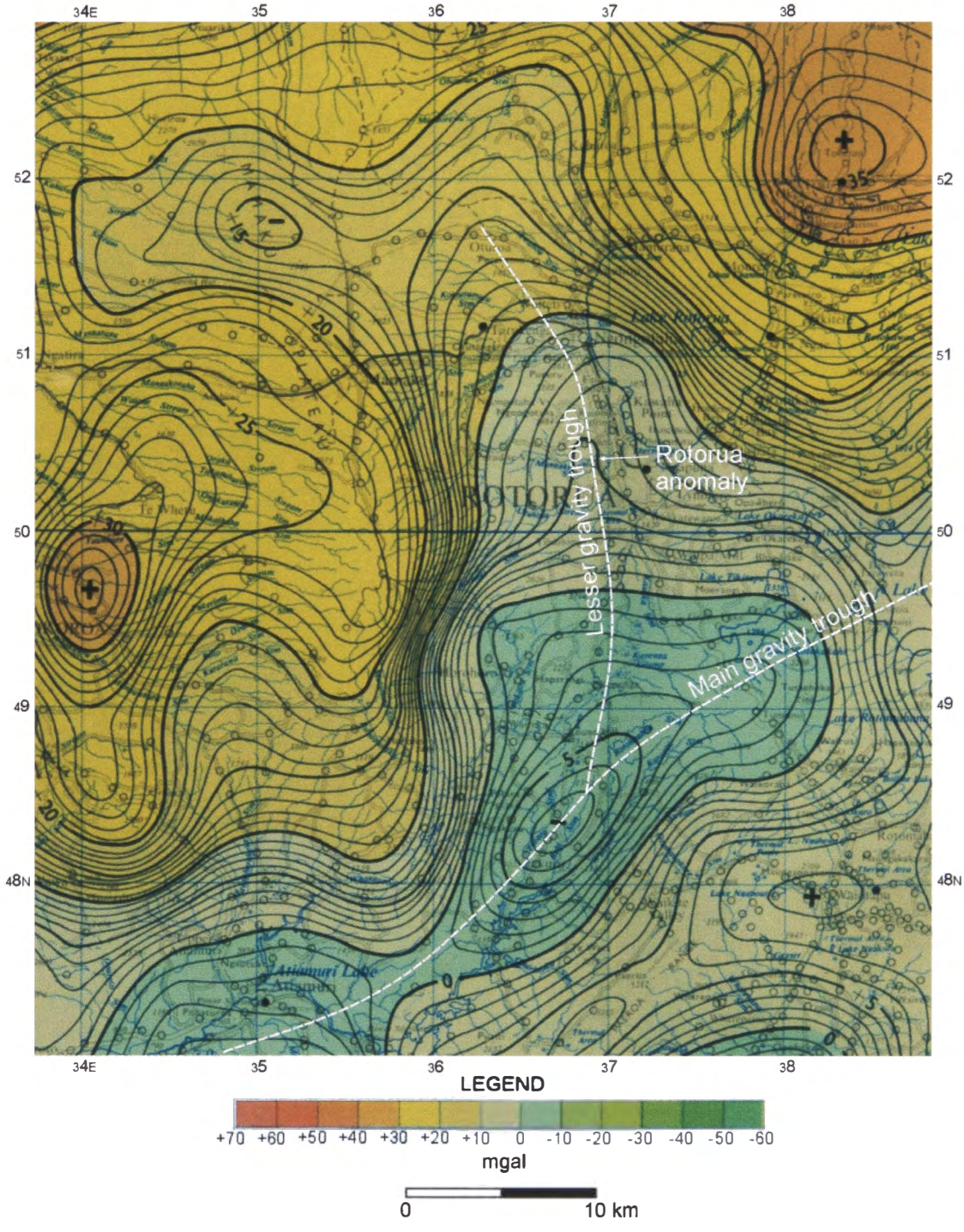

Figure 6.7. Part of Woodward and Ferry's (1973) gravity map. Rotorua Caldera is situated on a NNW-SSE trending gravity trough that branches off a larger gravity trough that extends NE-SW. A small low gravity anomaly can be seen southwest of lake Rotorua. Grid from NZMS 1.

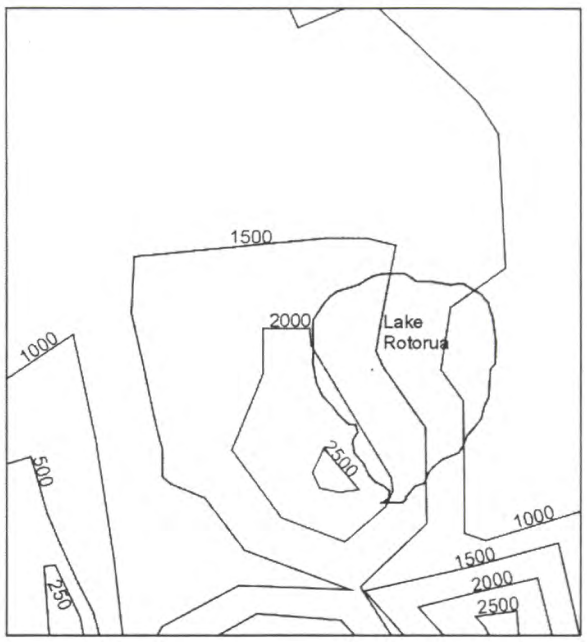

Figure 6.8. An enlargement of the area surrounding Rotorua taken from Rogan's (1982) gravity study of TVZ. The deepest basement anomaly was interpreted southwest of the lake. Numbers are calculated depths (metres) to basement below mean sea level.

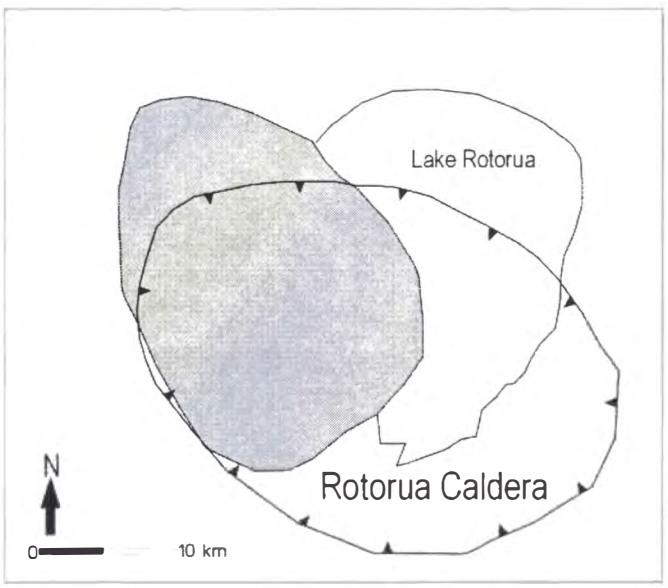

Figure 6.9. The shaded area depicts Rogan's (1982) interpretation of the area underlain by at least 1 km of non- or reversely magnetised material. The toothed line is Rogan's interpretation of the caldera boundary.

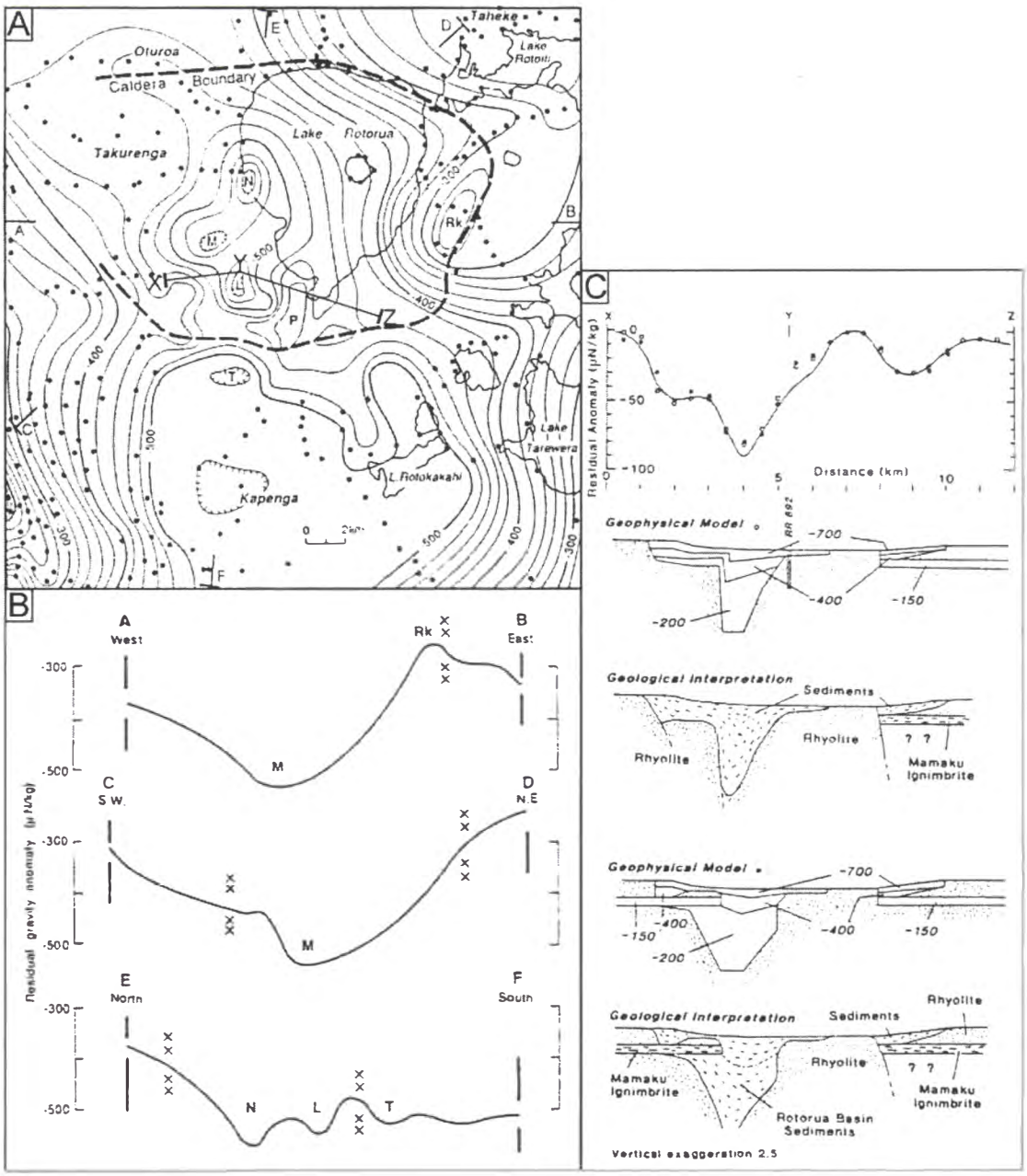

Figure 6.10. Hunt's (1992) gravity data. A) Residual gravity anomaly of Rotorua Caldera and surrounds (contour intervals are 20 μN/kg). B) Cross sections of residual gravity map. C) Possible interpretations of the depression's structure and fill.

in Fig. 6.10) Hunt suggests is due to the presence of low density material, probably sediment, >1 km deep. It is overlapped by the region under which Rogan (1982) indicates the presence of >1 km thick non- or reversely magnetised material. It seems rather coincidental that >1 km of sediment has collected in such an isolated steep sided pocket, as outlined by Hunt, that overlaps with an area of similar depth postulated by a previous worker (i.e. Rogan, 1982). It appears more likely that the area of deeper basement was caused by a caldera collapse event.

6.2.4 Geomorphology

The satellite image of Rotorua Caldera (from Landsat-4) clearly shows the elongation of its limit of deformation NE-SW with an embayment in the northwest (Fig. 6.11). In the southwest surrounding the gravity low are the rhyolite domes of Mt Ngongotaha, Pukehangi and Kawaha Point. A scarp north of the lake is clearly visible as is a scarp dissecting a pre-caldera rhyolite dome west of Mt Ngongotaha (Fig. 6.11). The dome in the middle of the lake is Mokoia Island. Tikitere Graben can be seen in the northeast disrupting the caldera outline. Streams flow towards Lake Rotorua in the northwest and their extents illustrate the area that has downsagged.

Northwest caldera embayment

Fumarolic mounds

Residual mounds are randomly distributed and seen over much of the proximal to medial area of the ignimbrite. They are particularly obvious in aerial photographs. The ignimbrite in these mounds is harder than other surrounding ignimbrite at the same stratigraphic level. Commonly they contain old fumarolic pipes around which the effects of vapour phase activity are evident. It is thought that vapours escaping through the ignimbrite have cemented it creating isolated areas of increased hardness. Later erosion has preferentially removed the ignimbrite outside the areas affected by fumarolic activity and left them protruding from the landscape. The cementing minerals are thought to be tridymite, cristobalite, alkali feldspar and albite. These minerals have been identified by XRD and EDAX in uMI, and are typically deposited from gases migrating through an ignimbrite (e.g. Bateman, 1965; Sheridan, 1970; Carr, 1981; Charles et al., 1986; McCormick, 1990; Papike et al., 1991; Streck and Grunder, 1995).

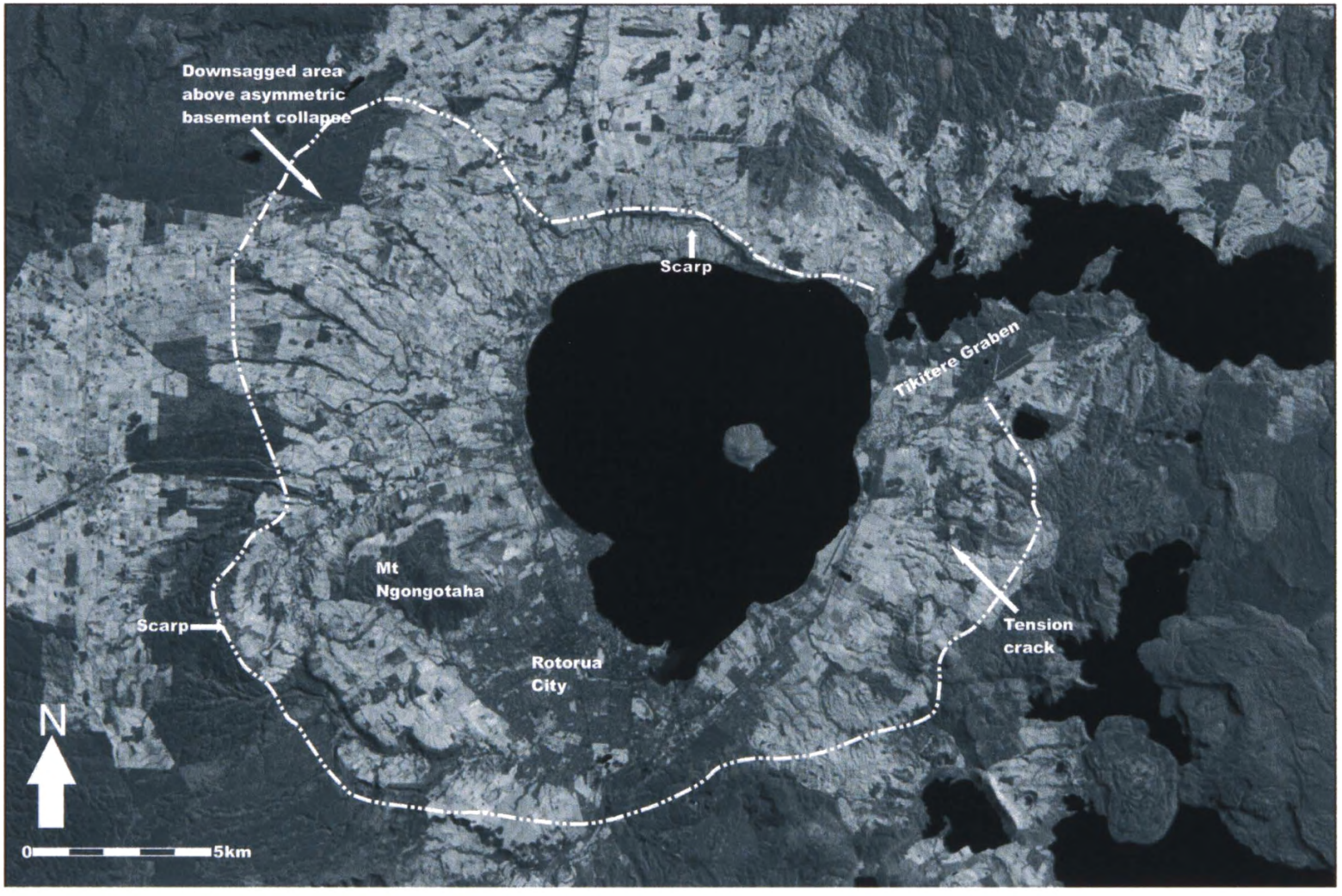

Figure 6.11. Satellite image of Rotorua showing major features outlined in the text. The embayment in the northwest is likely to have been strongly influenced by NW-SE striking faults. The influence of NE-SW striking faults (associated with the main axis of TVZ extension) can clearly be seen with the caldera forming an elliptical collapse structure with a long axis oriented NE-SW.

It is thought that higher concentrations of these minerals occur around the fumarolic conduits, thereby cementing the ignimbrite comprising the mounds.

Towards the northwest of Rotorua Caldera numerous narrow ridges and aligned tors have been identified from air photos (Figs 6.2, 6.6, and 6.12). These ridges and tors are aligned subparallel to the caldera margin. The ridges and tors protrude up to 20 m above the surrounding surface flaring out at their base often to 20 m in width, and they are up to 1.5 km long. A number of these ridges appear to branch off a scarp just inside the limit of caldera deformation (Figs 6.2, 6.6, and 6.13). Rare sections through the ends of the ridges contain fumarolic conduits (see Fig. 2.23), but instead of being point source vents they were fissures creating zones of cemented material (Fig. 6.14). They have been left upstanding in the same way as the mounds seen outside the caldera. Long fissures are interpreted to have formed in response to faulting or warping of the ignimbrite caused by forced folding or downsagging of the area during caldera formation (Fig. 6.14; see also section 8.5.1.). Streams in the area are deflected around these ridges standing as testament to their increased hardness. Sheridan (1970) described similar fumarolic structures in the Bishop Tuff.

Embayment margins

The scarp at the northern and northeastern margin of the embayment, off which some of these fumarolic structures propagate, is problematic. It forms a sinuous 5-6 km long line that begins near the fault scarp north of the lake (discussed below) and terminates in the forest in the northwest (Fig. 6.12). On the south side of the scarp the ground surface dips back towards Lake Rotorua and drainage is in the same direction. North of the scarp all streams flow away from the caldera. The scarp is interpreted to be near the limit of downsag and the caldera margin. Just beyond this scarp is a shorter curved lineament that may represent another similar scarp at an earlier stage of development (Fig. 6.13).

These may represent lines of extension associated with downsag being either tension fractures or head walls of slumps that had limited downslope movement. West and southwest of the scarp's termination, fumarolic ridges occur over a broader band for 6 km before disappearing at Orongohei (Fig. 6.6). Some linear features are present just

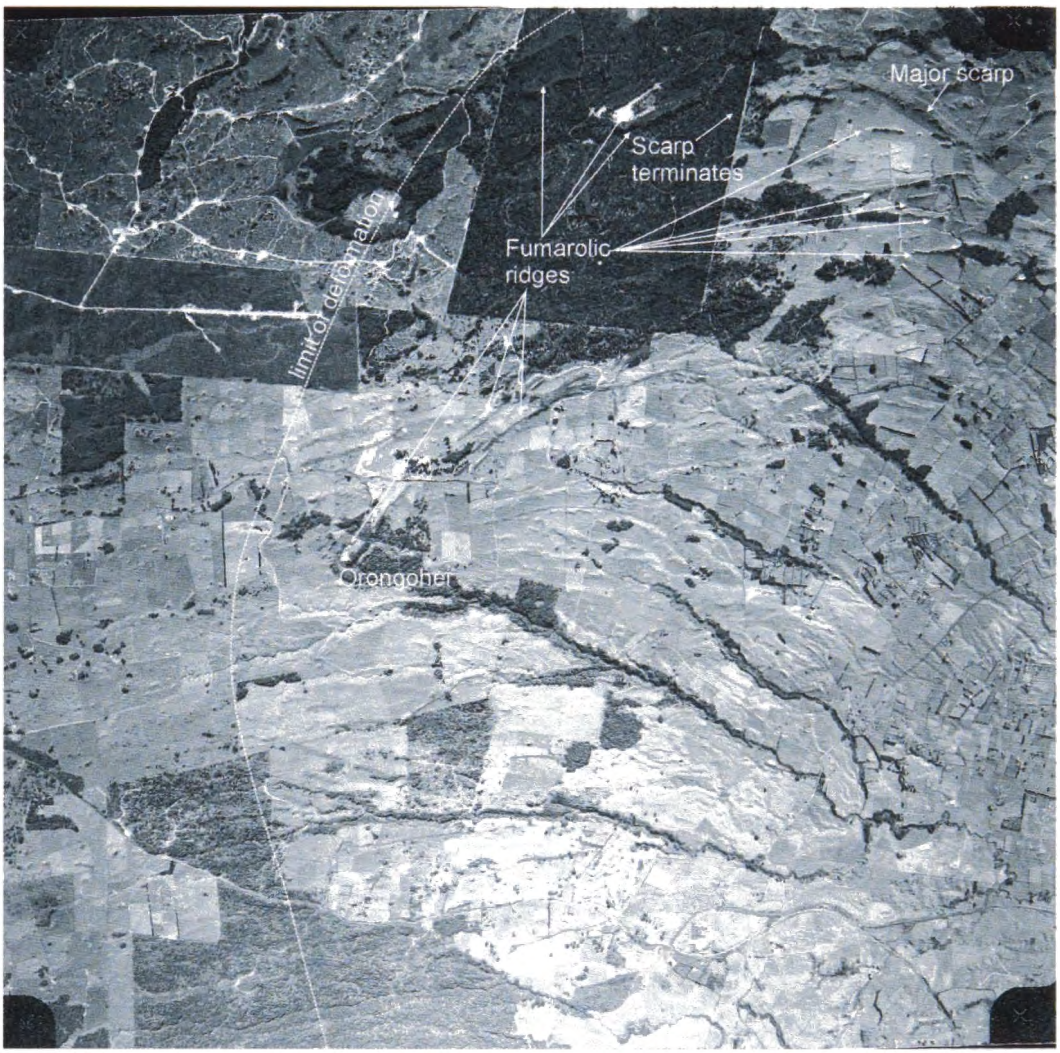

Figure 6.12. Aerial photograph of the northwest caldera embayment. Fissure fumarolic structures can be seen diverging from the scarp close to the caldera margin and are thought to have formed in response to downsag of hot Mamaku Ignimbrite. They are not found southwest of Orongohei. The scarp off which many of the ridges proliferate runs from Fryer dome paralleling the caldera margin before ending in the forest to the west. (Air photo made available by Environment Bay of Plenty, Whakatane).

beyond this scarp, but in much less abundance and are much shorter in length. Most branch off the main scarp. It is likely they were also generated in response to extension during caldera formation.

The embayment opening is well defined and flanked by two pre-caldera rhyolite domes (Endean dome and Fryer dome, Fig. 6.6). A NW-SE striking fault cuts the post-caldera Pukehangi dome and is in line with the southwestern flank of the embayment (Fig. 6.2 and 6.6). This fault may be a reactivated older structure that was involved in the caldera's development. The northeastern flank of the embayment is associated with the

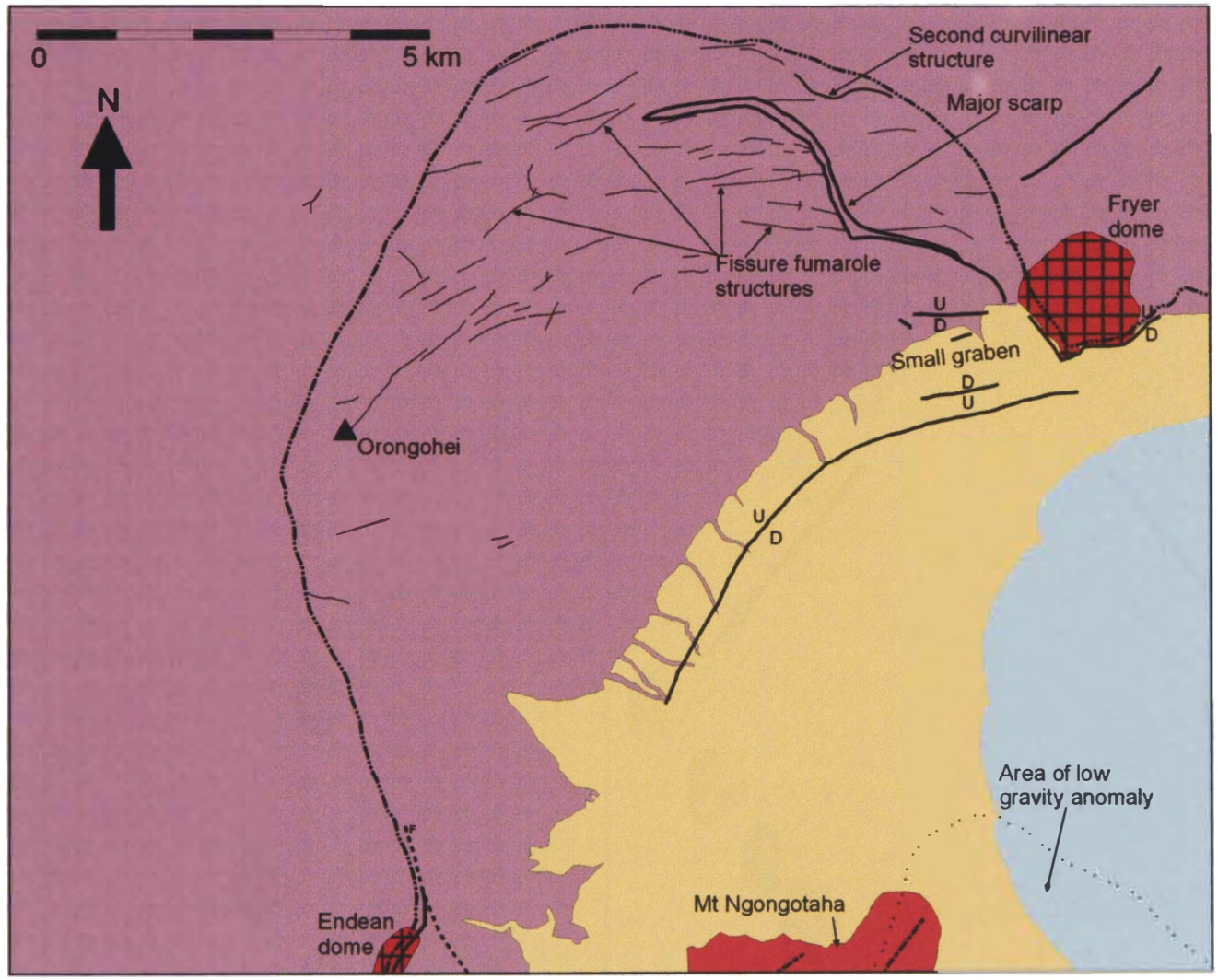

Figure 6.13. Close-up of the embayment in the northwest of the caldera showing the fissure fumarole structures, the embayment scarp, the fault at the embayment opening, and the small graben. The fissure fumarole structures are sub-parallel to the caldera margin and the low gravity anomaly and are thought to be related to extension caused by downsag of Mamaku Ignimbrite. The embayment is bounded by two pre-caldera rhyolite domes. Lithologies and symbols as for Figure 6.6 or back pocket.

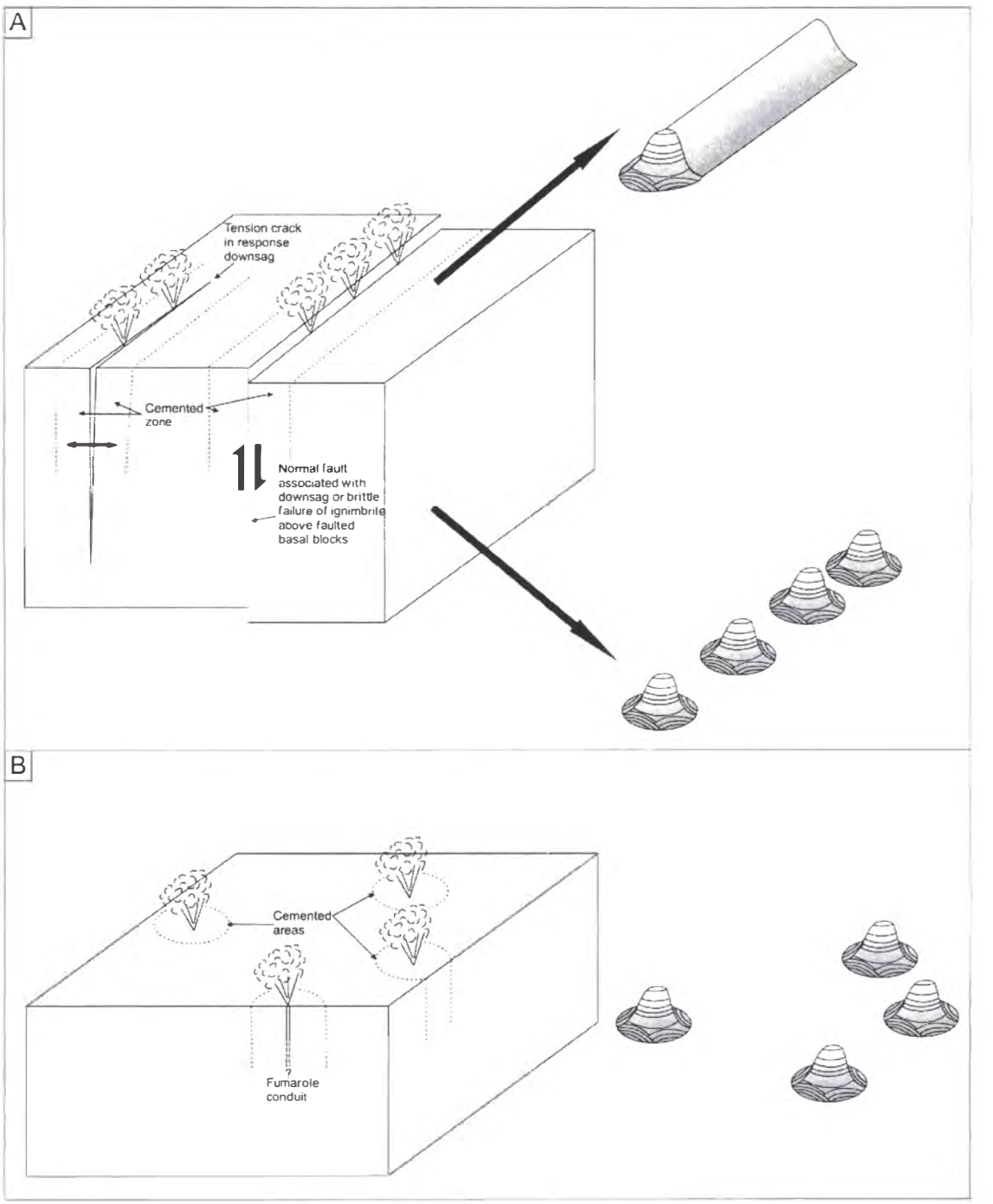

Figure 6.14. Formation of aligned fumarolic structures, fumarolic ridges, and randomly located fumarolic mounds. A) Around the margins of downsagged areas, tension cracks and faults create weakened zones along which gases preferentially ascend cementing linear-curvilinear zones. B) Where no such weaknesses prevail, gases discharge at randomly located vents creating structures with no preferred orientation. On erosion these structures are left as ridges or mounds (aligned or randomly distributed).

marginal scarp discussed previously and the northeastern and southwestern margins are thought to be controlled by NW-SE striking faults. It is interpreted that downsag occurs over a region of brittle basement collapse.

Surficial fault traces

Mamaku Ignimbrite begins to outcrop from beneath lake sediments approximately 5 km from the northwest embayment margin (Fig. 6.13). It outcrops in deeply entrenched streams and its emergence from beneath the lake sediments may signify the presence of a fault that would line up with two fault scarps at either end of the embayment.

Just inside the eastern end of the embayment is a small graben-like structure that has been identified from aerial photography (Fig. 6.13). This structure is difficult to determine from the ground due to the surface's hummocky nature and dissection of the area by streams. Such structures are sometimes seen associated with other calderas (e.g. Branney and Kokelaar, 1994) and may be of limited depth.

Northern margin fault

At the northern margin of the caldera is an obvious scarp that strikes approximately east-west and truncates two rhyolite domes (Fryer and Hamurana domes, Fig. 6.15). Between the two domes the scarp has probably been accentuated by wave erosion while the lake stood at higher levels. Flow lines present in Hamurana dome terminate at the scarp and small collapse features in Fryer dome show this scarp was ultimately created by fault movement and is not solely an erosional feature.

Western and southern margin faults

No single fault can be traced for any great distance along the western and southern caldera margins (Fig. 6.16). Instead a number of faults occur with extents that sometimes overlap.

South of the embayment, at the caldera's western margin, Endean dome has been dissected by a fault. Mamaku Ignimbrite, that must have been deposited as the caldera formed, surrounds the dome. Mamaku Ignimbrite also outcrops between Pukehangi

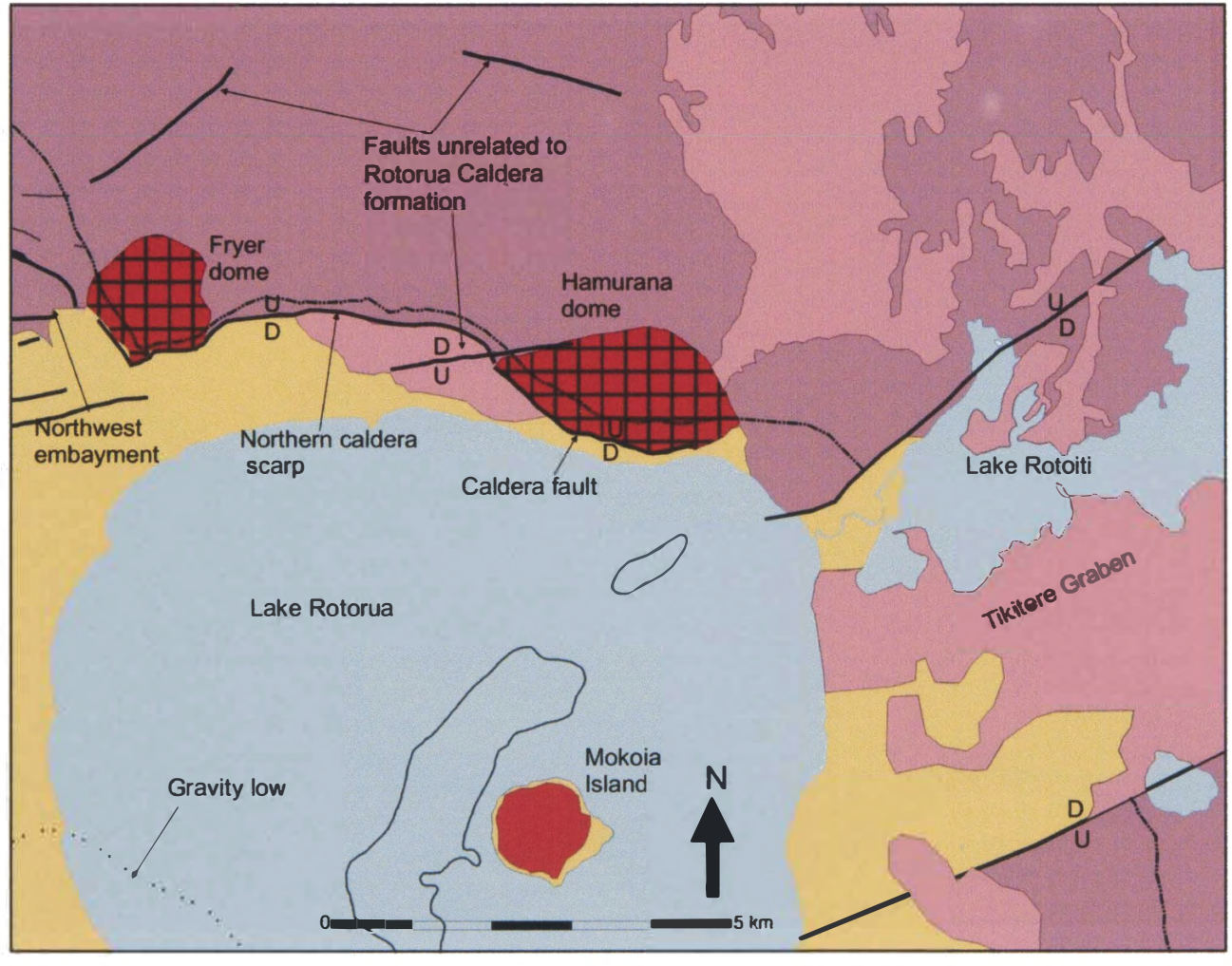

Figure 6.15. North and northeastern Rotorua Caldera. Structures relating to caldera formation in the northeast have been destroyed by the activity of Tikitere Graben and the eruption of Rotoiti Breccia. Tikitere Graben breaks the line bounding the limit of deformation associated with Rotorua Caldera's formation. The scarp at the northern caldera margin has likely been accentuated by wave action when the lake was at higher levels and perhaps by slumping of the caldera wall after formation. It is clearly fault related as the two rhyolite domes at its ends have been truncated by fault movement. For key see Figure 6.6 or back pocket.

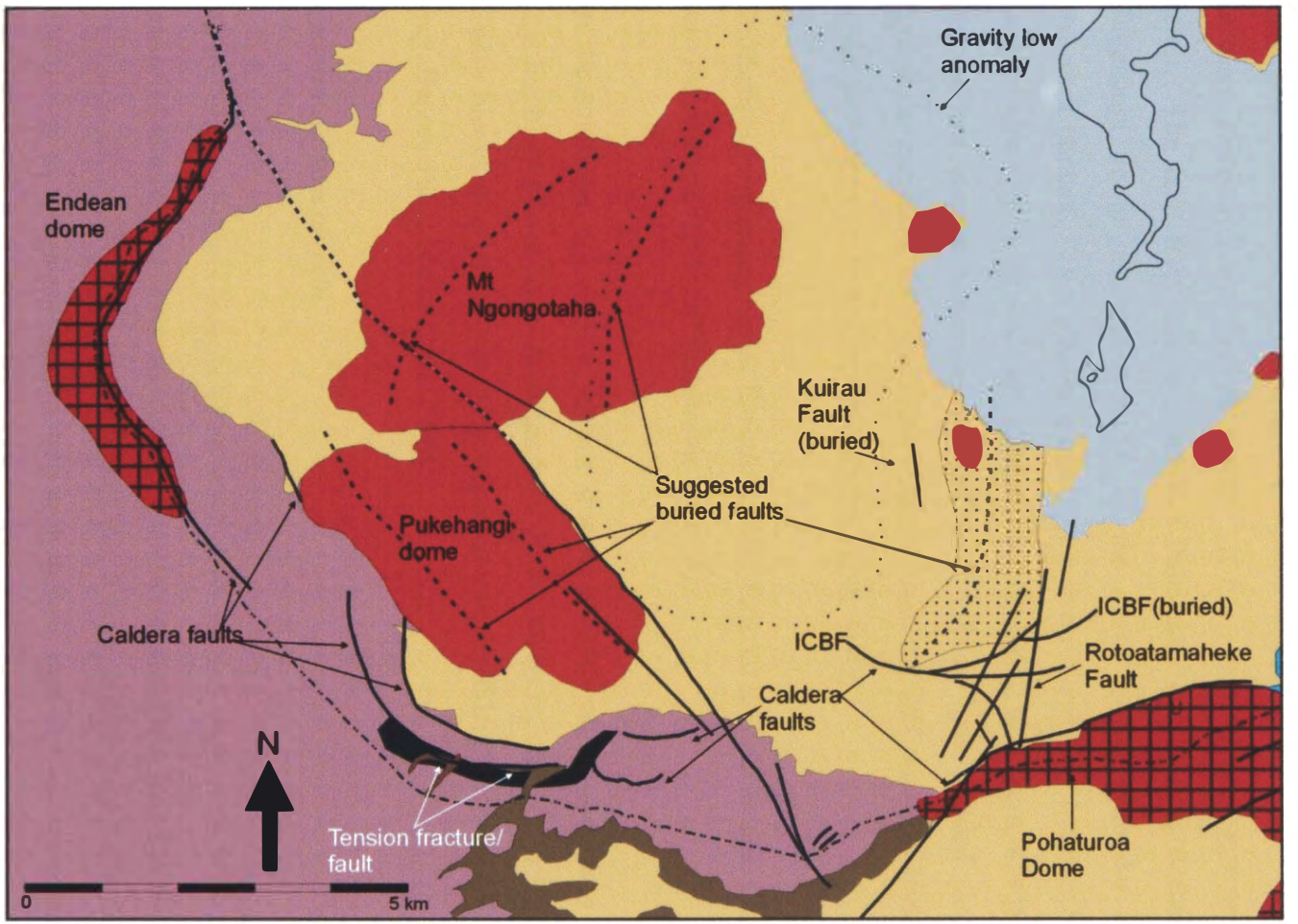

Figure 6.16. The southern and southwestern part of Rotorua Caldera. Post-caldera rhyolite domes surround the gravity low. Long axes of Pukehangi dome and Mt Ngongotaha are sub-parallel to the gravity low and are inferred to reflect the positions of underlying faults. There is no single fault marking a structural margin (cf. Lipman, 1984), displacements are instead taken up by a number of faults with extents that may overlap. Lithic lag breccias occur at the southwestern margin. Two stream tributaries are aligned in the south and may indicate the presence of a tension fracture. Faults and lineaments taken from Lloyd (1975), Bayrante (1984), Wood (1992), and this study. ICBF= Inner caldera boundary fault (Wood, 1992). Symbols and lithologies as for Figure 6.6 or back pocket.

rhyolite dome and Endean dome where it forms prominent bluffs that are also inferred to represent a fault. Both faults are interpreted to have formed during the collapse of the caldera.

South of Pukehangi dome a number of faults have been inferred based on Mamaku Ignimbrite outcrop and lineaments seen in air photos. Here, outcrop of Mamaku Ignimbrite rises suddenly from lake sediments similar to the bluff forming ignimbrite between Pukehangi and Endean domes. It has similarly been interpreted as a fault scarp. The fault trace inferred between Pukehangi and Endean domes is buried by Pukehangi dome resurfacing south of the dome at the Mamaku Ignimbrite-lake sediment contact. Two stream gullies (one is a tributary to Aorangi Stream and the other is close by to the east) are aligned both deviating from azimuths perpendicular to the caldera margin becoming parallel to it. They have eroded through Mamaku Ignimbrite exposing the underlying Pokai Ignimbrite, and possibly deviate in response to the presence of a fault or tension fracture (Fig. 6.16).

Southeast of Pukehangi dome the surface of Mamaku Ignimbrite again is tilted, dipping into the caldera, representing possible downsag.

In the southeast, pre-caldera rhyolite domes are also cut by a caldera fault. Faulted rhyolite blocks have been identified by C.P. Wood, (pers. comm., 1998) that are akin to slump blocks interpreted as contemporaneous with caldera formation at many calderas (e.g. Bacon, 1983; Nairn et al., 1994).

Eastern caldera margin

At the eastern caldera margin slope wash deposits and vegetation have mostly covered tension fractures. One tension fracture has been identified, is continuous and close to the caldera margin (Fig. 6.17). In air photos it is represented by a curvilinear lineament that seems to widen towards its two ends before tapering and pinching out. On the ground it comprises a flat area between two ridges that is up to 50 m wide and tapers at its northern and southern extremities. Towards the structure's northern end a cross section is exposed. At this locality the fracture is 15 m wide (its base is not exposed) and filled with bedded coarse sand (Fig. 6.18). The surface of Mamaku Ignimbrite is at

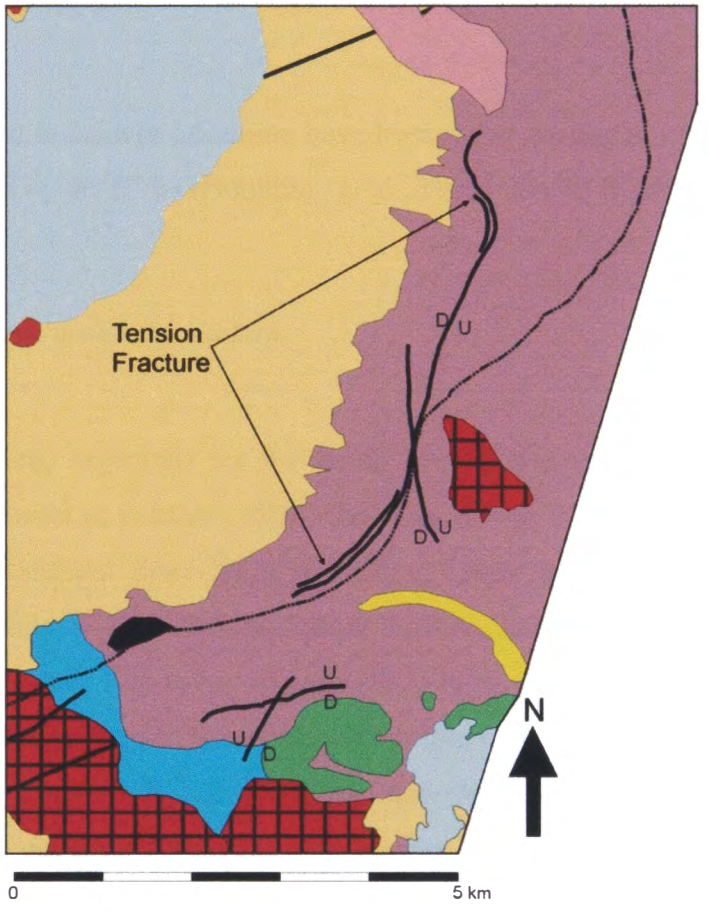

Figure 6.17. The eastern caldera margin showing the tension crack identified from aerial photography and interpreted to have been created by downsag of Mamaku Ignimbrite. For key see Figure 6.6 or back pocket.

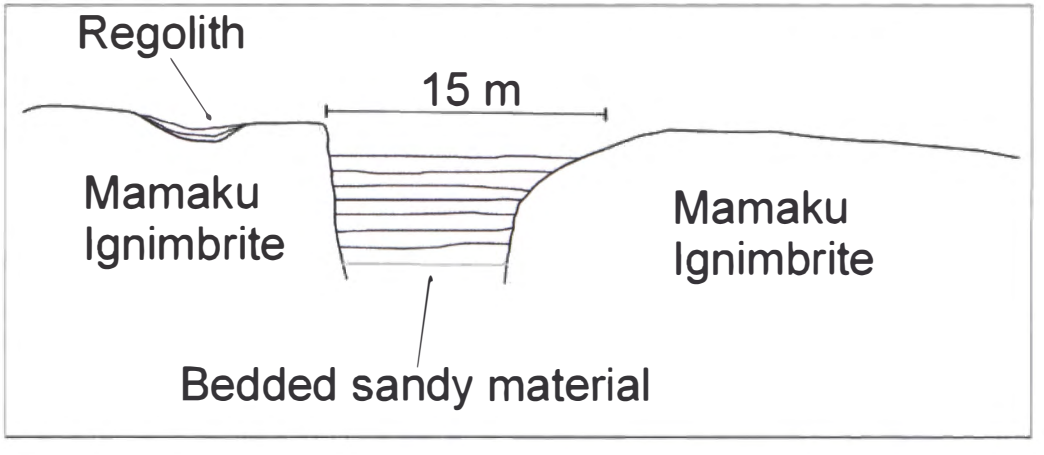

Figure 6.18. Section through the northern end of the tension fracture towards the eastern caldera margin. It is steep sided and filled with yellow, coarse, poorly sorted sand. The ignimbrite is not displaced on either side of the fracture, and it appears to have pulled apart, probably due to downsag of the ignimbrite during caldera formation.

the same elevation on either side and the structure is interpreted as a pull apart formed by downsag during caldera formation.

Northeast caldera margin

Structures related to caldera formation have been either destroyed by activity of Tikitere Graben or buried by the 65 ka (Houghton et al., 1995) Rotoiti Breccia.

Surface lineaments inside the caldera

Inside the caldera, especially in the south around the geothermal field, there are numerous lineaments (e.g. Lloyd, 1975; Bayrante, 1984; Wood, 1985; 1992; Fig. 6.16). Lloyd (1975) identified three NE-SW striking faults based on geomorphology and others based mainly on hydrothermal spring location and warm ground (including some that strike NNW-SSE; Fig. 6.16). Wood (1992) inferred the Kuirau Fault, also NNW-SSE striking, based on thermal activity and pointed out the Rotoatamaheke Fault that strikes N-S and displaces Pohaturoa Dome, and the ground surface, down to the east. Bayrante (1984) delineated numerous lineaments in air photos dominantly around the geothermal area, but also towards the southern caldera margin near Utuhina Stream (Fig. 6.5). Many of the faults identified within the caldera cut lake sediments and have been active since the caldera formed. They may be reactivated faults that were involved in caldera formation but cannot be said unequivocally to be so.

Beneath the lake a trench (20-25 m maximum depth; Fig. 6.6.) is present that runs north from Motutara Point past the west side of Mokoia Island before swinging around to a more NE-SW orientation (Irwin, 1969). It is subparallel to the regional extension axis and is thought to have formed post-caldera. At the south end of this trench is a 30-40 m deep depression (15-20 m deeper than the surrounding lake floor) that may represent an explosion crater (Grange, 1937).

A branch of the Horohoro Fault is truncated by the Pohaturoa Fault at the caldera boundary (Nairn, 1981). It may be present at depth beneath the caldera fill.

6.2.5 Geology

Lithic lag breccias

Lithic lag breccias are proximal deposits within ignimbrites (Wright and Walker, 1977; Walker, 1985) and are often interpreted as coincident with caldera collapse (e.g. Nairn et al., 1994; Branney and Kokelaar, 1997; Beresford and Cole, 2000). Outcrop of Mamaku Ignimbrite lithic lag breccias is limited due to forest cover, but they are found at the very top of the ignimbrite at the southern and southeastern caldera margins (Figs 6.6, 6.16, and 6.17). Their location indicates proximity to vent sites, possibly along adjacent faults. Where seen, the lower surface of the lag breccias dips towards the caldera. Their location and dip leave no doubt that they and the Mamaku Ignimbrite were sourced from Rotorua Caldera. Their gradational contact with uMI confirms that Mamaku Ignimbrite's source caldera is Rotorua. Areas of lithic concentration are also seen in uMI at a number of caldera margin localities (Fig. 6.6). Their presence at the top of the ignimbrite indicates a stage of caldera collapse late in the climactic eruption.

Andesite blebs

Andesitic blebs are found only in uMI. As outlined in chapter 4 the andesitic magma is thought to have resided in a sill beneath type 3 dacitic magma. Buoyancy and inertia factors would have impeded the withdrawal of the andesite magma (Blake and Ivey, 1986a and b) and it is interpreted that the andesite magma was forced to erupt late in the Mamaku Ignimbrite eruption as caldera collapse caused these restricting factors to be overcome.

Ignimbrite thickness

Intra- and extra-caldera ignimbrite thickness variation is also important in determining the presence of a caldera. Ignimbrites tend to pond in depressions (Wilson and Walker, 1982) and often the volume of erupted ignimbrite inside the caldera is comparable (subequal) to that of the outflow sheet (Lipman, 1984).

Just outside the caldera rim to the south, Mamaku Ignimbrite is approximately 40 m thick. To the north it is up to 145 m thick (Nathan, 1975). Inside the caldera the

ignimbrite is at least 279 m thick (Lamarche, 1992), and intra-caldera deposits of unknown Lithology (probably Mamaku Ignimbrite) may be >1 km thick (Rogan, 1982). The thickness variation indicates Mamaku Ignimbrite has ponded inside Rotorua depression lending further support to its definition as a caldera.

Post-caldera rhyolite domes

The largest of the exposed post-caldera rhyolite domes and dome complexes (Fig. 6.16) are located around the area of low gravity anomalies. Effusive volcanism is often associated with calderas after their collapse (e.g. Smith and Bailey, 1968; Lipman, 1984) and post-collapse rhyolite domes often extrude close to, or above, caldera forming faults (e.g. Lipman, 1984; Self et al., 1986) that become conduits for the ascending magma.

Mt Ngongotaha, the largest of the dome complexes found in Rotorua Caldera, was erupted from a fissure (J. Richnow, pers. comm., 1999), which suggests utilisation of a fault (or faults) for magma ascent and extrusion. Most of the other dome complexes in Rotorua Caldera have distinct long axes also suggestive of fissure/fault controlled eruptions. The orientations of these long axes are sub-parallel to the margins gravity low anomalies identified by Rogan (1982), and Hunt (1992). The distribution of the dome complexes around the area of deepest caldera collapse and orientation of long axes sub-parallel to the low gravity anomalies suggest eruption along the margins of the most deeply subsided blocks (block bounding faults). Dome locations have been used to infer the distribution of underlying caldera faults (Fig. 6.6 and 6.16).

Drill hole information

Drilling for geothermal water supply has been widespread in Rotorua Caldera, but most wells have not been logged in detail. Crafar (1974a) and Wood (1992) looked at 31 and 23 wells respectively in investigations of the geology and geothermal aquifers beneath Rotorua City. The only well logged by Crafar that penetrated Mamaku Ignimbrite was just southwest of Rotorua City, where the ignimbrite's upper surface was 120 m above sea level (280 m below the ground surface) while all of the wells logged by Wood either bottomed out in Mamaku Ignimbrite, or post-caldera rhyolite. The maximum thickness of Mamaku Ignimbrite drilled was 120 m, but the bottom was never reached. Based on

the elevations at Mamaku Ignimbrite was first encountered in drill core, Wood (1985) suggested the presence of the Inner Caldera Boundary Fault (ICBF). The ICBF is an east-west trending structure that Wood believes to be a buried scarp formed during caldera collapse (Fig. 6.6, and 6.16). It is also close to the southern boundary of a buried rhyolite complex (Fig. 6.6 and 6.16). The presence of the scarp would have inhibited incursion of the rhyolite lava any further to the south. Wood (1992) showed that the surface of Mamaku Ignimbrite steps down across at least one fault (ICBF) towards the area of the gravity anomalies (Fig. 6.19). Whether this step-faulting occurred during, or after, caldera collapse is equivocal, but the ICBF's orientation is sub-parallel to the gravity anomaly. Other scarps in Mamaku Ignimbrite are thought to be of caldera collapse origin and stratigraphic locations of lithic breccias indicate that some collapse occurred at a late stage in the ignimbrite's eruption, further suggesting that the step-faulting is related to caldera formation. From the drill hole data Wood (1992) suggested that the caldera subsided as "...kilometre-size blocks bounded by shallow rooted faults, aligned sub-concentrically to the region of greatest subsidence". This kind of step-faulting has been documented by Halinan (1991) at Guayabo Caldera (see section 8.5.1).

Mamaku Ignimbrite has also been documented at approximately 170 m depth near Rotorua airport on the eastern side of the lake (A.S. Cody, pers. comm., 2000).

6.3 Caldera structure

Ignimbrite thickness variation (intra- and extra-caldera), maximum lithic data, and location and dip of lithic lag breccias all prove that Mamaku Ignimbrite was erupted from a source in the Rotorua depression. It would be difficult to erupt such a volume of material without formation of a caldera.

More and more calderas are being described that do not conform to ideal structures. It may be that ideal structures, while in existence, are comparatively rare and that the form caldera collapse takes is governed by many factors other than the accumulation of magma and removal of support from a magma chamber roof. Pre-existing structures also play important roles in the morphological and structural development of calderas. Such structures may be related to the local tectonic environment, previous volcanism, and precursory tumescence.

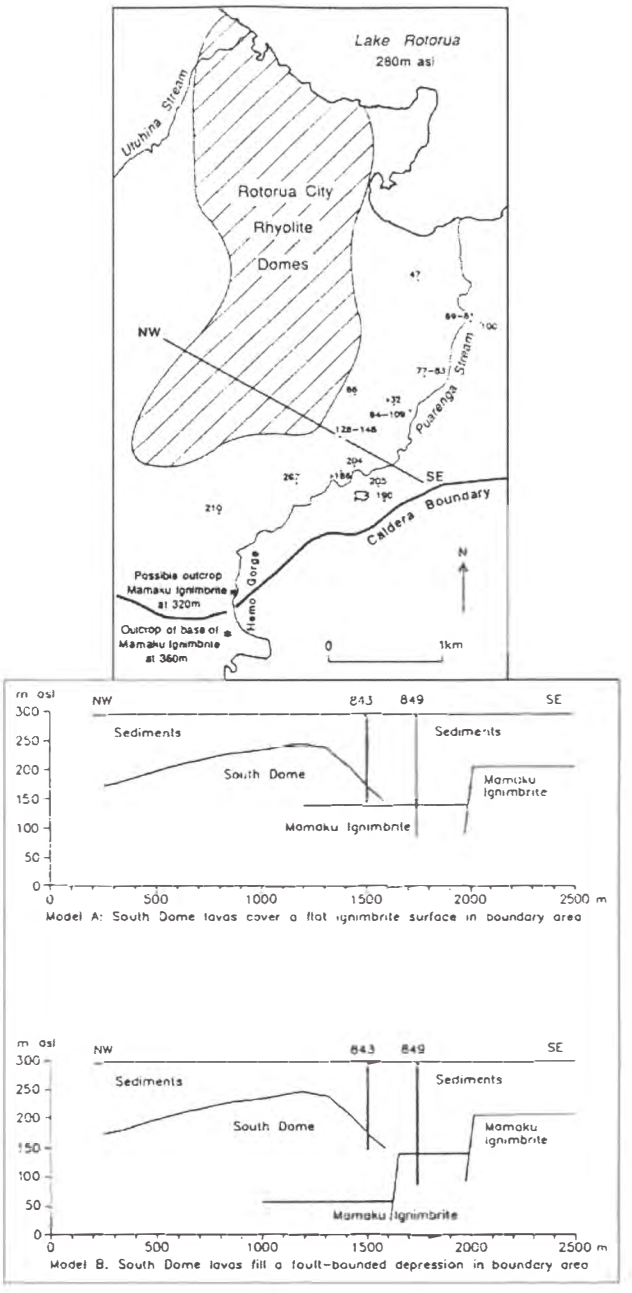

Figure 6.19. Wood's (1992) interpretation of subsurface structure of part of Rotorua Caldera based on drill core information. The cross sections are possible interpretations of the subsurface geology along the line NW-SE. The Mamaku Ignimbrite surface is viewed to step down towards the area of the deepest gravity anomaly.

Geomorphic, geological and geophysical information indicate that the structure of Rotorua Caldera is much more complex than can be explained by simple models postulated in the literature. The tectonic environment of TVZ makes formation of a simple caldera virtually impossible. No single ring fault encompasses the collapse structure at Rotorua and instead subsidence is thought to have taken place along pre-existing faults or crustal defects. Vent sites may also have been controlled by pre-

existing structures. It has features that can be attributed to downsag (to the northwest, southwest, and east), piston (beneath Rotorua City), trapdoor (asymmetric subsidences to the northeast and northwest), and piecemeal (numerous caldera related faults) collapse processes, but none of these describes the Rotorua Caldera's structure fully. A complete interpretation of Rotorua Caldera structure is made in chapter 8, but it can be summarised as a rhyolitic single event, asymmetric, multiple block, single locus caldera.

CHAPTER 7
Mokai Ignimbrite

7.1 Introduction

Martin (1961) identified an ignimbrite outcropping west of Maroa Volcanic Centre between Mokai township and Ongaroto Gorge (Waikato River; Fig. 7.1) and correlated it with the Mamaku Ignimbrite seen further north. Healy et al. (1964) mapped this ignimbrite, but regarded it as a separate unit and named it Mokai Ignimbrite. Since then, however, most workers have considered Mokai and Mamaku ignimbrites to be the same unit.

In this chapter the stratigraphic, field and chemical characteristics of the Mokai ignimbrite are outlined and its relationship to Mamaku Ignimbrite is discussed.

7.2 Previous Work

Previous work on Mokai Ignimbrite has mainly resulted from geothermal exploration, economic prospecting, and reconnaissance mapping by the Department of Scientific and Industrial Research (e.g. Healy et al., 1964, and Bibby et al., 1984). A major geothermal field is situated beneath Mokai (C.P. Wood pers. comm., 1997) and is now being used to generate electricity. Exploratory geothermal wells have been logged by staff of the Institute of Geological and Nuclear Sciences (IGNS).

Earlier work was carried out by BP Oil New Zealand Ltd. (especially in the Forest Rd area, Fig. 7.1; Fransen and Sharp, 1988) and IGNS (E.F. Lloyd, unpubl. data).

7.3 Distribution

Mokai Ignimbrite outcrops over a rectangular area covering c. 132-136 km^2 south of Lake Whakamaru in the northwestern part of Whakamaru caldera (Fig. 7.1). It outcrops in an 8 km wide zone extending 16.5-17 km north-south. The zone is flanked to the west by the Western Dome Belt (WDB) and to the east by rhyolite domes of the Maroa volcanic centre and Hauraki Fault (controlling Waipapa Stream Fig. 7.1). It may extend further south but does not outcrop.

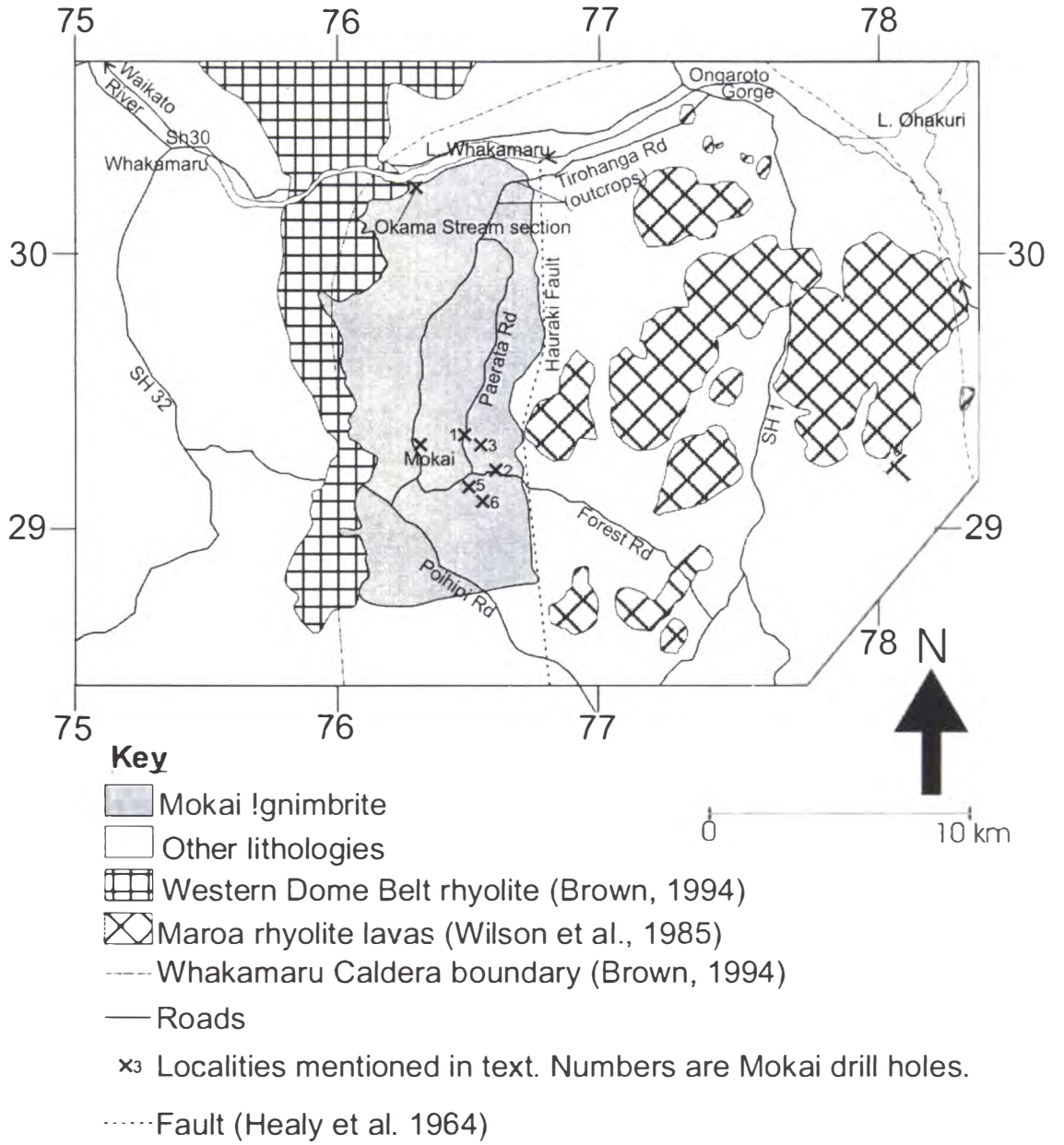

Figure 7.1. Location map showing distribution of Mokai Ignimbrite (grid from NZMS 262).

It appears that westward movement of the Mokai Ignimbrite was restricted by the older WDB, whereas exposed Maroa rhyolite domes are mostly younger (Wilson et al., 1986).

Pink vapour phase altered ignimbrite outcropping on Whangamata Rd 11.5 km south of Mokai is of similar appearance to the upper parts of both Mokai and Mamaku Ignimbrite, but it has a different paleomagnetic direction (G.M. Turner, pers. comm., 1999) and is regarded as a separate ignimbrite.

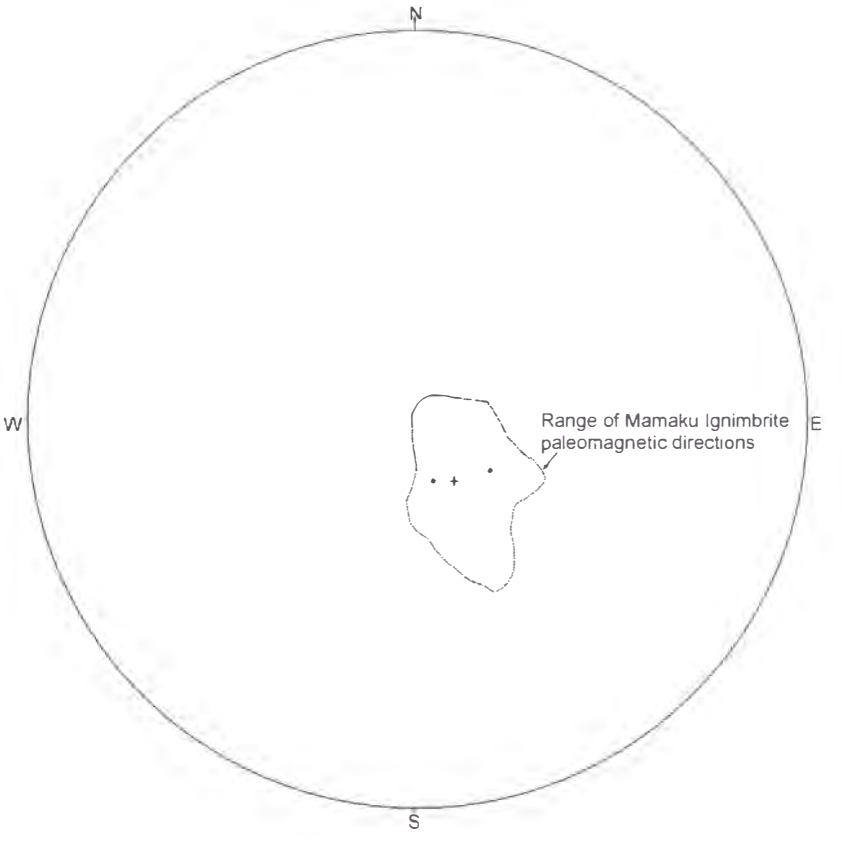

Figure 7.2. Paleomagnetic directions of Mokai Ignimbrite. The magnetic direction has a north pole in the equatorial Atlantic region (as does Mamaku Ignimbrite paleomagnetic data). Cross is from Tanaka et al. (1996), and dots and range of Mamaku paleomagnetic are from Shane et al. (1994).

7.4 Age and stratigraphic relations

$^{40}Ar/^{39}Ar$ dating of Mokai Ignimbrite was undertaken by Tanaka et al. (1996) and produced an age of 220 ± 10 ka. Paleomagnetic measurements have been made on samples from 3 sites by Tanaka et al. (1996; 1 site) and Shane et al. (1994; 2 sites). All measurements yield an equatorial Atlantic north pole (Fig. 7.2). Tanaka et al.'s (1996) measurements were made on samples taken below the extensively vapour phase altered top and so the paleomagnetic direction is accepted.

The paleomagnetic direction and $^{40}Ar/^{39}Ar$ dates of Mokai Ignimbrite are the same as those of Mamaku Ignimbrite (Tanaka et al., 1996). This has lead most workers to infer the two ignimbrites are part of the same unit.

Mokai Ignimbrite overlies Whakamaru Ignimbrite, which is downfaulted into Whakamaru Caldera. It also overlies older rhyolite lavas of Maroa volcanic centre (C.P.

Wood, unpubl. data) and the Western Dome Belt. In the field area it is overlain by Oruanui Ignimbrite and Taupo pumice (which is ponded in streams and gorges of the field area)

7.5 Lithology

Crystal content varies between 5 and 30 vol%. It does not appear to change regularly with stratigraphic position except at the base of the middle unit (see section 7.6) where it reaches 30 vol%. Crystals are euhedral to subhedral or broken and comprise plagioclase + iron/titanium oxides + quartz + orthopyroxene + clinopyroxene (augite) with trace amounts of hornblende and cummingtonite. Lithic content changes irregularly with stratigraphic position, and lithic fragments are often most abundant in upper parts of units. Lithic content ranges from 0-15 vol%.

7.6 Internal Stratigraphy

The Mokai Ignimbrite type section is designated as Okama Stream (T17/634040-634037-640034) south of Lake Whakamaru (Fig. 7.1), where it comprises at least 3 units separated by fine laminated ash deposits (Fig. 7.3), and is at least 100 m thick. Ponded Taupo Pumice and forest growth limits outcrop north of T17/634037. The base of Mokai Ignimbrite does not outcrop.

7.6.1 Ignimbrite units

Three units are exposed south of Lake Whakamaru (Fig. 7.3) and are all poorly to moderately welded. Lithification has imparted high induration to all units except for the vapour phase altered top.

The lowest unit is brown, crystal-poor (usually <10 vol% but locally up to 15 vol%), pumice-rich (15-50 vol%, usually 15-20 vol%), lithic-rich (5-20 vol%, usually <7 vol%) coarse ash and is at least 40 m thick. Superficial appearance is similar to Pokai Ignimbrite which was studied by Karhunen (1993). Pumice clasts are orange, lithic fragments are predominantly rhyolite, and the matrix is dark grey. Lithic content varies irregularly reaching a maximum of 15-20 vol% c.10 m from its top. M_L reaches 36 mm in the zone of highest lithic content decreasing to 29 and 25 mm at the top and

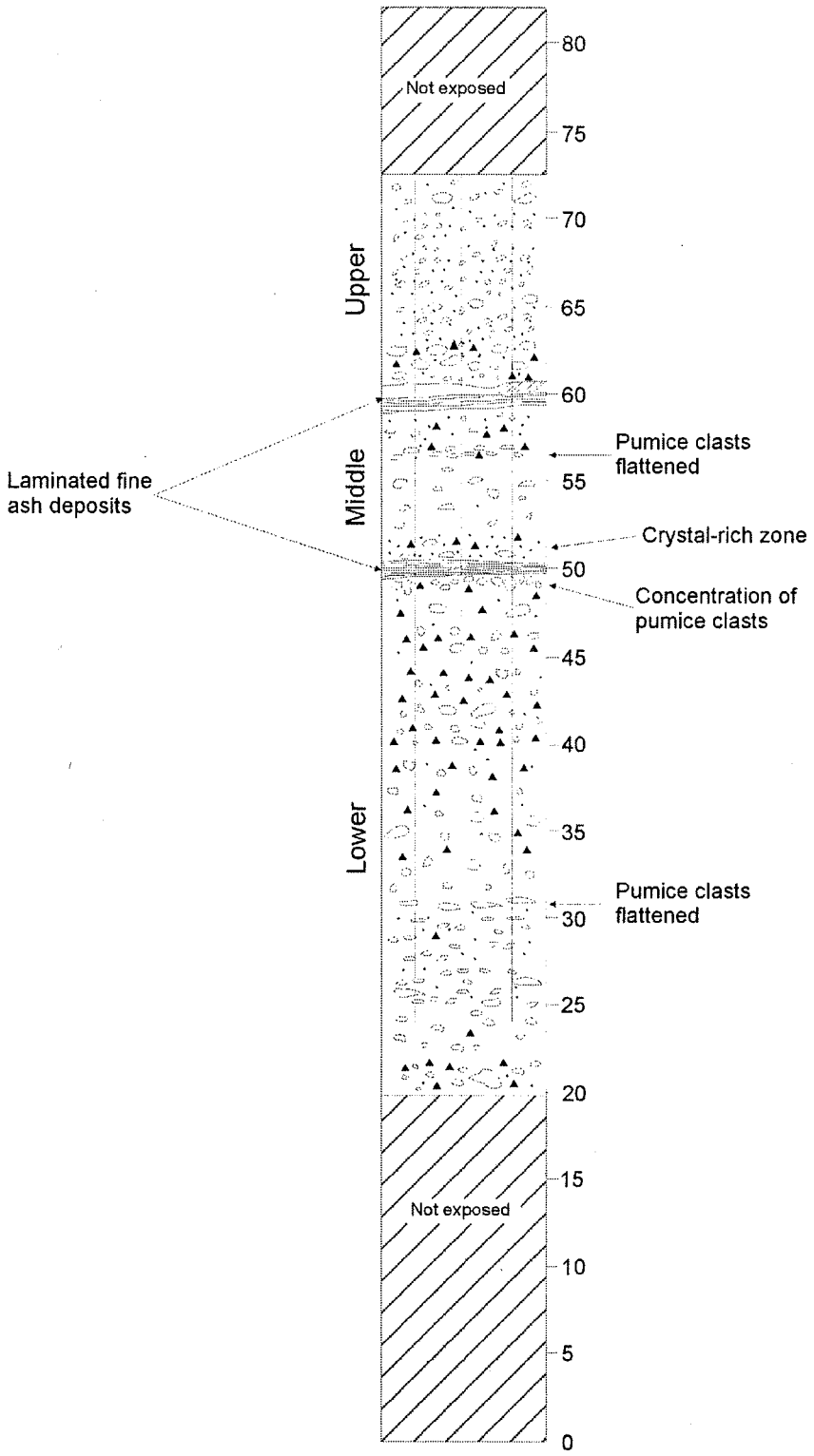

Figure 7.3. Graphic log of the Okama Stream section, the type locality of Mokai Ignimbrite. Lower, middle and upper units are separated by fine, laminated ash deposits. Open shapes are pumice clasts, triangles are lithic fragments, and dots are crystals. Units are metres.

lowest exposure respectively. Pumice content reaches a maximum of 50 vol% in a band at its upper surface. Maximum pumice (M_P) size varies irregularly throughout the unit reaching a maximum of 124 mm near the top of the unit. Just below the middle of the exposed unit, lithic content decreases to <1 vol%, crystal content rises to 15 vol%, and pumice clasts (10-15 vol%) are flattened. Lithic fragments sampled are all rhyolite lava.

The middle unit is 5-10 m thick, light brown, poorly to moderately welded, and comprises lithic fragments (5-10 vol%, M_L=29 mm), pumice clasts (3-15 vol%, Mp=72 mm) and crystals (15-30 vol%) in a fine to coarse ash matrix. Crystal content increases sharply towards the base of the unit (reaching 20-30 vol%). The higher crystal content at its base imparts a layer 2a-like (cf. Sparks et al., 1973) appearance. Pumice content decreases markedly in the top 2 m of this unit dropping from 10-15 vol% 2 m below the top to 2-3 vol% at the top. Three metres from the top of the unit pumice clasts are moderately flattened and devitrified. Above and below this pumice clasts are more open although long axes do have a horizontal preferred orientation. Lithic fragments decrease to a minimum 5 vol% in the zone of maximum pumice flattening and increase above and below this to between 7 and 10 vol%. Lithic fragments are almost entirely rhyolite lava.

The upper unit is pink, poorly welded, and poorly sorted with 5-15 vol% pumice clasts (M_P=73 mm), 0-5 vol% lithic fragments (M_L=28 mm) and 7-10 vol% crystals in a coarse ash matrix. Pumice clasts are devitrified and the pink colour is due to VPA. Lithic content decreases rapidly upward from the base and within 5 m is <1 vol%. Pumice content drops over the same distance from 10-15 vol% to 5 vol%.

Mokai Ignimbrite was emplaced as at least 3 units with enough time between deposition of each to allow respective tops to cool sufficiently to reduce welding and pumice flattening while allowing pervasive jointing (through all units and across unit boundaries) and a normal VPA profile (VPA increases upwards through the units with the upper unit affected by gas from those below). Jointing and VPA show that all three units cooled together whereas variations in welding and compaction of pumice clasts suggest a compound cooling unit.

In road cuts along Tirohanga and Poihipi roads (Fig. 7.1) Mokai Ignimbrite is grey-purple, massive, non-welded, not jointed, poorly to moderately indurated, and contains

pumice clasts (10-15 vol%), lithic fragments (<1-3 vol%), and crystals (5-20 vol%). Here the ignimbrite has been extensively affected by VPA and has devitrified. Lithic fragments are rhyolite lava and clasts of underlying units. Pumice clasts have totally devitrified and become powdery, similar to pumice clasts in uMI. Lack of outcrop at levels intermediate between the Okama Stream section and Tirohanga Rd prevents systematic study. Increased VPA is consistent with the VPA profile of the units in Okama Stream and the outcrops in Tirohanga Rd are inferred to be part of the upper unit.

Ash deposits have been identified at Okama Stream and 2 localities to the east. They form conspicuous bands, up to 1 m thick, separating the three units (Fig. 7.3, 7.4 and 7.5). The lower band is underlain by the zone of pumice concentration at the top of the lower unit. The deposits are grey-brown, finely laminated, fines-rich ashes with 0-5 vol% crystals and <2 vol% small pumice lapilli. Fine ash makes up at least 94 vol% of these bands. The upper ash deposit in Okama Stream contains 4 vol% normally graded small obsidian lapilli (M_L<4 mm) and is cross-stratified in some areas. Although equivocal, the small obsidian lapilli and cross-stratifications in the upper ash deposit indicate that it may have been deposited from a surge overriding the pyroclastic density current rather than by air fall. As with the rest of Mokai Ignimbrite the ash deposits have lithified post-deposition making sieve analysis impossible.

7.6.2 Mokai Ignimbrite in drill core

Mokai Ignimbrite has been penetrated in mineral prospecting drill holes around Forest Rd and geothermal exploration wells. Mineral exploration holes (logged by Fransen and Sharp, 1988) reached the top of the ignimbrite between 175 and 195 m beneath the ground but did not go through the base.

Exploratory geothermal wells were logged principally by C.P. Wood of IGNS (locations on Fig. 7.1). Boreholes show that Mokai Ignimbrite overlies Whakamaru Ignimbrite and older rhyolite lavas (Fig. 7.6). Thickness of Mokai Ignimbrite varies between 165 and 200 m, and is thickest towards the south in drill holes Mokai 5 and 6 (Fig. 7.7). The lower 70, 100 and 70 m is strongly welded in drill holes Mokai 3, 5 and 6 respectively (Fig. 7.7). Bores drilled more recently than Mokai 1-6 have encountered a paleosol at the base of Mokai Ignimbrite (C.P. Wood pers. comm., 1999).

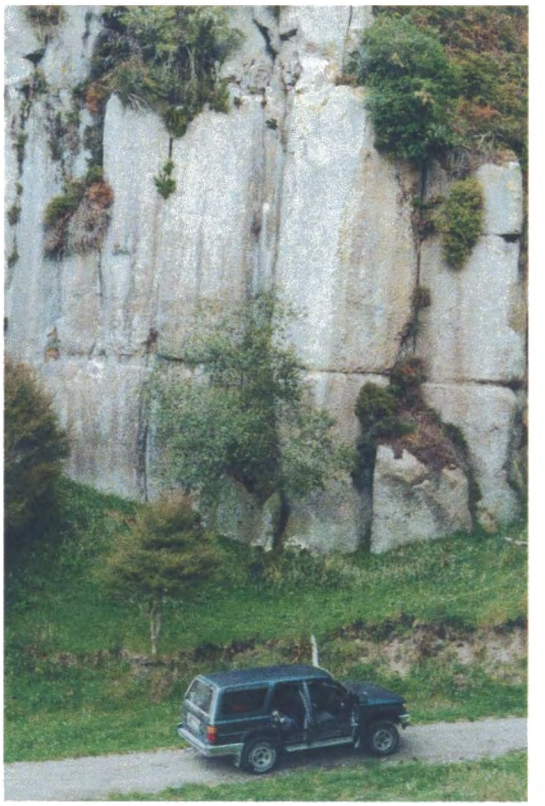

Figure 7.4. Photograph from the Okama Stream section showing the three units and ash deposits referred to in the text. The two ash deposits are prominent sub-horizontal bands. Jointing is pervasive and can be seen passing through all units and ash cloud deposits without deviation. Photograph courtesy of G. Leonard.

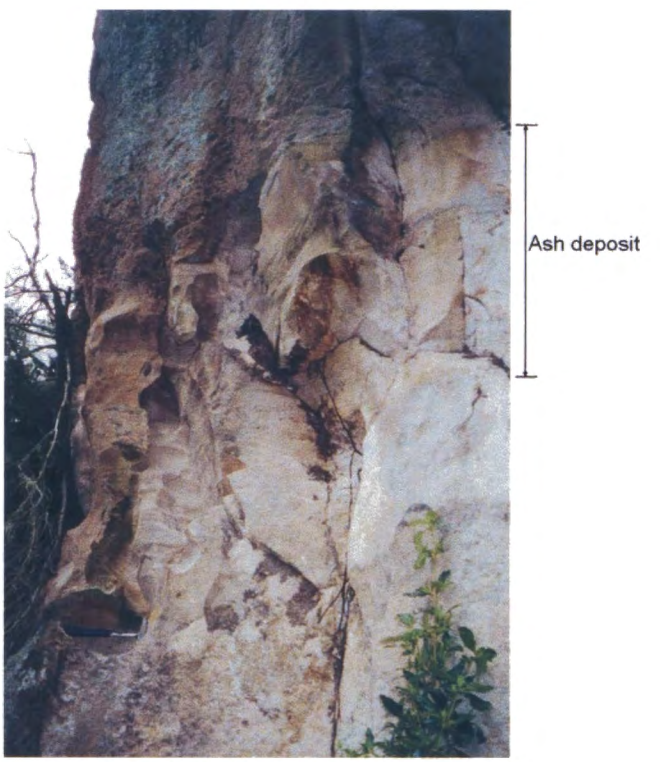

Figure 7.5. Close-up of the upper ash deposit showing relatively fine grain size (cf. ignimbrite above and below), and bedding. The ash deposit here is about 1 m thick.

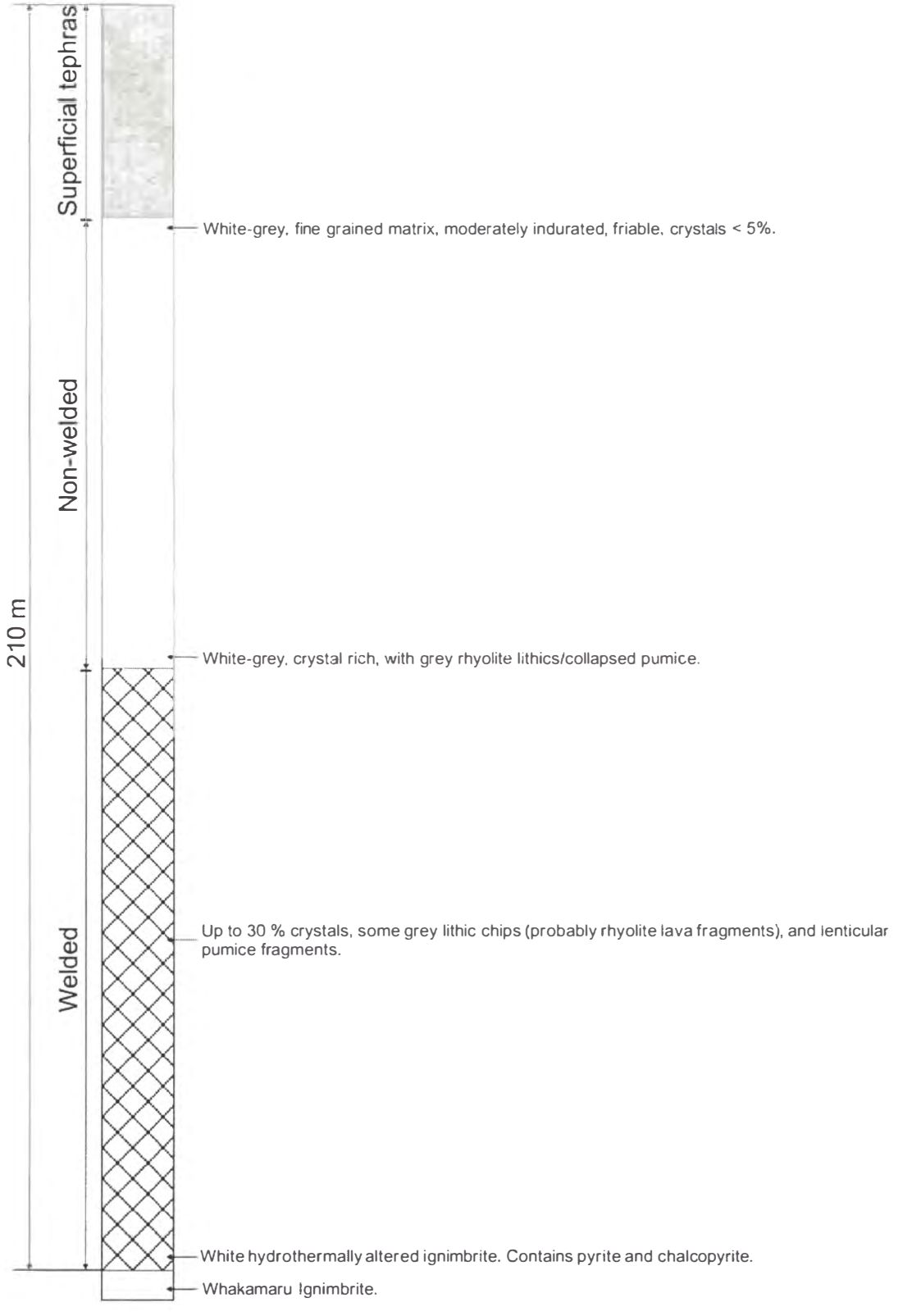

Figure 7.6. Log of Mokai 5 geothermal exploration well (from the surface to just below Mokai Ignimbrite. From C.P. Wood (unpublished data).

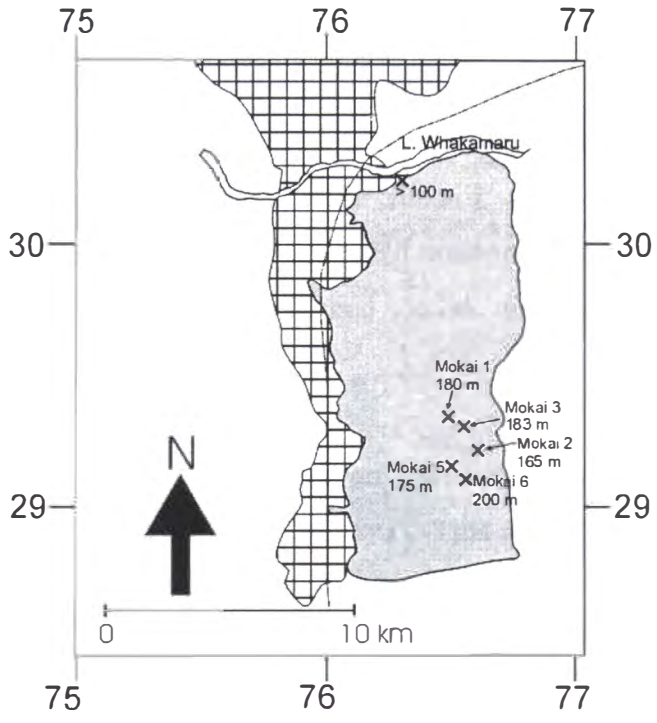

Figure 7.7. Mokai Ignimbrite thickness varies irregularly between drill holes. Such variations can be accounted for by paleotopography. Thicknesses taken from unpublished IGNS logs.

7.6.3 Lithic fragments

Fransen and Sharp (1988) and C.P. Wood (unpublished data) describe Mokai Ignimbrite from drill core as containing brecciated zones that are consistent with lithic-rich bands that outcrop in Okama Stream. Lithic fragments concentrate at irregular levels in each unit and lithic-rich bands have gradational upper and lower contacts. Their presence away from the base of the lower and middle units imparts crude layering and indicates changes in pyroclastic density current energy.

Lithic fragments in Mokai Ignimbrite are almost entirely rhyolite lava, with rare ignimbrite fragments. M_L varies between 4 and 50 mm irregularly stratigraphically. Clasts of lower Mokai Ignimbrite units are present in Tirohanga Rd outcrops indicating erosion of lower parts by succeeding pyroclastic density currents. The source of rhyolite lava fragments is equivocal. Older rhyolite domes flank the Mokai Ignimbrite to the north and west, and also underlie it. They are the most likely source of the lava fragments.

7.7 Thickness and volume

If outcrops in Tirohanga road cuts are added to the Okama Stream section the total thickness exposed is 160 m. The closest drill hole to this section is Mokai 1 where a total thickness of 180 m has been drilled. The Mokai 1 well is 8.5 km from the Okama stream section and ~6 km from the Tirohanga Rd outcrops. The base of the ignimbrite is likely within 80 m of the base of the logged section, and within 50 m of the base of the total section at Okama Stream.

Distribution of Mokai outcrop varies between 132 and 136 km^2. Using an average thickness of 181 m yields volumes 23.9-24.6 km^3. This range is very much a minimum volume. Limited outcrop extent prohibits more accurate volume estimates.

7.8 Petrography and geochemistry

X-ray fluorescence (XRF) and petrology were carried out on a small number of whole pumice samples from three localities in the lower and upper units. Only 8 had LOI <4 wt% and were used (4 from each upper and lower units). Pumice clasts from the upper unit were devitrified and affected by VPA and only used for comparison with those from the lower unit in ASI and TAS diagrams. Microprobe (EPMA) analyses were made on a single pumice clast from the lower unit to determine mineral and glass chemistry.

7.8.1 Pumice petrography

Pumice clasts from the lower unit are orange, weathered, fibrous, up to 30-40 vol% vesicles, and 5-10 vol% phenocrysts. The phenocryst population is dominated by plagioclase (5 vol%), orthopyroxene (1 vol%), clinopyroxene (0.5 vol%), and Fe/Ti oxides (1 vol%), with minor quartz (<1 vol%).

Upper unit pumice clasts are devitrified and have been affected by vapour phase alteration. They contain 5-10 vol% crystals that are dominated by plagioclase and quartz as mafic minerals have been all but destroyed by VPA. Where these mafic minerals once existed brown spots are now present.

Mafic blebs are present at all exposed levels of Mokai Ignimbrite. They characteristically have white bands (indicative of magma mingling; Fig. 7.8) and because of this were not analysed by XRF. They contain 20-25 vol% phenocrysts in a very fine holocrystalline groundmass. Phenocrysts comprise 10 vol% plagioclase, 3.5 vol% orthopyroxene, 3.5 vol% clinopyroxene, 2 vol% Fe/Ti oxides, 1-2 vol% olivine, and 1 vol% amphibole (Fig. 7.9).

7.8.2 Geochemistry

Raw pumice XRF data from the lower unit are given in table 7.1.

All pumice samples plot in the rhyolite field of the total alkali-silica diagram (Fig. 7.10) of Le Maitre (1989) and are peraluminous suggesting some degree of alteration (Fig. 7.11). Pumice clasts from the lower unit are partially weathered and alkalis may have been leached from them causing their ASI variation (Fig. 7.11). All pumice clasts in the upper unit are devitrified, have lower LOI, and appear less affected by leaching (Fig. 7.11). Trace and major element data plots within or near the range of type 2 Mamaku Ignimbrite pumice data (Figs 7.12 and 7.13) and normalised trace element variation (Fig. 7.14) in Mokai pumice clasts show little disparity from pumice chemistry of Mamaku Ignimbrite (with typical TVZ variation).

7.8.3 Mineral and glass chemistry

Plagioclase

Plagioclase is up to 2.5 mm long, euhedral to subhedral, commonly broken, and sometimes embayed due to resorption. Crystals are normally zoned, varying between An_{38-22} (Fig. 7.15a), and often contain inclusions of pyroxene, Fe/Ti oxides, and rarely glass.

Pyroxene

Pumice clasts contain 1-1.5 vol% pyroxene. The pyroxene assemblage is dominated by orthopyroxene with augite sometimes present. Pyroxene crystals are up to 2 mm long and 0.5 mm wide, sometimes euhedral, but more commonly broken. All are normally

Figure 7.1. An example of a mafic bleb from Mokai Ignimbrite. White bands are probably rhyolitic and indicate mingling of different composition magmas. The bleb shown also contains small exotic xenoliths.

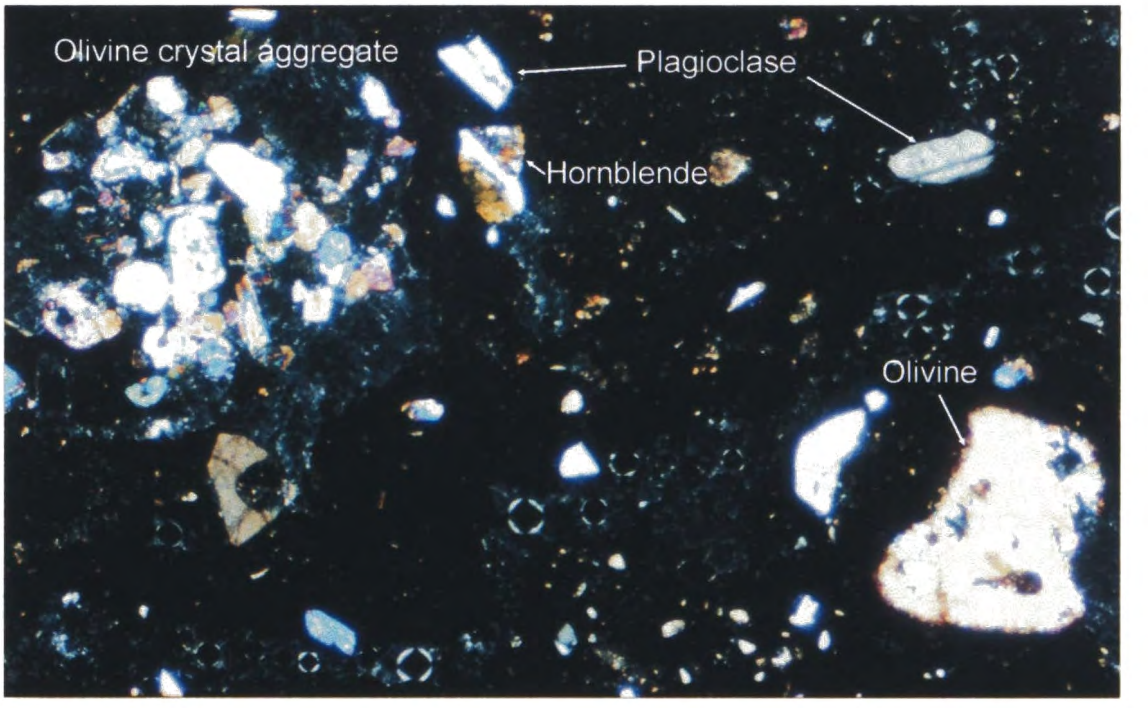

Figure 7.2. Photomicrograph of a mafic bleb from Mokai Ignimbrite using cross polarised light. They contain 20-25 vol% phenocrysts in a very fine holocrystalline groundmass. Note the regular occurrence of olivine phenocrysts, olivine crystal aggregates, and the low amount of amphibole even in the groundmass. Picture is 4 mm left to right.

Sample	MoP1	MoP2	MoP3	MoP6
Lab Number	32294	32295	32296	32298
SiO_2	70.57	68.69	69.49	70.14
TiO_2	0.28	0.3	0.29	0.26
Al_2O_3	15.04	16.39	15.92	15.54
Fe_2O_3	2.35	2.6	2.48	2.29
MnO	0.08	0.12	0.1	0.08
MgO	0.25	0.29	0.26	0.24
CaO	1.33	1.36	1.37	1.26
Na_2O	4.28	4.12	4.17	4.03
K_2O	2.94	2.75	2.79	2.99
P_2O_5	0.06	0.05	0.1	0.07
LOI	3.13	3.76	3.37	3.28
Total	100.31	100.43	100.34	100.18
V	10	12	15	10
Cr	4	6	5	6
Ni	3	3	3	3
Zn	63	81	74	66
Rb	237	264	257	232
Sr	10	11	1	11
Ba	744	744	699	826
La	25	23	18	24
Ce	66	76	62	74
Nd	41	26	31	26
Y	16	18	17	17
Nb	17	17	15	15
Pb	97	91	92	96
Zr	126	130	131	118
Th	10	9	9	10
Ga	35	34	32	33

Table 7.1. Whole rock geochemistry of the lower Mokai pumice clasts analysed.

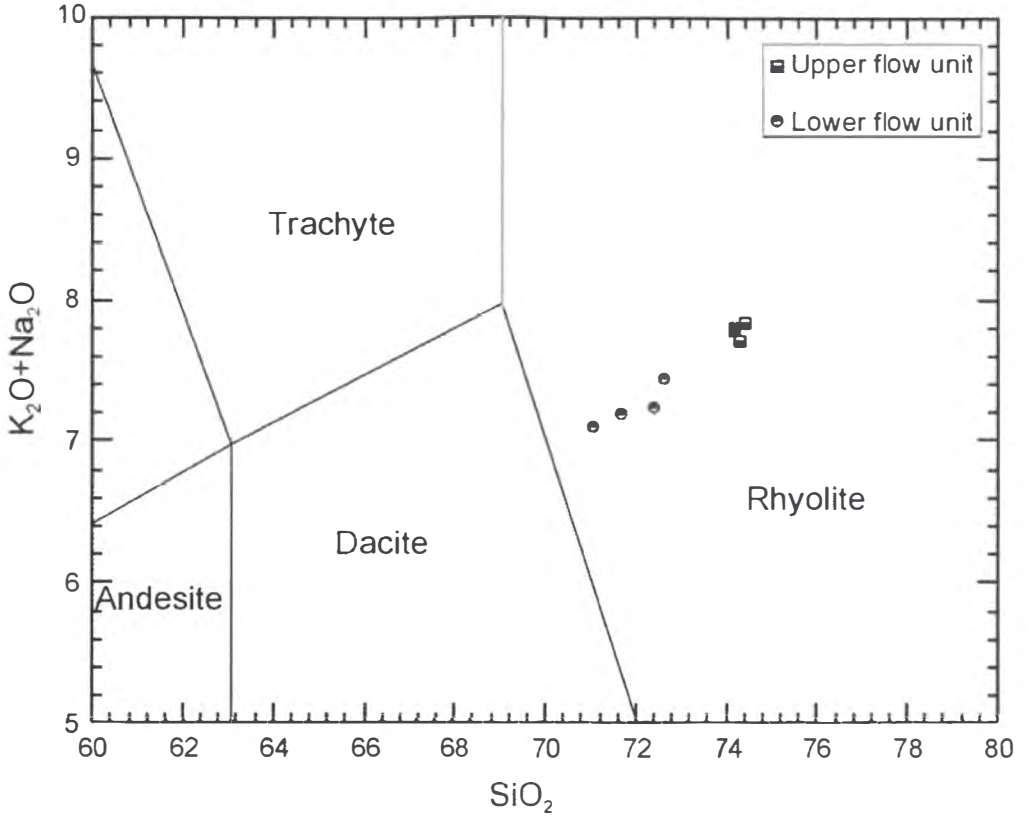

Figure 7.10. Total alkali silica plot of pumice chemistry from upper and lower units (after Le Maitre, 1989).

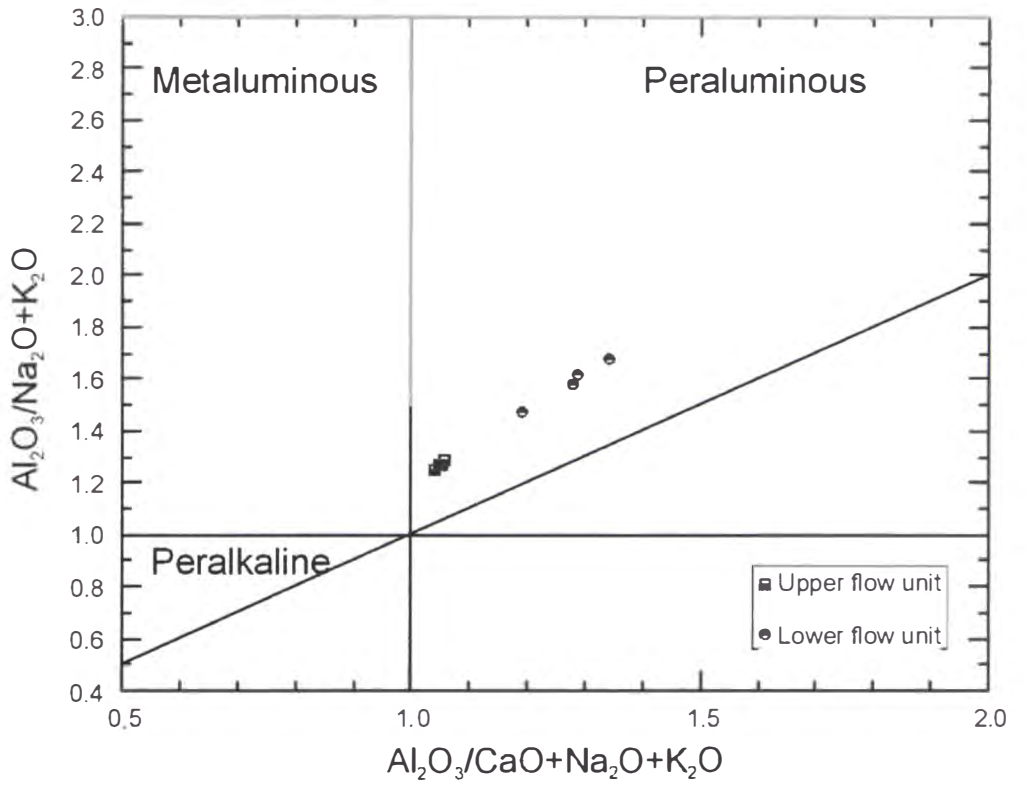

Figure 7.11. Alkalinity discrimination diagram after Pearce et al. (1984). The peraluminous nature of samples probably reflects leaching of alkalis after deposition.

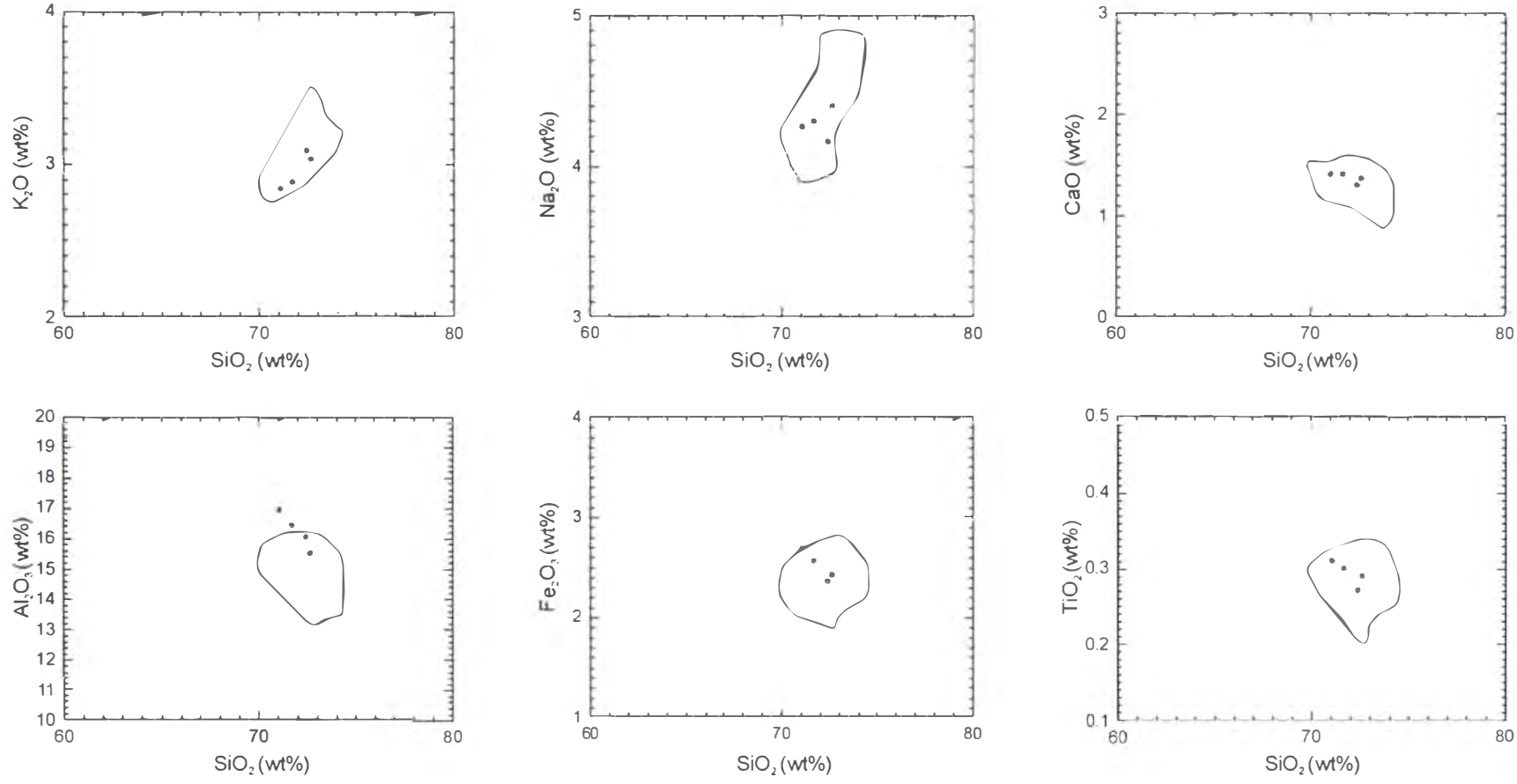

Figure 7.12. Selected major element plots for the lower unit of Mokai Ignimbrite pumice (dots). Outlined fields are those for type 2 pumice of Mamaku Ignimbrite. Most of the Mokai data plot within the type 2 pumice fields.

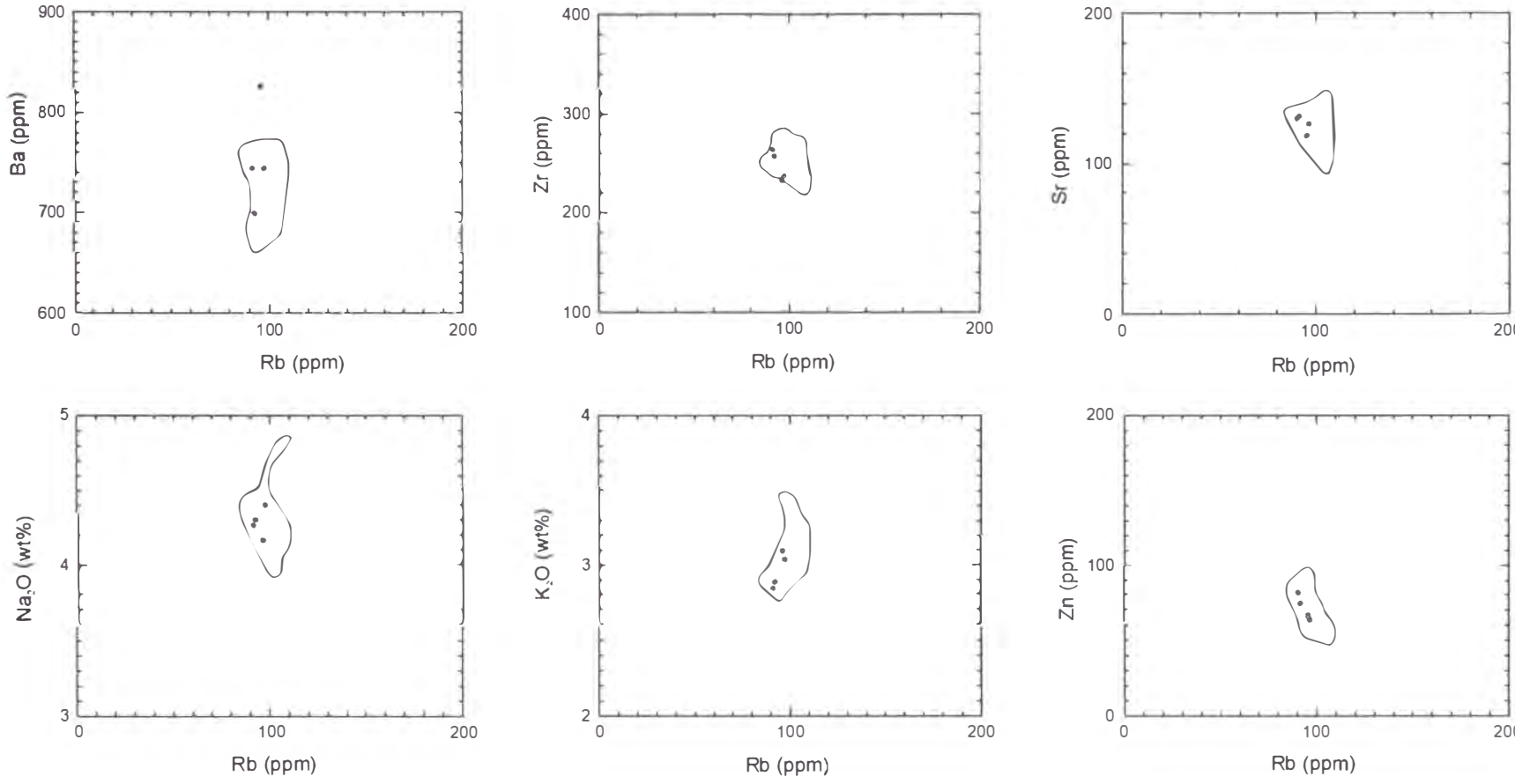

Figure 7.14. Selected trace and major elements plotted against Rb. Again, lower unit Mokai pumice (dots) plots almost entirely with the outlined fields of type 2 Mamaku pumice.

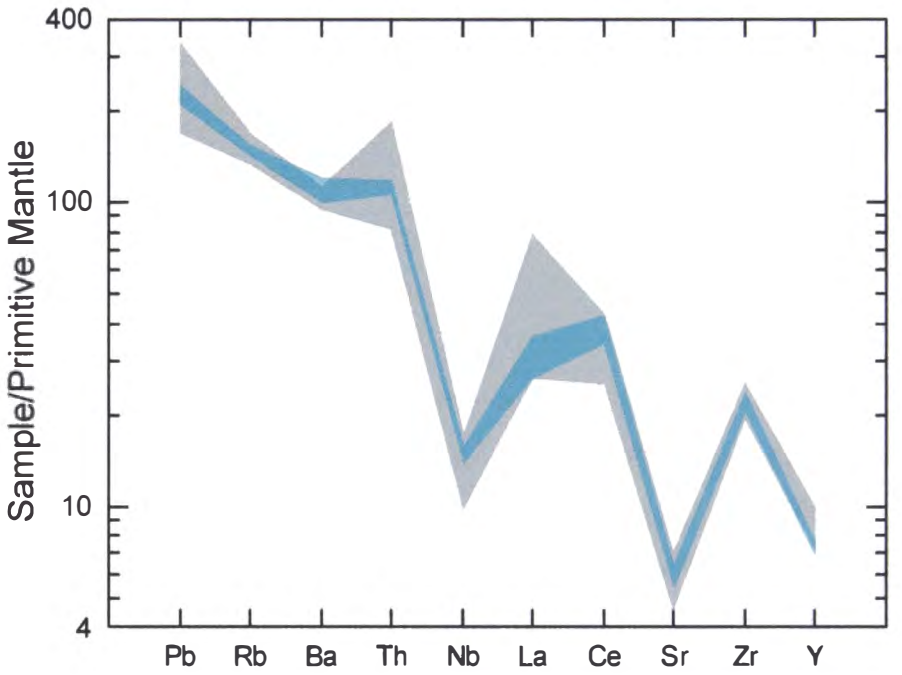

Figure 7.14. Comparison of trace element chemistry of rhyolitic pumice clasts from the lower unit of Mokai Ignimbrite and type 2 Mamaku Ignimbrite pumice clasts normalised against primitive mantle (from Sun and McDonough, 1989). The range of data is shaded blue and grey for Mokai and Mamaku Ignimbrites respectively. The range of Mokai Ignimbrite plots almost wholly within the range of type 2 Mamaku pumice clasts.

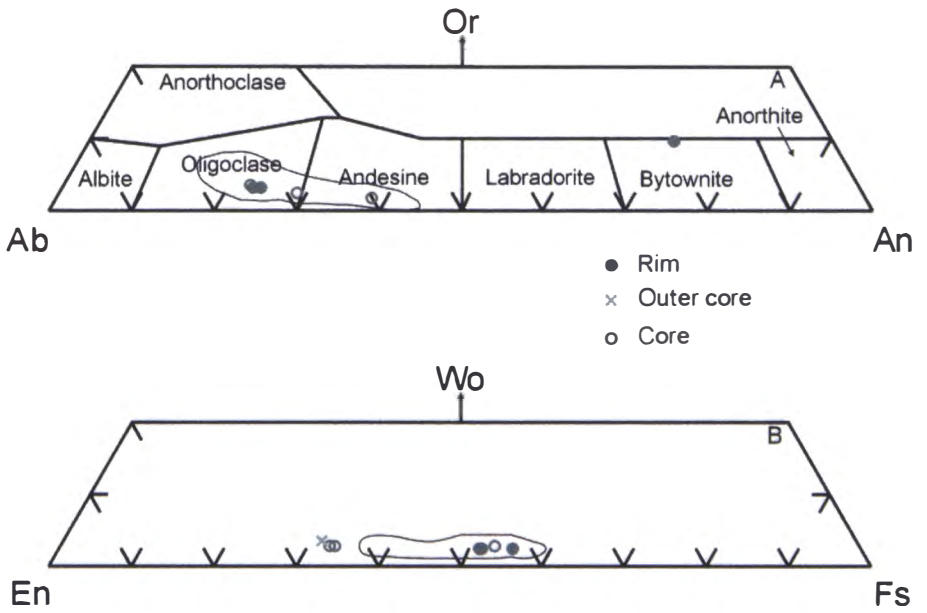

Figure 7.15. EPMA data for plagioclase (A) and pyroxene (B) phenocrysts from a Mokai pumice clast. Plagioclase plot almost wholly with the field of type 2 Mamaku pumice clasts (outlined) with one outlier, but the cores of two pyroxene phenocrysts are more En-rich than all Mamaku Ignimbrite pyroxene (outlined).

zoned ($En_{65-42}Wo_{2-4}Fs_{55-31}$) becoming more iron-rich towards their rims (Fig. 7.15b). Brown alteration can be seen along cracks and around the margins of some crystals.

Glass

Glass varies between 74-76 vol% SiO_2.

Fe/Ti oxides

EPMA analyses were carried out on magnetite and ilmenite pairs found as inclusions in pyroxene crystals. Only pairs found in the same pyroxene and in contact with the surrounding glass were analysed. Exsolved magnetite grains were avoided. Eruption temperature was calculated using the technique described by Ghiorso and Sack (1991) and found to be between 715-752 ^{o}C which is low compared with many other ignimbrites and suggests that Fe/Ti oxides analysed were not in equilibrium.

7.9 Source

In an effort to determine source direction M_L measurements were taken (as for Mamaku Ignimbrite) and plotted for all ignimbrite units seen in outcrop (Fig. 7.16), but the low total outcrop makes compilation of M_L isopleth maps difficult and there is no systematic variation in the three units, and an interpretation of such maps is questionable.

Nearly all lithic fragments measured were rhyolite lava and cannot be unequivocally designated as vent derived. It is more likely that the lithic fragments were stripped off surrounding domes during passage of the pyroclastic density current.

Thickness variations also show no systematic variation (Fig. 7.7). Thickness differences (between 165 and 200 m) are easily accomplished by paleotopographic variation.

The closest possible source for Mokai Ignimbrite is the Maroa Volcanic Centre, from which at least 3 other potentially caldera-forming ignimbrites were erupted (Korotai, Orakonui and Atiamuri; Houghton et al., 1995). The Kapenga structure is also close by, erupted during period IIIB (Fig. 1.5), and is another possible source.

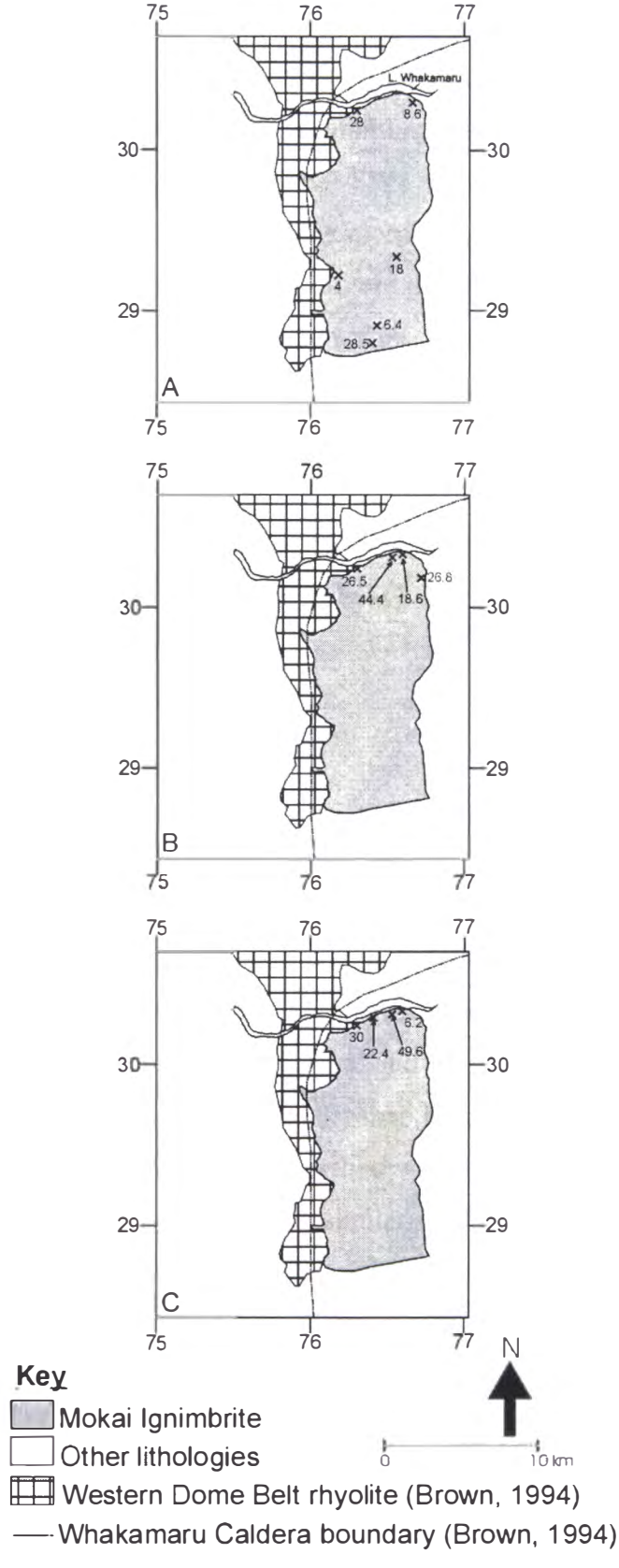

Figure 7.16. Maximum lithic maps for lower (A), middle (B), and upper (C) Mokai Ignimbrite units. M_L sizes exhibit no systematic variation.

The obvious scarp that marks the eastern boundary of exposed Mokai Ignimbrite is the Hauraki Fault trace. The significance of the fault is equivocal. It strikes at approximately 357°, orthogonal to Taupo Fault Belt, and creates a scarp up to 80 m high. Cole (1990) suggested the idea that a subordinate fault set strikes NW-SE in TVZ (Taupo Fault Belt striking predominantly NE-SW). These NW-SE striking faults are thought to have had a strong influence on the morphology of Rotorua Caldera (chapter 6). Kaingaroa Fault is known to bound the eastern margin of Reporoa Caldera and was a principal control during its formation (Beresford, 1997). In a similar way Hauraki Fault may delineate the western margin of Maroa Volcanic Centre and be a major control on the volcanism that occurs within it. If so, the fault must have been active either concurrently with eruption of Mokai Ignimbrite (as is the case with faults displacing Mamaku Ignimbrite in Rotorua Caldera) or Mokai Ignimbrite must predate collapse at Maroa. A current PhD study by G. Leonard should help clarify this relationship.

7.10 Discussion

Paleomagnetic directions and $^{40}Ar/^{39}Ar$ dates have all been used as evidence that Mokai and Mamaku ignimbrites are the same. The paleomagnetism and age of the Mokai Ignimbrite proves that it erupted contemporaneously with Mamaku Ignimbrite and major and trace element data for Mokai Ignimbrite pumice clasts is similar to that of type 2 Mamaku pumice clasts (Figs 7.13, 7.14, and 7.15). The phenocryst content of rhyolitic Mokai pumice clasts is slightly higher than Mamaku Ignimbrite pumice clasts, with plagioclase dominating (5 vol%) over orthopyroxene, Fe-Ti oxides, and quartz (up to 1 vol% each). Plagioclase chemistry is similar to that of type 2 Mamaku pumice clasts, while pyroxenes have slightly more En-rich cores.

Significant differences between the two ignimbrites include:

1) The three unit stratigraphy of Mokai Ignimbrite.
2) Compound cooling unit character of Mokai Ignimbrite.
3) Stratigraphic location of mafic blebs.
4) Petrography of mafic blebs.

Mamaku Ignimbrite comprises a single unit without internal boundaries which cooled as a single entity. Mokai Ignimbrite comprises at least three units within a compound

cooling unit. Mafic blebs are found at all stratigraphic levels in Mokai Ignimbrite, but andesite blebs occur only in upper levels of Mamaku Ignimbrite. Mafic blebs in Mokai Ignimbrite are characteristically banded (indicating mixing of rhyolitic and mafic magmas) with high amounts of olivine and low hornblende contents when compared to andesitic blebs from Mamaku Ignimbrite that are very low in olivine with a ground mass that is high in hornblende and are not banded.

The thickness of Mokai Ignimbrite is also important when assessing a Mokai-Mamaku relationship. Mokai Ignimbrite is up to 200 m thick 46 km from Rotorua. Mamaku Ignimbrite is >80 m (probably ≤100 m) under half the distance from Rotorua. These differences suggest that the two ignimbrites are different.

The controversy over whether the Mokai and Mamaku Ignimbrites are the same has not been fully resolved here. Geochemistry of the silicic pumice clasts from the two ignimbrites is very similar and they may be related at depth to the same magma source rocks whereas differences in outcrop morphology may indicate different vent systems (i.e. similar magmas with spatially different chambers and vents; N.B. trace element chemistry of Mokai pumice clasts analysed by B.F. Houghton and S.D. Weaver is quite different to that of Mamaku pumice clasts, see Fig. 3.17). Evidence found in this study suggests that the two are different ignimbrites. Ongoing work in the Maroa area (by G. Leonard) may help further resolve the Mamaku-Mokai issue.

CHAPTER 8
Discussion

8.1 Introduction

This section discusses Rotorua Caldera and the Mamaku Ignimbrite based on information provided in the preceding chapters. It also examines the applicability of caldera end-member structures to the Rotorua Caldera and suggests a better method of description. Probable emplacement mechanisms for Mamaku Ignimbrite are inferred based on internal stratigraphy, and the configuration of the magma chamber is deduced from variation in juvenile material within the ignimbrite. Withdrawal dynamics of the magma chamber are based on distribution of the juvenile components in the Mamaku Ignimbrite. The distribution of juvenile components and ignimbrite stratigraphy are used to infer the timing of caldera collapse.

8.2 Mamaku Ignimbrite

Mamaku Ignimbrite can be separated into a basal sequence and a main ignimbrite sequence. The main ignimbrite sequence can in turn be subdivided into lower (lMI), middle (mMI) and upper (uMI) ignimbrite based on crystal content, welding, intensity of vapour phase alteration and devitrification, the presence of andesite blebs, and variations in dominant lithic type (Fig. 8.1). Boundaries between the three are gradational. lMI grades into mMI over 0.2-2 m, but the boundary between mMI and uMI is much more difficult to determine. Welding decreases and devitrification and vapour phase alteration increase with height above the base of mMI and uMI characterised by totally devitrified pumice clasts, and the influx of mMI lithic fragments and andesitic blebs.

8.2.1 Source

It has been suggested that Mamaku Ignimbrite is sourced from both Kapenga and Rotorua calderas (I.A. Nairn and C.P. Wood pers. comm., 1999), with the lack of outcrop of Mamaku Ignimbrite in the Kapenga area suggesting that Kapenga Caldera may have collapsed concurrently with eruption of Mamaku Ignimbrite.

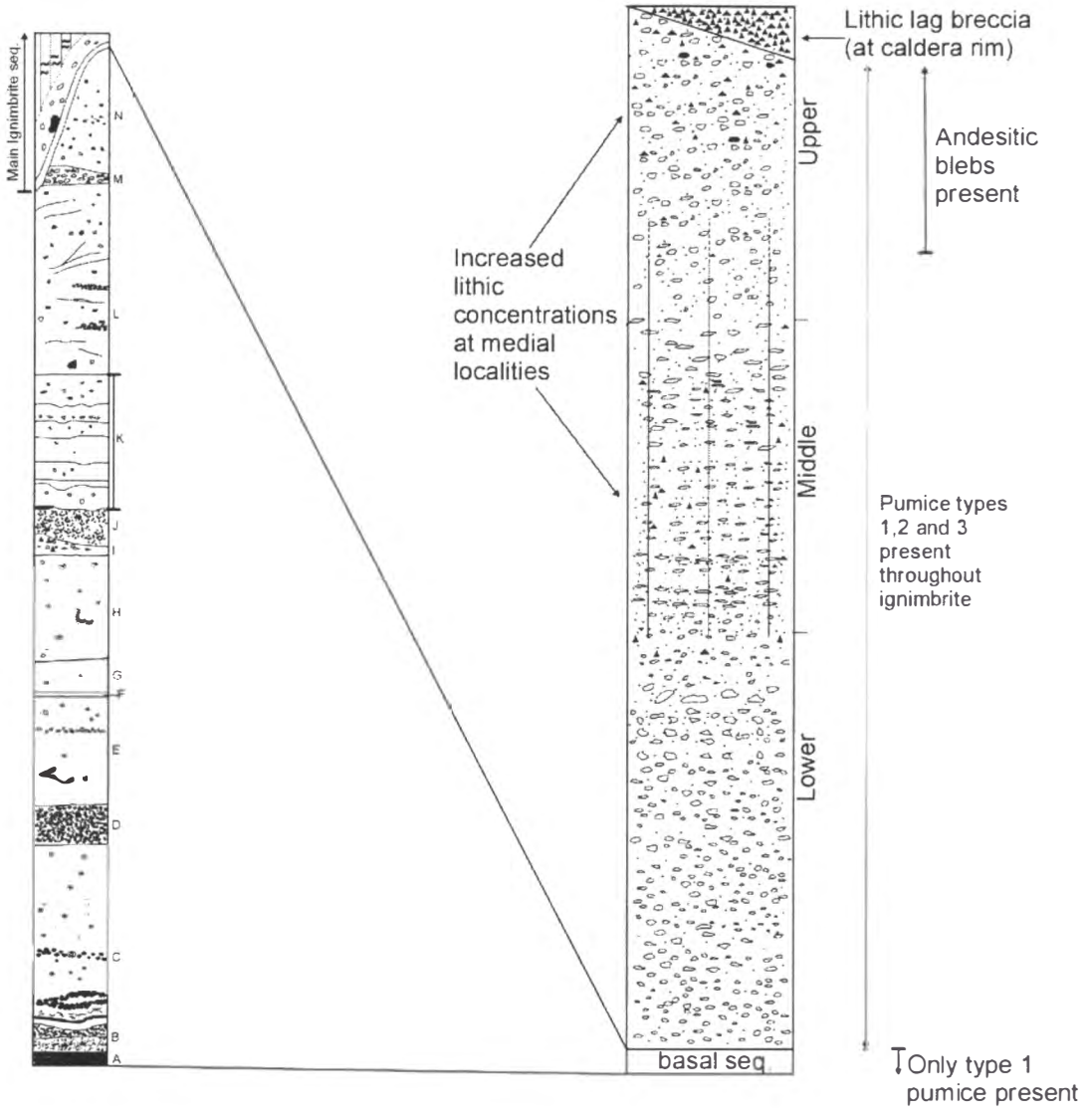

Figure 8.1. Composite diagram of Mamaku Ignimbrite stratigraphy based on the basal section at Pukerimu Rd, the type locality at Sutcliffe Rd, and Rotorua Caldera margin sites.

AMS flow direction indicators are oriented dominantly radially around Rotorua Caldera (Black, 1995) and M_L data and location of lithic lag breccias indicate that uMI was sourced solely from Rotorua Caldera. The coexistence of the different silicic pumice types throughout the deposit, and lack of flow unit boundaries in the ignimbrite, suggest that the source is the same for all stratigraphic levels. The rapid thickness variation of Mamaku Ignimbrite across the margin of Rotorua Caldera suggests the caldera was forming as the ignimbrite was erupted. The buried Kapenga structure is located in the Taupo Fault Belt, and extension and subsequent downfaulting within this zone since Rotorua Caldera's formation, is a more likely explanation for the lack of Mamaku Ignimbrite outcrop within Kapenga.

8.2.2 Mode of emplacement of Mamaku Ignimbrite

Deposition of ignimbrites from pyroclastic density currents remains controversial. Two main schools of thought exist, with deposition from pyroclastic density currents occurring across a range between the end-members of *en masse* emplacement (Sparks, 1976; Walker, 1983) and progressive aggradation (Fisher, 1966; Branney and Kokelaar, 1992). It is likely that a spectrum of depositional regimes exists, giving rise to the variety of deposits observed. The stratigraphy of the body (layer 2) of an ignimbrite that was deposited *en masse* reflects the internal layering of the body of its parent pyroclastic density current (Branney and Kokelaar, 1992), although the thicknesses are usually much different (Wilson and Walker, 1982). Layering within an ignimbrite that progressively aggraded reflects temporal variations of density current conditions, with stratigraphically higher layers deposited later than those beneath (Branney and Kokelaar, 1992).

Mamaku Ignimbrite is interpreted to have been deposited essentially by progressive aggradation although it does exhibit some features that are more characteristic of *en masse* emplacement.

A model describing the deposition of the Mamaku Ignimbrite sequence needs to account for:

1) Basal tephras.
2) Rip up clasts of Pokai Ignimbrite, and truncated lower basal tephra beds.
3) Presence of lithic lag breccias and lithic concentration zones at Rotorua Caldera rim in the top of uMI.
4) Local presence of elutriation pipes at the caldera rim.
5) Development of a 2a-like layer in lMI at Pukerimu Rd.
6) Vertical variations in pumice and lithic abundances and size without sharp contacts or flow unit boundaries.
7) Development of layer 1-like deposits beneath lMI and within mMI at Oropi Gorge (this study) and within uMI at Joyce and Belk roads (Morgan, 1986).

There appear to be no extensive time breaks between beds of the basal sequence, and they can be separated into packets of differing physical characteristics. Some beds

pinch and swell and, in places, truncate previously deposited beds indicating transitions between erosional and depositional phases. Upper beds of the basal sequence were eroded and pieces of Pokai Ignimbrite were ripped up during the arrival of lMI. All of these factors indicate changes in eruptive style and pyroclastic density current energy.

If Mamaku Ignimbrite was deposited *en masse* the contact between uMI and the lithic lag breccias should signify a flow unit boundary. However, the uMI matrix is continuous with that of the overlying lithic breccia, which therefore must be regarded as a proximal upper facies of uMI and not a deposit from a separate pyroclastic flow. Variations in pumice and lithic content and size through Mamaku Ignimbrite are gradational and there are no distinct flow unit boundaries. If lMI were emplaced *en masse*, a basal layer (layer 2a) would be normal, but a "2a-like" layer has been seen at only one, relatively distal, locality and is interpreted as having been deposited from a high particle concentration (non-particulate) density current.

Crystal-rich layers present at distal localities (Morgan, 1986; this study) are similar to ground surge (layer 1) deposits described by *en masse* advocates, but this type of deposit is not seen in medial or proximal locations where logs have been made. It may have been that as the pyroclastic current progressed further from source it became increasingly deflated until, in distal areas, it was moving in a dominantly non-particulate manner. Air would have been ingested at the front and layer 1-like deposits formed (similar to Druitt's (1998) description for emplacement of a high aspect ratio ignimbrite; Fig. 8.2). Crystal-rich lenses are also present within mMI and uMI at distal localities (Morgan, 1986; this study) that extend across some outcrops. Beyond these lenses the ignimbrite is gradational with no sharp flow unit boundary (see Fig. 2.14). These mMI crystal-rich lenses probably represent temporary changes in flow direction of the pyroclastic density current (probably in response to build up of the deposit) rather than a flow unit boundary.

A laminar flowing density current deposits an ignimbrite with distinct vertical variations according to the fluidisation and density of the current (e.g. Wilson, 1980). The vertical variations in Mamaku Ignimbrite are too complex to be deposited from a pyroclastic density current that moved in a laminar fashion and stopped entirely *en masse*. Vertical variations in pumice and lithic content and size (including pumice clast beds), erosion of earlier deposited beds, and lack of flow unit boundaries are consistent with

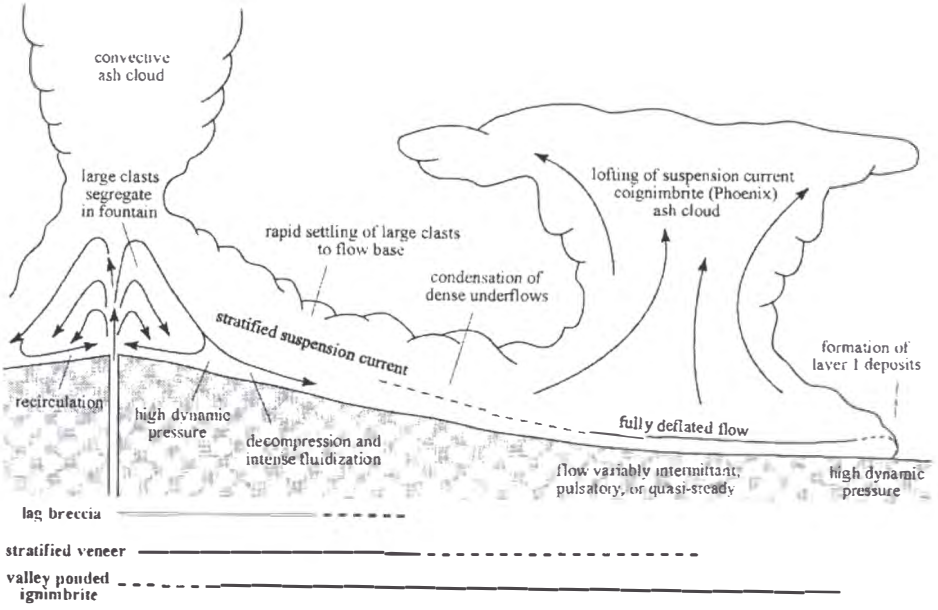

Figure 8.2. Druitt's (1998) depiction of a high aspect ratio ignimbrite forming pyroclastic flow morphology. Close to source, particles travel in suspension and larger clasts are deposited. Further away, the flow deflates allowing creation of "layer 1" deposits

deposition from a pyroclastic density current of variable energy that deposited progressively. Features close to source, such as gas segregation structures, illustrate high flow energy (Wilson, 1986). Crystal-rich ground layers and lenses at distal localities suggest that the density current had fully deflated and was travelling in a dominantly non-particulate fashion. The lensoidal nature of such bands in mMI suggests that Mamaku Ignimbrite was not deposited *en masse*. Mamaku Ignimbrite is thus interpreted to have been deposited from an unsteady pyroclastic density current that became less particulate as it travelled further from source.

8.3 The Rotorua magma system

8.3.1 Mamaku Ignimbrite magma chamber

Chemical differences between juvenile components in an ignimbrite indicate the coexistence of magmas of different composition located either in multiple chambers (Briggs et al., 1993; Brown et al., 1998) or separated in a single chamber as a result of density variation (Orsi et al., 1995; Civetta et al., 1996; Cambray et al., 1995).

Chemical variation in magma chambers can be caused by melting of different types of crust, discontinuous melting of the same crust (Hervig and Dunbar, 1992; Cambray et al., 1995), or by in situ crystallisation and fractionation of a single body of cooling magma along with varying amounts of assimilation of magma chamber wall rock (assimilation fractional crystallisation or AFC; Wolff et al., 1990) or by a combination of these. Magmas from different sources injected sequentially into the same magma chamber may remain separate due to density, temperature and viscosity contrasts (Trial and Spera, 1990).

Beresford and Cole (2000) found that more evolved pumice clasts in the Kaingaroa Ignimbrite had undergone plagioclase dominated crystal fractionation as delineated by the strong increase in Rb/Sr ratio (Sr is compatible in plagioclase, and plagioclase crystallisation depletes a large amount of Sr from the melt). The same is inferred for Mamaku Ignimbrite based on the same ratio. Rb/Sr increases steadily with SiO_2 from type 3 → type 1 pumice clasts suggesting types 1 and 2 magmas were formed due to fractionation of a type 3 parent. The systematic increase in K_2O and decrease in CaO with increasing SiO_2 also indicates fractionation of plagioclase from the melt as well as crystallisation of pyroxene. Fe_2O_3 and TiO_2 both decrease in a regular way with increasing SiO_2 (suggesting fractionation of pyroxene and Fe/Ti oxides), as do Zn and Zr with increasing Rb (probably controlled by crystallisation of pyroxene and zircon respectively), also suggesting fractionation of magma types 1 and 2 from type 3. Phenocrysts of basal sequence pumice clasts have chemistry similar to the more evolved type 1 magma and are thought to be the same.

The 3 types of Mamaku Ignimbrite pumice clast show evidence of eruption from a single zoned chamber. They lie on continuous chemical trends, and vector modelling shows that the most evolved pumice types can be derived from a type 3 magma parent by fractionating the dominant phenocryst phases (identified petrographically). Rare earth element, stable isotope chemistry, and/or reliable geothermometry needs to be obtained before zonation characteristics can be confirmed, but Mamaku Ignimbrite silicic pumice types have a wide trace element range when compared with other rhyolitic TVZ ignimbrites (see Fig. 3.17) further suggesting zonation of the source magma chamber. No distinct gaps are present on bivariate plots of Mamaku Ignimbrite geochemical data and the zonation of the Mamaku magma chamber is interpreted to have been gradational.

Andesitic blebs within uMI have a distinct normalised trace element trend, contain both augite and orthopyroxene, have quenched margins and represent a discrete magma, unrelated to the dacitic and rhyolite pumice types 1, 2, and 3. The andesite is considered to have been gently injected into the magma chamber where it accumulated at the base of type 3 magma. If the andesite magma had injected vigorously some degree of mixing with the silicic magma would be expected leading to a hybrid magma or banded pumice clasts as in the Waimihia pumice deposit (Blake et al., 1992) or those at Unzen and Soufriere Hills (Eichelberger et al, 2000). The presence of andesitic material only in uMI suggests it formed a sill-like layer within, or at the base of type 3 magma. The formation of a sill-like layer would inhibit its eruption until withdrawal dynamics overcame buoyancy differences acting to keep it in place (Blake and Ivey, 1986a and b).

8.3.2 Withdrawal of Mamaku Ignimbrite magma

Pumice types 1 to 3 are found together in lMI and are present throughout the sequence, whereas andesite blebs are found only towards the top of uMI. In the basal sequence only type 1 pumice clasts have been identified. No pumice clasts of mixed composition have been found in Mamaku Ignimbrite, and the coincidence of the pumice types 1, 2 and 3 at the same stratigraphic levels is considered to be due to co-eruption of different levels of the magma chamber.

Blake and Ivey (1986a, b) modelled magma withdrawal and eruption rates on the basis of buoyancy and viscosity forces acting in a zoned magma chamber. They considered that the style of zonation in an ignimbrite reflected the way in which the height of a withdrawal layer varied with time. Chaotic mixing and existence of pumice types in ignimbrite stratigraphy suggested single or ring vent sites were simultaneously tapping a range of magma compositions, coincident with minor collapse (Fig. 8.3). Deep collapse of a caldera was more likely to result in withdrawal from a thin layer that progressively discharged deeper portions of the magma chamber so that different magma compositions were stratigraphically separated in the resultant deposit (Fig. 8.3). Their models used only simple eruptions from central or ring vents, from a chamber of simple shape or zonation.

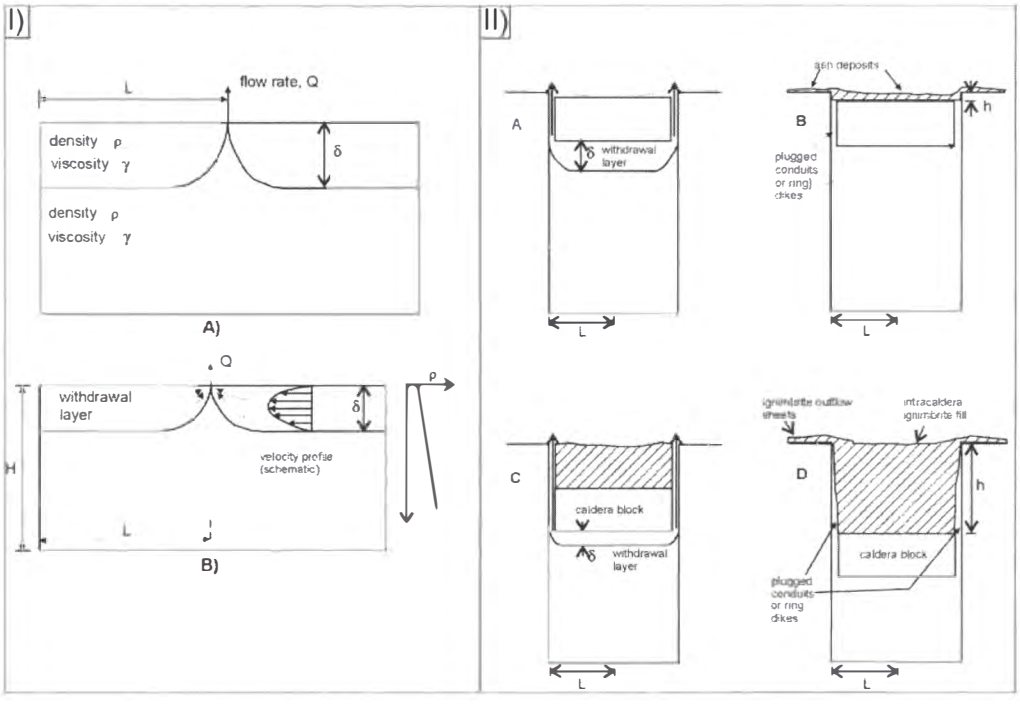

Figure 8.1. I) Blake and Ivey's (1986a) model of magma extraction from a zoned reservoir. Density and viscosity differences between the magmas must be overcome before they can be erupted together. II) Blake and Ivey's (1986b) model of the control of caldera collapse on magma withdrawal dynamics. Limited or slow caldera collapse leads to a deep zone of magma withdrawal (A and B) allowing co-eruption of different composition magmas. Rapid or deep collapse is interpreted as causing the eruption of narrow bands of the magma chamber (C and D) leading to a zoned deposit. δ= withdrawal layer thickness, L and H are the horizontal and vertical dimensions of the chamber, and ρ= magma density.

Any model of magma discharge from the Mamaku Ignimbrite chamber needs to account for:

1) Presence of only type 1 magma in the basal sequence.
2) Coincidence of pumice types 1, 2, and 3 throughout the main ignimbrite sequence.
3) Presence of andesitic blebs only in uMI.

Syn-eruption of multiple layers within a stratified magma chamber may be accomplished in two ways:

1) Withdrawal depth of the magma is greater than the collapse height of the caldera, resulting in discharge from a number of magma zones simultaneously (Blake and Ivey, 1986a and b).
2) Collapse of numerous caldera blocks, creating many conduits to the magma chamber and allowing withdrawal from various levels simultaneously.

Method 1 requires the collapse of a coherent plate, with eruption from its margins or a single central vent allowing magma extraction from discrete sites at the same depth. The second method is favoured for Rotorua because the likely collapse history of Rotorua Caldera involved multiple blocks, thereby creating multiple conduits (see section 8.5 below). However, both mechanisms may have contributed (Fig. 8.4). Only type 1 magma was tapped in the early stages of the Mamaku Ignimbrite eruption. Withdrawal of support for the chamber roof then initiated caldera collapse and resulted in co-eruption of all magmas from multiple vents. The greater density and lower buoyancy of the andesite magma would have impeded its withdrawal at this stage of the eruption (Blake and Ivey, 1986a). Only when full caldera collapse occurred, along with associated magma depressurisation, was the andesite magma destabilised enough to allow it to co-erupt with the rhyolitic magma. Thus, the presence of andesitic blebs in only uMI indicates downward migration of the zone of magma withdrawal during a late stage of caldera collapse.

8.3.3 Rhyolite domes of Rotorua Caldera

Pre- and post-caldera rhyolite lavas are located in and around Rotorua Caldera. There are no absolute ages for these domes but the lavas fall into 8 groups (pre- and post-caldera): Endean (pre-), Hamurana (pre-), Pohaturoa (pre-), Pukepoto Hill (pre-), rhyolite clasts in lithic lag breccias (pre-), Rotorua City rhyolite (post-), Mokoia Island (post-), and Hinemoa Point (post-). Pohaturoa dome has been related to Kapenga Caldera on petrographic grounds (Ewart, 1968) and Pukepoto Hill is more likely to have erupted from the Okataina Volcanic Centre (Nairn, 1989). On the basis of petrographic differences Endean, Hamurana, Mokoia Island, and Hinemoa Point rhyolites are thought to be unrelated to each other or to juvenile pumice clasts of Mamaku Ignimbrite. Isotope chemistry is needed to confirm a petrogenetic link between the Rotorua City rhyolite (RCR) and Mamaku Ignimbrite pumice clasts, but they have very similar phenocryst assemblages and their locations around the gravity low (marginal to the area

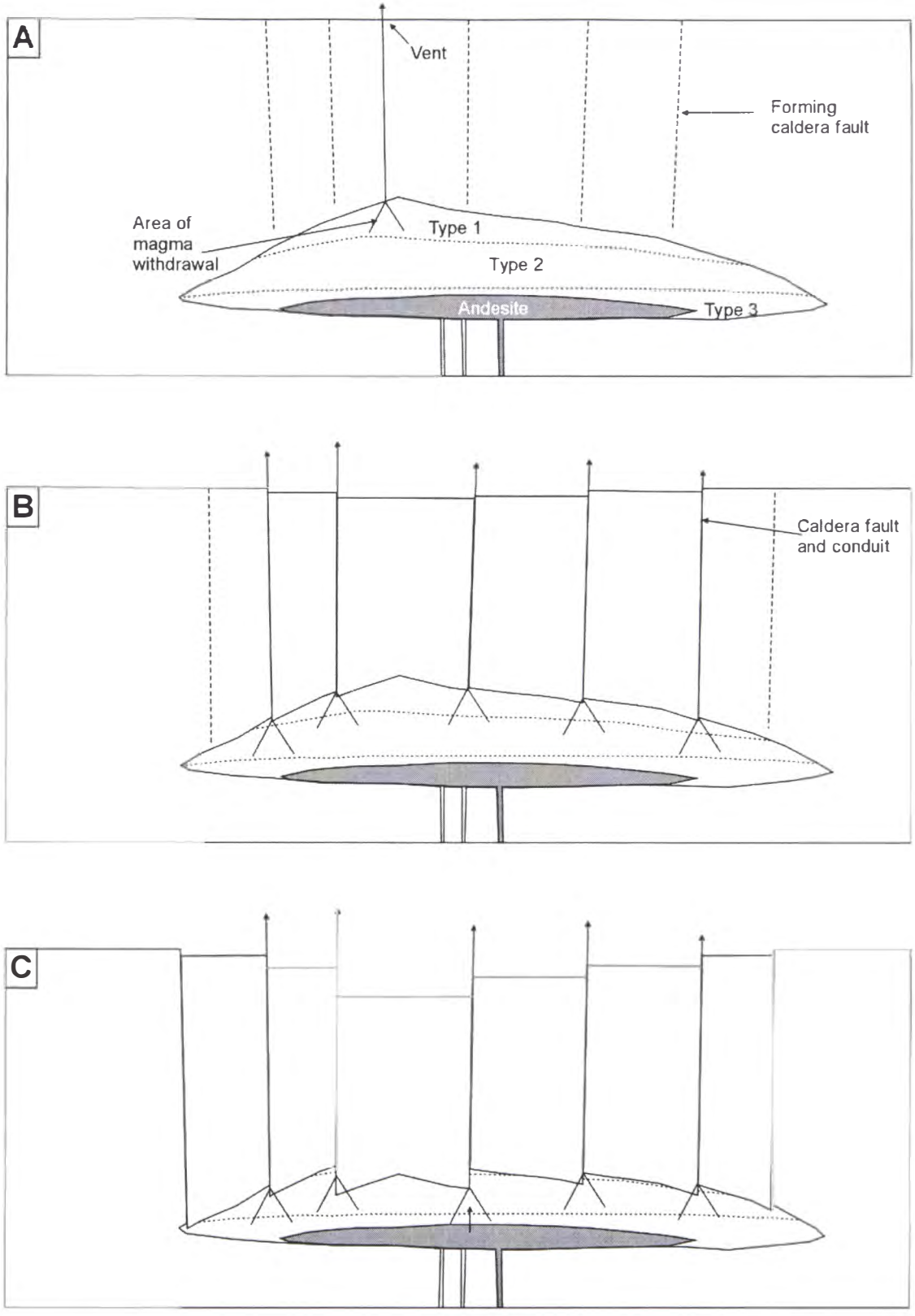

Figure 8.4. A schematic showing the interpreted pattern of magma withdrawal from the Mamaku chamber. A) The initial phase involved eruption of only type 1 magma. B) As the eruption proceeded caldera collapse began allowing the simultaneous eruption of magma from deeper levels and leading to the coexistence of types 1, 2, and 3 pumice at the same stratigraphic positions in the ignimbrite. C) Late in the eruption caldera collapse forced eruption of andesitic magma by causing withdrawal dynamics to overcome inertial and buoyancy forces acting to keep it in place.

of deepest caldera collapse) suggest that they are petrogenetically related. Fragments of rhyolite lava in lithic lag breccias also have similar phenocryst assemblages to Mamaku Ignimbrite pumice clasts, with mineral chemistry that is also very similar. The rhyolite lithic fragments may represent the initial stages of extrusion from the Mamaku Ignimbrite magma chamber, the domes produced completely destroyed or buried during caldera formation. The rhyolite lavas of Rotorua (except lag breccia clasts and RCR) most likely represent the eruptions of discrete, small volume magma reservoirs. Leonard et al. (submitted) suggest the presence of small isolated magma chambers beneath the Tarawera volcanic complex that are triggered to erupt by mafic magma intrusion and such a scenario is suggested for many of the small volume rhyolitic eruptives of TVZ (Smith et al., 2000). It seems likely that in TVZ there are periods in which magma accumulates in large magma chambers and erupts catastrophically producing calderas, but far more frequent is the formation of small magma chambers that erupt to create small volume rhyolite domes or tephra sequences.

8.3.4 Rotorua Caldera magma model

An overall model of magmatic activity at Rotorua Caldera needs to take into account:

1) Presence of three petrogenetically related pumice types.
2) Andesite blebs.
3) Mineralogically distinct pre- and post-caldera rhyolite lavas.
4) Post-caldera rhyolite lavas surrounding the gravity low (RCR) in Rotorua Caldera that are mineralogically very similar to juvenile Mamaku Ignimbrite pumice clasts.

The schematic diagram in Figure 8.5 is an interpretation of magmatic activity of Rotorua Volcanic Centre from immediately preceding the eruption of Mamaku Ignimbrite to the eruption of Mokoia and Hinemoa domes (interpreted as the youngest lavas outcropping in Rotorua Volcanic Centre; Healy, 1963; Kennedy et al., 1978; Nairn, in prep). The rhyolite domes of Rotorua Caldera, excluding those that surround the gravity low, are interpreted as having erupted from small discrete magma bodies.

Recent work by Eichelberger et al. (2000) is forcing a rethink of mechanisms of chemical zonation in ignimbrites and how zonation reflects magma chamber geometry;

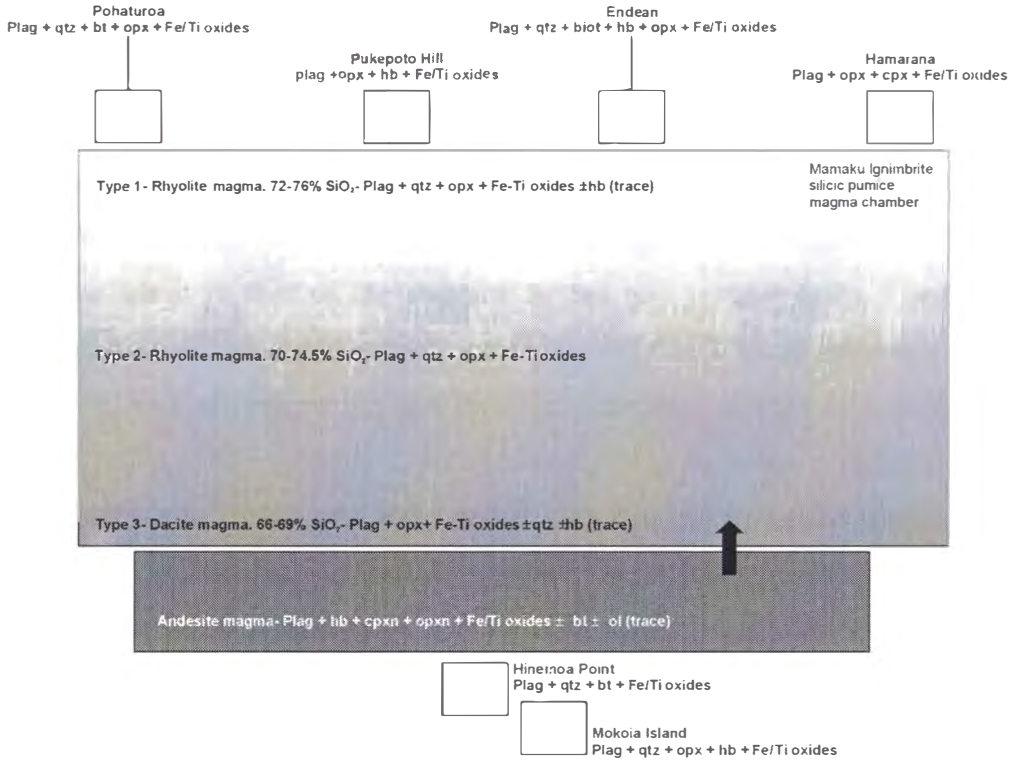

Figure 8.5. Schematic model of the Rotorua magma system. Position of the different magma chambers is based on relative age of eruption (inferred or known) with later erupted types placed lower in the diagram. No age relations can be determined for pre-caldera rhyolite dome chambers so they have been put at the same level. Lavas of Pukepoto Hill and Pohaturoa dome have been linked with other volcanic centres (Ewart, 1968; Nairn, 1989) but have been included here because of their locations at the caldera margin. RCR and the rhyolite lithic fragments in the lag breccias are thought to have been sourced from the same magma chamber as the Mamaku Ignimbrite. The andesite magma and the Mamaku Ignimbrite chamber were erupted at the same time.

the following is a summary of their findings. Zonation in the ignimbrite may be due to the rise of silicic magma coming in contact with, and then passing, resident mafic magma. Migration of the silicic magma is rapid. It is more buoyant than the mafic magma and erupts first followed subsequently by the extraction of the mafic melt. Mixing during the interaction of the two magmas causes gradational zonation in the ignimbrite. This has been demonstrated commonly in arc settings. In this situation mafic extrusions often precede and postdate the caldera-forming silicic event, and silicic pumice clasts are often crystal-poor to aphyric reflecting the rapid rise and eruption of the silicic melt (upon contact with the mafic magma). A much higher crystal content in mafic juvenile components relative to silicic pumice clasts would reflect this situation. Interaction of magmas in this way, Eichelberger et al. (2000) say, will create a more regular silicic-andesitic zonation than eruption from a silicic-over-andesitic layered

magma body. Also mixed or banded pumice clasts are often found in the resulting ignimbrite.

In Mamaku Ignimbrite andesitic blebs are only found in uMI, but silicic pumice clasts are found throughout, silicic pumice crystal content varies between 4 and 7 vol% (comparable with that of the andesite blebs), and pumice types 1 and 2 were likely derived from a type 3 parent (rather than types 2 and 3 being hybrids of type 1 and the andesitic magma) suggesting that the silicic magmas formed in a single chamber that was intruded by the andesite. Microphenocrysts in the andesite suggest a rapid change in crystallisation conditions and together with quenched margins and the lack of hybrid or banded pumice clasts in the Mamaku Ignimbrite suggest the andesite magma intruded the silicic chamber in a non-vigorous manner and not vice versa.

8.4 Mokai Ignimbrite

Similar paleomagnetic directions and $^{40}Ar/^{39}Ar$ dates have been used as evidence that Mokai and Mamaku ignimbrites are the same. Mokai Ignimbrite pumice clasts are similar to those of Mamaku Ignimbrite. Both have phenocryst assemblages dominated by plagioclase (5-15 vol%), with quartz, orthopyroxene, and Fe-Ti oxides comprising between 0.5 and 1 vol% each and trace amounts of hornblende and clinopyroxene. The only difference is that pyroxene is often more abundant than quartz in the Mokai pumice clasts. The crystal population of Mokai Ignimbrite matrix also differs slightly from that of Mamaku Ignimbrite in that pyroxene is again often more abundant than quartz in the former. Plagioclase again dominates.

The appearance and mineralogy of mafic blebs from Mokai Ignimbrite differ markedly from those found in the Mamaku. Mafic blebs were found in all Mokai Ignimbrite units. Such blebs are only found in the upper level of Mamaku Ignimbrite. Mafic blebs from Mokai Ignimbrite are characteristically dark grey with white bands suggesting mixing of mafic and rhyolitic magmas (as opposed to uniformly grey as occur in the Mamaku Ignimbrite). Mineralogy of the mafic blebs is very different between the two ignimbrites. Mokai mafic bleb phenocrysts comprise plagioclase (10 vol%), clinopyroxene (3.5 vol%), orthopyroxene (3.5 vol%), Fe-Ti oxides (2 vol%), olivine (1.5 vol%) and occasional hornblende crystals. The groundmass of Mokai mafic blebs is very fine grained and usually weathered making identification of crystal composition

difficult, but there is not the abundance of hornblende microphenocrysts as there is in the groundmass of andesitic blebs collected from Mamaku Ignimbrite. The amount of olivine is an important difference between mafic blebs in Mokai and Mamaku ignimbrites. Olivine was seen in only one mafic bleb sampled from Mamaku Ignimbrite where it comprised <1 vol%.

Thickness and ignimbrite stratigraphy are also important when assessing the Mokai-Mamaku relationship. The maximum thickness of distal Mamaku Ignimbrite seen is > 80 m (likely ≤ 100 m based on stratigraphy seen elsewhere) at Raparapahoe Stream, 21 km from Rotorua Caldera. The maximum thickness of Mokai Ignimbrite seen in drill core is 200 m, 46 km from Rotorua.

Mokai Ignimbrite can be separated into three units with intervening ash deposits. The same ash deposits can be seen in outcrops 2–2.5 km apart. Such ash deposits are not seen in Mamaku Ignimbrite, even at distal localities, where a dense pyroclastic current has been inferred. For the ash deposits to be present there must have been time breaks between successive pyroclastic flows sufficient to allow the ash to settle.

The top of the lower Mokai unit has a band of high pumice clast concentration that is overlain by an ash deposit, which is in turn overlain by the crystal-rich base of the middle unit. This sequence is typical of ignimbrites deposited from laminar, moderately to highly fluidised pyroclastic density currents that deposit en masse (Sparks et al., 1973; Sparks, 1976; Wilson, 1980). Stratigraphic variations in M_L and concentration of lithic and pumice clasts suggest progressive aggradation. Differences in pumice clast morphology within individual units suggest that each had cooled before deposition of the next unit. Boundaries between the units are sharp, but jointing is continuous and pervasive across all units indicating a compound-cooling unit.

Stratigraphic variation suggests that Mamaku Ignimbrite was emplaced progressively as a single unit (see chapter 2). The ash deposits, pumice variation and crystal content variation (in some units) show that Mokai Ignimbrite was emplaced as at least three distinct units each of which had time to cool prior to inundation of the area by the succeeding flow. Mamaku Ignimbrite is interpreted to have deposited from a density current that became progressively more concentrated as it got further from source and it could be suggested that this is responsible for the stratigraphic variation seen in the

Mokai area. However, even at distal localities Mamaku Ignimbrite aggraded progressively during a single event whereas three or more pyroclastic density currents deposited Mokai Ignimbrite.

Mokai Ignimbrite has similar whole pumice chemistry to Mamaku Ignimbrite, but this is true of many central TVZ ignimbrites; for example Pokai (Karhunen, 1993; Lynch-Blosse, 1998), Waimakariri (Lynch-Blosse, 1998; Morgan, 1986), and Matahina (Carr, 1983) ignimbrites. The similar chemistry does suggest that the two magmas are related at depth to the same or similar source rocks. The 200 m thickness of Mokai Ignimbrite is hard to reconcile with a Rotorua source when the thickest distal Mamaku Ignimbrite is probably ≤100 m less than half the distance away. The mineralogy and stratigraphic location of the mafic blebs, the three unit, and compound cooling unit stratigraphy of Mokai Ignimbrite also suggest it is not Mamaku Ignimbrite. Paleomagnetism, $^{40}Ar/^{39}Ar$, and fission track dates confirm that the two ignimbrites erupted more or less contemporaneously, but differences indicate that they are separate ignimbrites.

8.4.1 Periodicity of ignimbrite eruptions in TVZ

Houghton et al. (1995) have shown that the eruption of documented ignimbrites in TVZ has occurred over three main periods (I, II, and III, Fig. 8.6) separated by quiescent stages of 0.32 and 0.34 million years respectively. These three periods can in turn be split up into subperiods. Period III is divided into IIIA, IIIB, and IIIC. Mamaku and Mokai ignimbrites were erupted during period IIIB. Period IIIB lasted from 280ka-150 ka and resulted in eruption of 5 caldera forming ignimbrites: Kaingaroa, Kawerau, Ohakuri, Matahina, and Mamaku, and numerous smaller ignimbrite units. In addition, many tephra units have been delineated between distal Matahina and Mamaku correlatives (Manning, 1997) further confirming the vigorous volcanic activity that occurred in TVZ during this period.

This energetic activity resulted in a number of ignimbrites of the same or similar ages with comparable characteristics, that have been mistakenly correlated (e.g. Kawerau and Kaingaroa ignimbrites (Beresford, 1997)). The eruption of a voluminous ignimbrite is likely to cause significant disruption to the stress regimes within surrounding areas. It is possible that this disruption is great enough to trigger activity at an adjacent centre (e.g.

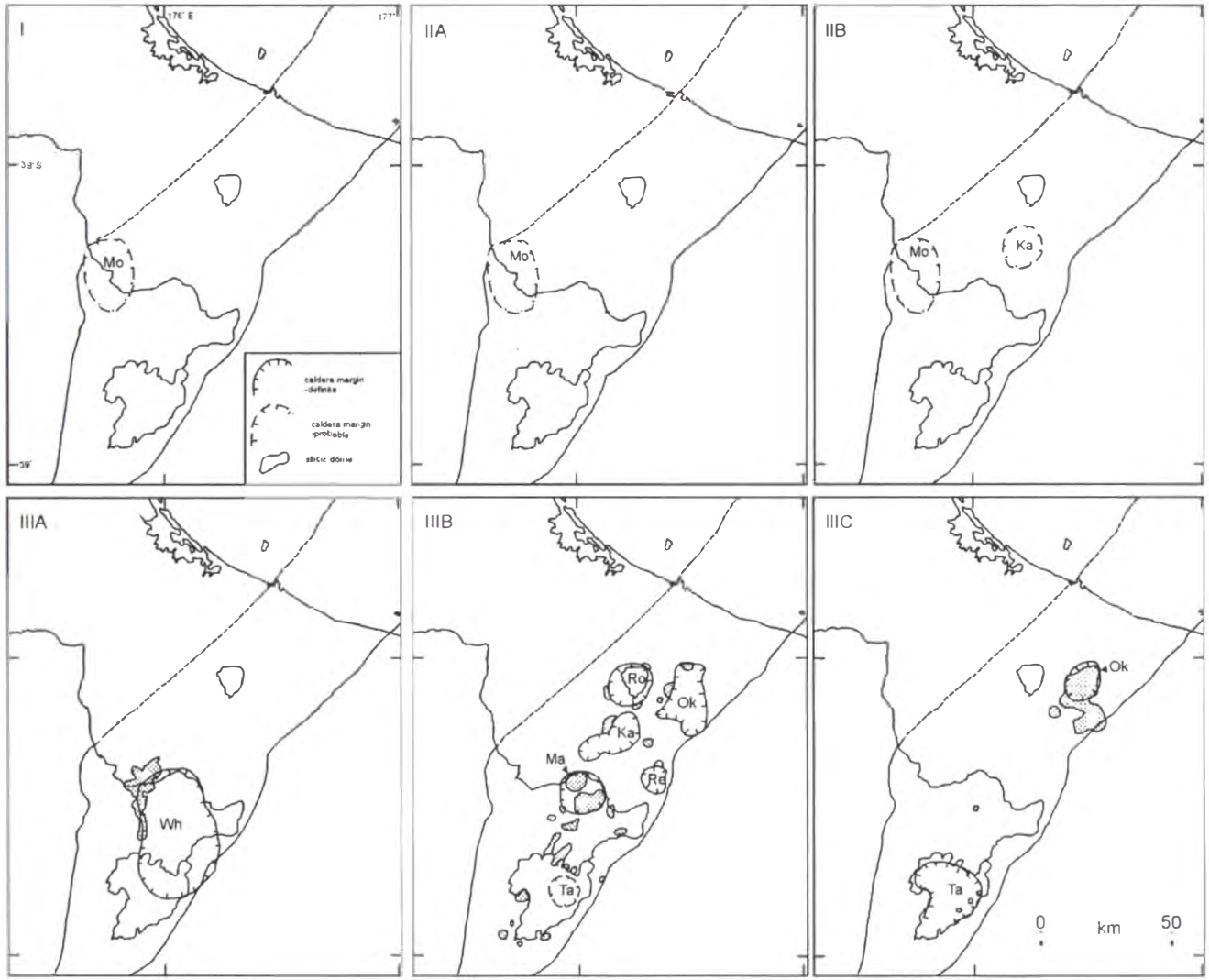

Figure 8.6. Maps showing the 3 period sequence of caldera forming activity in TVZ. I (1.68-1.53 Ma), IIA (1.21-0.89 Ma), IIB (0.77-0.68 Ma), IIIA (0.34-0.32 Ma), IIIB (0.28-0.15 Ma), and IIIC (0.065-present). Mo- Mangakino, Ka- Kapenga, Wh- Whakamaru, Ma- Maroa, Ok- Okataina, Re- Reporoa, Ro- Rotorua, Ta- Taupo. Mamaku and Mokai ignimbrites were erupted during period IIIB. Shaded areas are rhyolite domes. From Houghton et al. (1995).

Branney and Kokelaar, 1995; 1999), and that the eruption of Mamaku Ignimbrite triggered the eruption of Mokai Ignimbrite or vice versa.

Tectonism plays an important role in most types of volcanism and in TVZ volcanism and extension are intrinsically linked (Stern, 1987; Cole, 1990; Wright, 1992). Extension allows accumulation and emplacement of large magma bodies (Hutton and Reavy, 1992) and may or may not trigger their final eruption. Cambray et al. (1995) illustrate the possibility that extension can create the space into which a large rhyolitic body (or bodies) can be emplaced, but that it may be during the tectonically quiescent times that the eruption actually takes place (i.e. when pressure instabilities cannot be accommodated by further extension). Alternatively, extension can reduce the lithostatic load thereby promoting eruption from a chamber already residing in the crust. Major faults are known to be important factors influencing volcanism at many centres (e.g. Scafell Caldera (Branney and Kokelaar, 1995; 1999), Kaingaroa Fault and Reporoa Caldera (Beresford, 1997), the Tarawera vent alignment (Nairn, 1989)). At Scafell caldera magma evacuation of adjacent magma chambers has been interpreted to have triggered eruption from others nearby by activating volcano-tectonic faults (Branney and Kokelaar, 1995). The same may have occurred for the eruption of Mokai and Mamaku ignimbrites. It is impossible to tell which was erupted first, but it is thought that the eruption of Mamaku Ignimbrite, being of much larger volume, is more likely to have had the ability to trigger disturbance on a scale large enough to cause eruption at another centre.

8.5 Rotorua Caldera

End-member caldera structures have often been categorised as "type" structures. It has become clear during the course of this study that, although end-member structures exist, they are by no means the norm. In recent years significant advances have been made in understanding the complexities of caldera structures. As more calderas are studied geometric collapse relationships are increasingly shown to be affected by the tectonic environment, eruptive recurrence, and the volume and number of magma chambers evacuated.

Presence and dip of lithic lag breccias at marginal sites, intra- and extra-depression thickness variation of Mamaku Ignimbrite, faulted older rhyolite domes, location of

post-depression rhyolite domes, together with the presence of arcuate faults, tension fractures and fumarolic ridges, all indicate that the depression that contains Lake Rotorua is of caldera collapse origin. To interpret the structure of Rotorua Caldera use has been made of geophysical anomalies, distribution of rhyolite bodies, drill hole information, caldera geomorphology, and the stratigraphy of Mamaku Ignimbrite.

8.5.1 Structure

The insistence by Macdonald (1974) and Hunt (1992) that Rotorua is not typical of many calderas seen worldwide is true. In many cases a gravity anomaly exists in which the gravity contours are parallel to the caldera margins; for example Long Valley (Kane et al., 1976), La Primavera (Yokoyama and Mena, 1991), Toba (Nishimura et al., 1984, in Hunt, 1992), Taupo (Davy and Caldwell, 1997) and Mangakino (Woodward and Ferry, 1974), but this does not always occur. For example Whakamaru and Reporoa calderas do not have gravity lows concentric with their margins. The gravity low within Haroharo Caldera, although well defined, is only located in the caldera's southeast despite collapse being proved further north in Lake Rotoiti. The gravity and/or magnetic response generated by a caldera need not be parallel to its margins.

The sizes of the magnetic and gravity anomalies at Rotorua Caldera are both small when compared with all other TVZ calderas with the exception of Reporoa (Hunt (1999) indicated that the size of the gravity anomaly at Rotorua was small compared to other young calderas). This may be a function of the number of events involved in Rotorua's formation. Both Rotorua and Reporoa calderas were formed during the eruptions of single ignimbrites (Mamaku and Kaingaroa ignimbrites respectively; Beresford, 1997; Beresford and Cole, 2000; this study). All other calderas have undergone collapse in response to the eruption of at least two ignimbrites (Houghton et al., 1995). This multiplicity of activity at all other calderas may be responsible for the development of their well defined geophysical anomalies with deeper basement due to successive collapse events.

Halinan (1994), studying Guayabo Caldera in Costa Rica, utilised gravity surveys and borehole data to assess the structure of the caldera floor. The lowest gravity was not central to the caldera and not simply concentric with the caldera margin (Fig. 8.7a). Gravity transects (Fig. 8.7b) across the caldera yield a similar pattern to that illustrated

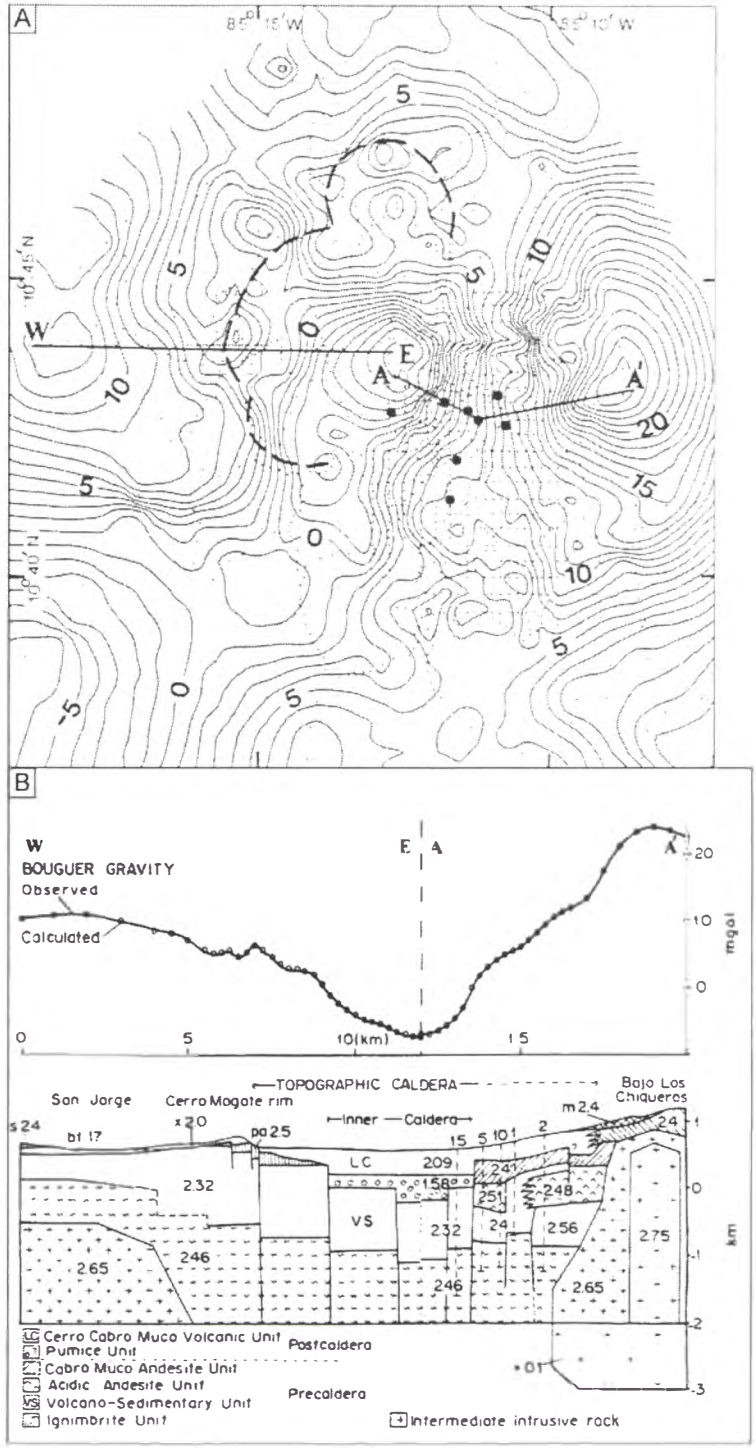

Figure 8.7. Guayabo Caldera, Costa Rica. A) The gravity anomaly does not have a simple geometric relationship with the caldera (dashed line represents the exposed caldera margin). B) A composite cross section of the gravity anomaly and the actual structure based on drill hole evidence (compare with Fig. 6.10). Rotorua is thought to have a similar step-faulted structure to Guayabo Caldera. From Halinan (1993).

by Hunt (1992) for Rotorua (see Fig. 6.10). Halinan views Guayabo Caldera as a funnel caldera produced by step-faulting of the caldera towards an area of deepest collapse (Fig. 8.7b). The same is also thought to be true for Rotorua Caldera. Rotorua Caldera is not thought to have collapsed in a totally piston-like manner, which would give rise to a simple gravity anomaly. Instead it is thought to have collapsed in a stepwise fashion with the caldera floor being broken up by pre-existing tectonic structures.

Caldera fill and volume

The volume of Rotorua Caldera has been estimated using a basement subsidence of 1.25-1.75 km (calculated by Rogan (1982) as >1 km), caldera fill of >1 km thickness (computed by Hunt (1992)) and using an elliptical asymmetric cone to approximate the caldera shape (see Appendix 7). The estimated volume of the caldera is approximately 120-163 km^3.

Volume of Mamaku Ignimbrite outflow is estimated as >225 km^3 but may have been as much as 283 km^3, which equates to volumes of approximately 96-121 km^3 DRE. The volume of intra-caldera rhyolite has been approximated by subtracting the volume of a cone that approximates the upper surface of intracaldera ignimbrite away from the total caldera volume (see Appendix 7). This suggests an intra-caldera volume of Mamaku Ignimbrite of 114 km^3 or 48.7 km^3 DRE. Total ignimbrite volume then is estimated at between 145-170 km^3 DRE, close to the volume calculated for the caldera. These close volume estimates suggest that Mamaku Ignimbrite is the only ignimbrite sourced from Rotorua Caldera.

Based on densities, Hunt (1992) suggested that the caldera fill (>1 km depth) was dominated by lake sediments. He also suggested that Mamaku Ignimbrite in the caldera is planar and of uniform thickness which, in his proposed geological cross-sections, was estimated at 100-110 m. Borehole evidence (Wood, 1992) indicates that the ignimbrite's thickness is greater than this and Larmarche's estimate of at least 279 m thickness at the southern margin, away from the low gravity anomalies, suggests that intra-caldera ignimbrite thickness is much greater than Hunt indicates. Rogan's (1982) suggestion that there is at least 1 km of non-magnetised material in the caldera closely agrees with Hunt's depth of fill estimate, and is assumed correct. Rogan further

suggested the fill comprised non- or reversely magnetised rock which is consistent with it being dominantly Mamaku Ignimbrite.

Faulting and caldera subsidence

Rotorua Caldera is one of only two single event calderas present in TVZ and it is only partially overlapped (spatially) by other caldera centres (Kapenga and Okataina). TVZ is a zone of active extension. This extension imparts a structural grain with faults preferentially striking NE-SW. A second wider spaced fault set is present that strikes NW-SE. Pre-existing faults can break up the area of a 'would-be' caldera into a number of blocks, each of which may subside at different rates, and may only interact slightly with one another during a collapse event. At Rotorua the number of faults breaking up the caldera floor is unquantifiable, but they are thought to be many because of 1) the prevalence of NE-SW striking structures further south of Rotorua, 2) the presence of NW-SE striking structures in TVZ, and 3) the apparent parallelism of geomorphic features in Rotorua Caldera and the structural trends of 1) and 2).

Caldera-forming faults are thought to underlie the post-caldera rhyolite domes surrounding the low gravity anomaly in the southwest of the caldera. They are also thought to underlie the margins of the embayment in the northwest and can be seen as scarps at the south, southwest and north caldera margins. A caldera-forming fault also truncates Pohaturoa dome in the southeast.

Walker (1984) used Rotorua as an example of a caldera that had formed by downsag, comparing it with Taupo and Bolsena (Italy) calderas. It appears that downsag has occurred in some, but not all parts of the caldera. Also it is more likely that downsag caldera subsidence can only occur where conditions favour forced folding (creating drape folds rather than buckle folds). The generation of such drape folds requires a rigid basement over which there is a cover sequence of sub-horizontal bedded or predominantly layered rocks (Stearns, 1978). The shape and trend of the fold is governed by some forcing member below (Stearns, 1978; Fig. 8.8). It has long been recognised that the passive bending of cover over steep basement faults cannot be accomplished in any mechanism that can maintain a length balanced cross section, rather the cover accommodates itself to the basement faulting by rigid-body rotation and internal deformation (Cosgrove and Ameen, 2000) i.e. either extension by faulting or

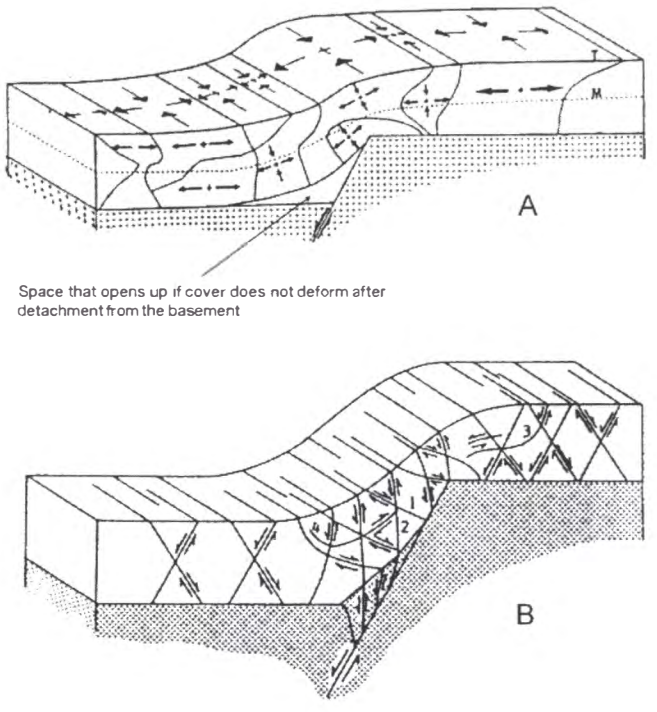

Figure 8.8. Showing Formation of a forced or drape fold. A) The cover rocks do not deform internally and detach from the underlying basement creating a triangular void. B) shows the way in which cover and basement rocks deform to overcome the space problem and areas of potential fault formation in the cover rocks. Arrows in A) delineate extension directions. After Cosgrove and Ameen (2000).

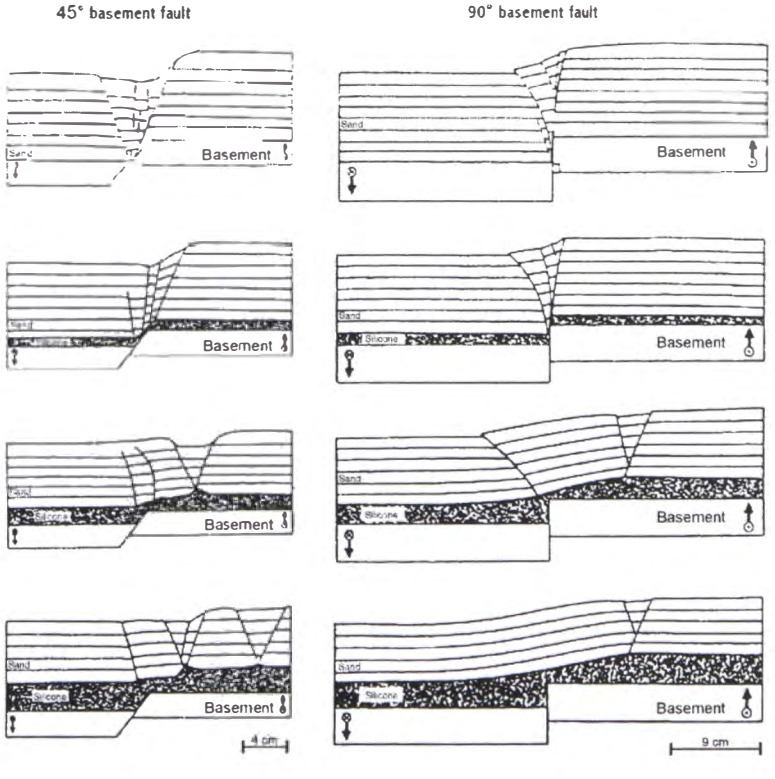

Figure 8.9. Showing the location of fractures in cover rocks above a basement fault. Fractures in cover rocks form above the fault and in cover above the footwall. From Richard (1990) and Richard (1991).

thinning of the cover must take place, or the cover detaches from the basement in a triangular zone at the base of the fault scarp, creating a void that must be filled (by fractured cover or basement rocks; Fig. 8.8). The amount of cohesion between the cover and basement and between the cover layers will determine the details of detachment, location of extensional faulting and the response to the footwall space problem. Analogue and computer modelling have demonstrated that commonly extension and small graben structures develop in areas from immediately above the basement fault to some distance behind its projection (Richard, 1990 in Cosgrove and Ameen, 2000; Fig. 8.9), and field studies show developing fractures concentrate in areas of maximum fold curvature (Lisle, 1994). The cover rocks tend to thin and separate from this zone of high extensional strain sagging towards the downthrown block (Fig. 8.9).

The exploded block diagram in Figure 8.10 (enlarged in the map pocket in the back of this thesis) is an interpretation of the structure of Rotorua Caldera, based on evidence outlined in chapter 6. Wood (1992) suggested that the formation of Rotorua Caldera involved blocks that were aligned sub-parallel to the area of deepest subsidence. This concept is supported in this study but here the caldera floor is viewed as broken up by faults, that strike both NE-SW and NW-SE, into numerous blocks not necessarily aligned sub-concentrically to the area of deepest subsidence. These blocks have subsided to different depths according to their proximity to the area of deepest collapse.

The block diagrams of Rotorua Caldera (Fig. 8.10, and those following) show brittle failure of the underlying basement rocks and older ignimbrites with thickening of Mamaku Ignimbrite into the space created. Newly deposited Mamaku Ignimbrite would have been less consolidated than underlying rocks and able to warp more easily, so the ignimbrite has been treated as a separate entity from the underlying rocks. It is hard to deform a thick mass of rock above a magma chamber by bending alone, especially when it is consolidated. Deforming a ≥3 km (geobarometry could not be calculated for Mamaku Ignimbrite, but Whakamaru is interpreted to have erupted from 3-6 km depth; Brown et al., 1998) vertical thickness of rock by pure downsag or trapdoor (the two cases in which warping of the rock is supposed to occur) requires an enormous amount of: i) extension at the surface, ii) disintegration and removal of rock at depth, or iii) widespread bed-over-bed sliding (see Fig. 5.7; Branney and Kokelaar, 1994). If the basement rocks beneath the TVZ volcano-sedimentary sequence are

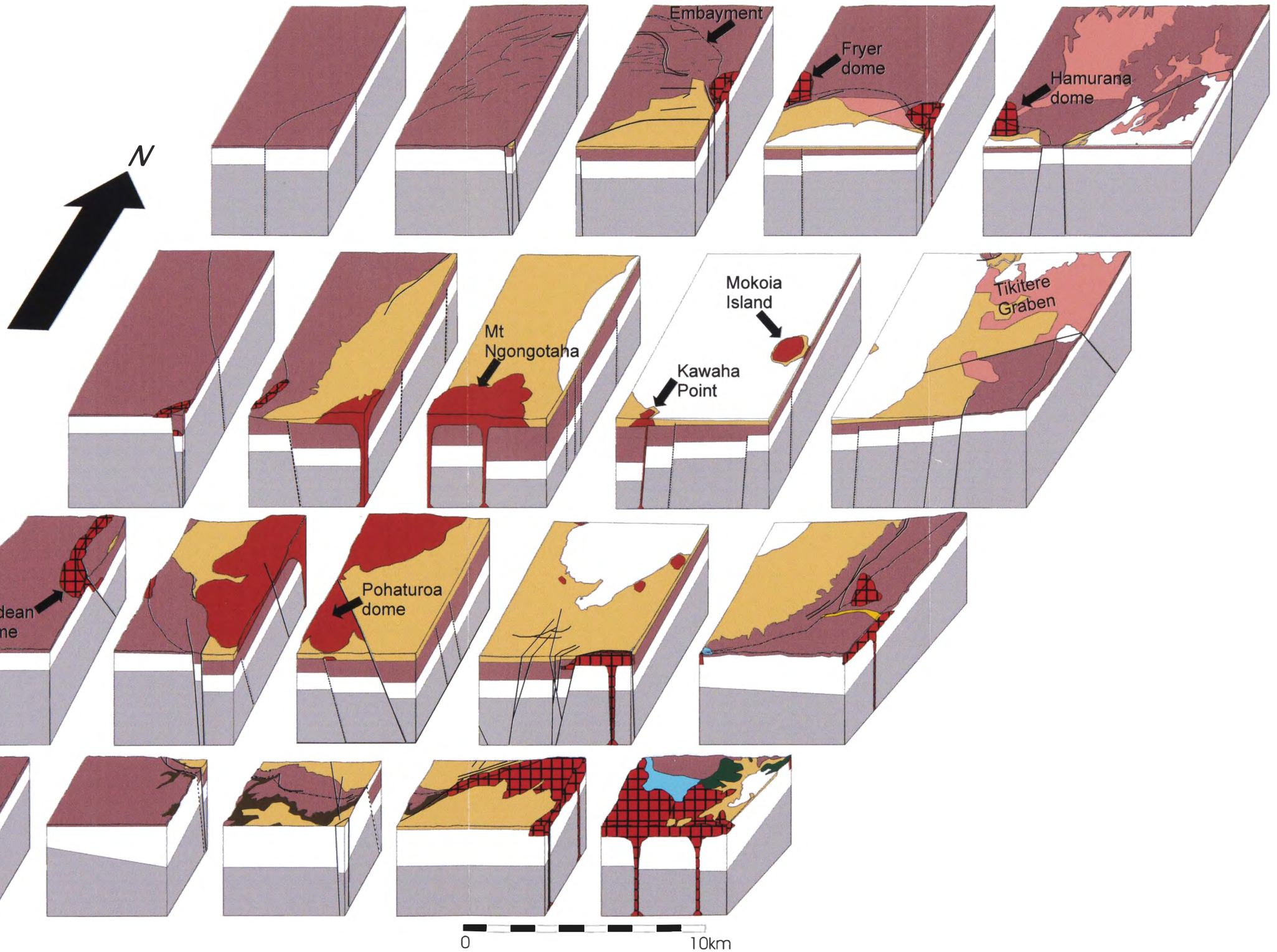

Figure 8.10. Exploded oblique view of Rotorua Caldera. The caldera floor is broken up into a number of blocks that increase in displacement to the southwest. Faults associated with caldera collapse have been used as conduits to erupt post-caldera rhyolite domes. The basement deforms brittly, and Mamaku Ignimbrite ponding in the depression is able to deform by downsagging. Faults striking northeast-southwest have much closer spacing than those striking northwest-southeast. Pre-caldera rhyolite domes have been truncated by caldera-forming faults. Enlargement in back pocket. Lithologies and symbols as for Fig. 6.6, back pocket.

Mesozoic greywackes and argillites (as found in a number of TVZ geothermal exploration wells (Wood et al., 1999)), they are likely to be complexly folded, further impeding downsag and trapdoor warping. It would be especially difficult to deform such rocks by warping them within the short time it takes a caldera to form. Basement rocks are much more likely to fail brittly under such conditions and in Figure 8.10 they have been broken up using normal dip slip faults. In contrast to greywacke, it would be comparatively easy to deform ignimbrite sheets above the basement, because they are likely to be thinner, less competent, and generally flat lying. However, cold, indurated, and possibly welded ignimbrites would bend only slightly before brittle failure would occur. Therefore the effects of downsag and trapdoor collapse are best seen in the Mamaku Ignimbrite itself. Even so, some deformation has been accommodated by cracking and faulting to produce the extensional features noted in the ignimbrite at the hinge regions of the downsag and fault scarps seen at the northern, southern, and southwestern margins.

Displacement of the blocks is greatest in the area of the low gravity anomalies and decreasing towards the caldera margins. In the area of the greatest gravity anomaly the basement is inferred to have collapsed more or less symmetrically in a piston-like fashion (Fig. 8.11) with fault location inferred based on rhyolite dome distribution.

Towards the northwest (Fig. 8.12) collapse is inferred to have occurred asymmetrically, with caldera floor blocks getting progressively deeper towards the area of maximum subsidence, forming an embayment in the caldera margin. The overlying Mamaku Ignimbrite has both filled the depression and been deformed by ongoing downsag. Numerous features support this idea, including the slope of the ground surface and presence of ignimbrite ridges towards the caldera margins. Other features of the embayment are its well defined margins, and the appearance of Mamaku Ignimbrite from beneath the lake sediments at its opening. The fumarolic ridges are interpreted to have formed in response to downsagging of the hot ignimbrite above an area of brittle basement collapse. Downsagging must lead to extension towards the margins of deformation as rocks accommodate stretching and bending. It is inferred that the extension caused a small amount of downslope creep or warping of the ignimbrite in the northwest that led to formation of narrow tension fractures or weakened zones along which fumarolic gases preferentially escaped (see Fig. 6.13). The ascent of vapours within the ignimbrite along these zones caused the cementation of a plane of ignimbrite

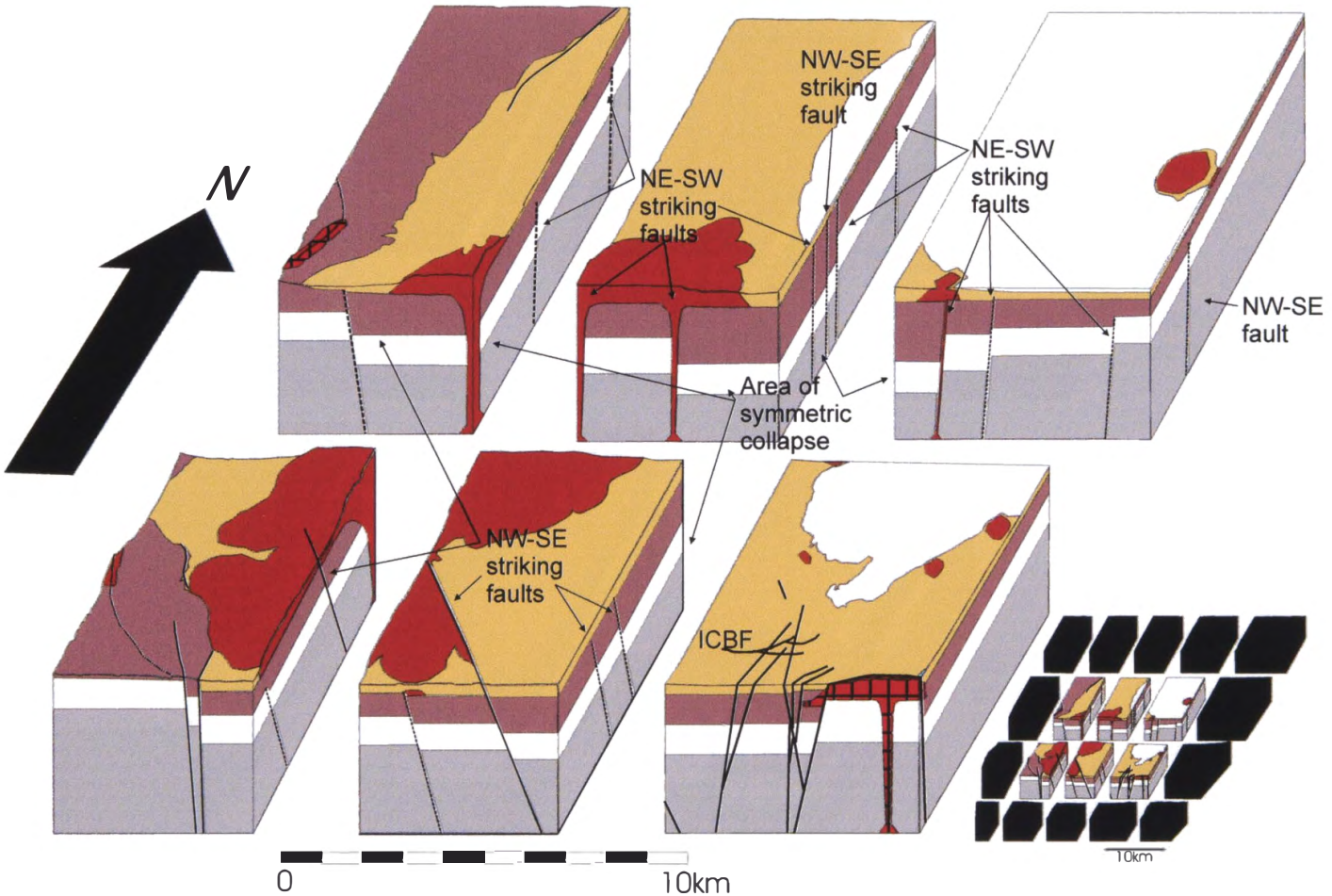

Figure 8.11. The area of deepest collapse is interpreted to have dropped in a symmetric piston-like manner with a smaller central block subsiding to the deepest level. NW-SE and NE-SW striking faults break up the caldera floor into numerous blocks allowing varying magnitudes of subsidence. Post-caldera rhyolite domes are though to have used faults as conduits. NW-SE striking faults are more prevalent here than in other parts of the caldera as it is the area of deepest subsidence. ICBF=Inner caldera boundary fault (Wood, 1992) Lithologies and symbols as for Figure 6.6, and back pocket.

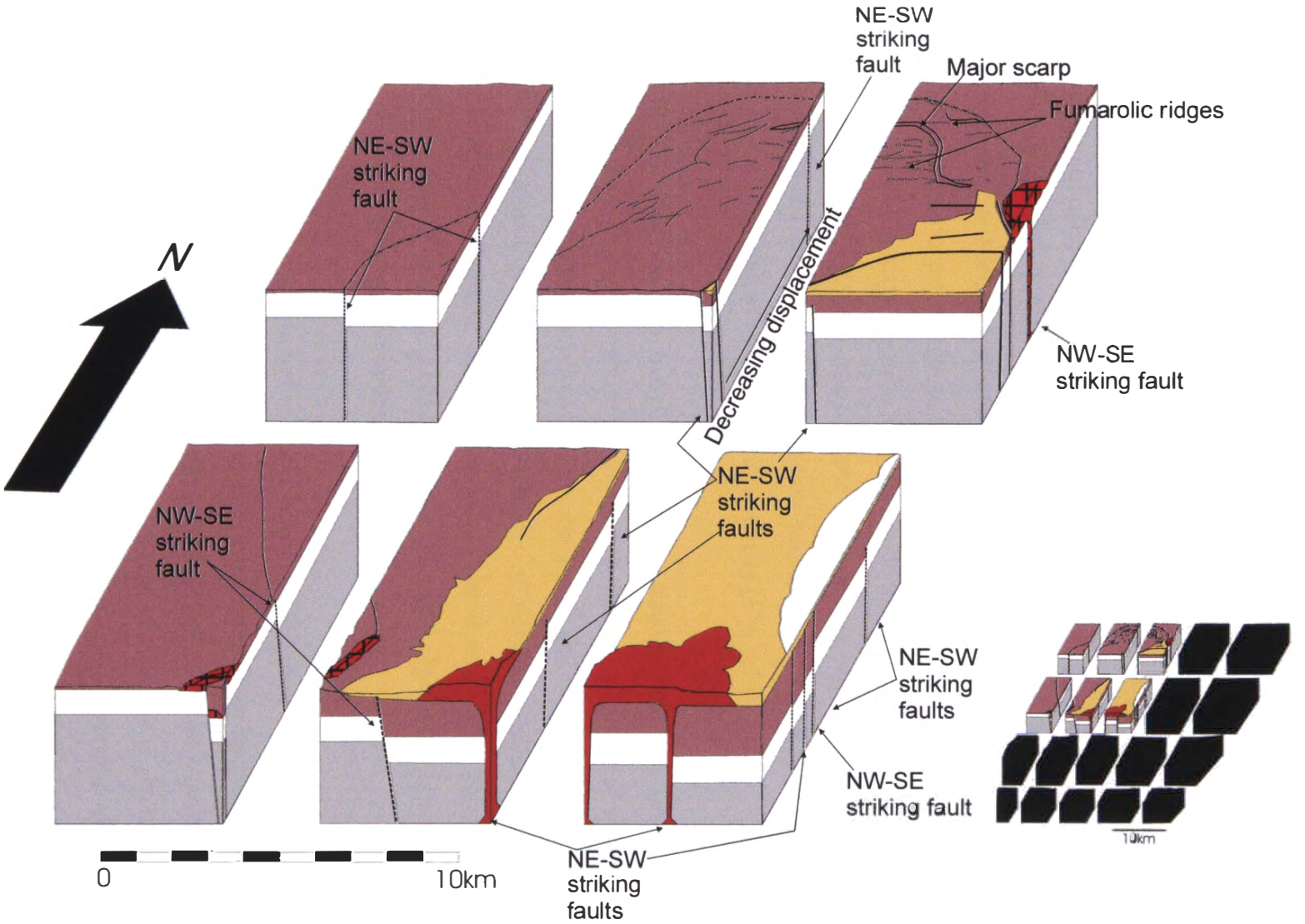

Figure 8.12. The embayment is bounded by NE-SW and NW-SE faults. The basement has deformed brittly, with overlying Mamaku Ignimbrite ponding, bending and faulting into the caldera. Caldera related subsidence increases towards the gravity low. Symbols and lithologies as for Figure 6.6, back pocket.

rather than a local point. At the opening of the embayment geomorphology and emergence of Mamaku Ignimbrite from beneath lake sediments suggest the presence of a fault running between Fryer and Endean domes. The northeastern and southwestern margins of the embayment are thought to reflect the positions of underlying NW-SE striking faults.

In the northeast, subsidence of the caldera floor is also thought to have occurred asymmetrically, with caldera floor blocks getting progressively deeper toward the gravity low (Fig. 8.13). Extensional features that would have marked the hinge of this collapse have been overprinted and destroyed. The scarp north of the lake indicates a fault that marks the margin of asymmetric collapse towards the caldera's northeast; the presence of the scarp suggests a greater single throw than occurs on any fault underlying the embayment. Asymmetric collapse in this area is oriented orthogonally to that which occurs in the embayment. The region where these two areas of asymmetric collapse intersect is the area of the low gravity anomaly (Fig. 8.14).

At the eastern caldera margin the tension fracture indicates downsag of Mamaku Ignimbrite. This is thought to have occurred above a step-faulted basement (Fig. 8.15) for reasons outlined previously. To the south and southwest gravity contours are slightly closer together and the subsidences of individual faulted blocks are interpreted to have been of greater single magnitudes than in many other parts of the caldera and the low gravity anomaly is closer to the south and southwest margin than it is to the NE, NW, and E reflecting the caldera's asymmetric nature.

From the preceding discussion it is evident that Rotorua Caldera cannot be classed as only one collapse type. Subsidence is interpreted to have taken place asymmetrically, deeper in the southwest, shallowing towards the north and northeast, and to have involved numerous fault-bound blocks, the size of which was governed by the spacing of pre-existing faults and their amount of displacement governed by their proximity to the area of maximum subsidence. The area of deepest subsidence is interpreted to be more symmetrical (piston-like), although morphology of the surrounding dome complexes suggests that this collapse cannot be assigned to a single ring fault, and geophysical evidence suggests that it contains up to three collapse blocks. Features consistent with downsag occur towards the northwestern (fumarolic ridges and small graben) and eastern (tension fracture) caldera margins, and are interpreted to have

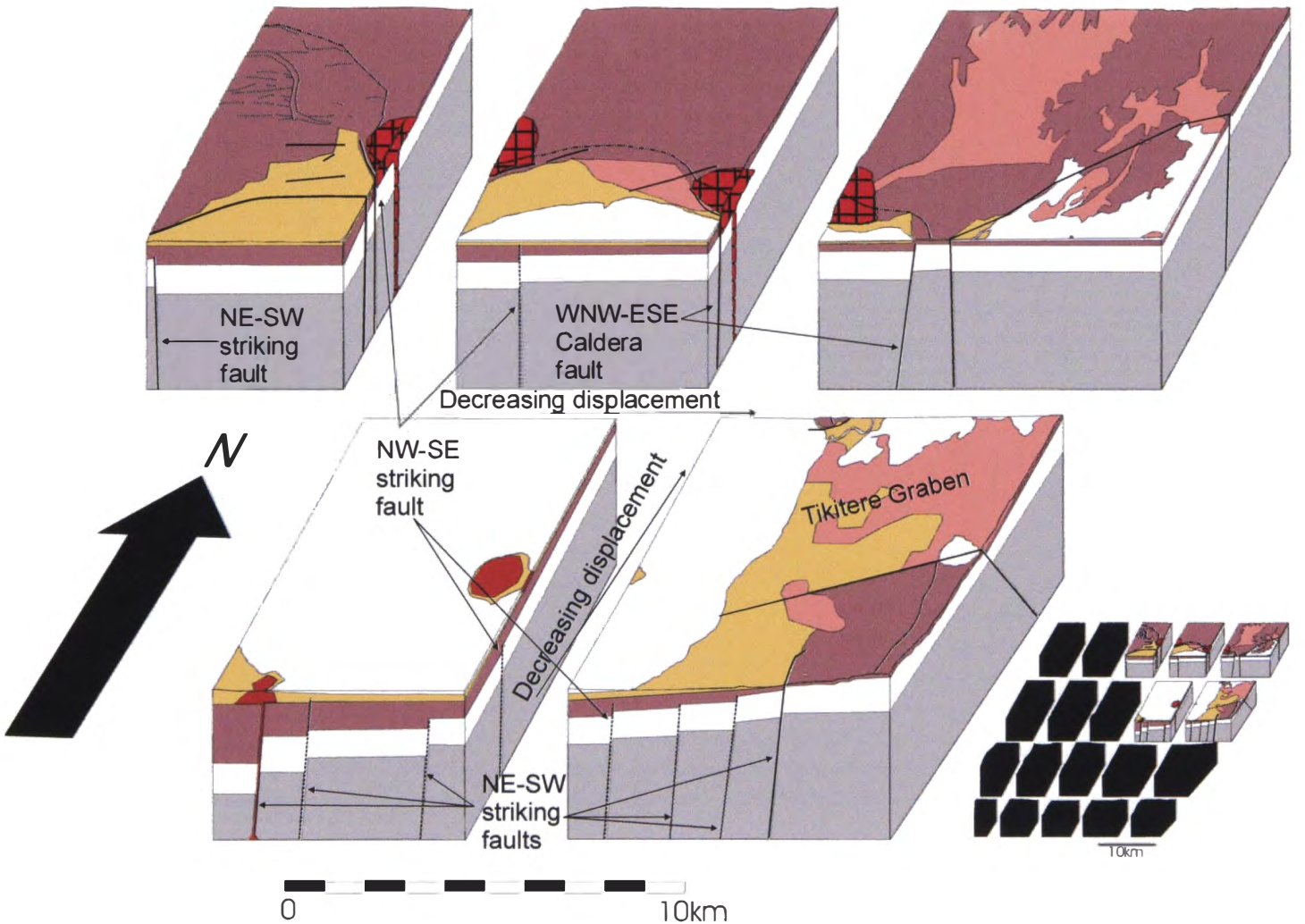

Figure 8.13. Northern and northeastern Rotorua Caldera. NE-SW structures have subsided asymmetrically; deeper to the southwest. Pre-caldera rhyolites at the northern caldera rim have been dissected by a fault that strikes generally WNW-ESE. Lithologies and symbols as for Figure 6.6, back pocket.

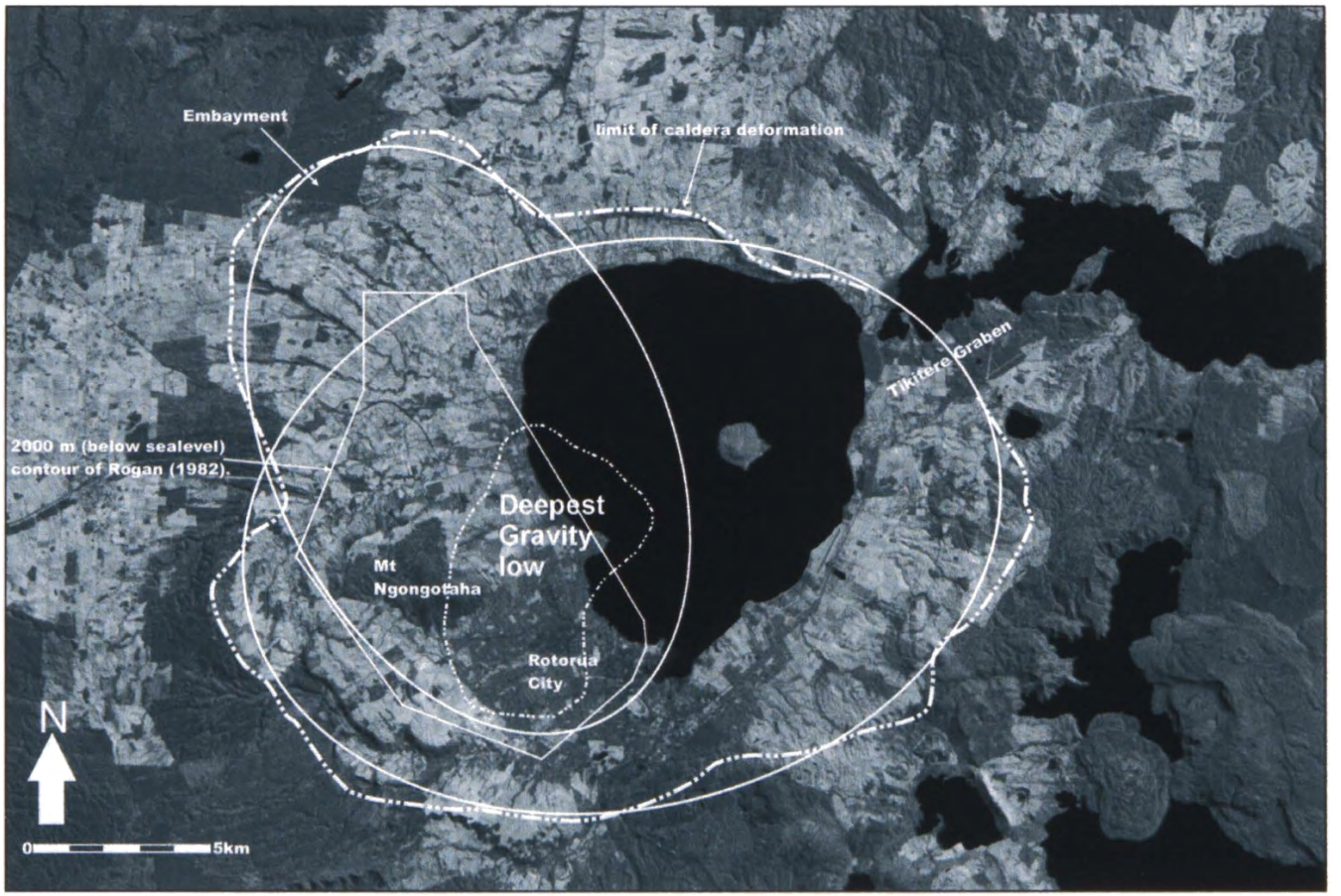

Figure 8.14. Satellite image of Rotorua Caldera showing the major features outlined in the text. The embayment in the northwest is likely to have been influenced by NW-SE striking faults. NE-SW striking features (parallel to the main axis of rifting) are interpreted to have greatly influenced caldera collapse that generated an elliptical structure (long axis oriented NE-SW). A second ellipse corresponding to the collapse of the embayment overlaps with the first in the area of the gravity anomaly.

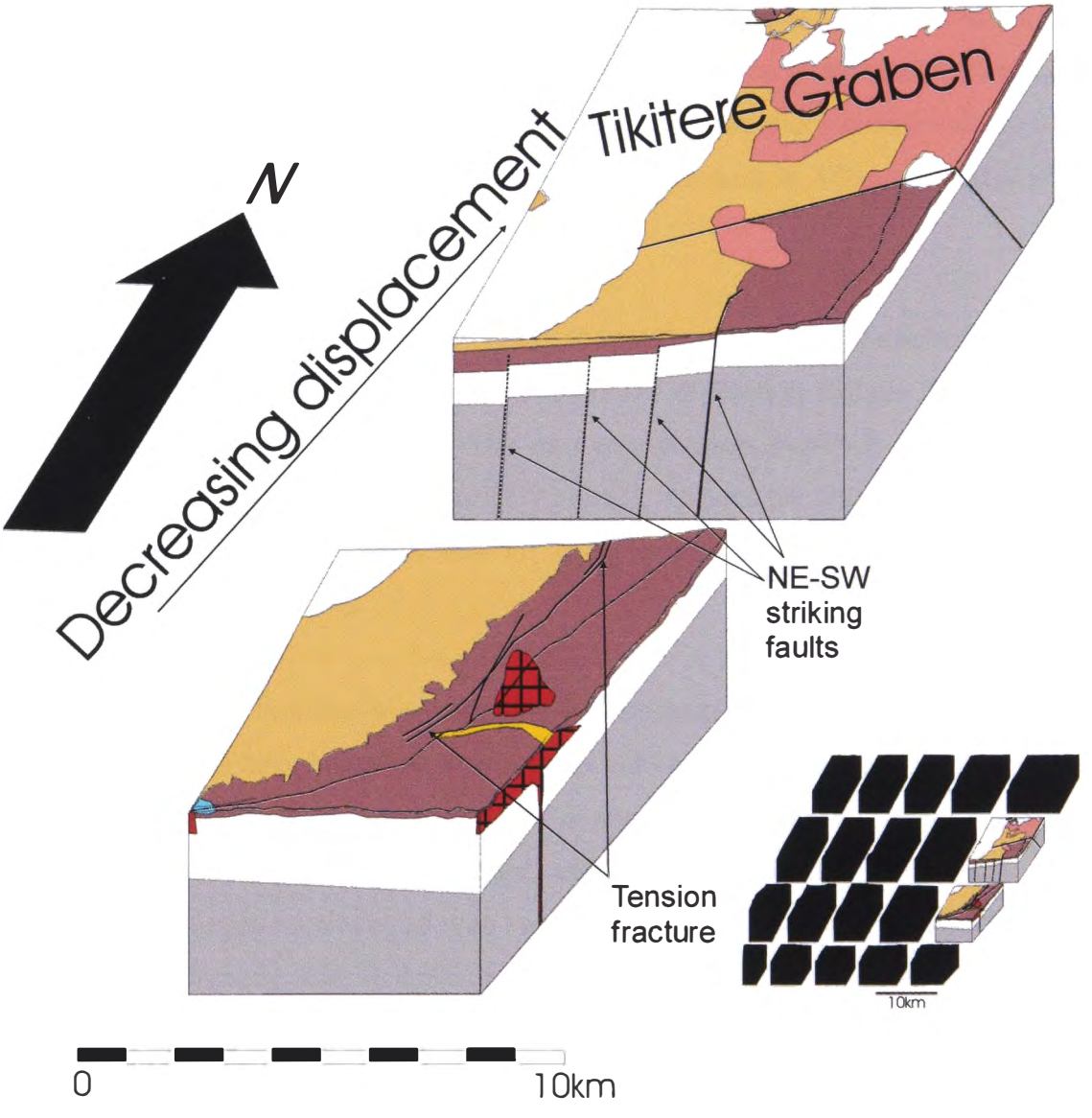

Figure 8.15. The eastern caldera margin. The basement is step-faulted into the caldera. Displacement down the faults decreases towards the northeast. Piano key-like movement of caldera floor blocks has been described by Kokelaar (1988), and a similar situation is envisaged here. The tension fracture has opened as Mamaku Ignimbrite has sagged down in response to basement faulting. Lithologies and symbols as for Figure 6.6, and back pocket.

formed above areas of brittle, step-faulted basement collapse. The northeastern and southwestern embayment margins (in the caldera's northwest) are oriented orthogonally to the dominant fault pattern, suggesting control by NW-SE striking faults which are otherwise concealed (Fig. 8.13). Trapdoor collapse also requires brittle failure of the basement at all margins of the subsiding block. If a coherent block subsides to a greater degree at one end than the other (i.e. asymmetrically) a trapdoor-like morphology is imparted. Extensional structures should be seen, in the erupted ignimbrite or surface rocks, where the subsidence is hinged. At Rotorua Caldera these structures are present in the northwest, but in the northeast have been buried by more recent volcanics of Okataina Volcanic Centre and destroyed by fault movement in Tikitere Graben (Fig. 8.13).

Analogue models indicate that reverse faults should dominate during caldera collapse, but it is assumed that normal faulting was dominant at Rotorua Caldera (and is most likely at other TVZ calderas also). This is likely because the TVZ is under active extensional stress and faulting is exclusively normal, whereas the laboratory models are carried out under static conditions with no acting external forces that would serve to complicate collapse processes.

Rotorua Caldera exemplifies a situation where regional fault structure and magma chamber evacuation have interacted to generate a caldera with a morphology that cannot be attributed to any single collapse process. Rotorua Caldera has characteristics that can be attributed to downsag, plate, trapdoor, and piecemeal collapse processes. The combination of numerous blocks all with varying displacements makes Rotorua Caldera piecemeal by Branney and Kokelaar's (1994) definition, but piecemeal does not describe the collapse process well. Collapse of the different blocks appears to have occurred sequentially away from an area of maximum down throw, with displacements that progressively decrease, that is not random or chaotic. An alternate and preferable way of describing the formation of Rotorua Caldera, according to the scheme introduced in chapter six, is as a rhyolitic, single event, asymmetric, multiple-block, single locus caldera. This description provides information on the dominant composition and collapse history of the caldera as well as indicating aspects of its overall geometry and morphology.

8.5.2 Timing of caldera collapse

Interpretation of the sequence of formation of Rotorua Caldera is shown in Figure 8.4 and is based on lithologic variation within Mamaku Ignimbrite (Fig. 8.1) taking into account the following:

1) Its extra- to intra-caldera thickness variation.
2) Stratigraphic location of lithic lag breccias and areas of higher lithic fragment concentration.
3) Welding in mMI.
4) Coexistence of the three pumice types throughout the deposit.
5) Location of andesitic blebs only in uMI.
6) Presence of only type 1 pumice clasts in the basal tephras.
7) Volume of the basal tephras.
8) Transition from eruption of the basal sequence material to main ignimbrite sequence material.

Exposed lithic lag breccias are at the top of the ignimbrite suggesting a major phase of collapse at the very end of the climactic eruption. There is also an increase in lithic abundance towards the middle of the ignimbrite sheet at medial distances from the caldera. This suggests that caldera collapse also occurred during an earlier stage of the eruption.

Just outside the caldera rim to the south, Mamaku Ignimbrite is approximately 40 m thick, whereas to the north it is up to 145 m thick (Nathan, 1975). Inside the caldera the ignimbrite is at least 279 m thick (Lamarche, 1992), and intra-caldera deposits of unknown lithology (probably Mamaku Ignimbrite) may be >1 km thick (Hunt, 1992; Rogan, 1982). If all of the caldera collapse occurred only at this late stage the difference in ignimbrite thickness between outflow sheet and intracaldera ignimbrite should not be great, and the ignimbrite should be buried at great depth beneath post-eruption infill. Some collapse must have occurred at an earlier stage in the eruption to allow ponding of Mamaku Ignimbrite inside the caldera.

Welding of mMI may have been enhanced by an increase in the mass eruption rate (MER). Presence of mMI lithics in uMI shows that welding was not solely due to

compaction. An increase in (MER) would increase the particle concentration of the pyroclastic density current and rate of deposition thereby promoting heat retention and welding. Any increase in MER must be associated with changes in vent dynamics suggesting an acceleration in the collapse rate of the caldera.

Coexistence of the different pumice types throughout the main Mamaku Ignimbrite sequence is thought to represent its eruption from numerous vents that tapped different levels of the magma chamber simultaneously. The vent sites were likely controlled by caldera faults that had propagated to the magma chamber. Andesite blebs are found only in upper Mamaku Ignimbrite and are thought to represent a sill that accumulated in the magma reservoir (Fig. 8.4). The andesite's withdrawal would have been impeded during early stages of the eruption due to buoyancy and inertia disparities between it and the more silicic magma (Blake and Ivey, 1986a and b), erupting only late in the eruption when these were overcome due to caldera collapse.

The basal tephras account for up to 10 km^3 of pyroclastic material and contain only type 1 pumice clasts. The eruption of the basal tephra sequence is interpreted as having tapped only the upper part of the magma chamber, and to have been of sufficient volume to have initiated caldera collapse.

The boundary between the basal sequence and the main ignimbrite sequence (and the associated change in magma withdrawal of one composition to three) signifies a radical change in the eruption dynamics i.e. a large increase in mass eruption rate. Such an increase in eruption rate may signify the onset of caldera collapse.

Formation of the caldera is interpreted to have started by the time the middle Mamaku Ignimbrite was erupted. It is postulated that collapse of the caldera was happening throughout the eruption of Mamaku Ignimbrite, but at different rates, accelerating during eruption of middle Mamaku Ignimbrite and again in the closing stages of the eruption. Collapse throughout the eruption is compatible the intra- and extra-caldera thickness variation, the stratigraphic coexistence of pumice types, and late extraction of andesitic blebs. Collapse at different rates is represented by the welding of mMI, and by the increased concentration of lithic fragments in mMI and uMI.

CHAPTER 9
Conclusions

This thesis presents findings from the first major study of Mamaku Ignimbrite and a reinterpretation of Rotorua Caldera structure and evolution.

Mamaku Ignimbrite is a mineralogically monotonous deposit comprising a single unit. It contains no detectable flow unit boundaries and was deposited progressively by a pyroclastic density current that became increasingly less particulate away from source.

Increasing size of lithic fragments and location of lithic lag breccias unequivocally prove that Rotorua Caldera is the source of uMI. Gradational uMI-mMI and mMI-lMI boundaries, and the presence of the same pumice types in uMI and lMI indicate that the whole ignimbrite was sourced from the same location.

Pumice clasts in Mamaku Ignimbrite can be grouped into three types. The more silicic pumice types can be derived from the least silicic type by up to 20 % crystal fractionation. Regular variations in whole pumice chemistry and large trace element concentration ranges, compared to other TVZ rhyolitic ignimbrites, suggest that Mamaku Ignimbrite was sourced from a zoned magma chamber.

Mokai Ignimbrite erupted contemporaneously with Mamaku Ignimbrite and the two have similar pumice chemistry. There are significant differences between the two and they are thus thought to be different.

Eruption of the Mamaku magma chamber probably began with the extrusion of rhyolite domes that were destroyed during the eruption of Mamaku Ignimbrite and became a major lithic lag breccia component. The climactic event commenced with withdrawal of only type 1 magma resulting in the deposition of the basal tephra sequence. Caldera collapse followed and numerous vents allowed the simultaneous eruption of all three silicic magma types present within the chamber. Andesitic magma was erupted only when forced to by continued caldera collapse. After caldera formation the domes of RCR extruded around the area of deepest caldera collapse were likely the last eruptives from the Mamaku magma chamber.

Other rhyolite domes of Rotorua are unrelated to Mamaku Ignimbrite and probably represent evacuation of small, isolated magma chambers typical of TVZ rhyolitic activity between caldera forming events.

TVZ is a zone of active rifting with orthogonal faults that greatly affect caldera structure, morphology and collapse. Rotorua is relatively simple when compared to most TVZ calderas. It is one of only two single event calderas with surface morphologies that are well preserved (the second being Reporoa). Typical caldera models cannot be applied to Rotorua Caldera, or indeed to any of the calderas of TVZ, as pre-existing structures lead to complex caldera floors.

Rotorua Caldera structure comprises a complex caldera floor that has been broken up into rectilinear blocks by orthogonal fault sets. It is elongate in two directions with NE-SW alignment controlled by the dominant TVZ fault pattern and the embayment in the NW governed by a more widely spaced NNW-SSE striking fault set. The caldera floor blocks have subsided asymmetrically to a maximum in the caldera's southwest which is coincident with the low gravity anomaly. The gravity low anomaly within Rotorua Caldera shows a lack of concentricity with the caldera margin and has been used to deny the caldera's existence. However, other calderas show similar gravity-morphology relationships and the large volume Mamaku Ignimbrite was sourced from Rotorua Caldera leaving little doubt about its presence.

The caldera began to form following the eruption of the basal tephra sequence. Collapse proceeded throughout the eruption of the main Mamaku Ignimbrite sequence with two periods of increased collapse rate during the eruption of mMI and uMI.

Rotorua Caldera has characteristics that can be attributed to a number of collapse processes. Decreasing subsidence towards the northeast and northwest indicate trapdoor (asymmetric) subsidence. Features relating to downsag are evident in the northwest and east, piston-like collapse has likely occurred in the area of the gravity low and the existence of numerous caldera floor blocks is consistent with piecemeal collapse. Current methods of describing calderas are deemed too restrictive. Rotorua Caldera is best described as a rhyolitic, single event, asymmetric, multiple-block, single locus caldera. Use of all these terms gives a much clearer picture of the caldera's characteristics and structural evolution.

Acknowledgements

Firstly I would like to thank my supervisors Professor Jim Cole and Dr Peter Wood (IGNS, Wairakei). Above all I thank Jim who suggested the Rotorua/Mamaku project and was full of encouragement throughout the fieldwork and thesis write up and continually had suggestions about future work. Peter always made time available in a busy schedule. His help and direction in the field, and suggestions during writing papers and this thesis were invaluable.

Professor Steve Weaver is thanked for all his help with geochemistry and petrology, for providing extra Mamaku pumice data and suggesting directions and possibilities for investigation. Steve is also thanked for proof reading various chapters of the thesis. Thank you to Associate Professor David Shelley for always helping with problem thin sections, questioning theories that I had (by providing numerous other potential explanations), and general interest in the work I was doing. I am indebted to Mrs Jocelyn Campbell who helped with structural interpretations of Rotorua Caldera reviewed chapters involving caldera structure and pointed out faults with my models. My gratitude is also owed Dr David Nobes for his help with geophysics and participation in a reconnaissance survey at various sites around Rotorua.

Scientists of IGNS, Drs Hugh Bibby, Andy Nicol, George Risk, Colin Wilson, and Mr Grant Caldwell are thanked for discussions involving caldera structure and ignimbrites. Mr Mike Rosenberg is thanked for access to core and rock samples held by IGNS. Dr Ian Nairn is also thanked for discussions about Rotorua and Mamaku Ignimbrite.

Professors Bruce Houghton, and Steve Self, and Dr Mike Branney are also thanked for discussions relating to eruptive processes and caldera collapse mechanisms.

Thanks are owed to all those I had discussions with, notably: Steve Beresford, Tasha Black, Stu Brown, Scott Bryan, Dave Dravitski, Stu Hildyard, Ted Lloyd, Blair Lynch-Blosse, Mitsuhiro Nakagawa, Jens Richnow, Phil Shane, Richard Smith, and Anekant Wandres.

To all the technical staff in the Department of Geological Sciences, University of Canterbury, a huge thank you for helping out with everything. To Rob Spiers for the multitude of thin and polished sections, Stephen Brown for help with XRF and XRD analyses, Cathy Knight for providing field equipment and access to Eng. labs, Jane Guise for help with magnetic mineral separation and allowing use of the project lab, John Southward for his patience with stupid questions and help with computer problems Kerry Swanson for all things photographic, Arthur Nicholas for slide scanning and presentation preparation, and Michelle Wright for employment contracts and Mason Trust advice. To all of you, THANK YOU.

Thank you also to the secretarial staff, Julie-Anne Hale and Joan Mawson. Sorry for keeping all those theses out past their due date Joan and Julie-Anne, I guess that constant harassment finally made me finish.

I am grateful to Dr John Patterson of the Analytical Facility, Victoria University of Wellington, for his guidance with the microprobe and to Neil Andrews of Plant and Microbial Sciences, University of Canterbury, for his instruction with SEM work.

Financial support was provided by a University of Canterbury doctoral scholarship and by the Mason Trust, both of which are gratefully acknowledged. Without the funding from these sources this study would not have become a reality. A Claude McCarthy Fellowship, awarded by the New Zealand Vice Chancellors Committee, funded attendance of the CEV workshop "Inside Silicic Calderas" in the UK. Attendance of this workshop became fundamental to the thesis with a huge understanding gained on caldera structure, and the Claude McCarthy Fellowship I also gratefully acknowledge.

I am deeply indebted to Will Esler, Ash Cody and their families in Rotorua. Ash and Will both assisted me in the field and provided relief and encouragement while I was in Rotorua, and when times were testing, often kept me on the straight and narrow.

Thanks are also deserved by numerous farmers around the Mamaku Plateau, Rotorua, and Mokai for permission to access their land. Superjet (Rotorua tour company) is thanked providing me with a trip out to Mokoia Island.

To the crew at University of Canterbury thanks for all your help. Many discussions with Karl Spinks resulted in ideas that have been included in this thesis. Anekant Wandres pointed out faults in geochemical plots and data presentation. Richard Jongens helped with AutoCAD problems. Graham Leonard helped out with Minpet, other computer problems, and proofread the thesis at a late stage. Darren Gravley also proofread parts of the thesis during the final week before submission. Discussions with Karl, Graham, Anekant and Darren all contributed to the final draft.

Flatties Hamish and Fi thankyou for helping with that late draft and the caldera paper, cooking yummy teas, and making home life enjoyable.

To my family thank you for your support, understanding, and encouragement during my entire time at university. To my sisters Helen, Penny, and Imogen, and brothers-in-law Grant and Mark, thank you for providing places to stay, encouragement and good humour throughout. To mum thanks for constantly offering help and checking up to make sure everything was OK. To dad, thank you for your encouragement and offers of help.

Finally thank you to Sarah for all your love and support, for keeping me sane, picking me up when I was down, and for providing very welcome and much needed breaks from University throughout this work.

Again to all those who kept me going, thank you.

References

Acocella, V., Cifelli, F., and R. Funiciello, 2000, Analogue models of collapse calderas and resurgent domes. Journal of Volcanology and Geothermal Research, v104, p81-96.

Acocella, V., and R. Funiciello, 1999, The interaction between regional and local tectonics during resurgent doming: the case of the island of Ischia, Italy. Journal of Volcanology and Geothermal Research, v88, p109-123.

Andersen, D.J., and D.H. Lindsley, 1988, Internally consistent solution models for Fe-Mg-Mn-Ti oxides: Fe-Ti oxides. American Mineralogist, v73, p714-726.

Aramaki, S., 1984, Formation of Aira Caldera, Southern Kyushu, ~22,000 years ago. Journal of Geophyical Research, v89B, p8485-8501.

Arth, J.G., 1976, Behaviour of trace elements during magmatic processes- a summary of theoretical models and their applications. Journal of Research of the United States Geological Survey, v4, p41-47.

Bacon, C.R., 1983, Eruptive history of Mount Mazama and Crater Lake Caldera, Cascade Range, U.S.A., Journal of Volcanology and Geothermal Research, v18, p57-115.

Bateman, P.C., 1965, Geology and tungsten mineralisation of the Bishop District, California. United States Geological Survey, Professional Paper, No. 470, 208p

Bayrante, L.F., 1984, Structural aspects of the S margin of Rotorua Caldera and their implications to the Rotorua geothermal field, North Island, New Zealand. Geothermal Institute Project Report, No 84.03, 79p.

Bemmelen, R.W. van, 1932, Over de genetische van negatieve vulkaanvormen. Geologie en mijnbouw, No. 1.

Bellamy, S., 1991, Some studies of the Te Wairoa Ignimbrites and the associated volcanic geology of the south western Okataina Volcanic Centre, Taupo Volcanic Zone. Unpublished MSc thesis, University of Waikato, Hamilton.

Beresford, S.W., 1997, Volcanology and Geochemistry of the Kaingaroa Ignimbrite, Taupo Volcanic Zone, New Zealand. PhD thesis, University of Canterbury.

Beresford, S.W., and J.W. Cole, 2000, Kaingaroa Ignimbrite, Taupo Volcanic Zone, New Zealand: evidence for asymmetric caldera subsidence of the Reporoa Caldera. New Zealand Journal of Geology and Geophysics, v43, p471-481.

Berryman, K., Beanland, S., and S. Wesnousky, 1998, Paleoseismicity of the Rotoitipakau Fault Zone, a complex normal fault in the Taupo Volcanic Zone, New Zealand. New Zealand Journal of Geology and Geophysics, v41, p449-465.

Bibby H.M., Dawson, G.B., Rayner, H.H., Stagpoole, V.M., and D.J. Graham, 1984, The structure of the Mokai Geothermal Field based on geophysical observations. Journal of Volcanology and Geothermal Research, v20, p1-20.

Bibby H.M., Dawson, G.B., Rayner, H.H., Bennie, S.L., and C.J. Bromley, 1992, Electrical resistivity and magnetic investigations of geothermal systems in the Rotorua area, New Zealand. Geothermics, v21, p

Black, T.M., 1995, Geochronology, correlation, and magnetic studies of Quaternary ignimbrites in the Taupo Volcanic Zone, New Zealand. Unpublished PhD thesis, University of Auckland.

Black, T.M., Shane, P.A.R., Westgate, J.A., and P.C. Froggatt, 1996, Chronology and palaeomagnetic constraints on widespread welded ignimbrites of the Taupo volcanic zone, New Zealand. Bulletin of Volcanology, v58, p226-238.

Blake, S., Wilson, C.J.N., Smith, I.E.M., and G.P.L. Walker, 1992, Petrology and dynamics of the Waimihia mixed magma eruption, Taupo Volcano, New Zealand. Journal of the Geological Society of London, v149, p193-207.

Blake, S. and G.N. Ivey, 1986a, Magma-Mixing and the dynamics of withdrawal from stratified reservoirs. Journal of Volcanology and Geothermal Research, v27, p153-178.

Blake S., and G.N. Ivey, 1986b, Density and viscosity gradients in zoned magma chambers, and their influence on withdrawal dynamics. Journal of Volcanology and Geothermal Research, v30, p201-230.

Branney, M.J., 1995, Downsag and extension at calderas: new perspectives on collapse geometries from ice-melt, mining, and volcanic subsidence. Bulletin of Volcanology, v57, p303-318.

Branney, M.J., 1988, The subaerial setting of the of the Ordovician Borrowdale Volcanic Group, English Lake District. Journal of the Geological Society of London, v145, p887-890.

Branney, M.J. and B.P. Kokelaar, 1992, A reappraisal of ignimbrite emplacement: progressive aggradation and changes from particulate to non-particulate flow during emplacement of high-grade ignimbrite. Bulletin of Volcanology, v54, p504-520.

Branney, M.J., and B. P. Kokelaar, 1997, Giant bed from a sustained catastrophic density current flowing over topography: Acatlán ignimbrite, Mexico. Geology, v25, p115-118.

Branney, M.J., and B.P. Kokelaar, 1994, Volcanotectonic faulting, soft-state deformation and rheomorphism of tuffs during development of a piecemeal caldera, English Lake District. Geological Society of America Bulletin, v106, p507-530.

Branney, M.J., and N.J. Soper, 1988, Ordovician volcano-tectonics in the English Lake Dustrict. Journal of the Geological Society of London, v145, p367-376.

Briggs, R.M., Gifford, M.G., Moyle, A.R., Taylor, S.R., Norman, M.D., Houghton B.F., and C.J.N. Wilson, 1993, Geochemical zoning and eruptive mixing in ignimbrites from Mangakino volcano, Taupo Volcanic Zone, New Zealand. Journal of Volcanology and Geothermal Research, v56, 175-203.

Briggs, R.M., Hall, G.J., Harmsworth, G.R.., Hollis, A.G., Houghton, B.F., Hughes, G.R., Morgan, M.D., and A.R. Whitbread-Edwards, 1996, Geology of the Tauranga Area. Occasional Report, No. 22, Department of Earth Sciences, University of Waikato, Hamilton, New Zealand. 56p.

Brown, G. and G.W. Brindley, 1980, X-ray diffraction procedures of clay mineral identification. In Brindley, G.W., and G. Brown (eds) *Crystal Structures of Clay Minerals and X-Ray identification*. Mineralogical Society of London. 405p.

Brown, S.J.A.., 1994, Geology and geochemistry of the Whakamaru Group Ignimbrites, and associated rhyolite domes, Taupo Volcanic Zone, New Zealand. Ph.D. thesis, University of Canterbury.

Brown, S.J.A., Wilson C.J.N., Cole, J.W., and J. Wooden, 1998, The Whakamaru group ignimbrites: evidence for reverse tapping of a zoned silicic magmatic system. Journal of Volcanology and Geothermal Research, v84, p1-37.

Buddington, A.F., and D.H. Lindsley, 1964, Iron-titanium oxide minerals and synthetic equivalents. Journal of Petrology, v5, p310-357.

Cagnoli, B., and D.H. Tarling, 1999, The reliability of anisotropy of magnetic susceptibility (AMS) data as flow direction indicators in friable base surge and ignimbrite deposits: Italian examples. Journal of Volcanology and Geothermal Research, v75, p309-320.

Campbell, S.D.G., Reedman, A.J., Howells, M.F., and A.C. Mann, 1987, The emplacement of geochemically distinct groups of rhyolites during the evolution of the Lower Rhyolitic Tuff Formation caldera (Ordovician), North Wales, U.K. Geological Magazine, v124, p501-511.

Cambray, F.W., Vogel, T.A., and J.G. Mills jr, 1995 Origin of compositional heterogeneities in tuffs of the Timber MountainGroup: the relationship between magma batches and magma transfer and emplacement in an extensional environment. Journal of Geophyical Research, v100, p15793-15805.

Carr, R.G., 1984, The Matahina Ignimbrite: Its evolution, including its eruption and post depositional changes. Unpublished Ph.D. thesis, University of Auckland.

Carr, R.G., 1981, A scanning electron microscope study of post-depositional changes in the Matahina Ignimbrite, North Island, New Zealand. New Zealand Journal of Geology and Geophysics, v24, p429-434.

Cas, R.A.F. and J.V. Wright, 1987, Volcanic Successions: modern and ancient. Chapman and Hall, London (publ.). 528p.

Charles, R.W., R.J. Vidale Buden and F. Goff, 1986, An interpretation of the Alteration Assemblages at Sulphur Springs, Valles Caldera, New Mexico. Journal of Geophysical Research, v91, No. B2, p1887-1898.

Civetta, L., Orsi, G., Pappalardo, L., Fisher, R.V., Heiken, G., and M. Ort, 1997, Geochemical zoning, mingling, eruptive dynamics and depositional processes – the Campanian Ignimbrite, Campi Flegrei caldera, Italy. Journal of Volcanology and Geothermal Research, v75, p183-219.

Clough, C.T., Maufe, H.B., and E.B. Bailey, 1909, The cauldron-subsidence of Glen Coe, and the associated igneous phenomena. Quarterly Journal of the Geological Society, London, v65, p611-678.

Cole, J.W., 1990, Structural control and origin of volcanism in the Taupo volcanic zone, New Zealand. Bulletin of Volcanology, v52, p445-459.

Cole, J.W., 1969, Gariboldi Volcanic Complex, Ethiopia. Bulletin Volcanologique, v33,p566-578.

Cole, J.W., Beresford, S.W., Burt, R.M., and A.B.H. Ritchie, 1996, Location and terminology of "caldera" structures in the Taupo Volcanic Zone. Geological Society of New Zealand Miscellaneous Publication v91A, p53

Cole, J.W., Brown, S.J.A., Burt, R.M., Beresford, S.W., and C.J.N. Wilson, 1998, Lithic types in ignimbrites as a guide to the evolution of a caldera complex, Taupo volcanic centre, New Zealand. Journal of Volcanology and Geothermal Research, v80, p217-237.

Cole, J.W., Darby, D.J., and T.A. Stern, 1995, Taupo Volcanic Zone and Central Volcanic Region: Backarc structures of North Island, New Zealand. In *Backarc Basins: Tectonics and Magmatism,* Brian Taylor (ed.). Published by Plenum Press, New York.

Cosgrove, J.W., and Ameen, M.S., 2000, A comparison of the geometry, spatial organization and fracture patterns associated with forced folds and buckle folds. In Cosgrove, J.W. and Ameen, M.S. (eds) *Forced Folds and Fractures.* Geological Society of London Special Publication 169, p7-21.

Cotton, C.A., 1922, Geomorphology of New Zealand. Government Printer, Wellington.

Crafar, W.M., 1974a, Well locations, Rotorua geothermal district. In *Geothermal Resources Survey: Rotorua Geothermal District*. Department of Scientific and Industrial Research Geothermal Report, no. 6, p46-52.

Crafar, W.M., 1974b, Geology of the Rotorua City Geothermal Area. In *Geothermal Resources Survey: Rotorua Geothermal District*. Department of Scientific and Industrial Research Geothermal Report, no. 6, p37-44.

Crook, C.N., and J. Hannah, 1988, Regional horizontal deformation associated with the March 2, 1987, Edgecumbe earthquake, New Zealand. Geophysical Research Letters, v14, p361-364.

Crosby, N., 1998, Quaternary geology and tephrostratigraphy of the north-north-eastern Rotorua region. Unpublished M.Sc. thesis, University of Waikato, Hamilton.

Dade, W.B. and H.E. Huppert, 1996, Emplacement of the Taupo Ignimbrite by a dilute turbulent flow. Nature, v381, p509-512.

Daly, R.A., 1914, Igneous rocks and the depth of the earth. New York

Darby, D.J., Hodgkinson, K.M., and G.M. Blick, 2000, Geodetic measurement of deformation in the Taupo Volcanic Zone, New Zealand: the north Taupo network revisited. New Zealand Journal of Geology and Geophysics, v43, p157-170.

Davy, B., 1992, Seismic reflection profiling on southern Lake Rotorua- Evidence for gas-charged lakefloor sediments. Geothermics, v21, p97-108.

Davy, B.W., and T.G. Caldwell, 1997, Gravity, magnetic and seismic surveys of the caldera complex, Lake Taupo, North Island, New Zealand, New Zealand. Journal of Volcanology and Geothermal Research, v81, p69-89.

Davey, F.J., Henrys, S.A., and E. Lodolo, 1995, Asymmetric rifting in a continental back-arc environment, North Island, New Zealand. Journal of Volcanology and Geothermal Research, v68, p209-238.

De Natale, G., Petrazzuoli, S.M., and F. Pingue, 1997, The effect of collapse structures on ground deformations in calderas. Geophysical Research Letters, v24, p1555-1558.

Decker, R.W., 1987, Dynamics of Hawaiian Volcanoes: An overview. In *Volcanism in Hawaii*. United States Geological Survey Professional Paper, v1350, p997-1018.

de Silva, S.L., 1991, Styles of zoning in central Andean Ignimbrites; insights into magma chamber processes. In Harmon, R.S., and Rapela, E.W., eds, Andean magmatism and its tectonic setting: Boulder, Colorado, Geological Society of America, Special Paper 265, p217-232.

Dravitzki, D.N.R., 1999, The volcanic history and lake sediment characteristics of Paradise Valley, Rotorua. Unpublished MSc thesis, University of Waikato, Hamilton.

Druitt, T.H., 1998, Pyroclastic density currents. In *The Physics of Explosive Volcanic Eruptions*. (Gilbert, J. S., and R.S.J. Sparks eds). Geological Society of London, special publicatio, No. 145, p145-182.

Druitt, T.H., Edwards, L., Mellors, R.M., Pyle, D.M., Sparks, R.S.J., Lanphere, M., Davies, M., and B. Barriero, 1999, *Santorini Volcano*. Geological Society, London, Memoir, No. 19.

Druitt, T.H., and R.S.J. Sparks, 1984, On the formation of calderas during ignimbrite eruptions. Nature, v310, p679-681.

Ellwood, B.B., 1982, Estimates of flow direction for calc-alkaline welded tufss and paleomagnetic data reliability from anisotropy of magnetic susceptibility measurements; San Juan Mountains, Southwest Colorado. Earth and Planetary Science Letters, v59, p303-314.

Ewart A., 1967, The petrography of the central North Island rhyolitic lavas. Part 1- Correlations between the phenocryst assemblages. New Zealand Journal of Geology and Geophysics, v10, p182-197.

Ewart A., 1968, The petrography of central North Island rhyolitic lavas, 2, Regional petrography including note on associated ash flow pumice deposits. New Zealand Journal of Geology and Geophysics, v11, p478- 545.

Ewart, A, and J. Healy, 1965, Rotorua- Volcanic Geology. Department of Industrial and Scientific Research Information Series, No. 50, p10-26.

Fitterman, D.V., 1988, Overview of the structure and geothermal potential of Newberry Volcano, Oregon. Journal of Geophysical Research, v93B, p10059-10066

Fisher, R.V., 1966, Mechanism of deposition from pyroclastic flows. American Journal of Science, v264, p350-363.

Fouque, F., 1879, *Santorin et ses eruptions*. Masson, Paris.

Franklin J.A., Volger, U.W., Szlavin, J., Edmond, J.M., and Z.T. Bieniawski, 1981, Suggested methods for determining water content, porosity, density, absorption and related properties, and swelling and slake-durability index properties. In E.T. Brown (editor) *Rock Characterization, Testing, and Monitoring: IRSM suggested methods.* Pergamon Press (Oxford) England. p81-168.

Fransen, P.J.B., 1982, Geology of of the western Mamaku Plateau and variations in the Mamaku Ignimbrite. Unpublished M.Sc. thesis, University of Waikato, Hamilton.

Fransen, P.J.B., and B.M. Sharp, 1988, BP Oil New Zealand Limited, Report on geology, geophysics and drilling, PL 31-1820 (Forest Rd North), Taupo.

Fridrich, C.J., Smith, R.P., DeWitt, E., and E.H. McKee, 1991, Structural, eruptive and intrusive evolution of the Grizzly Peak caldera, Sawatch Range, Colorado. Geological Society of America Bulletin, v103, p1160-1177.

Gamble, J.A., Wright, I.C., and J.A. Baker, 1993, Seafloor geology and petrology in the oceanic to continental transition zone of the Kermadec-Havre-Taupo Volcanic system. New Zealand Journal of Geology and Geophysics, v36, p427-435.

Gardner, J.E., and S. Tait, 2000, The caldera-forming eruption of Volcan Ceboruco, Mexico. Bulletin of Volcanology, v62, p20-33.

Ghiorso, M.S., and R.O. Sack, 1991, Fe-Ti oxide geothermometry: thermodynamic formulation and the estimation of intensive variables in silicic magmas. Contributions to Mineralogy and Petrology, v108, p485-510.

Given, I.A., 1973, *Mining Engineering Handbook.* Part City Press, New York.

Graham, I.J., Cole, J.W., Briggs, R.M., Gamble, J.A., and I.E.M. Smith, 1995, Petrology and petrogenesis of volcanic rocks from the Taupo Volcanic Zone: a review. Journal of Volcanology and Geothermal Research, v68, p59-87.

Grange L.I., 1937, The geology of the Rotorua-Taupo subdivision: Rotorua and Kaimanawa divisions. New Zealand Geological Survey Bulletin, No. 37, 132p.

Gudmundsson, A., 1987, Lateral magma flow, caldera collapse, and a mechanism of large eruptions in Iceland. Journal of Volcanology and Geothermal Research, v34, p65-78.

Gudmundsson, A., 1988, Formation of collapse calderas. Geology, v16, p808-810.

Gudmundsson, A., 1998, Formation and development of normal-fault calderas and the initiation of large explosive eruptions. Bulletin of Volcanology, v60, p160-171.

Gudmundsson, A., Marti, J., and E. Turon, 1997, Stress fields generating ring faults in volcanoes. Geophysical Research Letters, v24, p1559-1562.

Halinan, S., 1993, Non-chaotic collapse at funnel calderas: Gravity study of the ring fractures at Guayabo Caldera, Costa Rica. Geology, v21, p367-370.

Healy, J., 1963, Geology of the Rotorua district., Proceedings of the New Zealand Ecological Society, v10, p53-58.

Healy, J., 1964, Volcanic mechanisms in Taupo Volcanic Zone, New Zealand. New Zealand Journal of Geology and Geophysics, v7, p6-23.

Healy, J., Schofield, J.C., and B.N. Thompson, 1964, Sheet 5, Rotorua. Geological Map of New Zealand.

Herrero-Bervera E., Helsley C.E., Sarna-Wojcicki A..M., Lajoie K.R., Meyer, C.E., McWilliams, M.O., Negrini R.M., Turrin, B.D., Donnelly-Nolan, J.M., and J.C. Liddicoat, 1994, Age and correlation of a paleomagnetic episode in the western United States by $^{40}Ar/^{39}Ar$ dating and tephrochronology: the Jamaica, Blake or a new polarity episode? Journal of Geophyical Research, v99, p24091-24103.

Hervig, R.L., and N.W. Dunbar, 1992, Cause of chemical zoning in the Bishop (California) and Bandelier (New Mexico) magma chambers. Earth and Planetary Science Letters, v111, p97-108.

Hildreth, W., 1981, Gradients in silicic magma chambers: Implications for silicic magmatism. Journal of Geophyical Research, v86, p10153-10192.

Hildreth, W., 1991, The timing of caldera collapse at Mount Katmai in response to magma withdrawal toward Novarupta. Geophysical Research Letters, v18, p1541-1544.

Hildreth, W., and G.A. Mahood, 1986, Ring fracture eruption of the Bishop Tuff. Geological Society of America Bulletin, v97, p396-403.

Hildyard, S.C., Cole, J.W., and S.D. Weaver, 2000, Tikorangi Ignimbrite: a 0.89 Ma mixed andesite-rhyolite ignimbrite, Matahana Basin, Taupo Volcanic Zone, New Zealand. New Zealand Journal of Geology and Geophysics, v43, p95-107.

Hochstein, M.P., I.E.M. Smith, K. Regen-Lieb, and S. Ehara, 1993, Geochemistry and heat transfer processes in Quaternary rhyolitic systems of the Taupo Volcanic Zone, New Zealand. Tectonophysics, v223, p213-235.

Hochstetter, F. von., 1864, *Geology of New Zealand: Contributions to the geology of the provinces of Auckland and Nelson*. Translated from German and edited by C.A. Fleming, 1959. R.E. Owen, Government printer, Wellington. 319p.

Houghton, B.F., Wilson, C.J.N., McWilliams, M.O., Lanphere, M.A., Weaver, S.D., Briggs, R.M. and M.S. Pringle, 1995, Chronology and Dynamics of a large silicic magmatic system: Central Taupo Volcanic Zone, New Zealand. Geology, v23, p13-16.

Houghton, B.F., C.J.N. Wilson, E.F. Lloyd, J.A, Gamble, and B.P, Kokelaar, 1987, A catalogue of basaltic deposits within the Taupo Volcanic Zone. New Zealand Geological Survey Record, v18, p95-101.

Houghton B.F., Weaver, S.D., Wilson, C.J.N., and M.A. Lanphere, 1992, Evolution of a Quaternary peralkaline volcano: Mayor Island, New Zealand. Journal of Volcanology and Geothermal Research, v51, p217-236.

Howells, M.F., Campbell, S.D.G., Reedman, A.J., and S.P. Tunnicliff, 1987, A fissure-controlled acidic volcanic center (Ordivician) at Yr Arddu, North Wales. Geological Journal, v22, p133-149.

Hughes, G.R., 1993, Volcanic geology of the eastern Tauranga Basin and Papamoa Range. Unpublished M.Sc. thesis, University of Waikato.

Hunt, T.M., 1992, Gravity anomalies, caldera structure, and subsurface geology in the Rotorua area, New Zealand. Geothermics, v21, p65-74.

Irwin, J., 1969, Lake Rotorua, Provisional Bathymetry, Fish Research Division, Lake Series, 1: 15,840).

John, D.A., 1995, Tilted middle Tertiary ash-flow calderas and subjacent granitic plutons, southern Stillwater Range, Nevada: Cross section of an Oligocene igneous center. Geological Society of America Bulletin, v107, p180-200.

Johnson, R.W., 1969, Volcanic geology of Mt Suswa, Kenya. Philosophical Transactions of the Royal Society of London, Series A, v265, p383-412.

Jones, W.M., 1940, Variations of vertical magnetic intensity at Rotorua, and their relation to the thermal activity. New Zealand Journal of Science and Technology, v21B, p289-296.

Kane, M.F., Mabey, D.R., and R-L Brace, 1976, A gravity and magnetic investigation of the Long Valley caldera, Mono County, California. Journal of Geophysical Research, v81, p754-762

Karatson, D., Thouret, J.C., Moriya, I., and A. Lomoschitz, 1999, Erosion calderas; origins, processes, structural, and climatic control. Bulletin of Volcanology, v61, p174-193.

Karhunen, R.A., 1993, The Pokai and Chimp ignimbrites of the Taupo Volcanic Zone. Unpublished Ph.D. thesis. University of Canterbury.

Keiller, I.G., 1987, Geology of the Southern Mamaku Plateau. Unpublished BSc. Honours project. University of Otago.

Keith, T.E.C., 1984, Preliminary observations on fumarole distribution on fumarole distribution and alteration, Valley of Ten Thousand Smokes, Alaska. In "The United States Geological Survey in Alaska: Accomplishments during 1982." USGS circular 939, p82-85.

Kennedy, N.M., 1994, New Zealand tephrochronology as a tool in geomorphic history of the c. 140 ka Mamaku Ignimbrite Plateau and in relating oxygen isotope stages. Geomorphology, v9, p97-115

Kennedy, N.M., Pullar, W.A., and C.F. Pain, 1978, Late Quaternary land surfaces and geomorphic changes in the Rotorua Basin, North Island New Zealand. New Zealand Journal of Science, v21, p249-264.

Knight, M.D., Walker, G.P.L., Ellwood, B.B., and J.F. Diehl, 1986, Stratigraphy, paleomagnetism, and magnetic fabric of the Toba tuffs; constraints on the sources and eruptive styles. Journal of Geophysical Research, v91B, p10,355-10,382.

Kokelaar, B.P., 1993, Volcaniclastic density currents: Basic concepts and definitions. In J. McPhie (ed) *Explosive Volcanism: Processes and Products.* CEV Short Course, Canberra, p7.1-7.7.

Kokelaar, B.P., and M.J. Branney, *Inside silicic calderas (Snowdon, Scafell, and Glencoe, UK): Interaction of caldera development, tectonism and hydrovolcanism.* CEV Field Workshop, Guidebook. 150p.

Kokelaar, P., 1988, Tectonic controls of Ordivician arc and marginal basin volcanism in Wales. Journal of the Geological Society, London, v145, p759-775.

Komuro, H., 1987, Experiments on cauldron formation: a polygonal cauldron and ring fractures. Journal of Volcanology and Geothermal Research, v31, p139-149.

Komuro, H., Fujita, Y., and K. Kodama, 1984, Numerical and experimental models on the formation mechanism of collapse basins during the Green Tuff orogenesis of Japan. Bulletin Volcanologique, v47, p649-666.

Kuno, H., Oki, T., Ogino K., and S. Hirota, 1970, Structure of Hakone Caldera as revealed by drilling. Bulletin of Volcanology, v34, p713-725.

Lamarche, G., 1992, Seismic reflection survey in the geothermal field of the Rotorua Caldera, New Zealand. Geothermics, v21, p109-120.

Le Maitre, R.W. (ed), 1989, *A classification of igneous rocks and glossary of terms.* Blackwell, Oxford.

Legros, F., Kelfoun, K., and J. Marti, 2000, The influence of conduit geometry on the dynamics of caldera-forming eruptions. Earth and Planetary Science Letters, v179, p53-61.

Leonard, G.S., Cole, J.W., Nairn, I.A., and S. Self, submitted, Basalt triggering of the c.1350 AD Kaharoa rhyolite eruption, Tarawera Volcanic Complex, New Zealand. Journal of Volcanology and Geothermal Research.

Lipman, P.W., 2000, Calderas. In Sigurdsson, H. (editor-in-chief), *Encyclopedia of Volcanoes,* Academic Press, San Francisco (publ.). p643-662.

Lipman, P.W., 1997, Subsidence of ash-flow calderas: relation to caldera size and magma chamber geometry. Bulletin of Volcanology, v59, p198-218.

Lipman, P.W., 1984, The roots of ash flow calderas in western North America: Windows into the tops of granitic batholiths. Journal of Geophyical Research, v89B, p8801-8841.

Lipman, P.W., Self, S., and G. Heiken, 1984, Introduction to Calderas Special Issue. Journal of Geophyical Research, v89B, p8219-8221

Lipman, P.W., Dungan, M., and O. Bachman, 1997, Comagmatic granophyric granite in the Fish Canyon Tuff, Colorado: Implications for magma-chamber processes during a large ash-flow eruption. Geology, v25, p915-918.

Lisle, R.J., 1994, Detection of zones of abnormal strains in structures using Gaussian curvature analysis. American Association of Petroleum Geologists Bulletin, v78, p1811-1819.

Lloyd, E.F., 1975, Geology of Whakarewarewa hot springs. New Zealand Department of Industrial and Scientific Research Information Series, no. 111, 23p.

Lovering, T.S., 1957, Halogen acid alteration of the ash at fumarole NO. 1, Valley of Ten Thousand Smokes, Alaska. Bulletin of the Geological Society of America, v68, p1585-1604.

Lynch-Blosse, B.R., 1998, Ignimbrite Stratigraphy of the Southern Mamaku Region, North Island, New Zealand. Unpublished M.Sc. thesis. University of Waikato.

McCormick, T.C., 1990, Vapor-phase alteration in the Green Ignimbrite, Pantelleria. Eos, Transactions, American Geophysical Union, v71, p1700.

Macdonald, W.D., and H.C. Palmer, 1990, Flow directions in ash-flow tuffs; a comparison of geological and magnetic susceptibility measurements Tshirege Member (upper Bandelier Tuff), Valles Caldera, New Mexico, USA. Bulletin of Volcanology, v53, p45-59.

Macdonald, W.J.P., 1974, Geophysical Investigation of the Rotorua Geothermal District. In *Geothermal Resources Survey: Rotorua Geothermal District*. Department of Scientific and Industrial Research Geothermal Report, no. 6, p53-77.

Macleod, N.S., and D.R. Sherrod, 1988, Geologic evidence for a magma chamber beneath the Newberry Volcano, Oregon, Journal of Geophysical Research, v93B, p10067-10079.

McPhie, J., Doyle, M., and R. Allen, 1993, *Volcanic Textures: A guide to the interpretation of textures in volcanic rocks.* Tasmanian Governmaent Printing Office, Hobart (Publ.). 198p.

Mahood, G.A., 1983, Calderas in strongly peralkaline systems. Eos, Transactions of the American Geophysical Union, v64, No. 45, p883.

Mahood, G.A., 1984, Pyroclastic rocks and calderas associated with strongly peralkaline magmatism. Journal of Geophysical Research, v89B, p8540-8552.

Mahood, G., and W. Hildreth, 1983, Nested calderas and trapdoor uplift at Pantelleria, Strait of Sicily. Geology, v11, p722-726.

Mahood, G.A., and W. Hildreth, 1986, Geology of the peralkaline volcano at Pantelleria, Strait of Sicily. Bulletin of Volcanology, v48, p143-172.

Maniar, P.D., and P.M. Piccoli, 1989, Tectonic discrimination of granitoids. Geological Society of America Bulletin, v101, p635-643.

Manning, D.A., 1996, Middle-late Pleistocene tephrostratigraphy of the eastern Bay of Plenty, New Zealand. Quaternary International, v34-36(1), p3-12.

Marshall, P., 1905, The Geography of New Zealand. Whitcombe and Tombs, Wellington, New Zealand.

Marshall, P., 1912, Geology of New Zealand. Government Printer, Wellington, New Zealand. p107-114

Marshall, P., 1935, Acid rocks of the Taupo-Rotorua district. Transactions of the Royal Society of New Zealand. v64, p323-375.

Marti, J., Ablay, G.J., Redshaw, L.T., and R.S.J. Sparks, 1994, Experimental studies of caldera collapse. Journal of the Geological Society, London, v151, p919-929.

Marti, J. and A. Gudmundsson, 2000, The Las Canadas caldera (Tenerife, Canary Islands): an overlapping collapse caldera generated by magma-chamber migration. Journal of Volcanology and Geothermal Research, v103, p161-173.

Modriniak, N., 1949, Geophysical Investigation of Rotorua. New Zealand Journal of Science and Technology, v30, p1-19.

Moore, I., and P. Kokelaar, 1998, Tectonically controlled piecemeal caldera collapse: A case study of Glencoe volcano, Scotland. Geological Society of America Bulletin, v110, p1446-1466.

Moore, I. and P. Kokelaar, 1997, Tectonic influences in piecemeal caldera collapse and Glencoe volcano, Scotland. Journal of the Geological Society of London, v154, p765-768.

Morgan, M.D., 1986, Geology of the northern Mamaku Plateau. Unpublished M.Sc. thesis, University of Waikato.

Mori, J., and C. McKee, 1987, Outward-dipping ring-fault structure at Rabaul Caldera as shown by earthquake locations. Science, v235, p193-195

Mouginis-Mark, P.J., and M.S. Robinson, 1992, Evolution of Olympus Mons Caldera, Mars, Bulletin of Volcanology, v54, p347-360.

Murphy, R.P. and D. Seward, 1981, Stratigraphy, lithology, paleomagnetism and fission track ages of some ignimbrite formations in the Matahana basin. New Zealand Journal of Geology and Geophysics, v24, p325-331.

Munro, D.C., and S.K. Rowland, 1996, Caldera morphology in the western Galapagos and implications for volcano eruptive behaviour and mechanisms of caldera formation. Journal of Volcanology and Geothermal Research, v72, p85-100.

Nairn, I.A., 1974, Summary, comment and recommendations for drillhole sites. In *Geothermal Resources Survey: Rotorua Geothermal District.* Department of Scientific and Industrial Research Geothermal Report, no. 6, p114-120.

Nairn, I.A., 1989, Sheet V16 AC, Mount Tarawera. Geological Map of New Zealand 1:50,000.

Nairn, I.A. and Wood, C.P., 1987, Active Volcanoes and Geothermal Systems, Taupo Volcanic Zone. In *Active volcanoes and geothermal systems, Taupo Volcanic Zones.* New Zealand Geological Survey Record, No. 22, p5-84.

Nairn, I.A., Wood, C.P., and R.A., Bailey, 1994, The Reporoa caldera, Taupo Volcanic Zone: source of the Kaingaroa Ignimbrites. Bulletin of Volcanology, v56, p529-537.

Nappi, G., Antonelli, A., Coltorti, M., Milani, L., Renzulli, A., and F. Siena, 1998, Volcanological and petrological evolution of the eastern Vulsini District, central Italy. Journal of Volcanology and Geothermal Research, v87, p211-232.

Nappi G., Renzulli, A., and P. Santi, 1991, Evidence of incremental growth in the Vulsinian calderas (central Italy). Journal of Volcanology and Geothermal Research, v47, p13-31.

Nash, W.P., and H.R. Crecraft, 1985, Partition coefficients for trace elements in silicic magmas. Geochimica et Cosmochimica Acta, v49, p2309-2322.

Nathan, S., 1975, Notes on the petrology of the Mamaku Ignimbrite and associated rocks. Unpublished report. New Zealand Geological Survey, Rotorua.

Nathan, S., 1976, Geology of the Rotorua district. In Nathan, S. (compiler), Excursion Guide No. 55a and 56a, 25th International Geological Congress.

Nishimura, S., Abe, E., Nishida, J., Yokoyama, T., Dharma, A., Hehanussa, P., and F. Hehuwat, 1984, A gravity and volcanostratigraphic interpretation of the Lake Toba Region, North Sumatra, Indonesia. Tectonophysics, v109, p253-272.

Norrish, K., and J. Hutton, 1969, An accurate X-ray spectrographic method for the analysis of a wide range of geological samples. Geochimica et Cosmochimica Acta, c33, p431-453.

Oskarsson, N., 1981,The chemistry of Icelandic lava incrustations and the latest stages of degassing. Journal of Volcanology and Geothermal Research, v10, p93-111.

Odonne, F., Menard, I., Messonnat, G.J., Rolando, J.P., 1999, Abnormal reverse faulting above a depleting reservoir. Geology, v27, p111-114.

Orsi, G., Gallo, G., and A. Zanchi, 1991, Simple-shearing block resurgence in caldera depressions. A model from Pantelleria and Ischia. Journal of Volcanology and Geothermal Research, v47, p1-11.

Orsi, G., Civetta, L., D'Antonio, M., Di Girolamo, P., and M. Piochi, 1995, Step-filling and development of a three-layer magma chamber: the Neapolitan Yellow Tuff case history. Journal of Volcanology and Geothermal Research, v67, p291-312.

Ort, M.H., Rosi, M., and C.D. Anderson, 1999, Correlation of deposits and vent locations of the proximal Campanian Ignimbrite deposits, Campi Flegrei, Italy, based on natural remanent magnetisation and anisotropy of magnetic susceptibility. Journal of Volcanology and Geothermal Research, v91, p167-178.

Pakiser, L.C., 1961, Gravity, volcanism, and crustal deformation in Long Valley, California. United States Geological Survey Professional Paper, No. 424-B, pB250-B253.

Palladino, D.M., and G.A. Valentine, 1995, Coarse-tail vertical and lateral grading in pyroclastic flow deposits of the Latera Volcanic Complex (Vulsini, central Italy): origin and implications for flow dynamics. Journal of Volcanology and Geothermal Research, v69, p343-364.

Papike, J.J., 1992, The Valley of Ten Thousand Smokes, Alaska: A unique geochemistry laboratory. Geochimica et Cosmochimica Acta, v56, p1429-1449.

Papike, J.J., T.E.C. Keith, M.N. Spilde, K.C. Galbreath, C.K. Shearer and J.C. Laul, 1991, Geochemistry and mineralogy of fumarolic deposits, Valley of Ten thousand Smokes, Alaska: Bulk chemical and mineralogical evolution of dacite rich protolith.American Mineralogist, v76, p1662-1673.

Park, J., 1910, Geology of New Zealand. Whitcombe and Tombs, Wellington, New Zealand. p116-181

Pearce, J.A., Harris, N.B.W., and A.G. Tindle, 1984, Trace element discrimination diagrams for the tectonic interpretation of granitic rocks. Journal of Petrology, v25, p956-983.

Pettinga, J.R., Chamberlain, C.G., Yetton, M.D., Van Dissen, R.J., and G. Downes, 1998, Earthquake Source Identification and Characterisation. Canterbury Regional Council Publication No. U98/10.

Reck, H., 1936, Santorin, der Werdegang eines Inselvulkans und sein Ausbruch 1925-1928. Berlin. 3 vols

Reed, A.W., 1958, *Legends of Rotorua*. Reed publishing, Auckland. 163p.

Richard, P., 1990, Champs de Failles Audessus d'un Decrochment de Socle: Modelisation Experimentale. Unpublished PhD thesis, University of Rennes, France.

Richard, 1991, Experiments on faulting in a two layer cover sequence overlying a reactive basement fault with oblique slip. Journal of Structural Geology, v13, p459-470.

Ritchie, A.B.H., 1996, Volcanic Geology and Geochemistry of Waiotapu Ignimbrite, Taupo Volcanic Zone, New Zealand. Unpublished M.Sc. thesis, University of Canterbury.

Ross, C.S. and R.L. Smith, 1961, Ash-flow tuffs, their origin, geological relations and identification. United States Geological Survey, Professional Paper 366, p1-77.

Roche, O., Druitt, T.H., and O. Merle, 2000, Experimental study of caldera formation. Journal of Geophysical Research, v105B, p395-416.

Rochette, P., Lamarche, G., and C. Aubourg, 1992, Rock magnetism and interpretation of anisotropy of magnetic susceptibility. Reviews of Geophysics, v30, p4073-4088.

Rogan, M, 1982, A geophysical study of the Taupo Volcanic Zone, New Zealand. Journal of Geophyical Research, v87, p4073-4088.

Rollinson, H., 1993, *Using geochemical data: evaluation, presentation and interpretation*. Longman (publisher), 352p.

Roman-Berdiel, T., Gapais, D., and J.P. Bruin, 1995, Analogue models of laccolith formation. Journal of Structural Geology, v17, p1337-1346.

Rowland J.V., and R.H. Sibson, 1999, Extensional kinematics of the Ruaumoko rift system: Variable soft-linkage between offset spreading segments in the Taupo Volcanic Zone, New Zealand. Geological Society of New Zealand Miscellaneous publication, v107A, p141.

Rymer, H., van Wyk de Vries, B., Stix, J., and G. Williams-Jones, 1998, Pit crater structure and processes governing persistent activity at Masaya Volcano, Nicaragua. Bulletin of Volcanology, v59, p345-355.

Sack, R..O., and M.S. Ghirso, 1991, An internally consistent model for the thermodynamic properties of Fe-Mg-titanomagnetite-aluminate spinels. Contributions to Mineralogy and Petrology, v106, p474-505.

Sanderson, D.J., and Marchini, W.R.D., 1984, Transpression. Journal of Structural Geology, v6, p449-458.

Scandone, R., 1990, Chaotic collapse caldeas. Journal of Volcanology and Geothermal Research, v42, p285-308.

Schmincke, H-U., 1967, Cone sheet warm, resurgence of Tejeda caldera, and early geologic history of Gran Canaria. Bulletin Volcanologique, v31, p153-162.

Self, S., Goff, G., Gardner, J.N., Wright, J.V., and W.M. Kite, 1986, Explosive rhyolitic volcanism in the Jemez Mountains: Vent locations, caldera development and relation to regional structure. Journal of Geophyical Research, v91B, p1779-1798.

Self, S., and M.R. Rampino, 1981, The 1883 eruption of Krakatau. Nature, v294, p699-704.

Shane, P., Black, T., and J. Westgate, 1994, Isothermal plateau fission track age for the paleomagnetic excursion in the Mamaku Ignimbrite, New Zealand, and implications for late Quaternary stratigraphy. Geophysical Research Letters, v21, p1695-1698.

Shelley, D., 1993, Igneous and Metamorphic Rocks under the Microscope. Chapman and Hall (publ.). 445 pages.

Shepherd, A.D., 1991, Volcanology and petrology of the post-caldera rhyolite domes, Rotorua Volcanic Centre, New Zealand. Unpublished Bsc Hons thesis, Victoria University of Wellington, Wellington.

Sheridan, M.F., 1970, Fumarolic mounds and ridges of the Bishop Tuff, California. Geological Society of America Bulletin, v81, p851-868.

Sheridan, M.F., 1979, Emplacement of pyroclastic flows: A review. Geological Society of America Special Paper 180, p125-136.

Sigurdsson, H., and R.S.J. Sparks, 1978, Lateral magma flow within rifted Icelandic crust. Nature, v274, 126-130.

Simkin, T., and R.S. Fiske, 1983, "Krakatau 1883: The Volcanic Eruption and its Effects." Smithsonian Institution Press, Washington, DC.

Simkin, T., and K.A. Howard, 1970, Caldera collapse in the Galapagos Islands, 1968. Science, v169, p429-437.

Sissons, B.A., 1979, The horizontal kinematics of the North Island of New Zealand. Ph. D. thesis, Victoria University of Wellington.

Smith, E.G.C., and T.H. Webb, 1986, The seismicity and related deformation within the Central Volcanic Region, New Zealand. In Smith, I.E.M. (ed) *Late Cenozoic volcanism in New Zealand*. Royal Society of New Zealand Bulletin, v23, p112-133.

Smith, R.L., 1979, Ash-flow magmatism., In *Ash-flow Tuffs,* Chapin, C.E., and Elston, W.E. (eds). Geological Society of America, Special Paper 180, p5-28.

Smith, R.L., 1960a, Ash flows. Bulletin of the Geological Society of America, v71, p795-842.

Smith, R.L., 1960b, Zones and zonal variations in welded ash-flow tuffs. United States Geological Survey Professional Paper 354-F.

Smith, R.L., and R.A. Bailey, 1968, Resurgent cauldrons. In Coats, R.R., Hay, R.L., and C.A. Anderson (eds), *Studies in Volcanology*. Geological Society of America Memoir, V116, P613-662.

Smith, R.T., 1998, Eruptive and depositional models for units 3 and 4 of the 1.85 Ka Taupo Eruption. Ph.D. thesis, University of Canterbury.

Smith, R.T., and B.F. Houghton, 1995, Vent migration and changing eruptive style during the 1800a Taupo eruption: new evidence from the Hatepe and Rotongaio phreatoplinian ashes. Bulletin of Volcanology, v57, p432-439.

Sparks, R.S.J., S. Self and G.P.L. Walker, 1973, Products of Ignimbrite Eruptions. Geology, v1, p115-118.

Sparks, R.S.J., 1976, Grain size variations in ignimbrites and implications for the transport of pyroclastic flows. Sedimentology, v23, p147-188.

Spera, F.J., and J.A. Crisp, 1981, Eruption volume, periodicity, and caldera area: Relationships and inferences on development of compositional zonation in silicic magma chambers. Journal of Volcanology and Geothermal Research, v11, p169-187.

Stafford, D., 1999, *Pakiwaitara: Te Arawa Stories of Rotorua as told to Don Stafford*. Reed publishing, Auckland. 118p.

Stearns, D.W., 1978, Faulting and forced folding in the Rocky Mountains foreland. Geological Society of America Memoir 151, p1-37.

Stern, T.A., 1987, Asymmetric back-arc spreading, heat flux and structure associated with the Central Volcanic Region of New Zealand. Earth and Planetary Science Letters, v85, p265-275.

Steven, T.A., and P.W. Lipman, 1976, Calderas of the San Juan volcanic field, southwestern Colorado. United States Geological Survey Professional Paper 958, 35p.

Stimac, J., D. Hickmott, R. Abell, A.C.L. Larocque, D. Broxton, J. Gardner, S. Chipera, J. Wolff, E. Gauerke, 1996, Redistribution of Pb and other volatile trace metals during eruption, devitrification, and vapor-phase crystallization of the Bandelier Tuff, New Mexico. Journal of Volcanology and Geothermal Research, v73, p245-266.

Streck, M.J. and A.L. Grunder, 1995, Crystallization and welding variations in a widespread ignimbrite sheet; the Rattlesnake Tuff, eastern Oregon, USA. Bulletin of Volcanology, v57, p151-169.

Sun, S.-s. and W.F. McDonough, 1989, Chemical and isotopic systematics of ocean basalts: implications for mantle composition and processes. In Saunders, A.D., and M.J. Norry, *Magmatism in the Ocean Basins*. Geological Society Special Publication, No. 42, p315-345.

Sutton, A.N., Blake, S., and C.J.N. Wilson, 1995, An outline geochemistry of rhyolite eruptives from Taupo volcanic centre, New Zealand. Journal of Volcanology and Geothermal Research, v68, p153-175.

Taubeneck, W.H., 1967, Notes on the Glencoe Cauldron subsidence, Argyllshire, Scotland. Geological Society of America Bulletin, v78, p1295-1316.

Tanaka, H., Turner, G.M., Houghton, B.F., Tachibana, T., Kono, M. and M.O. McWilliams, 1996, Palaeomagnetism and chronology of the central Taupo Volcanic Zone, New Zealand. Geophysical Journal, v124, p1-16.

Tanakadate, H., 1930, The problem of calderas in the Pacific Region. Proceedings of the 4th Pacific Science Congress, Batavia, v2b, p730-744.

Thomas, L.J., 1973, *An Introduction to Mining*. R. Burton Printers Ltd, Sydney, 471p.

Thompson, B.N., 1958, Kaituna River Hydro Development. Geological Report on Te Akau, Te Tuararoa, and Pakotore schemes. Unpublished Report, New Zealand Geological Survey, Rotorua.

Thompson, B.N., 1963, Te Akau 18. Unpublished core log and report for the Kaituna River hydro scheme. Lodged with Institute of Geological and Nuclear Sciences, Wairakei.

Thompson, B.N., 1964, Quaternary volcanism of the Central Volcanic Region. New Zealand Journal of Geology and Geophysics, v7, p45-65.

Thompson, B.N., 1974, Geology of the Rotorua geothermal district. In *Geothermal Resources Survey: Rotorua Geothermal District*. Department of Scientific and Industrial Research Geothermal Report, no. 6, p10-36.

Tibaldi, A., and L. Vezzoli, 2000, Late Quaternary monoclinal folding induced by caldera resurgence at Ischia, Italy. In *Forced Folds and Fractures*. Geological Society of London Special Publication, No. 169, p103-113.

Trial, A.F., and F.J. Spera, 1990, Mechanisms for the generation of compositional heterogeneities in magma chambers. Geological Society of America Bulletin, v102, 353-367.

Valentine, G.A., 1987, Stratified flow in pyroclastic surges. Bulletin of Volcanology, v49, p504-520.

Verbeek, R.D.M., 1885, *Krakatau*. Batavia. 495p.

Vidal, V., 1961, *Explotation des Mines*. Dunod, Paris.

Walcott R.I., 1987, Geodetic strain and the deformational history of the North Island of New Zealand during the late Cainozoic. Philosophical Transactions of the Royal Society of London A, v321, p163-181.

Walker, G.P.L., 1988, Three Hawaiian calderas: An origin through loading by shallow intrusions? Journal of Geophyical Research, v93B, p14773-14784.

Walker, G.P.L., 1984, Downsag calderas, ring faults, caldera sizes, and incremental caldera growth. Journal of Geophyical Research, v89B, p8407-8416.

Walker, G.P.L., 1983 Grain-size characteristics of pyroclastic deposits. Journal of Geology, v79, p696-714.

Walker, G.P.L., 1985, Origin of coarse lithic breccias near ignimbrite source vents. Journal of Volcanology and Geothermal Research, v25, p157-171.

Walker, G.P.L., C.J.N. Wilson and P.C. Frogatt, 1981, An ignimbrite veneer deposit: the trail marker of a pyroclastic flow. Journal of Volcanology and Geothermal Research, v8, p409-421.

Walker, J.A., Williams, S.N., Kalamarides, R.I., and M.D. Feigenson, 1993, Shallow open-system evolution of basaltic magma beneath a subduction zone volcano: the Masaya Caldera Complex, Nicaragua. Journal of Volcanology and Geothermal Research, v56, p379-400.

Walker, R.T., 1928, Mineralized volcanic explosion pipes. Engineering and Mining Journal, v126, p895-898.

Wan, T., and J.W. Hedenquist, 1981, A reassessment of the structural control of the Broadlands Geothermal Field, New Zealand. Proceedings of the New Zealand Geothermal Workshop, 1981, p195-202.

Watson-Munro, C.N., 1938, Reconnaisance survey of the variation of magnetic force in the New Zealand Thermal Regions. New Zealand Journal of Science and Technology, v20B, p99-115.

Wheller, G.E., and R. Varne, 1986, Genesis of dacitic magmatism at Batur Volcano, Bali Indonesia: Implications for the origins of stratovolcano calderas. Journal of Volcanology and Geothermal Research, v28, p363-378.

Whitbread-Edwards, A.N., 1994, The volcanic geology of the Western Tauranga Basin. Unpublished M.Sc. thesis, University of Waikato.

Williams, H., 1941, Calderas and their origin. University of California publications. Bulletin of the Department of Geological Sciences, v25, p239-346.

Williams, H., and A.R. McBirney, 1979, *Volcanology*. Freeman, Cooper and Co., San Francisco (publ.). 397p

Williams, S.N., and R.E. Stoiber, 1983, "Masaya-type caldera"- Redefined as the mafic analogue of "Krakatau-type caldera". Eos, Transactions of the American Geophysical Union, v64, No.45, p877

Wilson, C.J.N., Houghton, B.F., and E.F. Lloyd, 1986, Volcanic history and evolution of the Maroa-Taupo Area, Central North Island. In *Late Cenozoic Volcanism in New Zealand,* I.E.M. Smith (ed.). Royal Society of New Zealand, Bulletin 23, p194-223.

Wilson, C.J.N., A.M. Rogan, I.E.M. Smith, D.J. Northey, I.A. Nairn and B.F. Houghton, 1984, Caldera Volcanoes of the Taupo Volcanic Zone, New Zealand. Journal of Geophysical Research, v89, p8463-8484.

Wilson, C.J.N., Houghton B.F., McWilliams, M.O., Lanphere, M.A., Weaver, S.D., and R.M. Briggs, 1995, Volcanic and structural evolution of Taupo Volcanic Zone: a review. Journal of Volcanology and Geothermal Research, v68, p1-28.

Wilson, C.J.N., and W. Hildreth, 1997, The Bishop Tuff: New insights from eruptive stratigraphy. Journal of Geology, v105, p407-439.

Wilson, C.J.N., and G.P.L. Walker, 1982, Ignimbrite depositional facies: the anatomy of a pyroclastic flow. Journal of the Geological Society, London, v139, p581-592.

Wilson, C.J.N., 1980, The role of fluidisation in the emplacement of pyroclastic flows: An experimental approach. Journal of Volcanology and Geothermal Research, v8, p231-249.

Wilson, C.J.N., 1986, Pyroclastic flows and ignimbrites. Scientific Progress, Oxford, v70, p171-207.

Wilson, C.J.N., 1993, Ignimbrites. In J. McPhie (ed.) *Explosive Volcanism: Processes and Products*. CEV Short Course, Canberra. Pp9.1-9.42.

Wilson, C.J.N., 1997, Emplacement of Taupo Ignimbrite. Nature, v385, p306-307.

Wilson, M., 1989, *Igneous Petrogenesis: A global tectonic approach.* Chapman and Hall. London. 466p.

Wisser, E., 1927, Oxidation subsidence at Bisbee, Arizona. Economic Geology, v8, p761-790

Wohletz, K.H. and M.F. Sheridan, 1983, Hydrovolcanic explosions II. Evolution of basaltic tuff rings and tuff cones. American Journal of Science, v283, p385-413.

Wolff, J.A., Worner, G., and S. Blake, 1990, Gradients in physical parameters in zoned felsic magma bodies: implications for evolution and eruptive withdrawal. Journal of Volcanology and Geothermal Research, v43, p37-55.

Wolff, J.A., and J.V. Wright, 1981, Formation of the Green Tuff, Pantelleria. Bulletin of Volcanology, v44, p681-690.

Wood, C.P., 1985, Geology of Mamaku water supply Drillhole. Unpublished report, New Zealand Geological Survey, Rotorua.

Wood, C.P., 1985b, Geology of the Rotorua geothermal field. In *The Rotorua Geothermal Field*. Technical Report of the Monitoring Programme 1982-1985, Ministry of Energy, p275-293.

Wood, C.P., 1988, Geology of Rotorua Caldera. Field Trip Guides. Geological Society of New Zealand miscellaneous publication, v41 b/c, p36-53.

Woodward, D.J. and L.M. Ferry, 1973, Sheet 5, Rotorua. Gravity Map of New Zealand, 1:250,000, Bouguer Anomalies. Department of Scientific and Industrial Research, Wellington, New Zealand.

Woodward, D.J. and L.M. Ferry, 1974, Sheet 8, Taupo. Gravtiy Map of New Zealand, 1:250,000, Bouguer Anomalies. Department of Scientific and Industrial Research, Wellington, New Zealand.

Wood, C.P., 1992, Geology of the Rotorua geothermal system. Geothermics, v21, p25-41.

Wright, J.V., and G.P.L. Walker, 1977, The ignimbrite source problem: Significance of a co-ignimbrite lag-fall deposit. Geology, v5, p729-732.

Wright, I.C., 1990, Late Quaternary faulting of the offshore Whakatane Graben, Taupo Volcanic Zone New Zealand. New Zealand Journal of Geology and Geophysics, v33, p245-256.

Yokoyama, I., and M. Mena, 1991, Structure of La Primavera caldera, Jalisco, Mexico, deduced from gravity anomalies and drilling results. Journal of Volcanology and Geothermal Research, v47, p183-193.

Yoshida, T., 1984, Tertiary Ishizuki cauldron, southwestern Japan arc: Formation by ring fracture subsidence. Journal of Geophyical Research, v89B, p8502-8510.

APPENDIX 1

Sample numbers, location and treatment

APPENDIX 1
Sample numbers location and treatment

Appendix 1 presents samples analysed during this thesis. Grid references are from NZMS 260. Abbreviations are as follows:

epma- Electron probe microanalyser
sem- Scanning electron microscope (x-ray energy dispersive analysis or EDAX was also carried out using SEM
ts- Thin section
xrd- X-ray diffraction
xrf- X-ray fluorescence

Sample #	Rock description	Location	Treatment
Mk1	Pink ignimbrite from fumarolic structure	U15/905498	ts
Mk2	Grey uMI	U16/766185	ts
Mk3	Grey ignimbrite with mMi lithics, uMI	U16/765185	ts
Mk4	Grey ignimbrite with mMi lithics, uMI	U16/765185	ts
Mk5	Grey ignimbrite with mMi lithics, uMI	U16/765185	ts
Mk6	Purple/pink ignimbrite, uMI	U15/883557	ts
Mk8	Pink uMI	U15/898531	ts
Mk9	Pink uMI	U15/973481	ts
Mk10	Mokai Ignimbrite	T17/661031	ts
Mk11	Pink ignimbrite, Whangamata Rd	T17/631817	ts
Mk12	Pink ignimbrite, Whangamata Rd	T17/631817	ts
Mk13	Grey mMI	U15/886554	ts
Mk14	Pink uMI	U14/991708	ts
Mk15	andesitic bleb in ignimbrite	U15/934483	ts
Mk16	uMI adjacent to fracture	U15/844474	ts
Mk23	uMI + granite lithic	U15/875449	ts
Mk24	Pokai/Waimakariri	U15/821683	ts
Mk25	mMI	U15/821683	ts
Mk26	mMI	U15/821683	ts
Mk27	uMI	U15/820684	ts
Mk28	mMI	U15/821683	ts
Mk29	mMI	U16/762193	ts
Mk30	mMI	U16/761191	ts
Mk31	mMI	U15/907556	ts
Mk32	mMI	U16/777178	ts
Mk33	Crimson uMI	U15/873452	ts
Mk34	Pink uMI	U15/832408	ts
Mk35	Grey uMI	U15/833408	ts
Mk36	uMI pumice	U16/011338	ts
Mk37	Andesitic bleb in ignimbrite	U16/033376	ts
Mk38	mMI	U14/995705	ts
Mk39	mMI	U14/992706	ts
Mk40	mMI	U14/995705	ts
Mk44	Grey uMI	U15/856272	ts
Mk46	uMI pumice	U15/833408	ts
Mk47	uMI pumice	U15/005465	ts
Mk48	lMI pumice	U15/876686	ts
Mk49	uMI pumice	U15/833408	ts
Mk53	uMI	U15/876686	ts
Mk54	uMI	U15/886442	ts
Mk55	Andesitic bleb in ignimbrite	U15/875467	ts
Mk57	Mokai Ignimbrite	T17/639905	ts
Mk58	uMI	T15/638468	ts
Mk59	Whakamaru Ignimbrite	T15/586429	ts
Mk60	Mamaku-like deposit of Ted Lloyd	T17/630093	ts
Mk61	lMI/mMI	U15/065418	ts
Mk62	lMI/mMI	U15/065418	ts
Mk63	mMI/uMI	U15/065418	ts
Mk64	Mamaku-like deposit of Ted Lloyd	T17/633083	ts
Mk65	Mamaku-like deposit of Ted Lloyd	T17/633083	ts
Mk66	Mokai Ignimbrite	T17/672930	ts
Mk67	Te Akau 5 drillcore 235 ft- uMI	U15/047549	ts
Mk68	Te Akau 5 drillcore 240 ft- uMI	U15/047549	ts
Mk69	Te Akau 5 drillcore 269 ft- uMI	U15/047549	ts
Mk70	Te Akau 5 drillcore 295 ft- uMI	U15/047549	ts
Mk71	Te Akau 5 drillcore 305 ft- uMI	U15/047549	ts
Mk72	Te Akau 5 drillcore 370 ft- uMI	U15/047549	ts

Sample #	Rock description	Location	Treatment
Mk73	Te Akau 5 drillcore 390 ft- uMI	U15/047549	ts
Mk74	Te Akau 5 drillcore 420 ft- uMI	U15/047549	ts
Mk75	Te Akau 5 drillcore 440 ft- lMI/uMI transition	U15/047549	ts
Mk76	Te Akau 5 drillcore 460 ft- mMI	U15/047549	ts
Mk77	Te Akau 5 drillcore 470 ft- mMI	U15/047549	ts
Mk78	Te Akau 5 drillcore 480 m- mMI	U15/047549	ts
Mk79	Te Akau 5 drillcore 487 m - mMI	U15/047549	ts
Mk80	Te Akau 5 drillcore 494 ft- mMI	U15/047549	ts
Mk81	Te Akau 5 drillcore 540 ft- mMI	U15/047549	ts
Mk82	Te Akau 5 drillcore 545 ft- mMI	U15/047549	ts
Mk83	mMI	U16/777177	ts
Mk85	lMI/mMI transition	U16/877318	ts
Mk87	lMI/mMI transition	U16/877318	ts
Mk88	lMI/mMI transition	U16/877318	ts
Mk89	Welded Mokai Ignimbrite- Mokai 1 drillcore	T17/650944	ts
Mk90	Welded Mokai Ignimbrite- Mokai 3 drillcore	T17/655943	ts
Mk91	Welded Mokai Ignimbrite- Mokai 4 drillcore	-	ts
Mk92	mMI	U16/761192	ts
Mk93	mMI	U15/821683	ts
Mk94	mMI	U15/821683	ts
Mk96	mMI	U15/783682	ts
Mk97	mMI/uMI transition	T15/665514	ts
Mk98	uMI	T15/665515	ts
Mk99	uMI	T15/664516	ts
Mk100	uMI	T15/664516	ts
Mk101	uMI	T15/665517	ts, sem
Mk102	Waimakariri	U14/821767	ts
Mk103	uMI	U14/826706	ts, sem
Mk104	mMI	U14/992706	ts
Mk105	lMI	U15/876686	ts
Mk106	mMI	U15/876686	ts
Mk107	mMI	U15/876686	ts
Mk108	mMI/uMI transition	U15/876686	ts
Mk109	uMI	U15/876686	ts
Mk110	uMI	U15/876687	ts
Mk111	uMI	U15/876687	ts
MKL1	mMI lithic	U15/905498	ts
MKL2	mMI lithic	U15/927473	ts
MKL3	mMI lithic	U15/927473	ts
MKL5	mMI lithic	U15/895503	ts
MKL7	Altered granite	U15/890505	ts
MKL8	mMI lithic	U15/936475	ts
MKL9	rhyolite lava fragment	U15/895503	ts
MKL11	rhyolite lava fragment	U16/744165	ts
MKL12	mMI lithic	U15/873436	ts
MKL13a	mMI lithic	U16/785205	ts
MKL13b,c	Whakamaru lithic	U16/785206	ts
MKL14	mMI lithic	U15/885403	ts
MKL15	mMI lithic	U15/824406	ts
MKL18	Andesitic bleb	U15/867455	ts
MKL19	Granite lithic	U16/883322	ts, xrf
MKL20	Granite lithic	U16/883322	ts, xrf
MKL21	Granite lithic	U16/883322	ts, xrf
MKL22	Andesitic bleb	-	ts
MKL23	Andesitic bleb	U15/883460	ts
MKL24	Mafic bleb	U16/033376	ts, xrf

Sample #	Rock description	Location	Treatment
MKL25	Andesitic bleb	U15/011473	ts
MKL26	Andesitic bleb	U15/937532	ts
MKL27	Granite lithic	U15/867455	ts
MKL29	Microdiorite lithic	U16/994341	ts
MKL30	Microdiorite lithic	U16/994341	ts
MKL31	Granite lithic	U16/994341	ts
MKL32	Microgranite lithic	U16/994341	ts
MKL33	Microgranite lithic	U16/894398	ts
MKL34	mMI block	U16/786205	ts
MKL35	mMI block	U16/786205	ts
MKL65	Leucogabbro	U16/025353	ts
MKP20	uMI pumice	U15/917507	ts
MKP21	uMI pumice	U16/884316	ts
MKP22	uMI pumice	U15/917507	ts
MKP23	uMI pumice	U15/917507	ts
MKP24	uMI pumice	U16/848354	ts
MKP25	expanded rhyolite fragment	U15/942480	ts
MKP26	lMI pumice	U16/762193	ts
MKP27	lMI pumice	U16/762193	ts
MKP29	lMI pumice	U16/738340	ts, xrf, epma
MKP30	uMI pumice	U16/887296	xrf
MKP32	lMI pumice	U16/716373	xrf
MKP33	lMI pumice	U16/716373	xrf
MKP34	uMI pumice	U16/709156	xrf
MKP35	lMI pumice	U16/716373	ts, xrf, epma
MKP36	lMI pumice	U16/738340	xrf
MKP37	lMI pumice	U16/738340	xrf
MKP38	lMI pumice	U16/738340	xrf
MKP39	lMI pumice	U16/738340	xrf
MKP40	lMI pumice	U16/738340	xrf
MKP41	lMI pumice	U16/737342	xrf
MKP42	lMI pumice	U16/737342	xrf
MKP43	lMI pumice	U16/737342	xrf
MKP44	uMI pumice	U16/709156	xrf
MKP45	uMI pumice	U16/709156	xrf
MKP46	uMI pumice	U16/709156	xrf
MKP47	uMI pumice	U16/887296	xrf
MKP48	lMI pumice	U16/737342	ts, xrf
MKP49	lMI pumice	U16/737342	xrf
MKP50	lMI pumice	U16/737342	xrf
MKP51	lMI pumice	U16/737342	xrf
MKP52	lMI pumice	U16/737342	xrf
MKP53	uMI pumice	U15/708438	xrf
MKP54	uMI pumice	U15/708438	xrf
MKP55	uMI pumice	U15/708438	xrf
MKP56	uMI pumice	T15/617477	xrf
MKP57	lMI pumice	U16/777177	xrf
MKP58	lMI pumice	U16/740340	xrf
MKP59	lMI pumice	U15/708438	xrf
MKP60	lMI pumice	U15/708438	xrf
MKP61	lMI pumice	U16/740340	ts, xrf
MKP62	uMI pumice	U16/709156	xrf
MKP63	lMI pumice	U16/737342	xrf
MKP64	lMI pumice	U16/716373	xrf
MKP65	lMI pumice	U16/737342	xrf
MKP66	lMI pumice	U16/716373	xrf

Sample #	Rock description	Location	Treatment
MKP67	uMI pumice	U15/715437	xrf
MKP68	basal tephra sequence	U16/719353	xrf
MKP69	lMI pumice	U16/719353	xrf
MKP70	lMI pumice	U16/786205	xrf
MKP71	uMI pumice	U16/887296	xrf
MKP72	basal tephra sequence	U16/777177	xrf
MKP73	lMI pumice	U16/716373	xrf
MKP74	Mokai pumice	T17/665043	xrf
MKP75	Mokai pumice	T17/634980	xrf
MKP76	uMI pumice	U15/867455	ts, xrf
MKP77	Mokai pumice	T17/665043	xrf
MKP78	Mokai pumice	T17/665043	xrf
MKP79	uMI pumice	U16/888316	xrf
MKP80	uMI pumice	U16/709156	xrf
MKP81	lMI pumice	U16/876686	ts, xrf
MKP82	uMI pumice	U16/884323	xrf
MKP83	uMI pumice	U16/867455	xrf
MKP84	uMI pumice	U16/867455	xrf
MKP85	lMI pumice	U16/738311	xrf
MKP86	uMI pumice	U16/867455	ts, xrf
MKP87	uMI pumice	U15/876571	ts, xrf
MKP88	uMI pumice	U16/883320	xrf
MKP89	lMI pumice	U16/738341	xrf
MKP90	lMI pumice	U16/738340	ts, xrf, epma
MKP91	lMI pumice	U16/737342	xrf
MKP92	uMI pumice	U15/859692	xrf
MKP93	lMI pumice	U15/876686	xrf
MKP94	lMI pumice	U15/876686	xrf
MKP95	lMI pumice	U15/876686	xrf
MKP96	lMI pumice	U16/761192	xrf
MKP97	lMI pumice	U16/761192	xrf
MKP98	lMI pumice	U16/761192	xrf
MKP99	lMI pumice	U16/761192	xrf
MKP100	lMI pumice	U15/876686	xrf
MKP101	lMI pumice	U15/876686	xrf
MKP102	lMI pumice	U15/876686	xrf
MKP103	lMI pumice	U15/876686	xrf
MKP104	lMI pumice	U15/876686	xrf
MKP105	lMI pumice	U15/876686	ts, xrf
MKP106	lMI pumice	U15/876686	xrf
MKP107	lMI pumice	U16/717373	xrf
MKP108	lMI pumice	U16/717373	xrf
MKP109	lMI pumice	U16/717373	xrf
MKP110	uMI pumice	U16/884316	xrf
MKP111	uMI pumice	U16/883316	xrf
MKP113	uMI pumice	U16/883315	xrf
MKP114	lMI pumice	U16/761192	xrf
MKP115	lMI pumice	U16/761192	xrf
MKP116	lMI pumice	U16/716363	ts, xrf, epma
MKP117	uMI pumice	U16/033365	xrf
MKP118	uMI pumice	U16/893323	xrf
MKP119	uMI pumice	U16/883319	xrf
MKP120	Andesitic bleb	U16/033363	ts, xrf
MKP121	uMI pumice	U16/917507	xrf
MKP122	uMI pumice	U16/332349	xrf
MKP123	uMI pumice	U15/892517	ts, xrf
MKP124	uMI pumice	U15/917507	xrf

Sample #	Rock description	Location	Treatment
MKP125	uMI pumice	U16/883320	xrf
MKP126	uMI pumice	U16/889318	xrf
MKP127	uMI pumice	U15/917507	xrf
MKP130	uMI pumice	U15/917507	xrf, sem
MKP131	uMI pumice	U15/917507	xrf, sem
MKP132	uMI pumice	U16/883316	xrf
MKP133	uMI pumice	U15/917507	xrf
MKP134	uMI pumice	U16/033365	xrf
MKP135	uMI pumice	U16/332349	xrf
MKP136	uMI pumice	U15/917507	ts, xrf
MKP137	uMI pumice	U15/917507	xrf
MKP138	uMI pumice	U16/033365	xrf
MKP139	uMI pumice	U15/789654	xrf
MKP140	uMI pumice	U15/917507	ts, xrf
MKP141	uMI pumice	U16/033365	xrf
MKP142	uMI pumice	U16/876335	xrf
MKP143	uMI pumice	U15/787160	xrf
MKP144	uMI pumice	U15/813606	xrf
MKP145	Mokai pumice	T15/665513	xrf
MKP146	uMI pumice	U15/917507	xrf
MKP147	uMI pumice	U16/034363	xrf
MKP148	lMI pumice	U16/761192	xrf
MKP149	uMI pumice	U15/102444	xrf
MKP150	lMI pumice	U16/874265	xrf
MKP152	Andesitic bleb	U16/027347	xrf
MKP153	lMI pumice	U16/738340	xrf
MKP154	uMI pumice	U16/882314	xrf
MKP155	basal tephra sequence pumice	U16/777177	epma
P3	uMI pumice	U15/833408	xrf
P4	lMI pumice	U15/876686	xrf
P10	uMI pumice	U15/824406	xrf
P11	uMI pumice	U14/895705	xrf
P16b	lMI pumice	U15/876686	xrf
P16c	lMI pumice	U15/876686	xrf
P17	uMI pumice	U15/973481	xrf
P18	uMI pumice	U15/833408	xrf
P19	uMI pumice	U15/891507	xrf
SUT101	lMI pumice	U16/738340	sem
RR1	Umarua	U15/847406	ts. xrf
RR2	RCR- Mt Ngongotaha	U16/880394	ts
RR3	RCR- Mt Ngongotaha	U16/913384	ts
RR4	RCR- Mt Ngongotaha	U16/881364	ts
RR5	RCR- Mt Ngongotaha	U15/914406	ts, xrf
RR6	RCR- Mt Ngongotaha	U16/904398	ts
RR7	RCR- Mt Ngongotaha	U16/904398	ts
RR8	RCR- Mt Ngongotaha	U16/881392	ts, xrf
RR9	RCR- Mt Ngongotaha	U16/901318	ts, xrf
RR10	RCR- Mt Ngongotaha	U16/913397	ts
RR11	RCR- Mt Ngongotaha	U16/905383	ts, xrf
RR12	RCR- Mt Ngongotaha	U16/876393	ts
RR13	RCR- Mt Ngongotaha	U16/898393	ts
RR14	RCR- Mt Ngongotaha	U16/915405	ts
RR15	RCR- Mt Ngongotaha	U16/881392	ts, xrf
RR16	Mokoia	U15/986413	ts, xrf
RR17	Mokoia	U15/986414	ts, xrf
RR18	Mokoia	U15/986413	ts

Sample #	Rock description	Location	Treatment
RR19	Hamurana	U15/991406	ts, xrf, epma
RR20	RCR- Pukehangi	U16/869348	ts, xrf
RR21	Hinemoa	U16/986373	ts, xrf
RR22	Hinemoa	U16/986371	ts, xrf
RR23	Hinemoa	U16/978362	ts, xrf
RR24	RCR- Ngongotaha	U16/873364	ts
RR25	RCR- Pukehangi	U16/894347	ts, xrf
RR26	RCR- Pukehangi	U16/894333	ts
RR27	RCR- Pukehangi	U16/874338	ts, xrf
RR28	Endean	U16/843363	ts, xrf
RR29	Endean	U16/842362	ts, xrf
RR30	Pukepoto Hill	U16/042361	ts
RR31	RCR- Kawaha Pt	U16/941390	ts
RR32	RCR- Kawaha Pt	U16/941390	ts, xrf, epma
RR33	RCR- Kawaha Pt	U16/945392	ts, xrf
RR34	RCR- Citizens Club borehole	U16/ 950358	ts, xrf
RR892	RCR- Buried dome, from 164 m depth of core (GNS)	U16/932363	ts
ROT328	RCR- Buried dome, from 22 m depth of core (GNS)	U16/932363	ts
Hemo	Pohaturoa	U16/945315	ts
MKR1	Expanded Rhyolite lithic- uMI lag breccia	U16/883322	ts, epma
F1	Fissure fill- Oropi Gorge	U15/875689	xrd
F2	Fissure wall- Oropi Gorge	U15/875689	xrd
F3	Fissure adjacent ignimbrite	U15/875689	xrd
F4	Fissure adjacent ignimbrite	U15/875689	xrd
F5	Yellow zone 1- Tauranga Direct Road	U15/874623	xrd
F7	Dark orange zone 1- Tauranga Direct Road	U15/874623	xrd
F8	Yellow zone 2- Tauranga Direct Road	U15/874623	xrd
F9	White zone 2- Tauranga Direct Road	U15/874623	xrd
F10	Pink/purple zone 2- Tauranga Direct Road	U15/874623	xrd
F11	Orange zone 2- Tauranga Direct Road	U15/874623	xrd
F12	Ignimbrite 4 m south of fumarole conduit	U15/895503	xrd
F13	Ignimbrite 3 m south of fumarole conduit	U15/895503	xrd
F14	Ignimbrite 2 m south of fumarole conduit	U15/895503	xrd
F15	Ignimbrite 1 m south of fumarole conduit	U15/895503	xrd
F16	Ignimbrite adjacent to fumarole conduit	U15/895503	xrd
F17	3 m north of conduit	U15/895503	xrd
F18	1 m north of fumarole conduit	U15/895503	xrd
F19	2 m north of fumarole conduit	U15/895503	xrd
F20	Coarse fissure fill	U15/895503	xrd
F21	Yellow sandy fissure fill	U15/895503	xrd
F22	Medium fissure fill	U15/895503	xrd
F23	Clay-like fissure fill	U15/895503	xrd
FF10	Fissure fumarole margin	U16/031354	sem
GRFM7	Fissure fumarole margin	U15/773468	sem
GRFM8y	Yellow fissure fumarole zone		
GRFM8rp	Red/purple fissure fumarole margin		
GRFM8m	Fissure fumarole margin		
MoP1	Mokai pumice	T17/653046	ts, xrf
MoP2	Mokai pumice	T17/653046	ts, xrf, epma
MoP3	Mokai pumice	T17/653046	xrf
MoP4	Mokai pumice	T17/653046	xrf
MoP5	Mokai mafic fragment	T17/652046	ts
MoP6	Mokai pumice	T17/652046	xrf
MoP7	Mokai pumice	T17/659044	xrf
MoP9	Mokai mafic fragment	T17/652046	ts

Sample #	Rock description	Location	Treatment
MoL1	Mokai mafic fragment	T17/673045	ts

APPENDIX 2

XRF analyses

APPENDIX 2
X-ray fluorescence analyses

Sample acquisition and preparation

Samples of pumice were analysed from lower and upper Mamaku Ignimbrite and andesitic blebs from uMI. Pumice clasts are analysed rather than whole rock ignimbrite as they are assumed to directly reflect the composition of the erupting magma. Whole rock samples often contain minute contaminants leading to erroneous magma composition correlations. Only single pumice clasts were analysed to preclude mixing of different compositions. Pumice clasts that were visibly altered were avoided and pumice that had greater than 3 wt% LOI not used for chemical interpretation. Pumice clasts from upper Mamaku Ignimbrite are entirely devitrified and were analysed for purpose of comparison with unaltered lower Mamaku pumice.

Pumice samples were washed with water and scrubbed to remove any matrix adhering to the surface, and dried overnight at 105 °C. The outside of any pumice clast that was altered, or could not be cleaned satisfactorily was removed using a diamond saw and rinsed under running water. Dried pumice clasts were crushed using a hammer or hydraulic ram and milled using a tungsten carbide concentric ring mill.

Rhyolite lava samples and plutonic lithic clasts were cleaned and dried before being crushed in a hydraulic ram and milled in the tungsten carbide ring mill.

All surfaces were thoroughly cleaned between samples to prevent contamination.

Sample analysis

Major element analyses were carried out on glass fusion beads. These beads were made by mixing 1.3 g of milled rock powder with 6.98 g of lithium tetraborate flux in platinum crucibles. The crucibles containing the mixture were heated to 1030 °C and the mixture melted, before being cooled, and reweighed to calculate loss on ignition. The mixture was then re-melted and poured into moulds to create 50 mm diameter beads. Platinum crucibles and moulds were thoroughly cleaned between samples to avoid cross contamination.

Trace element abundances were obtained from pressed powder pellets. The pellets measured either 30 mm or 50 mm diameter (depending on the amount of sample) and were a minimum of 4.5 mm thick. Pellets were created by mixing 6 or 11 g of rock powder with 16-20 drops of 7 % Mowiol solution, and hydraulically pressing the mixture into a flat disc. The hydraulic press and mixing beakers were thoroughly cleaned between samples to avoid contamination.

XRF analyses were carried out in a Phillips PW-2400 X-ray Fluorescence spectrometer by Stephen Brown at University of Canterbury following the general technique outlined by Norrish and Hutton (1969). Major element chemistry was determined using a rhodium tube set at 50 KV/55 mA, and trace element chemistry with a rhodium tube set at 60KV/46 mA. Only analyses that totalled 99.5 % ± 1 % that LOI < 3 % were accepted (N.B. all analyses made are listed). Major element compositions are quoted as hydrous in appendix tables but were recalculated anhydrous before being used and interpreted in the thesis. Total iron is given as Fe_2O_3. Some trace elements are quoted as a "less than" value indicating that its abundance is below the detection limit of the spectrometer. Accuracy of analyses are maintained by calibrating the XRF spectrometer using international standards.

Appendices have been separated according to the rock type analysed and data presented in the following order:

Appendix 2A- Silicic pumice clasts from lMI and uMI.
Appendix 2B- Andesitic blebs from uMI .
Appendix 2C- Plutonic lithics from Mamaku Ignimbrite.
Appendix 2D- Rhyolite lava of Rotorua Caldera
Appendix 2E- Mokai Ignimbrite pumice clasts.

Appendix 2A

Sample number	MKP29	MKP30	MKP31	MKP32	MKP33	MKP34	MKP35	MKP36	MKP37	MKP38	MKP40	MKP41
Lab number	31790	31791	31792	31793	31794	31795	31796	31797	31798	31799	31800	31801
Stratigraphic level	lMI	uMI	uMI	lMI	lMI	uMI	lMI	lMI	lMI	lMI	lMI	lMI
Pumice type	3	2	2	2	2	1	1	2	2	2	2	2
SiO_2	68.21	73.27	70.82	71.55	72.30	72.75	73.93	69.37	71.31	70.71	70.34	72.62
TiO_2	0.36	0.31	0.29	0.27	0.21	0.26	0.16	0.31	0.28	0.31	0.30	0.21
Al_2O_3	16.58	14.16	15.03	14.31	14.06	13.27	13.30	15.90	14.97	15.11	15.56	13.38
Fe_2O_3	2.92	2.70	2.46	2.26	1.82	2.19	1.53	2.39	2.07	2.41	2.38	1.94
MnO	0.06	0.09	0.08	0.08	0.07	0.08	0.06	0.06	0.06	0.06	0.06	0.06
MgO	0.45	0.17	0.35	0.31	0.22	0.29	0.14	0.33	0.30	0.34	0.31	0.22
CaO	1.69	1.26	1.51	1.43	1.33	1.35	0.82	1.41	1.33	1.32	1.39	1.16
Na_2O	4.15	4.62	4.30	4.19	4.12	4.05	3.63	4.17	4.27	4.12	4.26	3.98
K_2O	2.54	3.07	2.79	3.17	3.24	3.23	3.76	2.80	3.00	2.96	2.83	3.47
P_2O_5	0.02	0.04	0.02	0.05	0.03	0.02	0.02	0.02	0.02	0.02	0.02	0.02
LOI	3.15	0.49	2.54	2.19	2.34	2.17	2.93	3.62	2.43	2.72	2.96	2.10
Total	100.13	100.17	100.17	99.82	99.74	99.66	100.29	100.38	100.04	100.08	100.40	99.17
V	16	9	15	7		5	5	10	9	9	11	9
Cr	4	3	4	3		3	3	3	3	3	3	4
Ni	3	3	4	3		4	4	3	4	4	3	3
Zn	70	55	65	68		47	50	57	54	58	55	55
Zr	292	256	262	241		200	175	273	241	283	270	273
Nb	12	10	11	10		10	10	12	9	11	12	11
Ba	648	754	819	726		811	784	661	730	665	696	705
La	26	32	26	27		34	36	27	29	27	28	27
Ce	78	49	56	58		63	62	72	56	69	77	51
Nd	23	32	30	38		19	21	19	28	29	25	30
Ga	19	16	17	16		13	14	17	14	17	17	17
Pb	22	19	14	24		18	15	19	18	22	20	21
Rb	88	103	92	99		111	116	90	107	95	92	97
Sr	150	130	134	129		70	62	134	113	125	132	126
Th	23	11	12	12		12	14	13	15	14	16	13
Y	29	33	38	41		36	43	31	36	33	33	33

Appendix 2A

Sample number	MKP42	MKP43	MKP44	MKP45	MKP46	MKP47	MKP48	MKP39	MKP49	MKP50	MKP51	MKP52
Lab number	31802	31803	31804	31805	31806	31807	31808	31809	31810	31811	31812	31813
Stratigraphic level	lMI	lMI	uMI	uMI	uMI	uMI	lMI	lMI	lMI	lMI	lMI	lMI
Pumice type	1	1	1	2	2	2	2	2	1	1	2	2
SiO_2	73.79	74.28	75.39	69.78	70.31	74.92	70.83	71.39	71.89	74.07	72.62	70.93
TiO_2	0.19	0.16	0.14	0.41	0.25	0.26	0.29	0.22	0.19	0.15	0.21	0.25
Al_2O_3	12.87	12.76	12.36	14.57	13.19	14.03	14.71	14.94	13.50	12.81	13.46	14.46
Fe_2O_3	1.73	1.52	1.42	3.11	2.17	0.89	2.42	1.76	1.73	1.46	1.83	2.18
MnO	0.08	0.06	0.06	0.11	0.08	0.04	0.09	0.04	0.06	0.06	0.07	0.08
MgO	0.19	0.14	0.13	0.61	0.31	0.24	0.34	0.21	0.19	0.12	0.20	0.26
CaO	1.00	0.90	0.84	2.09	1.43	1.20	1.54	0.95	1.01	0.81	0.98	1.11
Na_2O	3.93	3.58	3.69	4.07	3.92	4.68	4.36	3.78	3.78	3.89	3.79	3.84
K_2O	3.64	3.97	3.73	3.02	3.15	3.17	2.91	3.34	3.44	3.54	3.46	3.15
P_2O_5	0.02	0.02	0.02	0.03	0.03	0.04	0.02	0.02	0.02	0.02	0.02	0.02
LOI	1.94	2.11	5.11	5.63	3.24	0.99	2.74	3.43	2.87	2.75	3.23	3.65
Total	99.37	99.49	102.87	103.42	98.08	100.45	100.25	100.08	98.67	99.66	99.86	99.93
V			4	22		6	10	7	5	4		
Cr			3	3		3	3	3	3	3		
Ni			4	3		3	3	3	4	5		
Zn			43	66		28	60	63	53	44		
Zr			148	342		234	262	227	198	164		
Nb			9	10		10	11	12	12	10		
Ba			790	730		727	751	754	860	804		
La			38	22		14	25	33	38	35		
Ce			57	56		38	69	59	60	57		
Nd			33	22		22	30	27	31	38		
Ga			13	16		15	17	16	13	14		
Pb			20	23		15	19	25	25	21		
Rb			124	90		105	92	102	110	120		
Sr			61	176		115	132	80	77	58		
Th			15	10		11	12	14	14	14		
Y			38	32		12	34	32	36	38		

Sample number	MKP53	MKP54	MKP55	MKP56	MKP57	MKP58	MKP59	MKP60	MKP61	MKP62	MKP63	MKP64
Lab number	31814	31815	31816	31817	31818	31819	31820	31821	31822	31823	31824	31825
Stratigraphic level	lMI	uMI	uMI	uMI	lMI	lMI	lMI	lMI	lMI	lMI	lMI	lMI
Pumice type	2	2	2	1	2	2	1	2	2	2	2	2
SiO_2	70.55	69.97	70.72	75.85	70.12	69.70	73.32	71.00	70.34	72.40	70.54	72.08
TiO_2	0.19	0.21	0.19	0.16	0.19	0.27	0.15	0.23	0.30	0.24	0.18	0.25
Al_2O_3	14.27	15.32	14.37	13.41	16.29	15.78	13.55	14.49	15.59	13.51	15.01	13.98
Fe_2O_3	1.99	2.10	1.87	1.61	1.93	2.14	1.61	1.97	2.21	2.04	1.83	2.12
MnO	0.07	0.08	0.07	0.04	0.05	0.05	0.05	0.06	0.05	0.07	0.06	0.07
MgO	0.20	0.20	0.17	0.07	0.14	0.28	0.11	0.22	0.32	0.26	0.14	0.27
CaO	0.93	1.02	0.89	0.49	0.82	1.08	0.72	1.03	1.35	1.48	0.81	1.29
Na_2O	3.89	3.59	3.90	3.26	3.11	3.75	3.46	3.78	4.15	4.12	3.51	4.11
K_2O	3.73	3.58	3.74	3.83	2.59	3.08	3.40	3.24	2.85	3.24	3.07	3.34
P_2O_5	0.02	0.03	0.02	0.02	0.02	0.02	0.02	0.02	0.02	0.02	0.02	0.05
LOI	3.59	3.76	3.83	1.21	4.47	3.62	3.15	3.64	2.98	2.27	4.50	2.41
Total	99.43	99.85	99.78	99.93	99.74	99.77	99.52	99.68	100.16	99.65	99.66	99.97
V		5	5	5		8			11			9
Cr		3	3	3		3			3			3
Ni		3	3	3		3			3			3
Zn		60	53	49		89			60			62
Zr		257	251	162		265			277			236
Nb		13	12	10		12			12			10
Ba		721	697	739		749			676			753
La		27	33	34		28			28			33
Ce		80	83	44		72			67			45
Nd		39	24	18		31			22			44
Ga		16	14	15		17			17			16
Pb		22	21	14		29			22			22
Rb		112	119	101		99			92			101
Sr		79	68	44		92			128			114
Th		17	17	13		16			14			14
Y		31	33	21		32			33			42

Appendix 2A

Sample number	MKP65	MKP66	MKP67	MKP68	MKP69	MKP70	MKP71	MKP72	MKP73	MKP76	MKP77	MKP78
Lab number	31826	31827	31828	31829	31830	31831	31832	31833	31834	31837	31838	31839
Stratigraphic level	lMI	lMI	uMI	lMI	lMI	lMI	uMI	lMI	lMI	uMI	uMI	uMI
Pumice type	2	2	2	2	1	2	1	2	2	1	2	2
SiO_2	72.27	71.54	73.06	68.07	74.17	71.74	75.86	68.48	71.87	76.11	74.09	74.05
TiO_2	0.27	0.28	0.24	0.27	0.16	0.18	0.14	0.30	0.26	0.15	0.28	0.26
Al_2O_3	13.62	14.16	13.65	16.18	13.01	15.30	12.50	16.43	14.09	12.79	13.73	13.98
Fe_2O_3	2.19	2.27	2.10	2.44	1.50	1.85	1.31	2.59	2.12	1.31	2.29	2.14
MnO	0.09	0.07	0.08	0.09	0.06	0.06	0.04	0.13	0.07	0.02	0.06	0.07
MgO	0.30	0.31	0.39	0.27	0.15	0.15	0.19	0.30	0.29	0.05	0.10	0.14
CaO	1.43	1.40	1.09	1.31	0.78	0.81	0.65	1.22	1.31	0.64	1.19	1.29
Na_2O	4.29	4.17	4.46	3.68	3.65	3.13	4.42	3.76	4.06	4.05	4.56	4.58
K_2O	3.20	3.21	3.14	2.84	3.67	2.80	3.79	2.61	3.21	3.73	3.25	3.10
P_2O_5	0.02	0.05	0.03	0.02	0.03	0.02	0.02	0.02	0.04	0.03	0.03	0.03
LOI	2.23	2.41	1.33	4.86	2.68	3.83	0.54	4.15	2.53	1.37	0.48	0.62
Total	99.90	99.87	99.56	100.03	99.85	99.86	99.45	99.98	99.85	100.19	100.05	100.26
V	10	7		9	3	5	3		10	5	11	9
Cr	3	3		3	3	3	3		3	3	3	3
Ni	3	3		3	3	3	3		3	3	3	3
Zn	56	61		89	52	64	32		67	27	44	42
Zr	237	264		262	177	199	148		236	158	233	233
Nb	10	10		13	10	12	6		10	7	9	10
Ba	737	732		823	805	862	757		742	784	716	745
La	28	31		34	38	52	28		30	30	26	25
Ce	56	45		73	60	63	39		53	50	61	53
Nd	36	31		37	36	41	28		33	15	38	22
Ga	15	16		18	14	17	13		16	14	15	15
Pb	18	18		118	20	25	12		23	16	13	13
Rb	100	99		87	115	103	138		101	137	115	106
Sr	122	123		100	58	60	57		114	57	115	118
Th	11	12		16	15	18	13		12	8	11	13
Y	36	42		35	43	40	19		42	11	41	24

Appendix 2A

Sample number	MKP79	MKP80	MKP81	MKP82	MKP83	MKP84	MKP85	MKP86	MKP87	MKP88	MKP89	MKP90
Lab number	31840	31841	31842	31843	31844	31845	31846	31847	31848	31849	31850	31851
Stratigraphic level	uMI	uMI	lMI	uMI	uMI	uMI	lMI	uMI	uMI	uMI	lMI	lMI
Pumice type	1	2	3	2	2	2	3	1	2	2	3	1
SiO_2	74.27	72.04	66.38	73.34	73.99	71.86	63.77	76.81	74.45	68.12	66.01	74.14
TiO_2	0.15	0.28	0.36	0.28	0.26	0.30	0.26	0.14	0.27	0.31	0.35	0.16
Al_2O_3	12.89	13.53	18.04	13.95	13.85	14.56	19.85	12.56	13.60	16.14	18.26	13.69
Fe_2O_3	1.46	2.30	2.99	2.43	2.14	2.75	2.43	1.24	1.87	2.63	2.93	1.33
MnO	0.03	0.09	0.09	0.08	0.05	0.05	0.06	0.03	0.06	0.10	0.09	0.03
MgO	0.07	0.34	0.41	0.27	0.13	0.08	0.27	0.06	0.24	0.35	0.04	0.12
CaO	0.67	1.48	1.67	1.48	1.16	1.20	1.01	0.65	1.20	1.54	1.73	0.76
Na_2O	4.03	3.99	4.11	4.84	4.43	4.33	3.08	4.01	4.63	4.26	4.06	3.76
K_2O	3.48	3.29	2.19	2.98	3.36	3.15	2.38	3.82	3.25	2.56	2.26	3.31
P_2O_5	0.03	0.02	0.02	0.04	0.03	0.04	0.04	0.04	0.02	0.03	0.02	0.02
LOI	2.63	1.96	3.41	0.68	0.70	2.16	7.25	0.86	0.54	4.26	3.96	2.85
Total	99.72	99.31	99.67	100.36	100.10	100.48	100.42	100.22	100.12	100.30	100.08	100.16
V	5		11	10	8	11	8	4	10	11	12	4
Cr	3		3	3	3	3	3	3	3	3	3	3
Ni	3		3	3	4	4	3	3	3	3	3	3
Zn	26		72	54	43	36	93	27	39	59	65	40
Zr	146		311	251	237	256	272	150	257	277	320	176
Nb	8		13	9	10	10	16	7	10	12	14	11
Ba	719		743	708	718	722	711	774	731	763	729	777
La	10		42	27	15	8	20	13	12	24	19	26
Ce	53		74	64	32	43	54	24	28	43	67	54
Nd	14		28	23	15	10	39	14	10	36	24	31
Ga	14		19	15	16	16	20	14	14	17	20	14
Pb	14		20	18	13	13	37	15	15	17	25	18
Rb	122		74	112	117	112	79	139	110	87	75	108
Sr	54		151	138	109	115	75	53	111	137	158	61
Th	9		14	10	7	7	20	7	7	12	16	12
Y	11		43	42	14	15	31	10	14	35	30	36

Appendix 2A

Sample number	MKP91	MKP92	MKP93	MKP94	MKP95	MKP96	MKP97	MKP98	MKP99	MKP100	MKP101	MKP102
Lab number	31852	31853	31854	31855	31856	31857	31858	31859	31860	31861	31862	31863
Stratigraphic level	lMI	uMI	lMI	lMI	lMI	lMI	lMI	lMI	lMI	lMI	lMI	lMI
Pumice type	2	2	3	3	3	1	2	2	1	2	1	2
SiO_2	70.78	71.72	62.12	66.65	69.67	74.73	71.24	68.94	73.49	70.33	72.61	70.36
TiO_2	0.28	0.33	0.39	0.33	0.32	0.13	0.25	0.38	0.18	0.30	0.17	0.29
Al_2O_3	14.42	15.02	21.56	18.11	15.46	12.32	13.43	14.70	12.72	15.16	14.40	15.12
Fe_2O_3	2.42	2.91	3.35	2.85	2.55	1.30	2.21	2.93	1.66	2.50	1.63	2.42
MnO	0.08	0.11	0.10	0.09	0.09	0.04	0.08	0.08	0.06	0.09	0.05	0.09
MgO	0.33	0.07	0.44	0.35	0.37	0.13	0.33	0.54	0.21	0.33	0.14	0.32
CaO	1.38	1.27	1.87	1.43	1.63	0.79	1.31	1.90	0.87	1.45	0.84	1.49
Na_2O	4.18	3.79	3.82	3.91	4.32	3.96	4.23	4.05	4.09	4.15	3.65	4.26
K_2O	2.99	3.35	1.63	2.30	2.79	3.67	3.24	3.11	3.63	2.89	3.45	2.85
P_2O_5	0.02	0.06	0.02	0.02	0.02	0.02	0.04	0.06	0.02	0.02	0.02	0.02
LOI	3.02	1.53	5.01	4.13	2.71	2.74	3.18	2.95	2.56	2.77	3.15	2.53
Total	99.90	100.16	100.29	100.16	100.23	99.82	99.54	99.63	99.48	99.99	100.10	99.74
V		12	10		12				6	11	3	11
Cr		3	3		3				3	3	3	3
Ni		4	3		4				4	3	4	3
Zn		52	108		75				46	94	68	83
Zr		277	370		284				185	273	182	262
Nb		10	15		11				10	11	11	11
Ba		717	938		748				732	751	803	747
La		35	48		29				32	33	35	32
Ce		57	71		53				65	62	59	67
Nd		30	44		10				16	10	13	36
Ga		18	23		16				14	17	15	17
Pb		15	23		20				17	24	21	22
Rb		115	56		91				122	95	112	95
Sr		134	172		144				69	125	62	128
Th		11	15		14				16	16	16	13
Y		32	47		38				36	44	38	42

Sample number	MKP103	MKP104	MKP105	MKP106	MKP107	MKP108	MKP109	MKP110	MKP111	MKP113	MKP114	MKP115
Lab number	31864	31865	31866	31867	31868	31869	31870	31871	31872	31886	31887	31888
Stratigraphic level	lMI	lMI	lMI	lMI	lMI	lMI	lMI	uMI	uMI	uMI	lMI	lMI
Pumice type	2	2	2	3	2	2	2	2	2	2	2	2
SiO_2	70.23	70.48	70.57	65.98	69.96	69.04	69.27	73.26	73.25	73.06	72.64	70.98
TiO_2	0.28	0.29	0.30	0.48	0.19	0.31	0.21	0.29	0.29	0.31	0.24	0.26
Al_2O_3	15.55	15.18	15.01	17.72	16.52	16.02	17.08	14.63	14.35	14.63	13.32	14.76
Fe_2O_3	2.31	2.38	2.46	3.57	2.02	2.72	2.11	2.46	2.66	2.66	2.13	2.41
MnO	0.08	0.08	0.09	0.09	0.06	0.11	0.09	0.08	0.10	0.09	0.07	0.07
MgO	0.31	0.30	0.37	0.60	0.18	0.39	0.20	0.14	0.10	0.16	0.30	0.31
CaO	1.51	1.36	1.50	2.02	0.82	1.56	0.96	1.07	1.00	1.12	1.38	1.26
Na_2O	4.23	4.24	4.20	3.99	3.22	4.04	3.43	4.13	4.15	4.19	4.20	3.96
K_2O	2.84	2.80	2.87	2.23	2.83	2.58	2.53	3.06	3.33	3.00	3.29	3.11
P_2O_5	0.02	0.02	0.02	0.03	0.02	0.02	0.02	0.03	0.04	0.03	0.04	0.02
LOI	2.72	2.83	2.73	3.73	4.27	3.16	4.24	1.19	1.01	1.10	2.36	2.87
Total	100.07	99.95	100.18	100.41	100.08	99.94	100.12	100.34	100.28	100.35	99.96	100.00
V	8	10	9	22	4			9	10	9	9	9
Cr	3	3	3	3	3			3	3	3	3	3
Ni	3	5	4	4	4			3	3	3	3	3
Zn	75	70	81	103	104			53	56	59	51	55
Zr	253	277	258	338	215			251	241	266	224	255
Nb	11	11	11	12	13			11	11	11	10	11
Ba	751	733	734	743	782			781	787	782	740	681
La	25	39	27	31	37			19	39	23	34	18
Ce	48	63	62	52	80			46	98	44	49	55
Nd	28	32	36	37	42			18	24	16	33	23
Ga	18	17	17	20	19			16	16	16	14	16
Pb	18	18	19	18	25			16	16	15	116	18
Rb	90	94	93	74	96			103	114	100	107	102
Sr	132	116	133	171	63			108	105	114	16	110
Th	12	12	13	14	19			11	12	10	11	11
Y	38	45	38	47	43			17	37	21	37	34

Appendix 2A

Sample number	MKP116	MKP117	MKP118	MKP119	MKP121	MKP122	MKP123	MKP124	MKP125	MKP126	MKP127	MKP128
Lab number	31889	31890	31891	31892	31894	31895	31896	31897	31898	31899	31900	31901
Stratigraphic level	lMI	uMI	uMI	uMI	uMI	uMI	uMI	uMI	uMI	uMI	uMI	uMI
Pumice type	2	2	2	1	2	2	2	2	2	1	2	2
SiO_2	72.76	71.84	72.14	77.22	74.08	73.56	72.18	74.34	68.40	76.45	73.72	68.28
TiO_2	0.25	0.32	0.33	0.15	0.28	0.28	0.32	0.27	0.30	0.16	0.28	0.32
Al_2O_3	13.87	15.10	14.58	12.49	13.82	14.13	14.75	13.84	14.96	13.08	14.39	16.77
Fe_2O_3	2.10	2.61	2.97	1.36	2.26	2.40	2.64	2.12	2.73	1.48	2.23	2.82
MnO	0.07	0.07	0.07	0.03	0.07	0.08	0.09	0.08	0.12	0.05	0.07	0.09
MgO	0.26	0.38	0.34	0.08	0.21	0.09	0.34	0.15	0.29	0.10	0.08	0.34
CaO	1.23	1.73	1.49	0.70	1.20	1.20	1.81	1.25	1.46	0.66	1.07	1.45
Na_2O	4.07	4.83	4.32	4.27	4.47	4.46	4.93	4.55	4.48	3.89	4.15	4.12
K_2O	3.31	2.70	2.99	3.67	3.14	3.13	2.73	3.07	2.79	3.62	3.12	2.53
P_2O_5	0.04	0.05	0.01	0.02	0.03	0.03	0.05	0.05	0.08	0.02	0.04	0.02
LOI	2.31	0.71	0.91	0.24	0.40	0.32	0.14	0.38	4.85	0.60	1.19	3.25
Total	100.27	100.34	100.15	100.22	99.97	99.69	99.98	100.08	100.46	100.11	100.33	100.00
V	7	12	9	5	10	13	12	8	10	6	8	9
Cr	3	3	3	3	3	3	4	3	3	3	3	3
Ni	3	3	3	3	3	3	3	3	3	3	3	3
Zn	69	45	306	32	44	48	42	47	50	31	46	190
Zr	233	274	276	155	256	254	267	245	278	165	261	303
Nb	10	11	10	9	10	11	10	9	10	9	8	12
Ba	740	693	714	781	722	714	713	735	661	853	749	810
La	25	6	45	21	31	10	25	58	35	41	36	34
Ce	60	26	48	58	63	39	45	72	55	62	55	78
Nd	36	10	53	18	24	10	22	53	25	46	20	14
Ga	15	17	16	13	15	15	16	15	15	13	16	19
Pb	22	14	20	14	15	19	11	22	17	15	14	139
Rb	101	91	107	128	110	106	93	106	90	129	109	82
Sr	107	164	145	56	108	114	166	113	128	52	105	138
Th	12	9	15	12	10	8	8	10	11	11	10	13
Y	42	15	41	22	36	18	27	54	25	43	48	38

Appendix 2A

Sample number	MKP129	MKP130	MKP131	MKP132	MKP133	MKP134	MKP135	MKP136	MKP137	MKP138	MKP139	MKP140
Lab number	31902	31903	31904	31905	31906	31907	31908	31909	31910	31911	31912	31913
Stratigraphic level	uMI	uMI	uMI	uMI	uMI	uMI	uMI	uMI	uMI	uMI	uMI	uMI
Pumice type	3	2	2	2	2	2	2	1	2	2	2	2
SiO_2	65.07	74.21	74.58	73.48	73.77	74.43	73.82	77.02	73.61	74.29	73.86	74.10
TiO_2	0.35	0.26	0.27	0.29	0.28	0.26	0.27	0.14	0.28	0.27	0.27	0.27
Al_2O_3	19.04	13.99	13.77	14.11	14.22	13.61	13.89	12.60	14.20	13.72	13.92	13.90
Fe_2O_3	2.96	2.17	2.14	2.50	2.24	2.08	2.23	1.39	2.32	2.14	2.32	2.20
MnO	0.13	0.07	0.06	0.08	0.06	0.05	0.08	0.04	0.08	0.06	0.06	0.07
MgO	0.40	0.09	0.16	0.15	0.12	0.24	0.16	0.10	0.20	0.26	0.11	0.18
CaO	1.53	1.12	1.23	1.18	1.11	1.21	1.23	0.73	1.36	1.27	1.15	1.30
Na_2O	3.82	4.31	4.56	4.56	4.25	4.63	4.60	4.20	4.62	4.68	4.19	4.61
K_2O	2.12	3.11	3.07	3.34	3.11	3.26	3.13	3.60	3.01	3.09	3.41	3.03
P_2O_5	0.02	0.04	0.04	0.04	0.04	0.03	0.05	0.03	0.05	0.04	0.04	0.05
LOI	4.47	0.97	0.48	0.56	0.98	0.39	0.66	0.42	0.52	0.36	0.84	0.54
Total	99.91	100.34	100.36	100.29	100.17	100.29	100.10	100.26	100.25	100.17	100.16	100.25
V	10	7	11	10	11	13	11	4	12	10	11	11
Cr	3	3	3	3	3	3	3	3	3	3	3	3
Ni	3	3	3	3	3	3	3	3	3	4	3	3
Zn	90	35	41	50	48	40	45	34	51	37	41	52
Zr	321	236	236	255	248	242	245	150	252	256	245	243
Nb	14	8	10	11	9	10	9	9	9	10	10	10
Ba	1009	764	745	752	753	735	729	772	763	728	732	721
La	51	66	62	24	43	19	23	37	65	31	34	46
Ce	134	58	70	66	53	36	48	60	75	46	56	64
Nd	30	42	50	31	42	25	11	27	57	10	42	44
Ga	21	16	15	15	16	16	15	14	16	16	17	16
Pb	42	23	19	15	15	13	19	20	16	10	13	24
Rb	70	107	106	114	106	110	109	126	102	108	118	105
Sr	138	106	112	119	106	113	114	54	125	118	108	116
Th	14	15	10	10	12	12	14	16	11	9	11	11
Y	41	63	40	29	42	15	24	39	46	22	35	41

Appendix 2A

Sample number	MKP141	MKP142	MKP143	MKP144	MKP145	MKP146	MKP147	MKP148	MKP149	MKP150	MKP153	MKP154
Lab number	31914	31915	31916	31917	31918	31919	31920	31921	31922	31923	32291	32292
Stratigraphic level	uMI	uMI	uMI	uMI	uMI	uMI	uMI	lMI	uMI	lMI	lMI	lMI
Pumice type	2	1	1	1	1	1	2	1	2	2	1	2
SiO_2	71.04	76.79	77.44	77.27	73.79	76.98	73.89	74.43	74.29	72.53	74.06	72.74
TiO_2	0.39	0.16	0.14	0.15	0.15	0.14	0.25	0.14	0.27	0.29	0.16	0.33
Al_2O_3	14.73	12.84	12.39	12.58	13.56	12.60	13.89	12.71	13.78	15.28	13.27	14.40
Fe_2O_3	3.29	1.25	1.27	1.25	1.31	1.32	2.09	1.42	2.20	2.51	1.54	2.73
MnO	0.09	0.02	0.04	0.03	0.04	0.04	0.05	0.05	0.08	0.07	0.06	0.07
MgO	0.46	0.05	0.05	0.05	0.09	0.09	0.24	0.12	0.14	0.09	0.13	0.14
CaO	1.62	0.72	0.53	0.58	0.72	0.71	1.30	0.80	1.10	0.96	0.81	1.47
Na_2O	4.78	4.31	3.82	3.83	3.87	4.09	4.69	3.95	4.31	3.45	3.78	4.82
K_2O	3.11	3.62	3.78	3.86	3.24	3.54	3.17	3.67	3.22	3.08	3.58	2.99
P_2O_5	0.06	0.02	0.02	0.02	0.02	0.03	0.09	0.02	0.03	0.03	0.02	0.05
LOI	0.66	0.53	0.67	0.60	3.07	0.51	0.57	2.54	0.83	1.98	2.81	0.55
Total	100.23	100.25	100.10	100.16	99.87	100.06	100.23	99.84	100.25	100.25	100.23	100.25
V	24	6	4	3		4	8		11	12	7	10
Cr	3	3	3	3		3	3		3	3	3	5
Ni	4	4	4	3		4	3		4	4	4	4
Zn	57	27	29	26		32	41		43	58	50	60
Zr	316	165	160	158		156	227		249	257	169	273
Nb	13	8	7	5		9	10		10	10	10	10
Ba	712	774	768	764		761	716		720	768	793	683
La	28	31	24	35		44	26		25	55	28	26
Ce	55	44	55	44		60	41		61	47	79	65
Nd	10	10	10	19		24	23		25	41	33	33
Ga	16	14	13	15		14	15		15	17	14	16
Pb	10	14	13	13		17	12		26	20	20	19
Rb	105	130	134	142		127	105		112	106	116	105
Sr	153	59	43	49		54	119		103	97	59	145
Th	8	11	12	11		12	10		11	12	13	9
Y	20	25	17	27		36	19		34	41	37	33

Sample number	P3	P4a	P4b	P10	P11	P16a	P16b	P17	P19
Lab number	30567	30569	30587	30577	30578	30583	30584	30585	30586
Stratigraphic level	uMI	lMI	uMI	uMI	uMI	lMI	lMI	uMI	uMI
Pumice type	2	2	2	1	1	2	2	2	2
SiO_2	74.27	70.25	70.76	75.60	75.11	73.57	71.51	73.97	75.42
TiO_2	0.28	0.29	0.28	0.14	0.15	0.27	0.28	0.28	0.21
Al_2O_3	13.68	15.11	14.89	12.48	12.23	13.62	14.41	13.84	12.76
Fe_2O_3	2.31	2.44	2.42	1.56	1.39	2.29	2.17	1.89	1.74
MnO	0.06	0.09	0.10	0.03	0.04	0.04	0.08	0.04	0.04
MgO	0.21	0.34	0.31	0.10	0.11	0.11	0.29	0.17	0.15
CaO	1.24	1.54	1.47	0.65	0.76	1.32	1.47	1.38	1.00
Na_2O	4.62	4.30	4.25	4.17	3.87	4.80	4.31	4.96	4.26
K_2O	3.30	2.82	2.93	3.89	3.60	3.19	2.97	3.18	3.42
P_2O_5	0.04	0.02	0.02	0.03	0.03	0.03	0.02	0.02	0.04
LOI	0.35	2.65	2.87	1.30	2.75	0.87	2.96	0.28	1.05
Total	100.35	99.84	100.31	99.95	100.05	100.11	100.47	99.99	100.09
V	8	8	8	5	3	9	7	8	7
Cr	4	3	3	3	3	8	3	3	4
Ni	3	3	3	3	3	3	3	3	3
Zn	45	83	93	31	41	29	62	31	34
Zr	227	253	248	151	152	230	240	233	190
Nb	9	9	9	5	8	7	9	7	7
Ba	758	761	803	776	782	727	754	732	800
La	17	26	23	12	28	29	26	28	16
Ce	35	63	61	30	62	47	68	63	27
Nd	10	28	13	10	29	16	28	35	10
Ga	16	17	16	14	13	16	16	15	14
Pb	6	12	15	31	15	15	14	<1	1
Rb	109	86	91	140	119	108	93	104	115
Sr	118	132	124	55	56	125	119	127	95
Th	3	7	9	4	10	12	9	7	3
Y	19	43	42	12	40	35	36	36	18

Appendix 2B

Sample number	MKP120	MKP152	MKL24
Lab number	31893	32290	32315
Straigraphic level	uMl	uMl	uMl
Rock type	andesite	andesite	basalt
SiO_2	58.35	60.46	48.44
TiO_2	0.97	0.96	1.76
Al_2O_3	17.63	15.04	20.96
Fe_2O_3	8.40	8.11	14.53
MnO	0.18	0.27	0.39
MgO	2.63	2.83	2.55
CaO	3.34	3.78	1.42
Na_2O	3.41	3.95	1.2
K_2O	1.97	2.26	1.35
P_2O_5	0.04	0.13	0.08
LOI	2.86	1.70	7.45
Total	99.72	99.49	100.13
V	168	120	276
Cr	36	22	12
Ni	14	6	6
Zn	196	237	382
Zr	209	189	241
Nb	10	9	27
Ba	742	615	572
La	5	70	10
Ce	28	39	37
Nd	13	54	25
Ga	18	18	22
Pb	26	9	19
Rb	81	130	76
Sr	164	172	30
Th	5	5	13
Y	19	28	31

Appendix 2C

Sample number	**MKL19**	**MKL20**	**MKL21**
Lab number	31787	31788	31789
Stratigraphic level	uMI	uMI	uMI
Rock type	granite	Hb/bt granite	Hb/bt granite
SiO_2	76.96	72.71	74.94
TiO_2	0.14	0.35	0.24
Al_2O_3	12.48	14.39	13.55
Fe_2O_3	1.36	2.69	1.97
MnO	0.02	0.06	0.04
MgO	0.12	0.48	0.28
CaO	0.59	1.74	1.45
Na_2O	4.14	4.69	4.55
K_2O	4.04	2.98	2.83
P_2O_5	0.01	0.01	0.01
LOI	0.21	0.23	0.26
Total	100.07	100.34	100.11
V	3	17	6
Cr	3	3	3
Ni	3	3	3
Zn	16	41	30
Zr	132	320	220
Nb	9	11	11
Ba	1030	689	820
La	29	23	14
Ce	51	43	41
Nd	15	21	24
Ga	14	16	15
Pb	12	9	9
Rb	126	92	83
Sr	38	155	129
Th	18	17	16
Y	22	26	20

Appendix 2D

Sample number	RR1	RR5	RR8	RR9	RR11	RR15	RR16	RR17	RR19	RR20	RR21	RR22
Lab number	32028	32029	32030	32031	32032	32033	32034	32035	32036	32037	32038	32039
Lava group	Umarua/Endean	RCR	RCR	RCR	RCR	RCR	Mokoia	Mokoia	Hamarana	RCR	Hinemoa	Hinemoa
SiO_2	72.97	75.05	75.59	74.91	75.42	74.25	73.89	73.69	73.48	75.42	71.14	71.63
TiO_2	0.29	0.19	0.19	0.19	0.20	0.20	0.25	0.24	0.35	0.19	0.30	0.29
Al_2O_3	14.55	13.52	13.53	13.61	13.60	13.74	13.91	13.02	14.39	13.19	14.94	14.60
Fe_2O_3	2.41	1.81	1.79	1.77	1.84	1.84	1.44	2.15	2.09	1.74	2.19	2.23
MnO	0.06	0.06	0.06	0.06	0.06	0.06	0.04	0.05	0.03	0.06	0.06	0.06
MgO	0.42	0.17	0.11	0.17	0.11	0.18	0.25	0.28	0.30	0.17	0.46	0.44
CaO	1.96	1.01	0.99	1.05	0.90	1.07	1.47	1.39	1.84	1.07	2.03	1.86
Na_2O	3.84	4.29	4.52	4.78	4.31	4.49	4.32	4.21	3.84	4.60	4.22	4.07
K_2O	3.04	3.49	3.18	3.17	3.35	3.18	2.90	3.21	3.15	3.37	2.79	2.81
P_2O_5	0.06	0.02	0.02	0.03	0.03	0.03	0.06	0.08	0.03	0.03	0.03	0.02
LOI	0.67	0.64	0.50	0.53	0.65	1.35	1.70	1.99	0.72	0.47	2.16	2.26
Total	100.26	100.26	100.48	100.26	100.45	100.41	100.22	100.32	100.20	100.31	100.31	100.28
V	29	14	14	13	12	13	16	23	27	12	26	24
Cr	7	4	3	3	5	5	5	3	3	3	4	4
Ni	4	4	3	3	3	3	3	3	3	3	3	3
Zn	40	50	37	48	49	55	35	43	31	51	39	48
Zr	154	228	228	223	221	230	186	179	219	220	181	168
Nb	7	11	11	11	10	10	9	8	7	10	8	8
Ba	832	841	931	823	842	851	758	716	722	779	770	748
La	27	32	34	26	24	32	23	23	22	28	15	14
Ce	54	76	73	74	63	62	60	79	69	83	60	61
Nd	13	18	20	21	17	24	17	23	37	45	10	10
Ga	14	15	15	15	15	15	16	14	14	14	15	15
Pb	11	20	15	18	18	20	17	15	13	18	12	14
Rb	72	106	81	94	110	104	96	107	105	107	94	100
Sr	160	75	81	83	75	82	125	107	154	80	163	149
Th	12	12	11	11	11	10	10	10	11	12	11	9
Y	18	37	36	32	27	36	26	31	23	36	25	22

Appendix 2D

Sample number	RR23	RR25	RR27	RR28	RR29	RR32	RR33	RR34
Lab number	32040	32041	32042	32043	32044	32045	32046	32293
Lava group	Hinemoa	RCR	RCR	Endean	Endean	RCR	RCR	RCR
SiO_2	72.78	75.40	75.39	74.23	73.60	75.52	75.36	77.13
TiO_2	0.21	0.19	0.19	0.31	0.28	0.21	0.20	0.13
Al_2O_3	14.85	12.92	13.30	13.77	14.28	13.39	13.14	12.95
Fe_2O_3	1.24	0.90	1.76	2.40	2.22	1.66	1.73	0.91
MnO	0.01	0.04	0.06	0.03	0.04	0.03	0.06	0.03
MgO	0.05	0.06	0.17	0.26	0.33	0.06	0.20	0.05
CaO	0.03	0.68	1.09	1.52	1.73	0.99	1.17	0.88
Na_2O	0.27	0.10	4.66	3.47	3.68	4.38	4.62	4.08
K_2O	1.23	2.37	3.20	3.37	3.18	3.32	3.27	3.53
P_2O_5	0.04	0.03	0.02	0.03	0.03	0.03	0.03	0.02
LOI	5.83	7.38	0.55	0.83	0.89	0.70	0.46	0.55
Total	100.47	99.97	100.40	100.23	100.25	100.27	100.23	100.25
	(+ 4% SO3)							
V	12	10	12	30	27	17	13	6
Cr	3	3	3	8	5	3	3	5
Ni	3	3	4	3	4	4	5	4
Zn	8	40	50	29	32	32	47	30
Zr	214	224	220	153	151	228	223	143
Nb	12	10	10	6	7	11	10	9
Ba	645	750	771	732	759	767	804	795
La	5	31	26	13	16	23	25	26
Ce	32	68	74	47	47	55	65	62
Nd	10	25	21	10	10	10	27	35
Ga	15	18	14	14	13	15	14	13
Pb	23	24	19	12	12	14	18	18
Rb	21	102	103	120	115	106	105	108
Sr	21	69	82	128	145	85	90	77
Th	12	11	10	11	12	12	10	13
Y	10	31	35	14	13	20	33	27

Appendix 2E

Sample number	MoP1	MoP2	MoP3	MoP4	MoP6	MoP7	MKP74	MKP75
Lab number	32294	32295	32296	32297	32298	32312	31847	31848
Flow unit	lower	lower	lower	upper	lower	upper	upper	upper
SiO_2	70.57	68.69	69.49	67.83	70.14	73.07	74.04	73.82
TiO_2	0.28	0.30	0.29	0.31	0.26	0.28	0.27	0.27
Al_2O_3	15.04	16.39	15.92	16.53	15.54	13.94	13.95	13.87
Fe_2O_3	2.35	2.60	2.48	2.63	2.29	2.52	2.29	2.28
MnO	0.08	0.12	0.10	0.10	0.08	0.07	0.06	0.16
MgO	0.25	0.29	0.26	0.29	0.24	0.29	0.10	0.18
CaO	1.33	1.36	1.37	1.42	1.26	1.32	1.25	1.26
Na_2O	4.28	4.12	4.17	4.16	4.03	4.33	4.58	4.60
K_2O	2.94	2.75	2.79	2.62	2.99	3.09	3.20	3.13
P_2O_5	0.06	0.05	0.10	0.13	0.07	0.09	0.03	0.04
LOI	3.13	3.76	3.37	4.25	3.28	1.43	0.43	0.60
Total	100.31	100.43	100.34	100.26	100.18	100.42	100.2	100.1
V	10	12	15	11	10	12	10	11
Cr	4	6	5	5	6	3	3	3
Ni	3	3	3	3	3	5	3	3
Zn	63	81	74	78	66	59	45	47
Zr	237	264	257	261	232	242	241	243
Nb	10	11	1	12	11	10	9	9
Ba	744	744	699	717	826	688	706	718
La	25	23	18	20	24	19	25	17
Ce	66	76	62	74	74	66	60	62
Nd	41	26	31	31	26	22	34	30
Ga	16	18	17	18	17	16	15	15
Pb	17	17	15	19	15	19	11	13
Rb	97	91	92	87	96	100	113	110
Sr	126	130	131	136	118	119	120	117
Th	10	9	9	10	10	12	9	12
Y	35	34	32	33	33	24	36	31

APPENDIX 3

EPMA analyses

APPENDIX 3

Electron probe microanalyser analyses

Mineral and glass chemistries were analysed using an electron probe microanalyser (EPMA) at the Analytical Facility, Department of Earth Sciences, Victoria University of Wellington, under the supervision of Dr John Patterson.

Sample preparation

Mineral mounts and polished thin sections were prepared on pumice samples from Mamaku and Mokai ignimbrites, an andesitic bleb from uMI, and two rhyolite lava samples from Rotorua Caldera. In an attempt to constrain the temperatures of the various magma types a portion of a corresponding pumice type was crushed using a mortar and pestle, sieved to remove the fine fraction and Fe/Ti oxides separated off using a hand magnet and Frantz isodynamic separator. Several runs through the magnetic separator were often required to part magnetite and ilmenite grains from the crushed pumice sample. Magnetite and ilmenite grains, and pyroxene with magnetite and ilmenite inclusions, were then handpicked using a binocular reflected light microscope and placed on doubled sided sellotape on a glass slide surrounded by an epoxy mould. The mould was then filled with epoxy resin and the sellotape peeled off after the epoxy had solidified, the resulting surface was then polished and the magnetic grains exposed. Rob Spiers of University of Canterbury prepared polished thinsections, and epoxy mounts.

Sample analysis

Samples were analysed using a JEOL 733 SuperProbe (wavelength dispersive) using an accelerating voltage of 15 kV and beam current between 8.1-8.2 μA. Standards were analysed before each session to calibrate the equipment. Where possible analyses were taken from both the cores and rims of crystals to assess any zoning characteristics. Outer core analyses were made if different outer compositions were evident from backscatter electron microscope images. The electron beam was typically 1-3 μm for

mineral spot analyses. For glass analyses the beam was widened to 20-30 μm and alkalis analysed first to minimise the effects of alkali migration.

Data was reduced using ZAF correction procedures by calculations built in to the computer program running the equipment. Lower detection limits (in wt%) were as follows: SiO_2= 0.03, TiO_2= 0.06, Al_2O_3= 0.03, FeO= 0.10, MnO= 0.10, MgO= 0.04, CaO= 0.05, Na_2O= 0.05, K_2O= 0.05, SrO= 0.13, BaO= 0.25, NiO= 0.13, Cr_2O_3= 0.1, and F= 0.12.

Total iron oxide data are stated as FeO. Cation calculations were undertaken using minpet2 software as follows: plagioclase on the basis of 32 oxygens, pyroxene, 6 oxygens; olivine, 4 oxygens; amphibole, 23 oxygens. EPMA data was manipulated using minpet2.

Microprobe data are listed as follows:
3A- Mamaku Ignimbrite pumice clasts.
3B- uMI andesitic blebs
3C- Rotorua rhyolite lithics
3D- Mokai Ignimbrite pumice and mafic bleb
Subheadings as follows:

i) Plagioclase
ii) Pyroxene
iii) Fe/Ti oxides (Olivine for andesitic blebs)
iv) Glass
v) Amphibole (Mamaku pumice only)

Appendix 3Ai: Mamaku plagioclase

Sample	MKP29	MKP29	MKP29	MKP29	MKP29	MKP29	MKP29	MKP29	MKP29	MKP29	MKP35	MKP35
Crystal analysed	1	1	2	2	4	4	6	6	7	7	1	1
Analysis location	c	r	c	r	c	r	c	r	r	c	c	r
SiO_2	63.65	61.98	60.21	62.76	55.91	60.46	55.12	57.06	59.87	61.53	62.55	60.31
TiO_2	0.06	0.01	0.05	0.02	0.06	0.07	0.09	0.08	0.13	0.04	0.00	0.00
Al_2O_3	24.67	23.60	24.77	24.17	22.36	22.39	26.65	25.54	22.31	22.58	23.17	24.89
FeO	0.31	0.15	0.30	0.22	0.21	0.29	0.36	0.34	0.25	0.18	0.33	0.39
MnO	0.04	0.00	0.06	0.16	0.02	0.00	0.19	0.18	0.06	0.06	0.06	0.22
MgO	0.03	0.00	0.09	0.07	0.06	0.02	0.04	0.05	0.03	0.03	0.00	0.01
BaO	0.08	0.10	0.09	0.02	0.20	0.02	0.19	0.28	0.18	0.29	0.08	0.13
CaO	5.79	5.04	6.32	5.07	4.80	4.25	9.04	7.80	4.51	4.24	4.96	6.42
Na_2O	5.66	7.31	7.60	7.63	8.25	8.43	6.40	7.10	8.35	9.01	8.51	7.71
K_2O	0.40	0.49	0.54	0.55	0.49	0.67	0.19	0.43	0.54	0.59	0.50	0.43
Total	100.69	98.68	100.03	100.67	92.36	96.60	98.27	98.86	96.23	98.55	100.16	100.51
Oxygen	32	32	32	32	32	32	32	32	32	32	32	32
Si	11.110	11.101	10.749	11.041	10.826	11.116	10.131	10.402	11.072	11.120	11.101	10.731
Al	5.071	4.978	5.208	5.007	5.099	4.848	5.768	5.483	4.859	4.806	4.843	5.216
Ti	0.008	0.001	0.007	0.003	0.009	0.010	0.012	0.011	0.018	0.005	0.000	0.000
Fe	0.045	0.022	0.045	0.032	0.034	0.045	0.055	0.052	0.039	0.027	0.049	0.058
Mn	0.006	0.000	0.009	0.024	0.003	0.000	0.030	0.028	0.009	0.009	0.009	0.033
Mg	0.008	0.000	0.024	0.018	0.017	0.005	0.011	0.014	0.008	0.008	0.000	0.003
Ba	0.005	0.007	0.006	0.001	0.015	0.001	0.014	0.020	0.013	0.021	0.006	0.009
Ca	1.083	0.967	1.209	0.956	0.996	0.837	1.780	1.523	0.894	0.821	0.943	1.224
Na	1.916	2.539	2.631	2.603	3.097	3.005	2.281	2.510	2.994	3.157	2.928	2.660
K	0.089	0.112	0.123	0.123	0.121	0.157	0.045	0.100	0.127	0.136	0.113	0.098
Total	19.341	19.727	20.011	19.808	20.217	20.024	20.127	20.143	20.033	20.110	19.992	20.032
Ab	62.0	70.2	66.4	70.7	73.5	75.1	55.6	60.7	74.6	76.7	73.5	66.8
An	35.1	26.7	30.5	26.0	23.6	20.9	43.4	36.8	22.3	20.0	23.7	30.7
Or	2.9	3.1	3.1	3.3	2.9	3.9	1.1	2.4	3.2	3.3	2.8	2.5

Appendix 3Ai: Mamaku plagioclase

Sample	MKP35	MKP35	MKP35	MKP35	MKP35	MKP35	MKP35	MKP35	MKP116	MKP116	MKP116	MKP116
Crystal analysed	2	2	3	3	4	4	5	5	1	1	3	3
Analysis location	c	r	c	r	c	r	c	r	c	r	c	r
SiO_2	63.71	64.57	59.42	61.57	60.66	64.27	66.82	65.87	54.42	63.48	62.87	63.31
TiO_2	0.01	0.13	0.12	0.06	0.07	0.01	0.04	0.02	0.15	0.00	0.09	0.10
Al_2O_3	22.93	21.89	24.99	23.85	24.36	22.24	22.99	22.74	27.35	23.34	23.24	22.99
FeO	0.23	0.36	0.23	0.21	0.16	0.20	0.30	0.17	0.25	0.27	0.24	0.34
MnO	0.04	0.12	0.00	0.09	0.05	0.06	0.02	0.00	0.23	0.04	0.07	0.04
MgO	0.02	0.00	0.00	0.00	0.00	0.00	0.00	0.01	0.07	0.01	0.03	0.04
BaO	0.11	0.01	0.00	0.21	0.10	0.11	0.10	0.00	0.15	0.20	0.24	0.00
CaO	3.93	3.87	6.75	5.14	6.01	3.65	3.82	3.60	9.71	5.17	4.76	4.21
Na_2O	8.91	8.66	7.83	8.36	8.55	9.19	9.02	9.05	6.01	8.07	8.83	8.85
K_2O	0.81	0.82	0.34	0.70	0.59	0.94	0.82	0.81	0.19	0.48	0.64	0.63
Total	100.70	100.43	99.68	100.19	100.55	100.67	103.93	102.27	98.53	101.06	101.01	100.51
Oxygen	32	32	32	32	32	32	32	32	32	32	32	32
Si	11.224	11.383	10.656	10.958	10.795	11.327	11.372	11.376	9.988	11.146	11.088	11.175
Al	4.757	4.545	5.278	4.999	5.105	4.616	4.608	4.625	5.912	4.826	4.827	4.779
Ti	0.001	0.017	0.016	0.008	0.009	0.001	0.005	0.003	0.021	0.000	0.012	0.013
Fe	0.034	0.053	0.034	0.031	0.024	0.029	0.043	0.025	0.038	0.040	0.035	0.050
Mn	0.006	0.018	0.000	0.014	0.008	0.009	0.003	0.000	0.036	0.006	0.010	0.006
Mg	0.005	0.000	0.000	0.000	0.000	0.000	0.000	0.003	0.019	0.003	0.008	0.011
Ba	0.008	0.001	0.000	0.015	0.007	0.008	0.007	0.000	0.011	0.014	0.017	0.000
Ca	0.742	0.731	1.297	0.980	1.146	0.689	0.697	0.666	1.909	0.973	0.899	0.796
Na	3.044	2.960	2.723	2.885	2.950	3.141	2.977	3.031	2.139	2.747	3.020	3.029
K	0.182	0.184	0.078	0.159	0.134	0.211	0.178	0.178	0.044	0.108	0.144	0.142
Total	20.003	19.892	20.082	20.049	20.178	20.031	19.890	19.907	20.117	19.863	20.060	20.001
Ab	76.7	76.4	66.4	71.7	69.7	77.7	77.3	78.2	52.3	71.8	74.3	76.4
An	18.7	18.9	31.6	24.4	27.1	17.1	18.1	17.2	46.7	25.4	22.1	20.1
Or	4.6	4.7	1.9	4.0	3.2	5.2	4.6	4.6	1.1	2.8	3.5	3.6

Appendix 3Ai: Mamaku plagioclase

Sample	MKP116	MKP116	MKP116	MKP116	MKP116	MKP155	MKP155	MKP155	MKP155	MKP90	MKP90
Crystal analysed	4	5	5	6	6	5	5	6	6	7	7
Analysis location	r	c	r	c	r	c	r	c	r	c	r
SiO_2	63.88	64.30	64.17	65.11	64.31	58.25	64.52	59.22	62.74	63.25	58.29
TiO_2	0.10	0.02	0.09	0.02	0.01	0.02	0.05	0.08	0.09	0.09	0.01
Al_2O_3	21.61	22.12	22.68	21.98	22.25	25.34	21.72	24.96	22.10	22.58	25.38
FeO	0.21	0.17	0.17	0.15	0.17	0.25	0.30	0.30	0.38	0.32	0.35
MnO	0.20	0.19	0.18	0.09	0.00	0.00	0.05	0.14	0.04	0.14	0.08
MgO	0.03	0.03	0.00	0.00	0.01	0.00	0.05	0.04	0.01	0.02	0.05
BaO	0.06	0.09	0.20	0.22	0.11	0.00	0.01	0.02	0.12	0.00	0.00
CaO	4.62	3.45	4.22	3.18	3.71	6.87	3.49	6.00	4.63	3.99	7.47
Na_2O	8.63	9.03	9.04	8.87	8.90	7.33	8.65	8.00	7.42	8.92	7.16
K_2O	0.54	0.85	0.77	1.01	0.78	0.45	1.04	0.45	1.09	0.70	0.37
Total	99.88	100.25	101.52	100.63	100.25	98.51	99.88	99.21	98.62	100.01	99.16
Oxygen	32	32	32	32	32	32	32	32	32	32	32
Si	11.344	11.360	11.238	11.444	11.352	10.573	11.427	10.670	11.282	11.223	10.533
Al	4.519	4.602	4.677	4.550	4.625	5.417	4.530	5.296	4.680	4.718	5.401
Ti	0.013	0.003	0.012	0.003	0.001	0.003	0.007	0.011	0.012	0.012	0.001
Fe	0.031	0.025	0.025	0.022	0.025	0.038	0.044	0.045	0.057	0.047	0.053
Mn	0.030	0.028	0.027	0.013	0.000	0.000	0.008	0.021	0.006	0.021	0.012
Mg	0.008	0.008	0.000	0.000	0.003	0.000	0.013	0.011	0.003	0.005	0.013
Ba	0.004	0.006	0.014	0.015	0.008	0.000	0.001	0.001	0.008	0.000	0.000
Ca	0.879	0.653	0.792	0.599	0.702	1.336	0.662	1.158	0.892	0.759	1.446
Na	2.972	3.094	3.070	3.023	3.046	2.580	2.971	2.795	2.587	3.069	2.509
K	0.122	0.192	0.172	0.226	0.176	0.104	0.235	0.103	0.250	0.158	0.085
Total	19.922	19.971	20.027	19.895	19.938	20.051	19.898	20.111	19.777	20.012	20.053
Ab	74.8	78.5	76.1	78.6	77.6	64.2	76.8	68.9	69.4	77.0	62.1
An	22.1	16.6	19.6	15.6	17.9	33.2	17.1	28.6	23.9	19.0	35.8
Or	3.1	4.9	4.3	5.9	4.5	2.6	6.1	2.5	6.7	4.0	2.1

Appendix 3Aii: Mamaku pyroxene

Sample	MKP29	MKP29	MKP29	MKP29	MKP29	MKP29	MKP29	MKP29	MKP29	MKP29	MKP35	MKP35
Crystal analysed	1	1	2	2	3	3	4	4	5	5	1	1
Analysis location	c	r	c	r	c	r	r	c	c	r	c	r
FeO	30.82	31.01	30.93	30.75	31.63	30.53	30.63	29.02	30.34	31.35	27.01	30.48
SiO_2	50.95	51.30	50.27	49.80	49.90	52.11	49.21	50.82	51.33	51.54	51.69	50.46
TiO_2	0.15	0.10	0.14	0.13	0.27	0.20	0.12	0.17	0.19	0.21	0.16	0.12
Al_2O_3	0.36	0.27	0.23	0.19	0.30	0.21	1.23	0.30	0.32	0.36	0.37	0.26
Cr_2O_3	0.07	0.06	0.00	0.10	0.01	0.02	0.00	0.00	0.01	0.01	0.00	0.07
MnO	2.24	2.27	2.10	2.32	2.17	2.08	1.88	1.99	1.75	2.17	1.64	2.47
NiO	0.00	0.12	0.17	0.11	0.02	0.04	0.23	0.27	0.00	0.12	0.10	0.00
MgO	15.56	15.04	15.33	14.27	15.18	14.98	13.66	16.58	15.46	14.73	18.28	15.50
CaO	1.23	1.23	1.38	1.19	1.17	1.11	1.09	1.23	1.25	1.19	1.28	1.17
Na_2O	0.00	0.00	0.00	0.00	0.00	0.00	0.00	0.00	0.00	0.00	0.00	0.00
K_2O	0.00	0.00	0.00	0.00	0.00	0.00	0.00	0.00	0.00	0.00	0.00	0.00
Total	101.38	101.40	100.55	98.86	100.65	101.28	98.05	100.38	100.65	101.68	100.53	100.53
Oxygen	6	6	6	6	6	6	6	6	6	6	6	6
Si	1.965	1.984	1.957	1.982	1.944	2.016	1.975	1.964	1.991	1.992	1.971	1.962
Al	0.016	0.012	0.011	0.009	0.014	0.010	0.058	0.014	0.015	0.016	0.017	0.012
Ti	0.004	0.003	0.004	0.004	0.008	0.006	0.004	0.005	0.006	0.006	0.005	0.004
Fe	0.994	1.003	1.007	1.023	1.031	0.988	1.028	0.937	0.985	1.013	0.861	0.991
Mn	0.073	0.074	0.069	0.078	0.072	0.068	0.064	0.065	0.058	0.071	0.12	0.081
Mg	0.895	0.867	0.890	0.847	0.882	0.864	0.817	0.955	0.894	0.849	0.972	0.899
Cr	0.002	0.002	0.000	0.003	0.000	0.001	0.000	0.000	0.000	0.000	0.000	0.002
Ni	0.000	0.004	0.005	0.004	0.001	0.001	0.007	0.008	0.000	0.004	0.003	0.000
Ca	0.051	0.051	0.058	0.051	0.049	0.046	0.047	0.051	0.052	0.049	0.052	0.049
Na	0.000	0.000	0.000	0.000	0.000	0.000	0.000	0.000	0.000	0.000	0.000	0.000
K	0.000	0.000	0.000	0.000	0.000	0.000	0.000	0.000	0.000	0.000	0.000	0.000
Total	4.000	4.000	4.001	4.001	4.001	4.000	4.000	3.999	4.001	4.000	4.001	4.000
Wo	2.525	2.554	2.845	2.538	2.403	2.340	2.396	2.535	2.614	2.486	2.607	2.413
En	44.449	43.456	43.968	42.352	43.374	43.947	41.781	47.542	44.977	42.814	51.808	44.485
Fs	53.025	53.990	53.187	55.109	54.223	53.712	55.823	49.923	52.409	54.701	45.584	53.101

Appendix 3Aii: Mamaku pyroxene

Sample	MKP35	MKP35	MKP35	MKP35	MKP35	MKP35	MKP35	MKP35	MKP116	MKP116	MKP116	MKP116
Crystal analysed	2	2	3	3	4	4	6	6	1	1	3	3
Analysis location	c	r	c	r	c	r	c	r	c	r	c	r
FeO	30.30	31.93	33.26	32.08	35.67	31.57	26.61	25.13	31.80	32.51	31.86	32.03
SiO_2	50.62	49.73	49.90	49.75	49.38	49.87	52.80	51.70	49.72	49.99	49.93	49.87
TiO_2	0.18	0.03	0.14	0.00	0.22	0.11	0.13	0.17	0.21	0.14	0.14	0.20
Al_2O_3	0.34	0.25	0.15	0.34	0.24	0.22	0.40	0.51	0.33	0.34	0.23	0.26
Cr_2O_3	0.04	0.05	0.04	0.07	0.07	0.01	0.09	0.02	0.04	0.15	0.09	0.04
MnO	1.94	2.24	2.34	2.25	2.32	2.61	0.88	1.01	2.07	2.30	2.44	2.48
NiO	0.06	0.14	0.10	0.10	0.03	0.05	0.03	0.08	0.00	0.13	0.00	0.00
MgO	16.02	14.19	13.42	13.68	11.63	13.69	19.83	19.88	14.79	14.26	14.46	14.15
CaO	1.20	1.16	0.88	0.94	1.22	0.91	0.78	1.06	1.14	1.20	1.31	1.10
Na_2O	0.00	0.00	0.00	0.00	0.00	0.00	0.00	0.00	0.00	0.00	0.00	0.00
K_2O	0.00	0.00	0.00	0.00	0.00	0.00	0.00	0.00	0.00	0.00	0.00	0.00
Total	100.70	99.72	100.23	99.21	100.78	99.04	101.55	99.56	100.10	101.02	100.46	100.13
Oxygen	6	6	6	6	6	6	6	6	6	6	6	6
Si	1.958	1.966	1.975	1.982	1.968	1.990	1.976	1.967	1.951	1.953	1.957	1.965
Al	0.015	0.012	0.007	0.016	0.011	0.010	0.018	0.023	0.015	0.016	0.011	0.012
Ti	0.005	0.001	0.004	0.000	0.007	0.003	0.004	0.005	0.006	0.004	0.004	0.006
Fe	0.981	1.056	1.101	1.068	1.189	1.053	0.833	0.799	1.043	1.062	1.044	1.056
Mn	0.064	0.075	0.078	0.076	0.078	0.088	0.155	0.191	0.069	0.076	0.081	0.083
Mg	0.924	0.836	0.792	0.812	0.691	0.814	0.979	0.969	0.865	0.830	0.845	0.831
Cr	0.001	0.002	0.001	0.002	0.002	0.000	0.003	0.001	0.001	0.005	0.003	0.001
Ni	0.002	0.004	0.003	0.003	0.001	0.002	0.001	0.002	0.000	0.004	0.000	0.000
Ca	0.050	0.049	0.037	0.040	0.052	0.039	0.031	0.043	0.048	0.050	0.055	0.046
Na	0.000	0.000	0.000	0.000	0.000	0.000	0.000	0.000	0.000	0.000	0.000	0.000
K	0.000	0.000	0.000	0.000	0.000	0.000	0.000	0.000	0.000	0.000	0.000	0.000
Total	4.000	4.001	3.998	3.999	3.999	3.999	4.000	4.000	3.998	4.000	4.000	4.000
Wo	2.465	2.437	1.858	2.009	2.591	1.950	1.565	2.157	2.366	2.488	2.716	2.304
En	45.794	41.481	39.424	40.678	34.372	40.820	55.363	56.296	42.715	41.134	41.719	41.232
Fs	51.740	56.082	58.718	57.314	63.036	57.230	43.072	41.546	54.919	56.378	55.565	56.464

Appendix 3Aii: Mamaku pyroxene

Sample	MKP116	MKP116	MKP116	MKP116	MKP116	MKP116	MKP116	MKP155	MKP155	MKP155	MKP155	MKP155
Crystal analysed	4	4	5	5	2	2	2	1	1	1	3	3
Analysis location	c	r	c	r	c	oc	r	c	oc	r	c	r
FeO	29.19	32.11	28.36	29.01	22.65	23.29	29.96	31.95	32.91	32.03	32.78	32.28
SiO_2	52.08	50.80	51.45	50.36	53.37	51.76	49.61	50.08	49.51	49.15	48.12	49.84
TiO_2	0.09	0.10	0.17	0.12	0.29	0.26	0.21	0.27	0.13	0.10	0.08	0.08
Al_2O_3	0.33	0.21	0.40	0.39	0.84	0.04	0.53	0.36	0.24	0.18	0.10	0.17
Cr_2O_3	0.03	0.25	0.00	0.14	0.11	0.00	0.10	0.12	0.09	0.02	0.03	0.00
MnO	2.64	2.20	2.00	1.81	1.62	1.58	2.10	2.34	2.33	2.77	2.25	2.33
NiO	0.04	0.00	0.02	0.08	0.15	0.00	0.03	0.22	0.08	0.16	0.00	0.80
MgO	16.91	13.68	17.35	16.87	21.06	20.21	15.75	14.99	13.32	13.71	13.55	13.64
CaO	1.11	1.20	1.28	1.26	1.60	1.48	1.36	0.98	0.99	0.95	1.16	0.91
Na_2O	0.00	0.00	0.00	0.00	0.09	0.08	0.00	0.04	0.01	0.01	0.00	0.00
K_2O	0.00	0.00	0.00	0.00	0.06	0.01	0.00	0.05	0.00	0.04	0.00	0.02
Total	102.42	100.55	101.03	100.04	101.84	98.71	99.65	101.40	99.61	99.12	98.07	100.07
Oxygen	6	6	6	6	6	6	6	6	6	6	6	6
Si	1.972	1.998	1.965	1.949	1.968	1.977	1.940	1.941	1.971	1.961	1.943	1.973
Al	0.015	0.009	0.018	0.018	0.037	0.002	0.024	0.016	0.011	0.008	0.005	0.008
Ti	0.003	0.003	0.005	0.003	0.008	0.007	0.006	0.008	0.004	0.003	0.002	0.002
Fe	0.924	1.056	0.907	0.939	0.699	0.744	0.979	1.035	1.095	1.069	1.108	1.068
Mn	0.085	0.073	0.083	0.082	0.246	0.224	0.07	0.077	0.079	0.094	0.077	0.078
Mg	0.955	0.802	0.970	0.950	0.963	0.979	0.918	0.866	0.791	0.816	0.815	0.805
Cr	0.001	0.008	0.000	0.004	0.003	0.000	0.003	0.004	0.003	0.001	0.001	0.000
Ni	0.001	0.000	0.001	0.002	0.004	0.000	0.001	0.007	0.003	0.005	0.000	0.025
Ca	0.045	0.051	0.052	0.052	0.063	0.061	0.057	0.041	0.042	0.041	0.050	0.039
Na	0.000	0.000	0.000	0.000	0.006	0.006	0.000	0.003	0.001	0.001	0.000	0.000
K	0.000	0.000	0.000	0.000	0.003	0.000	0.000	0.002	0.000	0.002	0.000	0.001
Total	4.001	4.000	4.001	3.999	4.000	4.000	3.998	4.000	4.000	4.001	4.001	3.999
Wo	2.242	2.551	2.605	2.582	3.209	3.019	2.815	2.015	2.104	2.012	2.448	1.939
En	47.523	40.467	49.128	48.093	58.767	57.355	45.353	42.893	39.388	40.401	39.793	40.443
Fs	50.235	56.982	48.267	49.326	38.025	39.626	51.833	55.091	58.508	57.587	57.759	57.618

Appendix 3Aii: Mamaku pyroxene

Sample	**MKP90**	**MKP90**	**MKP90**	**MKP90**	**MKP90**	**MKP90**
Crystal analysed	2	2	3	3	8	8
Analysis location	c	r	c	r	c	r
FeO	32.42	32.36	31.26	33.90	30.82	32.43
SiO_2	51.85	50.57	51.54	50.12	49.90	51.02
TiO_2	0.11	0.07	0.08	0.11	0.09	0.12
Al_2O_3	0.30	0.27	0.22	0.21	0.20	0.22
Cr_2O_3	0.00	0.10	0.23	0.15	0.06	0.00
MnO	2.14	2.06	2.38	2.32	2.07	2.24
NiO	0.12	0.18	0.06	0.00	0.10	0.00
MgO	15.21	13.89	15.87	13.73	14.79	13.72
CaO	1.27	1.03	1.06	0.98	1.13	1.03
Na_2O	0.00	0.00	0.09	0.08	0.10	0.10
K_2O	0.01	0.03	0.03	0.03	0.00	0.04
Total	103.43	100.56	102.82	101.63	99.26	100.92
Oxygen	6	6	6	6	6	6
Si	1.969	1.987	1.959	1.954	1.970	1.997
Al	0.013	0.012	0.010	0.010	0.009	0.010
Ti	0.003	0.002	0.002	0.003	0.003	0.004
Fe	1.030	1.064	0.993	1.105	1.018	1.062
Mn	0.069	0.069	0.077	0.077	0.069	0.074
Mg	0.861	0.813	0.899	0.798	0.871	0.801
Cr	0.000	0.003	0.007	0.005	0.002	0.000
Ni	0.004	0.006	0.002	0.000	0.003	0.000
Ca	0.052	0.043	0.043	0.041	0.048	0.043
Na	0.000	0.000	0.007	0.006	0.008	0.008
K	0.000	0.002	0.001	0.001	0.000	0.002
Total	4.001	4.001	4.000	4.000	4.001	4.001
Wo	2.569	2.180	2.145	2.026	2.384	2.182
En	42.814	40.908	44.679	39.488	43.413	40.441
Fs	54.617	56.912	53.177	58.486	54.203	57.377

Appendix 3Aiii: Mamaku Fe/Ti oxides

Sample	MKP29	MKP29	MKP29	MKP29	MKP29	MKP29	MKP29	MKP29	MKP29	MKP29	MKP35	MKP35	MKP35
Analysis area	1	1	1	1	3	3	4	4	5	5	1	1	1
Mineral	ilm	ilm2	mt	mt2	mt	ilm	mt	ilm	mt	ilm	mt	ilm	ilm2
SiO_2	0.10	0.05	0.10	0.12	0.06	0.12	0.16	0.00	0.15	0.02	0.16	0.04	0.07
TiO_2	50.78	50.38	12.79	13.17	12.18	49.60	12.64	51.74	12.95	51.82	11.46	50.71	51.14
Al_2O_3	0.07	0.11	1.05	1.04	1.06	0.07	1.18	0.05	1.06	0.06	1.08	0.05	0.06
FeO	48.72	47.65	80.66	79.22	79.29	48.53	80.67	47.26	80.00	47.93	81.24	47.32	46.99
MnO	1.43	1.49	0.79	0.79	0.96	0.90	1.02	1.33	0.98	1.54	1.09	1.80	1.62
MgO	0.77	1.01	0.54	0.49	0.47	0.70	0.63	1.54	0.57	1.18	0.41	0.93	0.96
CaO	0.07	0.01	0.06	0.03	0.05	0.04	0.04	0.01	0.05	0.16	0.07	0.08	0.01
Na_2O	0.00	0.00	0.00	0.00	0.00	0.00	0.00	0.00	0.00	0.00	0.00	0.00	0.00
K_2O	0.00	0.00	0.00	0.00	0.00	0.00	0.00	0.00	0.00	0.00	0.00	0.00	0.00
Cr_2O_3	0.00	0.20	0.05	0.05	0.11	0.00	0.01	0.00	0.12	0.01	0.00	0.20	0.00
NiO	0.23	0.00	0.11	0.00	0.00	0.12	0.15	0.04	0.14	0.03	0.07	0.00	0.23
Total	102.17	100.9	96.15	94.91	94.18	100.08	96.5	101.97	96.02	102.75	95.58	101.13	101.08

Sample	MKP35	MKP35	MKP35	MKP35	MKP35	MKP35	MKP35	MKP35	MKP35	MKP116	MKP116	MKP116	MKP116
Analysis area	1	2	2	2	2	3	3	4	4	2	2	3	3
Mineral	mt2	mt	ilm	mt2	ilm2	mt	ilm	mt	ilm	mt	ilm	mt	mt
SiO_2	0.07	0.02	0.08	0.09	0.02	0.06	0.01	0.03	0.02	0.05	0.03	0.04	0.11
TiO_2	12.22	11.77	51.97	11.54	52.06	50.88	51.35	51.06	45.25	12.06	50.27	50.37	10.02
Al_2O_3	1.11	1.08	0.07	1.02	0.10	0.04	0.10	0.07	0.02	1.12	0.08	0.08	1.18
FeO	80.93	80.85	47.06	80.06	47.80	47.33	47.02	45.58	47.80	80.45	49.13	49.89	80.80
MnO	0.88	0.93	1.50	1.03	1.73	1.64	2.00	1.71	1.77	0.81	1.38	1.38	0.86
MgO	0.46	0.48	0.86	0.46	0.80	1.01	1.01	1.02	1.05	0.35	0.70	1.01	0.36
CaO	0.06	0.04	0.04	0.10	0.02	0.06	0.08	0.09	0.00	0.04	0.04	0.03	0.06
Na_2O	0.00	0.00	0.00	0.00	0.00	0.00	0.00	0.00	0.00	0.00	0.00	0.00	0.00
K_2O	0.00	0.00	0.00	0.00	0.00	0.00	0.00	0.00	0.00	0.00	0.00	0.00	0.00
Cr_2O_3	0.03	0.00	0.08	0.11	0.07	0.00	0.12	0.20	0.03	0.09	0.06	0.07	0.01
NiO	0.22	0.06	0.18	0.00	0.00	0.03	0.00	0.00	0.00	0.00	0.03	0.00	0.11
Total	95.98	95.23	101.84	94.41	102.60	101.05	101.69	99.76	95.94	94.97	101.72	102.87	93.51

Appendix 3Aiii: Mamaku Fe/Ti oxides

Sample	**MKP116**	**MKP116**	**MKP116**	**MKP116**	**MKP90**	**MKP90**
Analysis are	4	4	5	5	3	3
Mineral	ilm	mt	ilm	mt	ilm	mt
SiO_2	0.09	0.09	46.16	0.01	0.07	0.2
TiO_2	50.26	12.04	0.01	51.55	50.05	11.41
Al_2O_3	0.00	1.06	0.06	0.09	0.07	0.98
FeO	48.88	80.08	50.82	46.70	46.75	80.83
MnO	1.50	0.95	2.43	1.39	1.72	0.84
MgO	1.01	0.40	0.07	1.29	0.97	0.43
CaO	0.09	0.04	0.13	0.01	0.01	0.02
Na_2O	0.00	0.00	0.00	0.00	0.01	0.00
K_2O	0.00	0.00	0.00	0.00	0.01	0.06
Cr_2O_3	0.00	0.00	0.01	0.03	0.08	0.01
NiO	0.14	0.08	0.09	0.80	0.03	0.10
Total	101.97	94.74	99.78	101.87	99.77	94.88

Appendix 3Aiv: Mamaku pumice glass

Sample	MKP29	MKP29	MKP29	MKP29	MKP116	MKP116	MKP116	MKP116	MKP116	MKP35	MKP35	MKP35
Analysis area	1	3	5	7	1	3	4	5	6	1	2	3
SiO_2	76.83	77.49	75.63	77.24	63.06	77.81	76.70	78.79	78.25	79.40	78.66	75.64
TiO_2	0.20	0.12	0.04	0.14	0.30	0.19	0.14	0.16	0.15	0.19	0.15	0.10
Al_2O_3	11.92	12.53	11.86	12.18	9.77	12.38	12.38	12.47	12.10	12.36	12.33	11.95
Fe_2O_3	0.55	0.28	0.48	1.13	0.21	1.13	1.20	1.19	1.09	0.91	1.01	0.96
MnO	0.08	0.17	0.10	0.13	0.08	0.19	0.06	0.13	0.07	0.03	0.08	0.19
MgO	0.06	0.00	0.04	0.12	0.01	0.08	0.08	0.09	0.09	0.09	0.08	0.10
CaO	0.21	0.43	0.74	0.79	0.41	0.61	0.67	0.50	0.53	0.64	0.41	0.52
Na_2O	1.89	2.04	5.42	3.40	2.70	2.39	2.26	2.59	2.57	2.46	2.52	5.92
K_2O	3.31	3.57	1.53	1.31	3.24	3.41	3.41	3.44	3.48	3.46	3.59	1.44
Total	95.05	96.63	95.84	96.44	79.78	98.19	96.90	99.36	98.33	99.54	98.83	96.82

Sample	MKP35	MKP35	MKP155	MKP155	MKP155	MKP155	MKP155	MKP155	MKP90	MKP90	MKP90	MKP90
Analysis area	5	5	1	2	5	6	6a	6b	4	5	7	8
SiO_2	77.50	75.82	73.73	70.70	73.49	74.12	73.76	73.42	75.41	75.57	75.96	72.46
TiO_2	0.12	0.27	0.11	0.10	0.17	0.09	0.10	0.13	0.22	0.08	0.25	0.15
Al_2O_3	12.33	12.32	12.13	11.53	11.85	12.03	12.01	12.03	12.03	12.03	12.21	11.81
Fe_2O_3	0.32	0.95	1.14	0.80	0.94	1.10	1.15	1.02	0.98	0.84	0.95	1.13
MnO	0.13	0.08	0.08	0.14	0.10	0.04	0.10	0.01	0.03	0.07	0.00	0.03
MgO	0.04	0.06	0.05	0.07	0.04	0.10	0.07	0.11	0.06	0.07	0.06	0.03
CaO	0.44	0.56	0.50	0.46	0.54	0.76	0.79	0.76	0.50	0.57	0.39	0.49
Na_2O	2.13	3.86	3.65	3.45	3.75	3.56	1.66	3.73	5.67	5.80	5.79	5.72
K_2O	3.56	3.81	3.89	3.59	4.02	3.74	3.49	3.49	1.61	1.83	1.66	1.68
Total	96.57	97.73	95.28	90.84	94.90	95.54	93.13	94.70	96.51	96.86	97.27	93.50

Appendix 3Av: Mamaku amphibole

Sample	**MKP29**	**MKP29**	**MKP90**
Crystal analysed	3	3	6
Analysis location	c	r	c
SiO_2	50.10	50.41	46.41
TiO_2	1.75	1.68	1.44
Al_2O_3	5.66	5.14	5.76
FeO	10.72	11.44	19.10
Cr_2O_3	0.13	0.15	0.09
MnO	0.59	0.43	0.90
MgO	18.37	17.37	11.23
CaO	10.88	10.57	9.83
Na_2O	2.17	1.86	1.71
K_2O	0.38	0.41	0.48
Total	100.62	99.31	96.86
Oxygen	23	23	23
Si	7.033	7.164	7.057
Al	0.936	0.861	1.032
Ti	0.185	0.180	0.165
Fe	1.258	1.359	2.429
Mn	0.070	0.052	0.116
Mg	3.844	3.680	2.546
Cr	0.014	0.017	0.011
Ca	1.636	1.610	1.602
Na	0.590	0.512	0.504
K	0.068	0.074	0.093
Total	38.634	38.509	38.555

Appendix 3Bi: Mamaku andesitic bleb plagioclase

Sample	**MKP120**	**MKP120**	**MKP120**	**MKP120**	**MKP120**	**MKP120**	**MKP120**	**MKP120**
Crystal analysed	1	1	4	4	6	6	10	10
Analysis location	c	r	c	r	c	r	c	r
SiO_2	56.03	64.90	60.19	61.55	57.97	58.80	56.46	60.88
TiO_2	0.05	0.30	0.04	0.08	0.10	0.05	0.05	0.07
Al_2O_3	27.12	19.15	24.91	22.70	26.31	25.54	26.77	23.34
FeO	0.43	0.71	0.31	0.31	0.29	0.26	0.35	0.23
MnO	0.12	0.00	0.01	0.01	0.03	0.06	0.08	0.04
MgO	0.05	0.04	0.01	0.01	0.04	0.03	0.09	0.00
BaO	0.40	0.65	0.02	0.07	0.08	0.05	0.13	0.23
CaO	9.68	0.92	6.42	4.64	7.89	7.15	8.89	5.29
Na_2O	6.21	6.07	8.02	8.60	6.98	7.50	6.70	8.42
K_2O	0.22	7.01	0.38	0.58	0.32	0.34	0.27	0.50
Total	100.31	99.75	100.31	98.55	100.01	99.78	99.79	99.00
Oxygen	32	32	32	32	32	32	32	32
Si	10.112	11.776	10.720	11.106	10.398	10.552	10.203	10.969
Al	5.764	4.092	5.225	4.824	5.558	5.398	5.697	4.952
Ti	0.007	0.041	0.005	0.011	0.013	0.007	0.007	0.009
Fe	0.065	0.108	0.046	0.047	0.044	0.039	0.053	0.035
Mn	0.018	0.000	0.002	0.002	0.005	0.009	0.012	0.006
MgO	0.013	0.011	0.003	0.003	0.011	0.008	0.024	0.000
Ba	0.028	0.046	0.001	0.005	0.006	0.004	0.009	0.016
Ca	1.872	0.179	1.225	0.897	1.516	1.375	1.721	1.021
Na	2.173	2.136	2.770	3.009	2.428	2.610	2.348	2.942
K	0.051	1.623	0.086	0.134	0.073	0.078	0.062	0.115
Total	20.10	20.01	20.08	20.04	20.05	20.08	20.14	20.07
Ab	53.1	54.2	67.9	74.5	60.4	64.2	56.8	72.1
An	45.7	4.5	30.0	22.2	37.7	33.8	41.7	25.0
Or	1.2	41.2	2.1	3.3	1.8	1.9	1.5	2.8

Appendix 3Bii: Mamaku andesitic bleb pyroxene

Sample	**MKP120**	**MKP120**	**MKP120**	**MKP120**	**MKP120**	**MKP120**	**MKP120**	**MKP120**	**MKP120**	**MKP120**
Crystal analysed	3	3	5	5	5	5	8	8	9	9
Analysis location	c	r	c	r	c	r	c	r	c	r
SiO_2	51.29	53.12	51.18	51.39	50.26	51.84	54.54	54.07	51.40	50.33
TiO_2	0.19	0.21	0.08	0.21	0.92	0.60	0.42	0.36	0.65	0.88
Al_2O_3	0.27	1.20	0.32	0.64	3.86	2.51	1.54	1.56	2.95	3.53
FeO	27.90	16.34	24.64	22.49	7.64	7.19	14.99	14.71	7.89	11.45
Cr_2O_3	0.11	0.17	0.12	0.22	0.47	0.36	0.09	0.17	0.39	0.01
MnO	1.79	0.50	1.53	1.30	0.22	0.28	0.53	0.54	0.33	0.32
NiO	0.08	0.00	0.09	0.10	0.19	0.00	0.10	0.02	0.16	0.04
MgO	17.82	26.28	19.77	20.74	15.70	16.51	27.46	27.74	16.43	15.55
CaO	1.07	1.82	1.17	1.32	20.85	21.55	1.64	1.61	20.03	18.06
Na_2O	0.06	0.05	0.04	0.01	0.31	0.24	0.07	0.01	0.27	0.32
K_2O	0.03	0.05	0.05	0.02	0.02	0.02	0.00	0.01	0.04	0.10
Total	100.61	99.74	98.99	98.44	100.44	101.10	101.38	100.80	100.54	100.59
Oxygen	6	6	6	6	6	6	6	6	6	6
Si	1.961	1.928	1.958	1.961	1.845	1.886	1.937	1.928	1.883	1.859
Al	0.012	0.051	0.014	0.029	0.167	0.108	0.064	0.065	0.127	0.153
Fe	0.893	0.496	0.789	0.718	0.234	0.219	0.446	0.439	0.242	0.353
Ti	0.005	0.006	0.002	0.006	0.025	0.016	0.011	0.010	0.018	0.024
Mn	0.058	0.015	0.050	0.042	0.007	0.009	0.016	0.016	0.010	0.010
Mg	1.016	1.422	1.127	1.180	0.859	0.895	1.454	1.475	0.897	0.856
Cr	0.003	0.005	0.004	0.007	0.014	0.010	0.003	0.005	0.011	0.000
Ni	0.002	0.000	0.003	0.003	0.006	0.000	0.003	0.001	0.005	0.001
Ca	0.044	0.071	0.048	0.054	0.820	0.840	0.062	0.061	0.786	0.715
Na	0.004	0.004	0.003	0.001	0.022	0.017	0.005	0.001	0.019	0.023
K	0.001	0.002	0.002	0.001	0.001	0.001	0.000	0.000	0.002	0.005
Total	3.999	4.000	4.000	4.002	4.000	4.001	4.001	4.001	4.000	3.999
Wo	2.181	3.532	2.382	2.707	42.697	42.796	3.156	3.089	40.621	36.943
En	50.542	70.953	56.001	59.183	44.735	45.620	73.523	74.060	46.361	44.258
Fs	47.276	25.515	41.617	38.110	12.568	11.585	23.321	22.851	13.018	18.799

Appendix 3Biii: Andesitic bleb olivine

Sample	**MKP120**	**MKP120**	**MKP120**	**MKP120**
Crystal analysed	2	2	7	7
Analysis location	c	r	c	r
SiO_2	38.51	38.31	39.11	38.60
TiO_2	0.00	0.02	0.11	0.17
Al_2O_3	0.05	0.08	0.04	0.04
FeO	21.01	21.01	20.57	22.36
MnO	0.34	0.44	0.51	0.38
MgO	40.01	40.10	40.58	39.41
CaO	0.71	0.16	0.18	0.17
Na_2O	0.00	0.06	0.05	0.03
K_2O	0.00	0.04	0.01	0.05
NiO	0.04	0.15	0.02	0.15
Total	100.67	100.37	101.18	101.36
Oxygen	4	4	4	4
Si	0.991	0.989	0.997	0.992
Al	0.002	0.002	0.001	0.001
Ti	0.000	0.000	0.002	0.003
Fe	0.452	0.454	0.439	0.481
Mn	0.007	0.010	0.011	0.008
Mg	1.535	1.544	1.543	1.510
Ca	0.020	0.004	0.005	0.005
Na	0.000	0.003	0.002	0.001
K	0.000	0.001	0.000	0.002
Ni	0.001	0.003	0.000	0.003
Total	3.008	3.010	3.000	3.006

Appendix 3Biv: Andesitic bleb groundmass

Sample	**MKP120**	**MKP120**	**MKP120**
Analysis	9	10b	11
SiO_2	57.92	60.79	66.51
TiO_2	0.12	0.06	0.02
Al_2O_3	26.00	22.13	18.44
FeO	0.65	0.76	0.33
MnO	0.00	0.23	0.09
MgO	0.04	0.05	0.03
BaO	0.21	0.23	0.18
CaO	7.78	4.26	0.70
Na_2O	7.08	5.85	6.62
K_2O	0.47	4.47	5.98
Total	100.27	98.83	98.90

Appendix 3Ci: Rotorua rhyolite plagioclase

Sample	**RR19**	**RR19**	**RR19**	**RR19**	**RR19**	**RR19**	**RR19**	**RR19**	**RR32**	**RR32**	**RR32**	**RR32**
Crystal analysed	2	2	5	5	7	7	10	10	1	1	6	6
Analysis location	r	c	c	r	c	r	c	r	c	r	c	r
SiO_2	56.92	58.57	52.96	61.63	56.39	56.62	56.34	57.56	60.01	60.79	59.15	58.64
TiO_2	0.09	0.06	0.01	0.01	0.01	0.01	0.09	0.00	0.04	0.08	0.14	0.03
Al_2O_3	25.71	24.87	25.93	25.49	26.61	26.17	26.73	25.62	25.58	25.18	25.14	25.01
FeO	0.37	0.23	0.22	0.42	0.24	0.23	0.34	0.32	0.26	0.34	0.30	0.21
MnO	0.00	0.17	0.00	0.05	0.02	0.08	0.09	0.03	0.14	0.08	0.07	0.02
MgO	0.11	0.05	0.01	0.03	0.01	0.01	0.04	0.03	0.03	0.02	0.06	0.00
BaO	0.00	0.00	0.00	0.00	0.04	0.11	0.00	0.00	0.00	0.00	0.34	0.16
CaO	7.81	6.75	8.16	7.00	8.50	9.31	8.86	8.12	6.92	6.90	7.45	6.82
Na_2O	6.71	7.15	6.71	7.40	6.23	6.44	6.62	6.74	7.34	7.01	7.38	7.64
K_2O	0.62	0.47	0.34	0.71	0.31	0.31	0.27	0.57	0.38	0.41	0.35	0.34
Total	98.34	98.32	94.34	102.74	98.36	99.29	99.38	98.99	100.70	100.81	100.38	98.87
Oxygen	32	32	32	32	32	32	32	32	32	32	32	32
Si	10.398	10.644	10.121	10.723	10.285	10.279	10.210	10.444	10.641	10.744	10.583	10.617
Al	5.531	5.323	5.836	5.223	5.716	5.595	5.704	5.475	5.342	5.241	5.297	5.333
Ti	0.012	0.008	0.001	0.001	0.001	0.001	0.012	0.000	0.005	0.011	0.019	0.004
Fe	0.057	0.035	0.035	0.061	0.037	0.035	0.052	0.049	0.039	0.050	0.045	0.032
Mn	0.000	0.026	0.000	0.007	0.003	0.012	0.014	0.005	0.021	0.012	0.011	0.003
Mg	0.030	0.014	0.003	0.008	0.003	0.003	0.011	0.008	0.008	0.005	0.016	0.000
Ba	0.000	0.000	0.000	0.000	0.003	0.008	0.000	0.000	0.000	0.000	0.024	0.011
Ca	1.529	1.314	1.671	1.305	1.661	1.811	1.720	1.579	1.315	1.307	1.428	1.323
Na	2.377	2.520	2.486	2.497	2.203	2.267	2.326	2.371	2.524	2.402	2.560	2.682
K	0.144	0.109	0.083	0.158	0.072	0.072	0.062	0.132	0.086	0.092	0.080	0.079
Total	20.078	19.993	20.236	19.983	19.984	20.083	20.111	20.063	19.981	19.864	20.063	20.084
Ab	58.70	63.90	58.60	63.10	56.00	54.60	56.60	58.10	64.30	63.20	62.90	65.70
An	37.80	33.30	39.40	33.00	42.20	43.60	41.90	38.70	33.50	34.40	35.10	32.40
Or	3.60	2.80	2.00	4.00	1.80	1.70	1.50	3.20	2.20	2.40	2.00	1.90

Appendix 3Ci: Rotorua rhyolite plagioclase

Sample	RR32	RR32	RR32	RR32	MKR1	MKR1	MKR1	MKR1	MKR1	MKR1	MKR1	MKR1
Crystal analysed	7	7	8	8	1	1	4	4	5	5	6	6
Analysis location	c	r	c	r	c	r	c	r	r	c	c	r
SiO_2	58.97	58.61	64.15	59.64	61.60	62.11	61.16	62.81	60.62	59.25	56.99	61.57
TiO_2	0.03	0.08	0.04	0.08	0.02	0.01	0.00	0.09	0.16	0.03	0.07	0.13
Al_2O_3	24.73	24.31	22.73	25.04	22.56	22.44	23.34	22.46	23.49	24.69	26.10	22.76
FeO	0.28	0.28	0.19	0.32	0.17	0.10	0.27	0.26	0.22	0.33	0.28	0.19
MnO	0.20	0.07	0.00	0.06	0.00	0.10	0.04	0.04	0.04	0.00	0.00	0.03
MgO	0.04	0.04	0.01	0.01	0.00	0.01	0.00	0.01	0.04	0.01	0.01	0.01
BaO	0.07	0.29	0.12	0.00	0.00	0.13	0.00	0.16	0.12	0.00	0.28	0.09
CaO	6.89	6.55	4.42	6.83	4.14	3.51	5.03	3.98	4.90	6.78	8.22	4.26
Na_2O	7.44	7.95	8.90	7.28	8.92	9.07	8.43	9.01	8.42	7.64	7.00	8.79
K_2O	0.38	0.32	0.57	0.36	0.75	0.87	0.07	0.87	0.55	0.41	0.25	0.72
Total	99.03	98.50	101.13	99.62	98.16	98.35	98.34	99.69	98.56	99.14	99.20	98.55
Oxygen	32	32	32	32	32	32	32	32	32	32	32	32
Si	10.659	10.673	11.248	10.685	11.148	11.213	11.029	11.206	10.953	10.686	10.341	11.109
Al	5.264	5.213	4.694	5.283	4.808	4.771	4.957	4.719	4.998	5.244	5.577	4.836
Ti	0.004	0.011	0.005	0.011	0.003	0.001	0.000	0.012	0.022	0.004	0.010	0.018
Fe	0.042	0.043	0.028	0.048	0.026	0.015	0.041	0.039	0.033	0.050	0.042	0.029
Mn	0.031	0.011	0.000	0.009	0.000	0.015	0.006	0.006	0.006	0.000	0.000	0.005
Mg	0.011	0.011	0.003	0.003	0.000	0.003	0.000	0.003	0.011	0.003	0.003	0.003
Ba	0.005	0.021	0.008	0.000	0.000	0.009	0.000	0.011	0.008	0.000	0.020	0.006
Ca	1.334	1.278	0.830	1.311	0.803	0.679	0.972	0.761	0.949	1.310	1.598	0.823
Na	2.608	2.807	3.026	2.529	3.130	3.175	2.948	3.117	2.950	2.672	2.463	3.075
K	0.088	0.074	0.128	0.082	0.173	0.200	0.016	0.198	0.127	0.094	0.058	0.166
Total	20.046	20.142	19.970	19.961	20.091	20.081	19.969	20.072	20.057	20.063	20.112	20.070
Ab	64.70	67.50	76.00	64.50	76.20	78.30	74.90	76.50	73.30	65.60	59.80	75.70
An	33.10	30.70	20.80	33.40	19.60	16.70	24.70	18.70	23.60	32.10	38.80	20.30
Or	2.20	1.80	3.20	2.10	4.20	4.90	0.40	4.90	3.20	2.30	1.40	4.10

Appendix 3Cii: Rotorua rhyolite pyroxene

Sample	RR19	RR19	RR19	RR19	RR19	RR19	RR19	RR19	RR19	RR19	RR32	RR32
Crystal analysed	1	1	4	4	6	6	8	8	9	9	9	9
Analysis location	c	r	c	r	c	r	c	r	c	r	c	r
SiO_2	52.46	51.66	51.88	51.28	52.78	51.62	52.22	51.13	51.48	49.44	51.96	51.27
TiO_2	0.17	0.23	0.10	0.08	0.24	0.09	0.07	0.21	0.20	0.22	0.15	0.26
Al_2O_3	0.79	0.75	0.47	0.39	0.30	0.41	0.40	0.62	0.55	0.99	0.30	0.36
FeO	23.10	24.34	24.87	26.35	21.56	25.25	27.00	25.83	25.47	11.96	27.36	27.59
Cr_2O_3	0.11	0.22	0.00	0.05	0.07	0.00	0.18	0.00	0.04	0.18	0.00	0.09
MnO	0.61	1.33	1.37	1.19	1.17	1.12	1.67	1.53	1.10	0.61	1.66	1.77
NiO	0.00	0.00	0.05	0.20	0.06	0.00	0.19	0.09	0.13	0.00	0.10	0.00
MgO	21.92	20.63	19.87	19.15	22.57	19.32	19.31	18.87	19.63	13.05	18.19	18.64
CaO	0.99	0.87	0.75	1.07	0.77	1.10	0.88	0.96	1.28	19.83	1.09	1.12
Na_2O	0.07	0.01	0.06	0.01	0.01	0.01	0.01	0.06	0.00	0.27	0.04	0.00
K_2O	0.05	0.05	0.00	0.00	0.00	0.04	0.00	0.05	0.00	0.02	0.01	0.02
Total	100.27	100.09	99.42	99.77	99.53	98.96	101.93	99.35	99.88	96.57	100.86	101.12
Oxygen	6	6	6	6	6	6	6	6	6	6	6	6
Si	1.954	1.947	1.975	1.958	1.974	1.980	1.956	1.960	1.956	1.926	1.976	1.943
Al	0.035	0.033	0.021	0.018	0.013	0.019	0.018	0.028	0.025	0.045	0.013	0.016
Fe	0.719	0.768	0.791	0.841	0.674	0.811	0.845	0.828	0.808	0.390	0.870	0.874
Ti	0.005	0.007	0.003	0.002	0.007	0.003	0.002	0.006	0.006	0.006	0.004	0.007
Cr	0.003	0.007	0.000	0.002	0.002	0.000	0.005	0.000	0.001	0.006	0.000	0.003
Mg	1.218	1.159	1.127	1.091	1.259	1.105	1.079	1.079	1.112	0.758	1.031	1.054
Ni	0.000	0.000	0.002	0.006	0.002	0.000	0.006	0.003	0.004	0.000	0.003	0.000
Mn	0.019	0.042	0.044	0.038	0.037	0.036	0.053	0.050	0.035	0.020	0.053	0.057
Ca	0.040	0.035	0.031	0.044	0.031	0.045	0.035	0.039	0.052	0.828	0.044	0.045
Na	0.005	0.001	0.004	0.001	0.001	0.001	0.001	0.004	0.000	0.020	0.003	0.000
K	0.002	0.002	0.000	0.000	0.000	0.002	0.000	0.002	0.000	0.001	0.000	0.001
Total	4.000	4.001	3.998	4.001	4.000	4.002	4.000	3.999	3.999	4.000	3.997	4.000
Wo	1.980	1.753	1.534	2.174	1.542	2.264	1.755	1.976	2.594	41.481	2.221	2.240
En	60.996	57.843	56.547	54.131	62.899	55.340	53.583	54.039	55.353	37.983	51.581	51.881
Fs	37.024	40.403	41.919	43.695	35.559	42.396	44.662	43.986	42.053	20.537	46.198	45.878

Appendix 3Cii: Rotorua rhyolite pyroxene

Sample	**MKR1**	**MKR1**	**MKR1**	**MKR1**
Crystal analysed	2	2	3	3
Analysis location		r	c	r
SiO_2	50.60	50.26	50.98	50.08
TiO_2	0.18	0.16	0.25	0.09
Al_2O_3	0.47	0.30	0.47	0.21
FeO	29.11	30.48	27.00	33.31
Cr_2O_3	0.00	0.20	0.05	0.00
MnO	2.16	1.94	1.55	2.43
NiO	0.00	0.08	0.08	0.00
MgO	17.24	15.62	18.30	14.05
CaO	0.88	1.00	1.28	1.17
Na_2O	0.00	0.11	0.00	0.08
K_2O	0.01	0.04	0.03	0.03
Total	100.65	100.19	99.99	101.45
Oxygen	6	6	6	6
Si	1.944	1.957	1.953	1.950
Al	0.021	0.014	0.021	0.010
Fe	0.935	0.992	0.865	1.085
Ti	0.005	0.005	0.007	0.003
Cr	0.000	0.006	0.002	0.000
Mg	0.988	0.907	1.045	0.816
Ni	0.000	0.003	0.002	0.000
Mn	0.070	0.064	0.050	0.080
Ca	0.036	0.042	0.053	0.049
Na	0.000	0.008	0.000	0.006
K	0.000	0.002	0.001	0.001
Total	3.999	4.000	3.999	4.000
Wo	1.785	2.081	2.610	2.405
En	48.659	45.223	51.919	40.191
Fs	49.556	52.696	45.471	57.403

Appendix 3Ciii: Rotorua rhyolite Fe/Ti oxides

Sample	**RR19**	**RR19**	**RR19**	**RR19**	**RR32**	**RR32**
Analysis area	8	8	11	11	9	9
mineral	mt	ilm	mt	ilm2	mt	ilm
SiO_2	0.07	0.00	0.18	0.08	0.15	0.04
TiO_2	81.05	11.42	1.03	51.49	2.33	47.48
Al_2O_3	0.22	1.48	0.57	0.08	2.45	0.17
FeO	15.41	77.15	88.69	45.88	87.63	49.21
MnO	0.17	0.41	0.60	1.58	0.28	1.16
MgO	0.30	0.62	0.29	1.29	0.61	1.29
CaO	0.05	0.11	0.06	0.06	0.04	0.02
Na_2O	0.00	0.00	0.09	0.00	0.00	0.01
K_2O	0.02	0.04	0.03	0.02	0.09	0.04
Cr_2O_3	0.14	0.22	0.13	0.14	0.03	0.16
NiO	0.03	0.03	0.07	0.00	0.03	0.02
Total	97.46	91.48	91.74	100.62	93.64	99.60

Appendix 3Civ: Rotorua rhyolite glass

Sample	RR19	RR19	RR19	RR19	RR19	RR32	RR32	RR32	RR32	RR32	MKR1	MKR1	MKR1
Analysis	9	7	8	9	10	3	6	7	9	9	4	6	7
SiO_2	77.44	76.17	63.78	77.87	76.46	66.29	95.85	93.87	94.72	95.56	64.34	88.22	64.15
TiO_2	0.24	0.23	0.15	0.21	0.31	0.22	0.13	0.12	0.02	0.08	0.11	0.04	0.21
Al_2O_3	12.52	12.62	19.07	12.52	12.87	18.70	0.74	1.39	0.80	0.96	17.39	0.56	17.38
FeO	0.49	0.51	0.23	0.22	0.29	0.31	0.07	0.07	0.16	0.01	0.31	0.05	0.46
MnO	0.06	0.05	0.06	0.01	0.09	0.18	0.05	0.03	0.01	0.08	0.00	0.00	0.15
MgO	0.05	0.06	0.08	0.03	0.01	0.01	0.03	0.05	0.02	0.04	0.04	0.00	0.00
BaO	0.00	0.48	0.00	0.00	0.35	0.29	0.12	0.11	0.09	0.18	0.39	0.30	0.07
CaO	2.10	2.71	1.00	1.87	2.38	0.83	0.04	0.10	0.05	0.04	0.35	0.05	0.42
Na_2O	4.49	4.16	3.42	5.15	4.88	6.36	0.41	0.38	0.38	0.35	4.37	0.30	4.52
K_2O	0.79	0.41	10.64	1.13	0.54	6.67	0.10	0.29	0.21	0.12	0.61	0.01	8.06
Total	98.18	97.40	98.43	99.01	98.18	99.86	97.54	96.41	96.46	97.42	87.91	89.53	95.42

Sample	MKR1	MKR1
Analysis	8	8
SiO_2	92.04	92.66
TiO_2	0.05	0.07
Al_2O_3	1.38	1.43
FeO	0.14	0.07
MnO	0.00	0.00
MgO	0.01	0.03
BaO	0.00	0.00
CaO	0.03	0.08
Na_2O	0.70	0.79
K_2O	0.08	0.07
Total	94.43	95.20

Appendix 3Di: Mokai plagioclase

Sample	**MoP2**	**MoP2**	**MoP2**	**MoP2**	**MoP2**	**MoP2**	**MoP2**
Crystal analysed	3	3	5	5	6	6	7
Analysis location	c	r	c	r	c	r	r
SiO_2	60.20	61.55	61.64	62.67	57.64	62.08	61.61
TiO_2	0.08	0.01	0.08	0.00	0.14	0.10	0.04
Al_2O_3	24.49	23.29	23.18	22.96	26.00	22.90	23.42
FeO	0.23	0.31	0.16	0.35	0.43	0.24	0.24
MnO	0.12	0.05	0.12	0.06	0.03	0.01	0.01
MgO	0.02	0.03	0.00	0.04	0.04	0.03	0.00
BaO	0.17	0.13	0.12	0.13	0.26	0.00	0.00
CaO	5.99	5.13	4.86	5.10	8.10	4.72	4.86
Na_2O	7.89	8.59	8.69	0.77	7.00	8.25	8.14
K_2O	0.41	0.58	0.60	0.58	0.30	0.57	0.55
Total	99.60	99.67	99.45	92.66	99.94	98.90	98.87
Oxygen	32	32	32	32	32	32	32
Si	10.789	11.010	11.039	11.594	10.382	11.131	11.054
Al	5.169	4.906	4.889	5.002	5.515	4.835	4.949
Ti	0.011	0.001	0.011	0.000	0.019	0.013	0.005
Fe	0.034	0.046	0.024	0.054	0.065	0.036	0.036
Mn	0.018	0.008	0.018	0.009	0.005	0.002	0.002
Mg	0.005	0.008	0.000	0.011	0.011	0.008	0.000
Ba	0.012	0.009	0.008	0.009	0.018	0.000	0.000
Ca	1.150	0.983	0.933	1.011	1.563	0.907	0.934
Na	2.742	2.979	3.018	0.276	2.445	2.868	2.832
K	0.094	0.132	0.137	0.137	0.069	0.130	0.126
Total	52.024	52.082	52.077	50.103	52.092	51.930	51.938
Ab	68.8	72.8	73.8	19.4	60.0	73.4	72.8
An	28.9	24.0	22.8	71.0	38.3	23.2	24.0
Or	2.4	3.2	3.4	9.6	1.7	3.3	3.2

Appendix 3Dii: Mokai pyroxene

Sample	**MoP2**	**MoP2**	**MoP2**	**MoP2**	**MoP2**	**MoP2**	**MoP2**
Crystal analysed	2	2	4	4	4	8	8
Analysis location	c	r	c	oc	r	c	r
SiO_2	51.36	50.96	51.33	53.54	50.61	52.41	50.11
TiO_2	0.12	0.23	0.39	0.34	0.17	0.21	0.07
Al_2O_3	0.28	0.21	1.03	1.30	0.29	0.68	0.28
FeO	30.89	32.04	19.66	19.41	29.35	20.28	29.84
Cr_2O_3	0.03	0.10	0.16	0.08	0.06	0.00	0.02
MnO	1.86	2.34	1.26	1.16	2.12	1.23	2.04
NiO	0.11	0.00	0.27	0.08	0.09	0.09	0.00
MgO	15.53	14.75	23.24	23.87	15.91	23.13	16.24
CaO	1.32	1.24	1.44	1.75	1.13	1.36	1.18
Na_2O	0.00	0.01	0.08	0.06	0.00	0.06	0.00
K_2O	0.00	0.03	0.03	0.01	0.02	0.07	0.00
Total	101.50	101.91	98.89	101.60	99.75	99.52	99.78
Oxygen	6	6	6	6	6	6	6
Si	1.978	1.967	1.918	1.942	1.975	1.949	1.952
Al	0.013	0.010	0.045	0.056	0.013	0.030	0.013
Fe	0.994	1.034	0.614	0.588	0.959	0.631	0.972
Ti	0.003	0.007	0.011	0.009	0.005	0.006	0.002
Mg	0.892	0.849	1.294	1.291	0.926	1.282	0.943
Mn	0.061	0.077	0.040	0.036	0.070	0.039	0.067
Ni	0.003	0.000	0.008	0.002	0.003	0.003	0.000
Cr	0.001	0.003	0.005	0.002	0.002	0.000	0.001
Ca	0.054	0.051	0.058	0.068	0.047	0.054	0.049
Na	0.000	0.001	0.006	0.004	0.000	0.004	0.000
K	0.000	0.001	0.001	0.000	0.001	0.003	0.000
Total	3.999	4.000	4.000	3.998	4.001	4.001	3.999
Wo	2.721	2.550	2.873	3.429	2.361	2.701	2.424
En	44.544	42.210	64.520	65.084	46.261	63.925	46.417
Fs	52.735	55.240	32.607	31.486	51.377	33.374	51.159

Appendix 3Diii: Mokai Fe/Ti oxides

Sample	**MoP2**	**MoP2**	**MoP2**	**MoP2**	**MoP2**	**MoP2**
Analysis area	4	4	8	8	8	8
mineral	ilm	mt	ilm	mt	mt2	ilm2
SiO_2	0.17	0.14	0.16	3.00	0.16	0.06
TiO_2	44.42	9.31	48.02	0.03	11.45	48.56
Al_2O_3	0.06	1.32	0.08	0.08	1.17	0.10
FeO	43.12	80.69	47.00	90.51	81.33	47.88
MnO	1.50	1.19	1.44	0.20	1.03	1.56
MgO	1.45	0.42	1.38	0.11	0.48	1.12
CaO	0.05	0.05	0.04	0.08	0.00	0.05
Na_2O	0.17	0.00	0.10	0.00	0.00	0.06
K_2O	0.11	0.05	0.01	0.00	0.00	0.05
Cr_2O_3	0.15	0.04	0.00	0.04	0.03	0.09
NiO	0.00	0.16	0.11	0.01	0.01	0.01
Total	91.20	93.37	98.34	94.06	95.66	99.54

Appendix 3Div: Mokai glass

Sample	**MoP2**	**MoP2**	**MoP2**	**MoP2**
Analysis area	1	3	5	7
SiO_2	75.14	74.41	75.28	75.95
TiO_2	0.14	0.15	0.27	0.16
Al_2O_3	11.95	12.09	12.11	11.60
FeO	0.36	0.32	0.34	0.43
MnO	0.04	0.13	0.09	0.04
MgO	0.00	0.00	0.04	0.07
BaO	0.00	0.33	0.34	0.28
CaO	0.40	0.53	0.45	0.71
Na_2O	3.83	4.01	3.91	3.99
K_2O	3.73	3.39	3.68	3.72
Total	95.59	95.36	96.51	96.95

APPENDIX 4

XRD analyses

Appendix 4
X-ray diffraction analyses

Sample preparation

Samples of pumice, ignimbrite and fumarole conduits from uMI and pumice clasts from lMI were taken and analysed by x-ray diffraction (XRD) to ascertain the effects of vapour phase alteration. All samples were crushed using a mortar and pestle with a small amount of ethanol added. The resulting mixture was applied to a glass slide and the ethanol allowed to evaporate off.

Most samples were analysed three times to ascertain the presence of clay following the method of Brown and Brindley (1980). The sample was first analysed air-dried and untreated. It was then treated with ethylene glycol and analysed a second time before being fired at 550 ^{o}C for an hour prior to the final analysis. Glycolation determines the presence of swelling clays as the corresponding peak shifts. Firing breaks down clay structure causing clay peaks to disappear.

Analytical procedure

XRD analyses were carried out using a Phillips PW-1729 X-ray generator and PW-1710 Diffractometer Control and $Cu_{K\alpha}$ (λ= 1.5418 Å). The control unit was operated via the software program "Visual XRD v2.6" with a step size between readings of 0.02° and rate of 0.02° s^{-1}. Traces were analysed and peaks matched using "Trace v4" software and standard PDF databases. Both "Visual XRD v2.6" and "Traces v4" were written by Diffraction technology Pty Ltd.

XRD results

XRD traces were first studied with using "Traces v4". The traces were then saved as text files, regraphed in Microsoft Excel™, and peaks labelled using CorelDRAW™.

Mineral abbreviations are as follows:

A-Andesine

Olig- Oligoclase

Ab- Albite

Or- Orthoclase

Opx- Orthopyroxene

Cr- Cristobalite

Tr- Tridymite

Q- Quartz

H- Halloysite 10 Å

F1 pattern

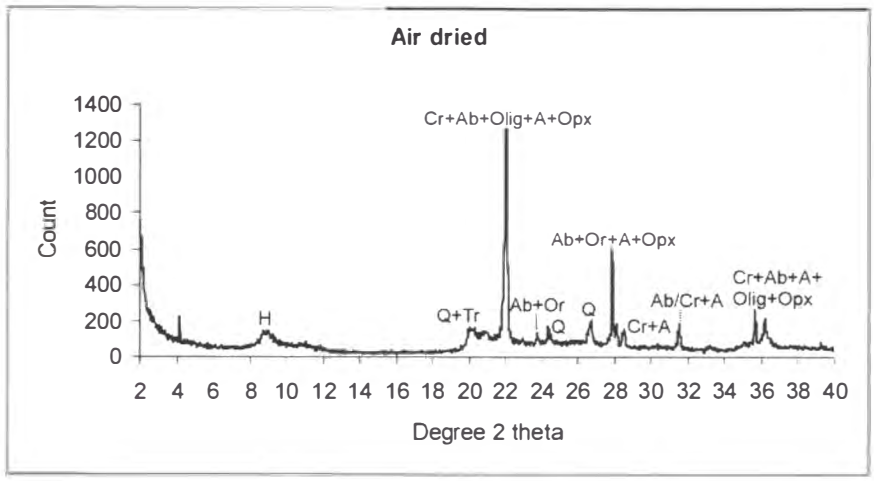
Air dried
Count
Degree 2 theta
Cr+Ab+Olig+A+Opx
Ab+Or+A+Opx
Cr+Ab+A+
Olig+Opx
Ab/Cr+A
Ab+Or
Q+Tr
Cr+A
H
Q

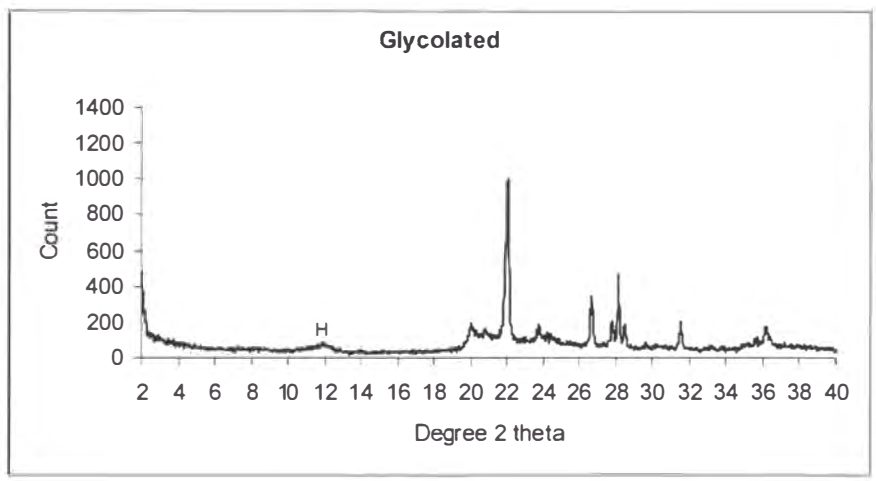
Glycolated
Count
Degree 2 theta
H

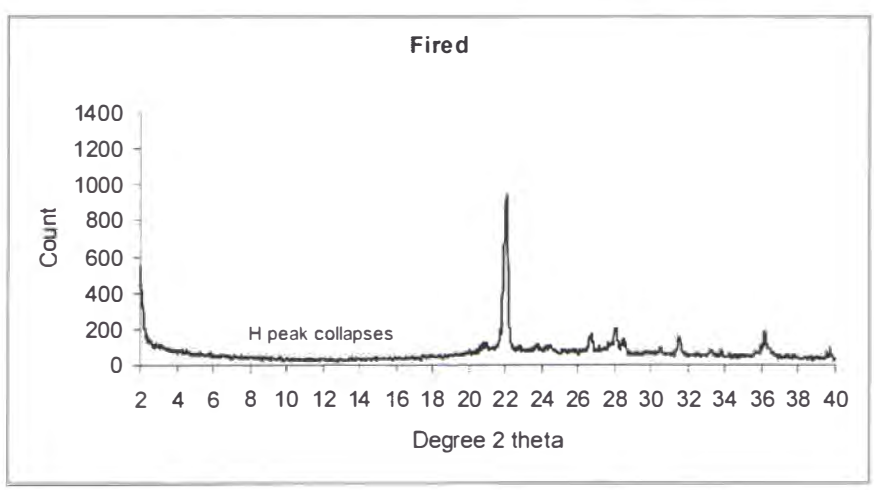
Fired
Count
Degree 2 theta
H peak collapses

F2 pattern

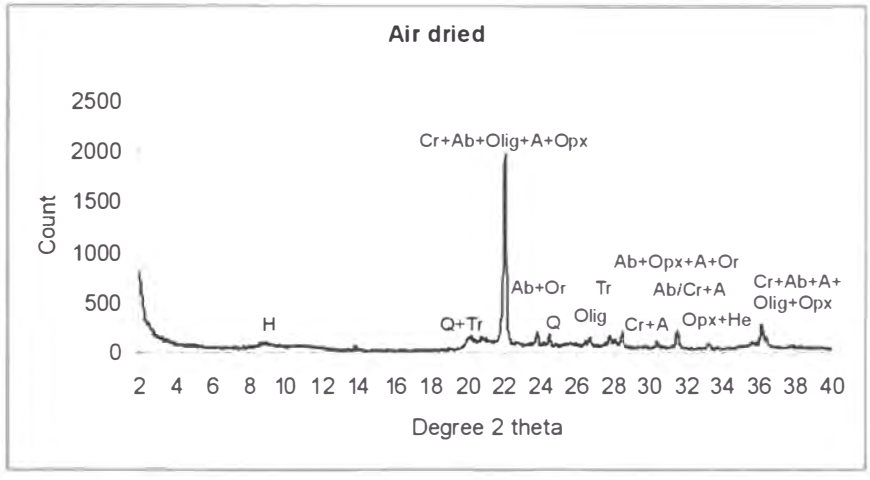
Air dried
Count
2500
2000
1500
1000
500
0
Cr+Ab+Olig+A+Opx
Ab+Or
Tr
Ab+Opx+A+Or
Ab/Cr+A
Cr+Ab+A+
Olig+Opx
H
Q+Tr
Q
Olig
Cr+A
Opx+He
2 4 6 8 10 12 14 16 18 20 22 24 26 28 30 32 34 36 38 40
Degree 2 theta

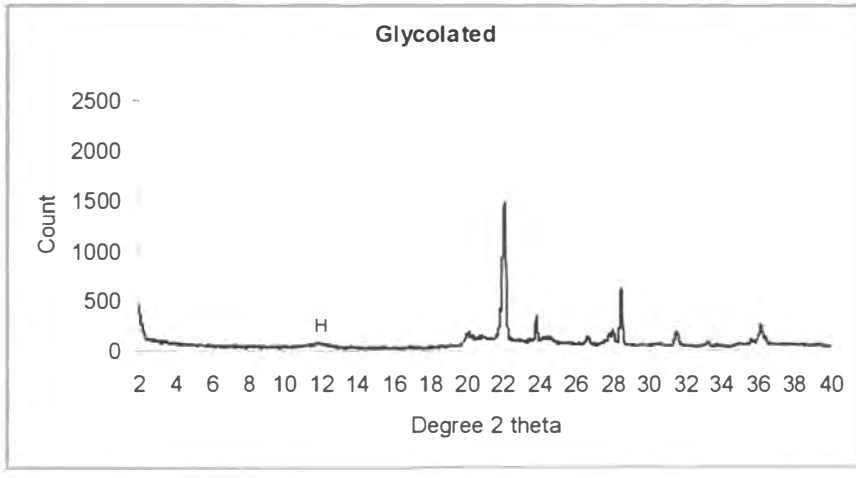
Glycolated
Count
2500
2000
1500
1000
500
0
H
2 4 6 8 10 12 14 16 18 20 22 24 26 28 30 32 34 36 38 40
Degree 2 theta

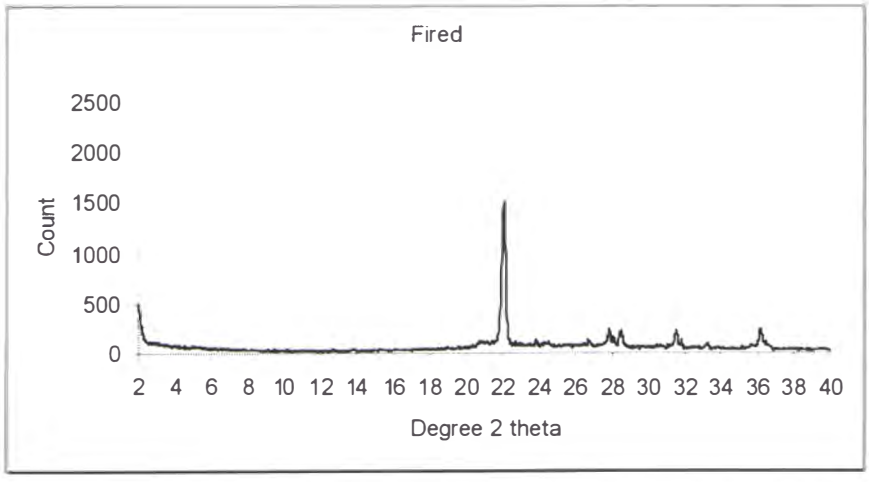
Fired
Count
2500
2000
1500
1000
500
0
2 4 6 8 10 12 14 16 18 20 22 24 26 28 30 32 34 36 38 40
Degree 2 theta

F3 pattern

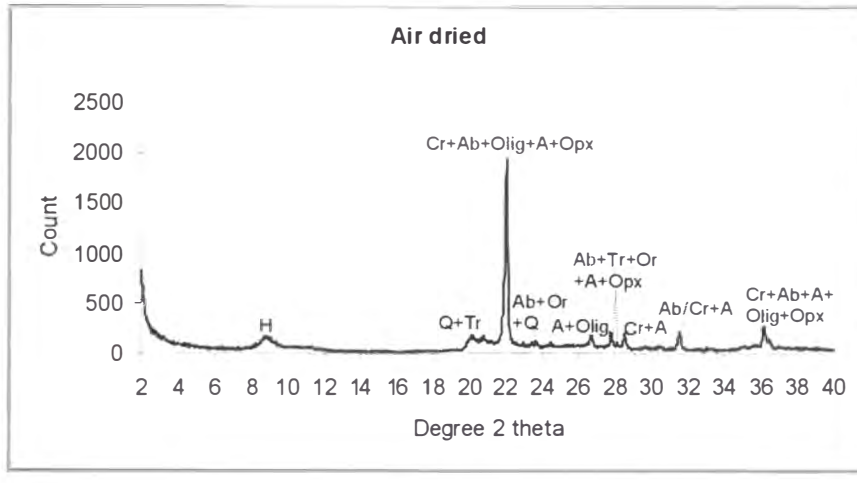
Air dried
Count
2500
2000
1500
1000
500
0
Cr+Ab+Olig+A+Opx
Ab+Tr+Or
+A+Opx
Ab+Or
+Q
Cr+Ab+A+
Olig+Opx
Ab/Cr+A
Q+Tr
A+Olig
Cr+A
H
2 4 6 8 10 12 14 16 18 20 22 24 26 28 30 32 34 36 38 40
Degree 2 theta

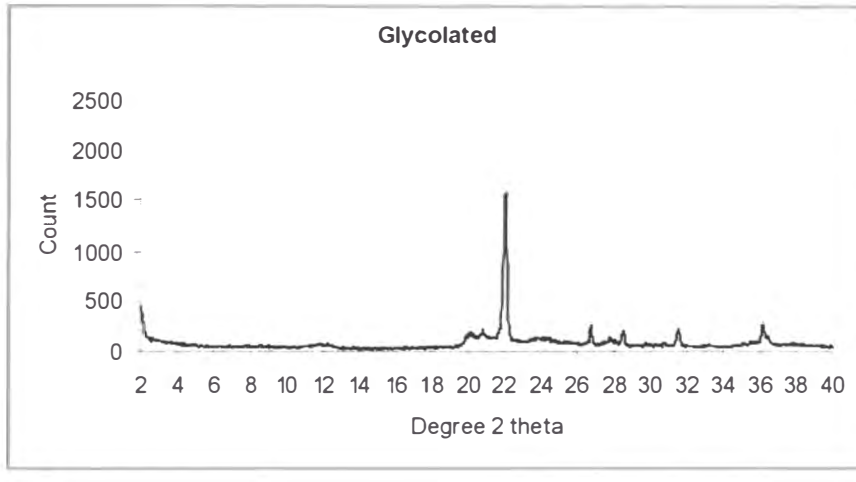
Glycolated
Count
2500
2000
1500
1000
500
0
2 4 6 8 10 12 14 16 18 20 22 24 26 28 30 32 34 36 38 40
Degree 2 theta

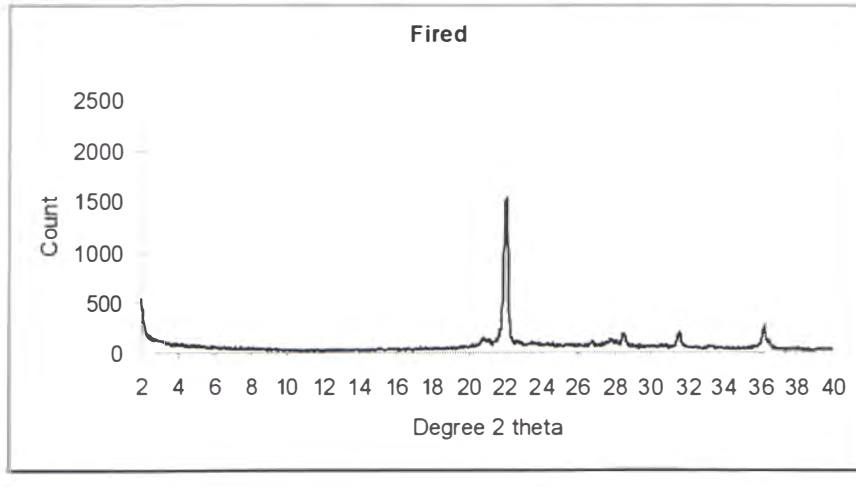
Fired
Count
2500
2000
1500
1000
500
0
2 4 6 8 10 12 14 16 18 20 22 24 26 28 30 32 34 36 38 40
Degree 2 theta

F4 pattern

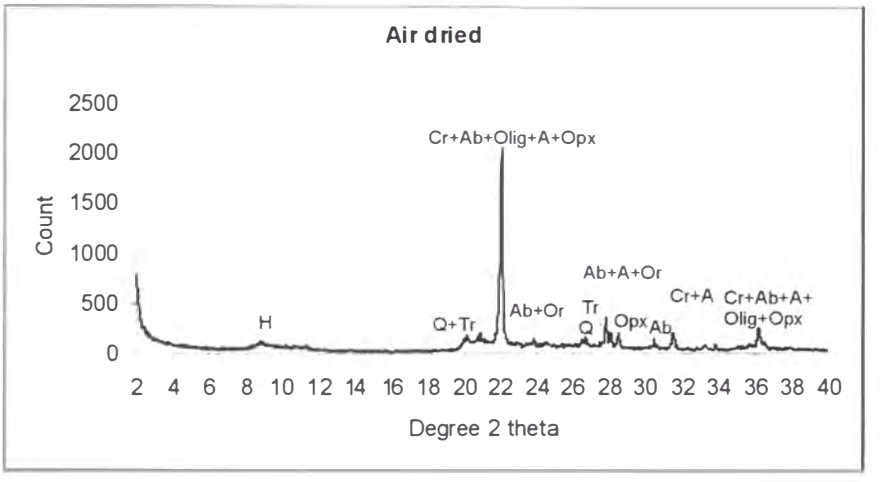
Air dried
Count
2500
2000
1500
1000
500
0
Cr+Ab+Olig+A+Opx
H
Q+Tr
Ab+Or
Ab+A+Or
Tr
Q
Opx
Ab
Cr+A
Cr+Ab+A+
Olig+Opx
2 4 6 8 10 12 14 16 18 20 22 24 26 28 30 32 34 36 38 40
Degree 2 theta

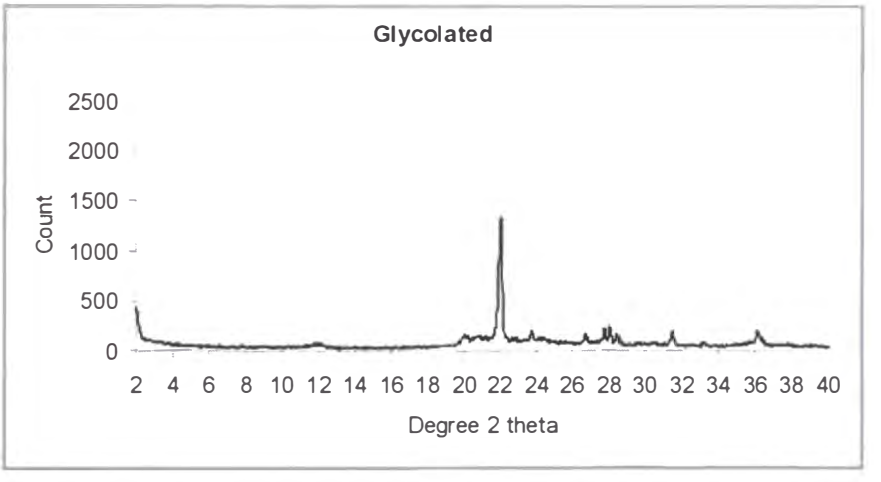
Glycolated
Count
2500
2000
1500
1000
500
0
2 4 6 8 10 12 14 16 18 20 22 24 26 28 30 32 34 36 38 40
Degree 2 theta

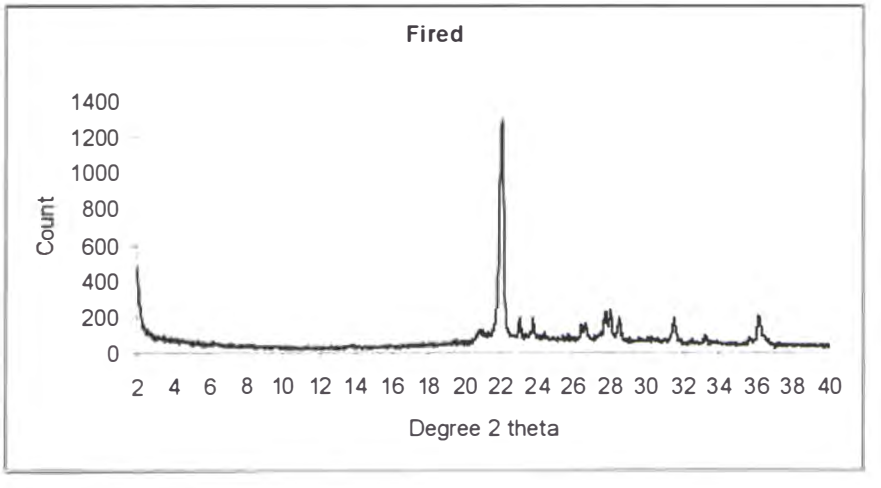
Fired
Count
1400
1200
1000
800
600
400
200
0
2 4 6 8 10 12 14 16 18 20 22 24 26 28 30 32 34 36 38 40
Degree 2 theta

F5 pattern

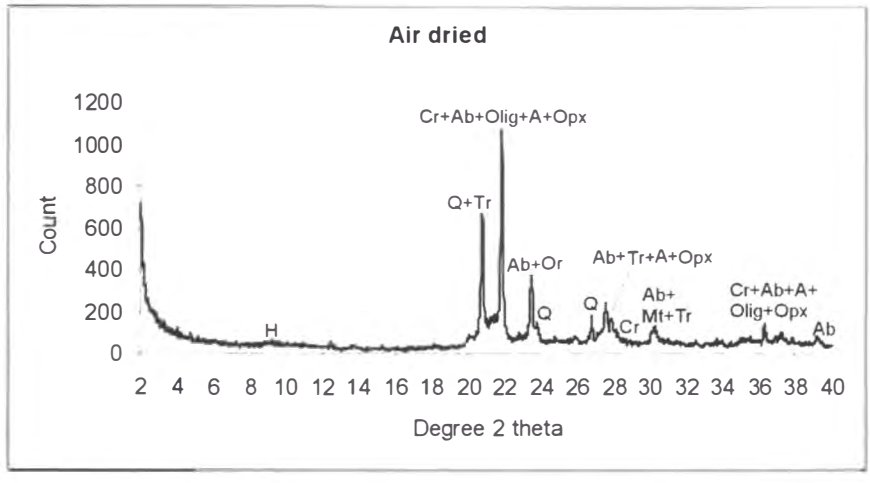
Air dried
Count
Degree 2 theta
Cr+Ab+Olig+A+Opx
Q+Tr
Ab+Or
Ab+Tr+A+Opx
Ab+ Mt+Tr
Cr+Ab+A+ Olig+Opx
H
Q
Cr
Ab

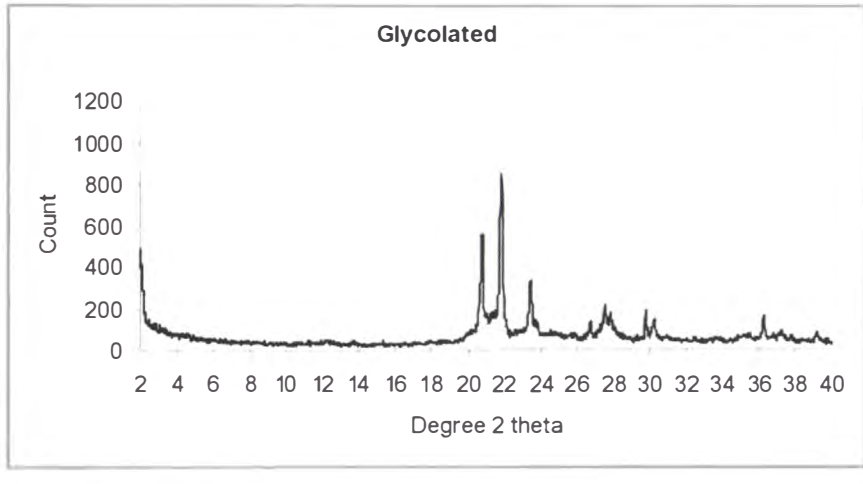
Glycolated
Count
Degree 2 theta

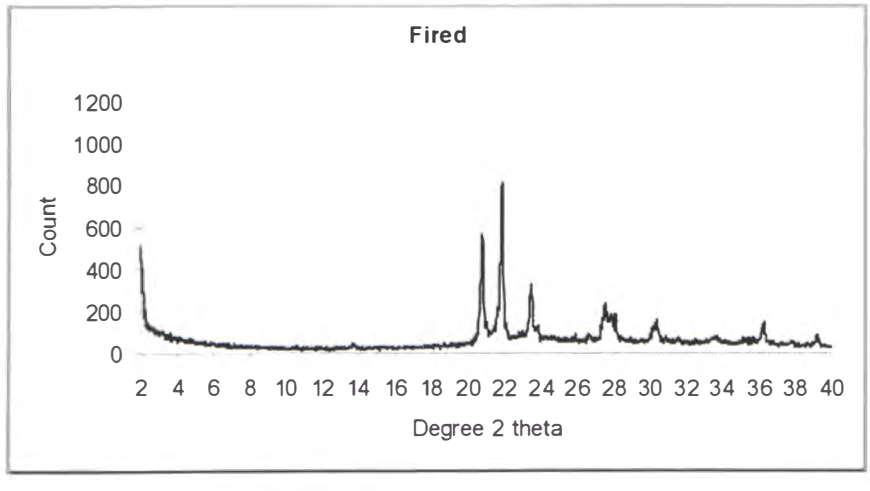
Fired
Count
Degree 2 theta

F7 pattern

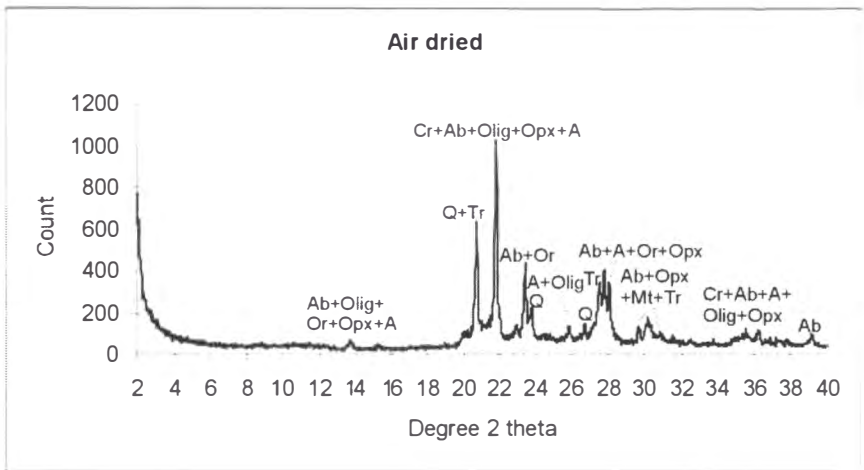
Air dried
Count
Degree 2 theta
Cr+Ab+Olig+Opx+A
Q+Tr
Ab+Or
Ab+A+Or+Opx
A+Olig
Q
Tr
Q
Ab+Opx
+Mt+Tr
Cr+Ab+A+
Olig+Opx
Ab
Ab+Olig+
Or+Opx+A

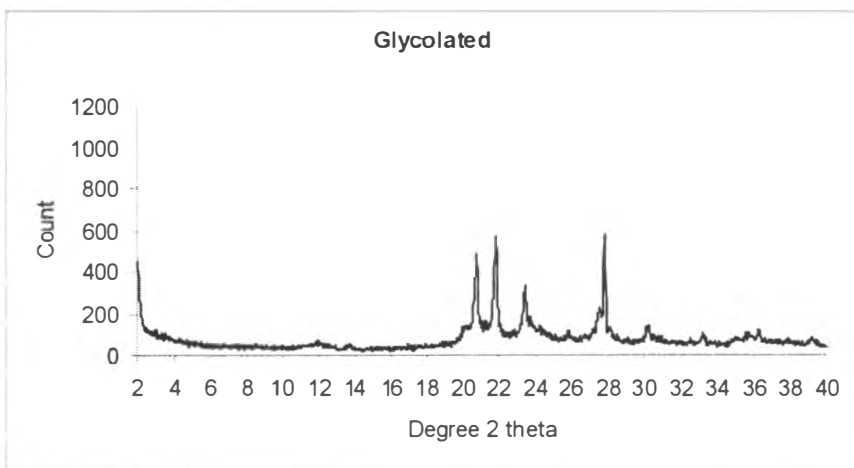
Glycolated
Count
Degree 2 theta

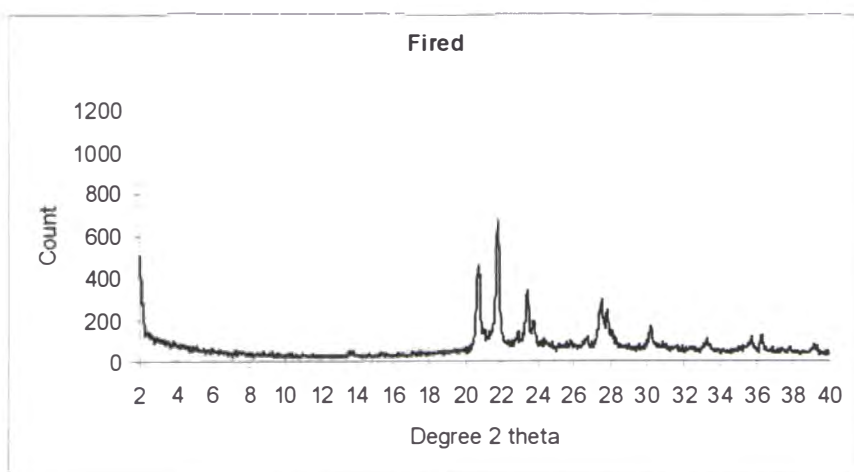
Fired
Count
Degree 2 theta

F8 pattern

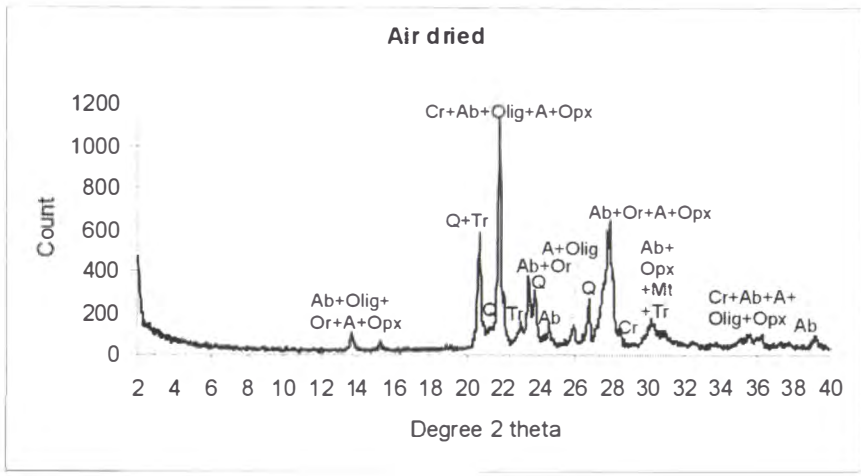
Air dried
Count
Degree 2 theta
Cr+Ab+Olig+A+Opx
Q+Tr
Ab+Or+A+Opx
A+Olig
Ab+Or
Ab+
Opx
+Mt
+Tr
Ab+Olig+
Or+A+Opx
Cr+Ab+A+
Olig+Opx
Ab
Q
Tr
Cr

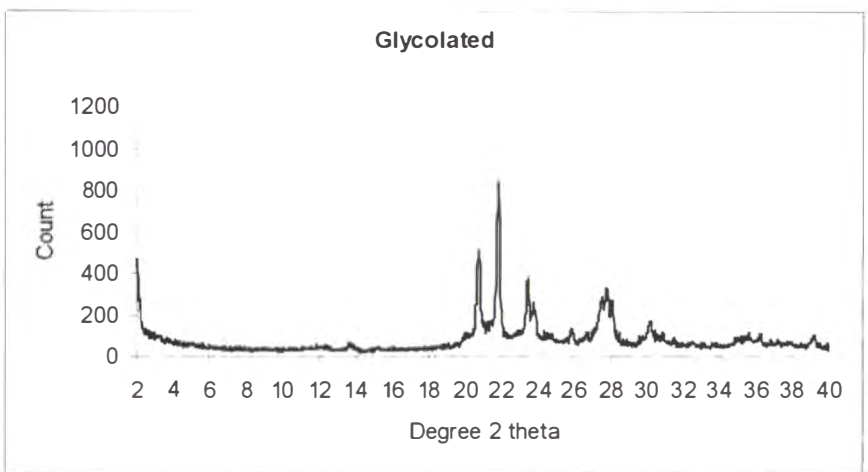
Glycolated
Count
Degree 2 theta

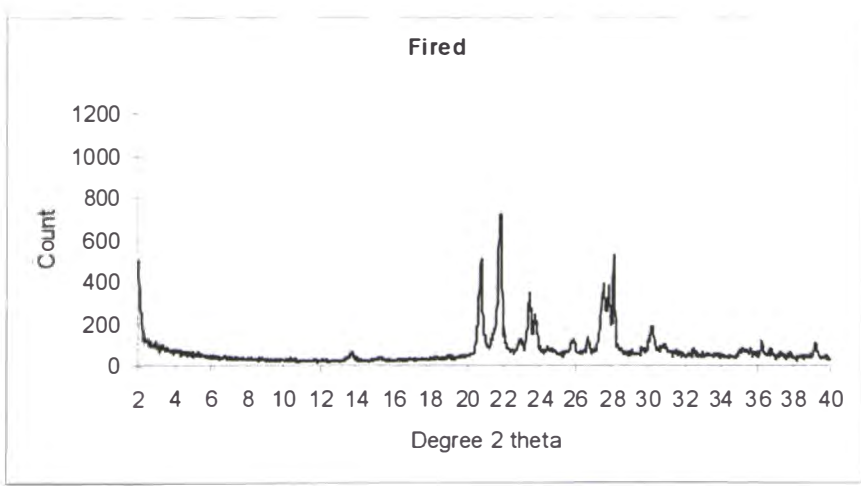
Fired
Count
Degree 2 theta

F9 pattern

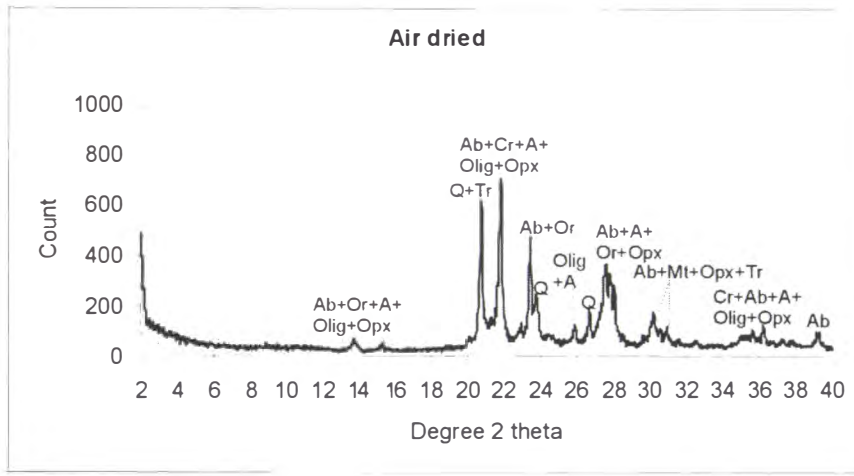
Air dried
Count
1000
800
600
400
200
0
Ab+Cr+A+
Olig+Opx
Q+Tr
Ab+Or
Olig
+A
Q
Ab+A+
Or+Opx
Ab+Mt+Opx+Tr
Cr+Ab+A+
Olig+Opx
Ab
Ab+Or+A+
Olig+Opx
2 4 6 8 10 12 14 16 18 20 22 24 26 28 30 32 34 36 38 40
Degree 2 theta

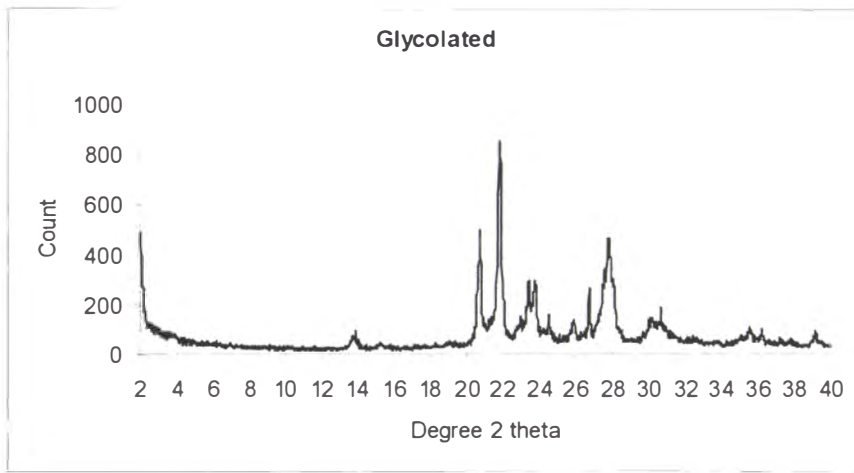
Glycolated
Count
1000
800
600
400
200
0
2 4 6 8 10 12 14 16 18 20 22 24 26 28 30 32 34 36 38 40
Degree 2 theta

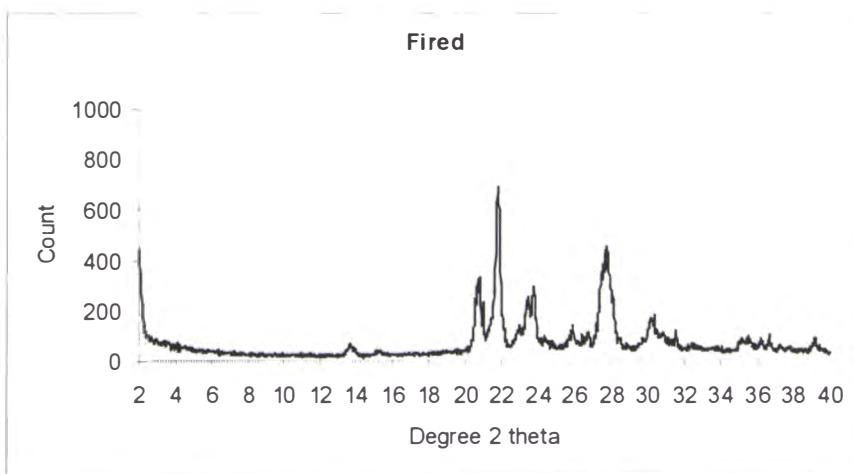
Fired
Count
1000
800
600
400
200
0
2 4 6 8 10 12 14 16 18 20 22 24 26 28 30 32 34 36 38 40
Degree 2 theta

F10 pattern

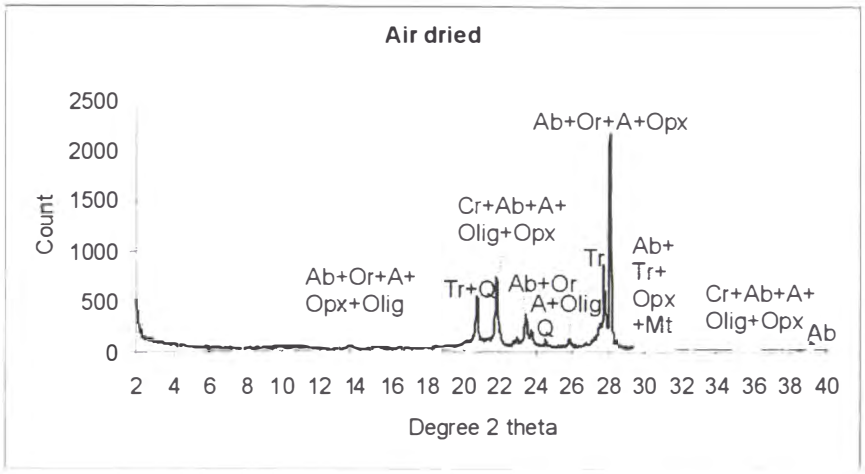
Air dried
Count
2500
2000
1500
1000
500
0
Ab+Or+A+Opx
Cr+Ab+A+
Olig+Opx
Tr
Ab+
Tr+
Opx
+Mt
Ab+Or+A+
Opx+Olig
Tr+Q
Ab+Or
A+Olig
Q
Cr+Ab+A+
Olig+Opx
Ab
2 4 6 8 10 12 14 16 18 20 22 24 26 28 30 32 34 36 38 40
Degree 2 theta

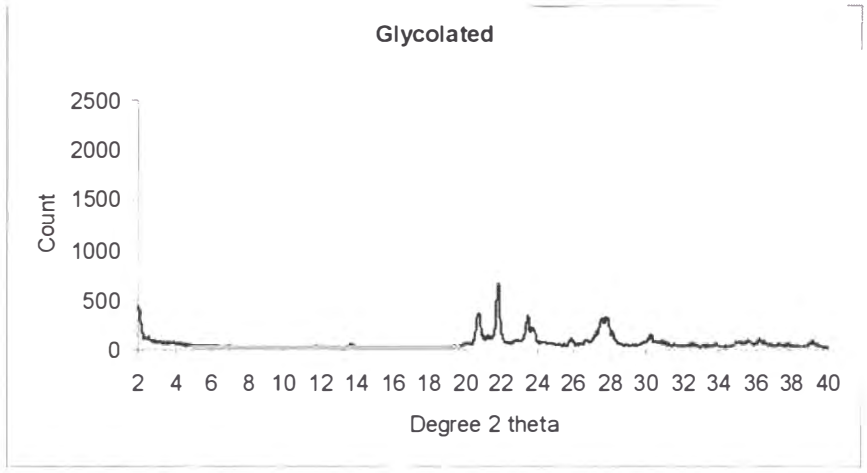
Glycolated
Count
2500
2000
1500
1000
500
0
2 4 6 8 10 12 14 16 18 20 22 24 26 28 30 32 34 36 38 40
Degree 2 theta

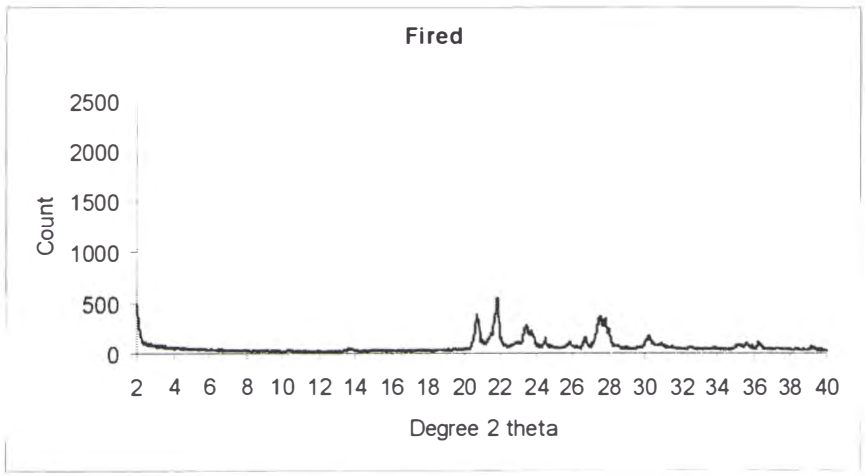
Fired
Count
2500
2000
1500
1000
500
0
2 4 6 8 10 12 14 16 18 20 22 24 26 28 30 32 34 36 38 40
Degree 2 theta

F11 pattern

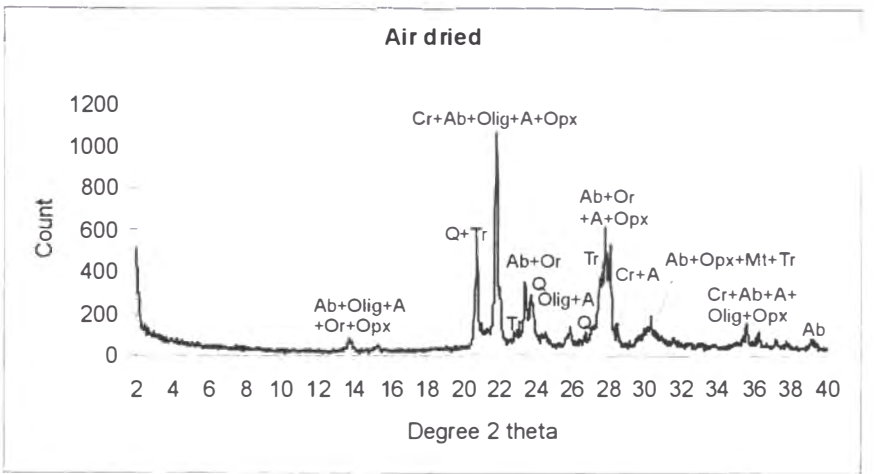
Air dried
Count
Degree 2 theta
Cr+Ab+Olig+A+Opx
Q+Tr
Ab+Or
Ab+Or
+A+Opx
Tr
Cr+A
Ab+Opx+Mt+Tr
Q
Olig+A
Ab+Olig+A
+Or+Opx
Tr
Q
Cr+Ab+A+
Olig+Opx
Ab

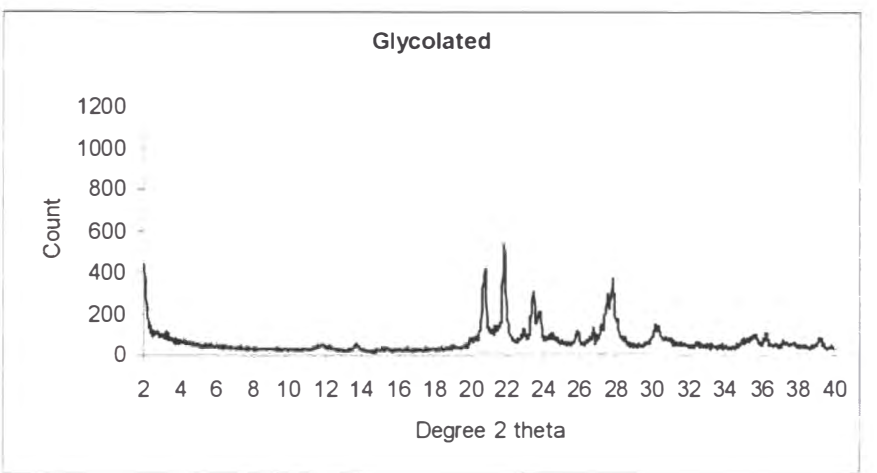
Glycolated
Count
Degree 2 theta

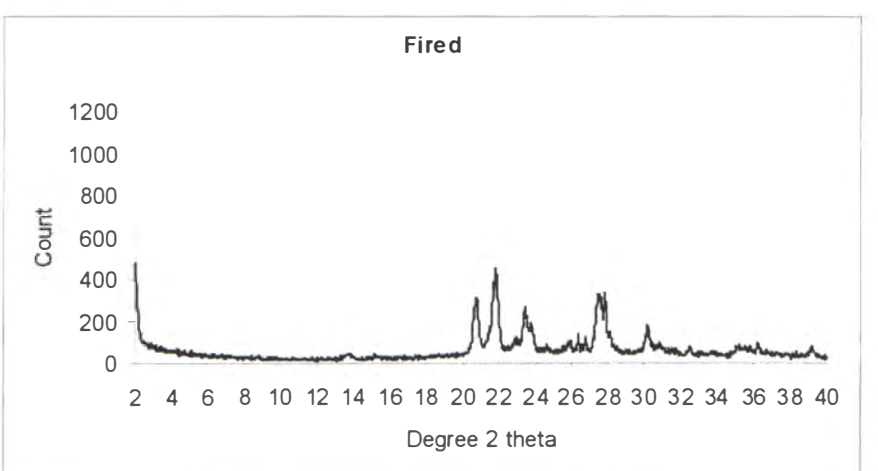
Fired
Count
Degree 2 theta

F12 pattern

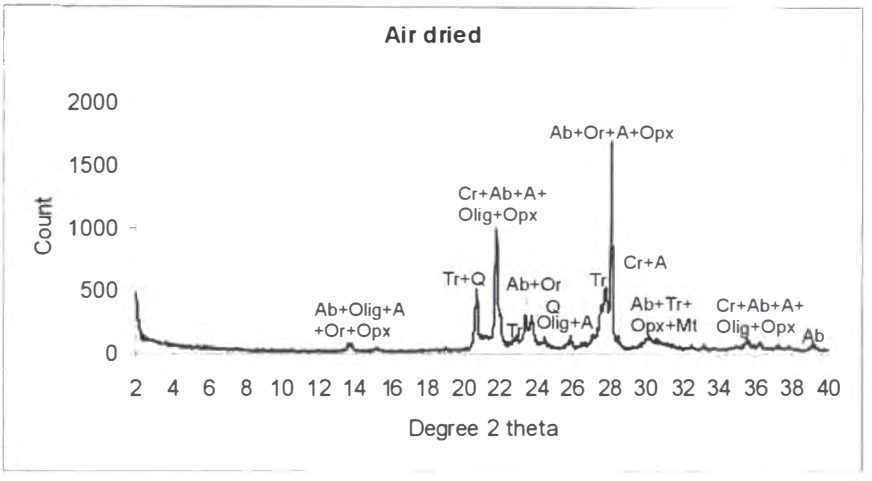
Air dried
Count
2000
1500
1000
500
0
Ab+Or+A+Opx
Cr+Ab+A+
Olig+Opx
Cr+A
Tr+Q
Ab+Or
Q
Tr
Olig+A
Ab+Olig+A
+Or+Opx
Ab+Tr+
Opx+Mt
Cr+Ab+A+
Olig+Opx
Ab
2 4 6 8 10 12 14 16 18 20 22 24 26 28 30 32 34 36 38 40
Degree 2 theta

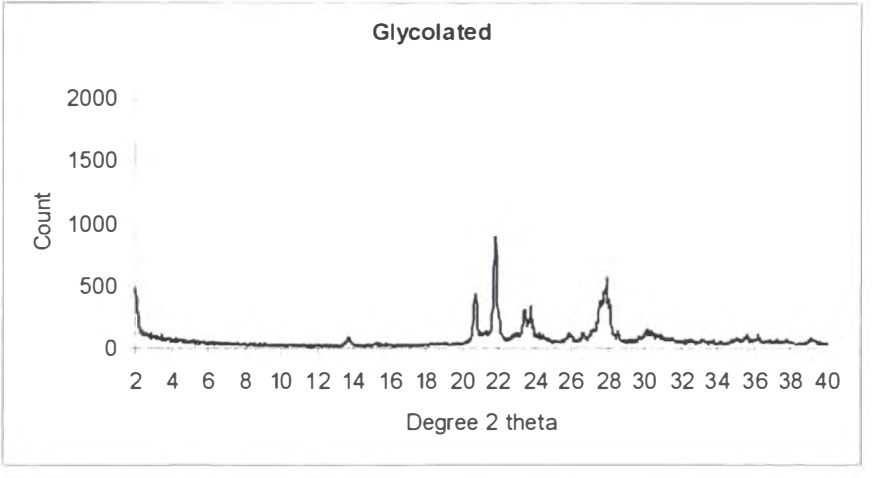
Glycolated
Count
2000
1500
1000
500
0
2 4 6 8 10 12 14 16 18 20 22 24 26 28 30 32 34 36 38 40
Degree 2 theta

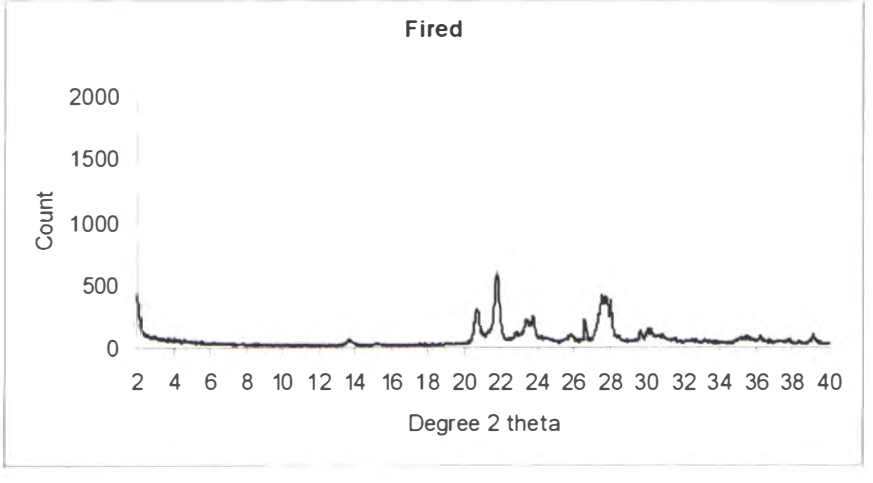
Fired
Count
2000
1500
1000
500
0
2 4 6 8 10 12 14 16 18 20 22 24 26 28 30 32 34 36 38 40
Degree 2 theta

F13 pattern

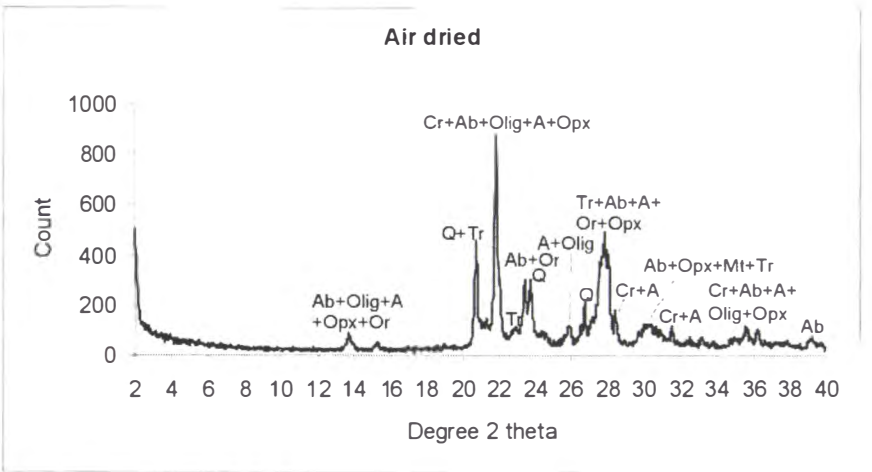
Air dried
Count
1000
800
600
400
200
0
Cr+Ab+Olig+A+Opx
Q+Tr
Ab+Or
Q
A+Olig
Tr+Ab+A+
Or+Opx
Ab+Olig+A
+Opx+Or
Tr
Q
Cr+A
Cr+A
Ab+Opx+Mt+Tr
Cr+Ab+A+
Olig+Opx
Ab
2 4 6 8 10 12 14 16 18 20 22 24 26 28 30 32 34 36 38 40
Degree 2 theta

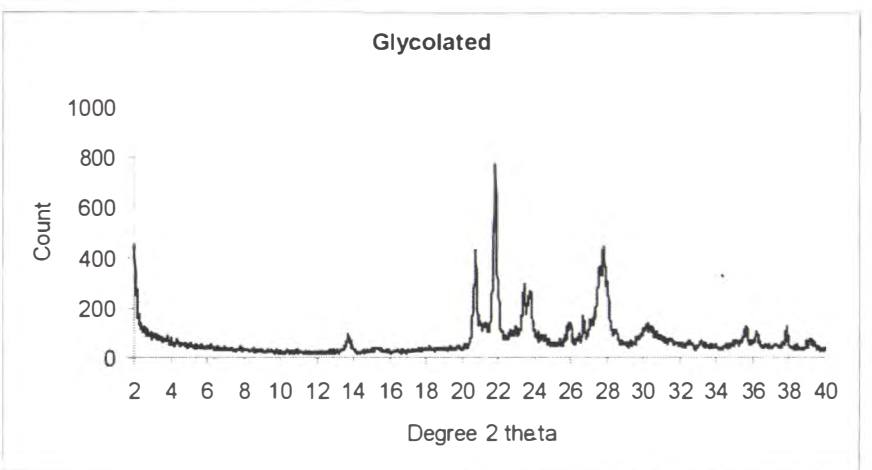
Glycolated
Count
1000
800
600
400
200
0
2 4 6 8 10 12 14 16 18 20 22 24 26 28 30 32 34 36 38 40
Degree 2 theta

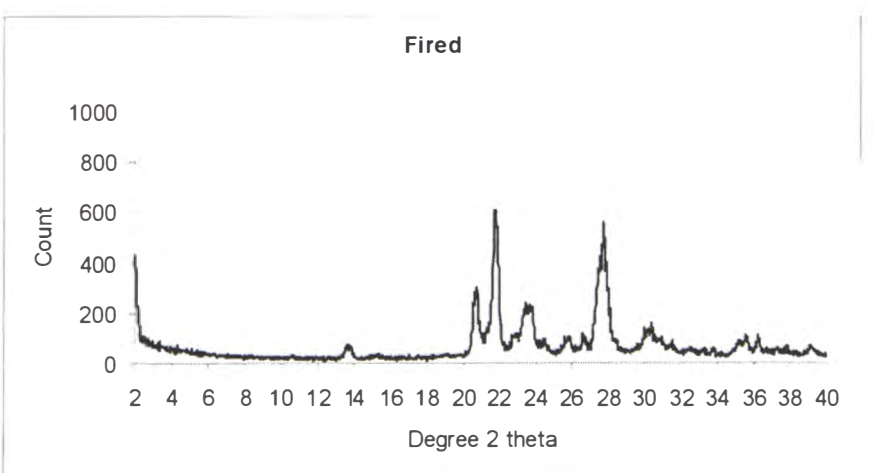
Fired
Count
1000
800
600
400
200
0
2 4 6 8 10 12 14 16 18 20 22 24 26 28 30 32 34 36 38 40
Degree 2 theta

F14 pattern

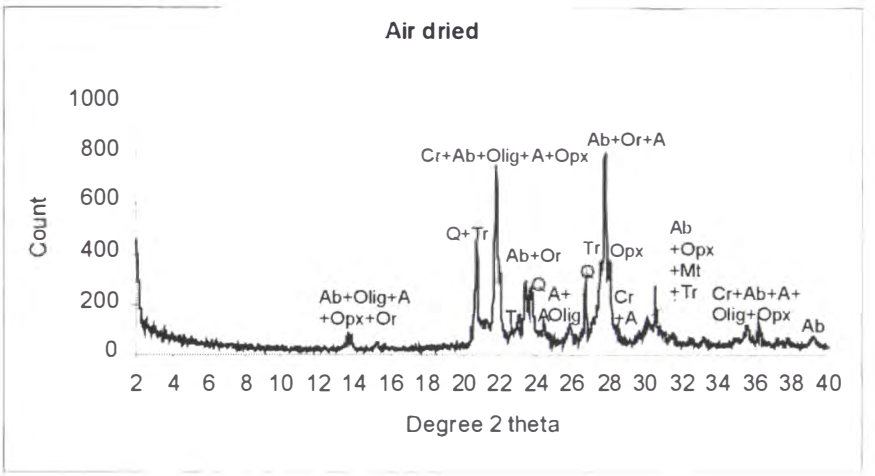
Air dried
Count
1000
800
600
400
200
0
Ab+Olig+A
+Opx+Or
Cr+Ab+Olig+A+Opx
Q+Tr
Ab+Or
Tr
Q
A+
AOlig
Ab+Or+A
Tr
Opx
Q
Cr
+A
Ab
+Opx
+Mt
+Tr
Cr+Ab+A+
Olig+Opx
Ab
2 4 6 8 10 12 14 16 18 20 22 24 26 28 30 32 34 36 38 40
Degree 2 theta

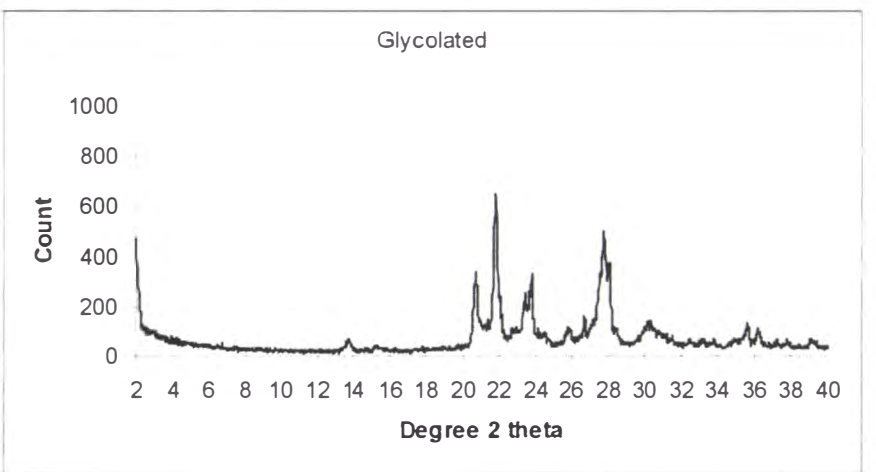
Glycolated
Count
1000
800
600
400
200
0
2 4 6 8 10 12 14 16 18 20 22 24 26 28 30 32 34 36 38 40
Degree 2 theta

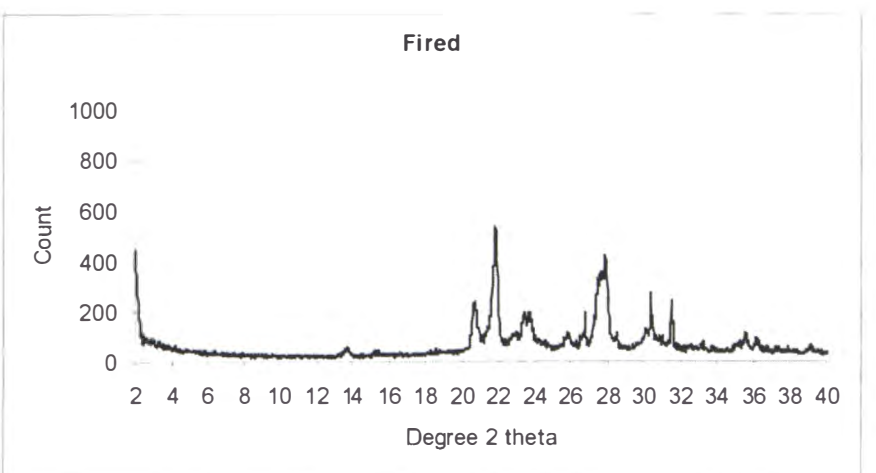
Fired
Count
1000
800
600
400
200
0
2 4 6 8 10 12 14 16 18 20 22 24 26 28 30 32 34 36 38 40
Degree 2 theta

F15 pattern

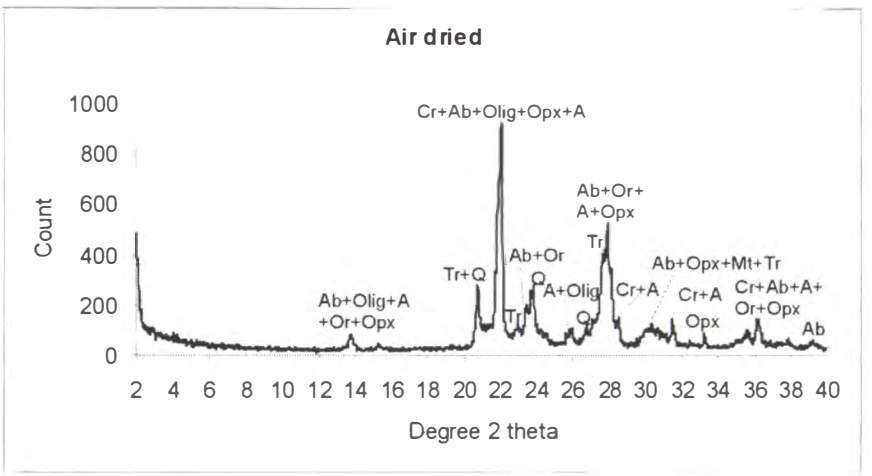
Air dried
Count
Degree 2 theta
Cr+Ab+Olig+Opx+A
Ab+Or+
A+Opx
Tr
Ab+Or
Tr+Q
Ab+Olig+A
+Or+Opx
A+Olig
Cr+A
Ab+Opx+Mt+Tr
Cr+A
Opx
Cr+Ab+A+
Or+Opx
Ab

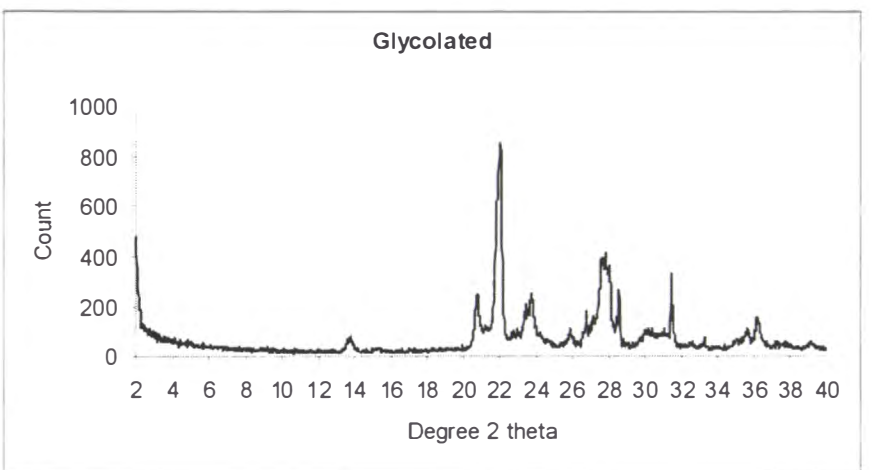
Glycolated
Count
Degree 2 theta

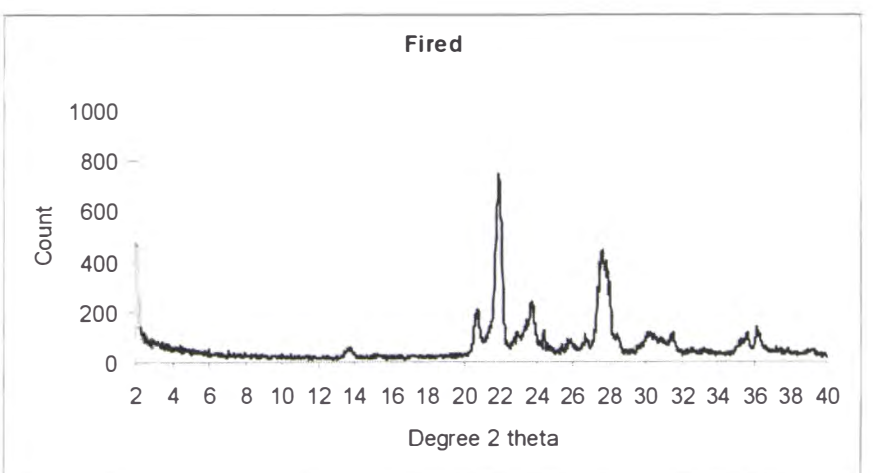
Fired
Count
Degree 2 theta

F16 pattern

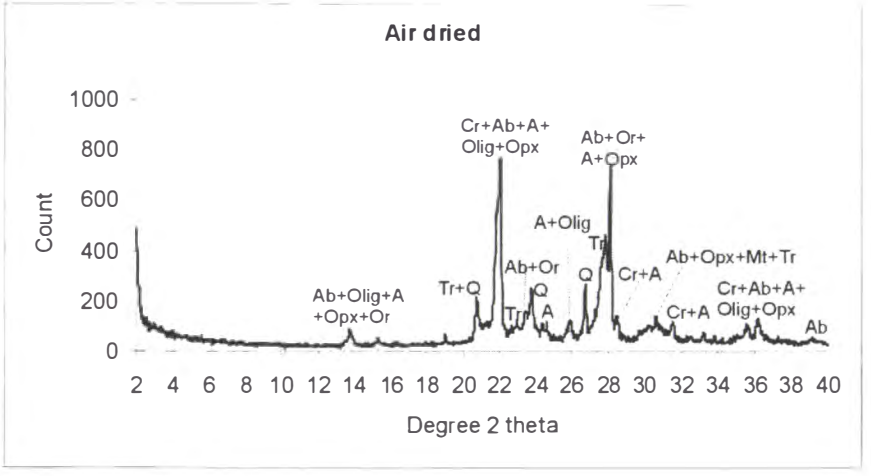
Air dried
Count
1000
800
600
400
200
0
Cr+Ab+A+
Olig+Opx
Ab+Or+
A+Opx
A+Olig
Tr
Ab+Or
Q
Cr+A
Ab+Opx+Mt+Tr
Ab+Olig+A
+Opx+Or
Tr+Q
Tr
Q
A
Q
Cr+A
Cr+Ab+A+
Olig+Opx
Ab
2 4 6 8 10 12 14 16 18 20 22 24 26 28 30 32 34 36 38 40
Degree 2 theta

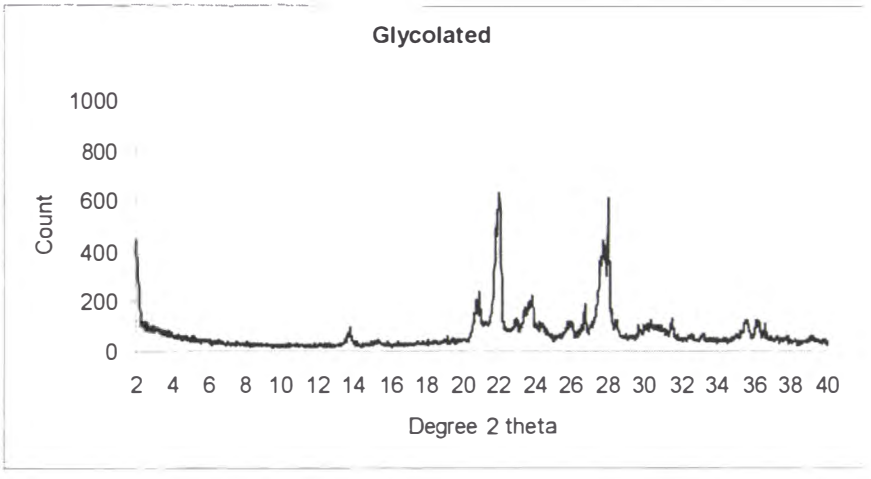
Glycolated
Count
1000
800
600
400
200
0
2 4 6 8 10 12 14 16 18 20 22 24 26 28 30 32 34 36 38 40
Degree 2 theta

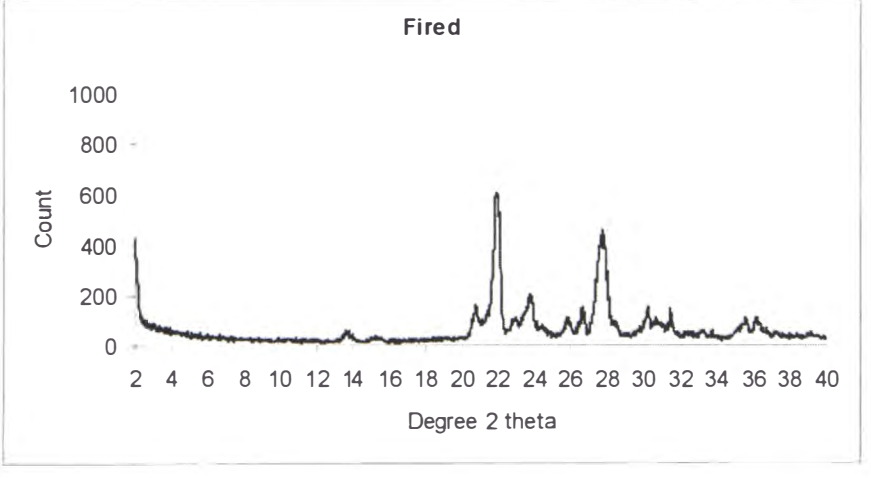
Fired
Count
1000
800
600
400
200
0
2 4 6 8 10 12 14 16 18 20 22 24 26 28 30 32 34 36 38 40
Degree 2 theta

F17 pattern

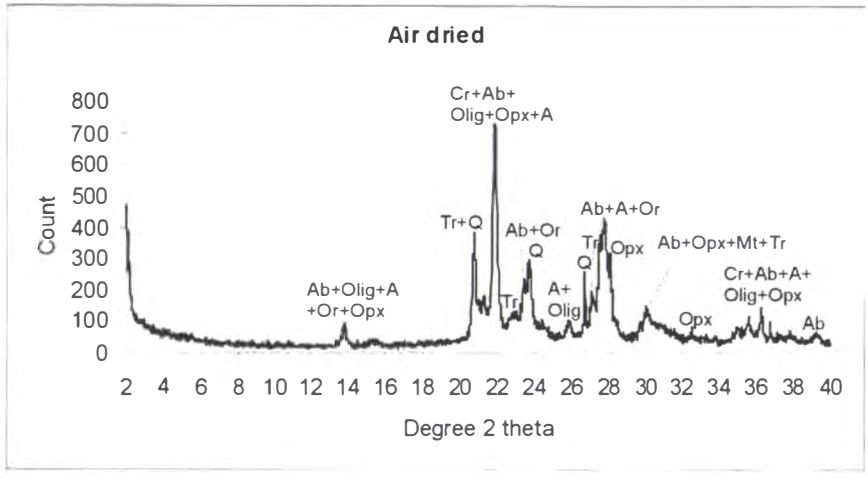
Air dried
Count
Degree 2 theta
Cr+Ab+
Olig+Opx+A
Tr+Q
Ab+Or
Q
Ab+A+Or
Tr
Opx
Q
Ab+Opx+Mt+Tr
Cr+Ab+A+
Olig+Opx
Ab+Olig+A
+Or+Opx
Tr
A+
Olig
Opx
Ab

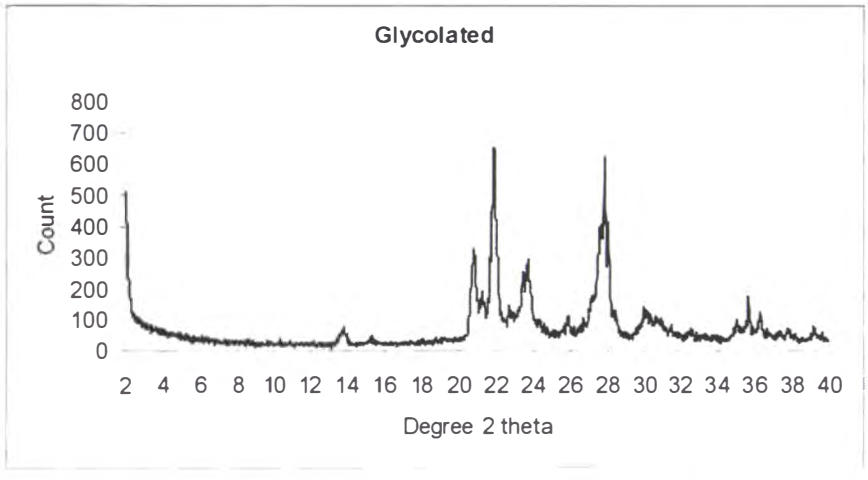
Glycolated
Count
Degree 2 theta

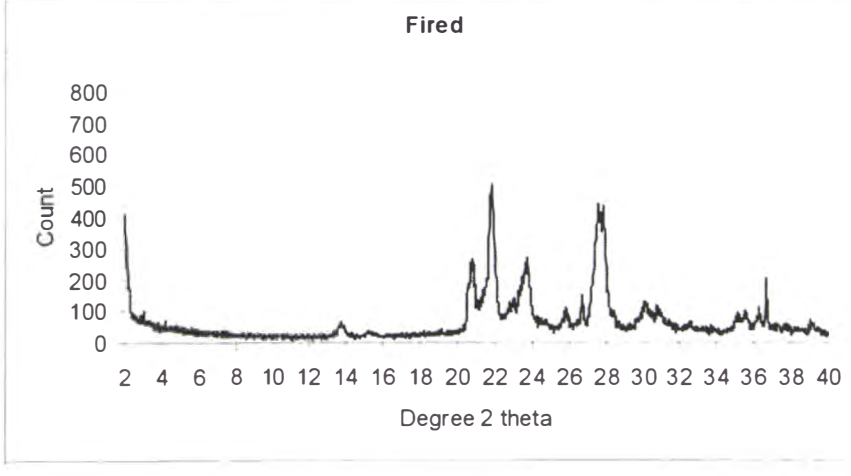
Fired
Count
Degree 2 theta

F18 pattern

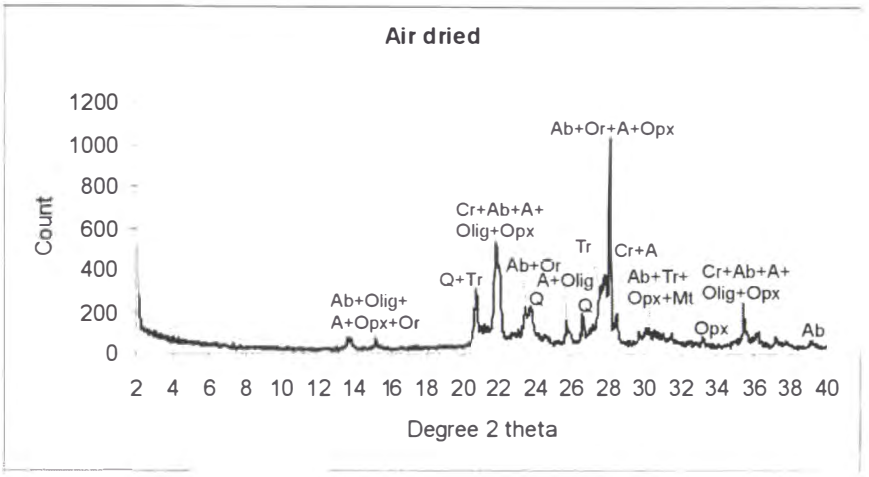
Air dried
Count
Degree 2 theta
Ab+Or+A+Opx
Cr+Ab+A+
Olig+Opx
Tr
Cr+A
Ab+Or
Q+Tr
A+Olig
Ab+Tr+
Opx+Mt
Cr+Ab+A+
Olig+Opx
Ab+Olig+
A+Opx+Or
Q
Q
Opx
Ab

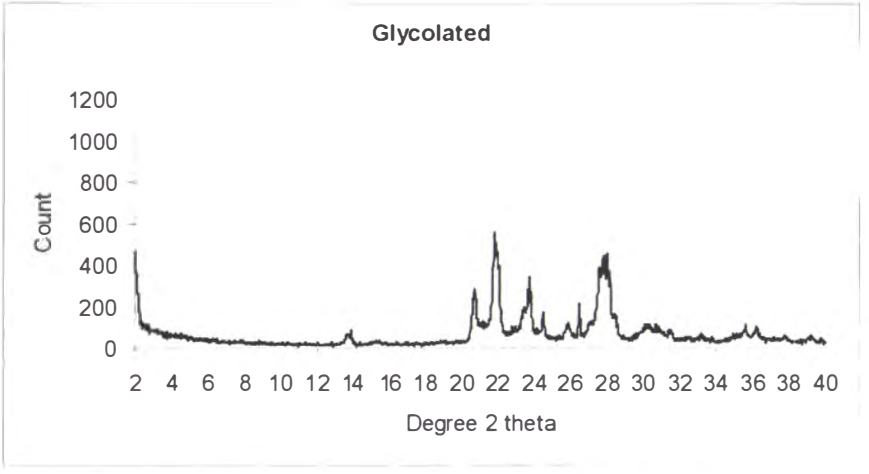
Glycolated
Count
Degree 2 theta

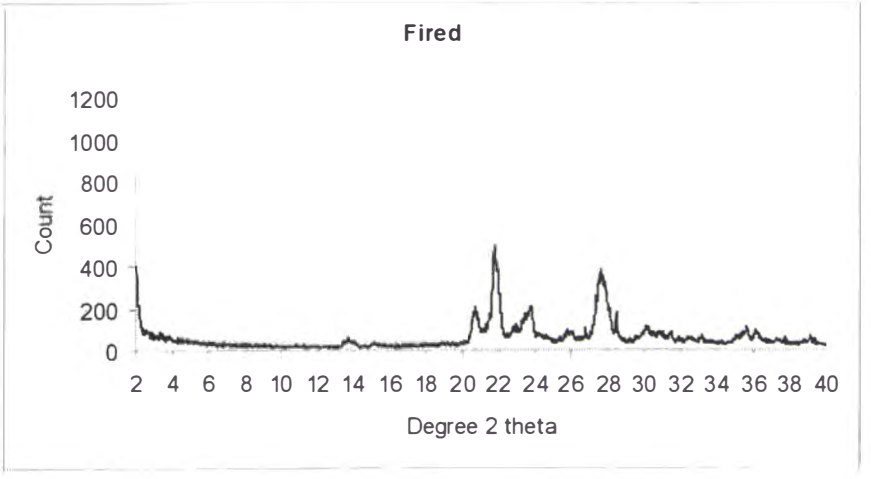
Fired
Count
Degree 2 theta

F19 pattern

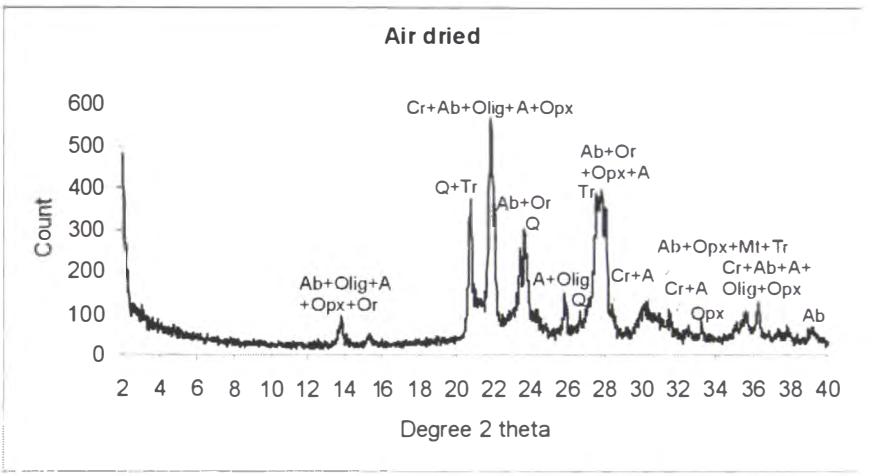
Air dried
Count
Degree 2 theta
Cr+Ab+Olig+A+Opx
Q+Tr
Ab+Or
Q
Ab+Or
+Opx+A
Tr
Ab+Opx+Mt+Tr
Cr+Ab+A+
Olig+Opx
Ab+Olig+A
+Opx+Or
A+Olig
Q
Cr+A
Cr+A
Opx
Ab

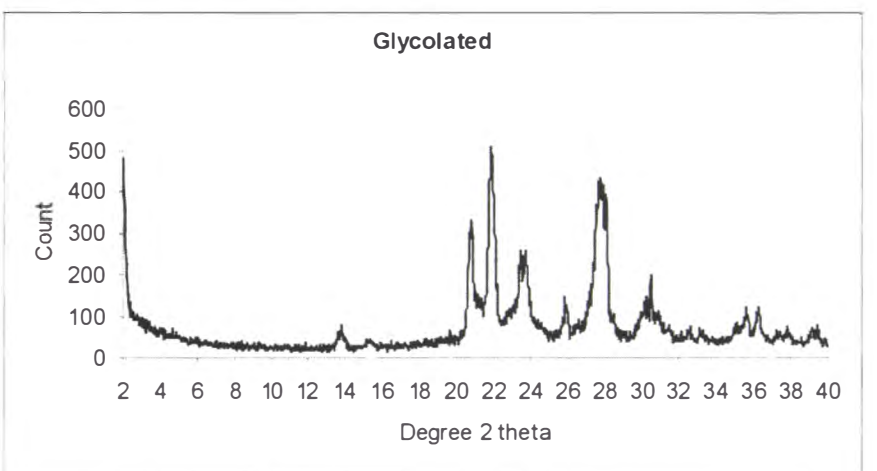
Glycolated
Count
Degree 2 theta

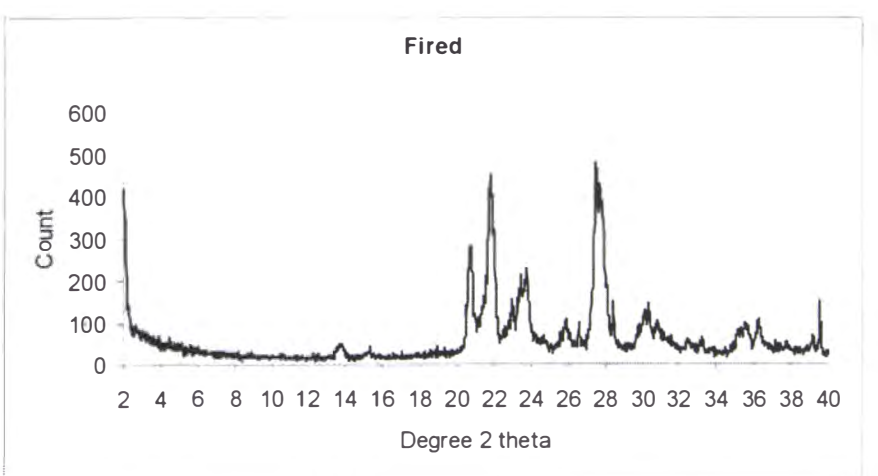
Fired
Count
Degree 2 theta

F20 pattern

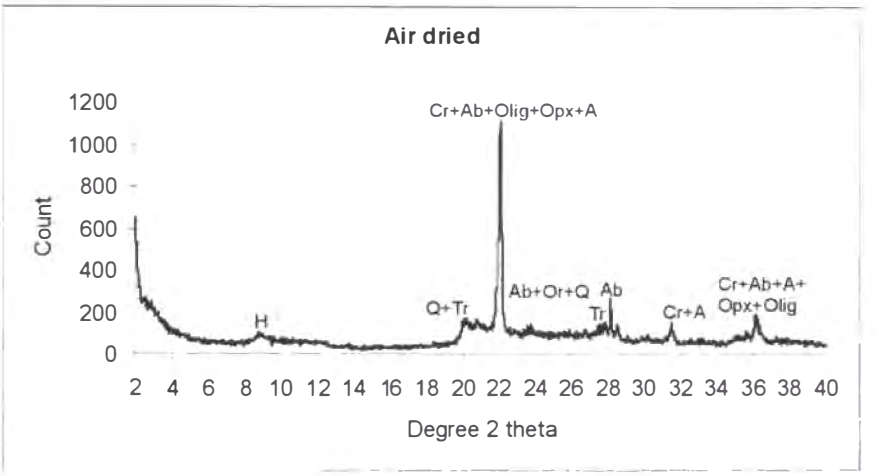
Air dried
Count
1200
1000
800
600
400
200
0
Cr+Ab+Olig+Opx+A
H
Q+Tr
Ab+Or+Q
Ab
Tr
Cr+A
Cr+Ab+A+
Opx+Olig
2 4 6 8 10 12 14 16 18 20 22 24 26 28 30 32 34 36 38 40
Degree 2 theta

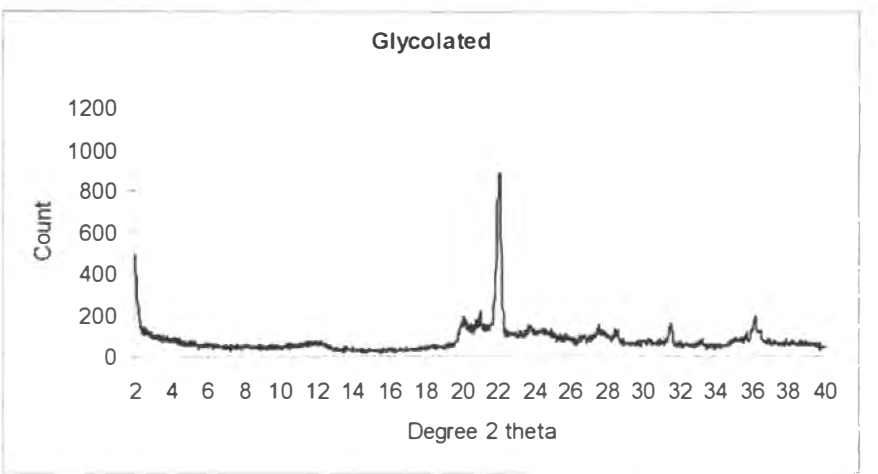
Glycolated
Count
1200
1000
800
600
400
200
0
2 4 6 8 10 12 14 16 18 20 22 24 26 28 30 32 34 36 38 40
Degree 2 theta

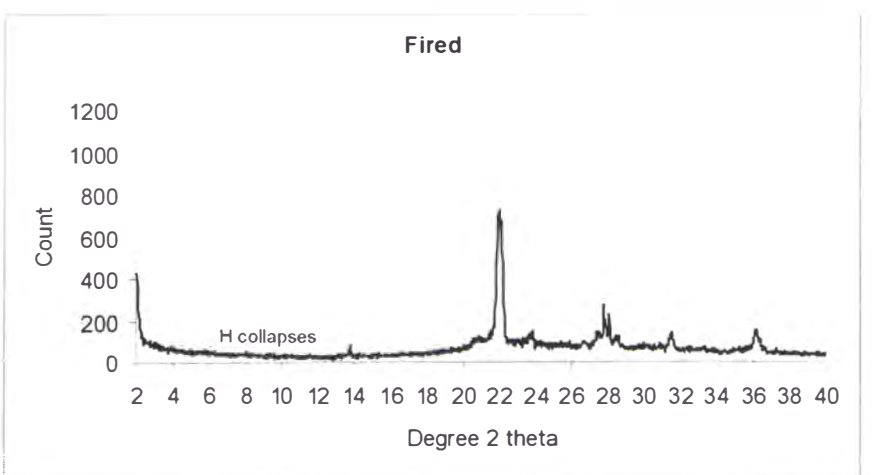
Fired
Count
1200
1000
800
600
400
200
0
H collapses
2 4 6 8 10 12 14 16 18 20 22 24 26 28 30 32 34 36 38 40
Degree 2 theta

F21 pattern

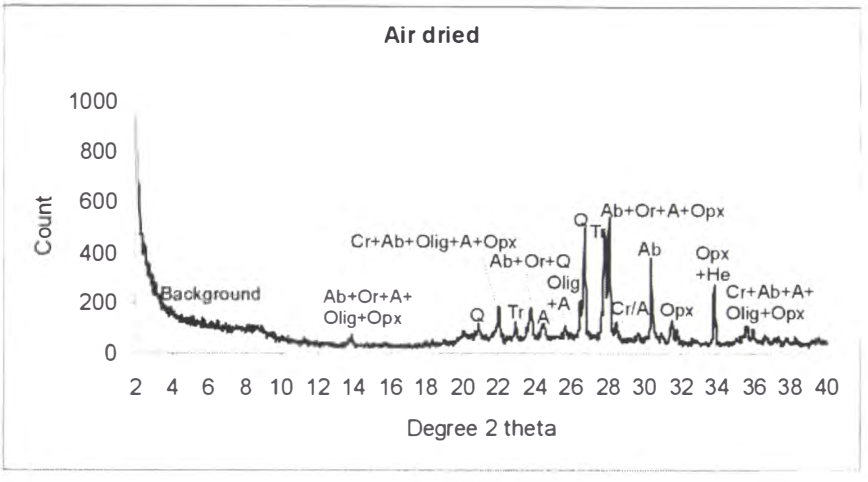
Air dried
Count
1000
800
600
400
200
0
Background
Ab+Or+A+
Olig+Opx
Cr+Ab+Olig+A+Opx
Ab+Or+Q
Olig
+A
Q
Tr
A
Q
Tr
Ab+Or+A+Opx
Ab
Opx
+He
Cr/A
Opx
Cr+Ab+A+
Olig+Opx
2 4 6 8 10 12 14 16 18 20 22 24 26 28 30 32 34 36 38 40
Degree 2 theta

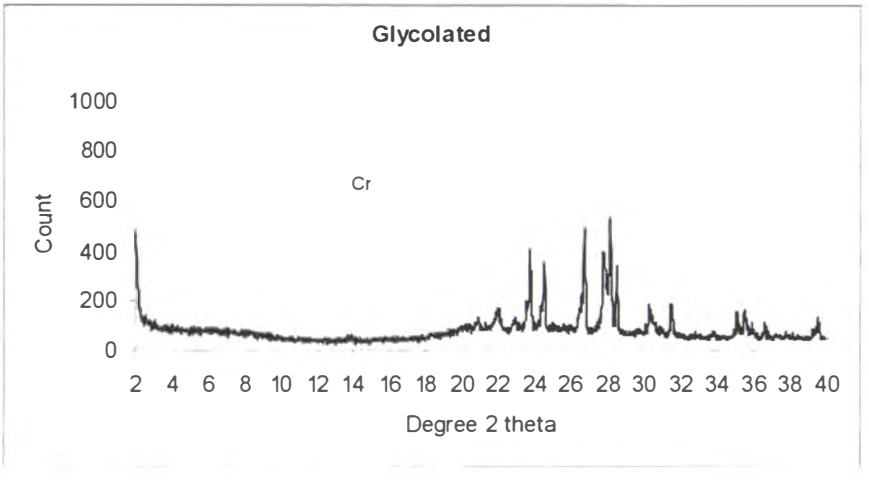
Glycolated
Count
1000
800
600
400
200
0
Cr
2 4 6 8 10 12 14 16 18 20 22 24 26 28 30 32 34 36 38 40
Degree 2 theta

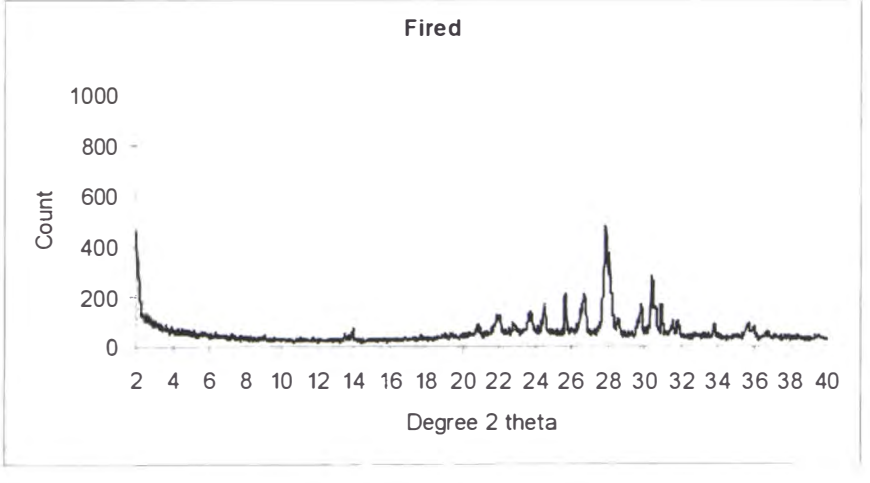
Fired
Count
1000
800
600
400
200
0
2 4 6 8 10 12 14 16 18 20 22 24 26 28 30 32 34 36 38 40
Degree 2 theta

F22 pattern

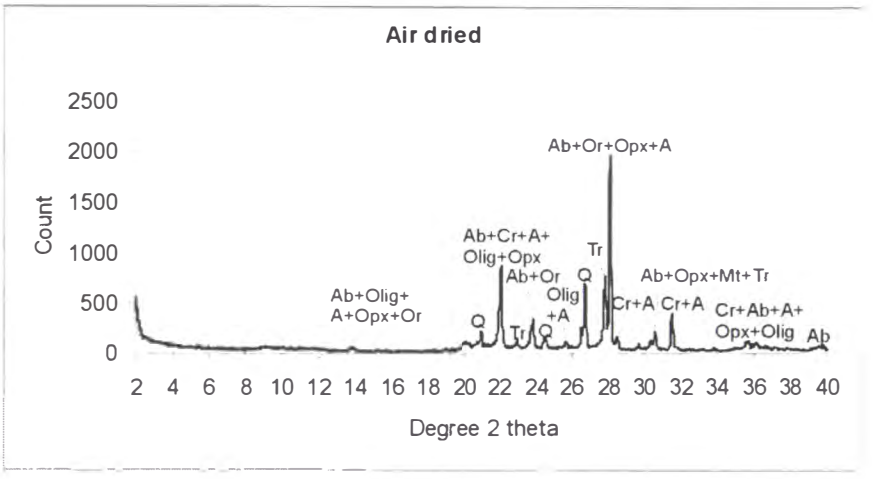
Air dried
Count
2500
2000
1500
1000
500
0
Ab+Or+Opx+A
Ab+Cr+A+
Olig+Opx
Tr
Ab+Or
Q
Ab+Opx+Mt+Tr
Ab+Olig+
A+Opx+Or
Olig
+A
Cr+A Cr+A
Cr+Ab+A+
Opx+Olig
Ab
2 4 6 8 10 12 14 16 18 20 22 24 26 28 30 32 34 36 38 40
Degree 2 theta

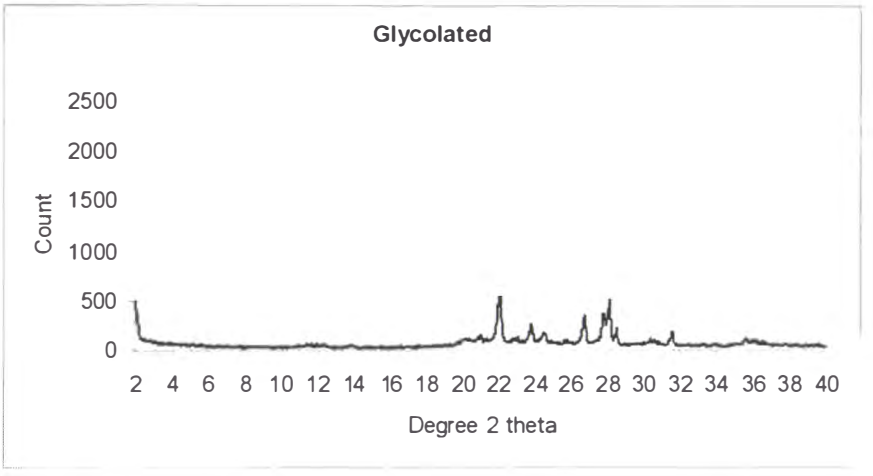
Glycolated
Count
2500
2000
1500
1000
500
0
2 4 6 8 10 12 14 16 18 20 22 24 26 28 30 32 34 36 38 40
Degree 2 theta

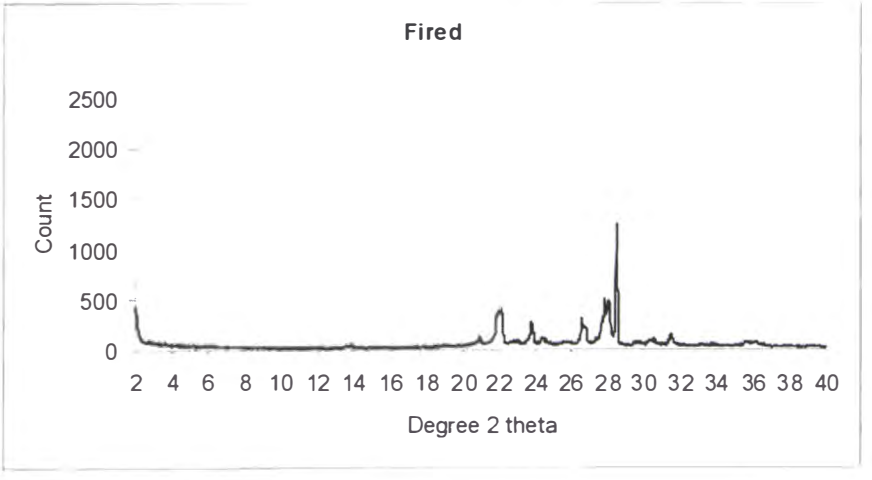
Fired
Count
2500
2000
1500
1000
500
0
2 4 6 8 10 12 14 16 18 20 22 24 26 28 30 32 34 36 38 40
Degree 2 theta

F23 pattern

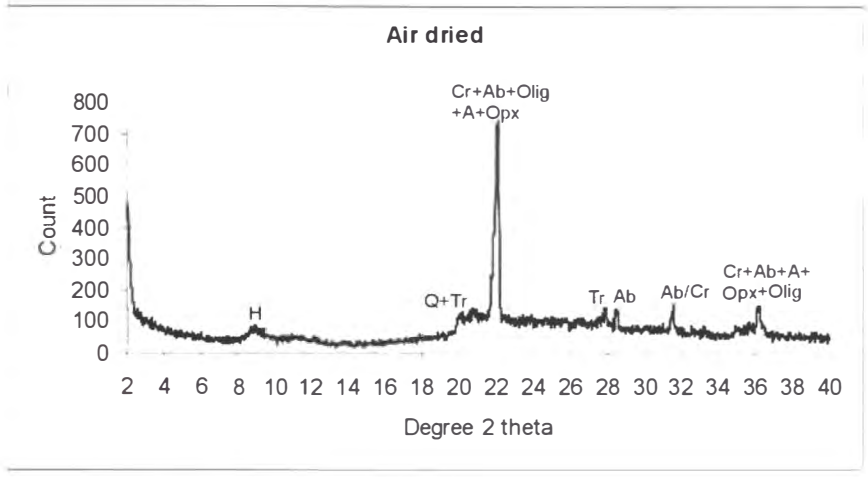
Air dried
Count
Degree 2 theta
Cr+Ab+Olig
+A+Opx
H
Q+Tr
Tr
Ab
Ab/Cr
Cr+Ab+A+
Opx+Olig

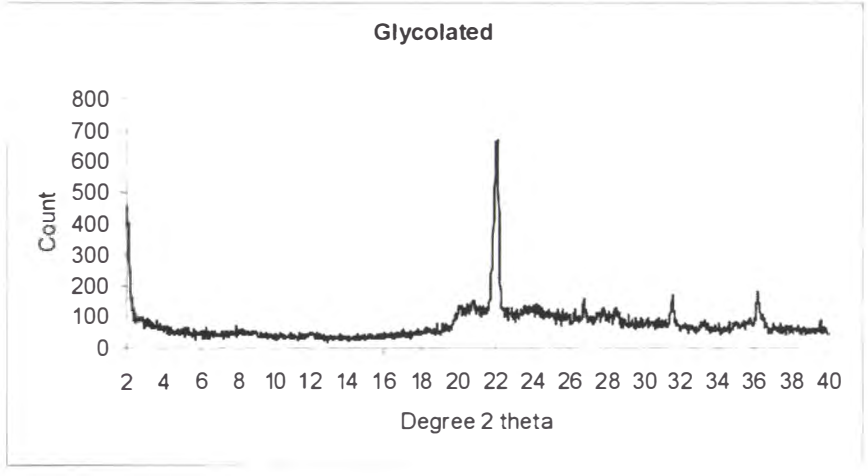
Glycolated
Count
Degree 2 theta

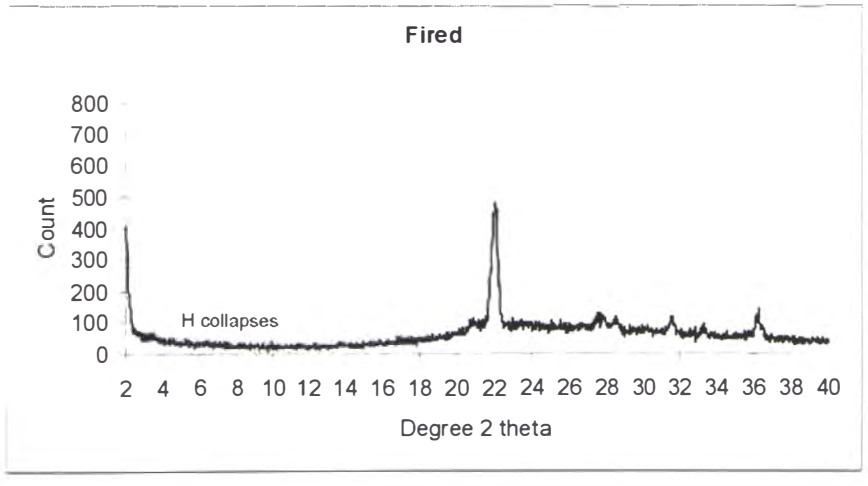
Fired
Count
Degree 2 theta
H collapses

Galaxy Rd fumarole 8 margin pattern

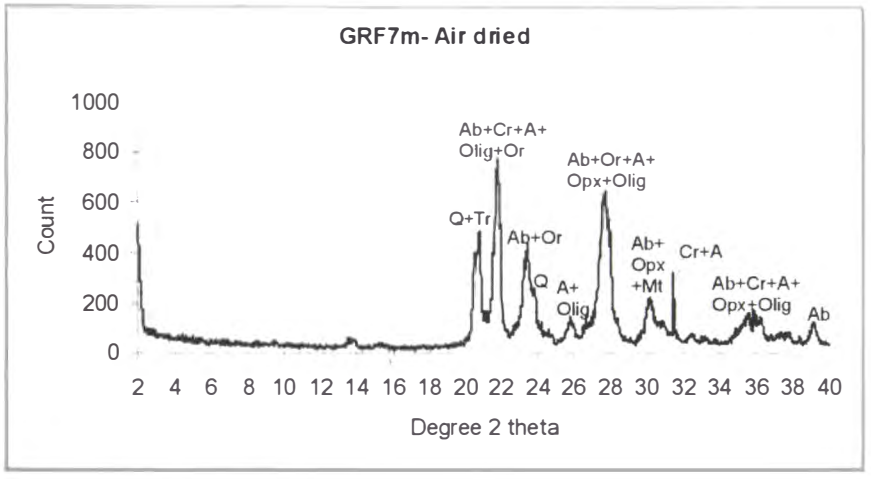

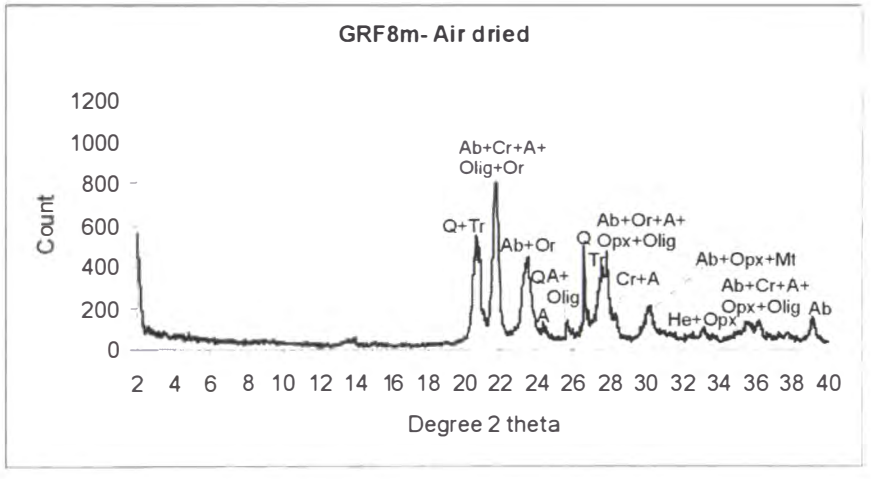

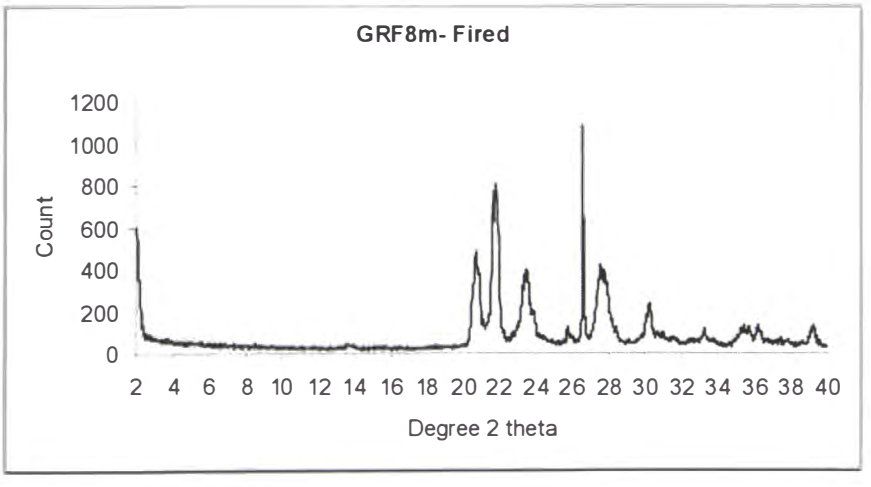

Galaxy Rd fumarole 8 red-purple zone pattern

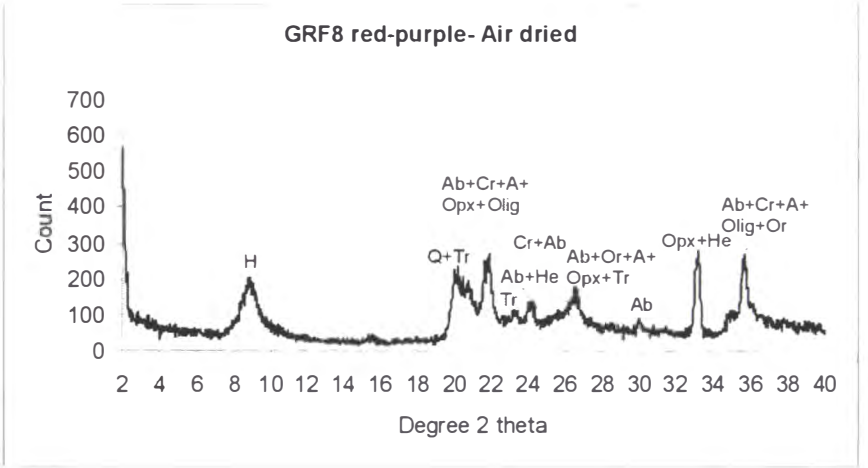

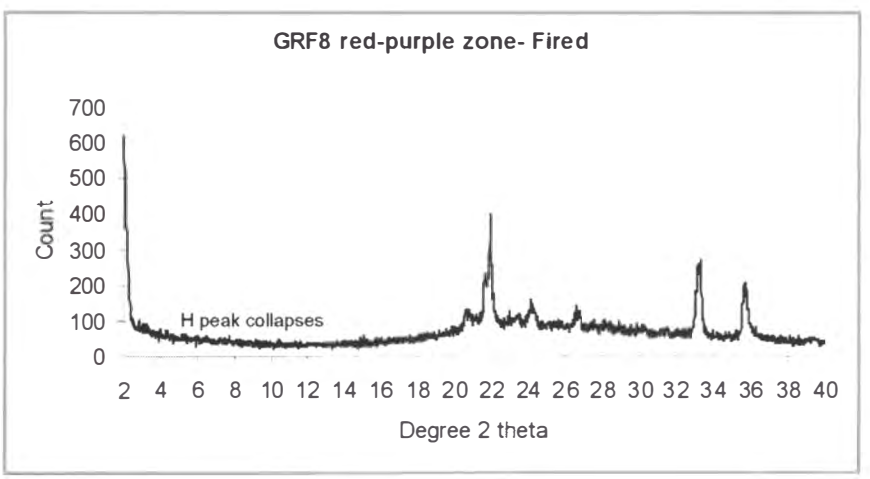

Galaxy Rd fumarole 8 yellow zone pattern

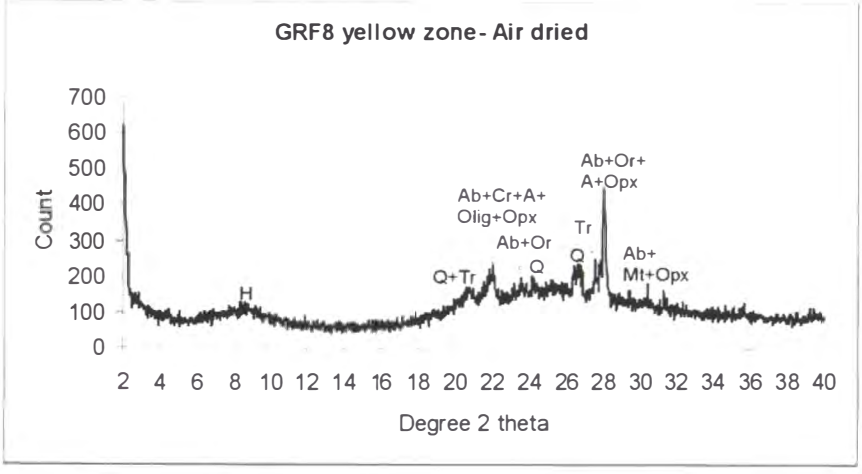

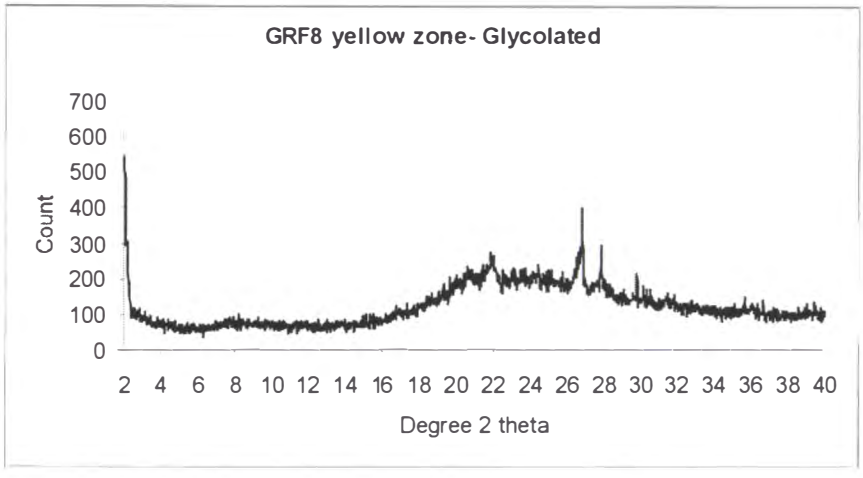

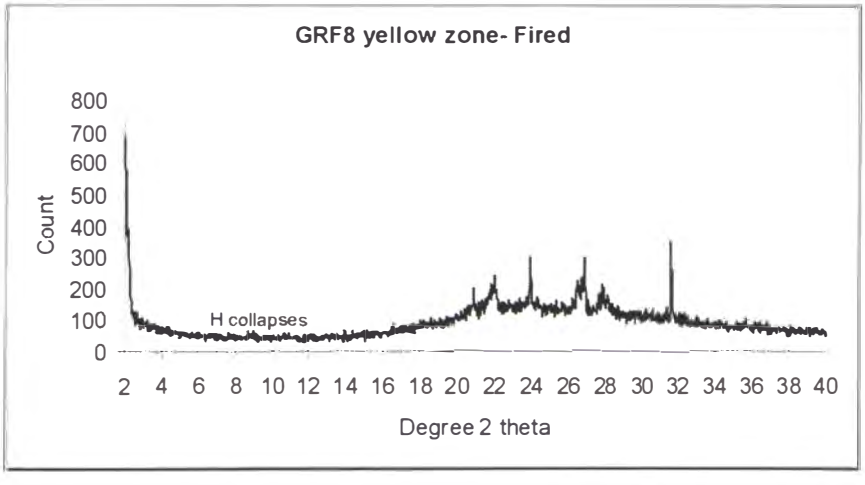

MKP105 (IMI) pattern

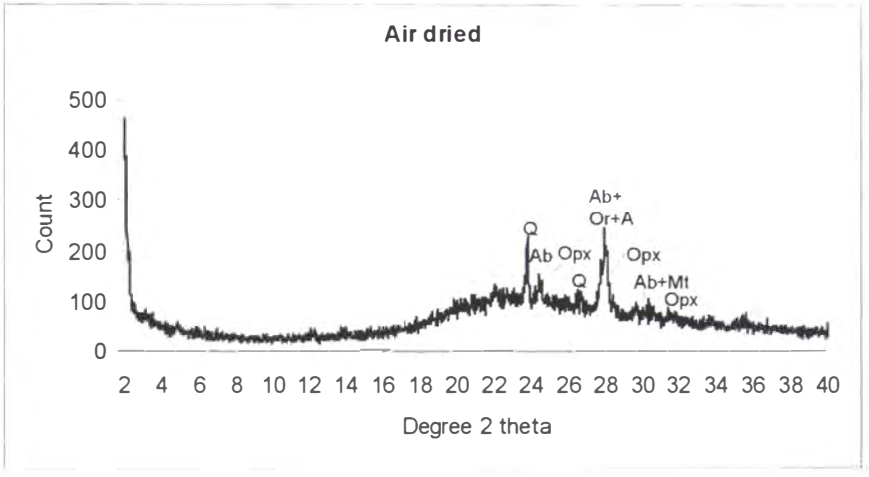

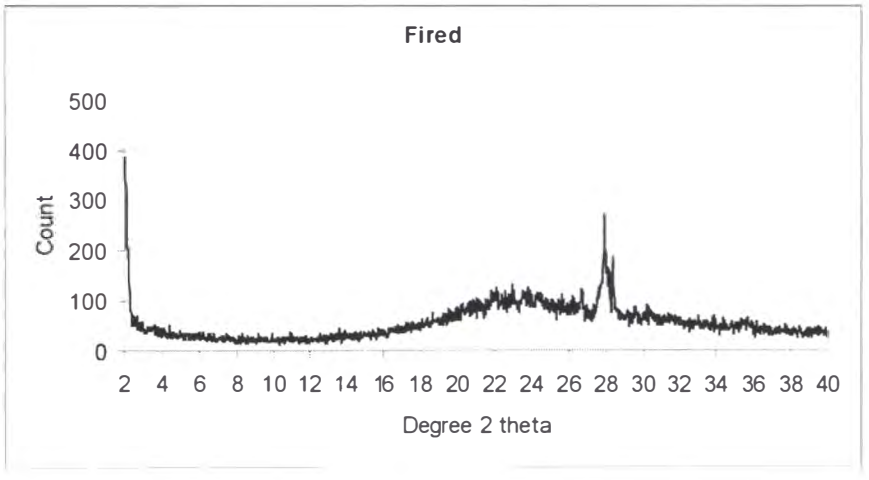

MKP110 (uMI) pattern

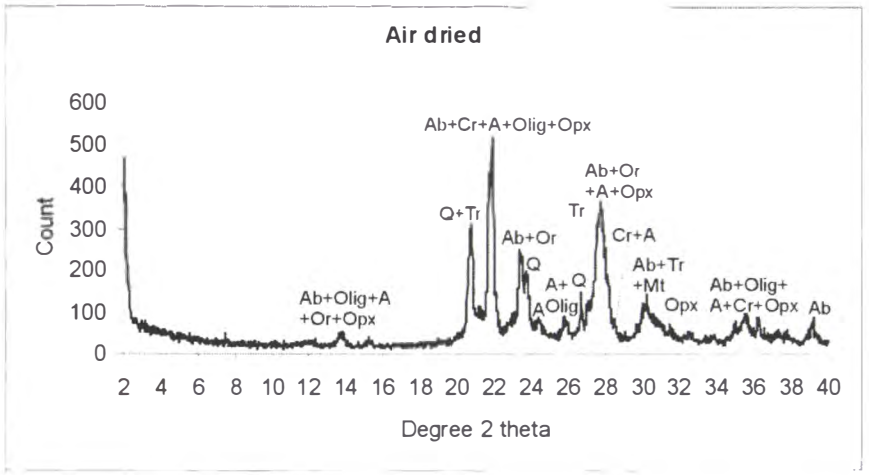

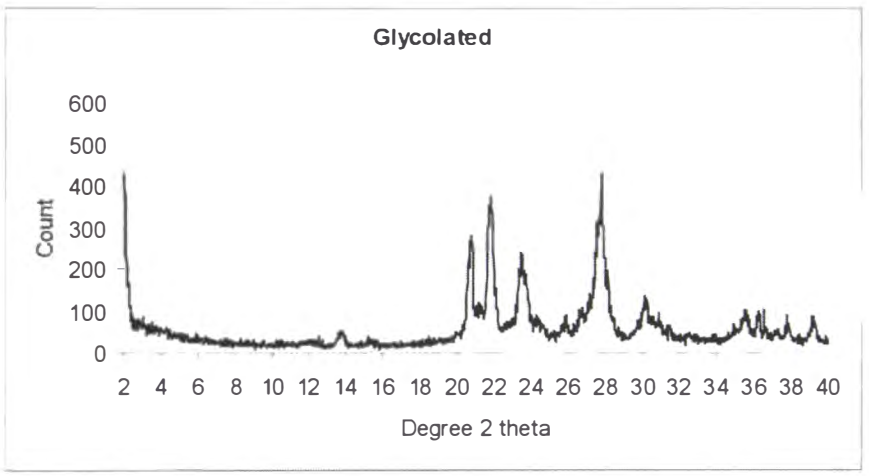

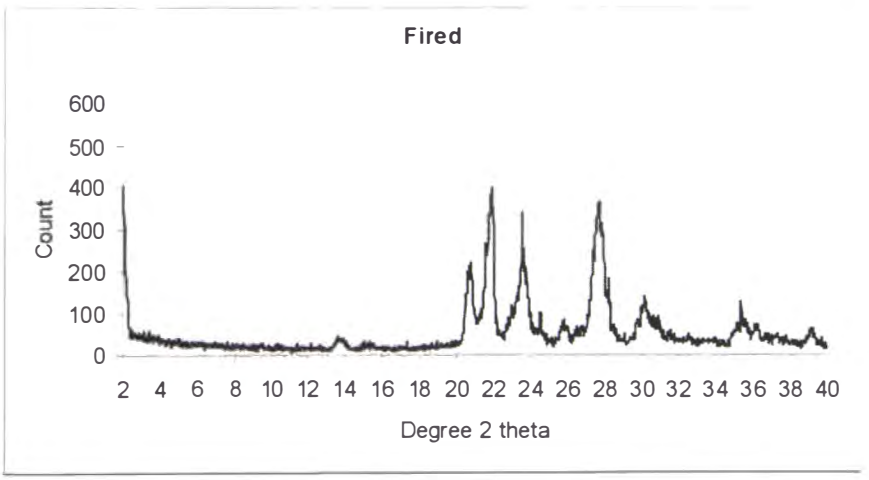

MKP111 (uMI) pattern

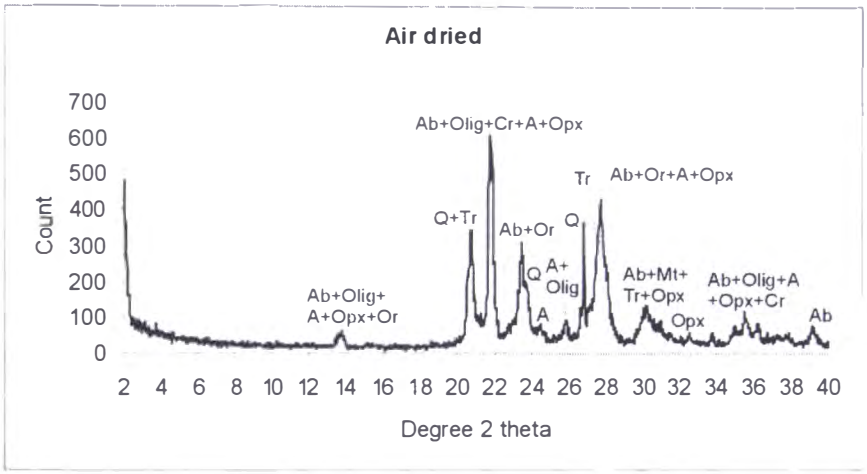

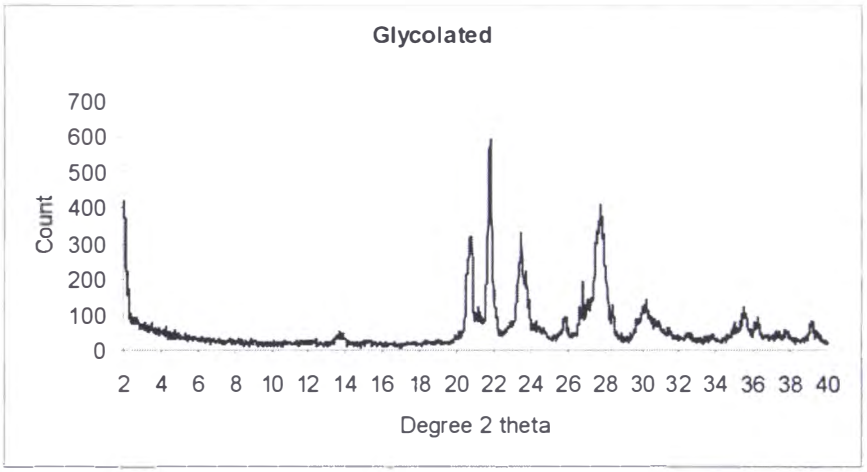

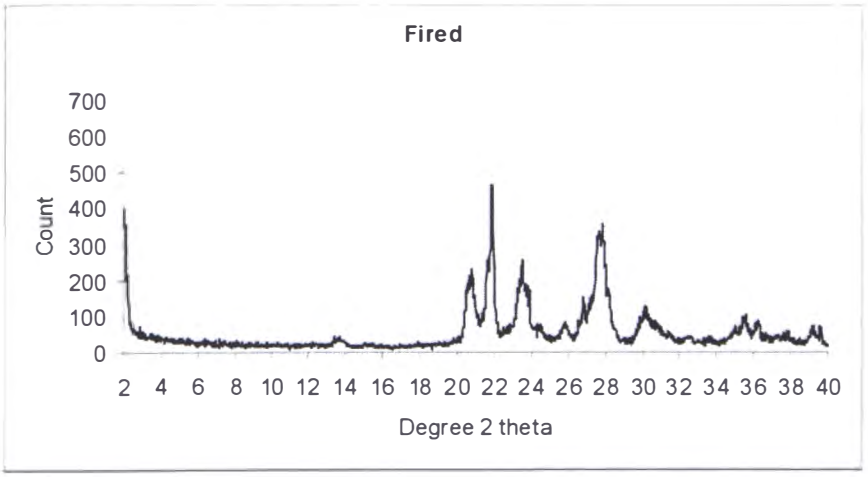

MKP134 (uMI) pattern

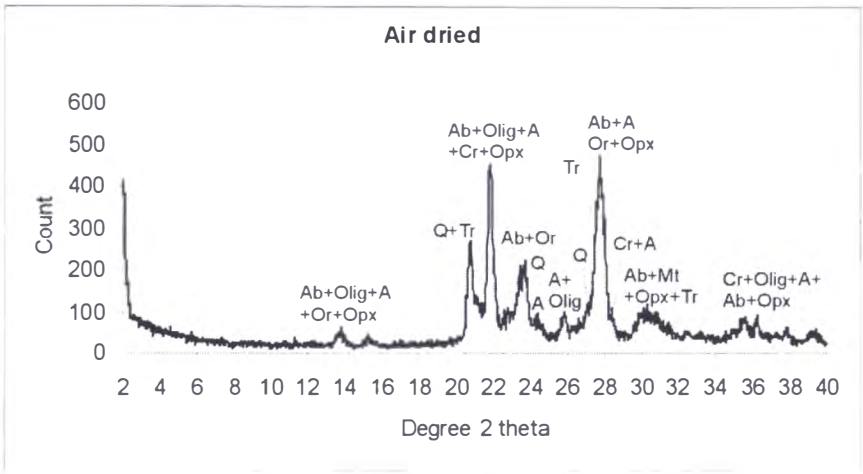

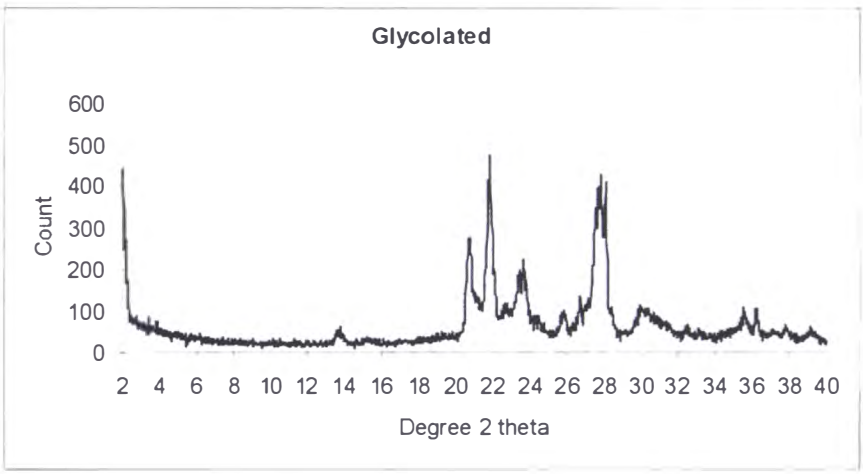

MKP29 (IMI) pattern

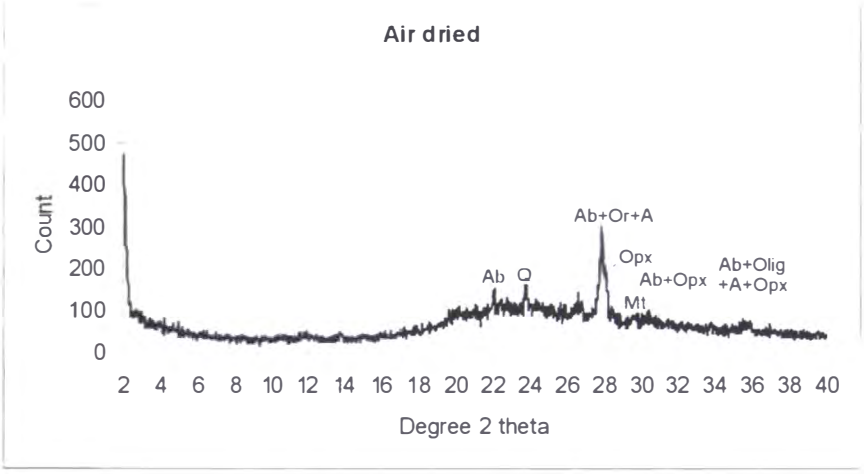

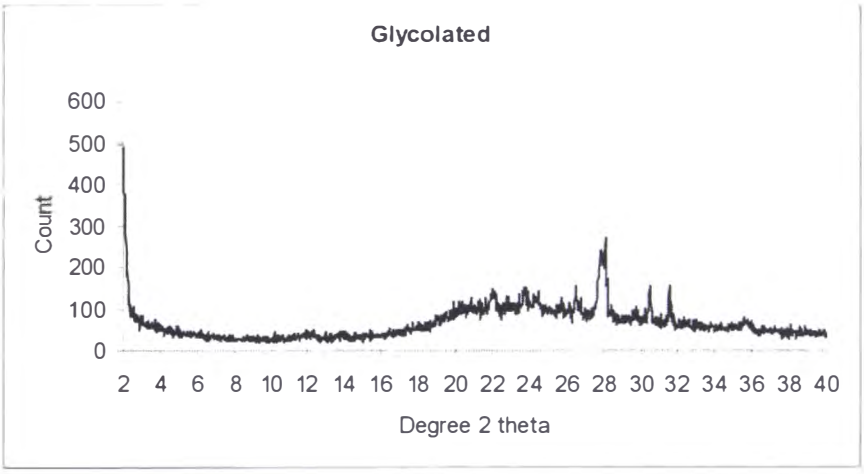

MKP35, MKP37, and MKP40 (IMI) pattern

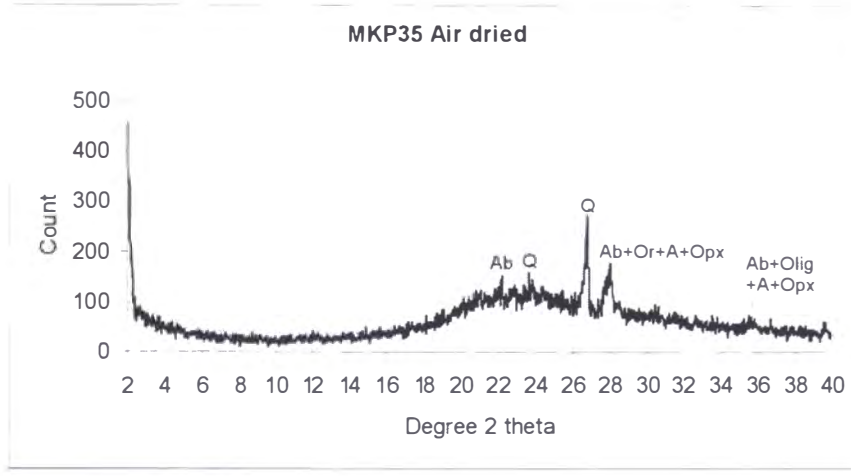

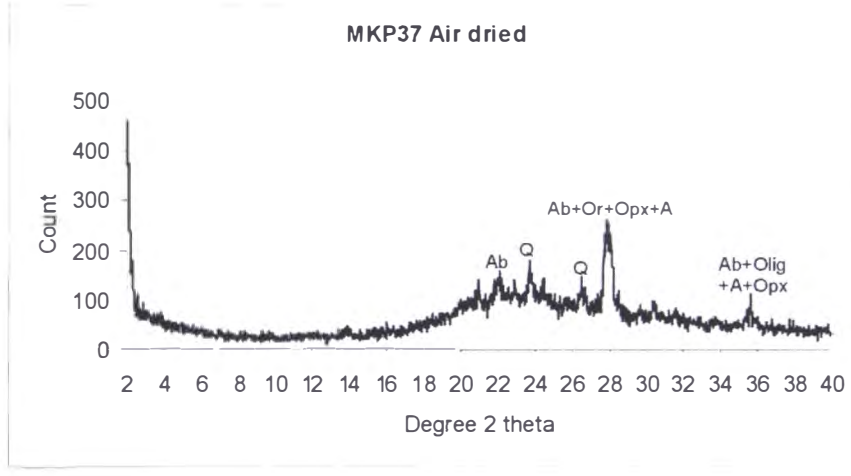

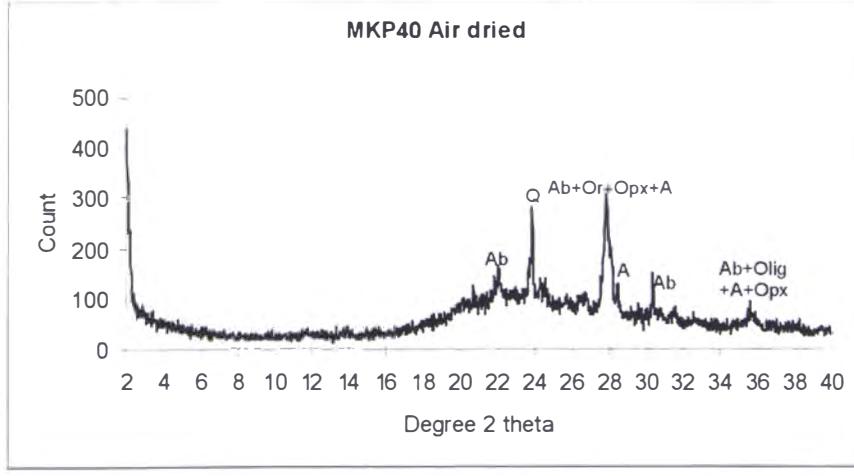

MKP36 (IMI) pattern

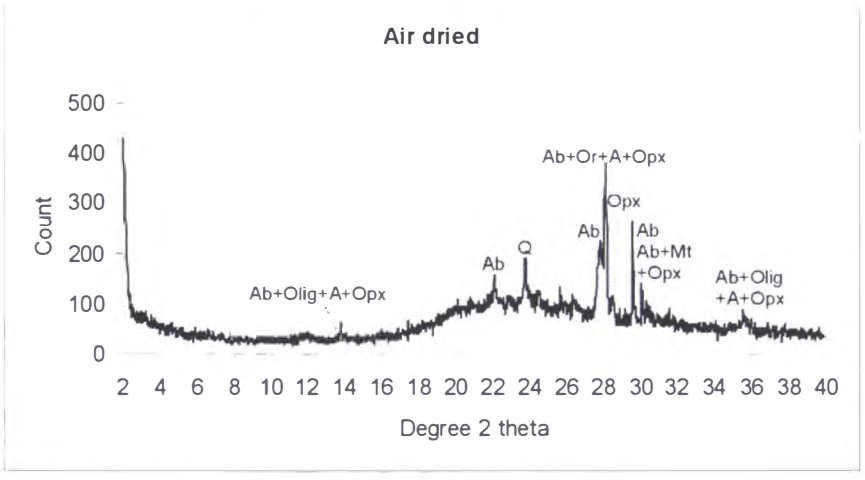

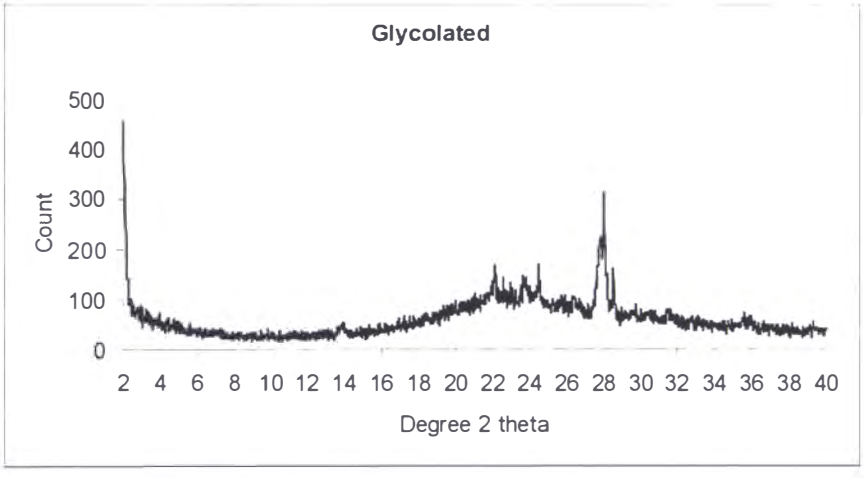

MKP117 and MKP121 (uMI) patterns

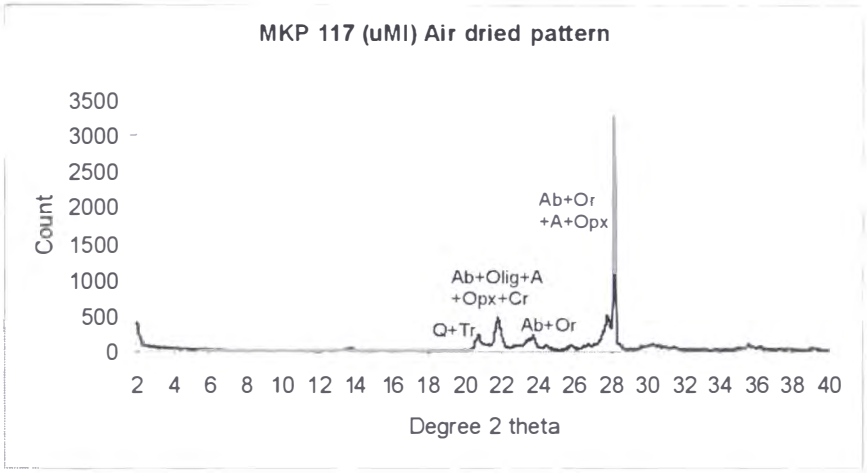

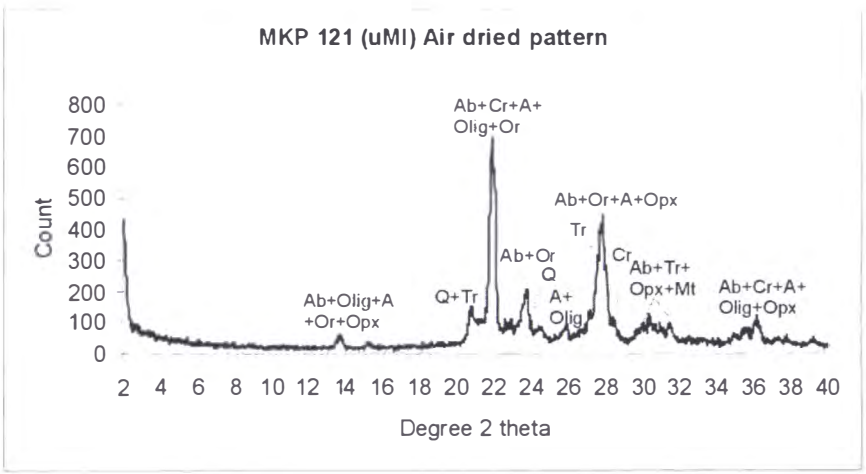

APPENDIX 5

Mamaku Ignimbrite graphic logs

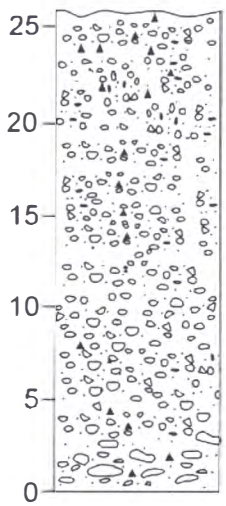

Very pale pink-brown, non-welded.
20 vol% pumice clasts, 5 vol % crystals,
5 vol% lithic fragments (mainly mMI).
M_n = 17,16,11,9,8 .

Pink-grey. non-welded, vapour phase altered,
20 vol% pumice clasts, 1 vol% lithic fragments. ~3 vol% crystals,.
M_n = 15,13,10,4,3.

Pink, non-welded, vapour phase altered
25 vol% pumice clasts, <1 vol% lithic fragments, 5 vol% crystals
M = 13,9,9,7,6.

Brown weathered, flattened pumice suggest
it was once welded, now poorly indurated,
7 vol% pumice clasts, ~2 vol% lithic fragments (rhyolite). 10 vol%
crystals. M_n = 16,19,5,4,4.

Leslie Rd log. From T15/637468.

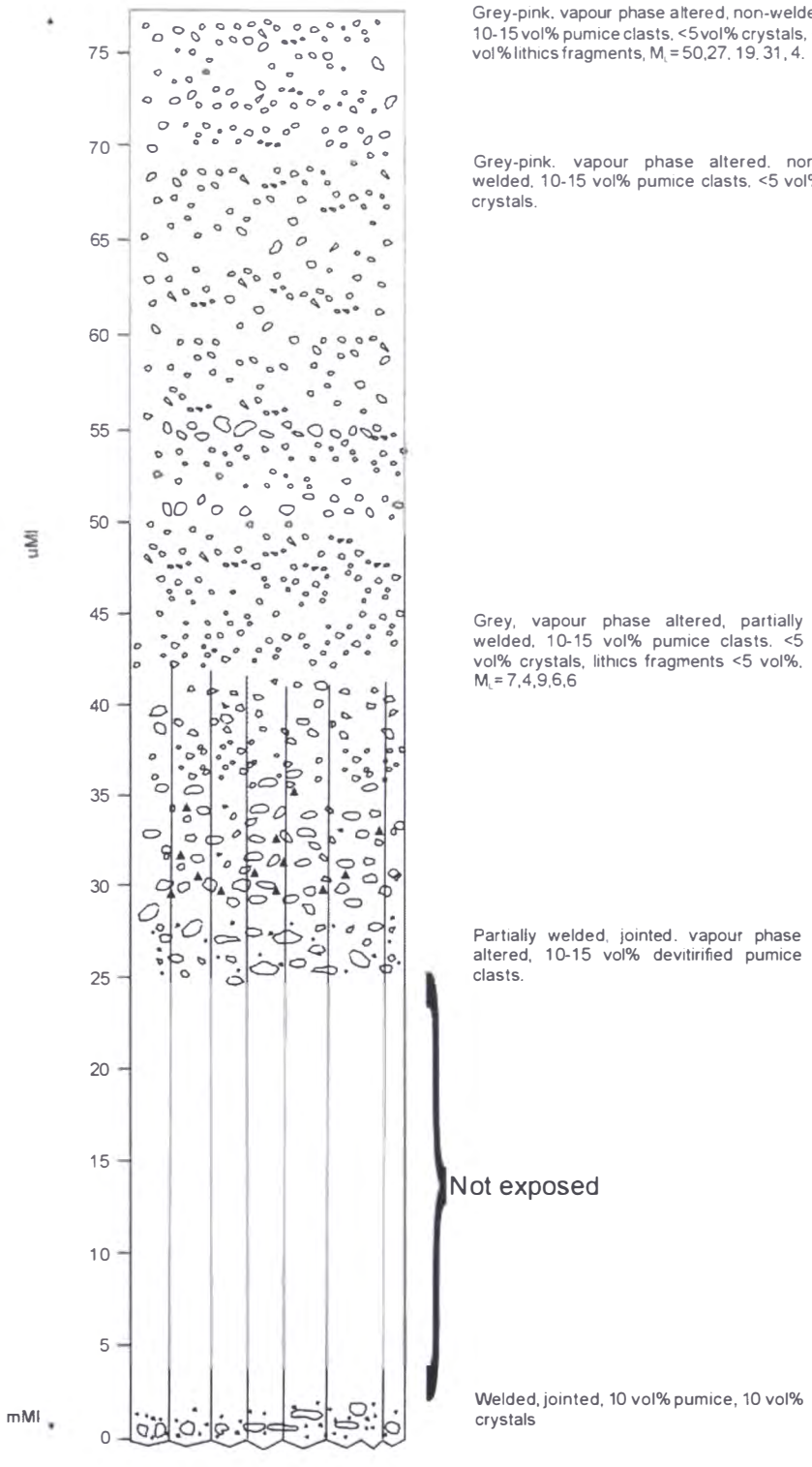

Omanawa River log. From U15/813606.

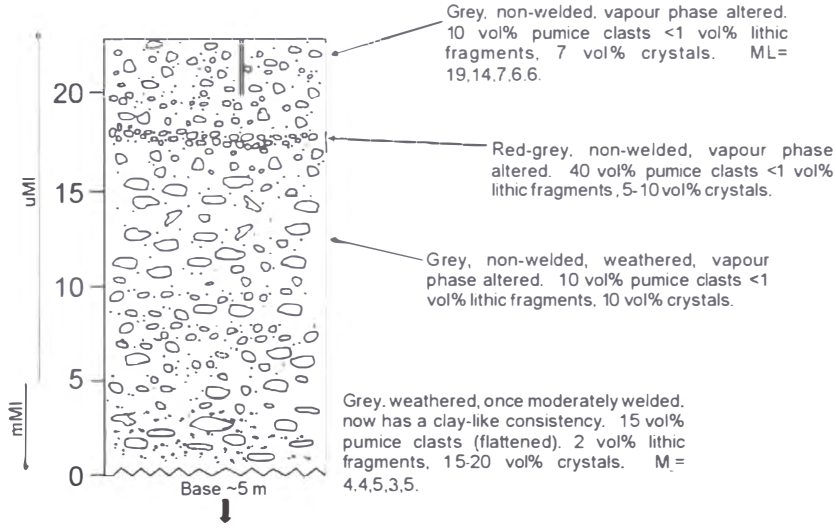

Lloyd Mandeno section. From U15/784684.

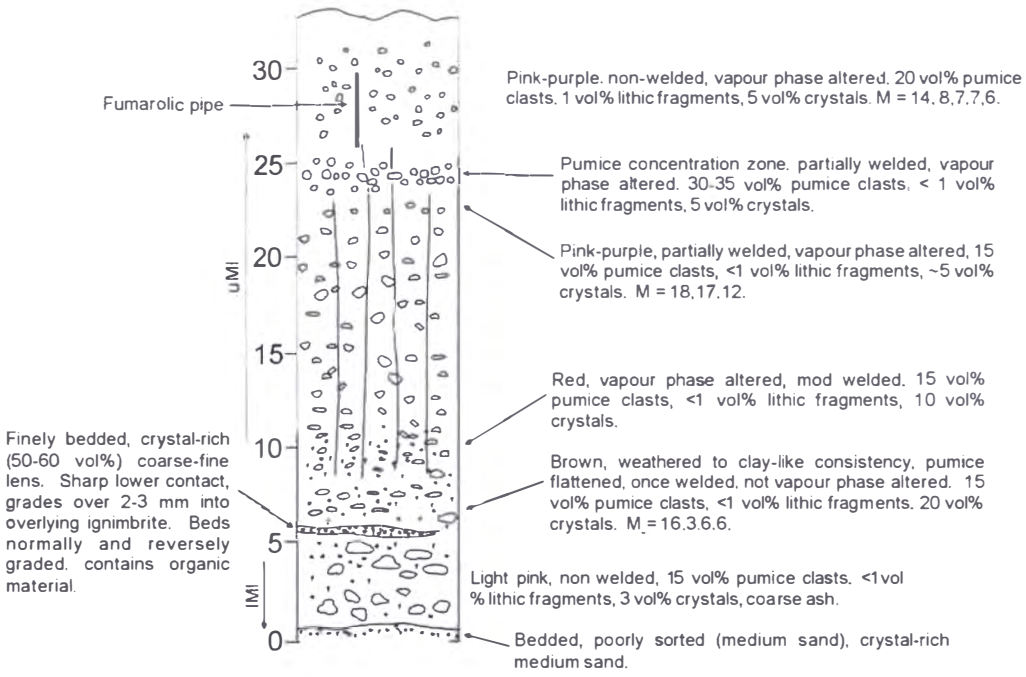

Oropi Gorge section. From U15/876676.

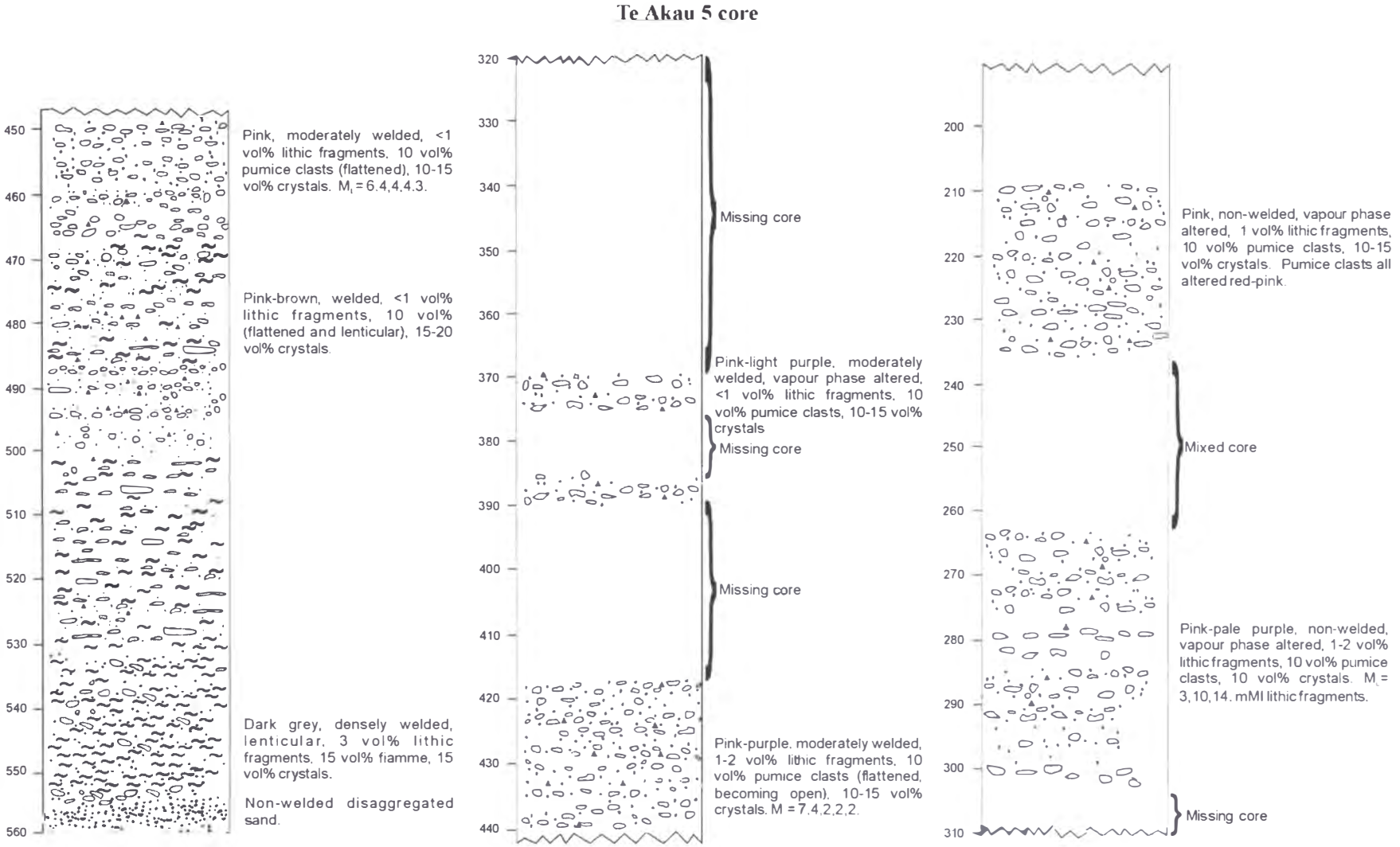

Mamaku Ignimbrite in the Te Akau5 drillcore, U15/047549. Units are feet below the surface.

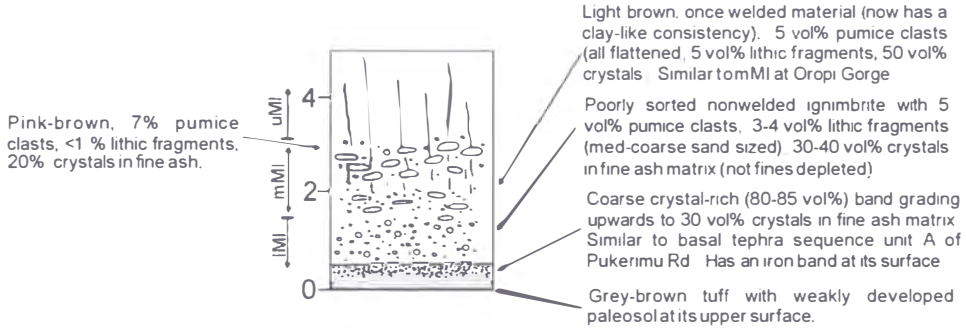

Mamaku Ignimbrite base, Lake Rotokawau, U15/065419.

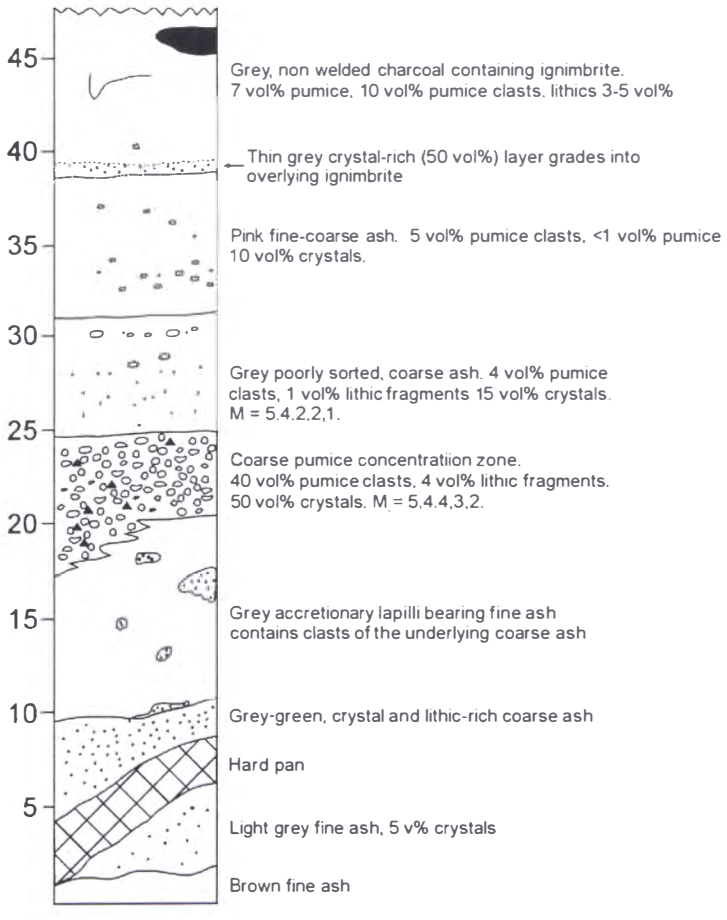

Basal tephra sequence at Pine Rd U16/761192.

APPENDIX 6

Density profiles

APPENDIX 6
Density profiles

Density of Mamaku Ignimbrite was calculated by three methods. The 1st involved extraction of the ignimbrite using a small can of known volume and weighing the resultant sample. Where the ignimbrite could not be sampled in such a way its density was calculated using a procedure outlined by Franklin et al. (1981) for irregular shaped samples, or cut into regular shapes, weighed, wrapped in a waterproof seal (of known weight and density), and submerged to ascertain its volume. Densities of rhyolite lavas were carried out using the method outlined by Franklin et al. (1981).

Density profiles were taken at Sutcliffe Rd starting at U16/738340, Oropi Gorge from U15/876686, and Pukerimu Rd (U16/777177). Rhyolite lava samples were taken from Mt Ngongotaha and Hamarana dome.

The density of Mt Ngongotaha was assumed to be the density of Mamaku Ignimbrite DRE and the Mamaku Ignimbrite volume prior to eruption based on this. The ratio of the average density of Mamaku Ignimbrite:Mt Ngongotaha rhyolite is 1:2.34. Volume of Mamaku Ignimbrite was divided by 2.34 to estimate its DRE volume.

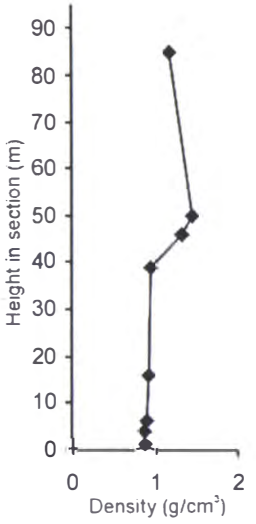

Sutcliffe Rd. From U16/738340.

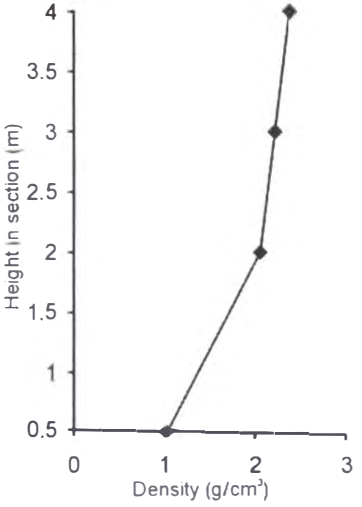

Pukerimu Rd. From U16/777177.

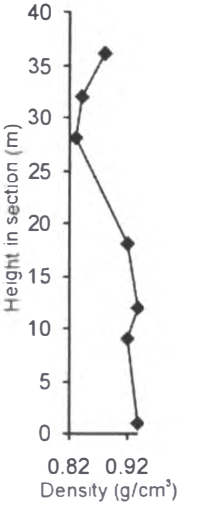

Oropi Gorge. From U15/876686.

APPENDIX 7

Caldera volume calculation method

APPENDIX 7
Caldera volume calculation method

Caldera volume was estimated using published geophysical models for Rotorua, and assuming a best-fit elliptical cone. An ellipse with approximately the same area (21×17 km) as the caldera was used as the upper cone surface and its maximum depth taken from the amount of collapse viewed in geophysical models to be between 1.25 and 1.75 km (Fig. A7.1). The caldera volume was then estimated as the volume of the cone using the formula:

$V = \frac{1}{3}Ah$

where V=volume, A= area of the cone top, and h= vertical depth of the cone.

The volume of intracaldera ignimbrite was estimated by subtracting the volume of a second cone with a lower boundary that followed the Mamaku Ignimbrite upper surface from the total caldera volume (Fig A7.1).

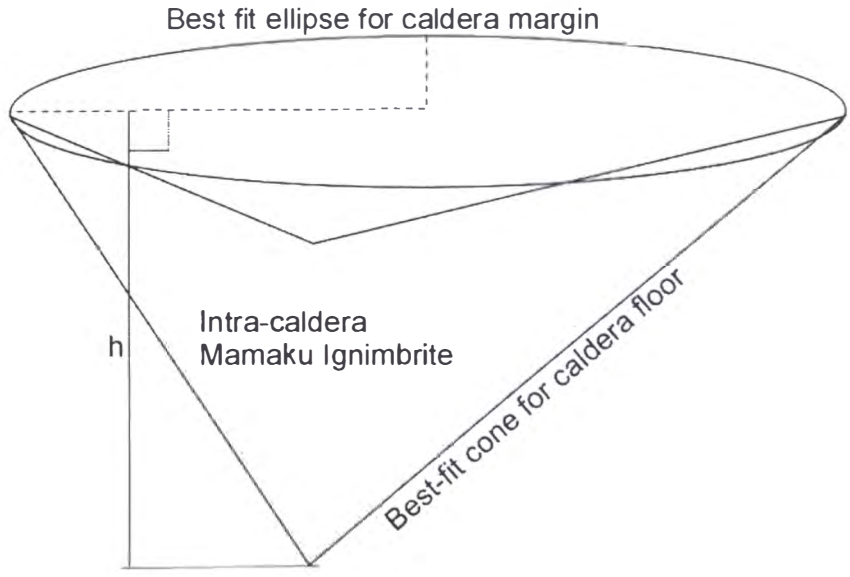

Figure A7.1. Estimating caldera and intra-caldera ignimbrite volumes using an elliptical caldera margin and conical base and ignimbrite upper surface.

APPENDIX 8

Asymmetric, multiple-block collapse at Rotorua Caldera, Taupo Volcanic Zone, New Zealand

submitted to
Bulletin of Volcanology

Asymmetric, multiple-block collapse at Rotorua Caldera, Taupo Volcanic Zone, New Zealand

D.M. Milner[1] · J.W. Cole[1] · C.P. Wood[2]

[1]Department of Geological Sciences, University of Canterbury, Private Bag 4800, Christchurch, New Zealand
email: d.milner@geol.canterbury.ac.nz, Fax: 64-3-3642769

[2]Institute of Geological and Nuclear Sciences, Wairakei Research Centre, Private Bag 2000, Taupo, New Zealand

Abstract

Calderas worldwide have been classified according to their dominant collapse styles, although there is a good deal of speculation about the processes involved. Recent laboratory experiments have tried to constrain these processes by modelling magma withdrawal and observing the effects on overlying materials. However many other factors also contribute to final caldera morphology. Collapse structure and evolution of Rotorua Caldera is interpreted based its geophysical response, geology and geomorphology of, and the stratigraphy of the Mamaku Ignimbrite. Rotorua Caldera is situated at the edge of the extensional Taupo Volcanic Zone, in which major faults strike NE-SW. A second, less dominant fault set strikes NW-SE. These two fault sets have a strong influence on the morphology of Rotorua Caldera. No one style of collapse can be applied to Rotorua Caldera; it was formed during a single eruption, but subsided as many blocks and shows features of trapdoor, piecemeal, and downsag types of collapse. Here Rotorua Caldera is described, according to its composition, activity and geometry, as a rhyolitic, single event, asymmetric, multiple-block, single locus collapse structure.

The Mamaku Ignimbrite is the only ignimbrite to have erupted from Rotorua Caldera. Extracaldera thickness of Mamaku ignimbrite is up to 145 m whereas inside the caldera it may be greater than 1 km thick. The timing of caldera subsidence is inferred from variations within the Mamaku Ignimbrite. The Mamaku Ignimbrite can be separated into a basal tephra sequence and main ignimbrite sequence. The main ignimbrite sequence contains no observable flow unit boundaries but can be split into lower, middle and upper parts based on crystal content, welding jointing, devitrification and vapour phase alteration. Juvenile clasts within the ignimbrite comprise three consanguineous pumice types and andesitic fragments. Only the most evolved pumice type occurs in the basal sequence. All three pumice types occur together throughout the main ignimbrite sequence whereas the andesitic fragments are only present in uMI.

Lithic lag breccias in uMI indicate a late stage of caldera collapse. Concentration of lithic fragments increases towards the middle of the ignimbrite may also reflect increased subsidence rate during an earlier stage. Collapse of Rotorua Caldera is thought to have occurred throughout the eruption of the main ignimbrite sequence of Mamaku Ignimbrite allowing simultaneous eruption of all the different pumice types.

Keywords: Caldera, Rotorua, Mamaku Ignimbrite, Taupo Volcanic Zone

Introduction

Large-scale withdrawal of magma from a chamber leads to instability of overlying rocks and formation of a volcanic depression or caldera (e.g. Williams, 1941). Calderas worldwide have been classified according to their dominant collapse style, such as simple piston, piecemeal, trapdoor, or downsag structures (e.g. Lipman, 1984, 1997, 2000). Walker (1984) was one of the first to indicate that many calderas have more than one mode of origin. He noted that downsag is a common collapse style, citing Rotorua Caldera, Taupo Volcanic Zone, New Zealand as one example, but that it commonly occurs in conjunction with other forms of collapse. Downsag is difficult to accommodate in thick consolidated piles of rock that are likely to deform brittly. Downsag will normally only occur at upper levels where relatively flat-lying and weak rocks are able to bend above competent caldera floor blocks. Recent studies confirm that caldera collapse mechanisms and associated structures are much more complex than they appear at the surface (e.g. Nappi et al., 1991; Branney and Kokelaar, 1994; Moore and Kokelaar, 1998; Kokelaar and Branney, 1999). For example, Branney and Kokelaar (1994) indicate that piecemeal collapse applies to situations where multiple magma bodies supply a number of vents, creating nested collapse structures, or when multiple dip-slip faults move separately due to magma withdrawal from a single chamber, to calderas in which the entire caldera floor down to the magma chamber is broken up into numerous small blocks. By this definition, piecemeal collapse has taken place at most calderas, whether or not one or a number of eruptions formed them.

Laboratory studies (e.g. Komuro et al., 1984; Komuro, 1987; Marti et al., 1994; Roche et al., 2000) are helping to constrain the types of structures that form when support is removed from beneath a set of strata. Comparisons have also been drawn between mine collapse subsidence and ice melt pits (Branney, 1995). The main points identified in these studies are that collapse often involves an inner block bounded by outward

dipping (reverse) faults at upper levels that steepen with depth, outside of which is a tilted block where faults are inward dipping (normal). These experimental analogues have enhanced understanding about how calderas collapse, but the resulting models lack verisimilitude because they have been carried out under conditions in which the external forces that always modify stress regimes around a magma chamber and cause added disruption to overlying strata are missing, and substances used for analogue crust in (laboratory models) commonly have uniform properties throughout, a condition that is not often found in nature.

The final morphology of a caldera will vary according to the way the caldera floor breaks up, whether the amount of vertical movement increases sequentially, or whether the blocks subside chaotically at more than one collapse centre. Depending on the tectonic setting of volcanic activity, many factors may contribute to a caldera's structure, collapse history, and final morphology.

Geological setting

Taupo Volcanic Zone (TVZ), New Zealand, is about 300 km long and up to 60 km wide (Fig. 1) and relates to subduction of the Pacific Plate beneath the Australian plate off New Zealand's east coast (Wilson et al., 1995). It can be split into northern and southern andesite dominated segments, and a central rhyolitic segment (Fig. 1; Houghton et al., 1995). TVZ is extending at ~7-12mm/year (Sissons, 1979; Walcott, 1987; Crook and Hannah, 1988; Darby et al., 2000) in a NW-SE direction along axes striking dominantly NE-SW (Fig. 2). A second, less dominant set of faults strikes NW-SE (Wan and Hedenquist, 1981; Cole, 1990). These faults may have been created under a transtensional stress regime (Cole, 1990), and they act as lines of weakness along which collapse preferentially takes place, so modifying the formation of a simple circular caldera. An alternative explanation for the NW-SE cross features is provided by Rowland and Sibson (in press), who regard them as "accommodation zones" between offset spreading centres. There are eight calderas or caldera complexes in TVZ (Wilson et al., 1995; 1984), varying from single-collapse structures such as Reporoa Caldera (Beresford and Cole, 2000) to multiple-collapse structures related to eruptions that occurred in much the same place (e.g. Taupo Caldera; Cole et al., 1998; Wilson et al., 1995), but separated by significant periods of time (Fig. 1). In places there is limited spatial overlap between calderas, adding to complications in developing simple caldera

structures. Rotorua Caldera formed during a single eruption, that of the c.225 ka Mamaku Ignimbrite (Shane et al., 1994; Houghton et al., 1995; Black et al., 1996).

Most previous work on Rotorua Caldera has concentrated on its geothermal activity, including heat flow and water properties. Lloyd (1975) was the first to look at Rotorua structurally, identifying faults subparallel to the caldera margin in the south of the caldera. Bayrantes (1984) looked at a larger area, documenting many lineaments and faults also in the southern part of the caldera, mainly associated with the geothermal field. Seismic studies of the Rotorua geothermal field and lake were carried out by Lamarche (1992) and Davy (1992) respectively. Wood (1985,1992) described the geology and hydrology of the field, and used drillhole data to determine the presence of blocks of Mamaku Ignimbrite which were progressively downfaulted from outcrop at the southern caldera rim, northwards towards the lake where they are concealed beneath lacustrine sediments and younger tephras.

In this paper the structure of Rotorua Caldera is studied. The caldera does not conform to simple end-member structures of current classification schemes and is described in terms of dominant composition, collapse geometry, structural make-up, and number of eruptive cycles involved in its formation. The characteristics of Mamaku Ignimbrite are introduced and are used to interpret caldera evolution.

Mamaku Ignimbrite

Outflow sheet

The Mamaku Ignimbrite is exposed around Rotorua Caldera in an outflow sheet of ~225 km^3 (in situ volume), dominantly in a 3100 km^2 fan extending north and west of the caldera (Fig. 3). Reconstruction of the original extents of the ignimbrite (following a method outlined by Streck and Grunder, 1995) indicates that it may have originally covered up to 3900 km^2 (283 km^3). The ignimbrite can be split into a basal tephra sequence and main ignimbrite sequence (Milner et al, submitted; Fig. 4). The main ignimbrite sequence can be divided into lower, middle and upper facies (Fig. 4), based on variations of welding, jointing, crystal content, lithic content, devitrification and vapour phase alteration.

The basal tephra sequence is a layered deposit up to 2.5 m thick that comprises up to 14 pyroclastic fall and density current beds (units a-n; Fig. 4). The lowest units (a-c) are fine grained, contain aggregates of fine ash, accretionary lapilli and considered phreatomagmatic. Units d-n contain charcoal fragments and no accretionary lapilli suggesting that the eruption had become dry. Grain size in units d-n is variable with up to 16 mm pumice, and small lithic lapilli (up to 5 mm) in a fine to coarse ash matrix. Units d-n contain occasional elutriation structures (usually surrounding charcoal fragments) and lenses of pumice concentration (up to 20 vol% pumice clasts), often have irregular boundaries and pinch and swell suggesting deposition by pyroclastic density current. Boundaries between the basal tephra sequence beds are sharp, but time breaks appear to be limited and the sequence represents the early phases of the Mamaku Ignimbrite eruption. Irregular boundaries between beds are thought to represent phases in which pyroclastic density currents were erosive, stripping earlier deposited material. Grainsize analysis, following methods outlined in Walker (1971), were carried out on beds a and m. Bed a has Md_ϕ= 1.3 and σ_ϕ= 1.3 consistent with airfall origin (Fig. 5). Bed m has Md_ϕ= 2 and σ_ϕ= 1.85 in the region of overlap between pyroclastic flow and fall on the Md_ϕ vs σ_ϕ plot (Fig. 5)

The main ignimbrite sequence is predominantly massive and contains no definable flow unit boundaries. Vertical changes in the sizes and contents of pumice and lithic clasts impart crude layering in places and are all gradational with the surrounding ignimbrite. Boundaries between lower and middle, and middle and upper Mamaku Ignimbrite are also gradational over 1-2 m and approximately 10 m respectively. The lower (lMI) to middle Mamaku Ignimbrite (mMI) is signified by an increase in welding and crystal content. Welding decreases and devitrification increases with height above the zone of maximum welding in mMI and uMI is represented by ignimbrite in which the glass shards and pumice fragments have become totally devitrified.

lMI is pale brown-yellow to white-grey, non-welded, non-jointed, mostly massive, poorly sorted, pumice-bearing (usually 7-10 vol%, but up to 20 vol% in lenses), lithic-poor (<1 vol%), crystal-bearing (7-10 vol%) ignimbrite with fine to coarse ash matrix. Grain size analysis was carried out following Walker (1971) and Md_ϕ found to vary between 1.1 and 3.3, and σ_ϕ to vary between 1.8 and 3.7. Glass shards in the ash matrix are cuspate, undeformed, vitric and unaltered. Maximum pumice diameter is 230 mm,

and pumice clast concentration reaches up to 15-20 vol% reflecting variations in density current energy (Fig. 4). Very rare lithic fragments are dominantly rhyolite lava.

mMI is light-brown to dark-grey, jointed, and very strongly welded. The crystal content is 17-26 vol% (the high crystal content relative to lMI is most likely due to loss of pore space during welding and compaction), fiamme 5-10 vol%, and lithic fragments 0-4 vol% (predominantly rhyolite lava up to 10 mm across; Fig. 4). Pumice clasts are all flattened (becoming fiamme up to 50 mm long), as are glass shards imparting a eutaxitic texture. The greater lithic content relative to lMI is believed to be original, not an artefact of welding. Fiamme long axes are all oriented sub-horizontally suggesting that welding in the outflow occurred predominantly by compaction. Some welding must have occurred immediately after deposition within the source area, however, as mMI fragments are the dominant lithic type in uMI. Grain size analysis of mMI could not be carried out due to the welded nature of the rock.

uMI is distinguished from mMI by its totally devitrified pumice, and is typified by the presence of andesitic juvenile fragments and clasts of mMI. The uMI matrix is grey, pink, red, or purple (due to vapour phase activity), non- to moderately welded, non-jointed, friable, fine to coarse ash. Crystal content varies between 10-15 vol%, lithic content 0-5 vol% (M_L=8 mm in medial exposures), and pumice clasts 10-20 vol% (up to 220 mm; Fig. 4). Glass in uMI has broken down into aggregates of feldspar and silica polymorphs (cristobalite and tridymite). Pumice clasts now comprise microspherulitic crystal aggregates and only relic structures of glass shards are present. The extremely friable nature of the altered pumice and glass shards obviates grain size analysis. Lithic fragments in uMI are dominantly pieces of mMI.

Lithic lag breccias and areas of high lithic concentration are present in the top of uMI at localities at, and within, the caldera margin. Exposures of lithic lag breccias are poor limited by forest cover to an area at the southern caldera margin, and a southeastern intracaldera locality (Fig. 6). The maximum thickness measured was only 1 m. Breccia clasts comprise 48.5 vol% rhyolite lava, 46 vol% mMI, 3.8 vol% older ignimbrites, and 1.7 vol% plutonic clasts (granite, diorite and very rare gabbro) and maximum clast size varies between 235 and 297 mm. uMI grades into breccias over approximately 100 mm into breccias comprising 80-90 vol% lithic fragments set in the same, pink, fine to coarse ash matrix as the uMI itself. Powdery, devitrified pumice of uMI type are also

found within the breccias. The similar matrix, pumice appearance, and gradational contact indicate the breccias are part of uMI, not some later unit.

Juvenile clasts in the Mamaku Ignimbrite comprise three consanguineous dacite-rhyolite pumice types and andesitic fragments described petrographically in Milner et al. (submitted). Pumice clasts range from dacite (66.0-69.7 wt% SiO_2; type 3) to rhyolite (type 2, 70.2-74.1 wt% SiO_2; type 1, 71.9-76.0 wt% SiO_2) and can be clearly distinguished by their Rb/Sr ratios (Fig. 7). Intrusion of the silicic chamber by the andesitic magma in a vigorous manner would have produced a mixed or hybrid layer (e.g. Blake et al., 1992). No mixed or hybrid silicic/andesite fragments have been found and the andesite is interpreted to have entered the silicic chamber in a non-vigorous manner accumulating as a sill-like layer beneath type 3 magma.

In the basal tephra sequence only the most siliceous evolved pumice type is present. In the main ignimbrite sequence all pumice types occur together at all stratigraphic levels due to simultaneous eruption. Andesitic fragments occur only in uMI.

The average size of vent-derived lithics in an ignimbrite is a useful method for identifying its immediate source (e.g. Wright and Walker, 1977; Walker, 1985). A contoured map of maximum lithic data (average of the 5 largest clasts at a given locality) and a graph of maximum lithic size vs distance from Rotorua Caldera indicates that Rotorua Caldera was the only source of the uMI (Fig. 8). Presence of the same pumice types throughout the main ignimbrite sequence, and gradational contacts between the stratigraphic parts suggest that all of the main ignimbrite sequence had the same source.

The stratigraphy of the Mamaku Ignimbrite reflects changes in the eruption dynamics and evolution of Rotorua Caldera. It is used to help interpret the timing of caldera collapse in a later section.

Intracaldera

Only the upper part of Mamaku Ignimbrite is exposed inside the caldera, towards its northwestern and eastern margins, otherwise intracaldera ignimbrite is not exposed. In the eastern Rotorua City area intracaldera Mamaku Ignimbrite is >120 m thick in a drill

hole (Wood, 1992), and 280 m is interpreted from a seismic reflection profile (Lamarche, 1992), 0.5 km and 1 km north of the southern caldera boundary respectively. Gravity data (Rogan, 1982) suggests there may be >1 km thickness of deposits (probably Mamaku Ignimbrite) filling the caldera.

Structure of Rotorua Caldera

Rotorua Caldera has an irregular shape, and the limit of deformation caused by collapse of the caldera is 21×22 km (Figs. 6 and 9). Its geometry can be defined by two ellipses creating a fault-controlled structural boundary of 21×20 km. One ellipse has a long axis oriented NE-SW and the second NW-SE running through an embayment in the NW caldera margin (Fig. 9). The margin is breached on the NE side by the Tikitere Graben (Fig. 6 and 9).

Downsag

The embayment in the NW is considered to be the result of asymmetric basement collapse above which Mamaku Ignimbrite deformed by downsag. The Mamaku Ignimbrite surface is tilted back (slope angle is ≤2°; Fig. 6) towards the caldera in the embayment which is interpreted to have formed during caldera collapse while the ignimbrite was still hot. The embayment is oriented orthogonally to the main axis of the caldera and the northeastern and southwestern margins are thought to reflect underlying NW-SE striking faults.

Residual mounds occur over much of the proximal-medial surface of the ignimbrite, and linear ridges and aligned mounds are present just inside the northwest caldera margin. Outside the caldera these mounds are approximately circular, up to 20 m high, vary between 25 and 60 m diameter and are composed of erosionally resistant ignimbrite cemented by minerals such as tridymite, cristobalite and alkali feldspar, which were deposited from ascending fumarolic gases after deposition. The ridges towards the northwest caldera margin are up to 20 m high, 20 to 30 m wide and up to 1.5 km long (Figs. 10 and 11). Aligned mounds are also up to 20 m high, and 20 to 30 m wide and they form discontinuous lines up to 900 m long. The depth that these fumarolic structures emanate from is unknown, but eroded stream channels up to 60 m deep deviate around them. The mounds and ridges usually have fumarolic conduits towards their centres (Fig. 11) surrounding which are various multi-coloured zones due to the minerals precipitated (hematite and magnetite have been identified in the ignimbrite

surrounding the fumarolic conduits). It is thought that the fumarolic ridges formed in response to downsagging of the hot Mamaku Ignimbrite during formation of Rotorua Caldera. Linear weakened zones or tension fractures caused by downsagging would have provided preferential pathways for fumarolic gases, giving rise to elongate rather than columnar cementation zones in the ignimbrite. Subsequent erosion left the harder cemented ignimbrite as upstanding ridges (Fig. 4) similar to those described by Sheridan (1970) in the Bishop Tuff.

Many of these fumarolic structures propagate from a curvilinear scarp that is traceable for 5.5 km (Fig. 6 and 10). The scarp has been interpreted as the headwall of a slump that had limited downslope movement and formed in response to extension associated with downsag. Some shorter structures apparent beyond this scarp may represent slump headwalls and linear fumarolic structures at earlier stages of development.

A tension fracture has been identified close to the eastern caldera margin. The fracture comprises a flat area between two ridges that is approximately 50 m, wide tapering towards its northern and southern ends (Figs. 6 and 9). Toward the northern end the fracture is 15 m wide, and filled with bedded, coarse sandy sediment. The bottom of the fracture is not exposed. The surface of Mamaku Ignimbrite is at the same elevation on either side of the crack and the fracture is interpreted as a pull-apart structure formed by downsag during caldera formation.

Southeast of Pukehangi dome the Mamaku Ignimbrite surface slopes towards the caldera reminiscent of downsag.

Faulting

Pronounced scarps at the southern, southwestern, and northern margins of the caldera, and are accentuated where they cut pre-caldera rhyolite domes (Fig. 6 and 9). Scarps are also represented where Mamaku Ignimbrite rises steeply from lake sediments in the south and southeast of the caldera. Collapse here does not appear to have occurred on a single fault, but by collapse down adjacent faults with overlapping extents. Scarps are likely to have been accentuated by avalanching of the sides as support was removed during caldera formation.

The scarp in the north strikes approximately east-west, truncates, and runs between two pre-caldera rhyolite domes (Hamarana and Fryer domes). Between the two domes Mamaku Ignimbrite is exposed discontinuously for 4.5 km. The visible maximum scarp height is 100 m below which it is covered by lake sediment and a younger ignimbrite from the Okataina Volcanic Centre.

No single fault can be traced for any great distance around the southwestern and southern caldera margins. South of the embayment Endean dome is cut by a fault (Fig. 9). Mamaku Ignimbrite that must have been depositing as the caldera formed surrounds the dome. Between Endean and Pukehangi domes Mamaku Ignimbrite forms prominent bluffs that are thought to be a fault scarp.

South of Pukehangi dome a number of faults have been inferred from aerial photography and outcrop distribution of Mamaku Ignimbrite. Mamaku Ignimbrite is juxtaposed lake sediments similar to the ignimbrite at the mouth of the embayment and the boundary likewise been interpreted as a fault. This fault is buried by Pukehangi dome and may join up with that seen west of the dome. Two stream gullies (one is a tributary to Aorangi Stream and the other is close by to the east) are aligned both deviating from azimuths perpendicular to the caldera margin becoming parallel to it. They have eroded through Mamaku Ignimbrite exposing the underlying Pokai Ignimbrite, and possibly deviate in response to the presence of a fault or tension fracture.

Buried blocks of rhyolite lava encountered in drill holes just inside the southern caldera margin (Wood, unpublished data) probably represent landslide debris from the pre-caldera Pohaturoa lavas.

More than 950 wells have been drilled in Rotorua for geothermal water supply, but only 20% have geological records, and of these only 23 penetrated into the Mamaku Ignimbrite (Wood, 1985, 1992). From drillhole stratigraphy, Wood (1985, 1992) postulated an inner caldera boundary fault which displaces the Mamaku Ignimbrite down towards the caldera centre by some 50 m, marks the southern boundary of the buried rhyolite and is just outside the -480 mgal contour (Fig. 6). Wood (1992) also postulated the presence of other step faults that drop the upper surface of the Mamaku Ignimbrite towards the gravity low.

Geophysical evidence

There has been a reluctance by geophysicists to accept the Rotorua basin as a volcanic collapse structure because it does not present the simple gravity anomaly of a circular hole filled with low-density deposits. Macdonald (1974) stated that "the geophysical evidence does not support the caldera hypothesis", a conclusion supported by Hunt (1992). Nonetheless, the gravity data are consistent with a more complex collapse hypothesis.

Rogan (1982) modelled gravity and magnetic data for Rotorua as part of a geophysical study of TVZ. Gravity stations and aeromagnetic flight lines, data and interpretations are shown in Figure 11. The basement was assumed to be Mesozoic greywacke, which outcrops on either side of the TVZ.

To interpret gravity Rogan (1982) used average densities of 2670 kg/m^3 for greywacke, and 2180 kg/m^3 for cover rocks (sediment, rhyolite, rhyolite tephras and ignimbrites) in the depth to basement calculations, and the density contrast rounded to 500 kg/m^3. A regional field was subtracted from the bouguer anomalies to remove the effect of the subducting slab. The regional field was defined where greywacke outcropped either side of the TVZ. Greywacke in areas outside TVZ was assumed to be continuous throughout the upper crust, and any anomalies inside the TVZ assumed therefore to be caused by accumulations of low density material. A three dimensional model was constructed using an inversion technique outlined by Woodward (1975) based on the gravity anomaly of a vertical triangular prism. Iterative inversion of the residual gravity anomalies was used to estimate the depths of the lower vertices of the prism.

Rogan's (1982) magnetic data was obtained aerially as a series of east-west flight lines 1.5 km above sea level separated by 3.6 km, and added to data already in existence. For modelling, mean magnetisations of 2.5 A/m were used for rhyolite lavas, and 0.3 A/m for pyroclastics and tuff breccias (magnetisation of the greywackes was negligible). The regional magnetic field was subtracted, and a correction of −100 nT added to the regional field so that the residual anomalies over magnetically undisturbed regions outside the TVZ were zero. A pseudogravity low pass filter of Baranov (1957) was applied to the data. The resulting magnetic anomalies thought to be equivalent to the gravity anomaly if the source rocks possessed a density contrast that is proportional to

magnetisation. Depths to basement were modelled in the same way as gravity, but carried out on pseudogravity.

Rogan's residual gravity data revealed two areas of low gravity generating an anomaly oriented north-south in a larger NNW-SSE trending low (Fig. 12 **A** and **B**). Modelling the gravity data Rogan (1982) found that the deepest basement (lowest gravity anomaly) occurs along the southwest side of Lake Rotorua in the southwestern part of the caldera, reaching 2500 m below sea level (Fig. 6a), some 1500 m lower than much of the surrounding basement. Her models produced from magnetic data show a maximum depth to basement of between 1000 and 1500 m. From the disparity between the two techniques Rogan (1982) suggested the presence of non- or reversely magnetised material at least 1 km thick. The Mamaku Ignimbrite has since been shown to have erupted during a magnetic excursion (Pringle Falls event) in which the North Pole was situated in an equatorial Atlantic position (Black et al., 1996; Tanaka et al., 1996). The intermediate magnetic direction of the Mamaku Ignimbrite probably masked the magnetic response of Rotorua Caldera measured by Rogan (1982) leading to the disparity of the basement depth calculations.

Hunt (1992) carried out a gravity survey with much closer station spacings and identified three gravity-low anomalies (Fig. 13) in close proximity to the deepest gravity anomaly of Rogan (1982). He modelled the data using mean wet densities of rhyolite lava (2150 ± 180 kg/m^3), sediment (1450 ± 90 kg/m^3 at the surface and 1830 ± 260 kg/m3 at depth) and Mamaku Ignimbrite (1700 ± 40 kg/m^3).

Hunt's (1992) residual bouguer maps show three adjacent areas of low gravity west and southwest of the lake suggesting an area of the caldera that has subsided to approximately the same level (Fig. 12). Two of these areas are close to those found by Rogan (1982) who used much wider station spacing. Cross sections through the gravity map indicate the asymmetric nature of the collapse structure (Fig. 12B). Hunt constructed 2½ dimensional models based on density contrasts relative to rhyolite lava adjusting them until their calculated response correlated well with that measured (Fig. 12C). In constructing the models a small regional gradient of 3 μm.kg^{-1}.km^{-1} was removed so that the anomalies near rhyolite outcrops was zero and the assumption made that the models extended 1 km north and 3 km south of the profile line. He found that numerous models could be constructed that could generate the gravity response seen but

that: 1) at least 1 km of low density material (probably mainly sediments) underlies the southernmost anomaly, 2) the edges of the rhyolite bodies are steep, 3) low density material such as sediment is thin or absent beneath the Mamaku Ignimbrite on the eastern side of Rotorua City, 4) it is not possible to determine from the gravity data whether Mamaku Ignimbrite occurs beneath the western part of the Rotorua City, but if it occurs at shallow depth (<1 km) it is likely to be underlain by low density material.

Both Rogan's and Hunt's data show a gravity anomaly that is elongate north-south and both models suggest the presence of low density material greater than 1 km thick beneath the low gravity anomaly. It is impossible to tell what this material is without a deep drillhole, but the discrepancy between the magnetic and gravity responses of Rogan (1982) suggests that it is probably Mamaku Ignimbrite. Both maps also show that the lowest gravity readings are closer to the southern and southwestern margin than to the northeast and north illustrating the caldera's asymmetric nature. Hunt's gravity sections through the caldera also indicate the asymmetry of the collapse structure.

Variations in gravity readings also suggest trapdoor-like collapse but with two areas of asymmetric subsidence one shallower towards the northwest caldera margin and a less obvious area shallower towards the northeast. Gravity readings increase at a lesser rate (albeit slightly) towards the northwest and northeast than they do towards the southeast or southwest indicating asymmetric subsidence.

Post-collapse volcanism

Effusive volcanism is often associated with calderas after their formation (e.g. Smith and Bailey, 1968; Lipman, 1984) and post-collapse rhyolite domes often extrude close to or above caldera-forming faults which are used as conduits for the ascending magma (e.g. Self et al., 1986; Lipman, 1984). Post-caldera rhyolite domes at Rotorua can be separated into three groups based on phenocryst content and assemblage. The rhyolite domes of Mokoia Island and Hinemoa Point have phenocryst populations and whole rock chemistries that are unlike Mamaku Ignimbrite pumice clasts and are not thought to be petrogenetically related. The phenocryst assemblage and whole rock and phenocryst chemistries of the lavas that surround the area of lowest gravity (-480 mgal) are similar to those of the silicic Mamaku Ignimbrite pumice and they are thought to have erupted from the same magma chamber.

The elongate morphology of the dome complexes (Fig. 6) around the --480 mgal gravity low suggests they were erupted from fault fissures (e.g. Richnow, 1999). We interpret those faults to bound the most deeply subsided blocks (block bounding caldera faults).

The convergence of the maximum lithic size isopleths on the area surrounded by the post-collapse domes and the --480 mgal gravity low also suggests that this area was the main site of eruption.

Timing of caldera formation

Interpretation of the sequence of formation of Rotorua Caldera needs to account for:

1) Presence of only type 1 pumice clasts in the basal tephras.
2) Coexistence of all pumice types throughout the main ignimbrite sequence.
3) Presence of andesitic fragments only in uMI.
4) Intra- and extracaldera thickness variations of Mamaku Ignimbrite.
5) Lithic lag breccias at he top of the ignimbrite
6) Stratigraphic variation within the extracaldera Mamaku Ignimbrite.

Only type 1 magma is present in the basal tephras whereas all pumice types occur together throughout the main ignimbrite sequence. To explain this, we propose that the opening phase of the eruption tapped only the most evolved magma in the top of the chamber possibly through a single vent. From then on coexistence of all silicic pumice types throughout the main ignimbrite sequence implies a huge increase in magma discharge rate. This phase of the eruption is interpreted as coincident with the onset of caldera collapse and the consequent generation of multiple which allowed access to different levels of the magma chamber (e.g. Blake, 1981).

Andesite fragments are found only in uMI and are thought to represent a sill-like body that accumulated at the base of the reservoir beneath the type 3 magma. Following Blake and Ivey (1986a and b) the density and inertia disparities between the silicic and andestic magmas would have impeded the withdrawal of the latter until the later stages when caldera collapse and high extraction rates allowed the denser andesite to discharge.

Just outside the caldera rim to the south, Mamaku Ignimbrite is approximately 40 m thick whereas to the north, extracaldera ignimbrite is up to 145 m thick (Nathan, 1976). Inside the caldera the ignimbrite is at least 280 m thick (Lamarche, 1992), and intracaldera deposits of unknown lithology (probably Mamaku Ignimbrite) may be >1 km thick (Rogan, 1982). If all the caldera collapse had occurred only at a late stage in the eruption the difference in thickness between outflow and intracaldera ignimbrite would not have been so great, and intracaldera ignimbrite would have been buried at great depth beneath post-eruption infill. Therefore, collapse must have occurred or been occurring at an earlier stage in the eruption to allow ponding of Mamaku Ignimbrite inside the caldera.

Lithic breccias in an ignimbrite are often interpreted to represent increases in magma discharge rate coincident with caldera collapse (e.g. Walker, 1985; Nairn et al., 1994). The location of the breccias at the top of the ignimbrite suggests a component of collapse occurred during late stages of the eruption.

Stratigraphy of the extracaldera ignimbrite also gives insights into the timing of caldera collapse (Fig. 4). The transition from deposition of the basal tephras to the main ignimbrite sequence indicates a dramatic increase in mass eruption rate that is probably associated with the initiation of caldera collapse. This is coincident with transition from extraction of one silicic magma type to the extraction of all three. Few lithic clasts occur in lMI, so the increase in lithic clast abundance seen in the medial mMI suggests a change in eruptive behaviour possibly coincident with an increasing rate of caldera collapse as the eruption passed its opening phases. Proximal mMI is not exposed so it is not known if lag breccias were deposited at this time. The welding of mMI may also be explained by an increase in the rate of collapse with the associated increase in mass eruption rate leading to high aggradation rates thereby allowing greater heat retention and promoting welding.

Formation of the caldera is thought to have been taking place at least by the time that the mMI was erupted. It is postulated that collapse of the caldera was happening throughout the eruption of Mamaku Ignimbrite, but at different rates, accelerating during the eruption's closing stages and possibly during the eruption of mMI. Collapse occurring throughout the eruption allows the intracaldera (280 to >1 km) and

extracaldera (40 to 145 m) thickness variation and coexistence of all the silicic pumice types at different stratigraphic levels in the ignimbrite, while collapse at different rates is represented by variation in lithic concentration in Mamaku Ignimbrite.

Discussion

Satellite imagery (Fig. 9) the caldera shows an NE-SW elongate structure with an embayment in the northwestern margin. Rotorua is one of only two calderas in TVZ that formed during single eruptive episodes. It occurs within a zone of active extension, which imparts a structural grain to the TVZ in which faults preferentially strike NE-SW (Fig. 2). A second, subsidiary, fault pattern strikes NW-SE. At Rotorua, the orthogonal fault sets allowed the caldera floor to break into a mosaic of blocks that subsided by increasing amounts towards a single collapse locus (Fig. 14). The location of Rotorua Caldera at the edge of the main zone of regional TVZ (Fig. 2) extension may have allowed the NW-SE striking fault set to have a greater influence on its collapse geometry than at other TVZ calderas. The embayment in the northwest is thought to reflect this influence as it is oriented orthogonally to the main structure.

For ≥4 km vertical thickness of rock to deform by pure downsag requires either an enormous amount either extension at the surface, or disintegration and removal of rock at depth, or widespread bed-over-bed sliding (Branney and Kokelaar, 1994). Roche et al. (2000) show in their analogue models that a tilted annular block surrounds the main subsiding block of a caldera. Near the surface the faults bounding the subsiding central block dip outward and are reverse, whereas faults in the tilted block are normal. The tilted block provides an explanation for an area of downsag surrounding a collapsing block. Another potential method to produce downsag subsidence is the creation of drape folds by forced folding. The generation of such drape folds requires a rigid basement over which there is a cover sequence of sub-horizontal or predominantly layered rocks; the shape and trend of the fold is governed by some forcing member below (Stearns, 1978; Fig. 15). Passive bending of the cover rocks cannot be accomplished by a mechanism that can maintain a balanced cross section, rather the cover accommodates itself to the basement by rigid-body rotation and internal deformation, i.e. either extension by faulting must take place, or the cover detaches from the basement in a triangular zone at the base of the fault scarp, creating a void that must be filled by fractured cover or basement rocks (Fig. 15; Cosgrove and Ameen, 2000). The amount of cohesion between the basement and cover layers will determine

the details of detachment, location of extensional faulting and response to the footwall space problem. Lines across which extension occurs strike parallel to the underlying fault (Cosgrove and Ameen, 2000) with the greatest concentration of faults occurring towards the site of maximum fold curvature (Lisle, 1994).

If the basement rocks beneath the TVZ volcano-sedimentary sequence are Mesozoic greywackes and argillites, as has been shown in a number of TVZ geothermal fields (Wood and Braithwaite, 1999), they are likely to be complexly folded, further impeding downsag deformation (Mesozoic greywackes in New Zealand have been interpreted as material of an accretionary prism (Mortimer, 1994 and others) and where observed at the surface are complexly folded). It would be especially difficult to deform such rocks by downsag over the short time it takes a caldera to form. Basement rocks are much more likely to fail brittly under such conditions, and in Fig. 14 they have been broken up using normal dip-slip faults. In contrast to greywacke, it would be comparatively easy to deform ignimbrite sheets within the TVZ sequence above the basement, because they are thinner, less competent, and are generally flat-lying. However, indurated and possibly welded ignimbrites would bend only slightly before brittle failure would occur, and the effects of downsag are best seen in the Mamaku Ignimbrite itself. Even so, some deformation would be accommodated by cracking and faulting to produce the extensional features noted in the ignimbrite at the hinge region of the downsag (zone of maximum curvature above the rigid fault block). These features are exposed as the fumarolic ridges towards the northwest caldera margin and tension fracture in the east. Trapdoor collapse also requires brittle failure of the basement at all margins of the subsiding block. If the block subsides to a greater degree at one end than the other (i.e. asymmetrically) a trapdoor-like morphology is imparted to the caldera. The ignimbrite at the surface will deform across the asymmetric structure by downsagging. Extensional structures should be seen, in the erupted ignimbrite or surface rocks, where the subsidence is hinged. At Rotorua these structures are present in the northwest, but in the northeast have been buried by subsequent activity of Okataina Volcanic Centre and destroyed by fault movement in Tikitere Graben (Fig. 4).

Analogue models indicate that reverse faults should dominate at the margins of the collapsing block, during caldera collapse, outside of which normal faults develop (Branney,1995; Acocella et al., 2000; Roche et al., 2000). Normal and reverse faults have been described in the field e.g. Grizzly Peak (normal faults; Fridrich et al., 1991)

and Rabaul (reverse faults; Mori and McKee, 1987). It is assumed that normal faulting was the mode at Rotorua caldera (and indeed at other TVZ calderas) and that subsidence took place along pre-existing structures. We believe this to be the case because the TVZ is under active extensional stress, and faulting is exclusively normal, whereas analogue models are carried out under conditions with no acting external forces that would serve to complicate collapse mechanisms and with no pre-existing structures that would act as preferential surfaces for movement.

Rotorua Caldera cannot be attributed to any one collapse type. Subsidence is interpreted from gravity data to have taken place in an asymmetric manner, deeper in the southwest, shallowing towards the northnorthwest and northeast, and is interpreted to have involved numerous fault-bound blocks, the size of which was governed by proximity to the area of maximum subsidence and spacing of pre-existing faults. The three gravity lows depict an area of the caldera that has subsided to more or less the same level (piston-like) although morphology of the surrounding dome complexes suggests that this collapse cannot be assigned to a single ring fault. Features consistent with downsag have been interpreted towards the northwest and east caldera margins. The embayment in the northwest is oriented orthogonally to the dominant fault pattern, suggesting control by concealed NW-SE faults. The block diagrams of Rotorua Caldera (Fig. 14) show brittle failure of the underlying basement rocks and older ignimbrites with thickening of Mamaku Ignimbrite (from 145 m to possibly >1 km) into the space created. Newly deposited Mamaku Ignimbrite would have been less consolidated than underlying rocks and able to warp more easily, so the ignimbrite has been treated as a separate entity from the underlying rocks. It is hard to deform a thick mass of rock above a magma chamber by downsag alone, especially when it is consolidated. The subsidence is inferred to have taken place on numerous faults rather than a single ring fault. A single ring fault with appreciable throw would generate a geophysical anomaly that was more obvious and concentric with the caldera margin (e.g. Toba Caldera, Nishimura et al., 1984). A step-faulted caldera would not generate simple, sharp concentric gravity patterns (e.g. Guayabo Caldera, Halinan, 1993). Rotorua Caldera does not have the sharp concentric gravity pattern observed at many calderas and as such has here been broken up by many faults which progressively step down towards the area of the lowest gravity anomaly.

Rotorua Caldera exemplifies a situation where regional fault structure and magma chamber evacuation have interacted to generate a caldera with a morphology that cannot be attributed to any single collapse style. The caldera has characteristics that can be attributed to downsag, trapdoor, and piecemeal collapse styles. Such terms give general ideas about a caldera's morphology, but are too restrictive when describing the overall structure. The combination of numerous blocks all with varying displacements makes Rotorua Caldera piecemeal by Branney and Kokelaar's (1994) definition, but piecemeal does not describe the collapse style well. Collapse of the different blocks appears to have occurred away from an area of maximum downthrow, with displacements that are progressively less (not chaotic; similar to Guayabo described by Halinan, 1993). A better description of Rotorua Caldera is as a rhyolitic, single event, asymmetric, multiple-block, single collapse locus caldera. Such a description provides information on the collapse history of the caldera as well as indicating aspects about its overall geometry, morphology, and dominant eruption composition.

Acknowledgements

We thank Hamish Kellahan for reviewing early versions of the manuscript and Dr Steve Beresford for helpful comments and criticisms. Reviews by J. Stix, T.H. Druitt, and an anonymous reviewer greatly improved the paper. Thanks also go to Karl Spinks, discussion with whom gave rise to many ideas outlined. DMM was funded by a University of Canterbury doctoral scholarship, with field expenses partly provided for by the Mason Trust, Department of Geological Sciences, University of Canterbury; both are gratefully acknowledged. A Claude McCarthy fellowship enabled participation of the CEV workshop "Inside Silicic Calderas: Interactions of caldera development, tectonism and hydrovolcanism" and is also gratefully acknowledged. CPW was partly funded by Foundation for Research, Science and Technology programme "Geological Hazards and their Mitigation", contract C050006

References

Acocella V, Cifelli F, Funiciello R (2000) Analogue models of collapse calderas and resurgent domes. J Volcanol Geotherm Res 104: 81-96

Baranov V (1957) A new method for intepretation of aeromagnetic anomalies. Geophys 22: 359-383

Bayrantes LF (1984) Structural aspects of the southern margin of the Rotorua Caldera and their implications to the Rotorua geothermal field, North Island, New Zealand. Project for Diploma in Energy Technology (Geothermal). Geothermal Institute, University of Auckland 79p

Beresford SW, Cole JW (2000) Kaingaroa Iginimbrite, Taupo Volcanic Zone, New Zealand: Evidence for asymmetric collapse of the Reporoa Caldera. N Z J Geol Geophys 43: p471-481

Bellamy S (1991) Some studies of the Te Wairoa Ignimbrites and associated volcanic-geology of the southwestern Okataina Volcanic Centre. MSc, University of Waikato, Hamilton

Berryman K, Beanland S, Wesnousky S (1998) Paleoseismicity of the Rotoitipakau Fault Zone, a complex normal fault in the Taupo Volcanic Zone, New Zealand. N Z J Geol Geophys 41: 449-465

Black TM, Shane PAR, Westgate JA, Froggatt PC (1996) Chronology and palaeomagnetic constraints on widespread welded ignimbrites of the Taupo volcanic zone, New Zealand. Bull Volcanol 58: 226-238

Blake S (1981) Eruptions from zoned magma chambers. J Geol Soc London 138: 281-287

Blake S, Ivey GN (1986a) Magma-Mixing and the dynamics of withdrawal from stratified reservoirs. J Volcanol Geotherm Res 27: 153-178

Blake S, Ivey GN (1986b) Density and viscosity gradients in zoned magma chambers, and their influence on withdrawal dynamics. J Volcanol Geotherm Res 30: 201-230

Blake S, Wilson CJN, Smith IEM, Walker GPL (1992) Petrology and dynamics of the Waimihia mixed magma eruption, Taupo volcano, New Zealand. J Geol Soc London 149: 193-207

Branney MJ (1995) Downsag and extension at calderas: new perspectives on collapse geometries from ice-melt, mining, and volcanic subsidence. Bull Volcanol 57: 303-318

Branney MJ, Kokelaar BP (1994) Volcanotectonic faulting, soft state deformation, and rheomorphism of tuffs during development of a piecemeal caldera, English Lake District. Geol Soc of Am Bull 106: 507-530

Cole JW (1990) Structural control and origin of volcanism in the Taupo volcanic zone, New Zealand. Bull Volcanol 52: 445-459

Cole JW, Brown SJA, Burt RM, Beresford SW, Wilson CJN (1998) Lithic types in ignimbrites as a guide to the evolution of a caldera complex, Taupo volcanic centre, New Zealand. J Volcanol Geotherm Res 80: 217-237.

Cosgrove JW, Ameen MS (2000) A comparison of the geometry, spatial organization and fracture patterns associated with forced folds and buckle folds. In: Cosgrove JW Ameen MS (eds) Forced Folds and Fractures. Geol Soc London Spec Publ 169: 7-21.

Crook CN, Hannah J (1988) Regional horizontal deformation associated with the March 2, 1987, Edgecumbe earthquake, New Zealand. Geophys Res Lett 14: 361-364

Crosby N (1998) Quaternary geology and tephrostratigraphy of the north-north-eastern Rotorua region. MSc, University of Waikato, Hamilton

Darby DJ, Hodgkinson KM, Blick GM (2000) Geodetic measurement of deformation in the Taupo Volcanic Zone, New Zealand: the north Taupo network revisited. N Z J Geol Geophys 43: 157-170

Davy B (1992) Seismic reflection profiling on southern Lake Rotorua- evidence for gas charged lake floor sediments. Geothermics 21: 97- 108

Fridrich CJ, Smith RP, DeWitt E, McKee EH (1991) Structural, eruptive and intrusive evolution of the Grizzly Peak caldera, Sawatch Range, Colorado. Geol Soc Am Bull 103: p1160-1177

Halinan S (1993) Non-chaotic collapse at funnel calderas: Gravity study of the ring fractures at Guayabo Caldera, Costa Rica. Geology 21: 367-370.

Healy J, Schofield JC, Thompson BN (1964) Geological Map of New Zealand, Sheet 5, Rotorua. Department of Scientific and Industrial Research, New Zealand.

Houghton BF, Wilson CJN, McWilliams MO, Lanphere MA, Weaver SD, Briggs RM Pringle MS (1995) Chronology and Dynamics of a large silicic magmatic system: Central Taupo Volcanic Zone, New Zealand. Geology 23: 13-16

Hunt TM (1992) Gravity studies in the Rotorua area, New Zealand. Geothermics 21: 65-74

Kokelaar BP, Branney MJ (1999) Inside Calderas: Interactions of caldera development, tectonism and hydrovolcanism. IAVCEI CEV/IUGG Field Workshop, July 7-18, 1999 guidebook, pp. 1-142

Komuro H (1987) Experiments on cauldron formation: a polygonal cauldron and ring fractures. J Volcanol Geotherm Res 31: 139-149

Komuro H, Fujita Y, Kodama K (1984) Numerical and experimental models on the formation mechanism of collapse basins during the Green Tuff orogenesis of Japan. Bull Volcanol 47: 649-666

Lamarche G (1992) Seismic reflection survey in the geothermal field of the Rotorua Caldera, New Zealand. Geothermics 21: 109-120

Lipman PW (1984) The roots of ash flow calderas in western North America: windows into the tops of granitic batholiths. J Geophys Res 89B: 8801-8841

Lipman PW (1997) Subsidence of ash-flow calderas: Relation to caldera size, and magma chamber geometry. Bull Volcanol 59: 198-218

Lipman PW (2000) Calderas. In: Sigurdsson H (ed-in-chief), Encyclopedia of Volcanoes. Academic Press, Boston London New York San Diego San Francisco Sydney, pp 643-662.

Lisle RJ (1994) Detection of zones of abnormal strains in structures using Gaussian curvature analysis. Am Assoc Pet Geol Bull 78: 1811-1819.

Lloyd EF (1975) Geology of Whakarewarewa hot springs. Dep Sci Ind Res Info Ser 111: pp 1-24

Macdonald WJP (1974) Geophysical Investigation of the Rotorua Geothermal District. In: Geothermal Resources Survey: Rotorua Geothermal District. Dep Sci Ind Res Geotherm Rep 6: 53-77.

Marti J, Ablay GJ, Redshaw LT, Sparks RSJ (1994) Experimental studies of caldera collapse. J Geol Soc London 151: 919-929

Milner DM, Cole, JW, Wood CP (submitted) The internal stratigraphy and chemistry of the Mamaku Ignimbrite, Taupo Volcanic Zone, New Zealand. To be submitted to J Volcanol Geotherm Res

Moore I, Kokelaar P (1998) Tectonically controlled piecemeal caldera collapse: A case study of Glencoe volcano, Scotland. Geol Soc Am Bull 110: 1446-1466

Mori J, McKee C (1987) Outward-dipping ring-fault structure at Rabaul Caldera as shown by earthquake locations. Science 235: 193-195

Mortimer N (1994) Origin of the Torlesse Terrane and coeval rocks, North Island, New Zealand. Int Geol Rev 36: 891-910

Nairn IA, Wood CP Bailey RA (1994) The Reporoa Caldera, Taupo Volcanic Zone: source of the Kaingaroa Ignimbrites. Bull Volcanol 56: 529-537

Nappi G, Rezulli A, Santi P (1991) Evidence of incremental growth at Vulsinian calderas (central Italy). J Volcanol Geotherm Res: 47: 13-31

Nathan S (1976) Geology of the Rotorua district. In Nathan S (ed), Excursion Guide No. 55a and 56a, 25th International Geological Congress.

Nishimura S, Abe E, Nishida J, Yokoyama T, Dharma A, Hehanussa P, Hehuwat F (1984) A gravity and volcanostratigraphic interpretation of the Lake Toba region, North Sumatra, Indonesia.

Richnow J (1999) Eruptional and post-eruptional processes in rhyolite domes. PhD thesis, University of Canterbury, Christchurch, New Zealand.

Roche O, Druitt TH, Merle O (2000) Experimental study of caldera formation. J Geophys Res 105B: 395-416

Rogan AM (1982) A geophysical study of the Taupo Volcanic Zone, N Z J Geophys Res 87B: 4073-4088

Rowland JV, Sibson RH (in press) Extensional kinematics of the Ruaumoko Rift System: Variable soft-linkage between offset spreading segments in the Taupo Volcanic Zone, New Zealand. N Z J Geol Geophys.

Self S, Goff G, Gardner JN, Wright JV, Kite WM (1986) Explosive rhyolitic volcanism in the Jemez Mountains: Vent locations, caldera development and relation to regional structure. J Geophys Res 91B: 1779-1798.

Shane P, Black T, Westgate J (1994) Isothermal plateau fission track age for the paleomagnetic excursion in the Mamaku Ignimbrite, New Zealand, and implications for late Quaternary stratigraphy. Geophys Res Lett 21: 1695-1698

Sheridan MF (1970) Fumarolic mounds and ridges of the Bishop Tuff, California, Geol Soc Am Bull 81: 851-868

Sissons BA (1979) The horizontal kinematics of the North Island of New Zealand. PhD thesis, Victoria University of Wellington, Wellington

Smith RL, Bailey RA (1968) Resurgent cauldrons. In Coats RR, Hay RL and Anderson CA (eds) Studies in Volcanology: A Memoir in Honor of Howell Williams. Geol Soc Am Mem 116: 613-662

Stearns DW (1978) Faulting and forced folding in the Rocky Mountains foreland. Geol Soc Am Mem 151: 1-37.

Streck MJ, Grunder AL (1995) Crystallization and welding variations in a widespread ignimbrite sheet; the Rattlesnake Tuff, eastern Oregon, USA. Bull Volcanol 57: 151-169

Tanaka H, Turner GM, Houghton BF, Tachibana T, Kono M, McWilliams MO (1996) Palaeomagnetism and chronology of the central Taupo Volcanic Zone, New Zealand. Geophys J Int 124: 1-16

Walcott RI (1987) Geodetic strain and the deformational history of the North Island of New Zealand during the late Cainozoic. Phil Trans Roy Soc Lon A 321: 163-181

Walker GPL (1971) Grain-size characteristics of pyroclastic deposits. J Geol 79: 696-714

Walker GPL (1984) Downsag calderas, ring faults, caldera sizes and incremental caldera growth. J Geophys Res 89B: 8407-8416

Walker GPL (1985) Origin of coarse lithic breccias near ignimbrite source vents. J Volcanol Geotherm Res 25: 157-171

Wan T, Hedenquist JW (1981) A reassessment of the structural control of the Broadlands geothermal field, New Zealand. 1981 Proc N Z Geotherm Workshop: 195-202

Williams H (1941) Calderas and their origin. University of California Publication, Dept Geol Sci Bull 25: 239-346

Wilson CJN, Rogan AM, Smith IEM, Northey DJ, Nairn IA, Houghton BF (1984) Caldera Volcanoes of the Taupo Volcanic Zone, New Zealand. J Geophys Res 89: 8463-8484

Wilson CJN, Houghton BF, McWilliams MO, Lanphere MA, Weaver SD, Briggs RM (1995) Volcanic and structural evolution of Taupo Volcanic Zone: a review. J Volcanol Geotherm Res 68: 1-28

Wilson CJN, Walker GPL (1982) Ignimbrite depositional facies: the anatomy of a pyroclastic flow. J Geol Soc Lon 139: 581-592

Wood CP (1985) Geology of the Rotorua geothermal field. In *The Rotorua Geothermal Field*. Tech Rep Mon Prog 1982-1985, Ministry of Energy: 275-293

Wood CP (1992) Geology of the Rotorua Geothermal System. Geothermics 21: 25-41

Wood CP, Brathwaite RL (1999) The basement at Kawerau geothermal field. Proc 21 N Z Geotherm Workshop 1999, Geothermal Institute, University of Auckland: 101-106

Woodward DJ, Ferry LM (1973) Sheet 5, Rotorua (1st ed.). Gravity Map of New Zealand 1:250,000, Department of Scientific and Industrial Research, Wellington

Wright JV, Walker GPL (1977) The ignimbrite source problem: Significance of a co-ignimbrite lag-fall deposit. Geology 5: 729-732

List of figures

Fig. 1. Outline of Taupo Volcanic Zone and calderas within it. a Location of TVZ in the North Island, New Zealand. A- andesite dominated, R- rhyolite dominated. b Calderas in TVZ 1 Rotorua, 2 Haroharo (in Okataina Volcanic Centre), 3 Kapenga, 4 Reporoa, 5 Mangakino, 6 Maroa, 7 Whakamaru, 8 Taupo. (After Houghton et al., 1995).

Fig. 2. Map of Taupo Volcanic Zone showing the prevalence of NE-SW striking faults. NW-SE striking structures are rarely identified at the surface. Solid lines are faults. Modified from Berryman et al. (1998).

Fig. 3. Current outcrop distribution of Mamaku Ignimbrite (shaded), around Rotorua Caldera. Current outcrop covers approximately 3100 km^2 but originally may have have been as high as 3900 km^2. Letters **A** and **B** are the sites of logs **A** and **B** in Figure 4.

Fig. 4. Stratigraphy of the Mamaku Ignimbrite basal tephra sequence (**A**) and main ignimbrite sequence (**B**). **A** The basal tephra sequence is made up of intercalated pyroclastic fall and density current beds. Lower beds (a-c) contain accretionary lapilli and aggregates of fine ash and are thought to be phreatomagmatic. Beds d-n contain fragments of charcoal and no accretionary lapilli suggesting dry eruption. Beds d-n also pinch and swell in places suggesting deposition from density current rather than by fall. **B** The main ignimbrite sequence can be split into upper, middle and lower facies based on variations in crystal content, welding, jointing, devitrification and vapour phase alteration, and lithic content and type. Pumice represented by open shapes, crystals by small spots and lithics by solid triangles. From Milner et al. (submitted).

Fig. 5. Granulometry of lower Mamaku Ignimbrite (lMI) and basal tephra sequence beds. Following Walker (1971). ■= basal tephra sequence bed a, •= basal tephra sequence bed m, ♦= lower Mamaku Ignimbrite.

Fig. 6. Geological map of Rotorua Caldera. The area of the lowest gravity anomaly is in the southwest of the caldera. Fissure fumarolic structures are present towards the northwest edge of the caldera. Faults have been inferred beneath rhyolite domes surrounding the gravity low. One main tension crack can be seen at the east caldera margin. At the northeast, formation of the Tikitere Graben and eruption of the Rotoiti Breccia have overprinted the Rotorua Caldera structure. Pre-caldera rhyolite domes were truncated as the caldera formed. ICBF denotes the inner caldera boundary fault postulated by Wood (1991). Map includes two lineaments defined by Lloyd (1975) and data from Nairn (1989), Bellamy (1991), and Crosby (1998).

Fig. 7. An Rb/Sr vs SiO_2 plot clearly separates the three silicic pumice types.

Fig. 8. Maximum lithic (M_L) isopleth map for upper Mamaku Ignimbrite. **A** Isopleths centre on the area southwest of Lake Rotorua, the inferred source of the upper part of the ignimbrite. Isopleth data and labels are in millimetres. B A graph of maximum lithic size versus distance from Rotorua for upper Mamaku Ignimbrite shows maximum lithic size decreases away from Rotorua. From Milner et al. (submitted).

Fig. 9. Satellite image of Rotorua Caldera showing major features outlined in the text. The embayment in the northwest is thought to have been strongly influenced by NW-SE striking faults. The influence of NE-SW striking faults (associated with the main axis

of rifting) can clearly be seen forming an elliptical collapse structure with a long axis oriented NE-SW.

Fig. 10. Aerial photograph of the northwest caldera embayment. Fissure fumarolic structures can be seen diverging from the scarp close to the caldera margin and are thought to have formed in response to downsag of hot Mamaku Ignimbrite. (Air photo made available by Environment Bay of Plenty, Whakatane).

Fig. 11. A quarried fumarolic structure reveals an internal conduit that splays at the top. Gases escaping up the conduit would have deposited minerals thereby cementing the ignimbrite and making it harder than in the surrounds. Material in the conduits is often eroded leaving a cavity, that may or may not be filled with younger material. **A** Photograph of the central portion of the fumarolic structure. **B** labelled diagram of the fossil fumarole interior. **C** Close up sketch of part of the fumarole conduit. The material inside the conduit is probably derived from the surrounding ignimbrite.

Fig. 12. Rogan's (1982) gravity and magnetic data and interpretations. **A** Bouguer anomalies over Rotorua (in milligals, dots are gravity stations). Two areas of low gravity are present west and southwest of Lake Rotorua. **B** Depth to basement calculated from the gravity data (contour labels are depth below mean sealevel in metres). **C** Rogan's residual total force magnetic anomalies of the Rotorua area (contours are in nanoteslas). **D** Depth to basement calculated from magnetic data. Rogan's calculations show a disparity in depth to basement of between 1 and 1.5 km which may be due to the abnormal magnetism of the Mamaku Ignimbrite. After Rogan (1982). Modified by permission of the American Geophysical Union

Fig. 13. Hunt's (1992) data and interpretation. A Residual gravity anomaly of Rotorua Caldera and surrounds (contour intervals are 20 μN/kg). B Cross sections of residual gravity map (along lines labelled). Crosses mark Hunt's caldera boundary. C Possible interpretations of the depression's structure and fill. Cross sections in B are similar to those for Guayabo Caldera (Halinan, 1993) and are not suggestive of a single ring fault of large displacement. Dots in A are gravity stations.

Fig. 14. Exploded oblique view of Rotorua Caldera. The caldera floor is broken up into a number of blocks that increase in displacement to the southwest. Faults associated with caldera collapse have been used as conduits to erupt post-caldera rhyolite domes. The basement deforms brittly, and Mamaku Ignimbrite ponding in the depression is able to deform by downsagging. Faults striking northeast-southwest have much closer spacing than those striking northwest- southeast. Faults have been placed on the map according to the location of postcaldera rhyolite domes, observed scarps inside and towards the caldera margin, and the margins of the northwest embayment. Pre-caldera rhyolite domes have been truncated by caldera-forming faults. Units and symbols as for Fig. 4.

Fig. 15. Showing Formation of a forced or drape folds showing the way in which cover and basement rocks deform to overcome the space problem and areas of potential fault formation in the cover rocks. From Cosgrove and Ameen (2000).

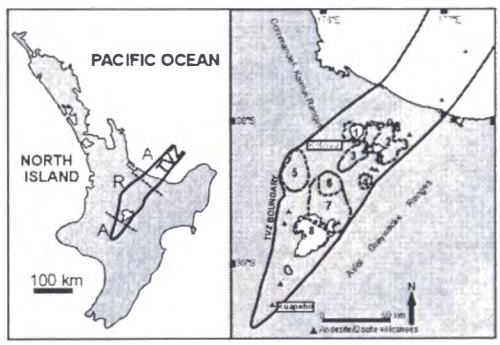

Fig. 1
Milner et al.

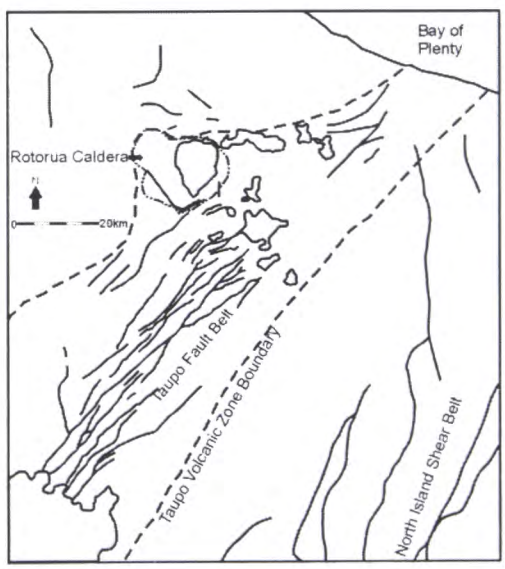

Fig. 2
Milner et al.

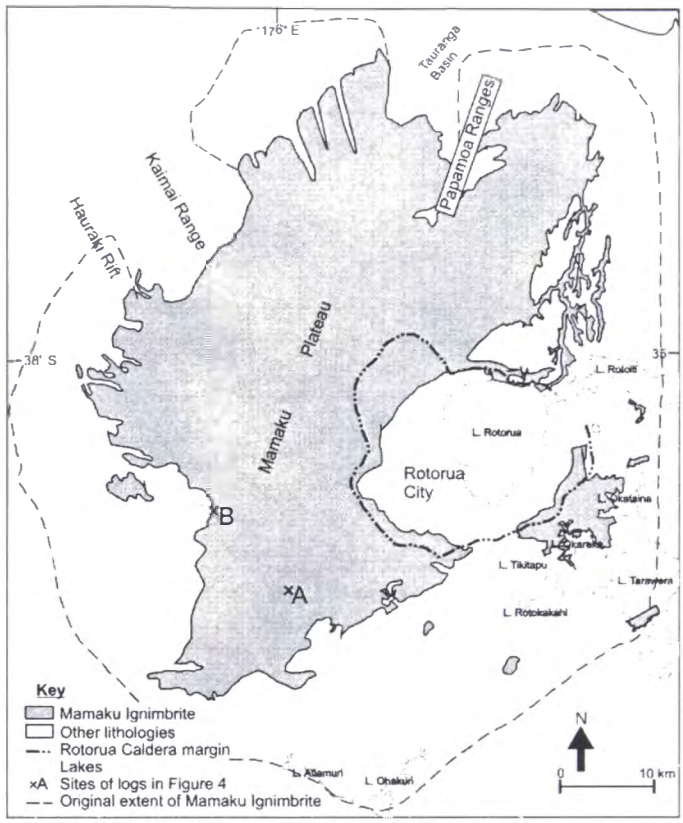

Fig. 3
Milner et al.

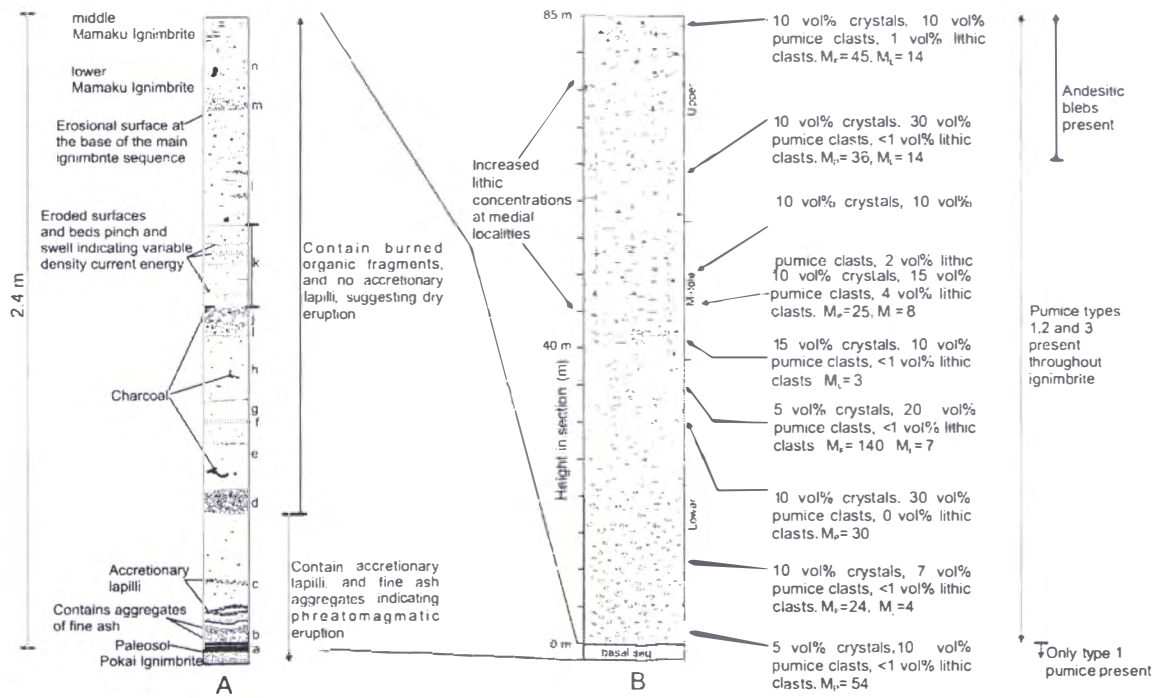

Fig. 4
Milner et al.

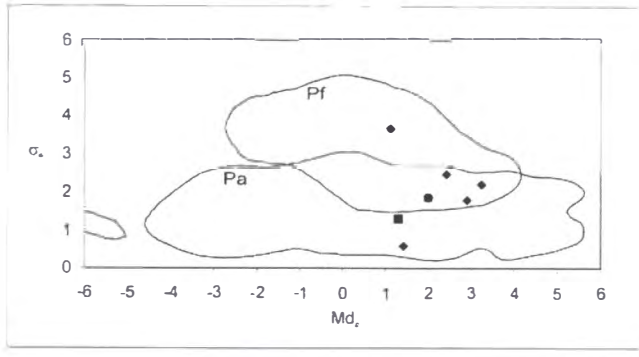

Fig. 5
Milner et al.

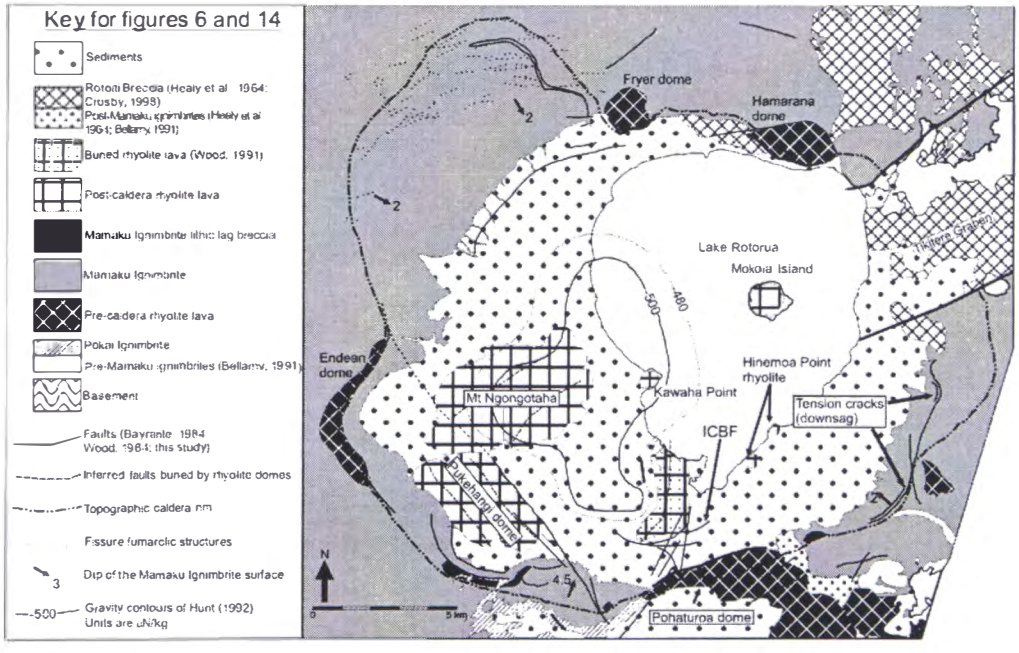

Fig. 6
Milner et al.

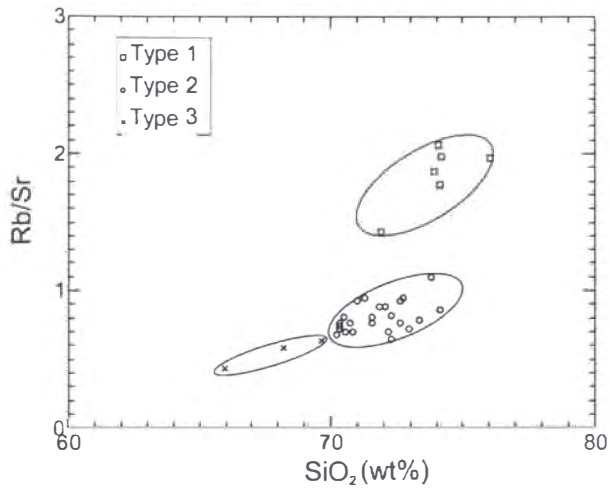

Fig. 7
Milner et al.

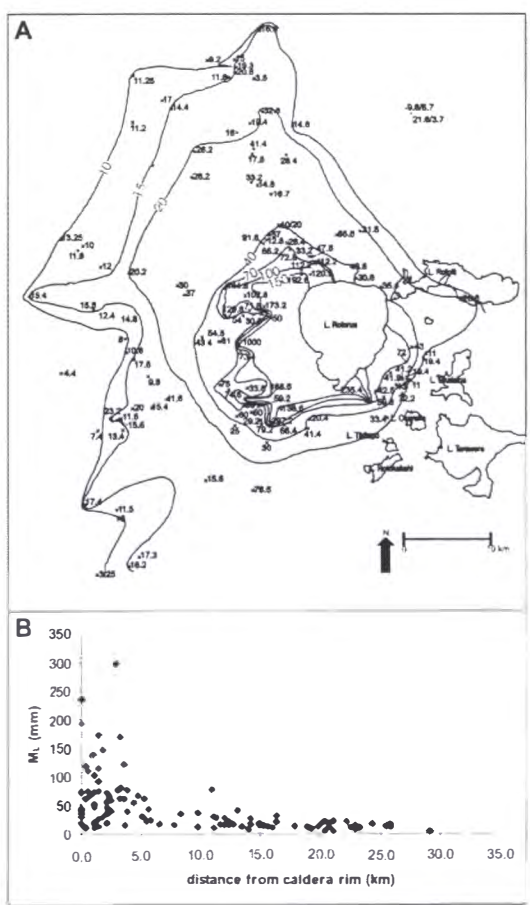

Fig. 8
Milner et al.

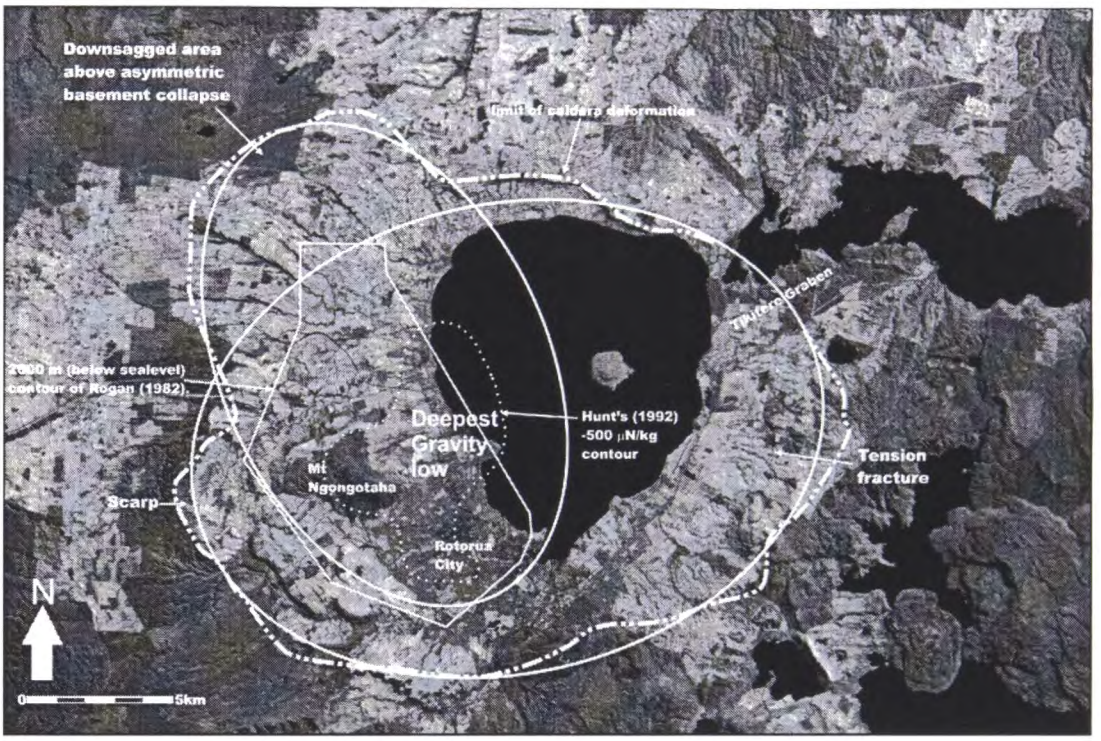

Fig. 9
Milner et al.

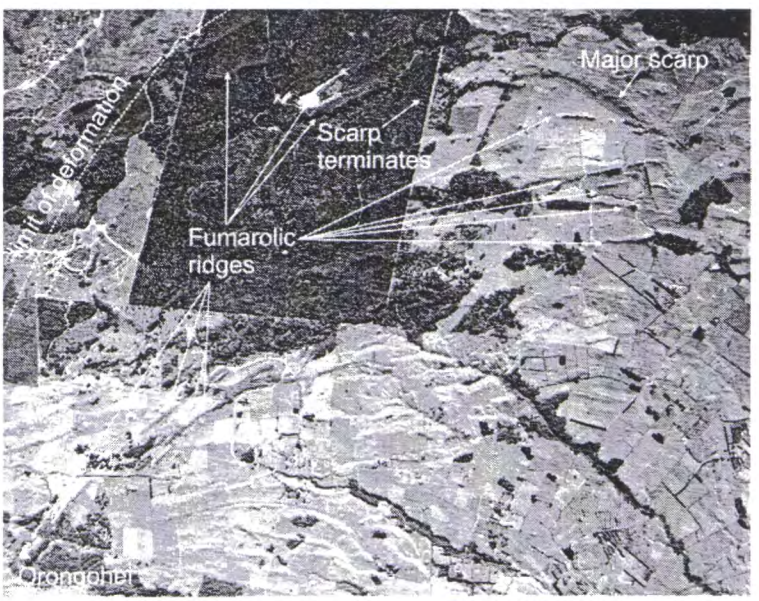

Fig. 10
Milner et al.

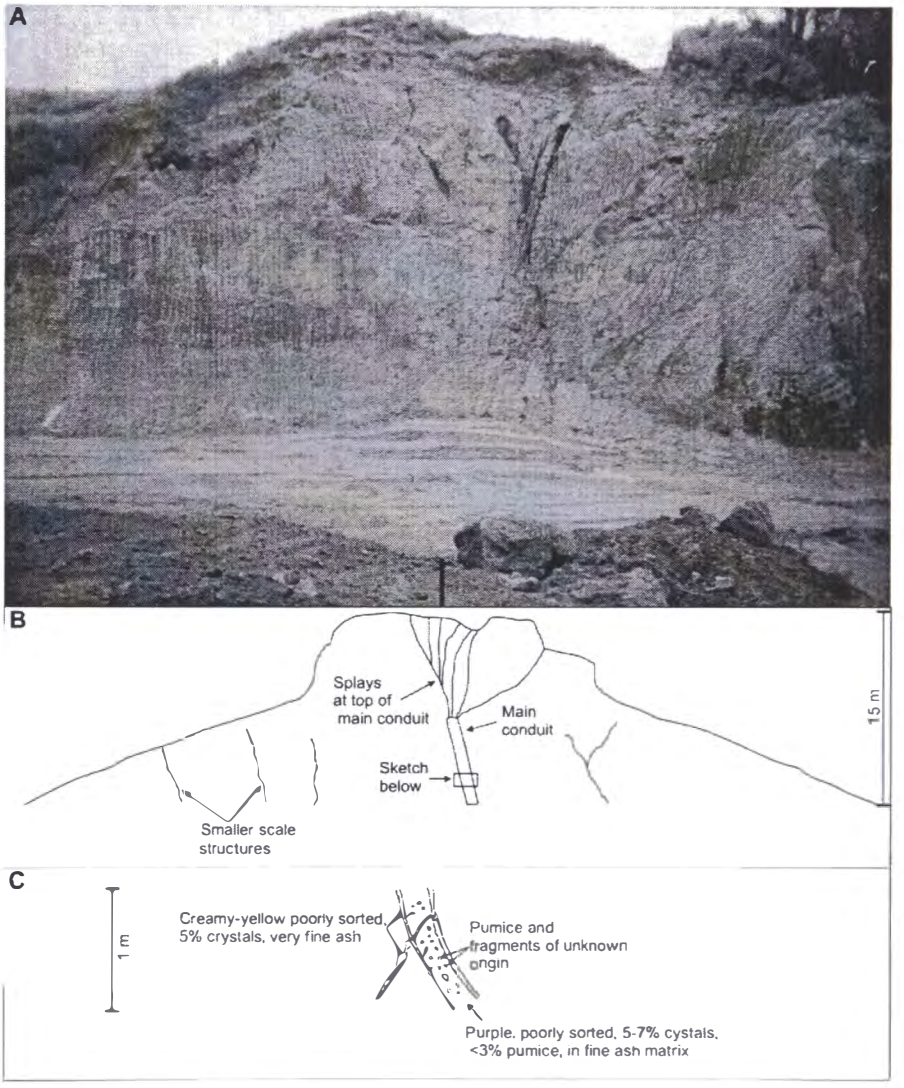

Fig. 11
Milner et al.

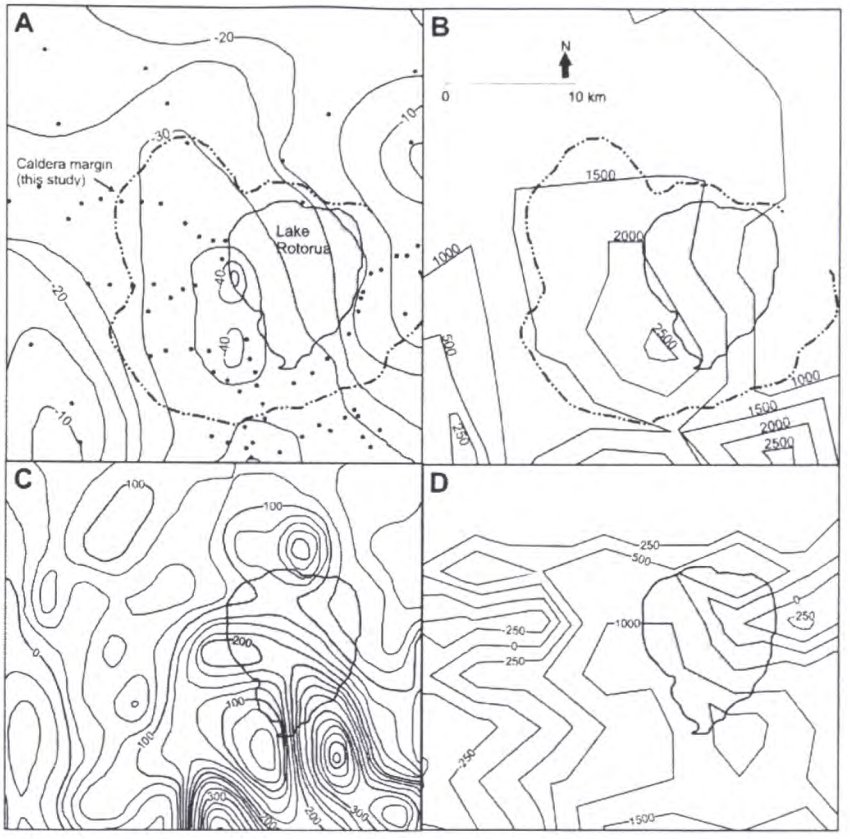

Fig. 12
Milner et al.

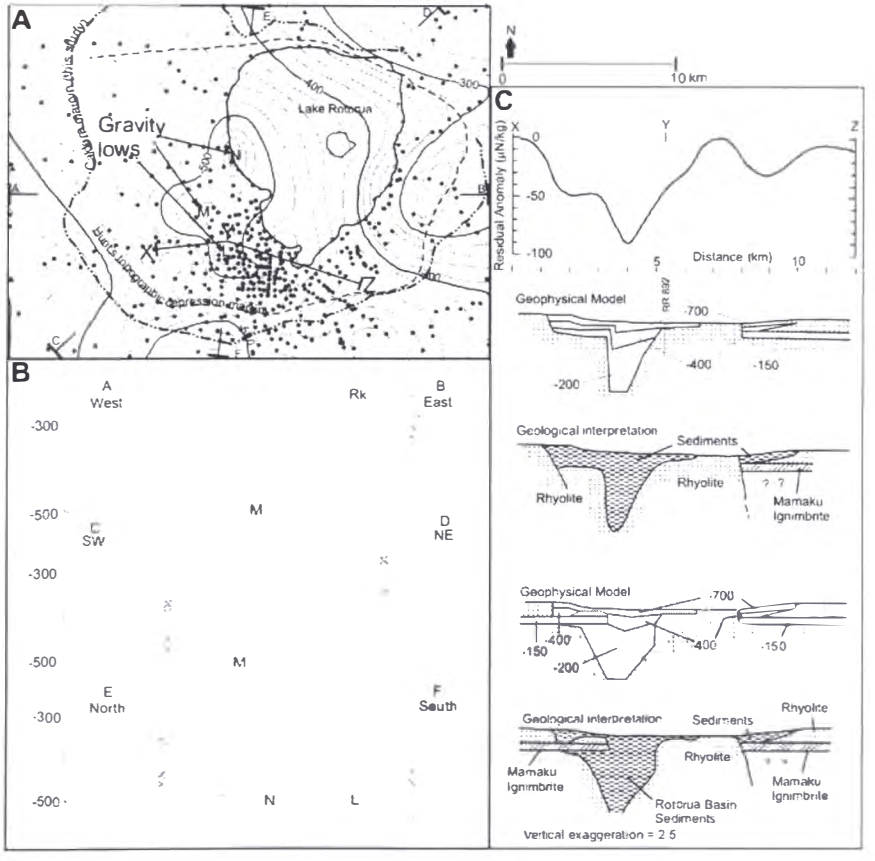

Fig. 13
Milner et al.

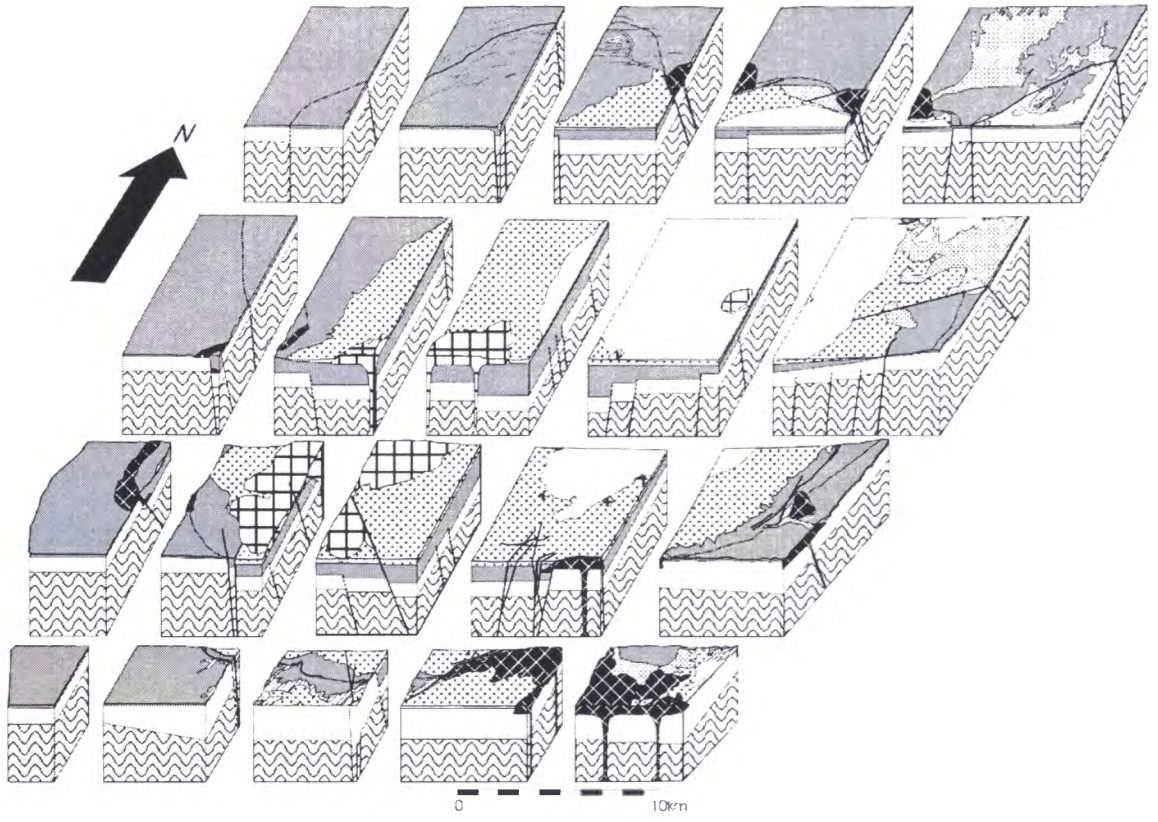

Fig. 14
Milner et al.

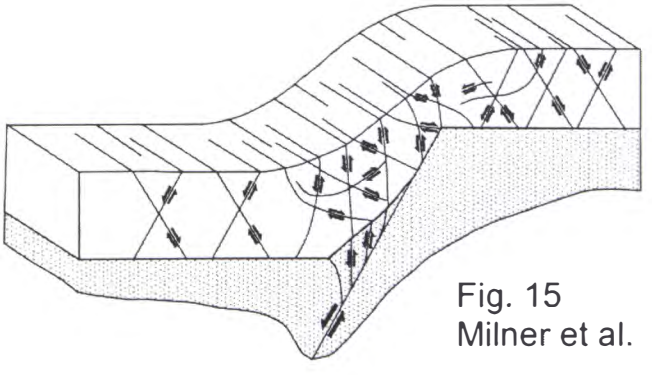

Fig. 15
Milner et al.

APPENDIX 9

Mamaku Ignimbrite; a caldera-forming ignimbrite erupted from a compositionally zoned magma chamber in Taupo Volcanic Zone, New Zealand

submitted to
Journal of Volcanology and Geothermal Research

Mamaku Ignimbrite; a caldera-forming ignimbrite erupted from a compositionally zoned magma chamber in Taupo Volcanic Zone, New Zealand

D.M. Milner[a*], J.W. Cole[a], and C.P. Wood[b]

[a] *Department of Geological Sciences, University of Canterbury, PB 4800, Christchurch, New Zealand*

[b] *Institute of Geological and Nuclear Sciences, Wairakei Research Centre, Private Bag 2000, Taupo, New Zealand.*

Abstract

Mamaku Ignimbrite was erupted from the Rotorua Caldera, Taupo Volcanic Zone, New Zealand, c.225 ka. Its outflow sheet forms a fan north, northwest and southwest of Rotorua, capping the Mamaku-Kaimai Plateau. Mamaku Ignimbrite can be divided into a partly phreatomagmatic basal sequence, and a main sequence which comprises lower, middle, and upper ignimbrite. Internal stratigraphy indicates that it was emplaced progressively from a pyroclastic density current of varying energy that became less particulate away from source. Gradational contacts between lower, middle, and upper ignimbrite suggest that it was deposited during one eruptive event the same source. Variations in lithic content and coexistence of different pumice types through the ignimbrite ignimbrite stratigraphy indicate that caldera collapse occurred throughout the eruption, but particularly during the eruption of middle Mamaku Ignimbrite and in the final stages of eruption of upper Mamaku Ignimbrite. Maximum lithic data and the location of lithic lag breccias in upper Mamaku Ignimbrite confirm Rotorua Caldera as the source. At least 120 m of geothermally altered intra-caldera Mamaku Ignimbrite occurs inside the caldera.

Pumice clasts in the Mamaku Ignimbrite are dacite to high-silica rhyolite and can be chemically divided into 3 types; high silica rhyolite (type 1), rhyolite (type 2) and dacite (type 3). All are petrogenetically related and types 1 and 2 may be derived by up to 20 % crystal fractionation from the type 3 dacite. All three types probably resided in a single, gradationally zoned magma chamber. Andesitic juvenile fragments are found only in upper Mamaku Ignimbrite and represent a discrete magma that was injected into the silicic chamber and is considered to have accumulated as a sill at the base of the magma chamber. The contrast in density between the andesitic and silicic magmas did not allow eruption of the andesite fragments during eruption of lower and middle Mamaku

Ignimbrite. Caldera collapse during upper Mamaku Ignimbrite created withdrawal dynamics that caused the andesitic magma to erupt.

Keywords: Mamaku Ignimbrite, Gradational Zonation, Magma Chamber, Taupo Volcanic Zone.

1. Introduction

The Taupo Volcanic Zone (TVZ; Fig. 1) has been active since 2 Ma (Houghton et al., 1995), and is a NE-SW striking volcano-tectonic depression and volcanic arc that is actively extending in a NW-SE direction at between ~7-12 mm/year (Sissons, 1979; Walcott, 1987; Crook and Hannah, 1988; Darby et al., 2000). The TVZ can be divided into southern andesite-dominated, central rhyolite-dominated, and northern-andesite dominated segments (Fig. 1; Wilson et al., 1995). Rhyolitic activity commenced ~1.6Ma and occurred during five periods: I (1.68-1.53 Ma), II (1.21-0.68 Ma), IIIA (0.34-0.32 Ma), IIIB (0.28-0.15 Ma), and IIIC (0.065 Ma-present) with the eruption of >15,000km^3 of predominantly rhyolitic volcanic deposits, making it the most productive, currently active rhyolitic centre on earth (Houghton et al., 1995; Wilson et al., 1995).

Heterogeneous pumice chemistry in pyroclastic deposits is often thought to represent tapping of either multiple magma batches or a zoned magma reservoir (Hildreth, 1979;1981). The stratigraphic variation of pumice types in an ignimbrite reflects the withdrawal dynamics of the magma chamber (Blake and Ivey, 1986a and b). Commonly pumice chemistry in ignimbrites is zoned, representing sequential tapping of compositional bands within the magma chamber. Normal zoning is reflected by the presence of the most evolved silicic pumice (usually representing the least dense magma) towards the base of the ignimbrite with progressively more mafic pumice up section. Occasionally reverse zoning may occur where the pumice is mafic at the base becoming more silicic upwards.

Internal lithologic variation of an ignimbrite can be used together with chemical zonation to determine eruption evolution, including changes in eruptive energy at vent, enlargement, and timing of caldera collapse.

Murphy and Seward (1981) originally dated it at 140 ± 80 ka (fission track estimate), but the large error made this suspect. Shane et al. (1994) later obtained an isothermal plateau fission track (ITPFT) age of 230 ± 12 ka, Houghton et al. (1995) an age of 220 ± 10 ka from $^{40}Ar/^{39}Ar$, and Black et al. (1996) 230 ± 10 ka also from ITPFT. Mamaku Ignimbrite was erupted during a geomagnetic excursion, which has been correlated with the 218 ± 10 ka (Herrero-Bervera et al., 1994) Pringle Falls event (Black et al., 1996; Tanaka et al., 1996). The age of the Mamaku Ignimbrite is considered in this paper to be c.225 ka.

Mamaku Ignimbrite is one of the most widespread ignimbrites of TVZ. It is the youngest welded ignimbrite of TVZ and it remains one of the least studied. This paper presents field and laboratory data obtained for the ignimbrite. The data has been used to constrain the ignimbrite source and to interpret possible mode of ignimbrite emplacement, magma chamber configuration and withdrawal dynamics. Structure and evolution of Rotorua Caldera is described in another paper (Milner et al., submitted), with collapse inferred from variations in pumice chemistry, and lithic content and is interpreted to have begun early in the eruption of Mamaku Ignimbrite, continuing until the eruption ceased.

1.1. Terminology

In Mamaku Ignimbrite welding zones have been described as non-welded, moderately welded, strongly welded, and densely welded following terminology outlined in Streck and Grunder (1995). **Non-welded** refers to friable ignimbrite in which pumice clasts are undeformed. **Moderately welded** is similar to "partially welded with pumice" of Streck and Grunder (1995) with pumice clasts showing signs of compaction, but samples are not vitreous and pumice clasts are often devitrified and vesicles frequently not seen. **Strongly welded** refers to their "partially welded with fiamme". The fiamme in the strongly welded ignimbrite are lenticular and have sub-horizontal long axes. **Very strongly welded** refers to ignimbrite that has become a dark grey-black vitrophyre with eutaxitic texture still observable in hand specimen.

Pumice clasts are highly vesicular, dacitic-rhyolitic glass that are pieces of the magma that filled the greatest proportion of the Mamaku Ignimbrite magma chamber, while a**ndesitic juvenile fragments** refer to a petrogenetically unrelated magma that intruded the silicic chamber and erupted with it. **Fiamme** are glassy lenses that represent compacted pumice clasts and their sub-parallel alignment (due to compaction) imparts a **eutaxitic** texture (as in McPhie et al., 1993).

2. Distribution, thickness and volume

2.1. Outflow Sheet

The outflow sheet forms a fan extending between Te Puke in the north and Atiamuri in the southwest, capping the Mamaku-Kaimai Plateau (Fig. 1). The surface of this plateau dips gently northwards at 2-3° to the northwest and west (Briggs et al., 1996) and the ignimbrite thins towards the Hauraki rift. Proximally the ignimbrite surface downsags towards Lake Rotorua (Milner et al., submitted). Southwest of Rotorua, Mamaku Ignimbrite appears to have flowed around the Horohoro rhyolite dome without over-topping it. East of the Horohoro dome it is faulted down into the Kapenga Caldera, where it is present in the Dillon drill hole in the Guthrie Graben (Fig. 1), and outcrops as an outlier on Kapenga Caldera's northeastern side. East of Rotorua outcrops extend as far as Lake Tarawera, but if present beyond, the ignimbrite has been concealed beneath younger volcanics from the Okataina Volcanic Centre (OVC). This is not considered likely however as it does not overlie older ignimbrites north or east of OVC.

The thickness of Mamaku Ignimbrite varies greatly outside its caldera, and is largely a function of the underlying topography and distance from inferred vent. Adjacent to the southern rim of Rotorua Caldera, it is 30-40 m thick, while at a locality 21 km northeast of the source an 80 m section is present with the base not exposed. 145 m of Mamaku Ignimbrite occurs in a drill hole 7 km north of the caldera (Nathan, 1975); the greatest thickness of outflow measured. A drill hole 11 km to the caldera's northeast (Fig. 1) penetrates 120 m (Fransen, 1982; this study), while thickness of 58 m has been drilled 5 km to the west (Wood, 1985). At the most distal localities Mamaku Ignimbrite thins to 2-5 m, or terminates in a scarp up to 20 m high.

The current outcrop area for Mamaku Ignimbrite is estimated at c.3100 km^2 using the method outlined by Streck and Grunder (1995), with total area once covered by the ignimbrite probably at least 3200 km^2, and possibly up to 3900 km^2 (Fig. 2). If an average thickness of 72.5 m is used, it gives potential volumes of 225 km^3, 232 km^3, and 283 km^3 for current outcrop, probable, and possible extents respectively (Fig. 2). Due to post-emplacement erosion total thickness and distribution estimates based on current outcrop are minima.

2.2. Intracaldera ignimbrite

Thickness of intracaldera ignimbrite has been estimated at ≥1000 m beneath Rotorua City by Rogan (1982, based on gravity and magnetic surveys; Fig. 2) and 279 m near the SE caldera rim by Lamarche (1992, seismic reflection surveys). Rogan (1982) found that the depth to basement in Rotorua Caldera was 1 km greater when calculated from gravity data than from magnetic data, and suggested this discrepancy resulted from the presence of at least a kilometre of non- or reversely magnetised material (Fig. 2). Mamaku Ignimbrite has since been shown to have an intermediate paleomagnetic direction (Tanaka et al., 1996; Black et al., 1996), which is consistent with this interpretation. The approximately 1 km thickness of ignimbrite within the caldera remains unproven, but is quite possible.

A drill hole has confirmed at least 120m of geothermally altered Mamaku Ignimbrite just inside the southern caldera (Wood, 1992).

3. Internal stratigraphy

The Mamaku Ignimbrite can be separated into a basal tephra sequence and a main ignimbrite sequence, which in turn can be subdivided into lower (lMI), middle (mMI) and upper (uMI) ignimbrite based on crystal content, welding, intensity of vapour phase alteration and devitrification (Fig. 3). Boundaries between the three are gradational. lMI grades into mMI over 0.2-2 m, but the boundary between mMI and uMI is much more difficult to determine. Welding decreases and devitrification and vapour phase alteration increase with height above the base of mMI. Where exposed, mMI grades into uMI over about 5-10 m.

3.1. Basal tephra sequence

The base of Mamaku Ignimbrite is exposed at six localities, and comprises a bedded sequence up to 2.5 m thick, with up to 14 pyroclastic fall and density current beds (units A-N, Fig. 4), overlying either 1m of brown tuff, the surface of which is a hard iron stained band, or the eroded surface of Pokai Ignimbrite on which a paleosol developed, or aeolian sand or fluvial sediment. The lowest units contain fine ash aggregates, accretionary lapilli, fine grained, and considered phreatomagmatic, and the basal sequence records a progressive change in eruptive style from an early wet phase to dry.

3.2. Main ignimbrite sequence

The main sequence of the Mamaku Ignimbrite is predominantly massive, mineralogically monotonous and has no definable flow units. In places it truncates the upper layers of the basal sequence. The ignimbrite varies vertically from a light grey, non-welded, unconsolidated, pumiceous and sandy deposit near the base, up through dark grey, welded and lenticular material to a pink-purple, devitrified and vapour phase altered top (Fig. 3). The ignimbrite is best exposed at Sutcliffe Rd (Fig. 1) where the full sequence of the ignimbrite is exposed, including some of the basal tephra sequence (units C-E, G, L-N).

3.2.1. Lower Mamaku Ignimbrite (lMI)

At the Mamaku Ignimbrite type section, lMI is 40-50m thick and comprises very pale brown-yellow to white-grey, non-welded, non-jointed, mostly massive, poorly sorted, pumice-bearing (7-10 vol%), lithic-poor (<1 vol%), crystal-bearing (7-10 vol%) ignimbrite with fine to coarse ash matrix. Pumice clasts are fibrous, vitric, and undeformed. Glass shards are also vitric and undeformed. Density varies between 0.79 g/cm^3 and 0.95 g/cm^3 and thickness between 1 m and 45 m (Thompson, 1958; Nathan, 1975; Fransen, 1982; this study).

Concentrations of pumice clasts define crude layers at some levels and are of two main types: 1) lenses of large pumice clasts (up to 230 mm diameter) with gradational upper and lower contacts, and 2) thin pumiceous bands (up to 30 mm thick), in which pumice

clast concentration may reach 15-20 vol% are present in lower parts of lMI and can be traced for the extent of some outcrops (up to 5-7 m) without thinning and without any sharp upper or lower contacts. These variations do not appear to be topographically related as they are often flat-lying and occur at levels well above the base of the ignimbrite. A third type was observed at only one locality towards the base of lMI. Here pumice clasts are up to 20 mm diameter, and comprise up to 30 vol% of the ignimbrite. This third type occurs immediately above, and parallel to, an area of moderate paleotopography and may have been caused by interaction of the density current with the underlying topography.

Lithics are almost all rhyolite lava with rare fragments of underlying ignimbrites, and towards its base, lMI contains rip up clasts of Pokai Ignimbrite, charcoal and parts of its own the basal sequence.

3.2.2. Middle Mamaku Ignimbrite (mMI)

The base of middle Mamaku Ignimbrite is indicated by a sudden increase in crystal content, welding, and jointing (Fig. 3). mMI is light-brown to dark-grey, jointed (spacing 0.5-4 m), strongly to very strongly welded (non-rheomorphic) ash, in places becoming vitrophyre. Crystal content is 17-26 vol%, pumice clasts 5-10 vol%, and lithics 0-4 vol%. Pumice clasts are flattened and become glassy and lenticular forming fiamme with flattening ratios (long axis/short axis) of 6-13 decreasing to 3-4 near the top. The matrix is brown and dominated by cuspate shards (slightly flattened depending on orientation) that impart, along with fiamme, a eutaxitic texture. Density is up to 2.2 g/cm^3 and mMI varies between 5-50 m thick. Lithics are sporadic, but are of increased concentration (cf. lMI), and are also dominantly rhyolite lava.

3.2.3. Upper Mamaku Ignimbrite (uMI)

Upper Mamaku Ignimbrite is grey-pink-red-purple, non- to moderately welded, non-jointed to jointed, friable, fine to coarse ash. Density varies between 0.84 and 1.1 g/cm^3; crystal content varies between 10-15 vol%, lithic content 0-2 vol% and pumice clasts 10-15 vol%. It can be distinguished from mMI by its totally devitrified pumice clasts, and is typified by the presence of irregularly shaped juvenile mafic fragments and presence of mMI lithics. Rare segregation or elutriation pipes occur in uMI exposures

near the Rotorua Caldera rim. They are 300-500 mm high × 50 mm wide, and contain lithic clasts of mainly mMI up to 50 mm diameter.

uMI has been extensively affected by post-depositional vapour phase alteration (VPA), which caused the colour variation from its original pale grey to pink-red-purple. Pumice clasts have devitrified and characteristic fibrous textures have been replaced by microspherulites of feldspar and silica. Microspherulites also occur at the margins of some primary crystals in the ignimbrite. The matrix often contains small needle-like crystals and aggregates of platy crystals, which X-ray diffraction (XRD) indicates are albite, alkali feldspar (needles), tridymite (plates) and cristobalite. Similar assemblages were identified in vapour phase affected parts of the Matahina Ignimbrite (Carr et al., 1981).

3.3. Layer 1-like deposits

At the base of lMI and within distal mMI to the north of Rotorua Caldera, sandy crystal-rich layers are present that appear similar to layer-1 deposits of Sparks et al. (1973) and have sharp boundaries. The layer beneath lMI is coarse-fine sand and contains pumice lapilli. In the same area a crystal-rich lens (up to 80 vol% coarse sand sized crystals with interstitial clayey material) with a maximum thickness of 120 mm is present, extending for 15 m along the outcrop, and is similar to those noted by Morgan (1986) at other localities. The lens in mMI and the layer beneath lMI are layer 1-like deposits produced from a fully deflated pyroclastic density current and are not seen at medial localities where extensive logs have been made. The lens in mMI pinches out over 15 m and beyond either end the ignimbrite is continuous without a visible break or flow unit boundary. The lens in mMI is interpreted as due to temporary migration of the pyroclastic density current direction perhaps, in response to deposit aggradation.

4. Source of Mamaku Ignimbrite

To determine Mamaku Ignimbrite source, measurements were made of the long axes of the 5 largest lithic clasts seen at 110 uMI sites (following Walker, 1985; Wright and Walker, 1977). The 5 values were averaged (M_L) and an isopleth map constructed (Fig. 5). M_L of uMI decreases from 192 mm at the northern margin of Rotorua Caldera to 11-

15mm at Oropi Gorge. North of Oropi Gorge lithic fragments are rare and were not measured. West and southwest M_L diminishes from 100-1000 mm near the caldera rim to 4–15mm at its western margin near Tokoroa and Atiamuri (Fig. 5). Lithic isopleths centre on the area southwest of Lake Rotorua (Fig. 5), with size clearly decreasing away from Rotorua Caldera (Fig. 6). M_L data from lMI and mMI is of little use due to lack of exposure close to Rotorua. They are inferred to have the same source as uMI due to the gradational boundaries between each level, similar petrography, and similar silicic pumice compositional groupings of lMI and uMI.

4.1. Lithic lag breccias

Lithic lag breccias occur at three caldera margin localities in the top of uMI, while lithic concentration zones have been found at a number of other caldera margin sites. Clasts of the lithic lag breccia comprise 46 vol% mMI, 48.5 vol% rhyolite lava, 3.8 vol% other older ignimbrites and 1.7 vol% plutonic clasts. Although uMI grades quickly (over c.100 mm) into lag breccia, the lithic clasts in the breccia are set in the same pink, fine-coarse matrix occurring in uMI, and devitrified pumice clasts typical of uMI are also present, demonstrating that the lag breccias are part of the ignimbrite, and are not a separate deposit. It is likely that lithic lag breccias are present at other localities, particularly along the southwest and west caldera margin, but the top of uMI is poorly exposed as a result of forest cover. Areas of high lithic concentration are exposed at and around the caldera margin (Fig. 1).

5. Petrography and mineral chemistry

Crystal content of the ignimbrite varies from 7-26 vol% depending on stratigraphic position and comprises plagioclase + quartz + clinopyroxene + iron/titanium oxides ± orthopyroxene with traces of hornblende and biotite. Crystal content is greatest (17-26 vol%) in the welded middle part of the ignimbrite and lowest (7-10 vol%) in its unwelded lower parts. It is generally lithic-poor with lithic abundance increasing in welded mMI and in uMI. This increase in crystal content is probably due to decrease in void space due to welding.

The most obvious petrographic differences between levels are in the textures of pumice clasts and glass shards, and variations in crystal concentration. All crystals are euhedral-subhedral or broken, and often contain stress cracks, probably caused by stresses imparted during eruption, trtansportation, and deposition.

5.1. Pumice petrography

Three types of Mamaku Ignimbrite pumice were first determined by their chemistry (see Geochemistry below) and can be distinguished petrographically, though not in hand specimen (percentages below quoted are by volume):

Type 1 (high SiO_2 rhyolite) pumice comprise 6-7 vol% phenocrysts, and up to 60 vol% vesicles. The phenocryst assemblage is plagioclase + quartz + orthopyroxene + Fe/Ti oxides ± augite (trace) ± hornblende (trace).

Type 2 (rhyolite) comprise 5-7 vol% phenocrysts and 30-60 vol% vesicles. Phenocrysts comprise plagioclase + quartz + orthopyroxene + Fe/Ti oxides ± augite.

Type 3 (dacite) pumice contains 4-5 vol% crystals and up to 60 vol% vesicles. The crystal assemblage plagioclase + orthopyroxene + Fe/Ti oxides ± quartz ± augite ± hornblende (trace).

Graphic intergrowths occur in type 1 pumice, and plagioclase and pyroxene often occur together in crystal aggregates in all pumice types, both are thought to be glomerocrysts stripped from the magma chamber walls.

5.2. Andesitic juvenile fragment petrography

Andesite occurs in uMI as irregularly shaped fragments up to 70 mm across which are dark grey-black, and massive with 4.5 vol% phenocrysts in a very fine-grained holocrystalline matrix. Pyroxene is the dominant phenocryst mineral (2 vol%), with plagioclase (1 vol%), amphibole (≤1 vol%), biotite (0.5 vol%), and trace amounts of olivine. Groundmass microphenocrysts comprise amphibole (~35 vol%), plagioclase (~45 vol%), and Fe/Ti oxides (10 vol%). The appearance of the mafic material in uMI

has implications for the eruption dynamics of Mamaku Ignimbrite. Crystallisation of the andesitic fragments occurred in two stages; firstly by growth of pyroxene and plagioclase phenocrysts up to 1.5 mm length, and later by hydrated crystallisation of the groundmass. Microphenocrysts comprising the groundmass are acicular; amphiboles are up to 0.3 mm long by 0.02 mm wide, and often splay at the ends, have fan or bowtie textures and, in extreme forms, are star-shaped. Plagioclase microphenocrysts are commonly skeletal and many have swallowtail terminations.

The shapes of groundmass amphibole and plagioclase indicate supercooling of the andesitic magma. The margins of some andesitic blebs are cracked, consistent with quenching on entering a cooler medium. The sudden change in conditions of crystallisation, groundmass crystal morphology and fracturing of the margins of the mafic clast indicate rapid cooling. The temperature difference between the silicic chamber and mafic magma would probably have been sufficient to cause the supercooling apparent in the andesitic fragments. Conversely the transfer of heat and perhaps volatiles from mafic magma may have caused vesiculation in the rhyolite thereby ultimately triggering its eruption.

5.3 Mineral chemistry

The dominant phenocryst in all Mamaku Ignimbrite pumice is plagioclase. Crystals are up to 2 mm long, euhedral-subhedral or broken, and sometimes contain stress cracks presumably induced during eruption. All plagioclase is normally zoned andesine-oligoclase varying between An_{31-17}, An_{31-16}, and An_{43-22}, for pumice types 1, 2 and 3 respectively. Plagioclase in andesitic fragments (An_{46-22}) is similar to that in type 3 pumice.

Pyroxene is the dominant mafic phenocryst in all pumice types, typically comprising 0.5-1 % (by volume). Minor augite is also present. Pyroxene crystals are up to 2 mm long and 0.25-0.5 mm in cross section. The orthopyroxene crystals are usually normally zoned, varying in the ranges $En_{56-34}Wo_{3-2}Fs_{63-43}$, $En_{59-40}Wo_{3-2}Fs_{57-38}$, and $En_{45-41}Wo_{3-2}Fs_{56-50}$ in pumice types 1, 2, and 3 respectively (Fig. 7), and $En_{43-39}Wo_2Fs_{59-55}$ in pumice from the basal tephra sequence. Orthopyroxene ($En_{74-50}Wo_{3-2}Fs_{47-23}$) and augite ($En_{46-44}Wo_{42-37}Fs_{19-12}$) coexist in andesitic fragments.

Iron/titanium oxides were analysed to obtain temperatures of the erupting magma and help identify zoning of the magma chamber. While crystals that showed visible signs of exsolution were avoided, the oxide pairs analysed were still found to be in disequilibrium.

Hornblende is present in trace amounts in pumice types 1 and 3. Andesitic fragments contain rare olivine (Fo_{85}) phenocrysts.

6. Geochemistry

6.1. Whole pumice chemistry

Whole pumice analyses from the lower ignimbrite range from dacite (66.0-69.7 wt% SiO_2; type 3 pumice) to rhyolite (70.2-76.0 wt% SiO_2; types 1 and 2) (Fig. 8a). The two types of rhyolitic pumice can clearly be identified on Rb/Sr ratios (Fig. 8b), while dacitic pumice is the third type.

Type 1 rhyolite pumice vary between 71.9-76.0 wt% SiO_2, and have low Zn, Zr, Sr, CaO, TiO_2, Al_2O_3, Na_2O, Fe_2O_3 and high Rb relative to pumice types 2 and 3, while in type 3 (dacite) pumice K_2O is low while Al_2O_3, Fe_2O_3, TiO_2, CaO, Sr and Zr are all high. Type 2 rhyolite pumice range between 70.2-74.1 wt% SiO_2 and have chemistry intermediate to pumice types 1 and 3 (Fig. 9).

Trace element spider plots (Fig. 10) show enrichment of large ion lithophiles (LILE) relative to high field strength elements (HFSE). Sr is most strongly depleted in type 1 pumice, consistent with lower CaO contents of this pumice type.

Vector modelling using Raleigh fractionation with the dominant phenocrysts of the various pumice types (Fig. 11) demonstrates that type 1 pumice compositions can be formed from a type 3 magma parent by 20 % crystal fractionation dominated by plagioclase and orthopyroxene.

The different pumice types are not separated stratigraphically in Mamaku Ignimbrite showing that they erupted simultaneously. Type 2 pumice is by far the most common type suggesting its magma dominated the pre-eruptive chamber. Pumice types 1, 2, and 3 lie on the same major and trace element trends (Figs 9 and 10) suggesting all 3 types are genetically related. No major compositional gaps exist between the three pumice types suggesting they evolved in a gradationally zoned magma chamber.

6.2. Andesitic fragments

Andesitic blebs range between 58.4-61.8 wt% SiO_2. They have different trace element trends to pumice types 1, 2, and 3 and are not considered consanguineous (Fig. 10).

7. Discussion

7.1. Chemical variation of the magma chamber

Chemical differences between juvenile components in an ignimbrite indicate the coexistence of magmas of different composition located in multiple chambers (Briggs et al., 1993; Brown et al., 1998) or separated in a single chamber as a result of density variation (Cambray et al., 1995; Orsi et al., 1995; Civetta et al., 1997).

Chemical variation in magma chambers can be caused by melting of different types of crust, or discontinuous melting of the same crust (Hervig and Dunbar, 1992; Cambray et al., 1995), or by *in situ* crystallisation and fractionation of a single body of cooling magma along with assimilation of magma chamber wall rock (assimilation fractional crystallisation or AFC; Wolff et al., 1990) or by a combination of the two processes.

Conclusive temperature data or stable isotope geochemistry is required to confirm the configuration of the Mamaku magma chamber, but pumice from Mamaku Ignimbrite show evidence of eruption from a single zoned reservoir. Slight but progressive changes in pyroxene composition, and the difference in plagioclase chemistry between type 3 and types 1 and 2 pumice, and the lack of large whole pumice compositional gaps further suggest zonation the silicic part of the magma chamber was gradational. The make up of the magma chamber has been inferred from probable densities of the

different magma compositions and the stratigraphic location of corresponding pumice clasts in the Mamaku Ignimbrite.

Beresford and Cole (2000) found that more-evolved pumice in Kaingaroa Ignimbrite resulted from plagioclase-dominated crystal fractionation, as indicated by the strong increase in Rb/Sr ratio, and the same is inferred for Mamaku Ignimbrite. Rb/Sr increases exponentially with increasing SiO_2 from type 3 to type 1 (Fig. 8b) suggesting types 1 and 2 magmas were formed by fractionation of a type 3 parent. The systematic increase in K_2O and decrease in CaO with increasing SiO_2 (Fig. 9) also indicates fractionation of plagioclase from the melt. Fe_2O_3 and TiO_2 both decrease in a regular way with increasing SiO_2, as do Zn and Zr with increasing Rb which, along with vector modelling, suggests fractionation of pyroxene from a type 3 parent was also important. Mineral chemistry of basal sequence pumice is similar to the more evolved type 1 pumices, and they are thought to be from the same magma.

Andesitic fragments of uMI have a distinct major and trace element trend, have quenched margins and represent a discrete magma, unrelated to the dacitic and rhyolite pumice types. The andesite magma is considered to have injected into the base of the magma chamber where it accumulated towards the base of type 3 magma. Mixed and striped pumice clasts have not been found in the Mamaku Ignimbrite and because of this the andesite magma is interpreted to have entered the silicic chamber in a non-vigorous manner. Its presence only in uMI suggests it collected as a sill-like layer at the base of type 3 magma.

A model of the proposed magma chamber immediately prior to eruption of Mamaku Ignimbrite is shown schematically in Fig. 12. Only erupted magma has been included in the diagram and layering in the chamber is based on probable density variation (due to a compositional gradient).

7.2. Comparison with other TVZ ignimbrites

Mamaku Ignimbrite pumice chemistry is compared with other TVZ pumice data in Fig. 13. The Zr range of Mamaku Ignimbrite pumice (221 ppm; Fig. 9) is large. Only Ohakuri pumice samples have a larger range, and the Ohakuri magma may have been

erupted from more than one magma chamber (Dr M. Nakagawa, pers. comm., 1997). Types 2 and 3 magma plot within the Rb-Sr range of other TVZ ignimbrites with type 1 plotting just outside (Fig. 13a). The Zn-Zr plot variation is also large relative to other TVZ ignimbrites (Fig. 13b). Both plots illustrate fractionation trends of the Mamaku Ignimbrite magma system similar to Whakamaru (Rb-Sr, and Zn-Zr), and Marshall (Zn-Zr) ignimbrites (Brown et al., 1998).

There has been considerable debate on the causes of zonation in the Taupo Volcanic Zone. Briggs et al. (1993) observed two styles of zoning in Mangakino ignimbrites: 1) ignimbrites with continuous compositional trends in major and trace elements and similar isotopic compositions (due to fractional crystallisation of a single magma body), and 2) those with major and trace element and isotopic compositions resulting from pre- and syn-eruptive mixing i.e. eruption of multiple magma bodies. They interpreted type 1 zonation as a function of long residence in a stable magma chamber. Homogeneous or weakly zoned ignimbrites from central TVZ (e.g. Taupo; Sutton et al., 1995 and Kaingaroa; Beresford and Cole, 2000) may have been erupted during periods of high rate of extension and high heat flow, which may have promoted strong convection in magma chambers, so preventing magma zonation (Briggs et al., 1993; Beresford, 1997). Whakamaru Ignimbrite, although sourced from a caldera that straddles the present day Taupo Fault Belt, was erupted following a quiescent period in TVZ activity (Houghton et al., 1995). Beresford (1997) suggested that it was this period of tectonic and volcanic stability that both allowed the large volume of magma to accumulate and to fractionate to the extent it did. This may be so, but the same argument does not hold for Mamaku Ignimbrite.

Mamaku Ignimbrite is the youngest welded ignimbrite of TVZ. It was emplaced during an energetic phase of TVZ activity, in which eruption of Matahina, Pokai and Kaingaroa ignimbrites also occurred (Houghton et al., 1995). The combined volume of intra- and extra-caldera Mamaku Ignimbrite of c. 170-180 km^3 DRE is one of the more voluminous eruptions recorded in TVZ. However, Rotorua Caldera is located at the edge of the zone of active extension (Rowland and Sibson, 1999) and as such may have been less affected by extension than other volcanic centres. In this situation, the location may have allowed accumulation and fractionation of the magma in the way described.

7.3. Withdrawal of the Mamaku Ignimbrite magma.

In the basal tephra sequence only type 1 pumice has been identified. Pumice types 1 to 3 are found together in lMI and are present throughout the main ignimbrite sequence, while andesitic fragments are found only towards the top of uMI. No pumice of mixed composition has been found in Mamaku Ignimbrite, and the coincidence of the magma types at the same stratigraphic levels is considered to be due to simultaneous eruption of all silicic magma types.

Blake and Ivey (1986a, b) modelled magma withdrawal and eruption rates on the basis of buoyancy and viscosity forces acting in a zoned magma chamber. They considered that the style of zonation in an ignimbrite reflected the way in which the height of a withdrawal layer varied with time. Chaotic mixing of different pumice types in an ignimbrite suggested multiple vent sites were simultaneously tapping a range of magma compositions, coincident with minor collapse. Deep collapse of a caldera was more likely to result in withdrawal from a thin layer that progressively discharged deeper portions of the magma chamber so that different magma compositions were stratigraphically separated in the resultant deposit. But their models relate to simple eruptions from central or ring vents, and from a chamber of simple shape and zonation.

Any model of magma discharge from the Mamaku Ignimbrite chamber needs to account for:

1) Presence of only type 1 magma in the basal sequence.
2) Coexistence of pumice types 1, 2, and 3 throughout the ignimbrite.
3) Presence of andesitic blebs only in uMI.

The co-eruption of different magma compositions from zoned chamber may be accomplished in two ways:

1) By having withdrawal depth of the magma is greater than the collapse height of the caldera, resulting in discharge from a number of magma zones simultaneously (Blake and Ivey, 1986a,b).

2) By collapse of numerous caldera blocks, creating many conduits for the magma chamber and allowing withdrawal from various levels simultaneously.

Method 1 requires the collapse of a coherent plate, with eruption from its margins or a single central vent allowing magma extraction from discrete sites at the same depth. The second method is favoured here because of the likely collapse history of Rotorua Caldera (Milner et al., submitted) although both mechanisms may have contributed (Fig. 14). Rotorua Caldera is located at the edge of an area of active extension (Fig. 15) in which there are two fault sets striking dominantly NE-SW and a wider spaced set striking NW-SE (Cole, 1990; Rowland and Sibson, 1999). These fault sets broke the caldera floor in to numerous blocks that subsided to different levels (Fig. 14), and they provided numerous potential conduits for the magma to ascend and depending on the location at which the faults intersected the magma chamber, tapped a number of compositional levels (Fig. 14). The magnitude of caldera subsidence increases sequentially towards a main locus suggesting the highest point of the underlying magma chamber and the area of greatest magma withdrawal.

Absence of types 2 & 3 pumice in the basal sequence indicates that only type 1 magma was tapped in the early stages of the Mamaku Ignimbrite eruption. Withdrawal of support for the chamber roof initiated caldera collapse and resulted in the opening of numerous conduits, and allowing the simultaneous eruption of all magmas from multiple vents. The strong density interface between sill-like andesite and other magmas would impede the andesites withdrawal at this stage of the eruption (Blake and Ivey, 1986a). Only when full caldera collapse occurred, along with associated magma depressurisation, was the andesite magma destabilised enough to allow it to co-erupt with the rhyolitic magma. Thus, the presence of andesitic blebs in only uMI indicates downward migration of the zone of magma withdrawal, during the main period of caldera collapse.

7.4. Mode of emplacement of Mamaku Ignimbrite

Deposition of ignimbrites from pyroclastic density currents remains controversial. Two main schools of thought exist, with deposition from pyroclastic density currents occurring across a range between the end-members of *en masse* emplacement (Sparks,

1976; Walker, 1983), and progressive aggradation (Fisher, 1966; Branney and Kokelaar, 1992). It is likely that a spectrum of depositional regimes exists giving rise to the variety of deposits observed. The stratigraphy of an ignimbrite that was deposited *en masse* reflects the internal layering of its parent pyroclastic density current. Layering within an ignimbrite that progressively aggraded reflects temporal variations of density current conditions, with higher layers deposited later than those beneath (Branney and Kokelaar, 1992).

A mechanism for emplacement of Mamaku Ignimbrite needs to account for:

1) Basal sequences.
2) Presence of lithic lag breccias and lithic concentration zones at Rotorua Caldera rim that are in gradational contact with uMI.
3) Local presence of elutriation pipes in the ignimbrite near the caldera rim, indicating high fluidisation of the parent pyroclastic density current (Wilson, 1986).
4) Rip up clasts of Pokai Ignimbrite, and truncated lower layers.
5) Vertical variations in pumice and lithic clast abundances and size without sharp contacts or flow unit boundaries.
6) Development of layer 1-like deposits beneath lMI and within mMI (this study) and uMI (Morgan, 1986) at distal localities.

There are no extensive time breaks between beds of the basal sequence, and they have dissimilar physical characteristics signifying changes in eruption style. Some beds pinch and swell and, in places, truncate previously deposited beds indicating changes in current energy. Upper beds of the basal sequence were eroded during the arrival of lMI suggesting a change in eruptive and current energy.

If Mamaku Ignimbrite was deposited *en masse* the contact between uMI and the lithic lag breccias should signify a flow unit boundary. However the uMI matrix is continuous with that of the overlying lithic breccia, which therefore must be regarded as a proximal upper facies of uMI, and not a deposit from a separate pyroclastic flow.

Variations in content and size of pumice and lithic clasts through Mamaku Ignimbrite are gradational and there are no distinct flow unit boundaries. If lMI were emplaced *en masse*, a basal layer (layer 2a) would be normal, but a 2a-like layer has been seen at only one, relatively distal, locality and is interpreted as deposited from a high particle concentration density current.

Crystal-rich layers present at distal localities (Morgan, 1986; this study) are similar to ground surge (layer 1) deposits described in *en masse* deposits, but in the Mamaku Ignimbrite are not seen in medial or proximal locations where extensive logs have been made. It is likely that, as with most pyroclastic density currents, the Mamaku pyroclastic density current became increasingly deflated as it progressed further from source until, in distal areas, it was moving in a dominantly non-particulate manner. Air may still have been ingested at the front and layer 1-like deposits formed (similar to Druitt's (1998) description for emplacement of a high aspect ratio ignimbrite). Crystal-rich lenses are present within mMI at distal localities (Morgan, 1986; this study) and probably represent a temporary changes in flow direction of the pyroclastic current. This is further evidence against *en masse* emplacement of Mamaku Ignimbrite.

The vertical variations are too complex to be deposited from a laminarly moving pyroclastic density current that stopped entirely *en masse*. Vertical variations in content and size pumice and lithic clasts, and erosion of earlier deposited beds are consistent with deposition from a pyroclastic density current of variable energy. Features close to source illustrate high flow energy. Stratigraphic variation further from source indicates deflation of the pyroclastic density current. Mamaku Ignimbrite is thus interpreted as deposited from an unsteady pyroclastic density current that became less particulate as it moved away from source.

8. Conclusions

There are three main types of pumice within the Mamaku Ignimbrite that range from dacite to high-silica rhyolite, and they occur throughout the deposit. The different pumice types indicate Mamaku Ignimbrite erupted from a gradationally zoned magma chamber. Andesitic fragments are found only in uMI, and are considered derived from a sill-like body that injected non-vigorously into the silicic chamber accumulating at the

base of type 3 magma. Its presence only in uMI reflects the density contrast between it and the more silicic magma, which inhibited its withdrawal till late in the eruption. When selected trace elements are compared to pumice chemistry of other TVZ ignimbrites, Mamaku Ignimbrite shows a wide range of compositional values consistent with a zoned magma chamber.

Mamaku Ignimbrite may be divided into upper, middle and lower ignimbrite based on variations in crystal content, welding, and amount of vapour phase alteration. The first eruption phase was phreatomagmatic, later becoming magmatic. Gradational boundaries between lower and middle, and middle and upper ignimbrite facies, and internal variations within the each facies and in the basal sequence suggest progressive aggradation from a sustained pyroclastic density current. Mamaku Ignimbrite was sourced from Rotorua Caldera during a single eruptive episode and deposited progressively from an unsteady pyroclastic density current that became less particulate as distance travelled increased.

Mamaku Ignimbrite is a good example of an ignimbrite derived from a compositionally zoned magma chamber that accumulated and fractionated during a period of intense volcanic activity in TVZ. Caldera collapse was initiated after the eruption of the basal sequence and continued throughout the eruption of Mamaku Ignimbrite. Caldera-related faults facilitated simultaneous withdrawal of magma from different depths, so that different types of pumice now coexist throughout the ignimbrite. During a later stage of the eruption, collapse and depressurisation of the magma chamber overcame the density contrast between a sill-like body of andesitic magma at the base of the chamber and overlying rhyo-dacite magma, allowing the different magmas to co-erupt.

Acknowledgements

This work is the result of a PhD study by DMM who was funded through a University of Canterbury Doctoral Scholarship and the Mason Trust, both are gratefully acknowledged. DMM is deeply indebted to Will Esler and Ash Cody, both of Rotorua, for help in the field. Carter Holt Harvey Ltd and Fletcher Forests are both thanked for allowing access to the field area. Thank you also to the technical staff at the Department of Geological Sciences, University of Canterbury. Reviews by Dr S.W. Beresford and S.C. Hildyard, and discussions with Prof. S.D. Weaver greatly improved the manuscript. Thanks are also due to Dr Mitsuhiro Nakagawa of Hokkaido University, Japan who provided samples, locations and analyses of Ohakuri Ignimbrite pumice.

References

Beresford, S.W., 1997, Volcanology and Geochemistry of the Kaingaroa Ignimbrite, Taupo Volcanic Zone, New Zealand. PhD thesis Canterbury Univ. Christchurch, New Zealand.

Beresford, S.W., Cole, J.W., 2000, Kaingaroa Ignimbrite, Taupo Volcanic Zone, New Zealand: evidence for asymmetric caldera subsidence of the Reporoa Caldera. NZ J.Geol.Geophys. 43, 471-481.

Berryman, K., Beanland, S., Wesnousky, S., 1998, Paleoseismicity of the Rotoitipakau Fault Zone, a complex normal fault in the Taupo Volcanic Zone, New Zealand. NZ J.Geol.Geophys. 41, 449-465.

Black, T.M., Shane, P.A.R., Westgate, J.A., Froggatt, P.C., 1996, Chronology and palaeomagnetic constraints on widespread welded ignimbrites of the Taupo volcanic zone, New Zealand. Bull. Volcanol. 58, 226-238.

Blake, S., Ivey, G.N., 1986a, Magma-Mixing and the dynamics of withdrawal from stratified reservoirs. J. Volcanol. Geotherm. Res. 27, 153-178.

Blake S., Ivey, G.N., 1986b, Density and viscosity gradients in zoned magma chambers, and their influence on withdrawal dynamics. J. Volcanol. Geotherm. Res. 30, 201-230.

Branney, M.J., Kokelaar, B.P., 1992, A reappraisal of ignimbrite emplacement: progressive aggradation and changes from particulate to non-particulate flow during emplacement of high-grade ignimbrite. Bull. Volcanol. 54, 504-520.

Briggs, R.M., Gifford, M.G., Moyle, A.R., Taylor, S.R., Norman, M.D., Houghton B.F., Wilson C.J.N., 1993, Geochemical zoning and eruptive mixing in ignimbrites from Mangakino volcano, Taupo Volcanic Zone, New Zealand. J. Volcanol. Geotherm. Res. 56, 175-203.

Briggs, R.M., Hall, G.J., Harmsworth, G.R.., Hollis, A.G., Houghton, B.F., Hughes, G.R., Morgan, M.D., Whitbread-Edwards, A.R., 1996, Geology of the Tauranga Area. Occasional Report, No. 22, Department of Earth Sciences, Waikato Univ. Hamilton, New Zealand. 56p.

Brown, S.J.A., Wilson C.J.N., Cole, J.W., Wooden, J., 1998, The Whakamaru group ignimbrites: evidence for reverse tapping of a zoned silicic magmatic system. J. Volcanol. Geotherm. Res. 84, 1-37.

Cambray, F.W., Vogel, T.A., Mills, J.G. jr, 1995 Origin of compositional heterogeneities in tuffs of the Timber MountainGroup: the relationship between magma batches and magma transfer and emplacement in an extensional environment. J. Geophys. Res. 100, 15793-15805.

Carr, R.G., 1981, A scanning electron microscope study of post-depositional changes in the Matahina Ignimbrite, North Island, New Zealand. NZ J.Geol.Geophys. 24, 429-434.

Civetta, L., Orsi, G., Pappalardo, L., Fisher, R.V., Heiken, G., Ort, M., 1997, Geochemical zoning, mingling, eruptive dynamics and depositional processes – the Campanian Ignimbrite, Campi Flegrei caldera, Italy. J. Volcanol. Geotherm. Res. 75, 183-219.

Cole, J.W., 1990, Structural control and origin of volcanism in the Taupo volcanic zone, New Zealand. Bull. Volcanol. 52, 445-459.

Crook, C.N., Hannah, J., 1988, Regional horizontal deformation associated with the March 2, 1987, Edgecumbe earthquake, New Zealand. Geophys. Res. Lett. 14, 361-364.

Darby, D.J., Hodgkinson, K.M., Blick, G.M., 2000, Geodetic measurement of deformation in the Taupo Volcanic Zone, New Zealand: the north Taupo network revisited. NZ J.Geol.Geophys. 43, 157-170.

Druitt, T.H., 1998, Pyroclastic density currents. In J.S. Gilbert and R.S.J. Sparks (Editors). The Physics of Explosive Volcanic Eruptions. Geol. Soc. London, Spec. Publ. 145, 145-182.

Fisher, R.V., 1966, Mechanism of deposition from pyroclastic flows. Am. J. Sci. 264, 350-363.

Fransen, P.J.B., 1982, Geology of of the western Mamaku Plateau and variations in the Mamaku Ignimbrite. M.Sc. thesis Waikato Univ. Hamilton, New Zealand.

Herrero-Bervera E., Helsley C.E., Sarna-Wojcicki A..M., Lajoie K.R., Meyer, C.E., McWilliams, M.O., Negrini R.M., Turrin, B.D., Donnelly-Nolan, J.M.,. Liddicoat, J.C, 1994, Age and correlation of a paleomagnetic episode in the western United States by $^{40}Ar/^{39}Ar$ dating and tephrochronology: the Jamaica, Blake or a new polarity episode? J. Geophys. Res. 99, 24091-24103.

Hervig, R.L., Dunbar, N.W., 1992, Cause of chemical zoning in the Bishop (California) and Bandelier (New Mexico) magma chambers. Earth Planet. Sci. Lett. 111, 97-108.

Hildreth, W., 1979, The Bishop Tuff: evidence for the origin of compositional zonation in silicic chambers. Geol. Soc. Am. Spec. Pap. 180, 43-75.

Hildreth, W., 1981, Gradients in silicic magma chambers: Implications for silicic magmatism. J. Geophys. Res. 86, 10153-10192.

Houghton, B.F., Wilson, C.J.N., McWilliams, M.O., Lanphere, M.A., Weaver, S.D., Briggs, R.M. Pringle, M.S., 1995, Chronology and Dynamics of a large silicic magmatic system: Central Taupo Volcanic Zone, New Zealand. Geology 23, 13-16.

Lamarche, G., 1992, Seismic reflection survey in the geothermal field of the Rotorua Caldera, New Zealand. Geothermics 21, 109-120.

McPhie, J., Doyle, M., Allen, R., 1993, *Volcanic Textures: A guide to the interpretation of textures in volcanic rocks.* Tasmanian Government Printing Office, Hobart (Publ.). 198p.

Milner, D.M., Cole, J.W., Wood, C.P., submitted, Asymmetric, multiple-block collapse at Rotorua Caldera, Taupo Volcanic Zone, New Zealand. Bull. Volcanol.

Morgan, M.D., 1986, Geology of the northern Mamaku Plateau. MSc thesis Waikato Univ. Hamilton, New Zealand.

Murphy, R.P. Seward, D., 1981, Stratigraphy, lithology, paleomagnetism and fission track ages of some ignimbrite formations in the Matahana basin. NZ J.Geol.Geophys. 24, 325-331.

Nathan, S., 1975, Notes on the petrology of the Mamaku Ignimbrite and associated rocks. Unpublished report. New Zealand Geological Survey, Rotorua.

Orsi, G., Civetta, L., D'Antonio, M., Di Girolamo, P., Piochi, M., 1995, Step-filling and development of a three-layer magma chamber: the Neapolitan Yellow Tuff case history. J. Volcanol. Geotherm. Res. 67, 291-312.

Rogan, M, 1982, A geophysical study of the Taupo Volcanic Zone, New Zealand. J. Geophys. Res. 87, 4073-4088.

Rowland, J.V., Sibson, R.H., 1999, Extensional kinematics of the Ruaumoko rift system: Variable soft-linkage between offset spreading segments in the Taupo Volcanic Zone, New Zealand. Geol. Soc. NZ Misc. publ. 107A, 141.

Shane, P., Black, T., Westgate, J., 1994, Isothermal plateau fission track age for the paleomagnetic excursion in the Mamaku Ignimbrite, New Zealand, and implications for late Quaternary stratigraphy. Geophys. Res. Let. 21, 1695-1698.

Sissons, B.A., 1979, The horizontal kinematics of the North Island of New Zealand. Ph. D. thesis, Victoria Univ. of Wellington, Wellington, New Zealand.

Sparks, R.S.J., 1976, Grain size variations in ignimbrites and implications for the transport of pyroclastic flows. Sedimentology 23, 147-188.

Sparks, R.S.J., Self, S., Walker, G.P.L., 1973, Products of Ignimbrite Eruptions. Geol. 1, 115-118.

Streck, M.J., Grunder, A.L., 1995, Crystallization and welding variations in a widespread ignimbrite sheet; the Rattlesnake Tuff, eastern Oregon, USA. Bull. Volcanol. 57, 151-169.

Sutton, A.N., Blake, S., Wilson, C.J.N., 1995, An outline geochemistry of rhyolite eruptives from Taupo volcanic centre, New Zealand. J. Volcanol. Geotherm. Res. 68, 153-175.

Tanaka, H., Turner, G.M., Houghton, B.F., Tachibana, T., Kono, M.. McWilliams, M.O, 1996, Palaeomagnetism and chronology of the central Taupo Volcanic Zone, New Zealand. Geophys. J. 124, 1-16.

Thompson, B.N., 1958, Kaituna River Hydro Development. Geological Report on Te Akau, Te Tuararoa, and Pakotore schemes. Unpublished Report, New Zealand Geological Survey, Rotorua.

Walcott R.I., 1987, Geodetic strain and the deformational history of the North Island of New Zealand during the late Cainozoic. Philos. Trans. R. Soc. London Ser. A, 321 163-181.

Walker, G.P.L., 1983 Grain-size characteristics of pyroclastic deposits. Journal of Geology, v79, p696-714.

Walker, G.P.L., 1985, Origin of coarse lithic breccias near ignimbrite source vents. J. Volcanol. Geotherm. Res. 25, 157-171.

Wilson, C.J.N., 1986, Pyroclastic flows and ignimbrites. Sci. Prog. (Oxford) 70, 171-207.

Wilson, C.J.N., Houghton B.F., McWilliams, M.O., Lanphere, M.A., Weaver, S.D., Briggs, R.M., 1995, Volcanic and structural evolution of Taupo Volcanic Zone: a review. J. Volcanol. Geotherm. Res. 68, 1-28.

Wolff, J.A., Worner, G., Blake, S., 1990, Gradients in physical parameters in zoned felsic magma bodies: implications for evolution and eruptive withdrawal. J. Volcanol. Geotherm. Res. 43, 37-55.

Wood, C.P., 1985, Geology of Mamaku water supply Drillhole. Unpublished Report New Zealand Geological Survey, Rotorua, New Zealand.

Wood, C.P., 1992, Geology of the Rotorua geothermal system. Geothermics 21, 25-41.

Wright, J.V., Walker, G.P.L., 1977, The ignimbrite source problem: Significance of a co-ignimbrite lag-fall deposit. Geology, v5, p729-732.

List of figures

Fig. 1. Current outcrop distribution of Mamaku Ignimbrite, location of study area, and locations mentioned in the text. Inset A: TVZ can be split into 3 segments, northern and southern andesite dominated segments (A) and a central rhyolite dominated segment (R) (Houghton et al., 1995). Inset B: Rotorua Caldera is situated in the northern part of the central segment. Outcrop of Mamaku Ignimbrite forms a fan north, northwest and southwest of Rotorua capping the Mamaku-Kaimai Plateau.

Fig. 2. Distribution of Mamaku Ignimbrite: Present outcrop (shaded), probable extent (dotted), and possible extent (dashed). Ignimbrite area and volume are discussed in the text.

Fig. 3. Stratigraphy of Mamaku Ignimbrite at the type section. Density and crystal content increase markedly in middle ignimbrite. Jointing starts in middle ignimbrite and gradually stops in the upper ignimbrite. Pumice compacts forming fiamme in middle ignimbrite. Open shapes are pumice, black triangles are lithics, and black spots are crystals.

Fig. 4. Graphic log of the basal sequence (A-N) at Pukerimu Road.

Fig. 5. Maximum lithic (ML) isopleths (in mm) for upper Mamaku Ignimbrite. Isopleths centre on the area southwest of Lake Rotorua, the inferred source of the ignimbrite. Contours are in mm.

Fig. 6. Maximum lithic size vs distance from Rotorua Caldera rim. Lithic size clearly decreases away from the rim of Rotorua Caldera.

Fig. 7. Pyroxene compositions for pumice types 1 (A), 2 (B), and 3 (C). The rims of pyroxene phenocrysts generally get more En rich from type 3 to type 1 pumice.

Fig. 8. A) Total alkali silica diagram (after Le Maitre, 1989) of lMI pumice, and andesitic blebs from uMI, pumice ranges from dacite to high silica rhyolite. B) Rb/Sr vs silica clearly separates the pumice types 1, 2, and 3. All major values have been recalculated anhydrous.

Fig. 9. Selected trace and major element harker diagrams. Types 1, 2 and 3 pumice lie on the same trends.

Fig. 10. Trace element spider plots for lMI pumice and andesitic clasts normalised by primitive mantle composition. Pumice types 1, 2, and 3 follow the same normalised path suggesting they are consanguineous. The andesitic juvenile fragment is notably depleted in Th, La and Ce compared to lMI pumice and has a trace element pattern discordant to lMI pumice types. This suggests that the andesite clasts are not related genetically to Mamaku Ignimbrite pumice. (Primitive mantle values from Sun and McDonough, 1989).

Fig. 11. Vector modelling of Raleigh fractionation of a type 3 parent magma. The trace element distribution of type 1 and 2 pumice can be achieved by 20% fractionation of orthopyroxene and plagioclase from a type 3 parent. Distribution coefficients are from Arth (1976) and Nash and Crecraft (1985), as quoted by Rollinson (1993).

Fig. 12. Schematic model of the Mamaku magma system.

Fig. 13. Comparison of Mamaku Ignimbrite pumice with other ignimbrites of TVZ. Mamaku Ignimbrite pumice lie on distinct fractionation trends similar to other ignimbrites. The range of Rb-Sr (A), and Zn-Zr (B) compositions for Mamaku pumice are large for Mamaku pumice, comparable only with Rb-Sr range of Whakamaru Ignimbrite, and Zn-Zr values of Ohakuri, and Marshall Ignimbrites. The large ranges suggest the Mamaku magma reservoir was zoned to a higher degree than most TVZ ignimbrites. TVZ ignimbrite data taken from B.F. Houghton and S.D. Weaver (unpublished data), Briggs et al., (1993), Brown (1994), and Sutton et al. (1995) as outlined in Brown (1994).

Fig. 14. The pattern of magma withdrawal from the Mamaku chamber. A) The initial phase involved eruption of only type 1 magma. B) As the eruption proceeded caldera collapse began and caused eruption from deeper levels in the magma chamber allowing mingling of type 1, 2 and 3 magmas. C) Late in the eruption caldera collapse and further depressurisation forced withdrawal of andesitic magma by causing withdrawal dynamics to overcome the inertial and buoyancy forces acting to keep it in place.

Fig. 15. Map of TVZ showing the prevalence of NE-SW striking structures. NW-SE striking structures are rarely identified at the surface. Rotorua Caldera is located towards the edge of the main axis of rifting in TVZ. This probably allows NW-SE striking structures to have a greater influence on the caldera morphology. Solid lines are faults. Modified from Berryman et al. (1998).

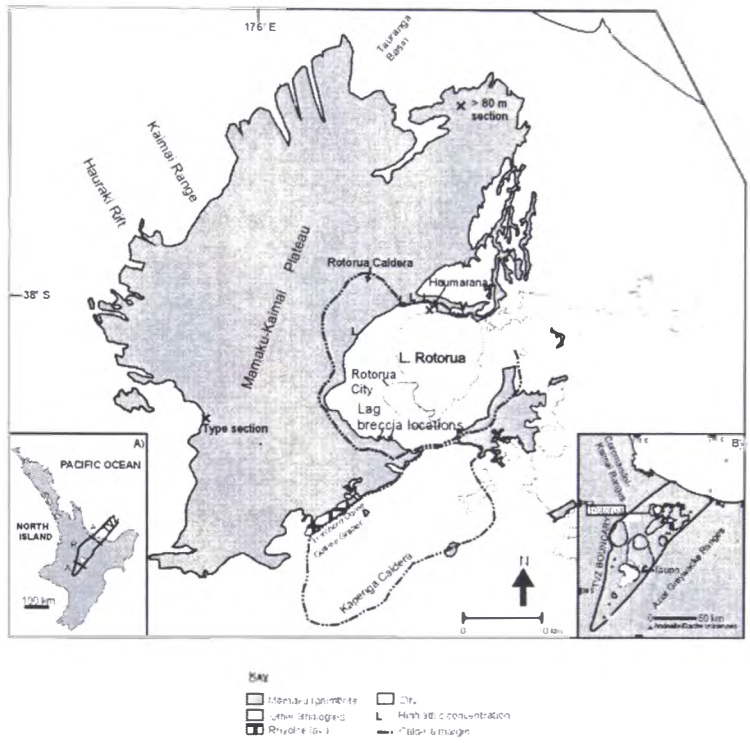

Fig.1. Milner et al.

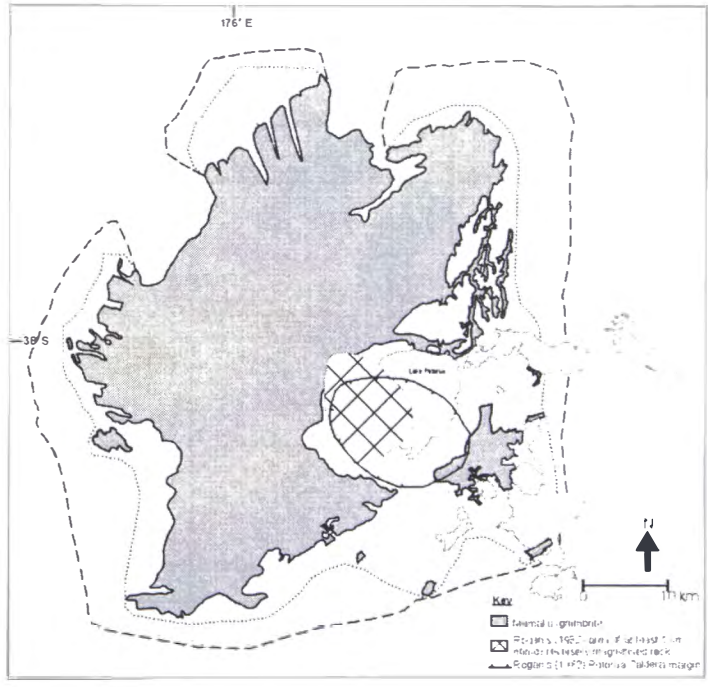

Fig. 2. Milner et al.

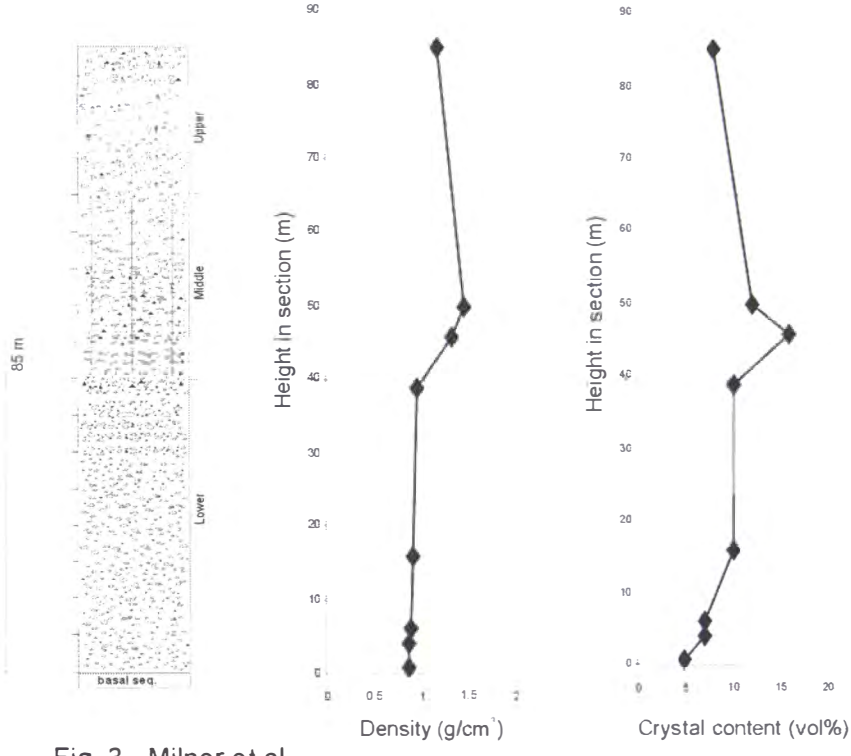

Fig. 3. Milner et al.

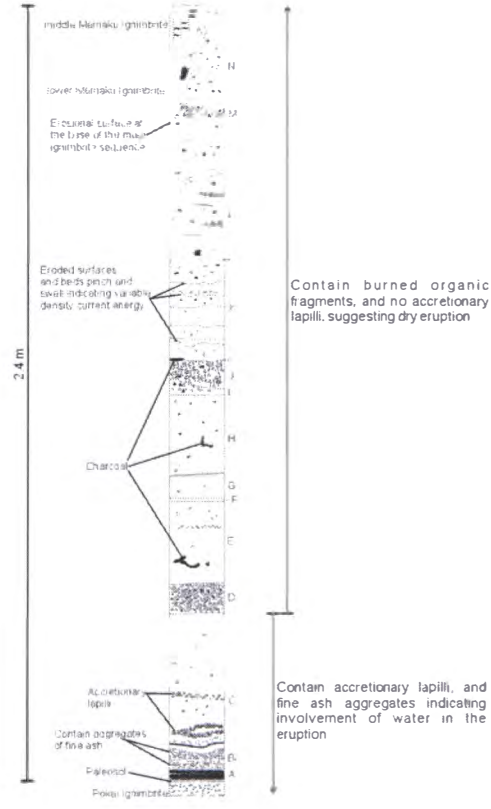

Fig. 4. Milner et al.

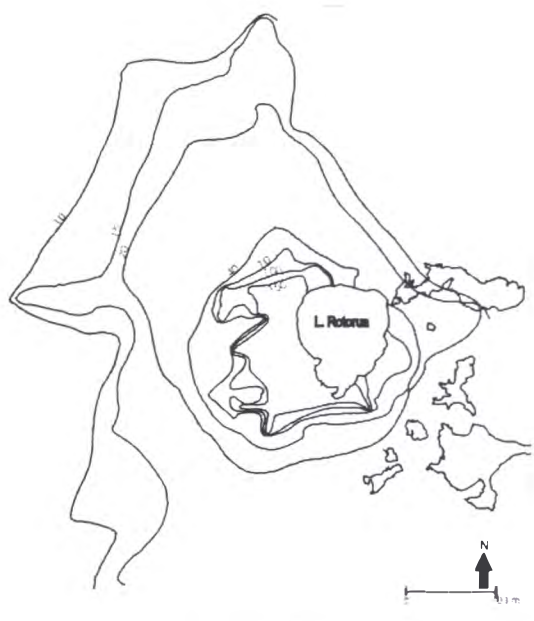

Fig. 5. Milner et al.

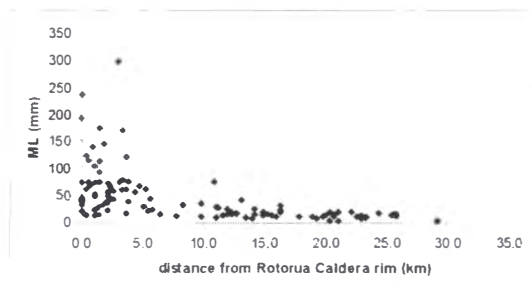

Fig. 6. Milner et al.

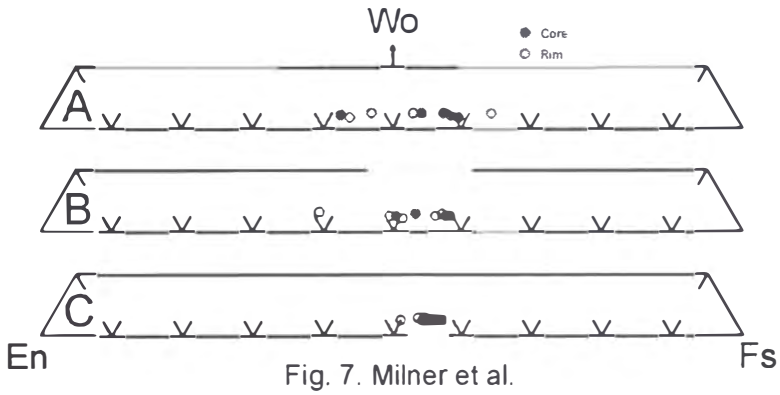

Fig. 7. Milner et al.

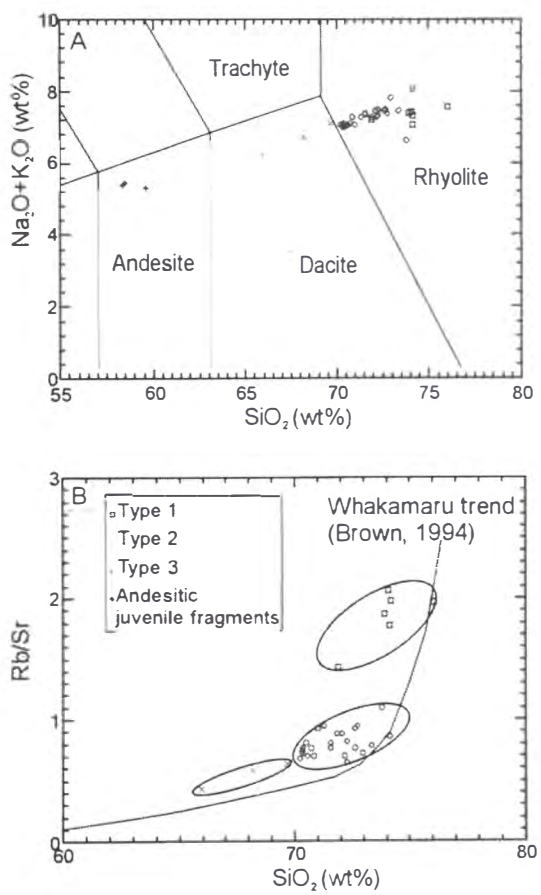

Fig. 8. Milner et al.

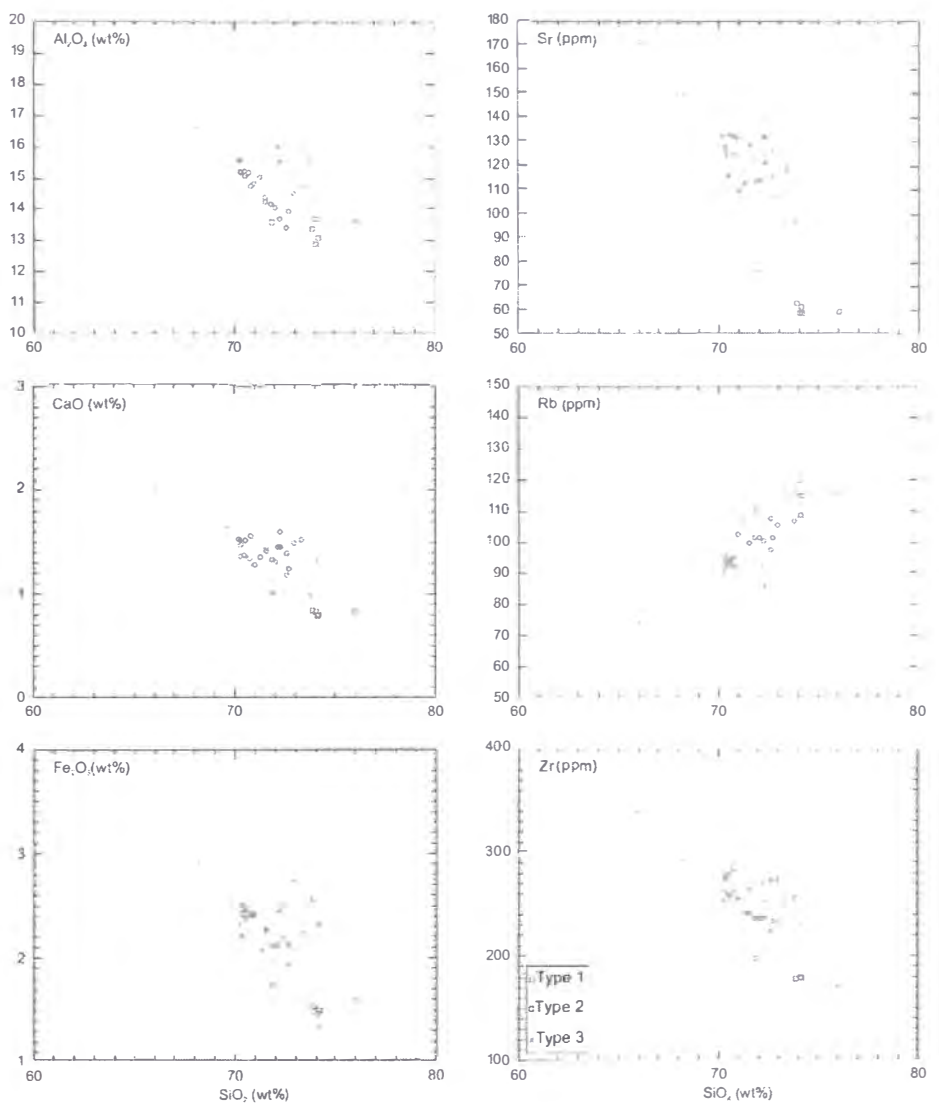

Fig. 9. Milner et al.

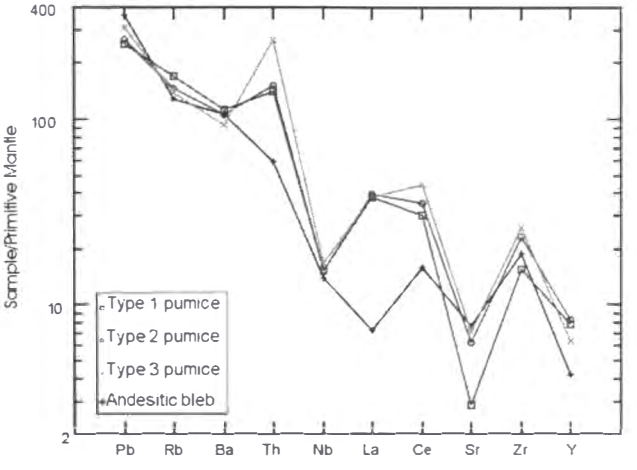

Fig. 10. Milner et al.

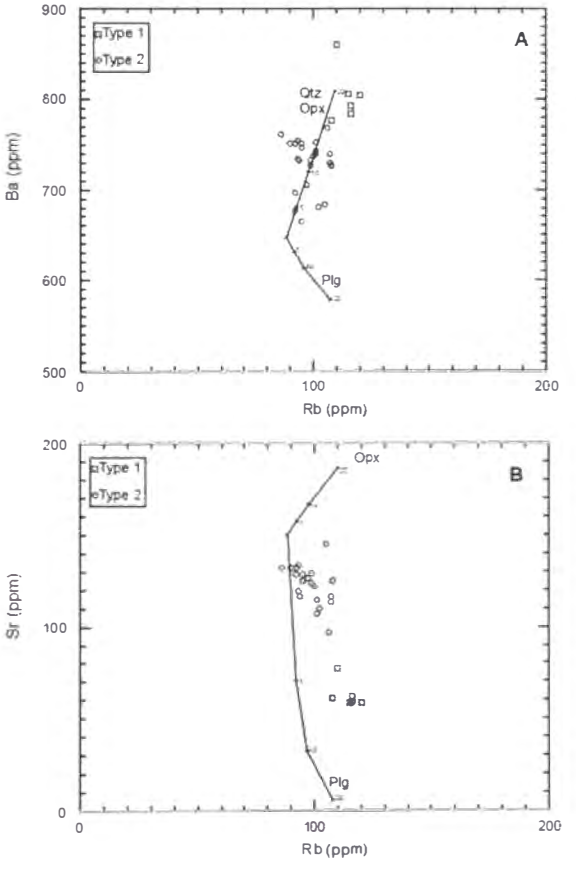

Fig. 11. Milner et al.

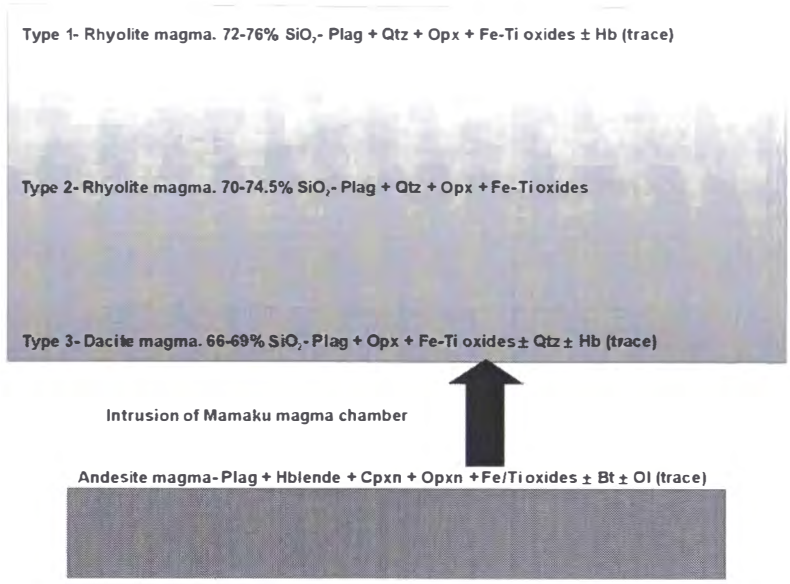

Fig. 12. Milner et al.

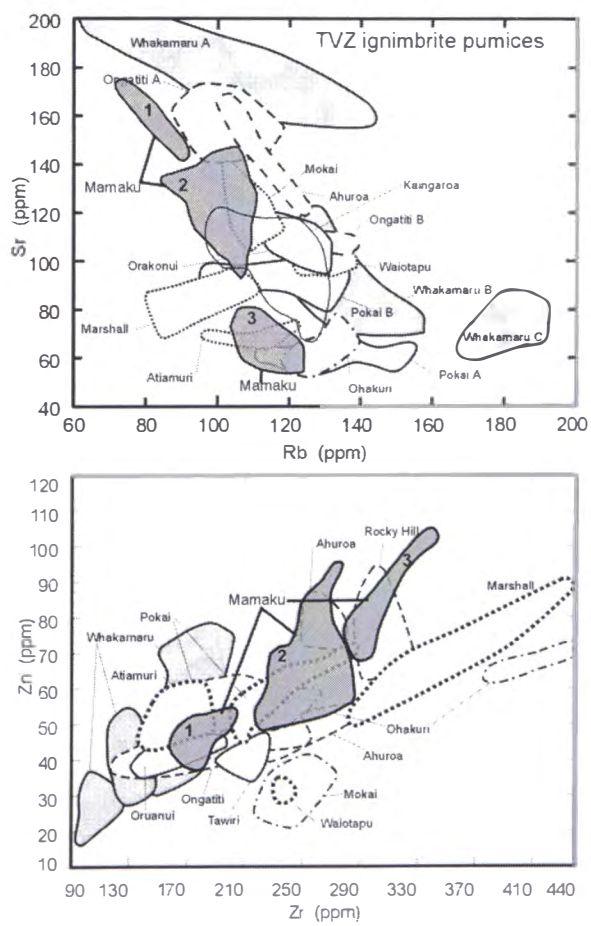

Fig. 13. Milner et al.

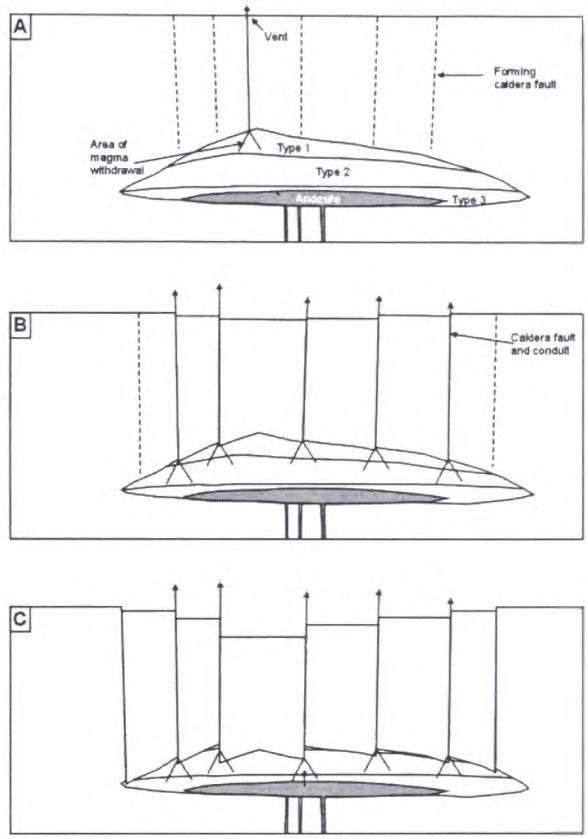

Fig. 14. Milner et al.

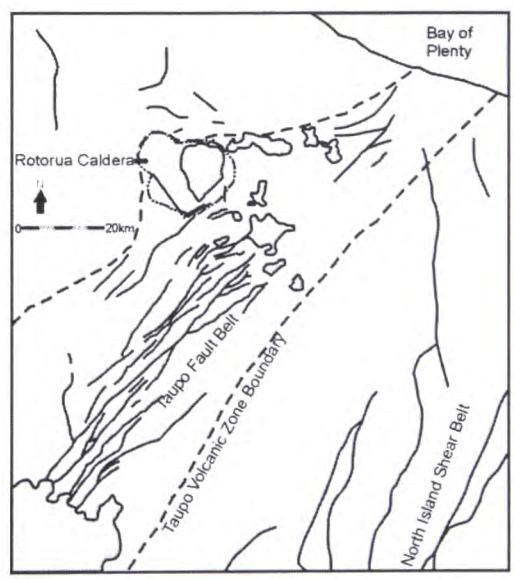

Fig. 15. Milner et al.